

**WESTERN SYDNEY**  
UNIVERSITY



---

The Radio Continuum Emission of Star  
Forming Galaxies at Low to High  
Redshift

Timothy James Galvin

---

A thesis submitted for the degree of  
Doctor of Philosophy  
at  
Western Sydney University

October 2019

Supervisors:  
Miroslav Filipović  
Nick Seymour  
Nick Tohill  
Josh Marvil

# Dedication

I want to dedicate this thesis to my Mum, Dad, Sam, Hannah, and Nanny Bet. They have given me nothing but love and support throughout my life. I hope this dedication is sufficient in return.

I was unable finish this in time for Nanny Bet to see it, but I know she would have been proud. I am also comfortable knowing that she probably would not have read it anyway. Rest easy!

# Acknowledgements

## Personal Acknowledgements

First and foremost, I would like to thank my supervisors Nick Seymour, Miroslav Filipović, Nick Tothil, and Josh Marvil, who worked with me over the past five years. Each of them has suffered countless conversations and endured my, admittedly tiresome, questions and remarks.

Nick Seymour especially invested countless hours helping me attain this point. When I started this project, I still considered myself a computing specialist, and I vividly remember getting confused over a luminosity function. I feel like it would be a disservice to him without making special mention of the time he has devoted to this work and all the effort he has made to make me a complete scientist.

Miroslav Filipović has been a fantastic primary supervisor who has helped me grow as a student. I want to thank him, especially for all the time, energy, and copious amounts of coffee he has invested in me.

Richard McDermid from Macquarie University was also a critical resource throughout my candidature. He commented on a number of proposals I had written and allowed me to ‘trojan horse’ them into the appropriate telescopic assignment committees. Without him, I would not have been able to operate the WIFES telescope, and there would not have been a Chapter 4! He invested a significant portion of his time and energy, helping me throughout this project, and his mentorship is deeply appreciated.

Academics Evan Crawford, Ain De Horta, Laurence Park, and Ray Norris were all kind enough to help answer questions and give advice when asked, and I would like to thank them for their help. At one point or another, each of them has helped me work through a problem I had been stuck on, and without them, I would surely be years behind where I am now.

I want to thank my fellow students in Y.2.30, including Andrew O’Brien, Jordan Collier, Kevin Grieve, Miranda Yew, Nicholas Ralph, Kieran Luken, and Greame Wong, who put up with me and my annoying antics. A lot of great memories have been made in that laboratory.

I also acknowledge Western Sydney University for the workspace and resources. In particular the technical and administration staff at the School of Computing Engineering and

Mathematics, including Rocky O’Leary, David Minard, Bruce Kneale, and Susan Henley.

As a sufferer of Choroideremia, I would like to acknowledge and thank the Choroideremia Research Foundation and all those who are associated with their efforts. Throughout my candidature, I have lost a fair amount of vision, mobility, and independence. Without the amazing advances the foundation has funded, I would have given up astronomy long ago. Special thanks go to Cory McDonald, Eric Hartman, John Oster, Beth Foss, Randy Wheelock, and Jeff Benelli, all of whom gave up their time and efforts to drive a search for a cure and inspired me not to give up.

### **Scientific Acknowledgements**

The Australia Telescope National Facility, being the group that manages the Australia Telescope Compact Array, deserves recognition for offering the Australia premier instruments under an open skies policy. I want to thank them for allowing me to design and conduct my experiments with complete support from them and their facilities.

The Australia Telescope Compact Array is part of the Australia Telescope National Facility which is funded by the Australian Government for operation as a National Facility managed by CSIRO.

This thesis includes archived data obtained through the Australia Telescope Online Archive (<http://atoa.atnf.csiro.au>). This scientific work makes use of the Murchison Radio-astronomy Observatory, operated by CSIRO. We acknowledge the Wajarri Yamatji people as the traditional owners of the Observatory site. Support for the operation of the Murchison Widefield Array (MWA) was provided by the Australian Government (NCRIS), under a contract to Curtin University administered by Astronomy Australia Limited. We acknowledge the Pawsey Supercomputing Centre which is supported by the Western Australian and Australian Governments.

This research has made use of the NASA/IPAC Extragalactic Database (NED) which is operated by the Jet Propulsion Laboratory, California Institute of Technology, under contract with the National Aeronautics and Space Administration.



# Contents

<b>List of Tables</b>	<b>v</b>
<b>List of Figures</b>	<b>vi</b>
<b>Abstract</b>	<b>ix</b>
<b>List of Abbreviations</b>	<b>xii</b>
<b>1 Introduction</b>	<b>1</b>
1.1 Star Formation History of the Universe . . . . .	1
1.2 Tracers of Star Formation . . . . .	2
1.2.1 Ultraviolet Continuum . . . . .	4
1.2.2 Optical Recombination and Forbidden Lines . . . . .	5
1.2.3 Radio Recombination Lines . . . . .	9
1.2.4 Infrared . . . . .	10
1.2.5 Composite Tracers of Star Formation . . . . .	13
1.2.6 Radio Continuum . . . . .	14
1.3 The Far-Infrared to Radio Correlation . . . . .	19
1.4 This Dissertation . . . . .	23
1.4.1 Overview . . . . .	23
1.4.2 Challenges in this Thesis . . . . .	26
1.4.3 Significance of this Work . . . . .	27
<b>2 Radio-Continuum Emission of Ultra-Luminous Galaxies</b>	<b>29</b>
2.1 Motivation . . . . .	29
2.2 Introduction . . . . .	31
2.3 Sample Selection . . . . .	32
2.4 ATCA data reduction . . . . .	33
2.5 The Far-IR to Radio Correlation . . . . .	38

2.5.1	Sources in Literature . . . . .	41
2.6	SED Modelling . . . . .	42
2.6.1	Emission Models . . . . .	43
2.6.1.1	Radio-Continuum . . . . .	43
2.6.1.2	Infrared . . . . .	43
2.6.1.3	SED Fitting . . . . .	44
2.7	Results . . . . .	49
2.7.1	SED Fits . . . . .	49
2.7.2	Comparison to Yun et al. (2001) sample . . . . .	50
2.7.3	Decomposed Radio to Far-IR . . . . .	52
2.7.3.1	Thermal Fraction . . . . .	52
2.7.4	Thermal and Non-Thermal Correlation with Far-IR . . . . .	54
2.7.5	Thermal Fraction and $q$ . . . . .	56
2.8	Discussion . . . . .	58
2.8.1	Object Selection . . . . .	58
2.8.2	Thermal Fraction, $q$ , and timescales . . . . .	59
2.8.3	Correlation of Decomposed Radio Luminosities . . . . .	64
2.9	Conclusions . . . . .	65
<b>3</b>	<b>Radio-Continuum Emission of Luminous Infrared Galaxies</b>	<b>66</b>
3.1	Motivation . . . . .	66
3.2	Introduction . . . . .	67
3.3	Data . . . . .	69
3.3.1	Source Selection . . . . .	69
3.3.2	ATCA Observations . . . . .	69
3.3.3	MWA . . . . .	72
3.3.3.1	Detected Sources . . . . .	72
3.3.3.2	Non-detections . . . . .	73
3.3.4	Archived Radio-Continuum Data . . . . .	75
3.3.4.1	Other . . . . .	75
3.4	Data Reduction . . . . .	77
3.4.1	Radio-Continuum . . . . .	77
3.4.1.1	Centimetre ATCA Calibration . . . . .	77
3.4.1.2	Millimetre ATCA Calibration . . . . .	77
3.4.1.3	Imaging . . . . .	82
3.4.1.4	Resolving structure . . . . .	83

3.5	SED Modelling . . . . .	85
3.5.1	Radio-Continuum Models . . . . .	85
3.5.1.1	Power Law . . . . .	85
3.5.1.2	Composition of Synchrotron and Free-Free . . . . .	85
3.5.1.3	Composition of Synchrotron and Free-Free with Free-Free Ab- sorption . . . . .	85
3.5.1.4	Multiple Free-Free absorption components . . . . .	86
3.5.2	Far-Infrared Emission . . . . .	87
3.5.3	Radio-Continuum Fitting and Selection . . . . .	88
3.5.3.1	Model Fitting . . . . .	88
3.5.3.2	Model Priors . . . . .	90
3.5.3.3	Model Selection . . . . .	92
3.6	Results . . . . .	93
3.6.1	Model Results . . . . .	93
3.6.2	Thermal Fraction . . . . .	96
3.6.3	Spectral curvature and emission measures . . . . .	105
3.6.4	Far-infrared to radio correlation . . . . .	106
3.7	Discussion . . . . .	109
3.7.1	Spectral Curvature-Physical Origin? . . . . .	109
3.7.2	Effects of FFA on low frequency extrapolations . . . . .	111
3.7.3	Synchrotron Spectral Index . . . . .	116
3.8	Conclusion . . . . .	118
<b>4</b>	<b>Optical Spectroscopy Data of LIRGS</b>	<b>120</b>
4.1	Motivation . . . . .	120
4.2	Background . . . . .	121
4.3	Wide-Field Spectrograph . . . . .	123
4.4	Optical Spectroscopic Data . . . . .	124
4.4.1	Data Reduction . . . . .	125
4.4.1.1	PYWIFES operation . . . . .	125
4.4.2	Extracting 1D Spectra . . . . .	127
4.4.3	PPXF . . . . .	130
4.4.4	Constraining the stellar continuum and transitions . . . . .	136
4.4.5	Dust attenuation correction . . . . .	145
4.4.6	Reddening curve . . . . .	149
4.5	Three Dimensional Spectra . . . . .	151



4.5.1	IRAS F00198–7926 . . . . .	151
4.5.2	IRAS F02364–4751 - A weak source . . . . .	155
4.6	Conclusions . . . . .	157
<b>5</b>	<b>Relating the Radio Continuum to other Star Formation Indicators</b>	<b>160</b>
5.1	Motivation . . . . .	160
5.2	Initial H $\alpha$ SFR comparisons . . . . .	163
5.2.1	Comparing optical features to radio-continuum components . . . . .	166
5.3	Discussion . . . . .	172
5.3.1	Electron Temperature Variation . . . . .	176
5.3.2	Optical and radio-continuum features of IRAS F00198–7926 . . . . .	180
5.4	Conclusions . . . . .	183
<b>6</b>	<b>Conclusions and Future Work</b>	<b>185</b>
6.1	Future work . . . . .	193
	Bibliography . . . . .	199
<b>A</b>	<b>Submitted Papers</b>	<b>220</b>
A.1	NGC 7793 . . . . .	220
A.1.1	NGC 7793 Paper . . . . .	220
A.2	M31 . . . . .	230
A.2.1	M31 Paper . . . . .	230
<b>B</b>	<b>WIFES Supplementary Data and Figures</b>	<b>256</b>
B.1	PPXF modelled galaxy spectra . . . . .	256
B.2	Resolved Optical Modelling . . . . .	263
B.3	Resolved Dust Obscuration . . . . .	270
B.4	Resolved Star Formation Rate . . . . .	277
B.5	PYWIFES Flux Calibration Issue . . . . .	283

# List of Tables

1.1	Composite SFR measures from Kennicutt et al. (2009)	14
2.1	ULIRG sample	32
2.2	ATCA frequency modes	34
2.3	ATCA ULIRG flux densities	37
2.4	Measurements available from the literature	39
2.5	Constrained model parameters for SFG sources	49
2.6	Constrained model parameters for AGN sources	49
2.7	Constrained parameters for Greybody models	50
2.8	SFR factors	61
3.1	LIRG sample overview	70
3.2	LIRG sample observation overview	71
3.3	MWA measurements	74
3.4	Archived ATCA data overview	75
3.5	Measurements obtained from the literature	76
3.6	Luminous Infrared Galaxy ATCA measurements	84
3.7	Overview of the natural log of the Bayes odds ratio from MultiNest	91
3.8	Constrained model parameters for LIRGS	95
3.9	Derived Emission Measures	106
3.10	Infrared to decomposed radio-continuum correlation coefficients	109
4.1	Standard WiFeS gratings	123
4.2	Overview of WiFeS observations	124
4.3	Example stellar template	134
4.4	Overview of constrained Balmer Ratio and SFR characteristics	148
5.1	SFR corner plot fitting results	165

# List of Figures

1.1	SFH of the Universe . . . . .	2
1.2	Common IMFs . . . . .	4
1.3	H $\alpha$ transition . . . . .	6
1.4	Hydrogen radio recombination lines . . . . .	10
1.5	Synchrotron Emission . . . . .	15
1.6	Bremsstrahlung Radiation . . . . .	17
1.7	Assumed starburst radio continuum spectral energy distribution . . . . .	18
1.8	Far-infrared to radio correlation . . . . .	20
1.9	Evolution of the far-infrared to radio correlation . . . . .	23
2.1	Limit of conventional radio telescopes . . . . .	30
2.2	The ATCA telescope . . . . .	33
2.3	Typical $(u, v)$ -coverage of our sample. . . . .	35
2.4	Comparison between $L_{60\ \mu\text{m}}$ and $q$ . . . . .	40
2.5	SED for SFGs in sample 1 . . . . .	45
2.6	Spectral energy distribution for non-detections in sample 1 . . . . .	47
2.7	Spectral energy distribution for AGNs in sample 1 . . . . .	48
2.8	Comparison between sample 1 and Yun et al. (2001) . . . . .	51
2.9	A comparison between spectral index and thermal fraction . . . . .	53
2.10	Far infrared vs decomposed radio-continuum . . . . .	55
2.11	Comparison between $q$ and thermal fraction . . . . .	57
2.12	SFH template . . . . .	60
2.13	Emission diagnostics through time using the assumed SFH . . . . .	62
2.14	Comparison between $q$ and thermal fraction with timescale overlay . . . . .	63
3.1	MIRIAD data reduction strategy for ATCA CABB data . . . . .	78
3.2	Initial MFCAL of millimetre bandpass . . . . .	79
3.3	Spectral slope of PKS 1921–293 after applying flux scaling . . . . .	80

3.4	Final spectrum of bandpass calibrator PKS 1921–293 . . . . .	81
3.5	Walkers through steps . . . . .	89
3.6	Parameter corner plot . . . . .	93
3.7	Radio-Continuum SEDs of LIRGS . . . . .	97
3.8	Comparison between 60 $\mu\text{m}$ and 1.4 GHz luminosities for sample 2 . . . . .	102
3.9	60 $\mu\text{m}$ luminosity vs $q$ for sample 2 . . . . .	103
3.10	Total infrared luminosities against constrained thermal fractions . . . . .	104
3.11	Infrared against decomposed radio-continuum components . . . . .	107
3.12	Infrared luminosities against the suppression factor . . . . .	111
3.13	SEDs without low frequency FFA . . . . .	113
3.14	SFR vs $\alpha_{\text{Synchrotron}}$ . . . . .	117
4.1	ANU 2.3 m telescope . . . . .	123
4.2	WiFeS Observing Software . . . . .	124
4.3	H $\alpha$ continuum map . . . . .	127
4.4	Initial one-dimensional WiFeS spectra . . . . .	128
4.5	Relative Flux Calibration Consistency . . . . .	129
4.6	Consistent spectral features . . . . .	131
4.7	Example stellar template . . . . .	132
4.8	Example of generation of stellar line template . . . . .	135
4.9	F00198–7926 PPXF fit . . . . .	137
4.10	Zoomed F00198–7926 PPXF fit . . . . .	138
4.11	Broaden optical spectra of IRAS F01268–5436 . . . . .	139
4.12	Broadened H $\beta$ emission lines of IRAS F01268–5436 . . . . .	140
4.13	AGN stellar continuum templates . . . . .	141
4.14	F01268–5436 PPXF fit . . . . .	143
4.15	Zoomed F01268–5436 PPXF fit . . . . .	144
4.16	$E(B - V)_{\text{gas}}$ and $E(B - V)_{\text{star}}$ comparison . . . . .	150
4.17	Gas distribution in IRAS F00198–7923 . . . . .	152
4.18	H $\alpha$ /H $\beta$ ratio of IRAS F00198–7926 . . . . .	153
4.19	Resolved SFR map of IRAS F00198–7926 . . . . .	153
4.20	Resolved H $\alpha$ fluxes from binned spaxels of IRAS F00198–7926 . . . . .	155
4.21	Resolved H $\alpha$ fluxes from binned spaxels of IRAS F00198–7926 . . . . .	155
4.22	IRAS F02364–4751 resolved spectroscopy . . . . .	156
4.23	IRAS F02364–4751 H $\alpha$ /H $\beta$ map . . . . .	157
4.24	IRAS F02364–4751 SFR map . . . . .	158

5.1	SFR corner plot . . . . .	164
5.2	LTS fitting example . . . . .	168
5.3	H $\alpha$ to radio component comparison . . . . .	170
5.4	H $\alpha$ to radio component comparison without FFA . . . . .	171
5.5	Composite SFR to radio component comparison . . . . .	173
5.6	H $\alpha$ to radio component comparison with thermal fraction colour overlay . . . . .	174
5.7	Radio free-free emission against H $\beta$ with electron temperature overlay . . . . .	177
5.8	Effects of varying assumed H $\alpha$ /H $\beta$ on the dust correction factor . . . . .	179
5.9	Dust corrected H $\alpha$ luminosity for IRAS F00198–7926 . . . . .	181
5.10	Resolved dispersion map of IRAS F00198–7926 . . . . .	182
6.1	Far-Infrared to radio correlation at 34 GHz . . . . .	195
6.2	Image of the ECDFS at 8.5 GHz . . . . .	196
6.3	Source counts at 8.5 GHz of objects in the ECDFS . . . . .	197
B.1	Optical spectroscopic PPXF fits . . . . .	257
B.2	Resolved optical spectroscopic PPXF fits . . . . .	264
B.3	Resolved dust obscuration maps . . . . .	271
B.4	Resolved Star Formation Rate maps . . . . .	277
B.5	Early H $\alpha$ diagnostic plot . . . . .	284

# Abstract

In this thesis, the radio-continuum emission of starburst galaxies is explored to understand the physical processes that trace star formation. Separating and constraining these processes require a broad, densely sampled spectral energy distribution that can be used to apply and constrain various radiative transfer models.

Existing tracers of star formation include a suite of multi-wavelength diagnostics, including UV, optical, infrared, nebular transitions, and radio continuum. At present, optical and near-infrared observations have been the most successful at probing the high redshift volume and constraining the star formation at the earliest epochs of the Universe. However, such approaches are critically flawed in that they are subject to the effects of dust obscuration, requiring sophisticated methods to recover the intrinsic luminosities of the optical tracers of star formation. In the high redshift Universe, these corrections are increasingly compromised and uncertain.

Radio-continuum measurements of star formation have the potential to be the most reliable in this high redshift regime because they are not affected by the presence of dust, allowing observers to acquire *uncompromised* measures of star formation. At frequencies below  $\sim 2$  GHz, the radio continuum is made up overwhelmingly by non-thermal synchrotron emission, produced by near light speed cosmic rays interacting with the large-scale magnetic structure of a galaxy. Although this type of emission is not a direct product of stars, it has been reasonably well calibrated to exploit the far-infrared to radio correlation to obtain a measure of star formation.

Our current understanding of the far-infrared to radio correlation suggests that there should be an evolution as a function of redshifts; however, observationally evidence both confirms and rejects this evolution hypothesis. As the far-infrared to radio correlation is the foundation of star formation rate indicators based on the radio continuum for frequencies where synchrotron emission is a significant component of the observed spectrum, there is a requirement to investigate, and if necessary repair, radio-based star formation rate measures in preparation for radio telescopes like the Square Kilometer Array.

Throughout my candidature, I have studied the spectral energy distribution of 30 local galaxies that were selected based on their high star formation rates, as indicated by their radio

and infrared emission data collected from existing surveys. Across a broad frequency range spanning 80 MHz to 50 GHz, the underlying physical processes driving the radio continuum have been disentangled. By comparing these products to other multi-wavelength indicators of star formation, we can begin to understand the radio-based tracers for faint star forming galaxies at high redshift that the next generation of radio telescopes will reveal.

This work is divided into two main sections. The first section explores the radio continuum emission of an initial sample of ultra-luminous infrared galaxies at moderately high redshifts. These sources have similar star formation rates to those expected at high redshift. They represent an ideal proxy for which we can begin to develop updated star formation rate measures that are compatible in this new parameter space. Data obtained from the Australian Telescope Compact Array can characterise the spectral energy distribution from 1.1 to 10 GHz. Using its wide-band correlator, these data almost covered this entire frequency range.

Least-squares fitting methods were employed to describe this spectrum as a combination of synchrotron and free-free emission. I applied the same fitting approach to similar sources available in the literature across a wide range of infrared luminosities to assess how their components can be parameterised as a function of the far-infrared to radio correlation. However, given the physical distance and brightness of this primary set of ultra-luminous galaxies, the obtained flux density measurements had low significance.

The approach was then expanded into a second set of 19 objects. Densely sampled data were collected across 80 MHz to 50 GHz using a combination of radio telescopes. Given the broad frequency coverage of these sources, we found a significant curvature of the observed spectra. These deviations from a simple power law could be attributed to the effects of free-free absorption, which suppresses the synchrotron emission, as well as the changing composition of the radio continuum with increasing frequencies. Further, I found evidence that for intense starburst galaxies, such as those triggered by recent merger effects, there can be multiple regions of free-free absorption with different optical depths.

Optical spectroscopy data for the second sample of 19 objects were also collected using the Australian National University's 2.3 metre WideField Spectrograph. These data covered a field of view of  $38'' \times 25''$  with spectral coverage from 3000 to 9500 Å and targeted the Balmer series of spectral emission lines, which trace the same emitting regions as free-free radio-continuum emission. If the effects of dust attenuation are correctly accounted for, these optical data will provide an excellent calibration tool independent from the far-infrared to radio correlation that could be used to investigate and constrain radio signatures of star formation.

The acquired optical spectroscopic data were modelled using the penalised pixel fitting method. While accounting for line-of-sight velocity dispersion effects, this procedure can re-

construct the underlying stellar continuum as the weighted sum of a set of stellar reference templates and simultaneously model spectral line emission and absorption features. This modelling was carried out in two forms.

Initially the three-dimension spectral data cubes were collapsed down to a one-dimensional spectrum by integrating the data over an area containing each object of interest. This procedure maximised the total signal-to-noise ratio of the targeted spectral line features in each object's spectra. Before measuring the star formation rate based on  $H\alpha$  luminosities, the effects of dust attenuation were first estimated using the Balmer decrement method. This approach compares the observed line ratios and the expected line ratios for assumed conditions. The difference between these two quantities provides a measure of the amount of dust present, which can then be used to attempt to quantify its effects. By collapsing the data cube into a one-dimensional spectrum, all positional information about the emission across each object is lost.

To preserve spatial information, this modelling was then applied to each data cube before they were collapsed into a one-dimensional spectrum. This approach compromised the total signal-to-noise ratio of all spectra, preventing the Balmer decrement method of dust correction from reliably being applied for most sources.

The modelled components of the radio-continuum and optical spectra, as well as other multi-wavelength quantities, were then compared to one another to obtain a global view of star formation indicators within each object. This comparison showed that the intrinsic  $H\alpha$  luminosities that were dust corrected using the Balmer decrement were inconsistent with other luminosities and measures of star formation. Potentially this could be because the optical depth of the  $H\alpha$  emission line was so poor that the Balmer decrement method could not properly recover the total intrinsic  $H\alpha$  luminosity. Alternatively, it may be that the data do not have a sufficient signal to accurately capture the entire extent of each object, which may also compromise the effectiveness of the Balmer decrement dust correction method.

Finally, the results of modelling the optical spectra before they were collapsed to a one-dimensional dataset suggests that there are complex morphologies. However, no dust correction could be performed for most of these objects as they did not contain sufficient signals in the Balmer emission lines, primarily the  $H\beta$ .



# List of Abbreviations

<b>AGN</b>	Active Galactic Nuclei
<b>ALMA</b>	Atacama Large Millimeter Array
<b>ANU</b>	Australian National University
<b>ASKAP</b>	Australian Square Kilometre Array Pathfinder
<b>ATCA</b>	Australia Telescope Compact Array
<b>ATNF</b>	Australia Telescope National Facility
<b>CABB</b>	Compact Array Broad-band Backend
<b>CCD</b>	charge-coupled device
<b>CDFS</b>	<i>Chandra</i> Deep Field South
<b>CR</b>	Cosmic Ray
<b>ECDFS</b>	Extended <i>Chandra</i> Deep Field South
<b>EM</b>	emission measure
<b>FFA</b>	Free-Free Absorption
<b>FIR</b>	Far Infrared
<b>FRC</b>	Far Infrared to Radio Correlation
<b>FITS</b>	Flexible Image Transport System
<b>FWHM</b>	Full Width Half Maximum
<b>GAMA</b>	Galaxy and Mass Assembly
<b>GLASS</b>	GAMA Legacy ATCA Southern Survey
<b>GLEAM</b>	Galactic and Extragalactic All-sky MWA Survey

<b>HESS</b>	High Energy Stereoscopic System
<b>HMS</b>	High-mass stars
<b>IC</b>	inverse-Compton
<b>IFU</b>	Integral Field Unit
<b>IMF</b>	Initial Mass Function
<b>IR</b>	Infrared
<b>IRAS</b>	Infrared Astronomical Satellite
<b>ISM</b>	Interstellar Medium
<b>ISO</b>	Infrared Space Observatory
<b>JVLA</b>	Jansky Very Large Array
<b>LIRG</b>	Luminous Infrared Galaxy
<b>LOFAR</b>	Low-Frequency Array for Radio astronomy
<b>LOSVD</b>	line of sight velocity dispersion
<b>LTS</b>	Least Trimmed Squares
<b>MWA</b>	Murchison Widefield Array
<b>NAS</b>	nod and shuffle
<b>NRAO</b>	National Radio Astronomy Observatory
<b>NVSS</b>	NRAO VLA Sky Survey
<b>ODR</b>	Orthogonal Diagonal Regression
<b>PPXF</b>	Penalized Pixel-Fitting
<b>SDSS</b>	Sloan Digital Sky Survey
<b>SED</b>	Spectral Energy Distribution
<b>SFG</b>	Star Forming Galaxy
<b>SFH</b>	Star Forming History
<b>SFR</b>	Star Formation Rate
<b>SKA</b>	Square Kilometre Array

**SKADS** Square Kilometer Array Design Simulation

**SUMSS** Sydney University Molonglo Sky Survey

**TAROS** Telescope Automation and Remote Observing System

**ULIRG** Ultra-Luminous Infrared Galaxy

**UV** UltraViolet

**VERITAS** Very Energetic Radiation Imaging Telescope Array System

**VIMOS** Visible Multi-Object Spectrograph

**VISTA** Visible-Infrared Survey Telescope for Astronomy

**VLA** Very Large Array

**VLASS** Very Large Array Sky Survey

**VLT** Very Large Telescope

**WiFeS** Wide Field Spectrograph

# Chapter 1

## Introduction

### 1.1 Star Formation History of the Universe

The star formation history of the Universe is one of the key components required to understand when, where, and how galaxies have built up their stellar mass. Being able to trace the bulk of mass that older stars make up is a somewhat solved problem. Older stellar populations emit the bulk of their emission at near-infrared frequencies, making instruments, including the Visible-Infrared Survey Telescope for Astronomy (VISTA), the *Spitzer Space Telescope*, and the *Hubble Space Telescope*, remarkably efficient at tracing the older stellar mass back to the earliest epochs of the Universe (Jarvis et al., 2015). A redshift ( $z = (\nu_{\text{emitted}} - \nu_{\text{observed}}) / \nu_{\text{emitted}}$ ) is a measure of how far light has been shifted because of the expansion of the Universe or because of relative movement. Objects with larger redshift values, which have either been spectroscopically measured or photometrically constrained, are more distant and represent a different period of the Universe's evolution. Building a library of a property (e.g., stellar mass) as a function of redshift allows astronomers to directly trace a feature from the birth of the Universe to the present day.

Understanding the rate at which stellar mass grows is a more difficult problem. Young stars are hotter, with their spectral energy distribution peaking more towards the blue colour region, causing the effects of dust obscuration to be much more pronounced (Takeuchi et al., 2005; Dole et al., 2006).

Characterising the cosmic Star Forming History (SFH) of the Universe is one of the fundamental goals of the Square Kilometre Array (SKA) and its pathfinder projects (Jarvis et al., 2015). Extensive studies have revealed that galaxies were their most active at a redshift of 2, before slowly dwindling to their current day rates (Madau et al., 1998; Seymour et al., 2008; Madau and Dickinson, 2014; Jarvis et al., 2015). Figure 1.1 highlights this particularly well.

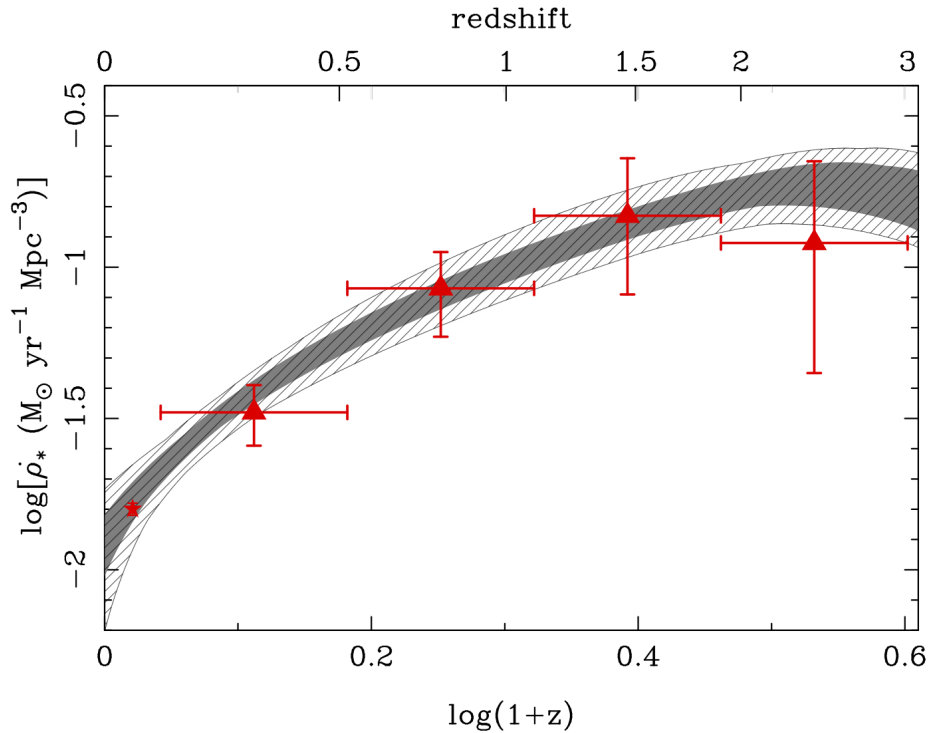


Figure 1.1: The co-moving SFH of the Universe taken from Seymour et al. (2008). The red triangles are from the VLA 1.4 GHz 13<sup>h</sup> *XMM-Newton/Chandra* Deep Field survey. The grey overlay are multi-wavelength composites from Hopkins (2004).

The grey highlighted regions trace the SFH as measured by the multi-wavelength indicators, including far-infrared, stellar transitions, and UV emission (Hopkins, 2004). Overlaid red markers are the SFH traced by radio-continuum emission at low frequencies of sources in the 13<sup>h</sup> *XMM-Newton/Chandra* Deep Field survey, as derived by Seymour et al. (2004, 2008).

The advent of large and deep all-sky surveys has led to considerable work attempting to understand the emission characteristics of young stars. Such surveys are critical for compiling a complete understanding of the galactic and mass evolution throughout cosmic time.

## 1.2 Tracers of Star Formation

Star Formation Rate (SFR) is the measure of the rate at which new stellar mass is formed. Typically, this star formation rate metric is expressed in units of solar masses per year ( $M_{\odot} \text{ yr}^{-1}$ ). Young stars, particularly those whose masses are above  $8 M_{\odot}$  (where  $1 M_{\odot} = 1.989 \times 10^{30}$  kilograms = 1 solar mass), have distinct features that are exhibited in various components across the multi-wavelength broadband Spectral Energy Distribution (SED) of an object.

Numerous researches have attempted to craft calibrated measures, based on components of

the observed electromagnetic spectrum, that produce consistent measures of the SFR. Such measures have been broadly consistent in the local Universe with well-understood systematics. Some studies have attempted to assess and recalibrate measures such that they are on a consistent scale, particularly at higher redshifts (Davies et al., 2016). Further complicating these SFR tracers for high redshift objects is the requirement of first applying a  $k$ -correction, which accounts for the *observed* emission being shifted from a higher *rest* frame emitting frequency. Some understanding of the typical SED has to be used and related to the appropriate manifestation of SFR.

A calibrated SFR indicator normalises a particular component of the observed emission into units of  $M_{\odot} \text{ year}^{-1}$ . An Initial Mass Function (IMF) is an empirically constructed probability function that describes a population of stars and their likely initial masses. When deriving an SFR indicator using physically motivated models, an IMF is adopted and integrated to obtain the final normalisation quotient. SFR tracers are sensitive to the choice of IMF, and when comparing different SFR calibrators, it is necessary to ensure consistency among the choice of IMF. An older IMF that is common in established SFR indicators is that of Salpeter (1955), which is described as a single power law across all mass limits:

$$\xi(m) \Delta m = \xi_0 \left( \frac{m}{M_{\odot}} \right)^{-2.35} \left( \frac{\Delta m}{M_{\odot}} \right), \quad (1.1)$$

where  $m$  is the mass in solar mass units  $M_{\odot}$  ( $1M_{\odot} \simeq 1.99 \times 10^{30} \text{ kg}$ ) and  $\xi_0$  is a constant representing the local stellar density. This single slope IMF is accurate for masses above approximately  $0.5 M_{\odot}$ , but with more recent studies, has been shown to overestimate the lower end of the mass function. More modern studies characterise IMFs as a continuous piecewise function. A popular example is from Kroupa (2001) who described IMF as

$$\xi(m) = \xi_0 m^{-\alpha_i}, \quad (1.2)$$

where

$$\begin{aligned} \alpha_0 &= +0.3 \pm 0.7 & , & \quad 0.01 \leq m/M_{\odot} < 0.08, \\ \alpha_1 &= +1.3 \pm 0.5 & , & \quad 0.08 \leq m/M_{\odot} < 0.50, \\ \alpha_2 &= +2.3 \pm 0.3 & , & \quad 0.50 \leq m/M_{\odot} < 1.00, \\ \alpha_3 &= +2.3 \pm 0.7 & , & \quad 1.00 \leq m/M_{\odot} \end{aligned} \quad (1.3)$$

To illustrate the difference between these two forms, both IMFs have been constructed in Figure 1.2. At low stellar masses, the difference is noticeable. Excluded from Figure 1.2 is the Eddington limit, which is a cap of the upper mass limit of new stars typically taken to be

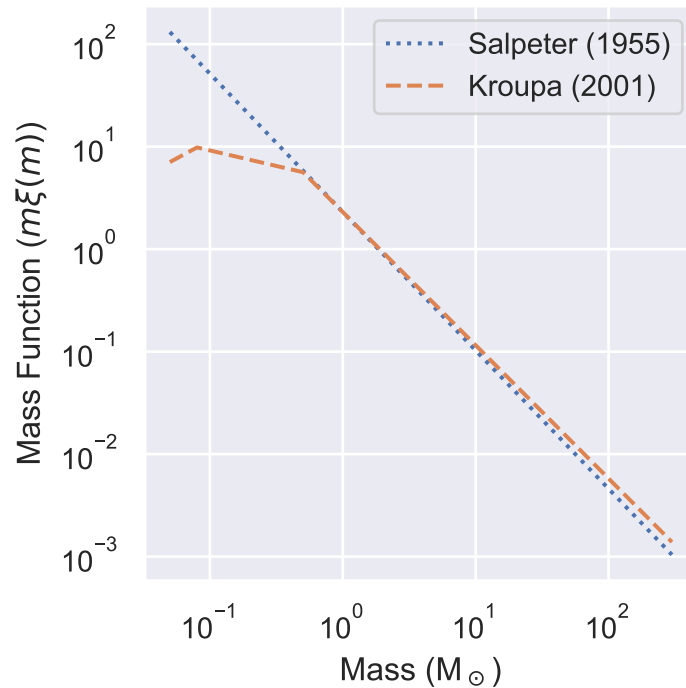


Figure 1.2: A simple comparison between the IMFs of Salpeter (1955) and Kroupa (2001). Both IMFs have been normalised to a common scale and are also scaled by and are logarithmically scaled by mass to better emphasise their differences.

$\sim 150 M_{\odot}$  (Kroupa and Weidner, 2003). At these masses, the incoming material being pulled under the influence of gravitation cannot overcome the outgoing light pressure.

This is a small overview limited only to notable IMFs used in key SFR tracers to be discussed and is not an exhaustive overview. Chabrier (2003, 2005) provide a more thorough overview of other available IMFs.

In the following sections, I provide a brief overview of various SFRs that are presented in the literature and outline the key advantages and disadvantages of each.

### 1.2.1 Ultraviolet Continuum

The most straightforward way of acquiring a measure on the rate of star formation is to observe the light directly from young stars. UltraViolet (UV) emission between 1250 to 2500 Å is the optimal wavelength for tracing young stellar populations (Kennicutt, 1998). Light in this regime avoids the Lyman- $\alpha$  forest, which is a series of absorption features produced by an electron in a neutral hydrogen atom moving to the lowest orbiting level that are prominent below  $\lambda < 1120$  Å (Lynds, 1971), and stellar features from older stars, namely absorption features from the Balmer series of transitions, above  $\lambda > 2500$  Å, as this is where the stars are the brightest with temperatures between  $10^7$  to  $10^9$  K.

Being able to observe the stellar light in this regime directly leads to star formation tracers which scale in linear proportion to the luminosity of an observed source. Via synthesis modelling, UV has been calibrated to be a star formation tracer of the form

$$\text{SFR} (\text{M}_{\odot} \text{yr}^{-1}) = 1.4 \times 10^{-28} L_{\nu} (\text{ergs s}^{-1} \text{Hz}^{-1}) \quad (1.4)$$

where  $L_{\nu}$  is a monochromatic luminosity of the UV emission taken in the wavelength range of 1250 to 2500 Å. Equation 1.4 is taken from Kennicutt (1998), who adjusted the calibration by Madau et al. (1998) to the Salpeter IMF (Salpeter, 1955) with mass limits between 0.1 to 100  $\text{M}_{\odot}$ .

At redshifts below 0.5, this wavelength range is not accessible to ground-based instrumentation because of atmospheric opacity, but the UV continuum of objects between redshift of 1 to 5 has been shifted to lower observer frame frequencies, where the atmosphere becomes transparent (Steidel et al., 1996).

Although the flat UV continuum makes Equation 1.4 relatively simple to apply, UV emission itself has issues that make its application difficult and may compromise its reliability in the high redshift Universe. The foremost being the effects of dust attenuation. Dust is optically thick to UV emission and effectively either scatters or absorbs a fraction of the intrinsic emission from the observed emission detected by instruments.

Methods do exist that attempt to characterise and consequently correct for the presence of dust. Radiative transfer models have been employed to attempt to consider the clumpy distribution of dust and incorporate extinction information encoded in the Balmer decrement (see the subsequent section §1.2.2 for an overview of the method) or infrared recombination lines (Calzetti, 1997; Kennicutt, 1998). Typical corrections to UV luminosities range between 0 to 3 magnitudes (Buat, 1992; Cortese et al., 2008; Mao et al., 2012). Even a modest amount of dust can significantly suppress UV emission (Madau and Dickinson, 2014). Calzetti (2013) described that dust corrections work mostly on ensembles of galaxies and not on individual objects themselves as the nature and amount of dust can vary widely between galaxies.

### 1.2.2 Optical Recombination and Forbidden Lines

Atomic transitions are a fairly direct method of tracing star formation rates in distant objects. High-mass stars (HMS) and their UV emissions bombard nearby gas clouds, ionising them. During recombination, where an electron transitions to a lower energy level of its bound atom, a corresponding photon is produced. The energy of this photon is directly related to the change in the energy level of the transitioning electron. Following the Planck-Einstein relation



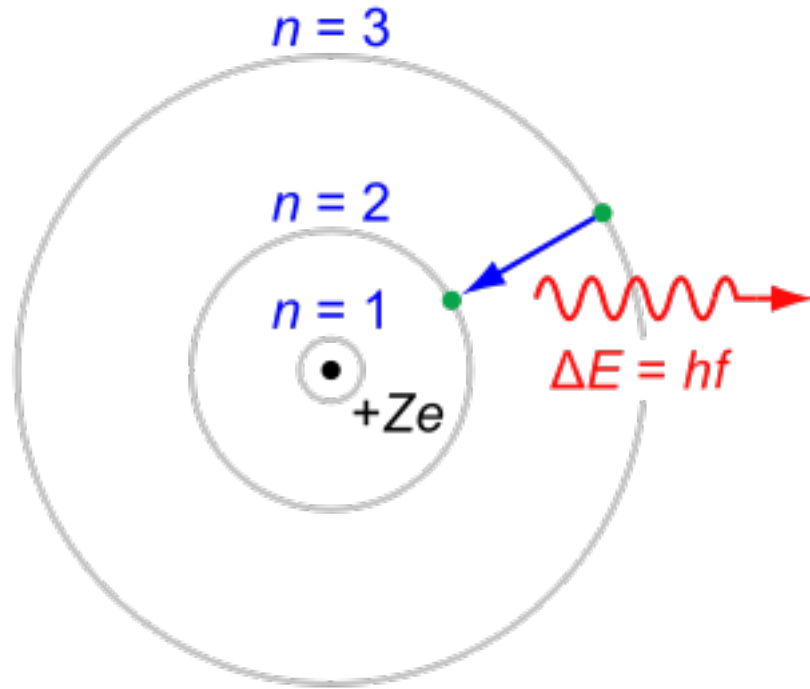


Figure 1.3: An example of an electron transitioning from the third to second orbiting level of a hydrogen atom. The energy difference between these orbiting levels produces a corresponding photon, whose frequency is quantised by Planck’s constant,  $h$ . This transition produces  $H\alpha$  emission. Image produced by Jabber Wok at the English language Wikipedia, CC BY-SA 3.0, accessible from <https://commons.wikimedia.org/w/index.php?curid=2639910>

(Einstein, 1905),

$$E = hf, \tag{1.5}$$

where  $E$  is the energy of a photon in Joules,  $h$  is Planck’s constant, taken as  $6.625 \times 10^{-34}$  Joules per second, and  $f$  is the frequency of a photon in Hertz. This relation dictates that light, and the photons that make it up, are quantised in increments of  $h$ . In the context of recombination lines, the energy released by an electron changing its orbiting level around its bound atom will produce a photon with a *corresponding* frequency. The relative motion of gas in a galaxy will typically shift emitted photons in the red and blue directions, producing emission over a relatively small bandwidth ( $\nu < 2$  MHz;  $\lambda < 60 \text{ \AA}$ ). Typically, these features are referred to as emission lines.

Studying the emission from these instances of recombination lines offers a powerful probe of star formation. One of the most accessible lines that is a remarkable tracer of HMS formation is the  $H\alpha$  transition of hydrogen, the state three to two transition of which emits at a wavelength of  $\lambda = 6562.8 \text{ \AA}$ .

There is an extensive collection of  $H\alpha$  surveys available in the literature, the most prominent of which being the Sloan Digital Sky Survey (SDSS) (Blanton et al., 2017). Commenced in 2000,

SDSS has produced high-quality spectra for over one million objects.  $H\alpha$  is attractive as a star formation rate indicator because the recombination transition it traces is directly tied to the ionisation rate of the HMS and is a relatively instantaneous emission mechanism. Its emitting wavelength, which largely avoids atmospheric opacity, also makes it observable from ground-based instruments.

Based on  $H\alpha$  emission, there have been several conversions calibrated in the literature to estimate star formation rates. Kennicutt et al. (1994) and Madau et al. (1998) have produced sound recipes of the form

$$\text{SFR} (M_{\odot} \text{ yr}^{-1}) = 7.9 \times 10^{-42} L(H\alpha) (\text{ergs s}^{-1}) \quad (1.6)$$

where  $L(H\alpha)$  is the  $H\alpha$  luminosity of a source. This has been calibrated assuming a Salpeter initial mass function and Case B recombination at an electron temperature of 10000 K, which are typical conditions for star forming galaxies (Osterbrock, 1989). Case B recombination refers to the ionised gas being optically thick, such that the gas would absorb a photon produced by an electron returning to its ground state. In the opposite scenario, called Case A recombination, is where the gas is optically thin and the photon can escape.

The main issue associated with the application of Equation 1.6 is acquiring the *intrinsic*  $H\alpha$  luminosity of an object. Similar to UV emission,  $H\alpha$  is susceptible to the effects of dust attenuation. This means that the *observed*  $H\alpha$  luminosity is only a fraction of the *intrinsic*  $H\alpha$  luminosity. Recovering an estimate of the amount of  $H\alpha$  obscured by dust is an essential step towards acquiring accurate star formation rate measures.

One of the more straight forward methods of characterising the degree of dust extinction is the use of a Balmer decrement (Domínguez et al., 2013). The Balmer decrement is an emission line diagnostic, in which often following typical Case B recombination scenarios, the ratio of lines in the Balmer series (including  $H\alpha$ ,  $H\beta$ , and  $H\gamma$ , for example) is taken to assess the amount of dust attenuation. For example, the expected ratio between the  $H\alpha$  and  $H\beta$  (State 4-2 transition;  $\lambda = 4861 \text{ \AA}$ ) is taken as 2.86. As the effects of dust attenuation are more severe at shorter wavelengths (Calzetti et al., 2000), any deviation from this expected  $H\alpha/H\beta$  ratio of 2.86 could be attributed to dust and subsequently corrected for. As  $H\alpha$  and  $H\beta$  have similar emitting wavelengths, most spectrographs can simultaneously observe both lines, making this approach reasonably straight forward.

Issues arise when  $H\beta$  is poorly constrained. This can be particularly troublesome when the  $H\alpha$  emission line, which is almost three times stronger, has a low signal-to-noise ratio detection itself. When  $H\beta$  is not robustly measured, uncertainties propagate through and over or under correct the  $H\alpha$  when following this Balmer decrement method of dust correction, particularly

if the  $H\alpha$  and  $H\beta$  lines are observed through two different filters with different throughput efficiencies (see the Wide Field Spectrograph (WiFeS) instrument overview in §4.3).

Alternate methods could be used to attempt to characterise dust attenuation. For example, the Penalized Pixel-Fitting (PPXF) algorithm (Cappellari and Emsellem, 2004; Cappellari, 2017) can use the stellar continuum in an observed set of optical spectra to constrain a reddening curve, such as the one presented by Calzetti et al. (2000). This algorithm attempts to deduce an optimal set of weights assigned to members of a stellar template reference library to replicate the shape of the observed stellar continuum of some source. A separate reddening curve can also be constrained throughout this procedure, allowing the stellar continuum itself to be used to obtain a reddening term. These two measures of dust, however, do not strictly probe the same dust screens of an object, meaning that they are not directly interchangeable. The Balmer decrement traces obscuration around young star forming regions, whereas the stellar continuum traces the obscuration of an older stellar population. Studies have empirically linked the dust attenuation of the stellar continuum to the dust attenuation of the recombination lines (Calzetti, 1997, 2013), but these are subject to a collection of effects.

Further complicating  $H\alpha$  as a star formation tracer presented in Equation 1.6 (as well as other transitions in the Balmer series) is that Active Galactic Nuclei (AGN) can also ionise HII regions<sup>1</sup>, which would then produce the nebular transitions calibrated for star formation (Netzer, 1990). To some degree, with either resolved spectra that can separate the AGN and star forming regions from one another, or by exploiting different velocity dispersion effects (as later performed in this thesis), nebular transitions not powered by star formation can be characterised and removed. In either case, high signal-to-noise spectra need to be able to identify and model these discrete sources, which is often difficult and when solved for simultaneously can produce degenerate solutions.

Forbidden lines, including [OII] and [OIII], refer to highly improbable transitions (Eddington, 1927). Although these forbidden lines are not a *direct* tracer of star formation, in that they are not tied to the ionisation rate of stars, there have been empirically calibrated measures in literature allowing them to be used as star formation rate tracers. Forbidden lines have the potential to be particularly useful diagnostics as  $H\alpha$ , the strongest of the Balmer series, is also the first that will be shifted out of the spectral aperture at sufficient redshifts.

The [OII]  $\lambda\lambda 3726, 3729 \text{ \AA}$  doublet has had particular focus as it represents a potential star formation tracer for redshifts between 0.4-1.5 (Kewley et al., 2004). Using spectra of 97 galaxies, Kewley et al. (2004) calibrated [OII] as a star formation rate tracer by comparisons with  $H\alpha$

---

<sup>1</sup>where a HII region is a region of interstellar hydrogen gas that is ionised

diagnostics. They published the relation

$$\text{SFR} (\text{M}_\odot \text{yr}^{-1}) = (6.58 \pm 1.65) \times 10^{-42} L([\text{OII}]) (\text{ergs s}^{-1}), \quad (1.7)$$

where  $L([\text{OII}])$ , the dust corrected  $[\text{OII}]$  luminosity, differs from the earlier published relation by Kennicutt (1998). Both sets though are calibrated against the Salpeter (1955) with 0.1 to  $100 \text{M}_\odot$  limits. The authors of both studies do stress that  $[\text{OII}]$  tracers are sensitive to both dust extinction and the metallicity content. For high redshift objects, where both characteristics are harder to constrain, there is an uncertainty for the reliability of this tracer, especially considering it is not directly tracing the ionisation rate of stellar populations. Even so, it could be useful in conjunction with other star formation tracer methods as a consistency check.

### 1.2.3 Radio Recombination Lines

Recombination lines are not limited to optical (or near optical) wavelengths. Following Equation 1.5, the frequency of the recombination lines is dependent on the energy difference between the transition states. There are many transitions which produce a radio photon that can be detected by a radio telescope. These recombination lines are not affected by the presence of dust, making them an ideal tool for probing SFR of distant galaxies.

There are many recombination lines in the radio regime (Lilley and Palmer, 1968). Generally speaking, the emitting frequency of a recombination line can be written as

$$\nu = R_{\text{Mc}} \left[ \frac{1}{n^2} - \frac{1}{(n + \Delta n)^2} \right], \quad (1.8)$$

where  $n$  is the energy level after a transition and  $\Delta n$  is the change in energy levels,

$$R_{\text{Mc}} = R_\infty \left( 1 + \frac{m_e}{M} \right)^{-1}, \quad (1.9)$$

with  $R_\infty$  being the Rydberg frequency of  $\approx 3.28 \times 10^{15} \text{Hz}$ ,  $m_e$  is the mass of an electron ( $9.109 \times 10^{-31} \text{kg}$ ), and  $M$  is the mass of the nucleus of an atom. These Equations are not limited to radio wavelengths and can be used to obtain the frequency of recombination for any transition and atom, including the optical emission lines described in § 1.2.2.

Hydrogen is the most abundant element in the Universe, and at radio wavelengths, hydrogen has many radio recombination lines. Figure 1.4 shows the various radio recombination lines of hydrogen following Equations 1.8-1.9 given the nucleus mass of hydrogen is  $1836.1 m_e$ .

For star forming galaxy Star Forming Galaxies (SFGs), radio recombination lines are pro-

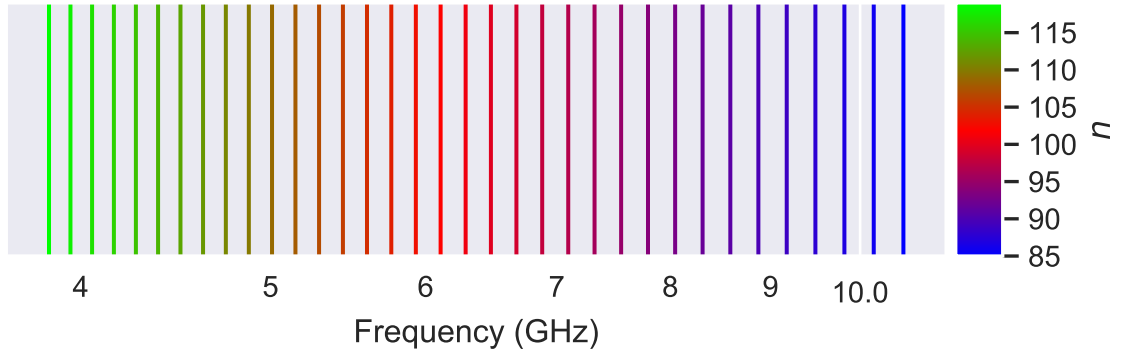


Figure 1.4: The hydrogen radio recombination lines at various frequencies denoted as vertical lines for a  $\Delta n = 1$  transition, with the end state being signified as the colour of each line.

duced in star forming regions as electrons cascade down the energy ladders. Although difficult, there are conditions where it is possible to derive an SFR measure using these transitions. Anantharamaiah et al. (2000) used the Very Large Array (VLA) to detect a series of hydrogen recombination lines towards Arp 220, the closest Ultra-Luminous Infrared Galaxy (ULIRG) whose radio emission is powered predominately by star formation with a weak active galactic nuclei AGN component. As a by-product of the spectral line observations, the radio continuum at 1.4, 8.2, 97.2 and 206.7 GHz were also obtained. Using these data collectively, they were able to constrain a model describing the physical conditions of gas and estimate its rate of ionisation. Adopting the IMF proposed by Miller and Scalo (1978) they obtained a SFR of  $\sim 240 M_{\odot} \text{ yr}^{-1}$ .

This approach of estimating SFR has not been widely utilised previously. Although the radio recombination lines are not affected by dust, they are relatively weak and require deep, sensitive radio observations across a wide range of frequencies to detect a sufficient number of transitions to constrain an assumed radiative transfer model accurately. In practice, this limits their use to bright and nearby objects.

#### 1.2.4 Infrared

Infrared emission is produced by clouds of heated dust that surround stars and are the same obscuring dust clouds that compromise UV and nebular tracers of star formation. The energy reradiated in the mid-to-far infrared region is the reprocessed stellar light component from stars. In particular, the bulk of energy stars absorb and re-radiate is produced by HMS, which burn hotter and are bluer, making them more susceptible to the effects of dust obscuration. At far-infrared wavelengths, the effects of dust obscuration are generally thought to be negligible. This is not entirely true for mid-infrared wavelengths, where highly dust-enshrouded areas can still be suppressed. However, it is generally regarded that infrared emission is a powerful probe

into the star formation rates of distant galaxies.

In the literature, it is generally assumed that for young SFG without a AGN component, the far-infrared is an excellent tracer of star formation. Young, newly birthed stars can heat the dust content of a galaxy to higher temperatures, producing a ‘warm’ component at  $\lambda \sim 60\mu\text{m}$  of dust near star forming regions and a cooler ‘infrared cirrus’ component at  $\lambda \sim 100\mu\text{m}$  (Helou, 1986; Kennicutt, 1998). Following a greybody spectrum, which approximates the infrared SED well and is a modification of a blackbody with a frequency-dependent emissivity term (Hildebrand, 1983), as the temperature of the heat dust increases, the peak of the emission profile shifts to shorter wavelengths. For a normal SFG made up of young stellar populations, this peak is observationally measured to be  $\approx 60\mu\text{m}$  (Calzetti, 2013).

With the advent of the Infrared Astronomical Satellite (*IRAS*) telescope, the infrared sky was observed at 12, 25, 60, and  $100\mu\text{m}$ , producing a remarkable dataset of 30,000 galaxies that could be used to characterise an infrared-based SFR tracer (Moshir et al., 1992). For the first order, assuming that young stars dominate the UV spectrum and infrared emission is optically thin, far-infrared luminosities can be considered calorimetric measures of star formation (Kennicutt, 1998).

Unfortunately, this simplified scenario is not often the completely correct case. In almost all galaxies, there exists, to some degree, a population of older stars. Without being able to resolve individual stars to separate younger and older populations from one another, the observed far-infrared also has a cooler dust component embedded in the warmer component that is heated by younger, hotter stars.

The introduction of AGN activity further complicates the use of infrared emission as an SFR indicator. AGN can also produce UV emission, and in dusty environments, it can heat nearby dust clouds, contributing to the observed infrared SED. With temperatures of approximately 100 K, the peak of this dust is closer to the mid-infrared (Kirkpatrick et al., 2012). Dust heated by stars, with temperatures between 50 to 100 K, peaks closer to the far-infrared. For unresolved objects, this mixture of dust temperatures produces a more complex SED. The use of infrared SED templates can disentangle the two features from one another through model optimisation methods. For resolved objects, the two dust components can be separated by their spatial distribution. The mid-infrared heated by AGN will be localised to the centre of an object, with the far-infrared heated by stars that are more extended and disperse.

Nevertheless, a bolometric infrared luminosity covering the 8 to  $1000\mu\text{m}$  range can be a reliable star formation measure, even when considering the possible complexity encoded in the

passband. Kennicutt (1998) calibrated such a conversion as follows:

$$\text{SFR} (M_{\odot} \text{ yr}^{-1}) = 4.5 \times 10^{-44} L_{\text{TIR}} (\text{ergs s}^{-1}), \quad (1.10)$$

where  $L_{\text{TIR}}$  is the bolometric luminosity between 8 to 1000  $\mu\text{m}$  obtained using models from Leitherer and Heckman (1995) and a Salpeter initial mass function. Kennicutt (1998) notes that Equation 1.10 applies to only starburst galaxies whose ages are less than  $10^8$  years. For more ‘normal’ galaxies, the combination of older stellar populations contributing to the infrared luminosities and potentially lower optical depth will lower the robustness of this bolometric infrared measure of star formation.

Furthermore, obtaining a  $L_{\text{TIR}}$  measurement is not trivial because often the required multi-wavelength data are not available. Overcoming this often requires infrared template fitting to, potentially, sparsely sampled infrared measurements. When these templates are of local galaxies extrapolated to higher redshifts, additional uncertainty due to dust emission properties can further compromise the total infrared derived star formation tracers.

More recently, monochromatic luminosities of components in infrared emission have become somewhat reliably calibrated tracers of star formation, although considerable care has to be taken while applying them. Calzetti et al. (2010) used a sample of 189 nearby galaxies with associated ground-based  $\text{H}\alpha$  images and infrared data at 24, 70, and 160  $\mu\text{m}$  from *Spitzer* (a space-based infrared telescope launched in 2003) to construct a global 70  $\mu\text{m}$  star formation tracer, where global is used to signify that this tracer is meant to be applied to measurements on galaxy-wide spatial scales. For smaller spatial regions, there are a further suite of 70  $\mu\text{m}$  star formation indicators derived by Li et al. (2010).

Similarly, studies in the literature have used 24  $\mu\text{m}$  luminosities as a probe of star formation on both local and global galactic scales. On the global scale, Wu et al. (2005), Zhu et al. (2008), and Kennicutt et al. (2009) found linear and near-linear relationships between the 24  $\mu\text{m}$  luminosities and other star formation rate indicators. Although these are generally consistent, it implies that the monochromatic infrared luminosity star formation tracing approach is challenging.

Such approaches, however, are difficult to reliably apply as they are susceptible to variation of intrinsic galactic properties. Measurements longer than 70  $\mu\text{m}$  trace cooler dust, heated by a population of smaller, older stars. Bands shorter than 20  $\mu\text{m}$  also trace emissions that are not exclusive to young stars (Crocker et al., 2013). Variations in dust content, distribution, and heating further complicate monochromatic infrared tracers of star formation (Calzetti, 2013).

Rest frame far-infrared measures that trace star formation in the high redshift Universe above redshifts of 2 are also currently limited by confusion, wherein confusion occurs when the

noise introduced by unresolved, faint background sources dominates the noise characteristics of an image. Once reached, there is no possibility of further integrating in a field to reach better sensitivities. Overcoming the confusion limit requires improving the angular resolution of an instrument. For space-based infrared instruments, this is currently not possible.

### 1.2.5 Composite Tracers of Star Formation

In the presence of dust UV, optical-based measures of SFR are compromised as a fraction of their emission is obscured. Similarly, infrared measures of SFR are only sensitive to the portion of emission that was absorbed and reradiated by dust. Built into each calibrated tracer is an additional component to compensate for the emission missed, making them statistically sound for samples of objects (Kennicutt, 1983; Calzetti et al., 1994, 2000). However, seemingly random errors may still be present for individual galaxies whose dust extinction effects are not typical or corrected well by this single additional calibration scaling component (Kennicutt, 1998).

There are calibrated SFR measures in the literature utilising two distinct emission tracers (Kennicutt et al., 2009; Hao et al., 2011; Kennicutt and Evans, 2012). These composite SFRs assume a simple energy balance model, where one tracer measures the SFR using light reradiated by heated dust (and is assumed to be isotropic) and the second measures the SFR of unobscured light (whether it is UV stellar light directly or emission or regions ionised by UV stellar light). Together they should be a more robust measure of SFR for individual objects as they better account for the potentially unique arrangement and distribution of obscuring dust.

The series of papers by Kennicutt et al. (2009) and Hao et al. (2011) provide a broad set of calibrated measures of the form

$$L(\lambda_1, \lambda_2)_{\text{corr}} = L(\lambda_1)_{\text{obs}} + a_{\lambda_2} L(\lambda_2), \quad (1.11)$$

where  $L(\lambda_1)_{\text{obs}}$  is the observed luminosity of a measure tracing unobscured light that would otherwise require a dust correction (e.g., UV or  $\text{H}\alpha$ ),  $L(\lambda_2)$  is the luminosity of an emission component produced by the heated obscuring dust (e.g. infrared),  $a_{\lambda_2}$  is a wavelength-dependent scaling term required to produce a linear combination of the two tracers, and  $L(\lambda_1, \lambda_2)_{\text{corr}}$  is a ‘dust corrected’ luminosity measure suitable to estimate SFRs. In the absence of infrared luminosities, it is possible to introduce the radio continuum as a measure to estimate the fraction of light absorbed by dust. Although radio emission is not a product of dust in itself, the Far Infrared to Radio Correlation (FRC) may be used to provide a first-order approximation.

Shown in Table 1.1 is an extract of Table 4 from Kennicutt et al. (2009) describing the various  $L(\lambda_1)_{\text{obs}}$  and  $L(\lambda_2)$  composite relations and the corresponding  $a_{\lambda}$  scaling term. Kennicutt et al.



Relation	SINGS	MK06	SINGS+MK06
$L(\text{H}\alpha)_{\text{obs}} + a^*L(24 \mu\text{m})$	$0.015 \pm 0.004$	$0.021 \pm 0.005$	$0.020 \pm 0.005$
$L(\text{H}\alpha)_{\text{obs}} + a^*L(\text{TIR})$	$0.0020 \pm 0.0005$	$0.0025 \pm 0.0006$	$0.0024 \pm 0.0006$
$L(\text{H}\alpha)_{\text{obs}} + a^*L(8 \mu\text{m})$	$0.010 \pm 0.003$		$0.011 \pm 0.003$
$L(\text{H}\alpha)_{\text{obs}} + a^*L_{1.4\text{GHz}}$	$0.41 \pm 0.13$	$0.39 \pm 0.10$	$0.39 \pm 0.10$
$L([\text{OII}])_{\text{obs}} + a^*L(24 \mu\text{m})$		$0.029 \pm 0.005$	
$L([\text{OII}])_{\text{obs}} + a^*L(\text{TIR})$		$0.0036 \pm 0.0006$	
$L([\text{OII}])_{\text{obs}} + a^*L(8 \mu\text{m})$	$0.016$		
$L([\text{OII}])_{\text{obs}} + a^*L_{1.4\text{GHz}}$		$0.54 \pm 0.10$	

Table 1.1: An extract of Table 4 from Kennicutt et al. (2009) describing the  $a_\lambda$  scaling term derived for various composite SFRs. SINGS and MK06 refer to the dataset used by Kennicutt et al. (2009) when constraining that relation.

(2009) constrained these scaling coefficients using the dust corrected  $\text{H}\alpha$  luminosities obtained from the SIRTf Nearby Galaxies Survey (SINGS; Kennicutt et al., 2003) and a survey of integrated spectrophotometry of 417 galaxies from Moustakas and Kennicutt (2006, referred to as MK06).

Kennicutt et al. (2009) provided two calibrated recipes allowing these composite luminosities to be converted to a SFR, based on either the Salpeter (1955) or Kroupa (2001) IMF. When using a Salpeter (1955) IMF and using  $\text{H}\alpha$  and total infrared luminosities, the SFR can be written as

$$\text{SFR} (\text{M}_\odot \text{yr}^{-1}) = 7.9 \times 10^{-42} [L(\text{H}\alpha)_{\text{obs}} + 0.0024L(\text{TIR})], \quad (1.12)$$

where  $L(\text{TIR})$  is the bolometric luminosity of 8 to 1000  $\mu\text{m}$  and  $L(\text{H}\alpha)_{\text{obs}}$  is the observed  $\text{H}\alpha$  luminosity. Both these quantities are in units of  $\text{ergs s}^{-1}$ . The 0.0024 constant is the scaling coefficient from Table 1.1 obtained when using the SINGS and MK06 datasets for this combination of SFR tracers.

### 1.2.6 Radio Continuum

Radio-continuum emission has the potential of being the most reliable method of obtaining SFR of distant objects, particularly in the early epochs in the Universe. Its key advantage over other methods outlined above is that it is not biased because of dust.

Over a broad frequency range, the radio continuum is made up of two distinct emission processes that are both tracers of HMS ( $\text{M}_\odot > 8\text{M}_\odot$ ). At frequencies below 10 GHz, non-thermal synchrotron emission is the most dominant process. Typically, synchrotron emission has a steep spectrum, with a nominal spectral index of  $\alpha = -0.8$ , where  $S_\nu \propto \nu^\alpha$ . At increasing frequencies, thermal free-free emission becomes the main mechanism in the radio continuum (Condon and Yin, 1990; Condon, 1992).

In the literature, synchrotron emission is a well-studied process that has been shown to be a well-calibrated tracer to SFR. The HMS that power the bulk of emission at Far Infrared (FIR) and optical wavelengths, end their lives as core-collapsed supernova. These supernovae accelerate electrons to relativistic speeds as their shock fronts interact with the Interstellar Medium (ISM). As these relativistic electrons propagate outwards, they interact with the galaxy's large-scale magnetic fields. This interaction leads to a change in acceleration as the relativistic electrons move around the field lines. Conservation of momentum dictates that this change in acceleration produces a corresponding photon. The low energy levels associated with this interaction lead to the production of low frequency radio emission. In Figure 1.5, I show a schematic illustration of the process. Synchrotron emission is a *delayed* tracer of star formation, taking more than  $10^7$  years for the relativistic electrons to lose their energy and diffuse in the large-scale galactic magnetic fields.

The low frequency radio continuum, which is overwhelmingly synchrotron emission in nature, as a tracer to SFR has been calibrated by exploiting the FRC, which shows a remarkably firm relationship between the radio continuum and the far-infrared spanning many magnitudes in luminosities and Hubble types. Yun et al. (2001) explored the FRC using data from the *IRAS* 1.2 Jy Sample (Strauss et al., 1990, 1992; Fisher et al., 1995) and the NRAO VLA Sky Survey (NVSS) (Condon et al., 1998) and used it to bootstrap far-infrared SFR calibrations to radio luminosities at 1.4 GHz. Using a Salpeter IMF with mass limits between 0.1 and  $100 M_{\odot}$ , their comparison yields the SFR tracer

$$\text{SFR} (M_{\odot} \text{ yr}^{-1}) = 5.9 \times 10^{-22} L_{1.4 \text{ GHz}} (\text{W Hz}^{-1}), \quad (1.13)$$

where  $L_{1.4 \text{ GHz}}$  is the 1.4 GHz luminosity of an object. At this frequency, the radio continuum is made up of mostly synchrotron radiation. Far-infrared emission, being mostly optically thin

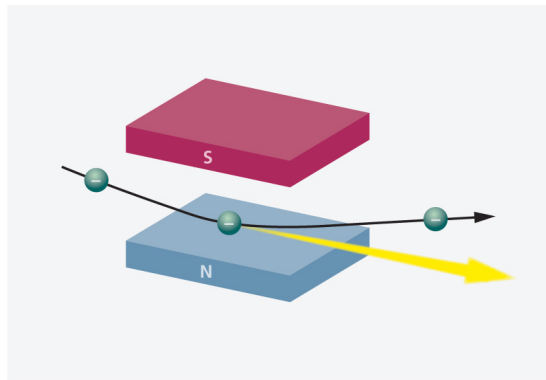


Figure 1.5: A diagram showing a photon of energy being emitted when the charged electron has its path changed from the magnetic field. Diagram taken from <http://www.psi.ch/media/the-swiss-light-source-sls>.

and sensitive to the same blue HMS which eventually produce synchrotron emission, is an ideal basis to calibrate this radio tracer of SFR.

Even so, work by Bell (2003) has shown that the FRC itself at low frequencies is not without issues. Low luminosity galaxies tend to have less dust (Wang and Heckman, 1996; Adelberger and Steidel, 2000; Hopkins et al., 2001; Sullivan et al., 2001; Bell and Kennicutt, 2001; Buat et al., 2002), and consequently, the far-infrared tracers could *underestimate* star formation. Because the observed FRC is linear in nature when considering the low frequency radio continuum, the natural interpretation is that there is also intrinsic behaviour in the synchrotron component of the radio continuum that is ‘balancing out’ the deficit in the far infrared and saving the FRC.

Using synchrotron emission as the basis of reliable SFR indicators, particularly in the high redshift Universe, is also associated with problems. First, synchrotron emission is not a process exclusive to star formation. AGN produces synchrotron emission far more vigorously than normal SFG. Care has to be taken when simply using the observed 1.4 GHz monochromatic luminosity of an object as the single tracer of SFR to ensure that there is no AGN contamination. Ignoring this possibility would mean that when AGN is present, the SFR implied by simply 1.4 GHz luminosity will overestimate the actual SFR. In the context of characterising the SFH of the Universe, researchers attempt to separate SFG from AGN objects (Seymour et al., 2008).

Similarly, synchrotron emission is known to have a variable spectral index. The synchrotron spectrum is related to the energy spectrum of the cosmic ray population, following

$$N(E) dE \approx K E^\delta dE, \quad (1.14)$$

where  $N(E) dE$  is the number of electrons of some volume between the energy levels  $E + dE$ . The parameter  $\delta$  corresponds to the slope of the Cosmic Ray (CR) distribution. Typically,  $\delta$  is taken to be  $-2.4$ . The parameter  $\delta$  is therefore tied directly to the history of star formation as well as electron cooling mechanisms, which include inverse-Compton losses and synchrotron self-absorption. Such cooling processes affect different energy levels in the cosmic ray distribution at different rates, leading to scenarios that can produce curved spectra. The synchrotron process itself exhibits faster electron cooling times at higher frequencies, which means that without a constant injection of relativistic electrons, the synchrotron component has an additional curvature component.

The second component that makes up the radio continuum is thermal free-free emission. Free-free emission, also sometimes referred to as Bremsstrahlung emission (which is German from ‘Braking Radiation’), describes a photon of energy created by the interaction of two

particles, often an electron and an atomic nucleus. Using a simplified classical model, when a travelling electron enters the Coulomb field of a secondary particle, usually an ion, it undergoes a period of deceleration. Because of energy conservation, this loss of kinetic energy results in the creation of a photon whose energy is equal to the difference in energy of the electron before and after the interaction. The term ‘free-free’ refers to both particles remaining independent and unbounded to one another both before and after the deflection. A schematic illustration of this process and the photon that is created are shown in Figure 1.6.

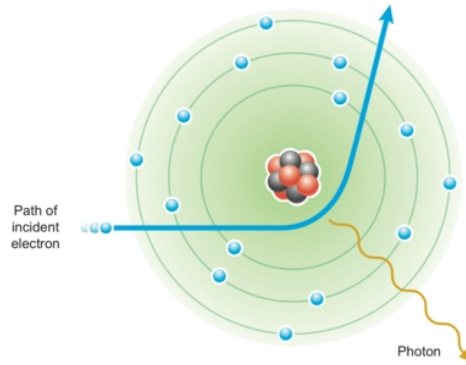


Figure 1.6: An illustration demonstrating how the Bremsstrahlung (free-free) emission occurs. The photon is created as an electron changes direction or is decelerated by a nearby ion. The path of the electron before and after the interaction with the ion is represented in green. The yellow arrow represents the emitted photon. Image taken from <http://titan.radonc.unc.edu/dose/aud30.gen.terms.01.html>

Because of its flat spectral index ( $\alpha = -0.1$ ; Condon and Yin, 1990), at low frequencies, isolating free-free component from the dominant synchrotron emission is difficult. Often, the only real method of characterising the free-free emission component is to acquire a set of flux density measurements over a broad frequency range and to perform model optimisation methods to disentangle it from the synchrotron and free-free components from one another (Condon, 1992).

Free-free emission is often assumed to be a far superior tracer of star formation when compared with synchrotron emission. For one, it is an instantaneous tracer of SFR because it probes the ionisation of HII regions that surround HMS. Murphy et al. (2012) showed in their study of resolved regions of star formation in nearby galaxies at 33 GHz that free-free emission is extremely sensitive to the current ionising photon rate of young stars, making it an ideal tracer of star formation. Secondly, at increasing frequencies, free-free emission becomes a more significant component of the observed radio continuum. Following this, as sources are observed at higher redshifts, the observed radio continuum is made up of an increasing amount of free-free emission, as the high frequency rest frame ( $\nu_{\text{rest}}$ ) radio continuum component gets shifted

to lower frequencies in the observed frame ( $\nu_{\text{obs}}$ ). This scaling follows

$$\nu_{\text{obs}} = \nu_{\text{rest}} / (1 + z), \quad (1.15)$$

where  $z$  is the redshift of an assumed object. Figure 1.7 shows the typical SED of a SFG. This SED is based on the radio continuum to far-infrared spectrum of M82, as published in Condon (1992). The radio continuum of M82 is modelled as being a combination of 90% steep spectrum synchrotron and 10% flat spectrum free-free emission at 1.4 GHz. At frequencies above 100 GHz, the infrared emission from heated dust produces a shape modelled well by a modified blackbody. To illustrate the effects of shifting from high to low frequencies, I included, as vertical lines, the equivalent rest frame frequency at observed 1.4 GHz and 9.0 GHz for redshifts of 1, 2, 3, and 4.

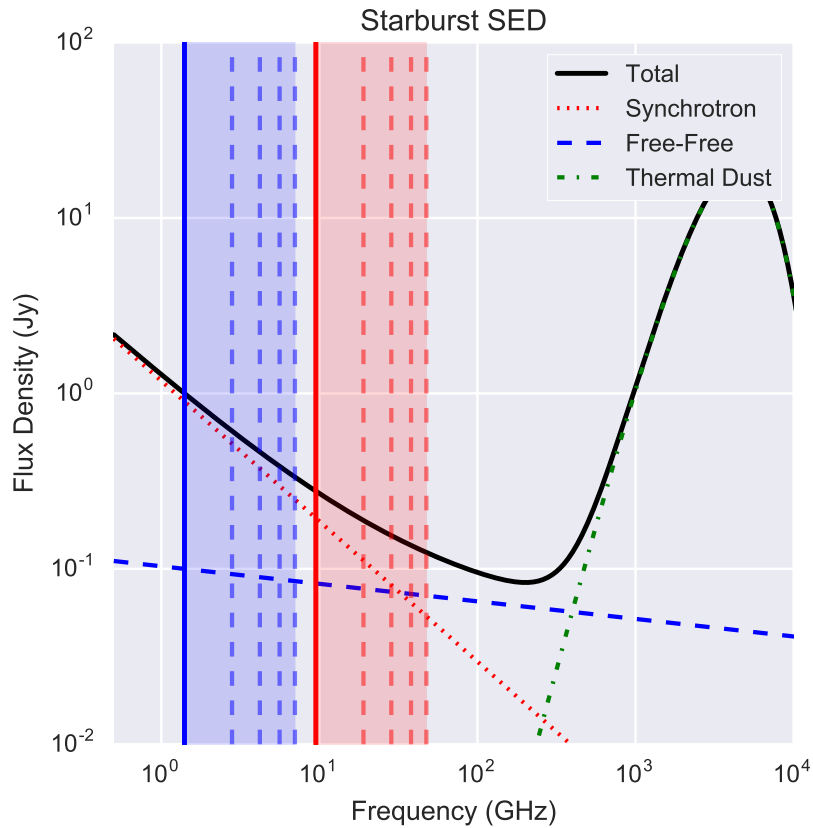


Figure 1.7: The observed radio-continuum and infrared spectrum of an assumed starburst galaxy based on M82 (see Fig. 1; Condon, 1992). The solid blue and red vertical lines represent the observed 1.4 and 9.5 GHz, respectively. The corresponding vertical dashed lines represent the rest frame frequency observed at a  $z$  of 1, 2, 3, and 4 moving from left to right.

Not included in the model presented in Figure 1.7 are the effects of inverse-Compton scattering, which have the effect of suppressing synchrotron emission at preferentially higher frequencies as a function of increasing redshifts, as well as known variability of the synchrotron spectral index.

Free-free emission is a process mostly taken to be associated with HMS formation (unlike synchrotron emission, which is also produced by AGN activity), and with increasing frequencies, becomes a larger component of the observed radio continuum Murphy (2009). It represents an ideal tracer of star formation for the SKA era.

Few studies have investigated the free-free emission component despite it being a near-instantaneous tracer of star formation with a fixed spectral index. Price and Duric (1992) investigated a sample of 31 galaxies with frequency data covering 408 MHz to 10.7 GHz. They found that with a modest frequency sampling the synchrotron and free-free components could be separated, and these model derivatives formed tight correlations with the far-infrared regions. The decomposition of synchrotron and free-free radio components by Niklas et al. (1997) also showed similar results, in that the individual components also form correlations with the far-infrared regions. This approach is limited by the availability of high frequency data, without which the free-free component can only be loosely constrained by the regions of the radio continuum that are overwhelmingly synchrotron in nature.

Observing resolved regions of star formation at a high frequency, where free-free emission can be directly observed, offers another opportunity to characterise radio continuum star formation rate indicators. Murphy et al. (2011) and Murphy et al. (2012) both used the Green Bank Telescope to acquire photometry at 33 GHz, a region where free-free emission begins to dominate over the steep spectrum synchrotron processes. In particular, Murphy et al. (2012) derived and calibrated radio continuum tracers of star formation that are independent of the far-infrared to radio correlation. They crafted an SFR indicator that weighs the observed radio continuum against the expected thermal fraction at a particular frequency. Approaching the problem in this direction requires an assumption of continuous star formation above 30 Myr because there is a time delay between the synchrotron and free-free emission tracers of star formation.

### 1.3 The Far-Infrared to Radio Correlation

A tight relationship exists between the far-infrared and radio continuum emission of galaxies. Typically, the correlation is taken as the far-infrared emission between 42.5 to 122.5  $\mu\text{m}$  (based on the 60 and 100  $\mu\text{m}$  IRAS measurements) and 1.4 GHz luminosities (Yun et al., 2001) but has also been shown to be present at 10  $\mu\text{m}$  (van der Kruit, 1973), total infrared luminosities (Bell, 2003), and 4.8 GHz (de Jong et al., 1985). The correlation has proved to be remarkably tight and present over many orders of magnitude and Hubble galaxy types (Helou et al., 1985; Condon, 1992; Yun et al., 2001).

One of the largest investigations of the FRC was work performed by Yun et al. (2001). In

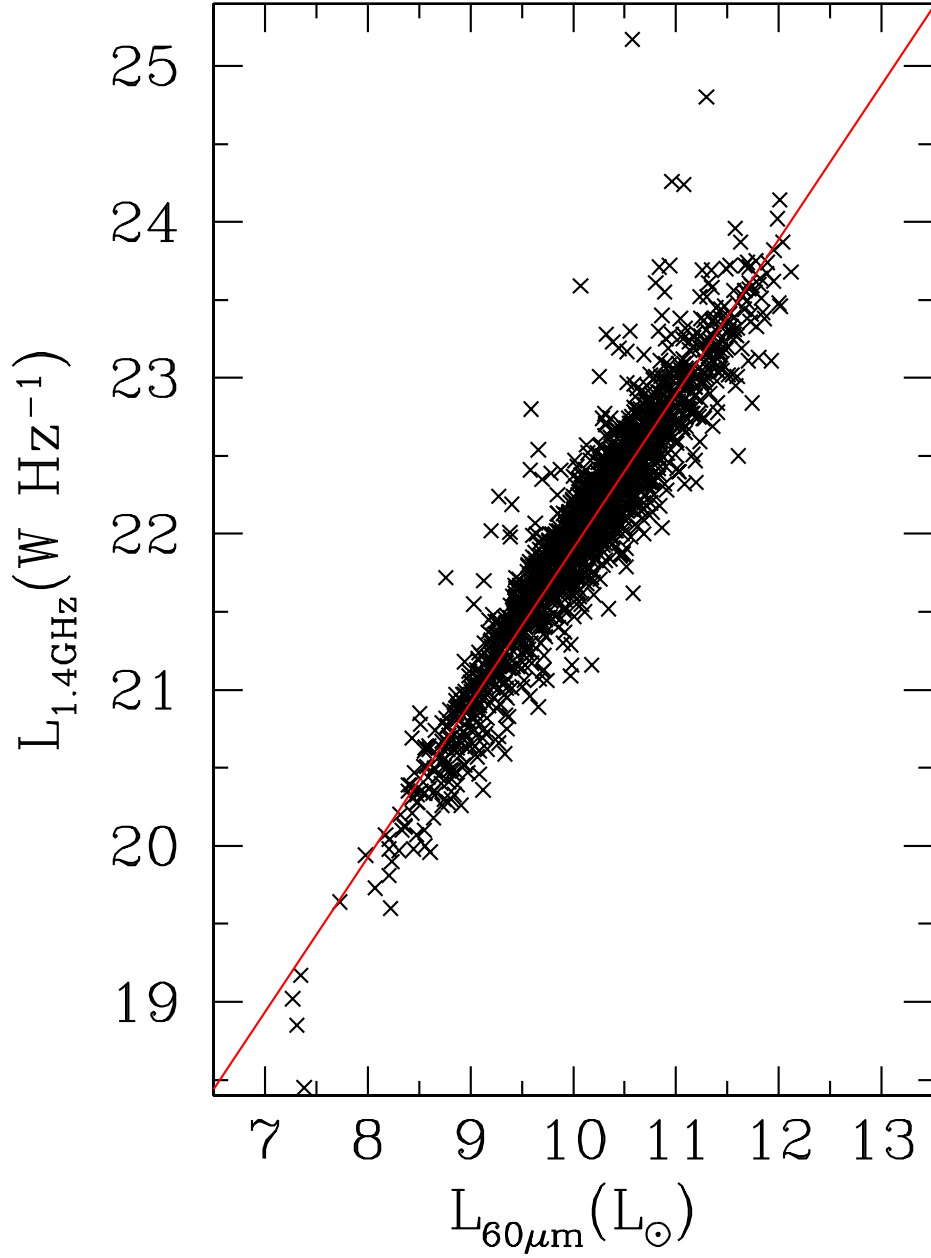


Figure 1.8: The observed far-infrared to radio correlation between the  $60\mu\text{m}$  and  $1.4\text{GHz}$  luminosities of 1,809 objects. A line of best fit, shown as the overlaid red line, represents a simple linear regression whose slope was found to be near unity. This figure has been taken from Yun et al. (2001) with minor editorial changes.

their study, they cross referenced the *IRAS* bright 2 Jy redshift sample (Strauss et al., 1990, 1992; Fisher et al., 1995) and NVSS. Figure 1.8 shows the observed FRC between the 60  $\mu\text{m}$  and 1.4 GHz luminosities of 1,809 galaxies they investigated. Using these objects, they fit a near-linear relation, formally constrained as

$$\log(L_{1.4\text{GHz}}) = (0.99 \pm 0.01) \log(L_{60\mu\text{m}}/L_{\odot}) + (12.07 \pm 0.08). \quad (1.16)$$

When first published by van der Kruit (1971) and van der Kruit (1973), it was initially unclear exactly how the two processes were so tightly coupled. Since then, significant work has gone into explaining the underlying physical drivers. Most models have tied the correlation to star formation, specifically H<sub>2</sub> formation. As mentioned in §1.2.6, the remarkably tight relation of the FRC has been exploited to calibrate radio-continuum star formation rate indicators (Condon, 1992; Yun et al., 2001).

Reliable tracers of star formation based on synchrotron radio-continuum emission are critically dependent on the FRC and require it to maintain its near-linear profile across all luminosities and redshifts. However, evidence already exists that suggests that the intrinsic nature of the FRC

- may not directly capture the true star formation rate of objects, and
- evolves as a function of redshift.

Bell (2003) investigated the FRC with a sample of galaxies that had far-ultraviolet, optical, infrared, and radio datasets. He found that at low luminosities, the far-infrared was not a reliable tracer of star formation because the dust clouds are optically thin to the UV. Consequently, star formation traced purely by far-infrared emission *underestimates* the true star formation rate of an object. Following this, if the radio continuum and specifically the synchrotron component at low frequencies, were accurate tracers of star formation, then there should be clear evidence of curvature at the low luminosity end of the FRC. The fact that the FRC is seen as linear implies that there is also a ‘suppression’ mechanism associated with the synchrotron component that would also cause radio-based star formation tracers to underestimate the true star formation rate. Bell (2003) suggests that because these low luminosity galaxies are smaller in size, this mechanism could be attributed to cosmic rays escaping the galaxies before they gyrate among the large-scale magnetic fields to produce synchrotron emission. The fact that these losses are roughly equal, thereby saving the linear shape of the FRC, is sometimes referred to as a ‘cosmic conspiracy.’

One of the initial interpretations of the FRC was described as being a manifestation of galaxies being efficient ‘calorimeters’ by Voelk (1989). A calorimeter is a tool that measures



the energy of particles. For this scenario, galaxies have to be optically thick to ensure that (1) all UV emission from young stars is reradiated as infrared by heated dust, and (2) all cosmic rays accelerated by supernova interact with magnetic fields to produce synchrotron emission. As both processes are tied to the SFR of HMS, FRC is a natural consequence.

Detailed analytical modelling presented by Lacki et al. (2010) and Lacki and Thompson (2010) further explained this concept while attempting to describe the ‘cosmic conspiracy’. Similar to Bell (2003), they argued that for galaxies with low surface density, the losses of cosmic rays escaping are balanced by low dust opacity. Although additional electron cooling processes such as Bremsstrahlung emission, ionisation, and inverse-Compton (IC), may decrease the radio emission in dense starbursts, these are countered by the production of secondary electron/positrons and the dependence of synchrotron frequency on energy (Lacki et al., 2010). Broadly, these various components are balanced to produce a linear FRC in the local Universe.

With increasing redshifts though a speculation that the FRC will evolve also exists. Murphy (2009) argued that although negligible in the local Universe, IC losses off the cosmic microwave background become an important consideration at increasing redshifts. IC scattering cools the same cosmic ray electrons that produce synchrotron emission, and with increasing redshifts, scale in proportion to  $(1+z)^4$ . For the FRC to maintain its constant ratio, at redshifts above 3, galaxies require magnetic field strengths over  $\sim 50 \mu\text{G}$  (Murphy, 2009).

In the literature, there is observational evidence that both confirms and rejects the FRC evolution hypothesis. Both Ivison et al. (2010) and Mao et al. (2011) explored FRC at high redshift ( $z > 1$ ) through stacking analysis. Although high redshift objects may not be directly observed because of their faint emission, the statistical average of undetected galaxies can be crafted by stacking images, centred on known positions of objects, on top of one another and taking a median or mean statistic for each pixel. The main conclusions of both studies were that there appears to be no change in the evolution in the FRC, although Ivison et al. (2010) did report a tentative break at a redshift of  $L_{1.4\text{GHz}} \sim 10^{22.7} \text{W Hz}^{-1}$ .

More recently, studies have reported statistically meaningful detections of FRC evolution. Calistro Rivera et al. (2017) performed broadband SED modelling using the radio continuum (four measurements below a frequency of 1.4 GHz), infrared, and UV wavelength bands. Of the roughly 1550 objects studied in the Boötes field, roughly half were modelled as being star forming in nature. The  $q$  parameter for these objects was derived ( $q$  being the logarithmic ratio between a component of the infrared region, typically the integrated 8-1000  $\mu\text{m}$  flux and the 1.4 GHz flux density) and compared with redshift data. This comparison was found, within a Bayesian framework, to require a redshift dependent term for adequate modelling, implying evolution in the FRC. The cornerstone figure of their work is included in this dissertation as

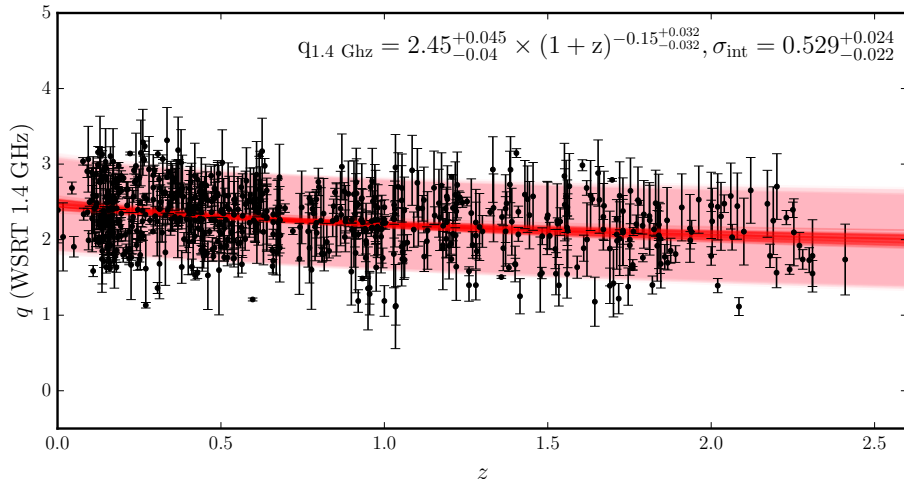


Figure 1.9: The modelled evolution of the infrared to radio correlation from Figure 14 of Calistro Rivera et al. (2017). The  $q_{1.4\text{GHz}}$  parameter is the logarithmic ratio between the integrated 8-1000  $\mu\text{m}$  infrared flux and 1.4 GHz flux density. Regions highlighted in red represented the likelihood regions modelled by Monte-Carlo simulations of the equation included in the upper right-hand of the figure. Black markers and their error bars were obtained by modelling the SED of objects in the Boötes field.

Figure 1.9.

These contradictory results suggest that the FRC is more complicated than originally thought and that perhaps the underlying physics is incomplete or misunderstood. Although in terms of the local Universe, the FRC and the radio continuum star formation tracers based on it have proved to be excellent tools to assess star formation, simple extrapolations into the high redshift Universe are not likely to be robust or reliable.

## 1.4 This Dissertation

### 1.4.1 Overview

Over the next decade, a series of new radio telescopes, built upon the most recent advances in technology, including Phased Array Feeds (Jeffs et al., 2008) and wide correlator broadband backends (Wilson et al., 2011), will become (or have already become) fully operational. Instruments including the low frequency MWA (Lonsdale et al., 2009; Tingay et al., 2013), the Low Frequency Array (van Haarlem et al., 2013), the Australian Square Kilometre Array Pathfinder (DeBoer et al., 2009; Schinckel and Bock, 2016), MeerKAT (Jonas, 2009), and the Karl G. Jansky VLA (Perley et al., 2011) are beginning to explore an entirely new volume of the Universe.

This work explores the radio continuum of local, luminous star forming galaxies, which can be considered an ideal representative sample of the types of faint, distant and highly active

SFGs that are expected to be revealed in the next generation of all-sky surveys.

Earlier studies of starburst galaxies have shown complex behaviour that requires a set of broadband radio frequency data to model and understand. Condon and Yin (1990) observed Markarian 325 with the VLA at 1.46, 4.85, and 8.4 GHz. In conjunction with other single dish data from 1.4 to 10.7 GHz, the authors constructed a radio-continuum model that describes the shape of the starburst. Functionally, their model consisted of a variable power law and normalisation component to account for the synchrotron spectrum and a second normalisation parameter for a fixed, near flat power law describing free-free emission.

Condon (1992) extended the work by Condon and Yin (1990) to include the effects of free-free absorption. Free-free absorption occurs when synchrotron emission passes through a region of thermal free-free emission. The effect suppresses synchrotron at a roughly exponential rate until a turnover in the spectrum has been reached. Subsequently, this model has become the basis for future studies investigating SFG. As a non-exhaustive list, key studies include Price and Duric (1992), Niklas et al. (1997), Clemens et al. (2010), Murphy et al. (2012), and Murphy et al. (2013).

Of particular relevance to this thesis are the effects of free-free absorption. Intense starburst galaxies, similar to those that are studied as part of this dissertation, have shown exceptionally complex behaviour that typically is not normally considered in more normal objects. Anantharamaiah et al. (2000) examined the radio continuum of Arp 220, the closest ULIRG and found that the radio recombination lines suggested three distinct turnovers caused by free-free absorption. When integrated over by a large radio synthesised beam, these turnovers result in ‘kinks’ in the radio continuum. Similarly, Clemens et al. (2010) investigated the radio continuum of 20 Luminous Infrared Galaxy (LIRG) ( $L_{40-120\mu\text{m}} > 10^{11} L_{\odot}$ ) and ULIRG ( $L_{40-120\mu\text{m}} > 10^{12} L_{\odot}$ ) from low (244 MHz) to high ( $> 23$  GHz), although rather sparsely with as few as four measurements. Their modelling and analysis also indicated the presence of multiple turnovers in the unresolved radio continuum, which the authors attribute to distinct regions of free-free absorption suppressing the synchrotron emission process.

For the future radio surveys that will be conducted by the next generation of radio telescopes to characterise the SFH of the Universe robustly, SFG themselves must be well understood. Our current set of radio-continuum tracers of star formation have worked well for objects in the immediate, local Universe, not only because the physics is well understood, particularly at low frequencies, but also because they are readily observable in large numbers. Scaling our understanding of these tracers to high redshifts requires a strong handle on the physics across a broad frequency range and higher-order complexities that would be shifted to lower observed frequencies.

Using robust statistical methods, I aim to characterise the overall shape over a broad contiguous frequency range to constrain the thermal free-free component of SFG. This type of emission has a flat spectral index and directly traces current star formation rates. Understanding its behaviour and how to calibrate it as an SFR indicator will be an exceptionally powerful tool for future high redshift surveys.

Initially, I explore a sample of twelve ultra-luminous infrared galaxies. These galaxies were selected to match the sample by Braun et al. (2011). The Australia Telescope Compact Array (ATCA) was used to collect 6 GHz of data spread across central frequencies of 2.1, 5.5, and 9.0 GHz. Once imaged, I collected the peak brightness of each source in our sample. Using these measurements, I then applied least-squares regression using a simple two power-law component model, representing the distinct steep spectrum synchrotron and flat spectrum free-free emission processes. I also constrained a modified blackbody model to all available infrared measurements for these galaxies.

I found that this sample of galaxies resides at the brightest tail of the FRC. The same modelling approach was then applied to 22 objects in the literature, which allowed me to explore how the synchrotron and free-free components constrained with the simple model behave as a function of increasing luminosity. Despite uncertainty from the modelling, arising mostly from sparse frequency sampling, I found that similar to earlier studies, there exists a strong relationship between the far-infrared and the decomposed radio-continuum components.

While investigating these sources, I noted that the signal-to-noise ratio (SNR) and the limited frequency sampling were significant hindrances. This was primarily due to the faintness of these objects, requiring a significant amount of observing time to improve upon. For this reason, I designed a new experiment that focussed that on a relatively nearby set of LIRGs.

The second sample of objects in this thesis was observed with a collection of telescopes producing a rich dataset. They were selected to be representative of the types of SFGs to be detected in future surveys. Using radio-continuum observations from ATCA, data obtained through a proposal I designed, which was awarded competitive time, I have collected 18.432 GHz of data across nine central frequencies from 2.1 to 46 GHz. These data were obtained with a variety of array configurations. Complimentary low frequency observations from the MWA covering 70 to 200 MHz were also incorporated into the final radio-continuum dataset.

With these radio-continuum data, I could produce a series of SEDs, which show interesting features that are not modelled by a simple power law. I found that at low frequencies, a clear flattening or turnover feature often occurs. Using a Bayesian framework for model fitting and selection, I attributed these effects to free-free absorption. For a significant fraction of sources in this sample, I also observed that with increasing frequencies, there is a clear steepening,

which is not expected given that the steep spectrum synchrotron emission should quickly be overwhelmed by free-free processes. I attribute this steepening to multiple regions of star formation.

Optical spectroscopy data were collected using the 2.3 metre Australia National University WiFeS for these sources. WiFeS, with its large  $38'' \times 25''$  field of view, could observe the spatially resolved objects with a single exposure. Between its red and blue arms, data covering 3300 to 9000 Å were obtained.

Applying the penalised pixel fitting (PPXF) algorithm to the summed spaxels in the datacube, I found strong stellar line detections. These lines include the Balmer series, which trace the same emitting matter as free-free emission. Applying dust corrections to the attenuated lines produces a measure independent from the FRC, which can be used to calibrate SFR measures.

For sources with sufficient signals, PPXF was applied to individual spaxels in the datacube. Analysis of these data for a selection of sources revealed clumps of stellar line emission and disturbed morphologies. This implies multiple regions of star formation, which may have been triggered by recent merger events. These distinct clumps support radio-continuum modelling, where a strong evidence of multiple emitting components can be found.

### 1.4.2 Challenges in this Thesis

The SFH of the Universe has been characterised well at redshifts below 2, but existing tracers of star formation are increasingly compromised at its earliest epochs.

UV emission tracers require space-based satellites to avoid the atmospheric opacity of Earth. Although UV emission is *direct*, making it in principle an excellent, prompt tracer, the presence of intermediary dust obscures a fraction of this light. A dust correction therefor needs to be derived and applied, which is increasingly difficult to apply when complex dust geometries and compositions, which cannot be resolved, obscure the light.

Similar to UV tracers, optical recombination lines, the most prominent of which being  $H\alpha$ , are tied to the ionisation rate of young stars. When unobscured, they are reliable, well-understood tracers. However, like UV emission, when obscured by dust, the *observed* recombination line no longer indicates the actual rate of star formation. Although the degree of dust obscuration can be characterised through a combination of methods, again, in the high redshift Universe, the methods are increasingly compromised and difficult to reliably apply. Forbidden lines, namely [OII], can probe higher redshifts, but they are not directly a product of star formation with tracers only being empirically calibrated. Furthermore, they are susceptible not only to dust attenuation but also to metallicities within the host system.

Infrared tracers of star formation are well calibrated and understood. Unlike UV and recombination methods, discussed previously, dust is mostly optically thin to infrared emission. The difficulty arises when the infrared SED comprises multiple components, including a cooler component whose dust is heated by an older stellar population, and a warmer component made up of hot, young HMS, and when in the presence of AGN, a third component with temperatures as high as  $\sim 100$  K. Apart from having to observe infrared emission from orbit, the main difficulty of infrared-based star formation tracers is that the telescopes are limited by confusion noise, as opposed to instrumental noise.

Radio-continuum emission offers a superb method for characterising the star formation rates of high redshift objects. Critically, radio emission is not affected by dust attenuation, making it an *unbiased* measure of star formation. Once the next generation of radio-continuum telescopes become operational, the earliest epochs of the Universe may be probed with a reliable indicator.

The issue explored in this thesis is how the radio continuum can be exploited to provide excellent characterisations of the star formation compatible with the high redshift Universe. Our current understanding of the physics that drive the radio continuum suggests that corrections have to be made to typical tracers currently used in the literature. Not only does the observed radio continuum become increasingly free-free, caused by the higher frequency continuum being shifted to lower frequencies, but it is also thought that inverse-Compton losses, which scale in proportion to  $(1+z)^4$ , will increasingly suppress the synchrotron emission at preferentially higher frequencies.

Exploring the radio continuum in representative sources is perhaps one of the most effective ways of characterising the behaviour of SFG, particularly those with high star formation rates ( $> 1000 M_{\odot} \text{ year}^{-1}$ ) that will be revealed by future radio continuum surveys.

### 1.4.3 Significance of this Work

Over the coming decade, a series of new radio-continuum surveys will begin to explore the high redshift Universe for the first time. The main driver of these new science products is merely new and updated technologies. For instance, the VLA, having had its correlator upgraded, operates as a completely new instrument (Perley et al., 2009). With wider spectral bandpasses and improved digital backends, the instrument is an order of magnitude more sensitive post-upgrade.

The National Radio Astronomy Observatory (NRAO) has for this reason begun a multi-year programme, dubbed the Very Large Array Sky Survey (VLASS), that will survey the radio continuum sky north of  $-40^{\circ}$  across a frequency of 2 to 4 GHz. With an estimated final sensitivity of  $64 \mu\text{Jy}$  and resolution of  $2.5''$ , this project will be near seven times more sensitive

than unresolved point sources and will have approximately 18 times more resolving power than the NVSS (Condon et al., 1998), which is the previous all-sky radio-continuum survey performed with the VLA before its upgrade.

In the Southern hemisphere, significant international investment has facilitated the construction of a series of next-generation telescopes. The Murchison Widefield Array (MWA), located in Western Australia, has been exploring the low frequency sky at frequencies between 80 to 320 MHz. The Galactic and Extragalactic All-sky MWA Survey (GLEAM) has had its full data release in Hurley-Walker et al. (2017), where 307455 sources were detected with 20 flux density measurements from 72 to 231 MHz. At the same site, the Australian Square Kilometre Array Pathfinder (ASKAP) instrument is nearing its completion (DeBoer et al., 2009; Schinckel and Bock, 2016). One of its key science programmes is the Evolutionary Map of the Universe (EMU) (Norris et al., 2011). Using the phased array feed receivers developed for ASKAP, the 30 square degree instantaneous field of view will be able to rapidly survey the southern sky. Throughout its complete project, with an expected one sigma RMS of  $\sim 10 \mu\text{Jy}$ , over 70 million objects will be detected.

What is particularly exciting about these new all-sky continuum surveys is the types of objects that will be detected. With the added sensitivity from modern technology, these surveys will detect predominately SFG out to moderately high redshifts. Existing radio-continuum surveys are limited to observing such objects in the local Universe, typically at redshifts below  $z < 0.15$ .

Radio-continuum emission, being free from the effects of dust obscuration, offers the most reliable method for characterising star formation rates in the earliest epochs of the Universe. In this space, optical and infrared tracers of this process either suffer from difficulties to characterise or unknown degrees of dust attenuation or are simply unuseable because of confusion.

At present, exploiting the radio-continuum information to probe these earliest epochs of the Universe requires considerable care and revision. As outlined previously, it is expected that our current set of radio-continuum star formation rate indicators will require re-calibration for the high redshift Universe. This re-calibration is not a straightforward problem as a collection of distinct effects need to be considered. This dissertation aims to characterise the radio-continuum components that make up the typical SFG that these future surveys will reveal.

Characterising the unique components of the radio continuum and how they relate to star formation will be a critical first step for correctly interpreting the outputs of deep, all-sky radio-continuum surveys in the future.

# Chapter 2

## Radio-Continuum Emission of Ultra-Luminous Galaxies

The work in this chapter (excluding §2.1 below) has been published in the ‘Monthly Notices of the Royal Astronomical Society’ journal as Galvin et al. (2016). Excluding minor editorial changes, I have further added and expanded Sections 2.4, 2.7.3.1 and 2.8.2.

### 2.1 Motivation

When designing surveys, an essential trade-off that has to be considered is the area footprint of the desired survey and the desired sensitivity of the survey. As telescope time is a finite resource, these two properties are at odds with one another. Either time is spent on a small number of sky positions to maximise sensitivity or more sky positions are visited with only a short integration time for each position. This scenario is illustrated in Figure 2.1, which highlights a collection of radio-continuum surveys and compares their sizes against their sensitivities.

Historically, all-sky radio surveys, which are shallow in terms of sensitivity but large in the pure number of detections, are predominately made up of AGN type sources, with detected SFG being relatively rare and almost certainly local. Future all-sky surveys being conducted with modern technologies will be far more sensitive to the population of distant SFG and will be the predominant class of objects detected. For instance, the EMU (Norris et al., 2011) is one of the key programmes of the ASKAP instrument. With a  $1\sigma$  sensitivity of  $10 \mu\text{Jy beam}^{-1}$ , it is expected to detect 70 million objects. Below a flux density of  $0.5 \text{ mJy}$  at  $1.4 \text{ GHz}$ , the majority of detected objects will be SFG with a median redshift of 1.1 (Norris et al., 2011).

Understanding the broadband radio continuum is an important step to prepare for these future surveys. For example, the observed  $1.4 \text{ GHz}$  emission of a source at a redshift of 4



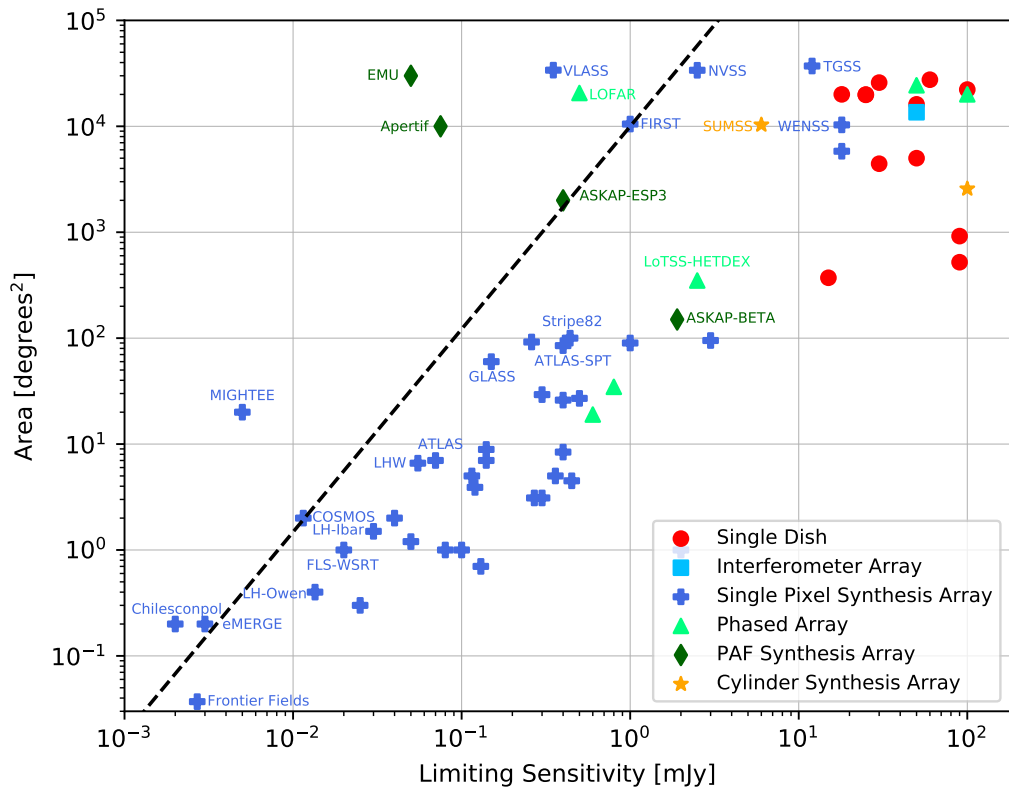


Figure 2.1: A comparison between the sensitivities and coverage area of existing radio-continuum surveys and planned surveys to be conducted by the next generation of radio-continuum instruments. This figure has been recreated using data collated by Norris et al. (2013).

corresponds to a rest frame frequency of  $1.4 \times (1 + 4) = 7$  GHz. At these frequencies, there is a significant shift in the composition of the radio continuum. The steep spectrum synchrotron emission quickly becomes swamped by the flat spectrum free-free emission. Inverse-Compton scattering also begins to suppress the high frequency synchrotron spectrum, whose effects are thought to scale with redshifts (Murphy, 2009). This further complicates the interpretation of radio emission of distant SFG.

## 2.2 Introduction

Radio-continuum surveys use, almost exclusively, the 1.4 GHz monochromatic luminosity of a galaxy to estimate SFRs. At this frequency, the spectrum predominantly comprises non-thermal synchrotron radiation caused by ultra-relativistic electrons accelerated by the shocks of supernovae of massive stars ( $M > 8M_{\odot}$ ) and may be used as a non-instantaneous tracer of star formation. However, a better tracer would be the thermal free-free emission originating from HII regions surrounding high-mass stars. This type of emission is not only a direct tracer of current SFRs of high-mass stars but also becomes the dominant emission mechanism at  $\nu \geq 10$  GHz. Thus, the method has the advantage of being capable of probing higher redshifts (Murphy et al., 2015). It is expected that the deep extra-galactic radio surveys produced by the next generation of radio telescopes (e.g., ASKAP, MeerKAT, Jansky Very Large Array (JVLA), LOFAR, eMERLIN, and SKA) will predominantly comprise powerful SFG at  $z \geq 1$  with radio luminosities consistent with very high formation rates ( $\geq 100 M_{\odot} \text{ yr}^{-1}$ ).

For radio observations to be a useful tracer for the SFR of distant, high redshift galaxies, first, it is necessary to understand how the radio-continuum components themselves may be related to the far infrared of the galaxy and how their relative strengths can be measured. Ultra-luminous infrared galaxies (ULIRGs;  $L_{\text{IR}}^{8-1000\mu\text{m}} > 10^{12} L_{\odot}$ ) represent classes of sources most analogous to those anticipated in future radio-continuum surveys. Price and Duric (1992) studied 31 galaxies in the local Universe ( $z < 0.02$ ) and showed that not only can the non-thermal and thermal components be separated but they can also form their own correlations with far-infrared luminosities. Understanding how these components evolve with increasing redshift will be required so that the FRC can continue to be used as a measure of SFR at high redshifts.

In this study, the FRC in a set of distant ULIRGs was investigated at redshifts between 0.2 and 0.5. Spectral energy distributions were constructed across multiple frequency domains to further investigate the astrophysics of FRC. A flat Universe was assumed, where  $\Omega_m = 0.3$ ,  $\Omega_{\lambda} = 0.7$ , and  $H_0 = 70 \text{ km s}^{-1} \text{ Mpc}^{-1}$ .

Table 2.1: A summary of the sources observed in the ATCA project C2696 and used in this study. The FIR luminosities have been taken from Spoon et al. (2009) and Braun et al. (2011). Phase calibrators used for each source are also provided.

Source Name IRAS	RA (J2000) (h m s)	Dec (J2000) ( $^{\circ}$ ' ")	$z$	$L_{\text{FIR}}$ $\log(L_{\odot})$	Phase Calibrator
F00183–7111	00:20:34.7	–70:55:27	0.327	12.95	2353–686
F00320–3307	00:34:28.5	–32:51:13	0.439	12.68	0008–264
00397–1312	00:42:15.5	–12:56:03	0.262	12.67	0036–216
00406–3127	00:43:03.2	–31:10:49	0.342	12.58	0008–264
02262–4110	02:28:15.2	–40:57:16	0.493	12.50	0153–410
02456–2220	02:47:51.3	–22:07:38	0.296	12.58	0237–233
03538–6432	03:54:25.2	–64:23:45	0.301	12.62	0235–618
F04565–2615	04:58:34.7	–26:11:14	0.490	12.78	0528–250
07380–2342	07:40:09.8	–23:49:58	0.292	12.54	0733–174
23515–2917	23:54:06.5	–29:01 :00	0.335	12.52	008–264
F23529–2119	23:55:33.0	–21:03:09	0.429	12.67	008–264
F23555–3436	23:58:06.5	–34:19:47	0.490	12.63	008–264

## 2.3 Sample Selection

We focussed on ULIRGs in this study as their high FIR emission indicates strong star formation, making them useful analogues of higher redshift galaxies which dominate deep radio surveys. A redshift range beyond the local Universe was chosen,  $z > 0.1$ , as local ULIRGs are rare and not always representative of distant ULIRGs.

Our sample was taken from Braun et al. (2011), who observed the CO(1-0) transition in a set of 11 ULIRGs. Braun et al. identified these sources from the NASA/IPAC Extragalactic Database (NED)<sup>1</sup> using the following criteria:

1. FIR detections at 60 and 100  $\mu\text{m}$
2. Spectroscopic redshifts between 0.2 and 0.5
3. Far-infrared luminosities (40-500  $\mu\text{m}$ )  $L_{\text{FIR}} > 10^{12.5} L_{\odot}$
4. Declinations south of  $-12^{\circ}$

The sample used here is based on that from Braun et al. (2011) who considered all objects matching these selection criteria known by NED at the time that the project was planned. IRAS F00183–7111 was also included as it has been extensively studied in the literature (Spoon et al., 2009; Norris et al., 2012; Mao et al., 2014, and references within). Referring to the Revised *IRAS* Faint Source Redshift Catalog (RIFSCz; Wang et al., 2014), an additional seven sources matching these criteria were noted and a further 12 with photometric redshifts that lie within this redshift range. To assess whether our sample was representative of all available sources, a series of two-sided Kolmogorov-Smirnov tests were performed on key intrinsic parameters listed

<sup>1</sup><http://ned.ipac.caltech.edu/>



Figure 2.2: Four of the six 22-m dishes that make up the ATCA radio interferometer. Image has been used with permission from Graeme Wong.

in the RIFSCz. The p-values returned in these tests showed no evidence to suggest that there is a different underlying distribution for most properties, including dust mass, as well as proxies for stellar mass and extinction. The FIR luminosities and derived SFRs of the sources matching these criteria, but not included here, are marginally lower ( $\sim 0.1$  dex) on average. However, this is not a significant bias because the goal of this project is to observe the most highly SFG.

## 2.4 ATCA data reduction

The 12 ULIRGs were observed using the Australian Telescope Compact Array (ATCA; Wilson et al., 2011), under project C2696 (PI: N. Seymour), for a 20-hour period during August 2012. Using the two 2.048 GHz spectral windows provided by the Compact Array Broad-band Backend (CABB) filters, a total 6.144 GHz of spectral information was collected at the central frequencies of  $\nu = 2.1, 5.5$  and 9.0 GHz. Although compact array broadband backend (CABB) can record 4.096 GHz simultaneously between the two independent spectral windows, at 2.1 GHz, the entire bandpass is covered by a single CABB spectral window, making the second window redundant.

ATCA is an Australia Telescope National Facility managed instrument located at the Paul Wild Observatory. It is made up of six 22-m dishes that have been configured to operate as a radio interferometer. Five of the six dishes (shown in Figure 2.2) reside on a stretch of a 3-km railway track, enabling them to be repositioned to form different array configurations. The sixth antenna is fixed a further 3-km away from the end of the railway track.

Band	Frequency Range (GHz)	Primary Beam	System Temperature (K)
L/S (16 cm)	1.1–3.1	42′–15′	45
C/X (4 cm)	3.9–11.0	12′–4′	36
K (15 mm)	16.0–25.0	2′	60
Q (7 mm)	30.0–50.0	70″	112
W (3 mm)	83.0–105.0	30″	724

Table 2.2: An overview of the frequency coverage offered by ATCA.

The sparsely distributed 6A ATCA array configuration was used to isolate sources in the sky. At  $\nu = 2.1$  GHz, this array configuration provides a restoring beam of roughly  $7''$ , although this can vary depending on the  $uv$ -sampling of our sources or the numbers of sub-bands imaged. This size was sufficient to prevent confusion effects, and based on the extracted source sizes for our sample from the SuperCosmos project (Hambly et al., 2001), avoids resolving out extended source structure, assuming that radio source sizes are no larger than optical source sizes.

Each source was observed for approximately 11 minutes at 2.1 GHz and 45 minutes at 5.5 and 9.0 GHz. Sources were observed at least five times at each frequency throughout the observing run. Short snapshots were ideal for this project because only an accurate flux density measurement for each source was needed. Shown in Figure 2.3 is the typical  $(u, v)$ -coverage obtained for each of the 12 objects.

The primary calibrator PKS1934-638 was used to provide flux density and bandpass calibration solutions across all central frequencies. A total of eight phase calibrators were used because of the spatial distribution of the programme sources (see Table 2.1).

The MIRIAD (Sault et al., 2011) and KARMA (Gooch, 2011) software packages were used for data reduction and analysis. The guided automated flagging MIRIAD routine PGFLAG was used in conjunction with more traditional MIRIAD flagging and calibration tasks for initial data reduction. Given the large fractional bandwidth provided by CABB, MFCLEAN (Sault and Wieringa, 1994) was used to deconvolve the multi-frequency synthesised dirty map.

Once a calibration solution was applied to each of the observations programme sources, they were then imaged individually across all frequency bands ( $\nu = 2.1, 5.5$ , and  $9.0$  GHz) using their complete bandwidth ( $\Delta\nu = 2.048$  GHz, minus the edge channels automatically flagged by ATLOD). A Briggs robust parameter corresponding to natural weighting was used to provide the maximum signal-to-noise. These preliminary images were produced to compare the calibration among the  $uv$ -datasets. During this stage, sources IRAS 07380-2342 and IRAS F23555-3436 (marked as black arrows in Figure 2.4) were not detected at any frequency. There is a known infrared AGN component associated with IRAS 07380-2342 (Han and Han, 2012, and references therein), boosting its FIR luminosity. The radio luminosity inferred from the FIR luminosity

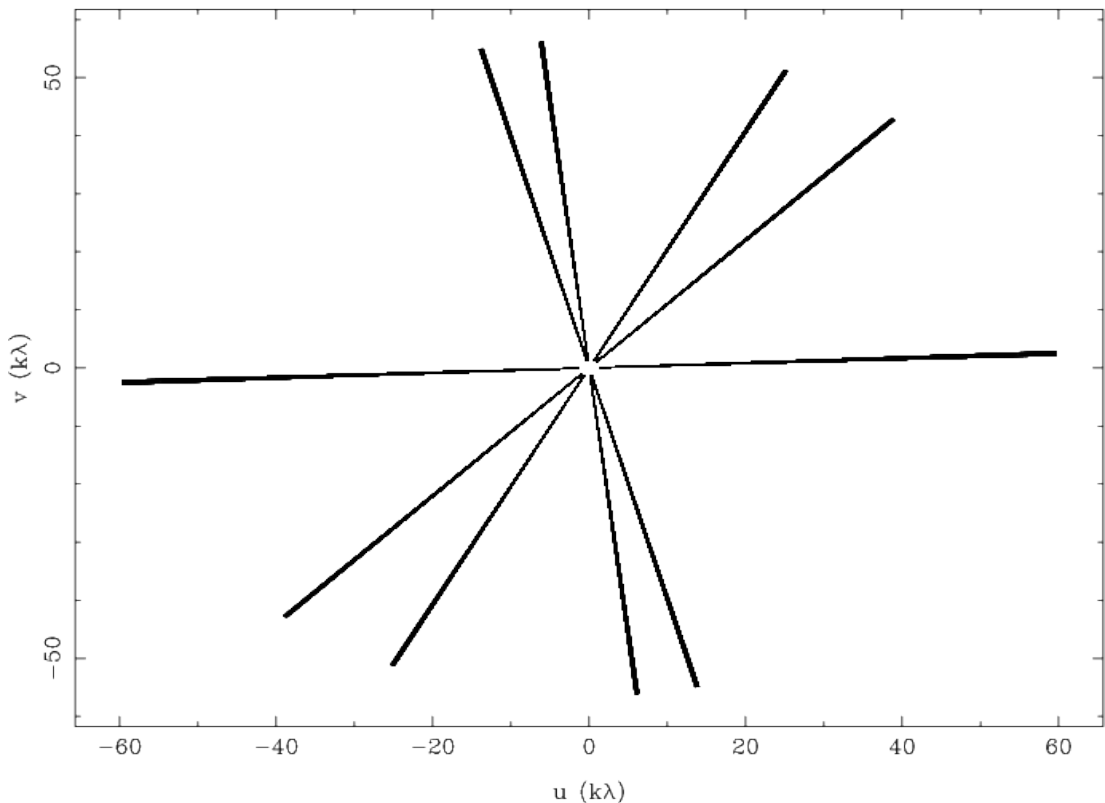


Figure 2.3: The typical  $(u, v)$ -coverage obtained for sources.

without the AGN component is consistent with our detection limits.

Images were then created with a consistent angular resolution to prevent emission from the extended structure being resolved at higher frequencies. This was done by convolving each of the higher frequency images with a Gaussian kernel derived so that each image shared a common resolution that matched the resolution of the lowest frequency image. We convolved the image to the desired resolution as the  $uv$ -coverage of the data is limited and clipping the  $uv$ -data would have increased the difficulty of the imaging processes of the remaining  $uv$ -data.

By exploiting the  $\sim 2$  GHz bandwidth provided by the ATCA CABB system, we could produce a more densely sampled SED of most sources. If there was a sufficient signal-to-noise ratio (SNR) in the fitted point source model ( $\text{SNR} > 8$ ) for a particular image, its corresponding  $uv$ -file would be split into two half bandwidth files. This  $uv$ -splitting considered the flagged channels to ensure that all split  $uv$ -files had a similar number of useable, unflagged channels. These two new  $uv$ -files were then re-imaged with natural weighting and their fitted flux values replaced the original. Again, the MIRIAD task CONVOL was used to produce a consistent resolution among image sets.

Point source models were fitted to each source of interest using the MIRIAD task IMFIT to estimate their integrated flux density and uncertainties. With such an approach, sources with

high SNR were split into multiple data points, which could be used to better constrain the radio-continuum emission models. A complete list of all convolving beam sizes and flux density measurements are presented in Table 2.3.

Table 2.3: ATCA integrated flux density measurements and convolving beam sizes obtained using the procedure described in §3.4.1.3. For each point, we list the central frequency, the measured flux density, and its associated uncertainty. In the case where there was sufficient signal-to-noise ratio to divide a  $uv$ -file into multiple segments, the extracted values for each segment are listed and are separated by a comma. Source names marked with a  $\dagger$  indicate which sources were not detected, and the values listed represent  $3\sigma$  upper limits only, while \* indicates sources classified as radio loud AGN based on their  $q$  parameter.

Source Name	Beamsize '' $\times$ ''		L Band 1.1 to 3.1 GHz		C Band 4.5 to 6.5 GHz		X Band 8.0 to 10.0 GHz
IRAS 00397–1312	23.6 $\times$ 6.2	$\nu$ (GHz)	2.10		5.50		9.00
		$S$ (mJy)	2.66		1.88		1.07
		$\Delta S$ (mJy)	0.47		0.14		0.18
IRAS 00406–3127	9.3 $\times$ 6.6	$\nu$ (GHz)	2.10		5.50		9.00
		$S$ (mJy)	3.40		1.78		1.22
		$\Delta S$ (mJy)	0.52		0.09		0.17
IRAS 02262–4110	13.0 $\times$ 7.9	$\nu$ (GHz)	1.60, 2.55		5.05, 6.00		9.00
		$S$ (mJy)	1.49, 1.31		0.79, 0.82		0.77
		$\Delta S$ (mJy)	0.22, 0.16		0.10, 0.11		0.05
IRAS 02456–2220	23.0 $\times$ 10.5	$\nu$ (GHz)	1.41, 1.87, 2.33, 2.79		5.04, 5.96		9.00
		$S$ (mJy)	2.92, 3.30, 2.55, 2.12		1.66, 1.37		1.18
		$\Delta S$ (mJy)	0.67, 0.40, 0.45, 0.46		0.28, 0.29		0.21
IRAS 03538–6432*	16.6 $\times$ 7.8	$\nu$ (GHz)	1.29, 1.52, 1.75, 1.98, 2.22, 2.45, 2.68, 2.91	4.69, 4.92, 5.15, 5.38, 5.62, 5.85, 6.08, 6.31	8.19, 8.42, 8.65, 8.88, 9.12, 9.35, 9.58, 9.81		
		$S$ (mJy)	44.80, 42.22, 37.29, 31.22, 29.33, 27.23, 23.94, 21.59	14.51, 13.79, 13.32, 12.75, 11.51, 11.12, 10.79, 9.60	7.31, 7.92, 7.09, 6.80, 6.40, 6.49, 5.62, 4.83		
		$\Delta S$ (mJy)	1.72, 1.14, 0.98, 0.63, 0.79, 0.64, 0.65, 0.64	0.23, 0.25, 0.29, 0.28, 0.23, 0.24, 0.20, 0.21	0.35, 0.31, 0.30, 0.33, 0.29, 0.40, 0.28, 0.30		
IRAS 07380–2342 $\dagger$	—	$\nu$ (GHz)	2.10		5.50		9.00
		$S$ (mJy)	<1.51		<0.86		<1.49
		$\Delta S$ (mJy)	—		—		—
IRAS 23515–2917	10.4 $\times$ 6.2	$\nu$ (GHz)	2.08		5.52		9.02
		$S$ (mJy)	1.40		1.24		0.92
		$\Delta S$ (mJy)	0.27		0.10		0.13
IRAS F00183–7111*	13.4 $\times$ 8.2	$\nu$ (GHz)	1.25, 1.49, 1.73, 1.96, 2.20, 2.43, 2.67, 2.91	4.69, 4.93, 5.17, 5.40, 5.64, 5.87, 6.11, 6.35	8.19, 8.43, 8.67, 8.90, 9.14, 9.37, 9.61, 9.85		
		$S$ (mJy)	306.50, 305.10, 264.70, 246.00, 225.30, 203.80, 189.30, 175.70	103.20, 97.99, 93.10, 87.15, 83.44, 79.47, 74.54, 71.06	51.81, 50.99, 48.87, 47.61, 46.21, 44.70, 43.03, 41.78		
		$\Delta S$ (mJy)	5.63, 3.56, 2.20, 1.89, 1.62, 1.55, 1.54, 1.47	1.23, 1.12, 0.98, 0.83, 0.81, 0.75, 0.77, 0.72	0.87, 0.92, 0.89, 0.87, 0.85, 0.72, 0.76, 0.87		
IRAS F00320–3307	8.9 $\times$ 6.7	$\nu$ (GHz)	2.08		5.52		9.02
		$S$ (mJy)	1.47		1.29		0.60
		$\Delta S$ (mJy)	0.07		0.07		0.05
IRAS F04565–2615*	18.7 $\times$ 10.8	$\nu$ (GHz)	1.41, 1.87, 2.33, 2.79	4.81, 5.27, 5.73, 6.19	8.31, 8.77, 9.23, 9.69		
		$S$ (mJy)	11.02, 9.47, 7.41, 7.05	4.36, 4.33, 3.79, 3.41	2.94, 2.58, 2.71, 2.06		
		$\Delta S$ (mJy)	0.63, 0.25, 0.32, 0.32	0.14, 0.15, 0.15, 0.15	0.24, 0.23, 0.31, 0.32		
IRAS F23529–2119*	25.4 $\times$ 9.6	$\nu$ (GHz)	1.41, 1.87, 2.33, 2.79	4.81, 5.27, 5.73, 6.19	8.31, 8.77, 9.23, 9.69		
		$S$ (mJy)	13.37, 9.69, 8.77, 6.81	5.60, 4.63, 4.63, 4.22	3.75, 2.90, 2.93, 2.46		
		$\Delta S$ (mJy)	1.86, 0.94, 0.92, 0.65	0.24, 0.22, 0.19, 0.16	0.30, 0.17, 0.38, 0.43		
IRAS F23555–3436 $\dagger$	—	$\nu$ (GHz)	2.10		5.50		9.00
		$S$ (mJy)	<1.05		<0.50		<0.93
		$\Delta S$ (mJy)	—		—		—



## 2.5 The Far-IR to Radio Correlation

The FRC has been parameterised by ‘ $q$ ’, defined as the logarithmic ratio between the far-infrared flux and 1.4 GHz flux density of an object:

$$q \equiv \log \left( \frac{\text{FIR}}{3.75 \times 10^{12} \text{ W m}^{-2}} \right) - \log \left( \frac{S_{1.4 \text{ GHz}}}{\text{W m}^{-2} \text{ Hz}^{-1}} \right) \quad (2.1)$$

where  $S_{1.4 \text{ GHz}}$  is in units of  $\text{W m}^{-2} \text{ Hz}^{-1}$ , and FIR is defined as

$$\text{FIR} \equiv 1.26 \times 10^{-14} (2.58 S_{60 \mu\text{m}} + S_{100 \mu\text{m}}) \text{ W m}^{-2} \quad (2.2)$$

where  $S_{60 \mu\text{m}}$  and  $S_{100 \mu\text{m}}$  are the 60 and 100  $\mu\text{m}$  band flux densities from *IRAS* in Jy (Helou et al., 1985).

Most SFGs have a  $q$  scattered around a value of 2.34. IR-excess sources ( $q \gtrsim 3$ ) may be highly obscured compact starburst galaxies or dust-enshrouded AGN, and some of the dispersion may be influenced, in part, by variations in extinction and dust temperature. Radio-excess objects ( $q \lesssim 1.6$ ) are caused by excess radio emission originating from an AGN component in the galaxy (Yun et al., 2001).

It is important to ensure that our sample remains free of radio loud AGN that may otherwise contaminate the results. To help determine the nature of each galaxy included in this study, their  $q$  values were evaluated. Initially, we estimated the flux density at 1.4 GHz, in the observed frame, using a fitted power-law to all radio-continuum measurements ( $S_\nu \propto \nu^\alpha$ ). Flux densities at 60 and 100  $\mu\text{m}$  from the *IRAS* faint source catalogue were used to calculate the FIR according to Equations 2.1 and 2.2. Although there would be a small change in  $q$  if it were derived in the rest frame (Seymour et al., 2009), there would be no change to how we have classified the sources in this study.

We compared our sources to those listed by Yun et al. (2001), who produced an infrared flux-limited ( $S_{60 \mu\text{m}} \geq 2 \text{ Jy}$ ) complete sample of 1 809 galaxies by identifying radio-counterparts for galaxies in the *IRAS* Redshift Survey using the NRAO VLA Sky Survey (NVSS) up to a redshift of 0.15. Our samples, however, exhibited redshifts in the range of  $0.2 < z < 0.5$  and targeted ULIRGs specifically, meaning that the far-infrared luminosity is often orders of magnitude higher than those seen by Yun et al. (2001). This infrared emission implies a higher SFR for these galaxies, as well as increased radio luminosities.

Of the Yun et al. (2001) sample<sup>2</sup> 98% of sources had  $L_{60 \mu\text{m}}$  luminosities that (once converted back to flux densities) were 2.6 times less than their reported  $S_{60 \mu\text{m}}$  fluxes. For this reason,

<sup>2</sup>the catalogue obtained from the ViZieR (<http://vizier.u-strasbg.fr>) catalogue service appears to be the source of the inconsistency, as Yun et al. (2001) present the correct luminosities in their study

Table 2.4: All additional flux density measurements collected from NED for each of the sources observed as a part of this study. For a measurement to be included, it was required to be a broad band measurement in the ranges  $0.1 \text{ GHz} < \nu < 100 \text{ GHz}$  or  $37 \mu\text{m} < \lambda < 500 \mu\text{m}$ . References are Helou and Walker (1988, HW88); Moshir (1990, M90); Condon et al. (1998, C98); Klaas et al. (2001a, K01); Spoon et al. (2009, S09).

Source Name IRAS	Frequency (GHz)	Flux Density (mJy)	Telescope	Reference
F00183–7111	1920.00	540.00±80.00	MIPS	S09
	3000.00	1190.00±119.00	IRAS	M90
	4200.00	1500.00±225.00	MIPS	S09
	5000.00	1200.00±83.70	IRAS	M90
F00320–3307	3000	869±156	IRAS	M90
	5000	430±60	IRAS	M90
00397–1312	1.40	2.80±0.50	VLA	C98
	3000	1900±170	IRAS	M90
	5000	1830±130	IRAS	M90
00406–3127	1.40	5.1±0.6	VLA	C98
	1470	320±100	ISO	K01
	1620	440±130	ISO	K01
	1860	630±190	ISO	K01
	2520	770±230	ISO	K01
	3000	994±169	IRAS	M90
	5000	718±57	IRAS	M90
02262–4110	3000	517±124	IRAS	M90
	5000	390±40	IRAS	M90
02456–2220	3000	1270±150	IRAS	M90
	5000	816±49	IRAS	M90
03538–6432	1470.00	620.00±186.00	ISO	K01
	1620.00	850.00±255.00	ISO	K01
	1860.00	1070.00±321.00	ISO	K01
	2520.00	1370.00±411.00	ISO	K01
	3000.00	1300.00±195.00	IRAS	M90
	5000.00	988.00±49.40	IRAS	M90
F04565–2615	3000.00	577.00±133.00	IRAS	M90
	5000.00	296.00±32.60	IRAS	M90
07380–2342	3000	3550±280	IRAS	HW88
	5000	1170±90	IRAS	HW88
F23529-2119	3000.00	627.00±132.00	IRAS	M90
	5000.00	327.00±55.50	IRAS	M90
23515–2917	1470	330±100	ISO	K01
	1620	480±140	ISO	K01
	1860	640±190	ISO	K01
	2520	800±240	ISO	K01
	3000	1060±160	IRAS	M90
	5000	648±58	IRAS	M90
F23555–3436	3000	711±157	IRAS	M90
	5000	305±54	IRAS	M90

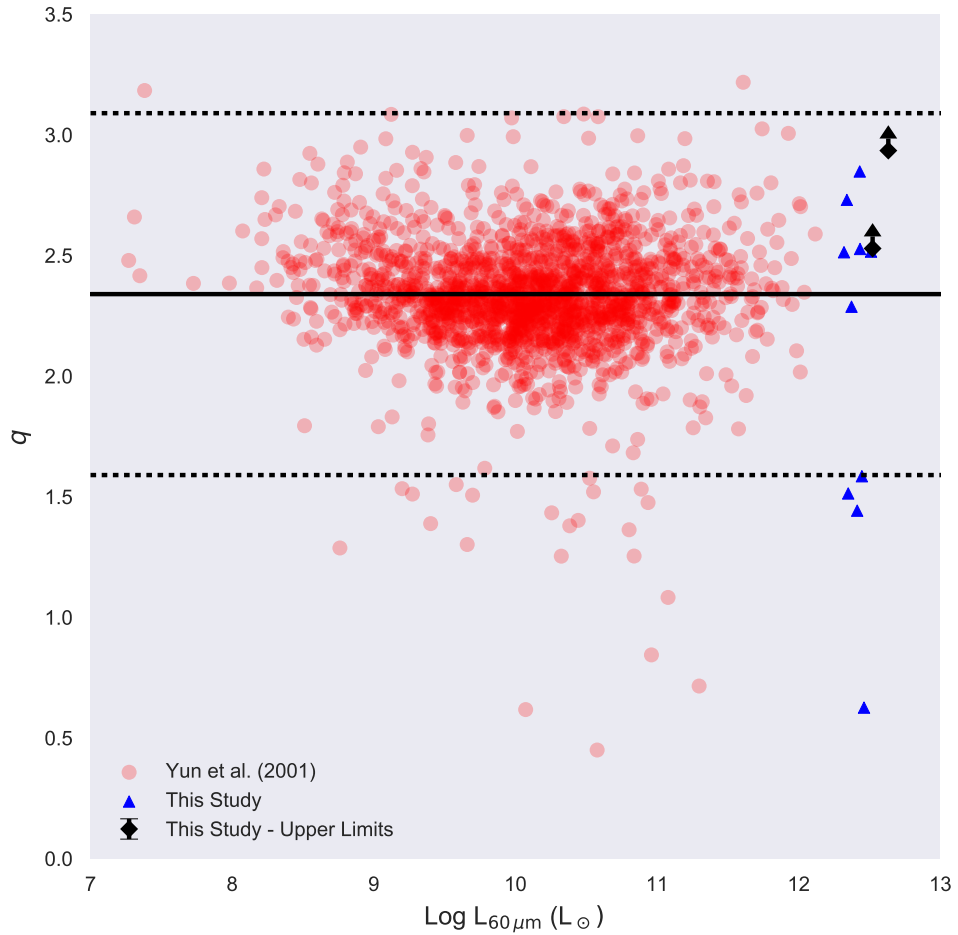


Figure 2.4: A comparison between the  $60 \mu\text{m}$  luminosity and the derived  $q$  of sources from Yun et al. (2001) and this study. The solid horizontal line represents the mean  $q = 2.34$ , as calculated by Yun et al. (2001). The dotted lines represent the radio-excess (*below*) and IR-excess (*above*) objects, defined as three times the standard deviation (SD) of  $q$  ( $\text{SD} = 0.25$ ) from the Yun et al. (2001) sample.

we re-derived the  $60\ \mu\text{m}$  luminosities of the Yun et al. sample using their reported  $60\ \mu\text{m}$  flux densities and distances. These re-derived  $60\ \mu\text{m}$  luminosities are used throughout this paper.

We compared derived  $q$  values of sources in Yun et al. (2001) and from this study as a function of *IRAS*  $60\ \mu\text{m}$  luminosities (Figure 2.4). We defined regions outside three standard deviations of the mean of the  $q$  parameter of samples from Yun et al. (2001) as being either radio or infrared excess. Sources 03538–6432, F00183–7111, F04565–2615, and F23529–2119 were classified as radio excess ( $q \lesssim 1.6$ ), which is indicative of AGN activity, and were thus excluded from subsequent analysis throughout this study. Sources classified as radio excess were consistent with the definition used by Yun et al. (2001), who defined radio-excess sources as those with five times the expected luminosity following the linear FRC. After removing these four sources, eight remained in our sample, two of which were radio upper limits. We also inspected the *IRAS*  $25\ \mu\text{m}$  and  $60\ \mu\text{m}$  flux density ratios and IR template fitting from Wang et al. (2014) of sources in our sample. Of the six sources with radio detections that were not classified as radio excess, only *IRAS* 02262-4110 possessed an elevated  $S_{25\mu\text{m}}/S_{60\mu\text{m}}$  ratio and included an AGN component in the fitted IR templates. We subtracted the AGN template (determined to be 6% and 2% at  $60\ \mu\text{m}$  and  $100\ \mu\text{m}$ , respectively) from the observed *IRAS*  $60$  and  $100\ \mu\text{m}$  flux densities which were then used throughout this study. All the remaining five sources had  $S_{25\mu\text{m}}/S_{60\mu\text{m}}$  ratios below 0.3 and were fitted exclusively by starburst type infrared templates. This indicates that there is no detectable AGN component in the  $60$  and  $100\ \mu\text{m}$  *IRAS* flux densities in the remainder of our samples. In terms of the radio-continuum, however, we could not completely dismiss the possibility of weak AGN contamination. Although the  $q$  parameter removes obvious radio loud AGN sources, a low luminosity AGN may be contributing a portion to the observed radio-continuum of sources in our sample. A review of the literature sources *IRAS* 00406–3127, *IRAS* 02262–4110, and *IRAS* 23515–2917 indicated that they have been classified as Seyfert type galaxies (Allen et al., 1991a; Klaas et al., 2001a; Véron-Cetty and Véron, 2006). To accurately characterise and correct for any AGN effects that may be present, we would need high resolution radio imaging to resolve the AGN core from extended star formation. Because we do not have these data, we have distinguished these three sources ‘Seyfert SFG’ in subsequent figures to avoid confusion.

### 2.5.1 Sources in Literature

Here, we briefly outline the literature available for the SFG and radio non-detection sources that remain in our sample.

*IRAS F00320–3307*: This source has not been classified in the literature. We classified it as SFG based on its location on the FRC.

*IRAS 00397–1312*: A compact starburst with clear PAH detections from the *Spitzer* spectrograph (Nardini et al., 2010).

*IRAS 00406–3127*: This has been classified as a Seyfert 2 type galaxy (Nardini et al., 2010). Roy et al. (1998) did not detect its radio AGN core using a 275 km array between the 64-m Parkes and 70-m Tidbinbilla antennae. Therefore, we assume that there is no significant radio AGN component in the observed radio-continuum.

*IRAS 02262–4110*: Véron-Cetty and Véron (2006) classified this object as a Seyfert 1 type galaxy based on the ratio of the  $H\beta/[OIII] \lambda 5007$  integrated line fluxes. However, given its soft X-ray luminosity, which is  $\log(L_x) = 45.1 \text{ erg s}^{-1}$ , and its power law exhibited from X-ray to FIR, this source could potentially be a broad line QSO. As its  $q$  parameter shows no excess emission, we assume that there is no significant AGN component that was observed in the radio-continuum. Likewise, the template fitting performed by Wang et al. (2014) suggests no significant AGN component in the FIR.

*IRAS 02456–2220*: There exists no classification of this source in the literature. We classified it as SFG based on its location on the FRC.

*IRAS 07380–2342*: This is one of the radio non-detected sources in our sample. Rowan-Robinson (2000) classified this object as a narrow-line AGN.

*IRAS 23515–2917*: A Seyfert 2 type galaxy (Nardini et al., 2010) that is possibly interacting with a nearby object (Allen et al., 1991b). This potential merger may have triggered a recent burst of star formation, causing the high luminosity seen in the radio spectrum and FIR. Its flat radio spectrum is currently being modelled as a starburst, in which optically thin free-free emission dominates across all frequencies. An alternative interpretation is that this flattening could be a result of the non-thermal component being suppressed by free-free absorption effects at the L band, thereby producing a higher thermal fraction. Comprehensive modelling would be needed with more complete radio-continuum data to analyse this alternate interpretation further.

*IRAS F23555–3436*: This is one of the radio non-detected sources in our sample, and there exists no classification of this source in the literature.

## 2.6 SED Modelling

We created comprehensive SEDs of each galaxy across the radio and infrared domains using ATCA CABB, *IRAS*, Infrared Space Observatory (*ISO*), and VLA data. These SEDs allowed the thermal, non-thermal, and dust emissivity components to be modelled and constrained.

## 2.6.1 Emission Models

### 2.6.1.1 Radio-Continuum

All galaxy radio SEDs were fitted with a SFG model, which is the sum of the thermal and non-thermal emission represented by two distinct power-law components (Condon, 1992, see Figure 1). This emission model was fitted to all ATCA and VLA flux density measurements in the range from 1.1 GHz to 10 GHz for each source. The emission model is

$$S_\nu(\nu) = A \left( \frac{\nu}{\nu_0} \right)^{\alpha_{\text{NT}}} + B \left( \frac{\nu}{\nu_0} \right)^{\alpha_{\text{T}}} \quad (2.3)$$

where  $\alpha_{\text{NT}}$  and  $\alpha_{\text{T}}$  are the spectral indices of non-thermal and thermal emission, assumed to be  $-0.8$  and  $-0.1$ , respectively, and  $A$  and  $B$  represent the fitted normalisation parameters. The reference frequency used,  $\nu_0$ , is  $1.4 \text{ GHz}/(1+z)$ .

The typical SFG model (Equation 2.3) is not an appropriate descriptor of the spectrum of sources with excess radio emission, which indicate a radio loud AGN component. Instead, an AGN model was fitted to their radio-continuum (Andreani et al., 2002). This expression can be described as a parabola-shaped curve in a log-log plane, as follows:

$$\text{Log}S_\nu(\nu) = C + \frac{1}{2D} (\text{Log}\nu - \text{Log}\nu_t)^2 \quad (2.4)$$

where  $\nu_t$  is 31.6 MHz and represents the frequency at which the plasma optical depth reaches unity (Andreani et al., 2002). The fitted free parameters were a normalisation factor,  $C$ , and the bend of the curve,  $D$ . Again, all flux density measurements in the range of 0.1 GHz to 10 GHz were used to constrain this model.

Depending on the overall SNR of the source in the radio domain, the number of data points to which this emission model was fitted varied. In the case of a weak source, as little as three data points ( $\Delta\nu = 2.048 \text{ GHz}$  for each of the three central frequencies) were used, whereas in the case of a high SNR source, as many as 24 data points ( $\Delta\nu = 256 \text{ MHz}$  for each of the 24 central frequencies) were used.

### 2.6.1.2 Infrared

In the infrared domain, a greybody emission model was fitted to the SED of each source and was used to describe the dust emissivity of each galaxy. A greybody model involves a modified blackbody, the emissivity of which is lower than 1 and is scaled with wavelength (Rouan, 2011).

The grey body model (Eq. 3.7) was fitted to the *IRAS* flux density measurements at  $\lambda = 60$  and  $100 \mu\text{m}$ , as well as any additional flux density measurements obtained from NED between

wavelengths of  $37\ \mu\text{m}$  to  $500\ \mu\text{m}$ .

$$S_\nu(\lambda) = N \times \left[ \left( \frac{60\ \mu\text{m}}{\lambda} \right)^{3+\beta} \times \frac{1}{e^{\frac{hc}{\lambda kT}} - 1} \right] \quad (2.5)$$

$S_\nu$  is the total power radiated in Jy at frequency  $\nu$  (in Hertz),  $T$  is the absolute temperature of the body in Kelvin,  $\beta$  is a power with a value between 1 and 2, representing the emissivity, and  $N$  is a normalisation.

Typically, this greybody model contains three free parameters ( $N$ ,  $\beta$ , and  $T$ ). As there were relatively few infrared flux density measurements that could be used, we assigned a fixed value of 1.5 to  $\beta$ . The remaining two parameters ( $T$  and  $N$ ) were allowed to vary for all greybody modelling that we performed.

### 2.6.1.3 SED Fitting

The Levenberg-Marquardt least-squares fitting algorithm was used to derive the best fit values for all emission models using all available flux density measurements in their observed frame of reference. We used the MPFIT algorithm (Moré, 1978; Markwardt, 2009) as implemented as the KMPFIT procedure in the KAPTEYN PYTHON module (Terlouw and Vogelaar, 2015) to constrain the radio-continuum and infrared modelling for these sources. Least-squares optimisation methods attempt to find the parameters,  $\theta$ , that minimise the  $\chi^2$  statistic,

$$\chi^2 = \sum_{i=0}^n \left( \frac{y_i - f(\theta, x_i)}{\sigma_i} \right)^2, \quad (2.6)$$

where  $x$ ,  $y$ , and  $\sigma$  are vectors of length  $n$  representing the frequency, flux, and associated flux uncertainty, respectively.  $f$  is the function that has to be optimised.

Using the optimised models, we estimated the 1.4 GHz and  $60\ \mu\text{m}$  rest frame flux densities, after shifting them to the observed frame. The final SEDs produced in this study are presented in Figures 2.5, 2.6, and 2.7 and comprise all flux density measurements used during emission modelling (see Tables 2.3 and 2.4), the best fit SFG, AGN, and greybody emission models. Although sources classified as AGN are not included in subsequent figures, we include their results here for completeness.

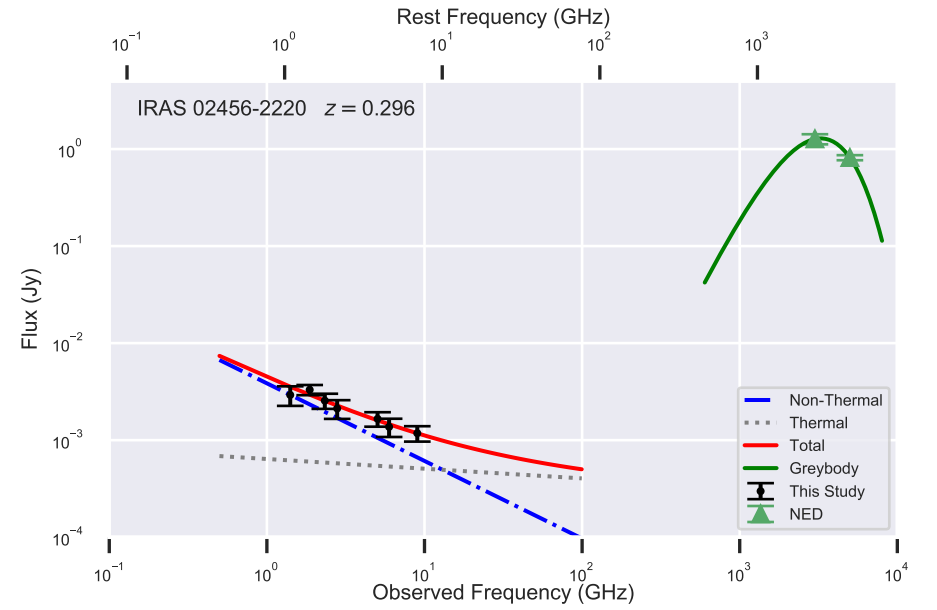
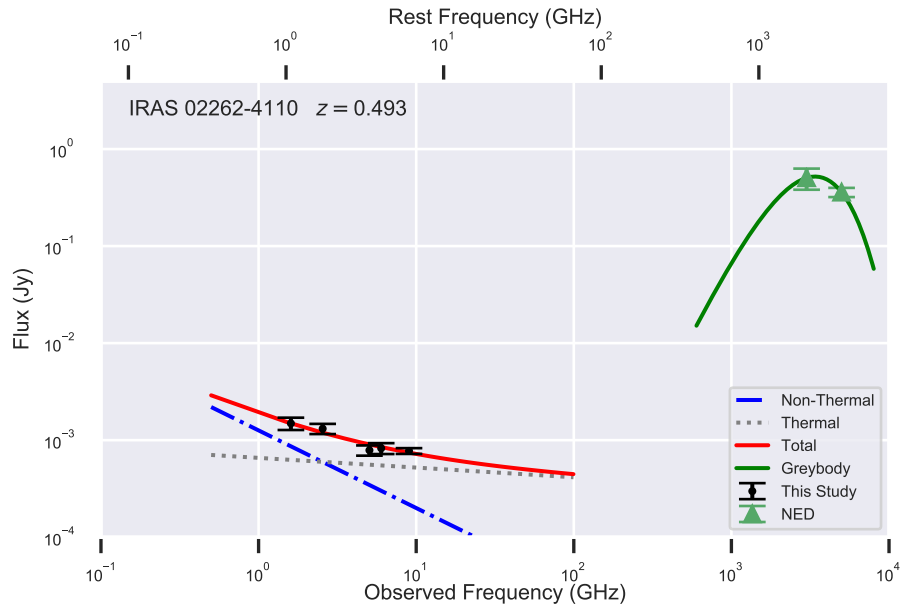
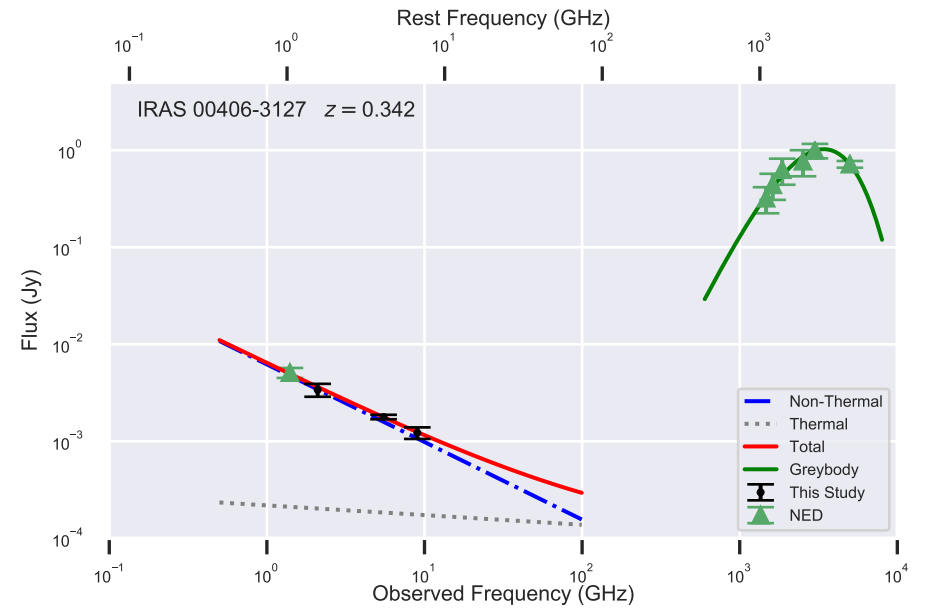
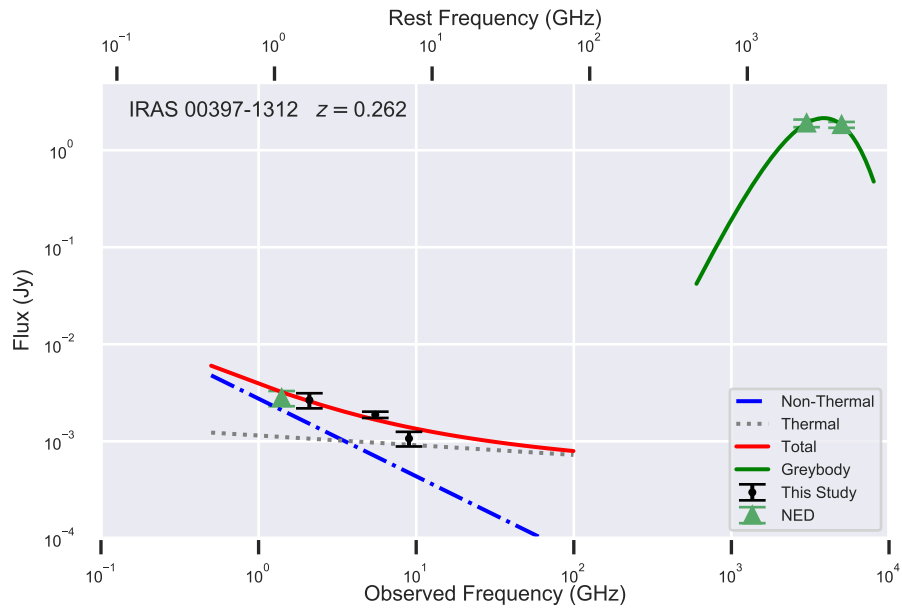


Figure 2.5: The SEDs of the SFGs from our ULIRG sample. These SEDs comprise all flux density measurements used during the emission modelling (see Tables 2.3 and 2.4), the SFG radio-continuum, and greybody emission models.



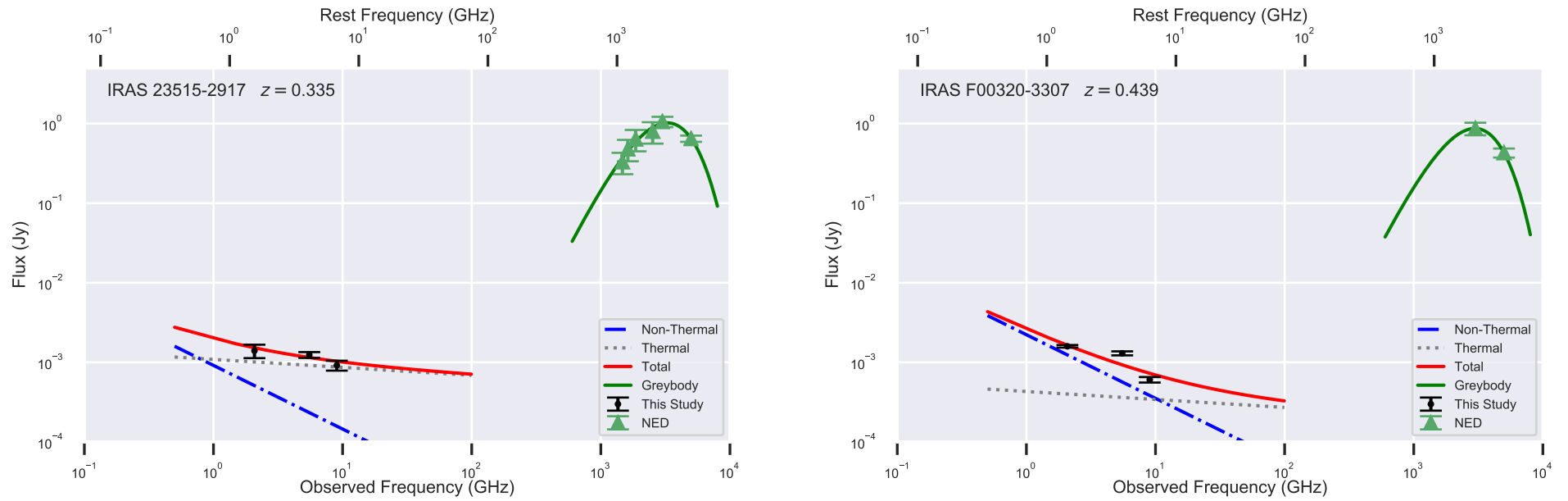


Figure 2.5 (cont.): The SEDs of the SFGs from our ULIRG sample. These SEDs comprise all flux density measurements used during the emission modelling (see Tables 2.3 and 2.4), the SFG radio-continuum, and greybody emission models.

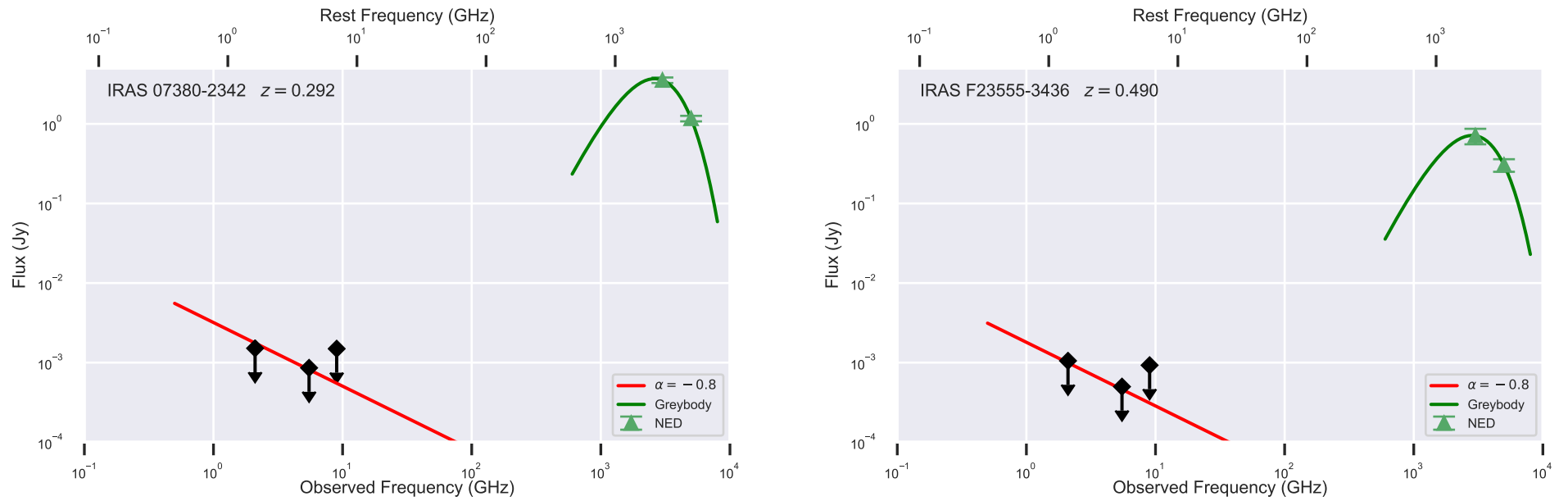


Figure 2.6: The spectral energy distributions of the radio non-detections (which is consistent with them being SFGs) from our ULIRG sample. These SEDs comprise all flux density measurements used during the emission modelling (see Table 2.4) and the fitted greybody emission model. The  $3\sigma$  upper limits are presented in sources with non-detections. The solid redline represents the scaled 5.5 GHz  $3\sigma$  upper limits assuming a spectral index of  $-0.8$ .

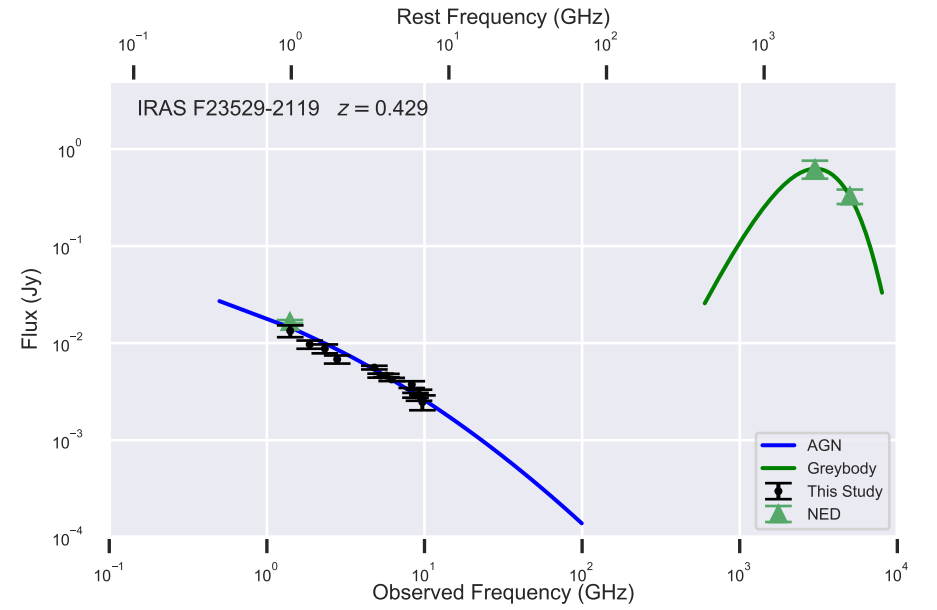
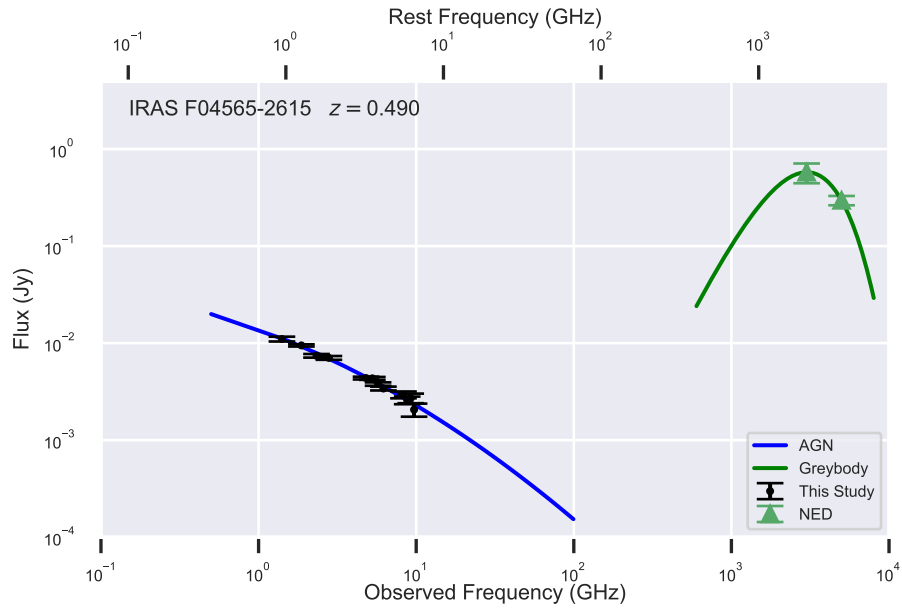
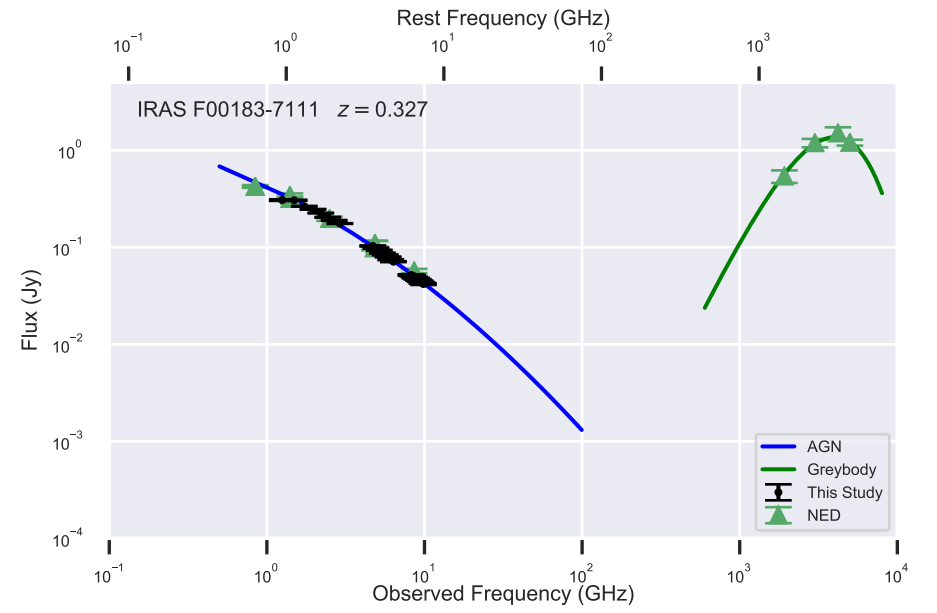
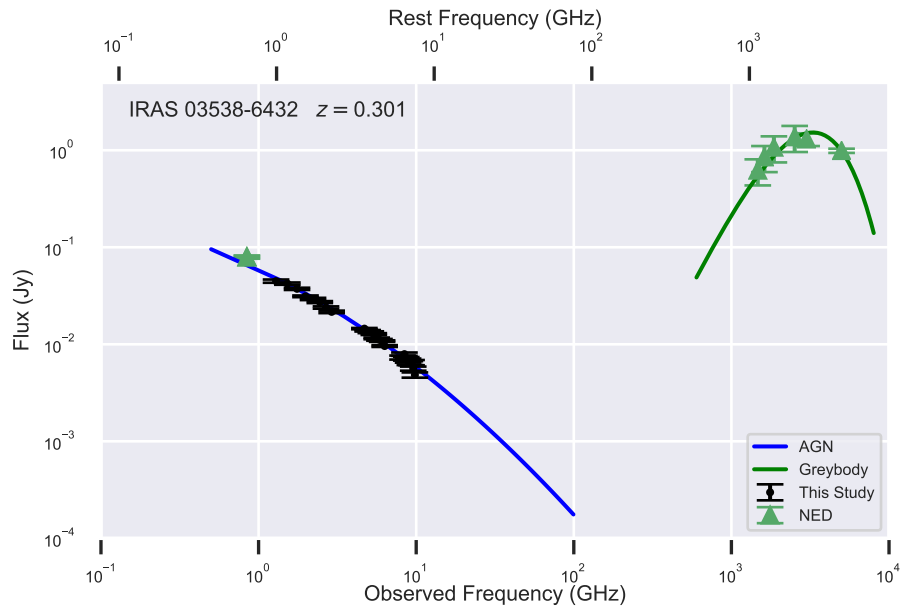


Figure 2.7: The spectral energy distributions of the AGNs from our ULIRG sample. These SEDs comprise all flux density measurements used during the emission modelling (see Table 2.4) and the fitted greybody emission model.

Source	Non-thermal	Thermal
IRAS	Normalisation	Normalisation
	(mJy)	(mJy)
F00320–3307	2.27±0.23	0.43±0.09
00397–1312	2.53±0.80	1.14±0.30
00406–3127	6.00±0.93	0.21±0.31
02262–4110	1.33±0.41	0.66±0.12
02456–2220	3.62±0.79	0.63±0.35
23515–2917	0.88±0.83	1.08±0.28

Table 2.5: The best fit normalisation parameters for the SFG emission model.

Source	DoF	Normalisation	Curvature	Reduced $\chi^2$
IRAS		(Jy)		
IRAS 03538–6432	24	-0.66±0.01	-1.97±0.00	4.99
IRAS F00183–7111	31	0.20±0.00	-1.99±0.00	7.88
IRAS F04565–2615	10	-1.42±0.03	-2.55±0.00	0.94
IRAS F23529–2119	11	-1.26±0.03	-2.36±0.00	2.81

Table 2.6: Best fit parameters for the AGN emission model. The uncertainties were derived during the fitting procedure.

## 2.7 Results

### 2.7.1 SED Fits

In Tables 2.5, 2.6, and 2.7, we present the fitted parameters and their uncertainties (where the uncertainty  $\sigma$  for parameter  $p$  is defined as  $\chi^2(p + \sigma) = \chi^2(p) + 1$ ; Bevington, 1969) which were derived from the fitting procedure. For four of the six sources, there were only two infrared flux density measurements available to constrain the greybody emission model, leaving no degrees of freedom. Table 2.7 includes both the fitted temperature ( $T$ ) parameter, derived using the least-squares fitting routine, and the rest frame temperature ( $T_e$ ), where  $T_e = T \times (1 + z)$ .

In total, six sources were fitted with an SFG emission model (see Table 2.5). Five of these six sources were dominated by synchrotron non-thermal emission, where the fitted uncertainties ranged between 2–30% of the corresponding best fit value. The fitted thermal components are not as well characterised because at low frequencies ( $\nu < 10$  GHz), the dominant emission mechanism is typically non-thermal. However, for the sixth source, IRAS 23515-2917, a strong thermal component can be observed with uncertainties similar to those of the best fit non-thermal components.

The rest frame dust temperatures (Table 2.7) for the six SFG type sources are fairly consistent and well constrained. Although we have restricted the parameter space by assigning a constant value to the dust emissivity  $\beta$  component, the temperatures agree with similar studies of starburst type objects with comparable luminosities (Yun and Carilli, 2002; Symeonidis et al., 2013; da Cunha et al., 2015).

Source IRAS	60 $\mu\text{m}$ Normalisation (Jy)	Fitted Temperature (K)	Rest Frame Temperature (K)
F00320–3307	0.76 $\pm$ 0.38	32.1 $\pm$ 2.4	46.2 $\pm$ 3.5
00397–1312	0.58 $\pm$ 0.15	41.6 $\pm$ 2.1	52.5 $\pm$ 2.7
00406–3127	0.48 $\pm$ 0.11	36.9 $\pm$ 1.5	49.5 $\pm$ 2.0
02262–4110	0.25 $\pm$ 0.16	36.6 $\pm$ 3.9	54.7 $\pm$ 5.6
02456–2220	0.74 $\pm$ 0.24	35.2 $\pm$ 1.8	45.6 $\pm$ 2.3
23515–2917	0.58 $\pm$ 0.13	35.3 $\pm$ 1.4	47.1 $\pm$ 1.9

Table 2.7: The best fit parameters for the greybody emission model. Models were constrained using all available flux density measurements in the range  $37 < \lambda < 500 \mu\text{m}$ . The Fitted Temperature is the  $T$  parameter derived during the fitting, whereas the rest frame temperature has an applied redshift correction such that  $T(1+z)$ .

## 2.7.2 Comparison to Yun et al. (2001) sample

The far-IR and radio luminosities calculated for sources in this project were compared to the sample compiled by Yun et al. (2001). This comparison (Figure 2.8) shows the SFGs from this study are in line with the FRC seen by Yun et al. (2001) with a small scatter. There is a deficit in the observed 1.4 GHz luminosity of the SFG from this study when compared with the expected 1.4 GHz luminosity based on the FRC. This can be attributed to our object selection method (see § 2.8).

Figure 2.8 includes the  $3\sigma$  1.4 GHz luminosity upper limits of the two sources that had no radio detections (IRAS 07380–2342 and IRAS F23555–3436). These upper limits were derived by scaling the  $3\sigma$  upper limits at 5.5 GHz to 1.4 GHz using a spectral index of  $-0.8$  ( $S_\nu \propto \nu^{-0.8}$ ) and applying a  $k$ -correction.

Because we re-derived the  $L_{60\mu\text{m}}$  values from the catalogue of Yun et al. (2001) (see §2.5), a new formal fit was calculated. To maintain consistency with Yun et al. (2001), no  $k$ -corrections were applied to sources in their sample. We also excluded AGN or outliers which would disproportionately affect the fitting routine based on their  $q$  value and luminosities. Specifically, sources were only included in the fitting process if they satisfied:

1.  $1.64 < q < 3.04$
2.  $6.5 < \log L_{60\mu\text{m}} < 13.5$
3.  $18.5 < \log L_{1.4\text{GHz}} < 25.5$

Applying these criteria to the original 1809 sources from Yun et al. (2001), 36 sources were removed. A formal fit to the remaining sources produced an observed radio-FIR luminosity correlation of

$$\log(L_{1.4\text{GHz}}) = 0.97 [\pm 0.01] \times \log\left(\frac{L_{60\mu\text{m}}}{L_\odot}\right) + 12.25 [\pm 0.07] \quad (2.7)$$

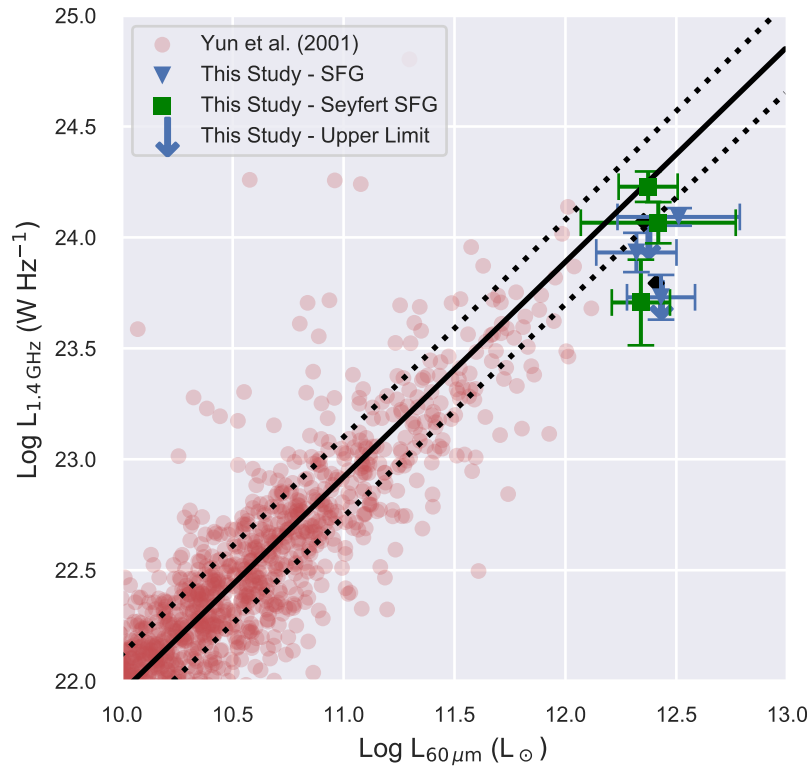


Figure 2.8: A comparison between the Yun et al. (2001) sample and those in this study. The solid and dotted lines represent the linear best fit and the uncertainty of the normalisation component of the Yun et al. (2001) sample. Radio and  $60\mu\text{m}$  luminosities of sources from this study have been  $k$ -corrected. Galaxies that were not detected in the radio in this project are represented by their 1.4 GHz luminosity upper limits, which have been scaled from their  $3\sigma$  5.5 GHz upper limits assuming a spectral index of  $-0.8$  and have been  $k$ -corrected.

Although the values of this formal fit are very similar to those of Equation 4 of Yun et al. (2001), there is a slight difference in the slope of the FRC, as well as a difference in the radio luminosity normalisation component corresponding to  $\sim 0.18$  dex. The fitted uncertainties of each free parameter are identical. We have included the normalisation uncertainties in Figure 2.8.

### 2.7.3 Decomposed Radio to Far-IR

To investigate the thermal and non-thermal radio-continuum properties of the Yun et al. (2001) sample, we cross referenced the 1809 sources in their sample to Dressel and Condon (1978), who used the Arecibo telescope to observe 2095 galaxies at  $\nu = 2380$  MHz, and the Green Bank 6 cm radio source catalogue (GB6; Gregory et al., 1996). We identified 22 sources common to all three catalogues using a matching radius of  $5''$  and  $20''$ . This provided us with three flux density measurements at  $\nu = 1.4, 2.38,$  and  $4.85$  GHz, from which we could obtain a spectral index and constrain the SFG emission model for these 22 sources.

#### 2.7.3.1 Thermal Fraction

As stated by Condon (1992), if integrated flux densities at three or four frequencies are used to fit the (unknown) non-thermal spectral index and the thermal fraction (defined as  $B/(A+B)$  from Eq. 2.3) simultaneously, the resulting non-thermal spectral index and thermal fraction are strongly correlated (Figure 2.9).

Here, we calculate the correlation between the thermal fraction and spectral index. Considering Equation 2.3 in terms of the thermal fraction  $TF$  at  $\nu_0$

$$S_\nu = S_{\nu_0} \left( TF_{\nu_0} \left( \frac{\nu}{\nu_0} \right)^{-0.1} + (1 - TF_{\nu_0}) \left( \frac{\nu}{\nu_0} \right)^{-0.8} \right) \quad (2.8)$$

and a simple power-law model of the form

$$S_\nu = S_{\nu_0} \nu^\alpha \quad (2.9)$$

then  $TF_{\nu_0}$  may be expressed in terms of the spectral index  $\alpha$  across frequencies  $\nu_0$  to  $\nu$  by

$$TF_{\nu_0} = \frac{\left( \frac{\nu}{\nu_0} \right)^{\alpha \nu_0} - \left( \frac{\nu}{\nu_0} \right)^{-0.8}}{\left( \frac{\nu}{\nu_0} \right)^{-0.1} - \left( \frac{\nu}{\nu_0} \right)^{-0.8}} \quad (2.10)$$

We have included this relationship in Figure 2.9, where the spectral index of Yun et al. (2001) sources are calculated over a frequency range of 1.4 to 4.85 GHz. Although this relationship is a product of the particular SFG emission model used, it may prove to be a useful diagnostic

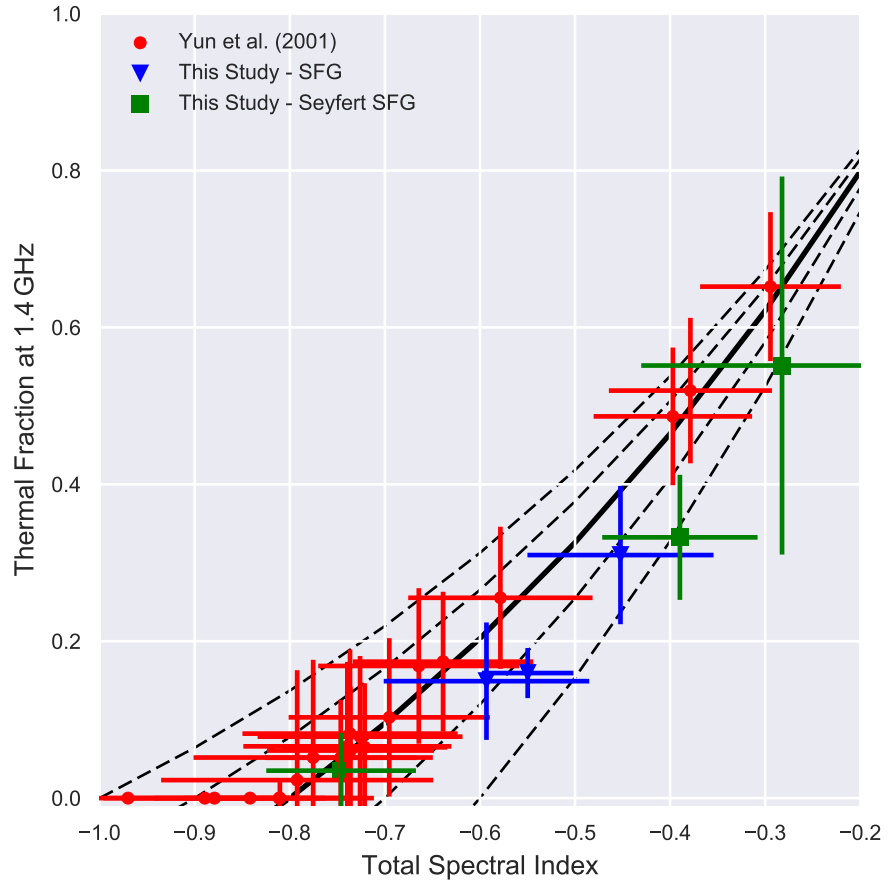


Figure 2.9: A comparison between the radio spectral index ( $\alpha_{1.4}^{4.8}$ ) and the fitted thermal fraction at 1.4 GHz (rest frame) of the SFGs or Seyfert SFGs from this study and 22 sources from Yun et al. (2001). Thermal and non-thermal radio luminosities were calculated in the rest frame at 1.4 GHz. The solid line represents the relationship between spectral index and the thermal fraction (see Equation 2.10) over a frequency range of 1.4 to 4.85 GHz. The dashed lines, from left to right, represent how the thermal fraction varies when values of  $-1.0$ ,  $-0.9$ ,  $-0.7$ , and  $-0.6$  are adopted as the spectral indices for non-thermal emission.



tool that could allow the spectral index of an object to be used as a proxy when estimating the ratio of thermal to non-thermal emission (as well as potentially other global properties).

In cases where the non-thermal spectral index varies from the adopted  $-0.8$  value, Equation 2.10 can be used to model the resulting thermal fraction and how it differs. As the spectral index becomes flatter, the thermal fraction becomes more resilient to varying values of non-thermal spectral indices. This effect can be seen in Figure 2.9 because the thermal fraction tracks showing the effect of varying the non-thermal spectral index converge as the spectral index increases towards zero.

Synchrotron and free-free emission are caused by different fundamental physical processes with their own timescales, so the thermal fraction could potentially be used as an initial estimate of the age of a SFG. A high thermal fraction can indicate a young galaxy that has yet to have time to propagate electrons from supernova shocks to emit non-thermal radio emission. Likewise, a low thermal fraction may imply an older galaxy because the instantaneous thermal emission is less due to a dwindling SFR, whereas the ejected relativistic electrons, which produce non-thermal emission, are still propagating throughout the galaxy.

#### 2.7.4 Thermal and Non-Thermal Correlation with Far-IR

Using the deconstructed radio-continuum emission components from both Yun et al. (2001) and this study, we could estimate the thermal and non-thermal luminosities at 1.4 GHz for each source. In Figure 2.10 we show how these radio luminosities, derived from the fitted emission components of Equation 2.3, correlate with the  $60\ \mu\text{m}$  luminosities.

These general correlations were obtained from a subset of the Yun et al. (2001) sample derived by applying simple selection criteria. To ensure an adequate fit, we excluded sources from Yun et al. (2001) if their  $q$  values were less than 1.64 or if the reduced  $\chi^2$  of the fitted SFG model was greater than 5. This was done to ensure that the SFG model was appropriate and was an adequate fit for the available data points. Additionally, if a source had a negligible thermal luminosity ( $\text{Log } L_{1.4\text{GHz}}^T < 19$ ), it was also excluded while fitting for both the thermal and non-thermal to infrared luminosity correlations. In total, there were 15 of the 22 thermal and non-thermal data points remaining after these criteria were applied to the sample of Yun et al.. A bootstrapping method was also used while fitting the correlation because it helped provide appropriate uncertainties given the relatively small sample size. Only the measurements from the sample of Yun et al. were used when fitting these correlations. This was done to (1) remain consistent with Figure 2.8 and (2) assess which, if any, of the decomposed components of our ULIRG sample were away from the expected trend set by the Yun et al. sample.

The non-thermal radio luminosity at 1.4 GHz, shown in Figure 2.10 (top), is strongly cor-

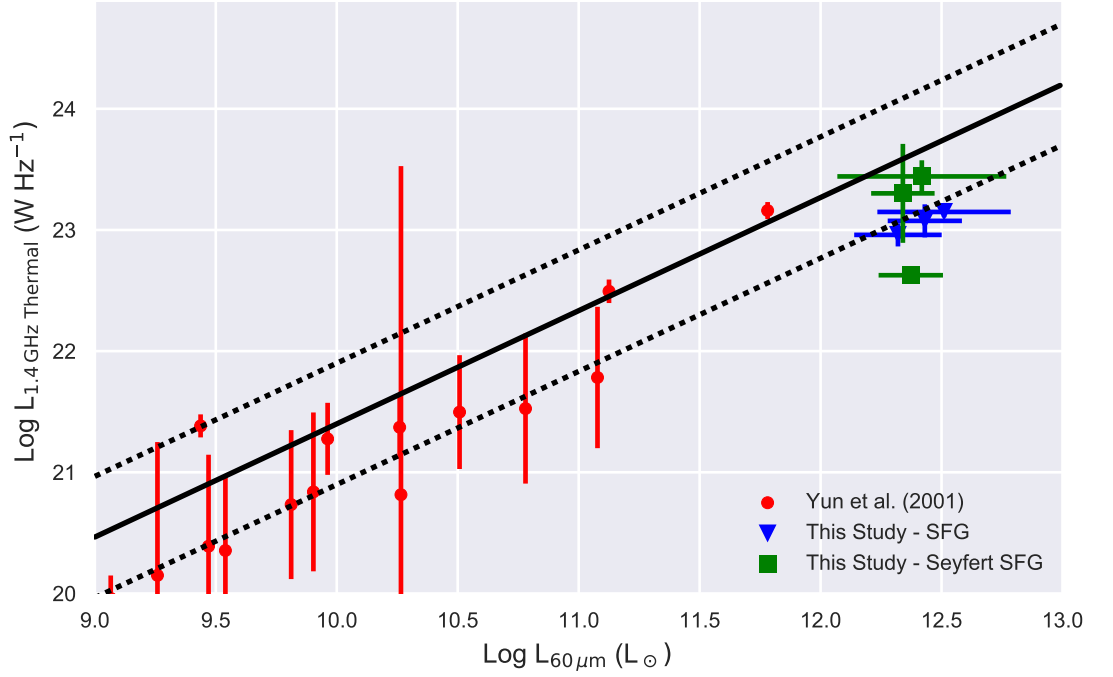
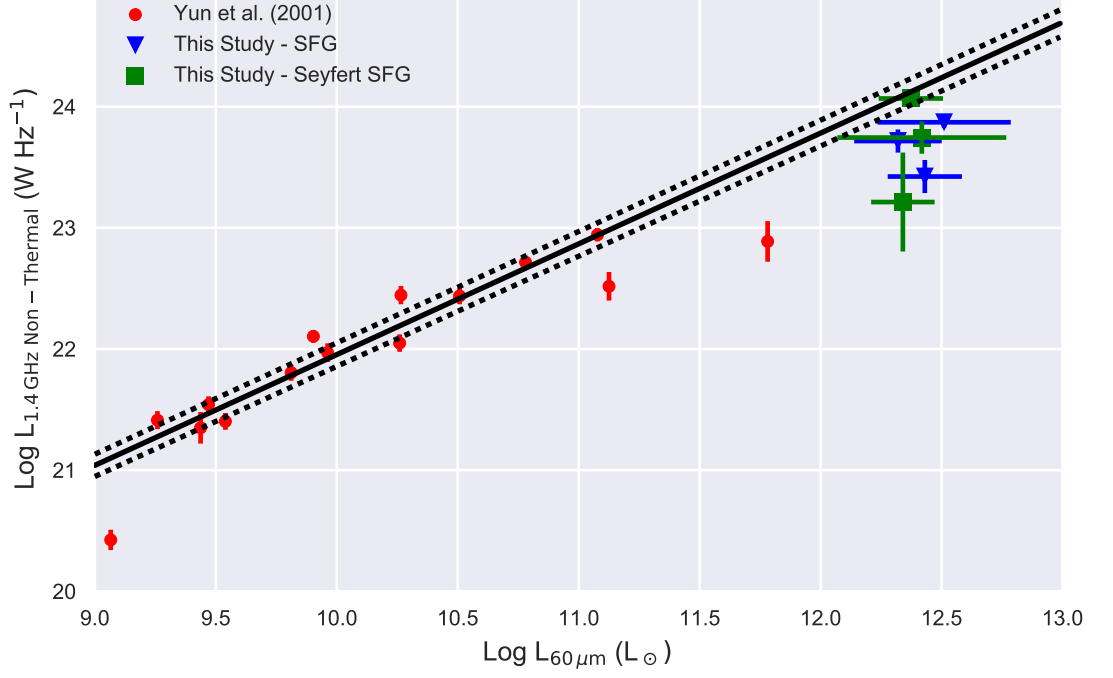


Figure 2.10: (*Top*) Comparison between the  $60\mu\text{m}$  and the fitted non-thermal 1.4 GHz luminosity of 15 sources from Yun et al. (2001) and the 6 SFG or Seyfert SFG sources from this study. We fit a relation to the 15 Yun et al. (2001) sources, which is presented as a solid line. The dotted lines represent uncertainty of the fit. (*Bottom*) A comparison between the  $60\mu\text{m}$  and the fitted thermal 1.4 GHz luminosity of 15 sources from Yun et al. (2001) and 5 SFG sources from this study. The solid and dotted lines represent a fitted relation and the uncertainties of the normalisation component fitted to the 15 Yun et al. (2001) sources.

related to the  $60\ \mu\text{m}$  luminosity. We could fit a trend to the 15 Yun et al. (2001) galaxies:

$$\log(L_{1.4\text{GHz}}^{\text{NT}}) = 0.916 [\pm 0.004] \times \log(L_{60\ \mu\text{m}}/L_{\odot}) + 12.80 [\pm 0.04] \quad (2.11)$$

where  $L_{1.4\text{GHz}}^{\text{NT}}$  is the non-thermal luminosity at 1.4 GHz. These parameters were constrained using the fitted results of 10000 randomly selected subsamples of the 15 sources (with repetition allowed).

At  $L_{60\ \mu\text{m}} < 10^{11}L_{\odot}$ , this correlation is especially strong, with little scatter from the best fit correlation. Towards the upper end of the fitted correlation, there appears to be a slight increase in the scatter with 2 sources roughly 0.2 dex below the main trend. This increased scatter is also seen in the SFG sources from this study (although possibly subject to our object selection method). These SFGs were not part of the data used to constrain this trend, only the Yun et al. sample.

Likewise, the thermal radio luminosity at 1.4 GHz is also shown to be correlated with  $60\ \mu\text{m}$  luminosities in Figure 2.10 (bottom). We fit a correlation to the Yun et al. (2001) luminosity estimates using the bootstrapping method outlined above:

$$\log(L_{1.4\text{GHz}}^{\text{T}}) = 0.93 [\pm 0.05] \times \log(L_{60\ \mu\text{m}}/L_{\odot}) + 12.10 [\pm 0.51] \quad (2.12)$$

where  $L_{1.4\text{GHz}}^{\text{T}}$  is the thermal luminosity at 1.4 GHz. The uncertainties of the fitted components, especially the normalisation component, are higher when compared with the fitted non-thermal trend.

### 2.7.5 Thermal Fraction and $q$

We compared the estimated thermal fraction at 1.4 GHz obtained from the fitted SFG models to the  $q$  parameter (Figure 2.11) for sources from this study and Yun et al. (2001). Sources whose fitted spectral index was outside the range of  $-0.8 < \alpha < -0.1$  were excluded from Figure 2.11 because thermal fractions of sources whose values are outside this range cannot be represented by the SFG model in its current form (returned as either 100% or 0%, as demonstrated in Figure 2.9).

Figure 2.11 shows that the mean  $q$  value of Yun et al. (2001) (represented as a dashed line) appears to mark a transition from low thermal fractions to increased values accompanied by larger intrinsic scatter. For the 18 sources where  $q < 2.34$ , we find the mean and SD of the thermal fraction to be 0.08 and 0.12, respectively. Of the 8 sources where  $q > 2.34$ , the mean and SD of their thermal fraction correspond to 0.38 and 0.18, respectively. A two-sided Kolmogorov-Smirnov test with each of these groups returns a p-value below 1%, indicating that

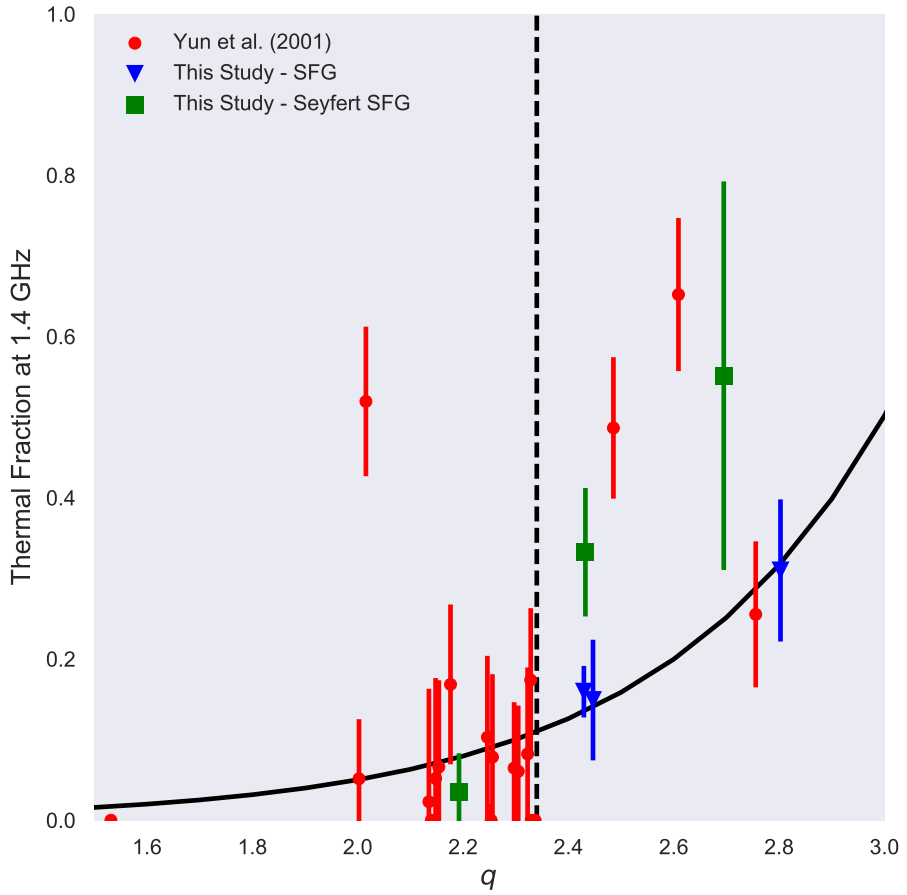


Figure 2.11: A comparison between the  $q$  parameter against the fitted thermal fraction at 1.4 GHz (rest frame) of the 6 detected SFGs or Seyfert SFGs from this study and 20 sources from Yun et al. (2001). The dashed vertical line represents the mean  $q$  value of Yun et al. (2001) ( $q = 2.34$ ). The solid line is Equation 8 from Marvil et al. (2015) and relates the  $q$  parameter to a thermal fraction.

there are two different underlying distributions present.

Marvil et al. (2015) show that the  $q$  parameter may be related to the thermal fraction of a source, such that

$${}^{\text{IR}}f_{\text{tf}1.4} = 1.7 \times 10^{q-3.53}, \quad (2.13)$$

where  ${}^{\text{IR}}f_{\text{tf}1.4}$  is the thermal fraction at 1.4 GHz estimated using the far infrared and total 1.4 GHz luminosity from NVSS. This relationship was constructed by considering SFR conversion factors based on radio thermal emission originating from resolved HII regions (Murphy et al., 2011) and IR (Kennicutt, 1998), allowing the radio thermal emission component to be described in terms of the total FIR emission. Because the  $q$  parameter and this derived expression share this common FIR term, the thermal fraction can be expressed in terms of  $q$ . The solid line shown in Figure 2.11 represents this relationship (Equation 2.13). Sources with small values of  $q$ , which would classically be described as radio excess, could alternatively be interpreted as having low thermal fractions using this relation (Marvil et al., 2015). This implies that ULIRGs are a relatively short lived phenomena, an idea further explored in §2.8.2.

## 2.8 Discussion

We constrained the multiple radio emission components that make up a typical luminous SFG (at higher redshifts and luminosities). This type of modelling shows that there exists a measurable thermal emission component that contributes to the radio-continuum at  $\nu < 10$  GHz. Although the uncertainties associated with the thermal components are high for three of the six fitted SFG models, these uncertainties can be attributed to the frequency range of flux density measurements used in the radio-continuum and low thermal fractions. Typically, the thermal component of an SFG does not become a significant fraction of the radio-continuum till frequencies above 10 GHz. We find it encouraging that despite a lack of measurements in this regime, we were still able to estimate this mechanism. Once the 10 to 100 GHz frequency range is sampled, a more robust SFG model can be constrained.

### 2.8.1 Object Selection

We specifically focussed on ULIRGs in this study for two reasons. First, they are a useful representative sample of the types of active galaxies (in terms of star formation and luminosities) which are expected to be detected at higher redshifts with the next generation of radio telescopes, including ASKAP, MeerKAT, Jansky Very Large Array (JVLA), Low-Frequency Array for Radio astronomy (LOFAR), eMERLIN, and SKA. Second, the strong emission seen in the

infrared indicates high SFR. Assuming that the non-thermal emission is a delayed tracer of star formation, we expect that the thermal component would be a significant fraction of the radio-continuum at 1.4 GHz, allowing it to be more easily disentangled from the overall spectrum. This property is especially applicable to high redshift objects, where the observed 1.4 GHz radio flux density will include a larger fraction of thermal emission than observed in local galaxies. Given that of the six SFG galaxies identified here, five were fitted with a measurable thermal component, this seems to be a valid approach.

A side effect of our selection criteria is, as mentioned in §2.7.2, an apparent deficit in the radio luminosity of the six SFG objects from this study, given the fitted FRC. A source must have a far-infrared luminosity in excess of  $10^{12.5} L_{\odot}$  to be included in our sample. Although we successfully identified galaxies with high SFR and a measurable thermal component, our method also had the effect of selecting sources with a higher mean  $q$  value once AGN contamination was corrected, thereby producing the radio luminosity deficiency that was observed.

To confirm the origin of our higher  $q$  values, we obtained the Revised IRAS-FSC Redshift Catalogue (RIFSCz; Wang et al., 2014) and applied the same selection criteria as described in §2.3, with the exception of replacing item 3 ( $L_{\text{FIR}} > 10^{12.5} L_{\odot}$ ) with the requirement for a source to have a  $60 \mu\text{m}$  flux  $> 0.5$  Jy. This amended criterion targeted the region between the upper limit of the Yun et al. (2001) sample and our own. After removing all sources without a listed 1.4 GHz flux density, there were 26 objects whose properties matched the amended selection criterion (including sources, IRAS F00397-1312 and IRAS F00406-3127, from this study). We found that this sample is equally scattered around the FRC from Yun et al. (2001), extrapolated to higher luminosities.

## 2.8.2 Thermal Fraction, $q$ , and timescales

One of the properties of the fitted SFG emission model is that the thermal fraction is tied closely to the spectral index of a galaxy (Figure 2.9). This relationship allows an estimate of the thermal fraction, obtained from the spectral index, to be used without the need for detailed SED modelling. For instance, this thermal fraction may be used to indicate the starburst age of a particular galaxy. The thermal emission, caused by free-free type interactions between particles in ionised clouds of hydrogen surrounding HMS, is an instantaneous emission characterised by a relatively flat spectrum. In contrast, the steep spectrum of the synchrotron emission is delayed due to the lifespan of OB stars ( $\sim 10^7$  years) and the time required for relativistic electrons, ejected from the shocks of supernovae, to diffuse ( $\sim 10^4$  years).

Figure 2.11 shows that sources with higher values of  $q$  ( $q > 2.34$ ) tend to have a larger thermal fraction. Additionally, the thermal fraction of sources in this region have a larger

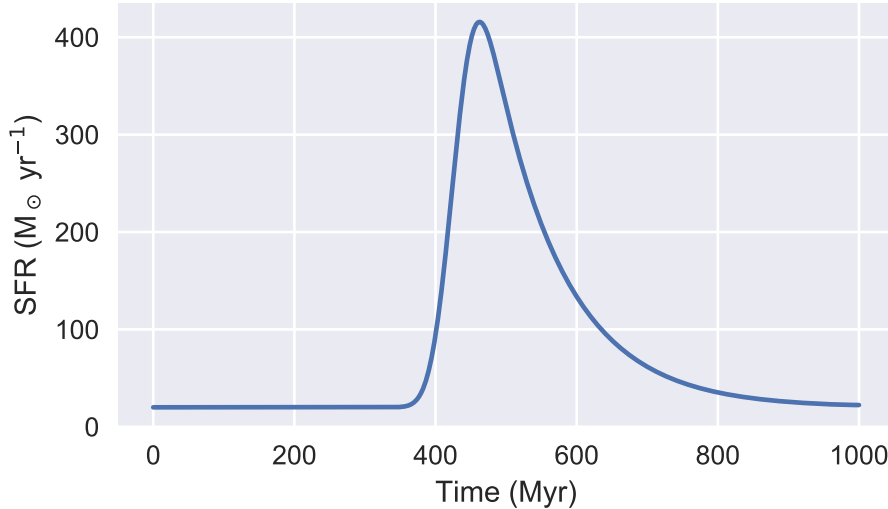


Figure 2.12: The SFH constructed for an assumed starburst galaxy.

scatter than that seen in the radio sources with lower values of  $q$  ( $q < 2.34$ ). Potentially, this may be explained by the timescales associated with each emission mechanism, as well as the duration of the starburst itself. A younger starburst will have a high thermal fraction and a high value of  $q$  as the non-thermal emission is delayed and absent from its radio-continuum. As the starburst ages,  $q$  and the thermal fraction will decrease because of the increase in the time-delayed, non-thermal radio emission and also because of the declining SFR reducing the amount of instantaneous thermal emission.

The scatter of the thermal fraction when compared against  $q$  could be influenced by the duration of the starburst. For instance, if star formation ceases before the non-thermal emission commences, the  $q$  parameter will possibly increase if the IR emission persists longer than the thermal emission but will then decrease once the IR emission begins to decline. Once the non-thermal component commences, the thermal fraction will quickly decline and  $q$  will decrease almost as rapidly. Alternatively, if the non-thermal emission begins to contribute to the radio-continuum while star formation is still ongoing, the thermal fraction and  $q$  will decrease more gradually.

To investigate this time scale effect and how it may influence the scatter seen in the thermal fraction and  $q$  parameter, a template model was constructed describing SFH of an assumed starburst galaxy. In this template, the steady-state SFR for  $\sim 380$  Myr was encoded, at which point the template builds to a peak and exponentially decays across  $\sim 50$  and  $\sim 300$  Myr, respectively. The SFH template constructed here is shown in Figure 2.12.

Using conversion factors for SFR to luminosity for various emission processes and a delay to account their associated timescales, I then tracked how the emission diagnostics evolve through

Emission Process	SFR to emission Factor	Delay Myr
FIR	$\text{SFR}/3.88 \times 10^{-44}$	35-45
free-free	$\text{SFR}/4.6 \times 10^{-28}$	5-15
Synchrotron	$\text{SFR}/6.64 \times 10^{-29}$	100-110

Table 2.8: An overview of the SFR conversion factors and delayed possible range of time offsets applied to the assumed starburst SFH. SFR conversion factors have been taken from Murphy et al. (2011).

the life of a starburst using the assumed SFH. To build in uncertainty, 100 samples were drawn from a range of timescales for each mechanism. I outlined the conversion factors and time scale delays in Table 2.8. The time delay offsets adopted are consistent with those summarised by Kennicutt and Evans (2012). Although they do not explicitly list timescales for the synchrotron and free-free component, the 1.4 GHz radio band presented by Kennicutt and Evans (2012) was considered to be an appropriate delay for the synchrotron process as at these frequencies, the radio continuum is almost entirely synchrotron in nature. Likewise, although Kennicutt and Evans (2012) made no specific mention of the timescales of free-free emission, they do provide an estimate of the  $\text{H}\alpha$  delay. As both free-free radio-continuum emission and  $\text{H}\alpha$  are produced by the same ionisation process, I considered this to be an appropriate substitute.

Using the properties outlined above, I could then estimate how various emission diagnostics vary as a function of the assumed SFH, as demonstrated in Figure 2.13. By drawing offsets from a range of possible values, I constructed a crude confidence interval.

With this model, as a colour overlay, the  $q$  parameter and thermal fraction histories (as shown in Figure 2.13) were added onto Figure 2.14, where the colour of the track represents time. I overlaid 100 tracks, each with different time delay offsets.

Exploiting the different emission processes in this manner may help recover the age and state of an observed starburst reliably. Currently, these properties may be recovered from broadband template modelling across the infrared, optical, or ultraviolet emission bands (Farrah et al., 2003; Symeonidis et al., 2013; Cappellari et al., 2013; Cappellari, 2017; da Cunha et al., 2008). These methods require flux density measurements, reliable emission templates, and sophisticated model optimisation methods to characterise the observed SED.

This approach, however, projects objects into a parameter space that requires only a minimal set of observed flux densities. My work shown in Figure 2.14 suggests that the scatter and placement of objects may be used to infer the starburst ages without having to rely on model optimisation methods. To assess the effectiveness of this method, however, a larger sample of objects is needed with enough data to perform existing template modelling optimisation approaches to compare against. In the future, I plan to use objects in the Extended *Chandra*



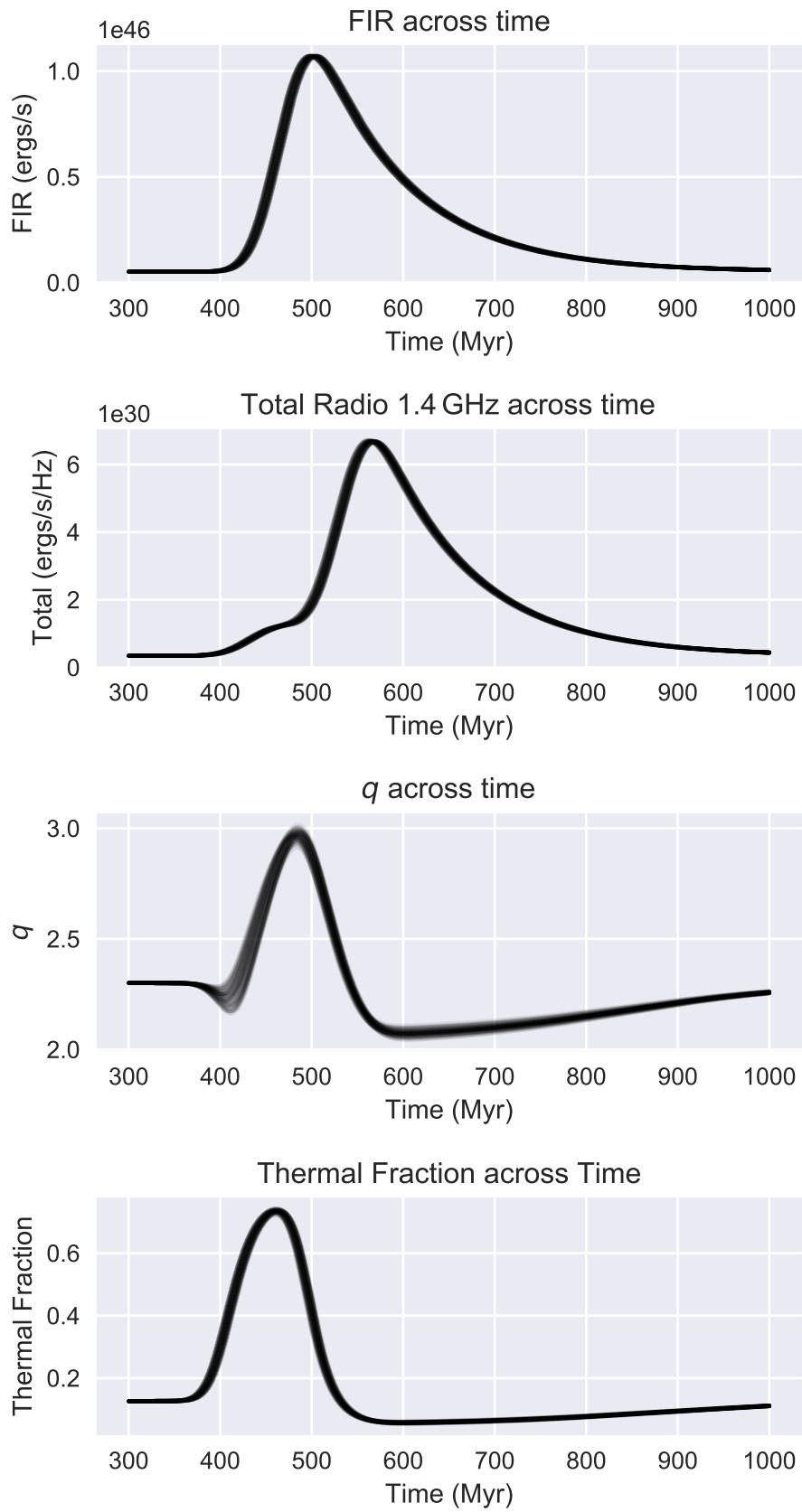


Figure 2.13: Various emission diagnostics after applying emission delays to the assumed starburst SFH.

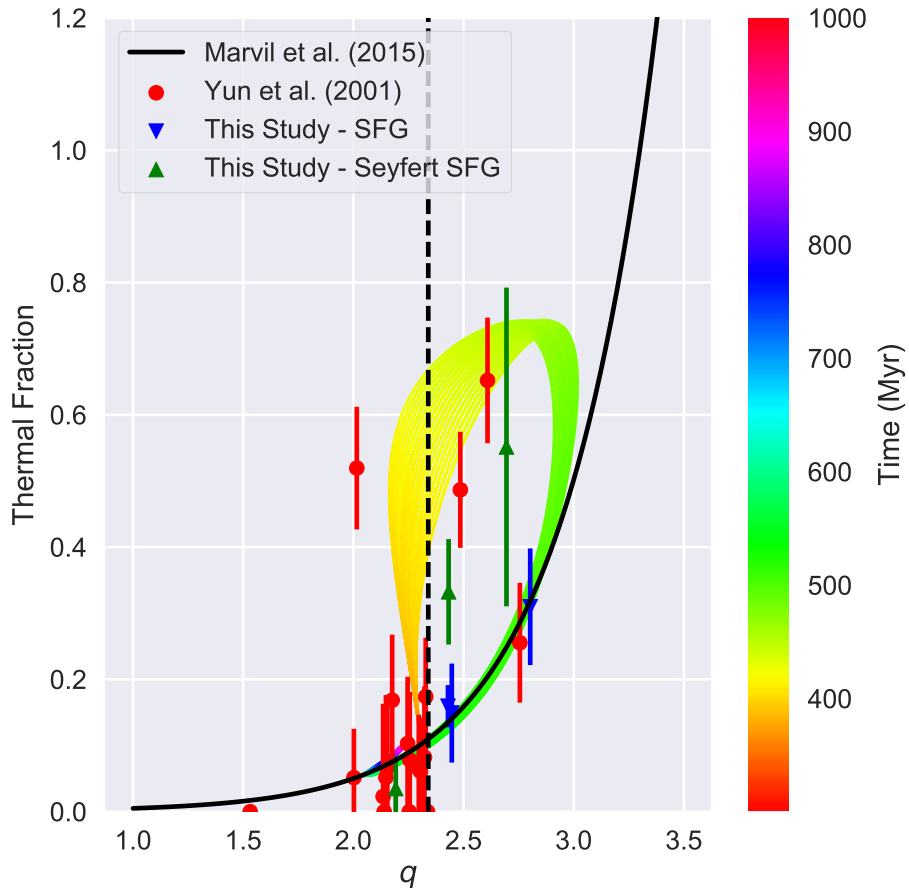


Figure 2.14: A comparison between the  $q$  parameter against the fitted thermal fraction at 1.4 GHz (rest frame) of the six detected SFGs or Seyfert SFGs from this study and 20 sources from Yun et al. (2001). The dashed vertical line represents the mean  $q$  value of Yun et al. (2001) ( $q = 2.34$ ). The solid line is Equation 8 from Marvil et al. (2015) and relates the  $q$  parameter to a thermal fraction. As a colour overlay, I included the tracks that objects in this space would follow using an SFH template of an assumed starburst galaxy and various SFR indicators.

Deep Field South to this end as it has been studied extensively by a range of superb instruments, including Atacama Large Millimeter Array (ALMA) and the Very Large Telescope (VLT), out to high redshifts.

### 2.8.3 Correlation of Decomposed Radio Luminosities

Through the application of the SFG emission model, the thermal and non-thermal luminosities could be estimated through a collection of 28 sources across the two studies. These decomposed components themselves correlate with  $60\ \mu\text{m}$  luminosity across many orders of magnitudes like that of the traditional FRC (Figure 2.10). Although these trends are present, the thermal to  $60\ \mu\text{m}$  luminosity correlation is less constrained. Given that the 22 sources from Yun et al. (2001) had their SFG model constrained with only three measurements across a frequency range dominated by non-thermal emission, the thermal component of the resulting fit will inherently carry with it a higher uncertainty. Consequently, the resulting fitted trend is less well constrained as the non-thermal correlation.

During the fitting of these correlations, we elected to fit only to sources from the Yun et al. (2001) sample and not to include the SFG sources from this study. This was done because, as outlined above, our sample of the SFG type objects tend to move towards high  $q$  (as can be seen in Figure 2.8) and would have diminished the effectiveness of the fitted correlations when using the decomposed radio luminosities. As previously discussed, sources that were selected for inclusion in this study were based on their high total far-infrared luminosities as it is likely that this excess infrared emission originated from a high rate of star formation and possibly a younger stellar age. Although this approach helped to identify sources where we could constrain the thermal radio-continuum properties of our sample, it resulted in sources with higher  $q$ .

We note that although the non-thermal to  $60\ \mu\text{m}$  luminosity correlation is clearly well characterised by the Yun et al. (2001) sample, SFG type sources from this study do not follow it nearly as strongly as the lower luminosity sources. We see this in the intrinsic scatter of the non-thermal 1.4 GHz luminosity of the 6 SFG objects from our study. Given that the uncertainties of the fitted non-thermal component in our SFG modelling were small, it is likely that this luminosity deficiency is caused by the timescales associated with non-thermal emission in these presumably young galaxies. A physical interpretation of this effect is that these galaxies are young enough that the cosmic ray electrons accelerated by the shock fronts of supernovae are yet to completely be transformed to synchrotron.

## 2.9 Conclusions

Using ATCA data, the intrinsic thermal and non-thermal emission was measured that comprises the radio-continuum. The ULIRGs included as part of this study, with their high infrared luminosities and vigorous star formation, are an excellent representative sample of the class of galaxies that are observed in the current and future of deep, extra-galactic radio surveys. Understanding the physical contribution of star formation process to the radio regime is necessary to characterise these distant galaxies. To this end, the following was shown through the emission modelling of this study:

- The intrinsic thermal and non-thermal emission components that make up the radio-continuum can be separated with as few as three flux density measurements. The steep spectrum of non-thermal emission can be easily distinguished from the relatively flat spectrum of thermal emission.
- Both the thermal and non-thermal emission components form their own well defined correlations with the  $60\ \mu\text{m}$  luminosities. Like the FRC, these correlations exist over many orders of magnitude with relatively small scatter.
- The thermal fraction of a fitted SFG model is tied closely to the fitted spectral index of the object. Given the wide bandwidth filters now fitted on the ATCA and the Karl G. JVLA, this will be very useful in obtaining initial estimates of the thermal emission of star forming galaxies without having to fit a complete SFG model to its radio-continuum.
- With increasing values of  $q$ , there is an increase in the value and scatter of the thermal fraction. This could be due to the differing time scales associated with thermal and non-thermal radio emission originating from HMS formation. Galaxies with younger starbursts may have a higher  $q$  and thermal fraction because of the delayed non-thermal emission mechanism. Likewise, galaxies with older starbursts may have a lower  $q$  and thermal fractions due to declining SFRs (thereby reducing the amount of instantaneous thermal emission) and increasing non-thermal emission from earlier bursts of star formation.

## Chapter 3

# Radio-Continuum Emission of Luminous Infrared Galaxies

The work in this Chapter has been published in the Monthly Notices of the Royal Astronomical Society Journal. Excluding minor editorial changes, I have added Section 3.1, expanded the description of the data reduction method, and included an additional figure highlighting the potential link between the star formation rate of objects and the intrinsic cosmic ray distribution spectral index.

### 3.1 Motivation

An issue encountered during the investigation of the radio-continuum emission of the sample of ultra-luminous galaxies in Chapter 2 was the decomposition of the synchrotron and free-free components. Although these components could be separated, the uncertainties for the free-free emission were high. The flat spectral shape of the free-free emission and the lack of high frequency information, where synchrotron is far less prominent, meant that the model optimisation methods could not place strong constraints on this component. The sparse frequency coverage also meant analysis similar to Clemens et al. (2010), who detected a ‘kink’ in the radio-continuum spectrum which they attributed to free-free absorption with high emission measures, could not be performed.

Sources selected for study in Chapter 2 had redshifts in the range of 0.2 to 0.5. At these, their faint emission required long integration times. Using the ATCA 2 GHz broadband filters, most star forming objects in this 12 source sample were detectable only by summing the data across the complete 2 GHz band, i.e. by inverting all data into a single image. Such an approach leads to loss of spectral index information across each band and potentially makes higher-order

curvature features undetectable.

For these reasons, under the guidance of my supervisory panel, I designed an experiment to acquire more detailed broadband radio-continuum data for a larger sample of sources. The motivation was to better constrain the distinct synchrotron and free-free emission processes across a broader frequency range. When designing the experiment and selecting sources, it was expected that the MWA GLEAM project (Wayth et al., 2015; Hurley-Walker et al., 2017) would also provide data that would be incorporated into the dataset at frequencies lower than those possible with ATCA. At the commencement of source selection, these were not yet available. It was expected that free-free absorption would form a component of the required modelling, so the Sydney University Molonglo Sky Survey (SUMSS) (Bock et al., 1999; Mauch et al., 2003), which surveyed the southern sky at 843 MHz, formed a critical component of the selection criteria.

## 3.2 Introduction

Understanding the SFH of the Universe is a key scientific goal of the Square Kilometre Array (SKA; Prandoni and Seymour, 2015) and its pathfinder projects (Norris et al., 2011). Radio-continuum emission offers a unique advantage over other wavebands as it is impervious to the effects of dust attenuation and can provide an unbiased view into the SFR of distant galaxies through cosmic time (Jarvis et al., 2015). Current critical radio-continuum SFR indicators, based mostly on the 1.4 GHz luminosity, have been calibrated against far-infrared (FIR) measures using the far-infrared to radio correlation (FRC; Condon, 1992).

The FRC itself is a tight, linear relationship across many order of magnitude between the far-infrared and radio-continuum luminosities of galaxies (Yun et al., 2001; Bell, 2003; Mao et al., 2011). Its existence comprises three individual emission processes that are all manifestations of high-mass star (HMS;  $M_{\odot} > 8 M_{\odot}$ ) formation.

Far-infrared (FIR) emission, spanning 40 to 120  $\mu\text{m}$ , originates from widespread dust cirrus heated by UV and optical emission from a combination of mostly young HMS and an older stellar population. The observed radio-continuum is a superposition of two individual mechanisms, the most prominent at low frequencies being non-thermal synchrotron emission. This process is thought to be formed from relativistic electrons, accelerated by the remnants of Type II and Type Ib supernova of HMS, interacting with large-scale galactic magnetic fields. Although synchrotron emission makes up roughly 90% of the radio-continuum at 1.4 GHz of normal galaxies, it is a delayed tracer to SF, taking more than  $10^7$  years for the electrons to diffuse (Condon, 1992).

Thermal free-free emission is the second mechanism that makes up the radio-continuum. Its underlying process is powered by the ionisation of HII regions by UV flux from HMSs. Unlike synchrotron emission, it is a direct, near-instantaneous tracer of SFR. Despite this, it is relatively unused as a radio-continuum SFR indicator because of its flat spectral index ( $\alpha = -0.1$ ) and the fact that at low frequencies, where the survey speeds of radio telescopes are the most efficient, the spectrum is overwhelmingly dominated by synchrotron. Isolating free-free emission requires either model fitting using a broad, densely sampled radio-continuum spectral energy distribution (SED; Price and Duric, 1992; Galvin et al., 2016) or high frequency observations ( $\nu > 20$  GHz) where synchrotron emission is mostly absent (Murphy et al., 2012).

Although calibrating the radio-continuum SFR measures through FRC has been proven to be effective in the local Universe ( $z < 0.15$ ), there remains considerable uncertainty as to how their reliability will scale with increasing redshifts. Murphy (2009) argues that because of a combination of the changing composition of the radio-continuum with increasing frequencies and the suppression of synchrotron emission scaling in proportion to  $(1+z)^4$ , there should be an evolution in the observed frame FRC. Ivison et al. (2010) and Mao et al. (2011) both used image stacking techniques for observational evidence to demonstrate no change in the FRC up to redshifts of 2, suggesting that the physical origin of the FRC may be more complex than first thought.

Future radio-continuum surveys expected from the SKA and its pathfinder projects will explore the high redshift Universe ( $z > 0.15$ ). In this parameter space, it is expected that distant, faint star forming galaxies (SFG), whose SFRs are in excess of  $100 M_{\odot} \text{ yr}^{-1}$ , will be the predominant class of objects detected with these surveys. Work by Clemens et al. (2010) also showed that the effects of free-free absorption, particularly in the case of multiple star forming regions with different optical depths, will further complicate the observed radio-continuum. Correctly interpreting the emission properties that trace star formation will require an improved understanding of the underlying physical mechanisms and how they can be characterised through their diverse SEDs.

In this study, we investigate the intrinsic emission components of 19 powerful star forming luminous infrared galaxies (LIRGS), which are ideal representative sources of distant SFGs, at redshifts between 0.0627 and 0.227. A series of comprehensive radio-continuum SEDs is constructed, ranging between 80 MHz up to 50 GHz with the aim of isolating the thermal free-free component and identifying the effects of free-free absorption (FFA) at low frequencies. As the free-free emission (1) is a direct tracer of SFR, (2) is a flat spectral slope, and (3) originates from the same HII regions that power stellar hydrogen emission lines, it is an excellent candidate to craft SFR measures that are compatible with the high redshift SFGs that will be revealed

with SKA and its pathfinder projects. For our sample of objects, we have also acquired optical spectroscopy data using the WiFeS instrument (Dopita et al., 2007, 2010). We will subsequently analyse the optical spectroscopic data in conjunction with this radio-continuum modelling in a subsequent series of papers.

We assume a flat Universe, where  $\Omega_m = 0.277$ ,  $\Omega_\lambda = 0.733$  and  $H_0 = 70.2 \text{ km s}^{-1} \text{ Mpc}^{-1}$  following Komatsu et al. (2009).

### 3.3 Data

#### 3.3.1 Source Selection

In this study, we selected a sample of all known southern ( $\delta < -30^\circ$ ) LIRGS, defined as having IR luminosities greater than  $L_{8-1000\mu\text{m}} > 10^{11} L_\odot$ . These objects were specifically targeted due to their high SFR, as this implies that there would be a measurable thermal component in their radio-continuum. These types of objects are analogous to the types of distant SFG which are expected to predominately comprise the next generation of future deep surveys.

The sample constructed for this study was obtained using the Revised *IRAS* Faint Source Catalog (Wang et al., 2014). We identified all sources with a  $60 \mu\text{m}$  flux density in excess of  $1.4 \text{ Jy}$  ( $S_{60\mu\text{m}} > 1.4 \text{ Jy}$ ) and a spectroscopic redshift between  $0.067 < z < 0.227$ . This was done not only to target galaxies with high SFR but also to allow for future ground-based observations of the Paschen- $\alpha$  ( $\text{Pa}\alpha\lambda 18750$ ) hydrogen recombination line, which is a relatively un-attenuated measure of star formation. Potential sources were cross referenced with the SUMSS catalogue (Mauch et al., 2013) to obtain radio flux densities at 843 MHz. Sources with a detectable AGN component, as seen in a deviation from the FRC based on their SUMSS measurement (see the  $q$ -parameter defined below), their optical spectra, or those flagged as quasi-stellar objects by Wang et al. (2014) were also excluded from further consideration. Our final sample of 20 sources, along with their spectroscopic redshifts, IR luminosities, and SFRs, are presented in Table 3.1.

#### 3.3.2 ATCA Observations

For over five non-consecutive nights, 19 of the 20 sources in our sample (IRAS F14378-3651 was dropped because of LST constraints) were observed across 11 central frequencies (Table 3.2) using the Australia Telescope Compact Array (ATCA; Wilson et al., 2011) under the project code C2992 (PI: Galvin). With the CABB filters, a spectral window of 2.048 GHz was available for each of the targeted central frequencies. In total, this provided roughly 22.5 GHz of coverage from 1.1 to 94.0 GHz. We adopted a snapshot imaging approach because of the diverse LST



Name <i>IRAS</i>	RA J2000	Dec J2000	$z$	$L_{\text{IR}}$ 8 - 1000 $\mu\text{m}$
F00198-7926	00:21:53.6	-79:10:07.79	0.07	12.12
F00199-7426	00:22:07.0	-74:09:41.89	0.10	12.22
F01268-5436	01:28:47.7	-54:21:25.62	0.09	11.97
F01388-4618	01:40:55.9	-46:02:53.32	0.09	12.08
F01419-6826	01:43:17.1	-68:11:24.12	0.08	11.8
F02364-4751	02:38:13.9	-47:38:11.34	0.10	12.05
F03068-5346	03:08:20.9	-53:35:17.66	0.07	11.9
F03481-4012	03:49:53.8	-40:03:41.03	0.10	11.86
F04063-3236	04:08:18.9	-32:28:30.35	0.11	12.07
F06021-4509	06:03:33.6	-45:09:41.12	0.16	12.23
F06035-7102	06:02:54.1	-71:03:10.48	0.08	12.15
F06206-6315	06:21:01.2	-63:17:23.81	0.09	12.2
F14378-3651	14:40:59.0	-37:04:32.24	0.07	12.07
F18582-5558	19:02:24.0	-55:54:08.56	0.07	11.63
F20117-3249	20:14:55.3	-32:40:00.50	0.10	11.92
F20445-6218	20:48:44.1	-62:07:25.35	0.11	11.95
F21178-6349	21:21:53.8	-63:36:43.68	0.07	11.63
F21292-4953	21:32:36.2	-49:40:24.74	0.14	12.39
F21295-4634	21:32:49.4	-46:21:03.93	0.07	11.72
F23389-6139	23:41:43.5	-61:22:52.62	0.09	12.14

Table 3.1: Complete source sample used throughout this study. IRAS F14378-3651 was ultimately excluded from further processing because of LST constraints.

range of our sample. To help optimise efficiency, we grouped sources based on their positions to share phase reference calibrators. This was important because at high frequencies, an increasingly large fraction of time is lost to calibration overheads, including array pointing calibrations and more frequent phase reference scans.

On the first night on 4<sup>th</sup> October 2014, we targeted the Q and W band frequencies and used a H214 hybrid configuration. This compact array configuration was selected to help prevent resolving outsource structures. PKS 1921-293 (RA,DEC J2000: 19:24:51.05, -29:14:30.12) was used as the bandpass calibration, while Uranus was used to provide a flux density scale. Because of the high frequency, pointing calibrations were performed between each slew greater than 10°. A full hour angle synthesis was not possible because of the considerable overheads required for obtaining observations at these frequencies. Instead, we selected to observe each source for a single 15-minute exposure and measure the flux of each source in the  $uv$ -plane exclusively. Although normally, a single cut in the  $uv$ -plane would introduce source confusion, the H214 hybrid array, with two antennae along the north-south spur, provided enough spatial coverage to sample the  $uv$ -plane adequately enough to isolate our sources in the sky. Elevated path noise only allowed us to observe six sources at the W band central frequencies. Ultimately these W band data were discarded due to difficulties during calibration.

Centimetre data were collected over a number of individual observing runs. Initially, L

Central Frequency GHz	Band	Array	Date Observed	LAS "
2.1	L/S	6A	23-01-2015	89.0
5.0	C/X	6A	27-01-2015	37.4
5.0	C/X	750C	29-12-2015	275.3
6.8	C/X	6A	27-01-2015	27.5
6.8	C/X	750C	29-12-2015	201.7
8.8	C/X	6A	27-01-2015	21.2
8.8	C/X	750C	29-12-2015	155.9
10.8	C/X	6A	27-01-2015	17.31
10.8	C/X	750C	29-12-2015	127.0
17.0	K	6A	23-01-2015	11.0
17.0	K	750C	31-12-2015	80.9
17.0	K	H168	06-09-2016	60.5
21.0	K	6A	23-01-2015	8.9
21.0	K	750C	31-12-2015	65.3
21.0	K	H168	06-09-2016	49.0
45.0	Q	H214	4-09-2014	17.0
47.0	Q	H214	4-09-2014	15.9
89.0	W	H214	4-09-2014	8.6
93.0	W	H214	4-09-2014	8.2

Table 3.2: An overview of the ATCA data (Project code: C2993, PI: Galvin) obtained as part of this study. All data used the compact array broadband backend, giving a total of 2.048 GHz per central frequency. The Largest Angular Scale (LAS) that each array is sensitive to.

and K-band data were collected on 23<sup>rd</sup> January 2015 in a 6A array configuration. We used PKS 1934–638 to provide a flux density calibration for both bands. For K-band data taken on this night, PKS 1921–293 was used as a bandpass calibrator. During this initial 12 hour observing run, each source was observed for at least 5 minutes across at least 3 cuts. A phase calibrator was also visited at least once every ten minutes. Subsequent K-band data were collected on 30<sup>th</sup> December 2015 and 26<sup>th</sup> September 2016 in compact 750C and H168 array configurations. Data obtained in the 750C array configuration used the same observing strategy outlined above. For the H168 array K observing band, we elected to dwell on each source for a single 10 minute block of time across a single 4 hour block of green time. This ‘single block’ approach minimised the total time lost to overheads, while the addition of the north-south spur adequately sampled the inner most  $uv$ -region. A phase reference scan was made after each source.

The C/X band frequencies were obtained across two separate observing runs totalling roughly 17 hours. The first, performed on 27<sup>th</sup> January 2015 for 12 hours, used a sparsely distributed 6A configuration. On 29<sup>th</sup> December 2015, we again revisited the sample in a compact 750C array. For both observing sessions, PKS 1934–638 was used as a bandpass calibrator and flux density scale. In total, across both observing runs, each source was observed for roughly 7 minutes with at least 4 cuts.

Because of the wide range of LST of our sources, we could not ensure a consistent amount of integration time equally spread across the  $uv$ -space for our complete sample. Traditionally, this would be a problem for widefield image deconvolution because of the poorly constrained instrumental response, but as we are primarily interested a known source at the phase centre of each pointing. Hence, our major obstacle is to try to prevent resolving source structure with increasing frequencies. The inclusion of a short baseline data from 750C, H214, and H168 array configurations for the C/X and K bands and a natural weighting scheme helped in this regard. Collectively, the combination of data was sensitive to roughly the same angular scales.

### 3.3.3 MWA

Low frequency data were obtained from the SKA-LOW precursor, the MWA. Located in Western Australia, it comprises 2048 dual polarisation dipole antennae capable of operating between 70 to 320 MHz with an instantaneous frequency coverage of 30.72 MHz.

One of its key science products, entitled the GaLactic and Extragalactic MWA Survey (GLEAM, Wayth et al., 2015), is imaging the low frequency sky for declinations south of  $+30^\circ$ . The survey itself covers 30000 square degrees to an  $\approx 90\%$  completeness level at 160 mJy. A complete description of the observing, calibration, imaging, and post-image calibration strategies is presented by Hurley-Walker et al. (2017). GLEAM is the largest fraction bandwidth all-sky survey to date, with the final catalogue containing twenty sub-band flux density measurements for each source across the MWA frequency range. The internal flux calibration is better than 10% on the Baars et al. (1977) scale and can vary as a function of sky position.

Source identification and extraction in GLEAM (as outlined by Hurley-Walker et al., 2017) was performed using the AEGEAN software package (Hancock et al., 2012). An initial deep image covering the frequency range of 170-231 MHz was used to extract an initial reference catalogue. After applying quality control measures, the flux density of each source in this reference catalogue was measured in the twenty 7.68 MHz narrow-band images that span the complete 72 to 231 MHz frequency range of MWA (Hurley-Walker et al., 2017). With this forced photometry mode and the decreasing sensitivity at low frequencies, the low frequency sub-band fluxes often had an  $\text{SNR} < 5\sigma$ .

#### 3.3.3.1 Detected Sources

We inspected the GLEAM catalogue to obtain possible low frequency flux densities for our sample of galaxies. Owing to the low resolution of GLEAM, which is around  $120''$ , we compared potential matches by eye<sup>1</sup> to ensure that they were genuine detections in a non-confused field. We

<sup>1</sup>using the GLEAM postcard server found at [http://mwa-web.icrar.org/gleam\\_postage/q/form](http://mwa-web.icrar.org/gleam_postage/q/form)

found sources IRAS F00198–7926, IRAS F01268–5436, IRAS F02364–4751, IRAS F03068–5346, IRAS F03481–4012, IRAS F04063–3236, IRAS F21292–4953, and IRAS F23389–6139 had clear counterparts in the catalogue. Source IRAS F06035–7102, being in the direction of the Large Magellanic Cloud, was not included in this release of GLEAM. Subsequent source extraction was performed for a small region surrounding it using the GLEAM pipeline. For each detected source, GLEAM could provide twenty flux density measurements spanning 72 to 230 MHz, in roughly 8 MHz increments.

### 3.3.3.2 Non-detections

For sources in our sample without a reliable MWA detection, we used the `PRIORISED` option available in `AEGEAN` to estimate the flux density and uncertainty in the GLEAM broad band images. These broad band images were at central frequencies of 88, 115, and 155, each with 30 MHz of frequency coverage, and 200 MHz with 60 MHz of bandwidth. They were chosen in place of the twenty 8 MHz images as their wider bandwidth improved noise characteristics. `PRIORISED` allows the user to fix properties of some source (including its position) and specify characteristics of the MWA synthesised beam while fitting for an object. Using this method, we could obtain a further set of low significance measurements for sources IRAS F00199–7426, IRAS F01388–4618, IRAS F01419–6826, IRAS F06021–4509, IRAS F06206–6315, IRAS F18582–5558, IRAS F20117–3249, IRAS F20445–6218, IRAS F21178–6349, and IRAS F21295–4634.

A similar approach is undertaken for the GLEAM survey. An initial source catalogue is produced for a wide-band image covering 170-230 MHz. This catalogue is then used as a base model for subsequently finding sources on the narrow-band image. All detected components in the wide-band image are first scaled to account for the changing MWA synthesised beam as a function of frequency. Next, `AEGEAN` will optimise the model with only the peak of each component allowed to vary. Although the narrow-band images may have a component with a low significance, the initial model obtained on the wide-band image is used as *a-priori* knowledge about a source and its location. This makes it possible to avoid using an upper limit based on the local RMS in cases where a source is of low significance.

All MWA GLEAM measurements described in Sections 3.3.3.1 and 3.3.3.2 are listed in Table 3.3.

Source <i>IRAS</i>	MWA GLEAM											
	76 MHz (mJy)	84 MHz (mJy)	88 MHz (mJy)	92 MHz (mJy)	99 MHz (mJy)	107 MHz (mJy)	115 MHz (mJy)	119 MHz (mJy)	122 MHz (mJy)	130 MHz (mJy)	143 MHz (mJy)	151 MHz (mJy)
F00198-7926	47.9±121.6	-	-	237.4±97.8	226.4±106.4	101.2±63.3	5.7±48.1	-	179.9±50.0	218.9±47.0	39.5±34.0	156.4±39.6
F00199-7426	-	-	141.0±53.9	-	-	-	-	25.6±25.6	-	-	-	-
F01268-5436	361.9±81.2	237.9±60.0	-	83.7±48.9	28.0±48.6	87.7±38.3	122.5±33.4	-	123.9±30.2	135.5±29.4	147.5±30.0	112.1±25.7
F01388-4618	-	-	32.4±32.4	-	-	-	-	15.2±15.2	-	-	-	-
F01419-6826	-	-	31.0±31.0	-	-	-	-	36.6±14.5	-	-	-	-
F02364-4751	32.5±73.8	139.6±54.3	-	73.6±45.5	27.3±43.3	2.3±35.7	68.0±29.6	-	98.8±27.7	69.2±24.7	52.4±17.5	41.4±15.4
F03068-5346	-	170.0±52.5	-	46.3±45.3	77.9±44.0	98.3±33.3	91.4±28.3	-	74.1±25.2	83.2±24.3	80.2±21.5	38.9±18.7
F03481-4012	-	80.4±59.0	-	93.2±52.3	114.5±48.6	138.7±37.3	69.4±29.9	-	75.0±28.2	64.0±25.0	76.0±24.8	66.4±22.2
F04063-3236	195.1±76.5	-	-	-	-	54.2±37.3	34.9±30.1	-	29.4±28.1	20.7±25.6	18.3±21.3	44.4±19.0
F06021-4509	-	-	38.7±38.7	-	-	-	-	20.9±20.9	-	-	-	-
F06035-7102	898.0±144.6	568.7±97.2	-	686.1±101.7	712.2±106.6	634.5±81.8	530.8±67.7	-	536.6±65.2	510.9±62.0	474.8±56.0	465.7±54.3
F06206-6315	-	-	30.8±30.8	-	-	-	-	14.3±14.3	-	-	-	-
F18582-5558	-	-	40.4±40.4	-	-	-	-	21.8±21.8	-	-	-	-
F20117-3249	-	-	201.0±47.8	-	-	-	-	131.0±39.2	-	-	-	-
F20445-6218	-	-	43.7±43.7	-	-	-	-	20.0±20.0	-	-	-	-
F21178-6349	-	-	47.9±47.9	-	-	-	-	20.6±20.6	-	-	-	-
F21292-4953	40.8±80.3	140.7±65.0	-	50.5±56.8	51.1±47.1	135.1±39.2	61.0±29.8	-	96.4±26.8	79.9±25.4	71.2±19.3	51.1±16.5
F21295-4634	-	-	28.7±28.7	-	-	-	-	17.4±17.4	-	-	-	-
F23389-6139	114.8±62.1	140.2±50.7	-	123.3±48.0	145.2±43.6	191.0±39.4	202.2±34.9	-	181.1±35.5	229.3±33.5	298.3±31.4	268.4±28.8
Source <i>IRAS</i>	MWA GLEAM											
	155 MHz (mJy)	158 MHz (mJy)	166 MHz (mJy)	174 MHz (mJy)	181 MHz (mJy)	189 MHz (mJy)	197 MHz (mJy)	200 MHz (mJy)	204 MHz (mJy)	212 MHz (mJy)	220 MHz (mJy)	227 MHz (mJy)
F00198-7926	-	149.7±38.3	68.6±34.1	188.8±42.2	135.1±40.5	81.0±36.9	156.3±39.2	-	108.2±38.5	114.5±40.4	137.0±41.5	-
F00199-7426	67.5±19.1	-	-	-	-	-	-	37.4±12.0	-	-	-	-
F01268-5436	-	118.6±23.8	65.8±22.0	88.1±22.7	79.0±22.2	102.9±22.0	85.1±23.1	-	97.4±19.1	51.6±18.2	58.5±18.0	86.6±19.6
F01388-4618	20.1±7.4	-	-	-	-	-	-	25.6±5.7	-	-	-	-
F01419-6826	9.8±9.8	-	-	-	-	-	-	19.3±19.3	-	-	-	-
F02364-4751	-	58.5±13.8	52.8±13.2	61.2±14.7	27.0±12.2	57.5±12.7	61.1±12.6	-	40.9±14.5	21.7±12.8	61.7±13.7	29.1±13.6
F03068-5346	-	104.2±18.4	107.4±18.6	91.7±17.9	74.0±15.7	96.7±16.5	77.0±16.7	-	74.3±14.3	74.3±14.4	49.7±12.3	62.7±13.0
F03481-4012	-	40.1±21.2	59.4±20.2	25.2±20.4	84.4±21.4	91.4±21.4	70.6±19.4	-	57.0±15.1	70.3±15.2	62.2±15.1	82.3±15.6
F04063-3236	-	22.3±18.0	40.8±16.2	3.1±15.5	31.0±13.3	15.8±12.9	40.5±12.2	-	47.0±14.2	10.4±12.5	47.9±13.3	58.2±14.1
F06021-4509	48.8±14.2	-	-	-	-	-	-	7.4±7.4	-	-	-	-
F06035-7102	-	483.9±54.9	480.6±55.2	534.6±60.5	458.3±54.4	465.5±54.6	375.6±48.2	-	436.4±52.7	412.5±49.9	366.9±45.4	408.6±49.9
F06206-6315	30.8±8.8	-	-	-	-	-	-	23.5±8.4	-	-	-	-
F18582-5558	21.9±21.9	-	-	-	-	-	-	12.6±12.6	-	-	-	-
F20117-3249	22.2±22.2	-	-	-	-	-	-	86.5±15.4	-	-	-	-
F20445-6218	16.8±16.8	-	-	-	-	-	-	15.6±15.6	-	-	-	-
F21178-6349	14.2±14.2	-	-	-	-	-	-	13.0±13.0	-	-	-	-
F21292-4953	-	78.2±17.4	47.9±14.8	23.0±15.3	55.5±16.2	24.0±15.2	82.0±16.7	-	72.7±17.4	43.9±17.9	28.6±16.6	49.5±17.3
F21295-4634	10.5±10.5	-	-	-	-	-	-	21.7±8.0	-	-	-	-
F23389-6139	-	239.4±27.4	273.0±27.5	239.8±26.3	286.6±31.7	317.2±30.7	292.4±29.5	-	272.5±29.2	250.0±27.6	269.6±26.6	255.5±26.8

Table 3.3: An overview of all radio-continuum measurements obtained from the MWA GLEAM project (Wayth et al., 2015). Sources with more than 20 measurements were taken directly from the MWA GLEAM catalogue (Hurley-Walker et al., 2017). Otherwise, sources with only four measurements at frequencies of 88, 119, 155, and 200 MHz were obtained using the PRIORISED option available in the AEGEAN packages.

Project	Date	$\nu$ (GHz)	RA (J2000)	DEC (J2000)
C222	21-6-1993	4.8	00:22:08.4	-74:08:31.95
	21-6-1993	8.6	00:22:08.4	-74:08:31.95
C539	5/7-1-1998	4.8	22:39:09.4	-82:44:11.00
	5/7-1-1998	8.6	22:39:09.4	-82:44:11.00
	27/28-1-1998	4.8	22:39:09.4	-82:44:11.00
	27/28-1-1998	8.6	22:39:09.4	-82:44:11.00
	27-1-2002	1.4	22:39:09.4	-82:44:11.00
	27-1-2002	2.5	22:39:09.4	-82:44:11.00

Table 3.4: An overview of the archive ATCA data identified for this project. All observations used the old ATCA correlator, providing only 128 MHz of bandwidth.

### 3.3.4 Archived Radio-Continuum Data

The Australian Telescope Online Archive<sup>2</sup> (ATOA) was used to search for existing ATCA data of sources in our sample. Projects C222 and C593 were found to have observed IRAS F00199–7426 and IRAS F23389–6139, respectively. Their bandwidth was limited to 128 MHz as they were taken using the old ATCA correlator. We have summarised these observations in Table 3.4.

#### 3.3.4.1 Other

We sourced any radio-continuum or far-infrared flux density measurements from the literature for each of our sources. Initially, we collected measurements from the photometry tables for our sample tracked by the online NED<sup>3</sup> tool.

Additional far-infrared measurements were obtained from the *AKARI* space telescope (Murakami et al., 2007). With the exception of IRAS F21295–4634 and IRAS F23389–6139 all sources in our sample were detected at 90  $\mu\text{m}$  in the *AKARI* All-Sky Survey Point Source Catalog (Yamamura et al., 2010). Brighter sources were also detected at 65 and 140  $\mu\text{m}$ . These measurements were not included in the photometry tables retrieved from NED. We have listed all measurements obtained from either NED, with references to their origin or Yamamura et al. (2010), in Table 3.5.

An image of the LMC at 20 cm presented by Hughes et al. (2006, 2007) was used to obtain a single flux density measurement at 1.4 GHz for IRAS F06035–7102. This was particularly important as our L/S band ATCA data for this source was difficult to image and was ultimately discarded because of its sparse  $(u, v)$ -sampling and the complexity of the LMC field.

<sup>2</sup><http://atoa.atnf.csiro.au/>

<sup>3</sup><http://ned.ipac.caltech.edu/>

Source	SUMSS	NVSS	PMN	IRAS		AKARI	ISOPHOT						
IRAS	843 MHz (mJy)	1.4 GHz (mJy)	4.85 GHz (mJy)	3000 GHz (Jy)	5000 GHz (Jy)	3330 GHz (Jy)	4160 GHz (Jy)	1470 GHz (Jy)	1620 GHz (Jy)	1860 GHz (Jy)	2520 GHz (Jy)	3150 GHz (Jy)	4930 GHz (Jy)
F00198–7926	36.7±3.0	–	–	2.9±0.3	3.1±0.2	–	2.4±0.2	–	–	–	–	–	–
F00199–7426	40.8±3.6	–	–	6.4±0.5	4.2±0.3	5.4±0.5	4.4±0.3	3.9±0.3	3.0±0.9	4.2±1.3	5.3±1.6	7.5±2.3	–
F01268–5436	20.3±1.6	–	–	2.3±0.2	1.7±0.2	2.5±0.5	1.6±0.1	–	–	–	–	–	–
F01388–4618	19.7±1.4	–	–	3.7±0.3	2.9±0.3	–	2.8±0.2	–	–	–	–	–	–
F01419–6826	12.5±1.1	–	–	2.5±0.2	2.2±0.1	–	2.8±0.2	–	–	–	–	–	–
F02364–4751	29.7±1.9	–	–	5.0±0.4	2.8±0.2	4.0±0.5	3.2±0.2	–	–	–	–	–	–
F03068–5346	28.9±2.2	–	–	4.0±0.3	3.4±0.2	–	2.9±0.2	3.1±0.3	1.4±0.4	1.7±0.5	–	–	–
F03481–4012	21.9±1.7	15.8±1.1	–	2.6±0.2	1.8±0.1	–	1.6±0.1	–	–	–	–	–	–
F04063–3236	11.9±1.6	11.5±1.2	–	2.1±0.2	1.8±0.1	–	1.7±0.2	–	–	–	–	–	–
F06021–4509	10.9±1.3	–	–	2.4±0.3	1.6±0.1	–	1.4±0.1	–	–	–	–	–	–
F06035–7102	152.0±10.7	–	–	5.7±0.4	5.1±0.3	4.8±0.3	4.5±0.2	4.6±0.3	1.4±0.4	2.0±0.6	2.9±0.9	5.2±1.6	5.0±1.5
F06206–6315	22.6±1.6	–	–	4.6±0.4	4.0±0.2	4.0±0.3	3.5±0.2	3.5±0.3	1.5±0.5	1.9±0.6	2.9±0.9	4.6±1.4	4.2±1.3
F18582–5558	12.0±1.2	–	–	–	1.9±0.2	–	1.8±0.1	–	–	–	–	–	–
F20117–3249	54.4±3.5	57.1±3.4	–	–	1.5±0.1	–	2.3±0.2	–	–	–	–	–	–
F20445–6218	17.8±1.4	–	–	2.9±0.3	2.2±0.1	2.9±0.4	2.1±0.2	–	–	–	–	–	–
F21178–6349	10.2±1.4	–	–	2.0±0.2	1.6±0.1	–	1.4±0.1	–	–	–	–	–	–
F21292–4953	28.5±1.9	–	–	3.1±0.3	2.5±0.2	3.5±0.6	2.5±0.2	–	–	–	–	–	–
F21295–4634	18.2±1.4	–	–	3.2±0.3	2.4±0.2	–	–	–	–	–	–	–	–
F23389–6139	166.0±9.7	–	59.0±8.5	4.3±0.3	3.6±0.2	–	–	–	1.5±0.5	2.0±0.6	2.8±0.9	4.0±1.2	3.3±1.0
													3.9±1.2

Table 3.5: An overview of all flux density measurements obtained from the literature that were used for sources in our samples. ‘–’ denotes sources without a measurement for that survey or instrument. References: SUMSS - Mauch et al. (2013), NVSS - Condon et al. (1998), PMN - Gregory et al. (1994), IRAS - Moshir (1990), AKARI - Yamamura et al. (2010), ISOPHOT - Klaas et al. (2001b).

## 3.4 Data Reduction

### 3.4.1 Radio-Continuum

#### 3.4.1.1 Centimetre ATCA Calibration

The MIRIAD (Sault et al., 2011) and KARMA (Gooch, 2011) software packages were used for data reduction and analysis. The guided automated flagging MIRIAD routine PGFLAG was used in conjunction with more traditional MIRIAD flagging and calibration tasks to perform an initial data reduction. A workflow summary of the calibration process is shown in Figure 3.1. Given the wide bandwidth of the CABB system, appropriate MIRIAD tasks used the NFBIN option to derive a frequency-dependent calibration solution.

#### 3.4.1.2 Millimetre ATCA Calibration

At increasing frequencies, the ATCA flux density calibrator becomes fainter. Although its flux density model is now well understood for frequencies up to 50 GHz, meaning it can be continued to be used to establish a consistent flux scale across all observing bands, it is not a suitable bandpass calibrator.

For an accurate bandpass calibration to be derived, a strong source has to be observed. It is suggested that a SNR of 100 should be achieved per channel. This guideline requires a Jansky level source. Hence, a source other than PKS 1934–638 needs to be used.

This presents a problem during data reduction. The wide bandwidth receivers of ATCA allow the spectral shape of a source to be observed in a single observation. When calibrating the bandpass shape using a sufficiently strong source, the spectral slope of the source should be known. At centimetre wavelengths, the known spectral model of PKS 1934–638 can be included when deriving bandpass corrections. For other sources, where there a reliable flux model is not known, the MIRIAD task MFCAL will assume that the source has a flat spectral shape. An example of this is shown in Figure 3.2. This is not a reasonable spectral shape for most sources, and more than likely never will be.

The bandpass solutions and absolute flux reference scale derived and applied using the standard CABB calibration workflow (shown in Figure 3.1) can be incorrect for high frequency data. An incorrect bandpass calibration can lead to additional error in the flux scale applied to sources. This issue would be more pronounced in sub-band fluxes and can affect the modelled spectral shape of objects. To produce a more reliable bandpass solution, and hence more correct absolute flux scale, the spectral shape of PKS 1921–293 (or any bandpass calibrator) can be recovered and subsequently leveraged for use as an absolute flux calibrator.

To achieve this, after applying the initial bandpass solutions to the flux calibrator PKS 1934–638,



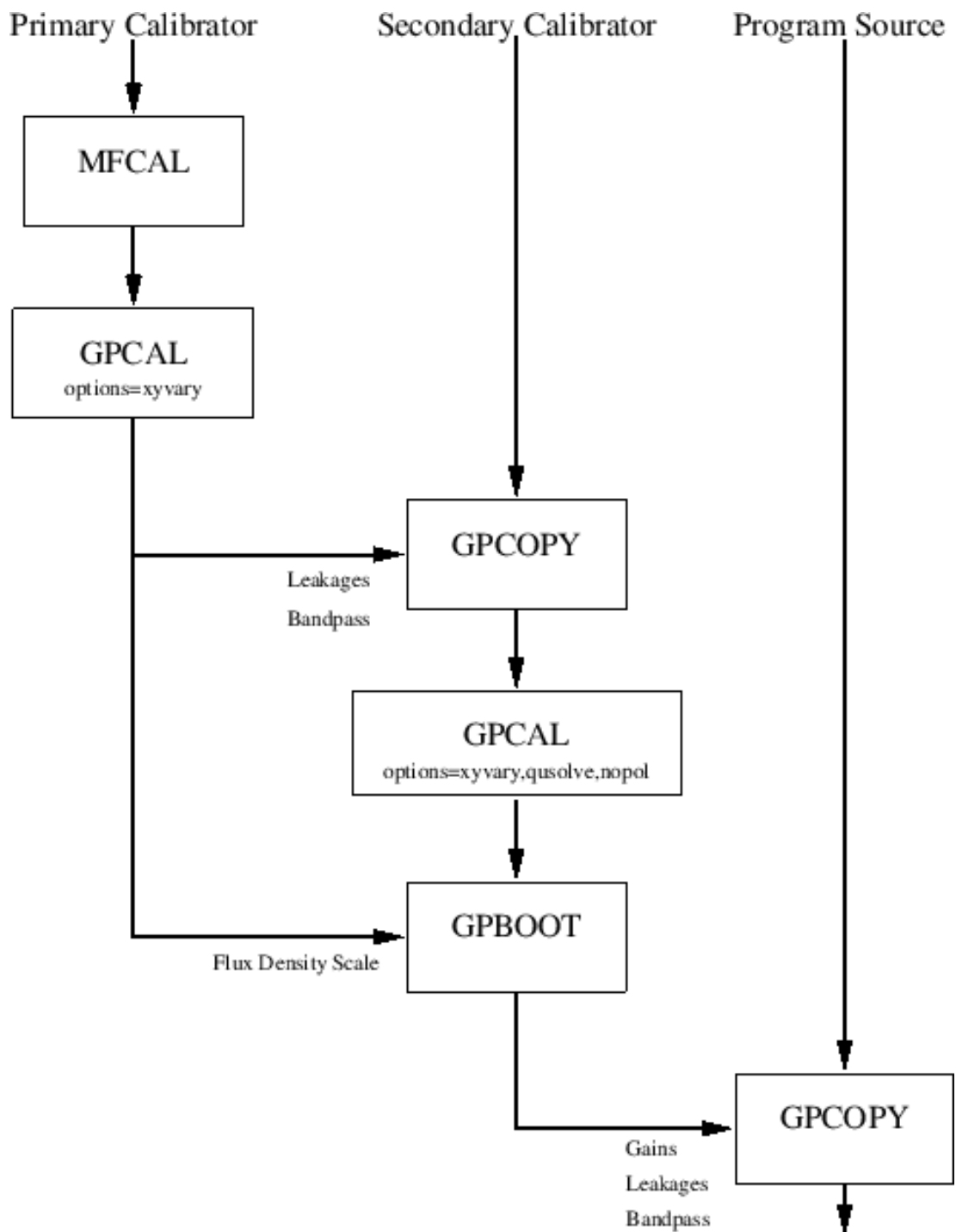


Figure 3.1: An overview of the typical MIRIAD data reduction strategy for ATCA CABB radio-continuum data. This Figure has been taken from the MIRIAD User Guide, accessible at <https://www.atnf.csiro.au/computing/software/miriad/userguide/node87.html>.

Stokes I, Spectrum Measurement: Source 1921–293

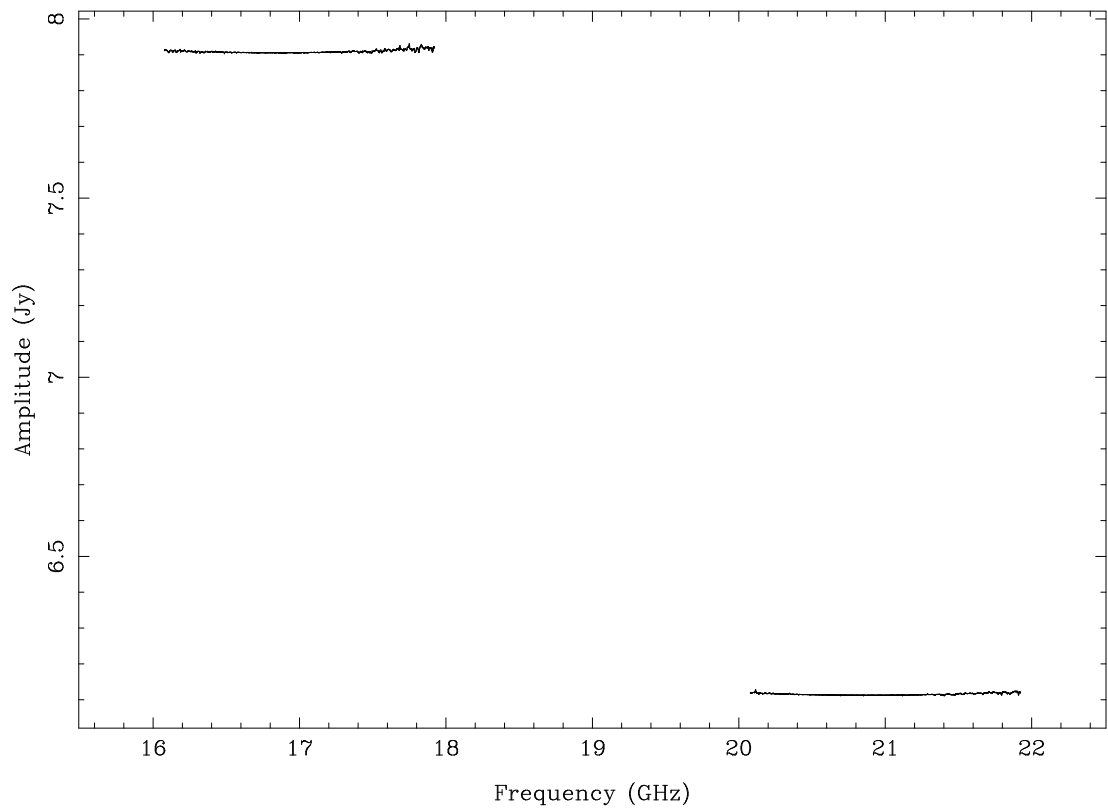


Figure 3.2: The spectrum of PKS 1921–293 after applying an initial bandpass solution derived using MFCAL for two ATCA CABB bands centred at 19 GHz and 21 GHz.

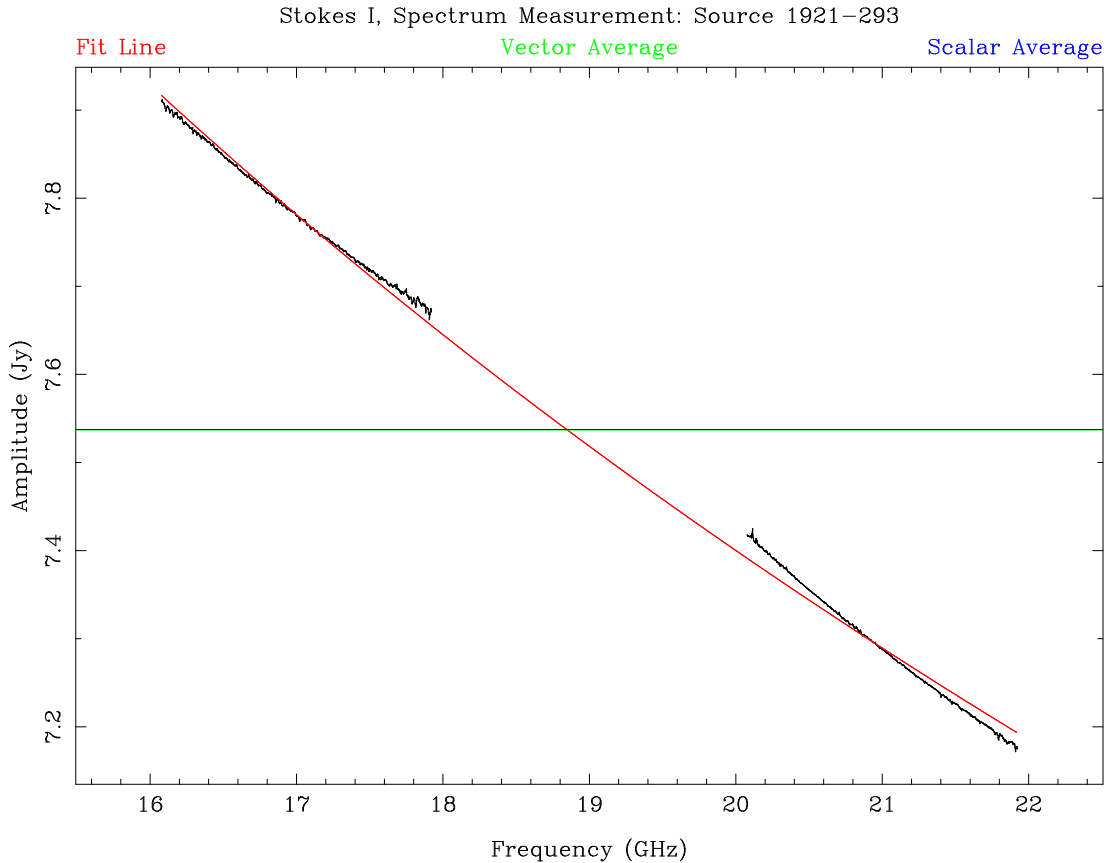


Figure 3.3: The spectral slope of the bandpass calibration PKS 1921–293 after applying the absolute flux scaling corrections derived from PKS 1934–638. The two ATCA CABB bands, which were previously both flat, show a strong trend. A spectral index, as shown as a red line, is constrained using information from both bands.

an absolute flux scaling correction is derived. As MIRIAD is aware of the spectral shape of PKS 1934–638, these solutions will correctly account for the source slope. Once derived, they are then applied back to PKS 1921–293 with the task GPBOOT. The case when the spectrum of PKS 1921–293 is recovered is shown in Figure 3.3. Although there is now a strong trend between the two separately calibrated CABB bands, there is a slight residual left after constraining a simple power law. This residual is non-physical and an artefact of the false assumption of a flat spectrum used during the initial bandpass calibration.

The residual error can be removed by using the constrained spectral index as a user provided model to MFCAL as it produces its bandpass calibration solutions. When this is included, the final spectrum of PKS 1921–293 can be treated as known to produce a more reliable bandpass calibration, and hence more accurate flux density, for subsequent sources. At this stage, the calibration solutions of PKS 1921–293, which include bandpass corrections and absolute flux scaling, may be transferred to secondary phase calibrators. The final spectrum, with bandpass corrections applied, is shown in Figure 3.4.

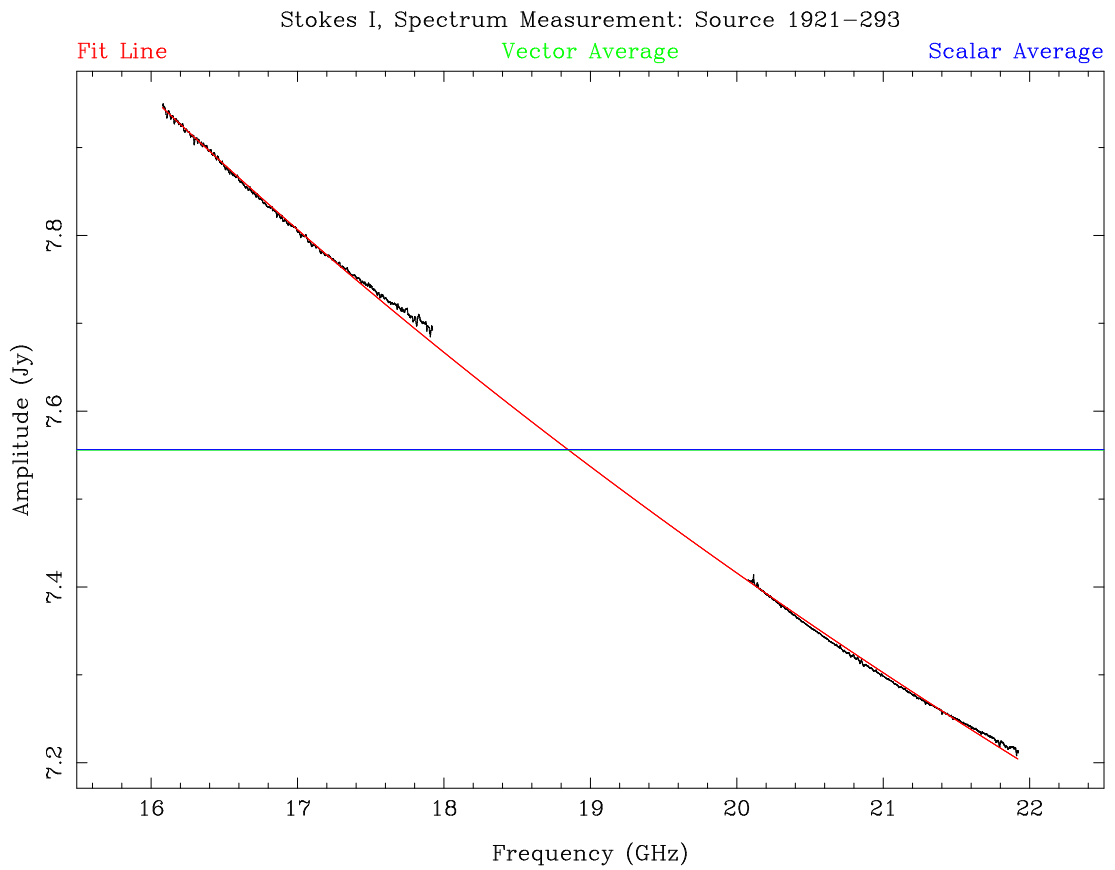


Figure 3.4: The spectral slope of the bandpass calibration PKS 1921–293 after applying the absolute flux scaling corrections derived from PKS 1934–638 and final bandpass solutions solved for using a user provided model. The red line highlights the best fit spectral index constrained in Figure 3.3.

### 3.4.1.3 Imaging

Once a calibration solution was applied to each of the observational programme sources, the centimetre data were then imaged individually across all frequency bands using their complete bandwidth ( $\Delta\nu = 2.048$  GHz, minus the edge channels automatically flagged by ATLOD). A Briggs robust parameter value of 2, corresponding to natural weighting, was used to provide the maximum SNR at the cost of producing a larger synthesised beam. Given the large fractional bandwidth provided by CABB, MFCLEAN (Sault and Wieringa, 1994) was used to deconvolve the multi-frequency synthesised dirty map. MIRIAD tasks RESTOR and LINMOS were used in conjunction to deconvolve sidelobe artefacts and primary beam correction was performed while accounting for the spectral index of the clean components. These preliminary images were produced to inspect and compare the applied calibration solution among the  $uv$ -datasets for each source.

An iterative procedure, similar to that used by Galvin et al. (2016), was used to exploit the generous 2 GHz bandwidth provided by the ATCA CABB system. Initially, each CABB band was imaged individually using the recipe outlined above. Next, the MIRIAD task IMFIT was used to constrain each source of interest using a single point source model. If the extracted peak flux density was above a SNR of 8, the CABB dataset would be split into an increasing number of sub-bands and reprocessed. We also ensured that each sub-band had a fraction bandwidth larger than 10% so that MFCLEAN could safely be used. Given sufficient signal-to-noise across all sub-bands, this iterative procedure would continue to a maximum of four sub-bands. We utilised the LINE parameter in INVERT to ensure each image shared an equal amount of unflagged channels. With such an approach, sources with high SNR were split into multiple data points, which could be used to better constrain the radio-continuum emission models (see § 3.5.1).

For the high frequency Q and W band observations observed for this project, we used the MIRIAD task UVFIT to fit a single point source model directly to the  $uv$ -data for each source. We elected to not iteratively increase the number of sub-bands (similar to the process outlined above) or include a spectral index as a parameter while fitting to the visibilities (implemented in the MIRIAD task UVSFIT) because at these frequencies, the fractional bandwidth is below 5% and spectral variation would be difficult to constrain.

For archived data, where only 128 MHz of data were available, the NFBIN option was not used during typical calibration procedures<sup>4</sup>. A joint deconvolution method was applied to applicable datasets, namely those from C539, to minimise the resulting noise characteristics. Otherwise normal imaging procedures were used to deconvolve the beam response and apply primary beam corrections to all images. The task IMFIT was used to fit a point source model

---

<sup>4</sup><http://www.atnf.csiro.au/computing/software/miriad/userguide/>

to sources of interest. Image residuals were inspected to ensure an adequate fit.

#### 3.4.1.4 Resolving structure

We examined the outputs of the iterative imaging process, including the modelled point source residuals, SUMSS images, and the initial SEDs that the imaging pipeline produced to assess whether our data was resolving components of an object. This review showed that our 4 cm data for IRAS F06035–7102 was detecting extended structures distinct from the main component of the source and within the SUMSS source. Therefore, we applied a convolving beam to produce a final resolution of  $45 \times 45''$  (the same size of the SUMSS restoring beam) to all images above a frequency of 4 GHz for this source, which was used to extract peak flux densities. We added an additional 10% error in quadrature for these measurements.

To assess whether there were other sources in our sample with similar diffuse features, we compared the peak fluxes obtained by fitting a point source model to all images before and after they were convolved with a Gaussian kernel, as well as the integrated flux of a Gaussian model fitted to the non-convolved image. We found that there was weak evidence of structure for IRAS F21292–4953 above frequencies of 6 GHz. Convolved peak flux density measurements were therefore used for images between  $4.0 < \nu < 22.0$  for this source. Otherwise, there were no other sources showing flux densities that were inconsistent among these methods.

IRAS F23389–6139, however, showed that the 4 cm C/X bands was roughly  $\sim 6$  mJy below the ATCA pre-CABB fluxes from project C539 and the trend seen between 3 to 17 GHz. During investigation, we found that measurements made using the visibilities directly with the MIRIAD task UVFIT produced results that were in excellent agreement with the rest of the data. We believe that this difference in peak flux densities was a combination of clean bias and imaging artefacts that could not be deconvolved due to the sparse  $(u, v)$ -sampling.

Our typical restoring beams were  $20 \times 10''$  in the L-band,  $10 \times 5''$  in the C/X band, and  $5 \times 3''$  in the K-band. For each image, we also computed the brightness temperature sensitivity. We compared this to the model from Condon (1992) normalised to 1 K at 1.4 GHz, which is the median brightness temperature of a face on a spiral galaxy (Condon et al., 1998). The brightness temperatures of our images was all higher than this lower limit.

All ATCA flux density measurements obtained under the project code C2993 are listed in Table 3.6.

Source IRAS	This Study																									
	1.5 GHz (mJy)	1.6 GHz (mJy)	1.8 GHz (mJy)	2.0 GHz (mJy)	2.2 GHz (mJy)	2.4 GHz (mJy)	2.6 GHz (mJy)	2.8 GHz (mJy)	4.4 GHz (mJy)	4.5 GHz (mJy)	5.0 GHz (mJy)	5.5 GHz (mJy)	5.6 GHz (mJy)	6.3 GHz (mJy)	6.8 GHz (mJy)	7.2 GHz (mJy)	7.3 GHz (mJy)	8.3 GHz (mJy)	8.8 GHz (mJy)	9.2 GHz (mJy)	17.0 GHz (mJy)	21.0 GHz (mJy)	43.1 GHz (mJy)	48.1 GHz (mJy)		
F00198–7926	19.4±1.2	–	–	14.9±1.0	–	12.3±0.9	–	11.0±0.9	10.4±0.7	–	9.7±0.6	–	8.9±0.6	8.0±0.6	–	–	6.7±0.5	–	5.7±0.4	–	3.5±0.3	2.7±0.3	1.5±0.2	1.4±0.3		
F00199–7426	19.0±1.2	–	–	16.9±1.1	–	14.3±0.9	–	13.3±0.9	10.7±0.7	–	9.9±0.6	–	8.6±0.6	7.8±0.6	–	–	6.6±0.5	–	5.0±0.4	–	3.4±0.2	2.5±0.3	1.5±0.2	2.0±0.3		
F01268–5436	10.2±0.8	–	–	8.4±0.7	–	7.4±0.7	–	7.2±0.6	5.0±0.4	–	4.2±0.4	–	3.5±0.4	3.4±0.3	–	–	2.9±0.2	–	1.9±0.3	–	1.8±0.2	1.4±0.3	1.0±0.1	1.1±0.2		
F01388–4618	9.2±0.8	–	–	8.3±0.7	–	8.4±0.7	–	7.8±0.6	6.4±0.4	–	5.9±0.4	–	5.5±0.4	4.6±0.3	–	–	4.0±0.3	–	3.2±0.3	–	2.0±0.2	1.8±0.3	0.9±0.1	1.2±0.2		
F01419–6826	7.0±0.6	–	–	7.0±0.5	–	6.6±0.6	–	4.8±0.7	4.2±0.3	–	3.6±0.3	–	3.1±0.3	2.9±0.2	–	–	2.7±0.2	–	2.2±0.2	–	1.6±0.2	1.0±0.2	–	1.3±0.3		
F02364–4751	17.5±1.1	–	–	14.0±0.9	–	12.1±0.8	–	12.2±0.8	8.9±0.5	–	7.3±0.4	–	6.8±0.4	5.8±0.4	–	–	5.2±0.4	–	3.6±0.4	–	2.9±0.2	2.2±0.2	1.4±0.1	1.2±0.2		
F03068–5346	–	–	9.5±1.0	–	–	–	–	6.0±0.9	–	–	6.9±0.6	–	6.4±0.8	–	–	–	4.4±0.6	–	4.4±0.3	–	3.6±0.4	2.7±0.3	1.7±0.1	2.0±0.2		
F03481–4012	11.3±0.7	–	–	10.5±0.6	–	8.7±0.6	–	8.3±0.6	5.9±0.4	–	6.1±0.4	–	5.3±0.4	4.8±0.3	–	–	3.8±0.3	–	3.0±0.3	–	2.2±0.2	1.8±0.3	0.9±0.1	0.7±0.2		
F04063–3236	7.4±0.5	–	–	6.5±0.5	–	5.5±0.5	–	5.3±0.5	4.8±0.4	–	5.5±0.3	–	4.8±0.3	5.0±0.3	–	–	3.9±0.3	–	2.9±0.3	–	1.8±0.2	1.3±0.3	0.8±0.1	–		
F06021–4509	7.1±0.6	–	–	7.5±0.6	–	6.8±0.6	–	5.8±0.6	4.8±0.3	–	4.8±0.3	–	4.4±0.3	4.2±0.2	–	–	3.6±0.2	–	3.0±0.2	–	1.7±0.2	1.1±0.2	1.2±0.2	1.3±0.3		
F06035–7102	–	–	–	–	–	–	–	–	20.6±2.8	–	20.1±2.6	–	17.8±2.2	16.1±2.0	–	–	13.4±1.6	–	11.0±1.2	–	7.0±2.2	5.1±2.3	1.8±0.2	2.0±0.3		
F06206–6315	15.5±0.9	–	–	14.6±0.9	–	14.7±0.9	–	13.2±0.8	11.4±0.6	–	10.5±0.6	–	9.4±0.5	8.8±0.5	–	–	7.7±0.4	–	6.6±0.4	–	3.5±0.4	2.8±0.3	1.5±0.2	2.3±0.3		
F18582–5558	6.7±0.6	–	–	7.1±0.6	–	7.0±0.6	–	7.4±0.6	6.0±0.5	–	5.8±0.5	–	5.5±0.5	5.0±0.5	–	4.8±0.5	–	4.3±0.4	–	3.9±0.3	2.3±0.2	2.0±0.3	0.8±0.1	–		
F20117–3249	49.7±2.5	–	–	44.7±2.3	–	41.2±2.2	–	36.8±2.0	25.4±1.7	–	23.4±1.7	–	19.2±1.6	16.2±1.4	–	–	13.0±1.4	–	9.8±1.1	–	7.1±0.6	5.1±0.6	2.9±0.1	2.3±0.2		
F20445–6218	9.0±0.6	–	–	8.2±0.6	–	7.1±0.5	–	6.0±0.5	4.7±0.4	–	3.8±0.4	–	3.5±0.4	3.2±0.3	–	–	2.8±0.3	–	2.4±0.3	–	1.7±0.2	1.4±0.2	0.9±0.1	–		
F21178–6349	–	5.1±0.5	–	–	4.0±0.4	–	–	2.8±0.5	–	2.2±0.2	–	1.6±0.3	–	–	–	–	1.6±0.2	–	–	–	0.7±0.2	–	–	–		
F21292–4953	–	–	16.6±1.8	–	–	–	–	11.6±1.2	–	–	9.7±1.0	–	–	–	–	–	8.0±0.9	–	–	–	7.5±0.9	–	6.4±0.6	4.4±0.7		
F21295–4634	10.1±0.8	–	–	10.2±0.8	–	7.5±0.8	–	4.4±0.7	3.7±0.5	–	4.1±0.5	–	3.2±0.5	3.0±0.5	–	–	2.3±0.4	–	1.9±0.3	–	1.8±0.2	1.1±0.3	0.5±0.1	–		
F23389–6139	117.8±6.0	–	–	100.4±5.1	–	91.3±4.7	–	82.3±4.3	56.1±0.8	–	49.2±0.9	–	41.8±0.9	37.1±0.9	–	–	28.2±1.0	–	–	–	25.0±0.6	–	10.4±0.3	8.3±0.6	3.9±0.2	3.8±0.3

Table 3.6: An overview of all radio-continuum flux density measurements produced using ATCA data obtained under the project code C2993 as a part of this study. ‘–’ denotes sources without a measurement for the central frequency. All measurements at 43.1 and 48.1 GHz were obtained by modelling each object directly from the visibilities using UVFIT. Measurements between 4 and 10 GHz for IRAS F23389–6139 were also obtained with UVFIT from the visibilities directly.

## 3.5 SED Modelling

### 3.5.1 Radio-Continuum Models

The coverage of our radio-continuum data was broad, covering 80 MHz to 50 GHz, we elected the size of our sample so as to fit a series of increasingly complex models to all sources. All modelling was performed in the rest frame with a reference frequency, of  $\nu_0 = 1.4$  GHz, unless stated otherwise.

#### 3.5.1.1 Power Law

Initially, we fit a simple power law (‘PL’) to all available flux density measurements, in the form of

$$S_\nu = A \left( \frac{\nu}{\nu_0} \right)^\alpha. \quad (3.1)$$

The terms  $A$  and the spectral index,  $\alpha$ , are treated as free parameters and represent a normalisation component and gradient of the slope in logarithmic space.

#### 3.5.1.2 Composition of Synchrotron and Free-Free

We can model the radio-continuum as the sum of two distinct power laws. One representing the steep spectrum non-thermal synchrotron emission, and the second describing the flat spectral thermal free-free emission, following the form

$$S_\nu = A \left( \frac{\nu}{\nu_0} \right)^\alpha + B \left( \frac{\nu}{\nu_0} \right)^{-0.1}, \quad (3.2)$$

where  $A$  and  $B$  are treated as free parameters and represent the synchrotron and free-free normalisation components, respectively. The free parameter  $\alpha$  represents the synchrotron spectral index, and depending on the history of injected cosmic rays, is known to vary (Niklas et al., 1997). We label this model as ‘SFG NC’.

#### 3.5.1.3 Composition of Synchrotron and Free-Free with Free-Free Absorption

When synchrotron and free-free emission are in a coextensive environment, synchrotron emission can be attenuated by free-free absorption (FFA) processes, producing a low frequency turnover. This attenuation depends upon the flux density and spatial distribution of the ionised free-free emission with respect to the non-thermal synchrotron emission. If the frequency of this turnover from free-free absorption is parameterised by  $\nu_{t,1}$ , then the optical depth can be described as



$\tau = (\nu/\nu_{t,1})^{-2.1}$ . Following Condon (1992) and Clemens et al. (2010), we describe this more complete model (labelled as ‘C’ throughout) as

$$S_\nu = (1 - e^{-\tau}) \left[ B + A \left( \frac{\nu}{\nu_{t,1}} \right)^{0.1+\alpha} \right] \left( \frac{\nu}{\nu_{t,1}} \right)^2, \quad (3.3)$$

where  $\nu_t$  is the turnover frequency where the optical depth reaches unity, and  $\alpha$  is the spectral index of the synchrotron emission.  $A$  and  $B$  represent the synchrotron and free-free emission components. We fit for  $A, B, \nu_{t,1}$  and  $\alpha$  simultaneously. To minimise model degeneracy, particularly in the case when normalisation components are subject to the  $\nu^2$  scaling in the optically thick regime, we replace the  $\nu_0$  term, set to 1.4 GHz in other models, to instead be the turnover frequency parameter for each component.

#### 3.5.1.4 Multiple Free-Free absorption components

Model ‘C’ assumes a single screen of thermal free-free plasma attenuating the synchrotron emission produced by relativistic electrons. Although this model was derived from observations of the irregular, clumpy galaxy Markarian 325 (Condon and Yin, 1990), Clemens et al. (2010) present a set of LIRGS whose radio-continuum show a number of high frequency ‘kinks’ which could be attributed to multiple turnover features. Their interpretation suggests that when multiple star forming regions with different compositions or geometric orientations are integrated over by a large synthesised beam, like in the case of an unresolved galaxy, the observed radio-continuum could be complex.

Following this, we include an additional set of increasingly complex models that aim to capture these higher-order features.

First, we assume a single relativistic electron population that produces the synchrotron emission that is inhomogeneously mixed with two distinct regions of star formation with distinct optical depths. This model (labelled ‘C2 SA’) may be described as

$$S_\nu = (1 - e^{-\tau_1}) \left[ B + A \left( \frac{\nu}{\nu_{t,1}} \right)^{0.1+\alpha} \right] \left( \frac{\nu}{\nu_{t,1}} \right)^2 + (1 - e^{-\tau_2}) \left[ D + C \left( \frac{\nu}{\nu_{t,2}} \right)^{0.1+\alpha} \right] \left( \frac{\nu}{\nu_{t,2}} \right)^2, \quad (3.4)$$

where  $\tau_1$  and  $\tau_2$  describe the optical depths of component one and two (each parameterised with their own turnover frequency  $\nu_{t,1}$  and  $\nu_{t,2}$ ), respectively,  $A$  and  $C$  are the normalisation parameters for the synchrotron mechanism, and  $B$  and  $D$  scale the free-free component.  $\alpha$  is

the spectral index of the single synchrotron population.

To account for sources where the low frequency SED does not indicate a turnover due to free-free absorption, we construct a model similar to ‘C2 1SA’ in the form of

$$S_\nu = \left(\frac{\nu}{\nu_0}\right)^{-2.1} \left[ B + A \left(\frac{\nu}{\nu_0}\right)^{0.1+\alpha} \right] \left(\frac{\nu}{\nu_0}\right)^2 + (1 - e^{-\tau_2}) \left[ D + C \left(\frac{\nu}{\nu_{t,2}}\right)^{0.1+\alpha} \right] \left(\frac{\nu}{\nu_{t,2}}\right)^2. \quad (3.5)$$

The model and its parameters, with the exception of  $\tau_1$  which has been removed, behave the same way as ‘C2 1SA’. The reference frequency for the low frequency component is parameterised as  $\nu_0$  and is set to 1.4 GHz. We maintain this form as it allows the parameters  $A$  and  $B$  to be more directly comparable to  $C$  and  $D$ . We label this model as ‘C2 1SAN’. Although functionally this model is similar to ‘C2 1SA’, we include it for sources which may have a high frequency turnover but no data to support low frequency curvature. Without its inclusion, it is possible that the Bayesian model selection methods (discussed in the next section) may prefer a simpler model that does not attempt to model a low frequency turnover component.

Next, we relax the single spectral index constrain. Although this introduces an additional parameter, its physical motivation is based on a galaxy merger, where two distinct systems merging drives a new burst of star formation. The electron distribution could, in such a scenario, comprise two different populations. We express this model as

$$S_\nu = (1 - e^{-\tau_1}) \left[ B + A \left(\frac{\nu}{\nu_{t,1}}\right)^{0.1+\alpha} \right] \left(\frac{\nu}{\nu_{t,1}}\right)^2 + (1 - e^{-\tau_2}) \left[ D + C \left(\frac{\nu}{\nu_{t,2}}\right)^{0.1+\alpha_2} \right] \left(\frac{\nu}{\nu_{t,2}}\right)^2, \quad (3.6)$$

where parameters carry the same meaning as in ‘C2 1SA’ except we introduce parameters  $\alpha$  and  $\alpha_2$  to characterise the synchrotron spectral indices of component one and component two, respectively. We label this model simply as ‘C2’.

### 3.5.2 Far-Infrared Emission

Heated dust from normal type galaxies, traced by far-infrared emission and approximated well by a greybody, begins to contribute a non-negligible fraction of the observed continuum at frequencies above 100 GHz (Condon, 1992). A greybody is an optically thin, modified blackbody

spectrum written as

$$S_\nu(\lambda) = I \times \left[ \left( \frac{60 \mu\text{m}}{\lambda} \right)^{3+\beta} \times \frac{1}{e^{\frac{hc}{\lambda kT}} - 1} \right], \quad (3.7)$$

where  $S_\nu$  is the flux density in Jy at frequency  $\nu$ ,  $T$  is the absolute temperature of the body in Kelvin,  $\beta$  represents the power-law variation of the emissivity with wavelength, and  $I$  is the normalisation. The  $\beta$  component encodes properties of the distribution of dust grains and their sizes with typical values in the range of 1 to 2 (Hildebrand, 1983; Smith et al., 2013). To appropriately constrain these additional free parameters, we collect all measurements for each source up to  $\lambda = 500 \mu\text{m}$  available from the literature (summarised in Table 3.5).

For each radio-continuum model described in Equations 3.1–3.6, we add a greybody component. The near orthogonal free-free and infrared emission components (specifically the Rayleigh-Jeans property of the greybody) allow us to reduce associated uncertainties for the thermal free-free emission while fitting each SED.

### 3.5.3 Radio-Continuum Fitting and Selection

#### 3.5.3.1 Model Fitting

While fitting our SED models, we followed a similar fitting approach as described by Callingham et al. (2015). An ‘affine invariant’ Markov chain Monte-Carlo ensemble sampler (Goodman and Weare, 2010), implemented as the EMCEE<sup>5</sup> PYTHON package (Foreman-Mackey et al., 2013), was used to constrain each of the described radio-continuum models for each source in our sample. This particular sampling method offers an efficient method for searching for a parameter space using a set of ‘walkers’ for regions of high likelihood during model optimisation. These walkers are relatively insensitive to dependencies or covariance among the free parameters being optimised. Figure 3.5 shows an example of a model with five parameters being optimised. I initialise the walkers in a small Gaussian ball around a region selected using simple least square fitting. The walkers slowly explore the immediate parameter space before settling into a stationary distribution.

Assuming independent measurements whose errors are normally distributed, the log likelihood function that EMCEE attempts to maximise is expressed as

$$\ln \mathcal{L}(\theta) = -\frac{1}{2} \sum_n \left[ \frac{(D_n - f(\theta))^2}{\sigma_n^2} + \ln(2\pi\sigma_n^2) \right] \quad (3.8)$$

where  $D$  and  $\sigma$  are two vectors of length  $n$  containing a set of flux density measurements and their associated uncertainties, and  $f(\theta)$  is the model used to optimise using the parameter

<sup>5</sup><https://github.com/dfm/emcee>

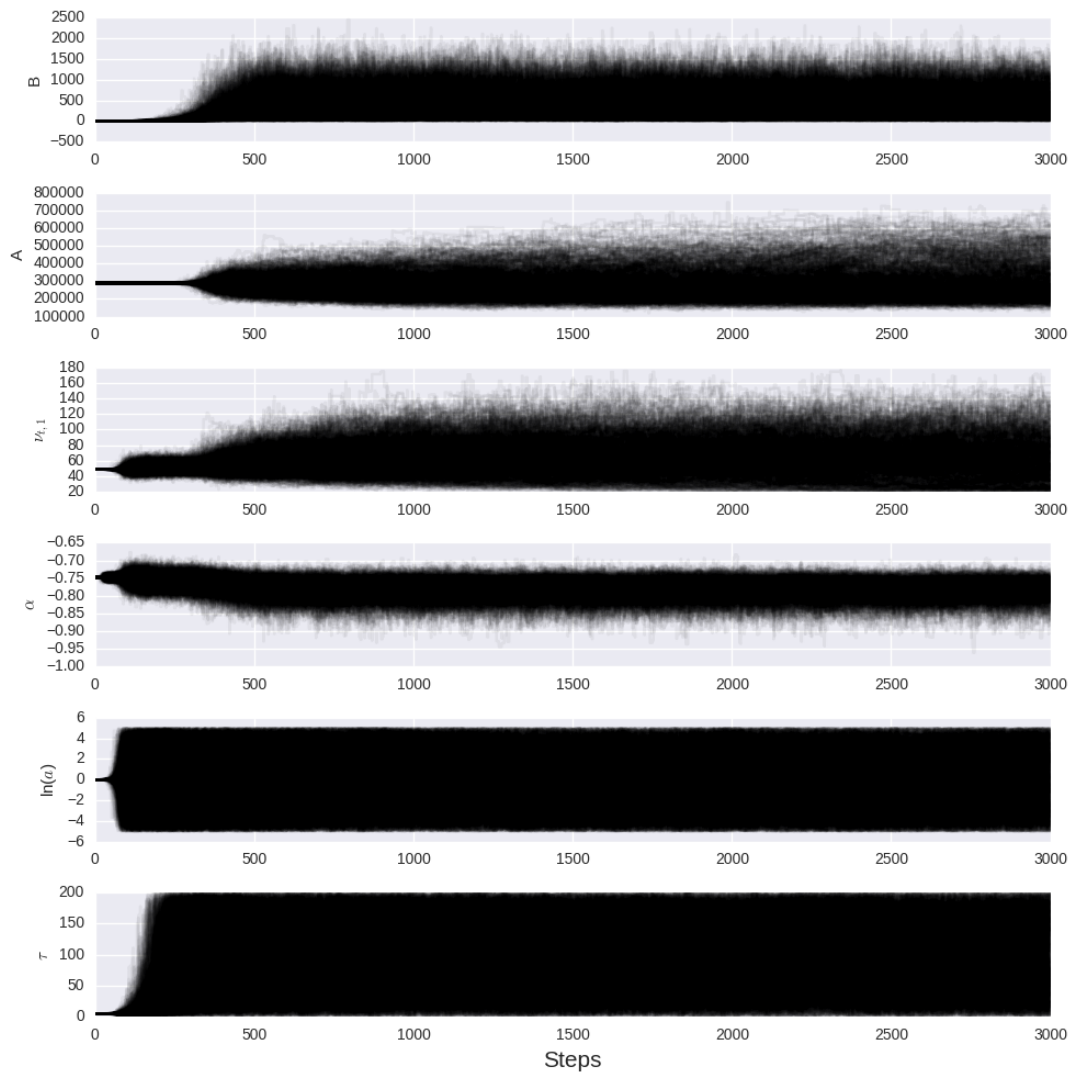


Figure 3.5: Example of the walkers converging for a model.

vector  $\theta$ .

As stated in Section 5.4 of Hurley-Walker et al. (2017), MWA GLEAM 7.68 MHz sub-band measurements have correlated errors, which violate an underlying assumption of Equation 3.8. This covariance was introduced by a combination of self-calibrating visibility data across 30.72 MHz before creating the final set of twenty sub-band images with 7.68 MHz widths and their methods of applying primary beam and absolute flux scaling corrections. Although this could be accounted for with an appropriate covariance matrix, whose off-diagonal elements represent the degree of correlation for a pair of sub-band fluxes, at present, such a matrix is not known. Without accounting for this, any inferences made from constrained models could be biased or incorrect.

We therefore adopted, as part of our fitting routines, a Matérn covariance function, which aims to model the off-diagonal elements of the unknown MWA GLEAM data covariance matrix. This is a radial type covariance function which assumes that measurements closer together (for our problem closer together in frequency space) are more correlated than those further apart. The form we adopt while performing all SED fitting is

$$k(r) = a^2 \left( 1 + \frac{\sqrt{3}r}{\gamma} \right) \exp \left( -\frac{\sqrt{3}r}{\gamma} \right), \quad (3.9)$$

where  $k$  is the parameterised Matérn covariance function,  $r$  is the  $\Delta\nu$  between a pair of flux density measurements.  $a$  and  $\gamma$  are quantities constrained by EMCEE. The PYTHON module GEORGE<sup>6</sup> (Ambikasaran et al., 2014) was used to implement and manage the Matérn covariance function and supply the log likelihood for only the GLEAM flux density measurements of some model given  $\theta$ . This was then summed with the log likelihood obtained using Equation 3.8 for the independent flux density measurements and  $\theta$  parameter vector. Note that the addition of  $a$  and  $\gamma$  increased the free parameters for each model by two. This covariance matrix modelling was not used for sources with a single measurement of MWA GLEAM flux density.

### 3.5.3.2 Model Priors

When constraining models within a Bayesian framework, ‘priors’ describe any known or likely conditions for each parameter in some  $\theta$  set. Such priors can be as simple as limits to enforce a strict value range, or as complex as defining some distribution that the ‘true’ value of a parameter is likely to take. Such priors should include known conditions of some parameter. The sampled posterior that the walkers construct can be sensitive to the conditions encoded as parameter priors, particularly if complex prior distributions are used. Therefore, we use uniform priors which simply enforce a range of values some parameter is allowed to take.

---

<sup>6</sup><https://github.com/dfm/george>

Source <i>IRAS</i>	PL	SFG NC	C	C2 1SAN	C2 1SA	C2
F00198–7926	-12.0	-13.2	-15.8	-10.4	<i><b>0.0</b></i>	<i>-0.9</i>
F00199–7426	-15.4	-17.0	-1.4	<i><b>0.0</b></i>	-1.9	-2.2
F01268–5436	-7.1	<i><b>0.0</b></i>	-2.2	-4.7	-5.1	-5.2
F01388–4618	-12.6	-14.3	<i><b>0.0</b></i>	-3.0	-3.7	-4.5
F01419–6826	<i><b>0.0</b></i>	-1.4	<i>-0.9</i>	-2.3	-2.9	-2.0
F02364–4751	-28.5	-30.1	<i><b>0.0</b></i>	-2.6	-2.4	-1.9
F03068–5346	-9.4	<i>-0.3</i>	<i><b>0.0</b></i>	<i>-0.9</i>	-2.6	-1.6
F03481–4012	<i><b>0.0</b></i>	-1.4	-3.5	-6.5	-3.8	-4.5
F04063–3236	-23.2	-24.8	-30.4	-9.5	<i><b>0.0</b></i>	-1.3
F06021–4509	-8.5	-10.2	-10.4	-1.8	<i>-0.0</i>	<i><b>0.0</b></i>
F06035–7102	-53.9	-55.1	-21.7	<i><b>0.0</b></i>	-1.7	-5.4
F06206–6315	-65.8	-67.2	-29.4	-23.1	<i><b>0.0</b></i>	<i>-0.3</i>
F18582–5558	-24.9	-26.5	-22.9	<i>-0.3</i>	<i>-1.1</i>	<i><b>0.0</b></i>
F20117–3249	-148.5	-150.0	-18.7	<i><b>0.0</b></i>	-7.5	-4.3
F20445–6218	-1.9	-3.3	<i><b>0.0</b></i>	-1.3	-3.3	-1.3
F21178–6349	-2.5	-3.2	<i><b>0.0</b></i>	-4.1	-1.6	-2.1
F21292–4953	<i><b>0.0</b></i>	-1.8	-4.3	-3.3	-5.9	-5.9
F21295–4634	-20.3	-21.9	<i>-0.1</i>	<i><b>0.0</b></i>	-2.0	<i>-1.0</i>
F23389–6139	-1451.1	-1452.6	-211.6	-146.5	<i><b>0.0</b></i>	<i>-1.1</i>

Table 3.7: An overview of the natural log of the Bayes odds ratio from the MULTINEST fitting of each model to every source. For each source, the values presented below are the evidence values for each model divided by the most preferred model (i.e. model with the highest evidence value). As the natural log of ratio is presented, the most preferred models have values in this table equal to  $\log_e(1) = 0$  (Bold-italic typeface with blue background). Less preferred models therefore have more negative numbers. Models where the ratio is less than  $\log_e(3) = 1.1$  are considered indistinguishable from the most preferred model (italic typeface with green background).

Uniform priors are also referred to as being ‘uninformed’ as no likely distribution has been supplied to the Bayesian fitting frameworks.

Throughout our model fitting, we ensured that normalisation parameters A, B, C, and D remain positive and that the spectral index parameters  $\alpha$  and  $\alpha_2$  remain in the range of  $-0.2 > \alpha > -1.8$ , the turnover frequencies are between 10 MHz to 40 GHz, and the  $a$  and  $\gamma$  parameters of Equation 3.9 are between  $-500$  mJy to  $500$  mJy and 1 to 200 MHz respectively.

These priors are founded on the sound assumptions that flux densities are positive emission processes, and we can only constrain turnovers within the range where we have data (note that some SED begins to flatten before the optical depth reaches unity). We construct the limits of the spectral index parameters  $\alpha$  and  $\alpha_2$  to allow a diverse range of values in the literature (Condon and Yin, 1990; Niklas et al., 1997; Clemens et al., 2010). For the Matérn covariance parameters  $a$  and  $\gamma$ , we make no assumption about their value and set their priors to be broad enough such that to encompass all GLEAM data.

### 3.5.3.3 Model Selection

A Bayesian framework grants the ability to objectively test whether the introduction of additional model complexity (where additional complexity is not restricted to an increasing set of nested models) is justified by an improved fit that is not simply a symptom of overfitting. The evidence value,  $\mathcal{Z}$ , is defined as the integral of the complete parameter space. Although computationally difficult to numerically compute, especially in the case of increasing parameter dimensions, recent algorithms have proven to be adept at obtaining reliable estimates of its value. MULTINEST (Feroz et al., 2009) uses a nested sampling method to obtain an estimate of the  $\mathcal{Z}$  value.

Among the  $\mathcal{Z}$  values of competing models  $M_1$  and  $M_2$ , one is able to determine whether a model is preferred over another given a set of data. The Bayes odds ratio between the evidence values  $\mathcal{Z}_1$  and  $\mathcal{Z}_2$  for models  $M_1$  and  $M_2$  is constructed as

$$\Delta\mathcal{Z} = e^{(\mathcal{Z}_1 - \mathcal{Z}_2)} \quad (3.10)$$

The evidence supporting  $M_1$  over  $M_2$  is considered ‘very strong’ with a  $\Delta\mathcal{Z}$  in excess of 150. If  $\Delta\mathcal{Z}$  is between  $150 > \Delta\mathcal{Z} > 20$  or  $20 > \Delta\mathcal{Z} > 3$ , then it is seen as either ‘strong’ or ‘positive’ evidence (respectively) supporting  $M_1$  over  $M_2$ . When  $\Delta\mathcal{Z}$  is less than 3, then  $M_1$  and  $M_2$  are indistinguishable from one another. This scale was established by Kass and Raftery (1995) and is considered the standard ladder for preferred model selection.

We summarise the results of the Bayes odds ratio test for all models in Table 3.7 and highlight the most preferred model with any of its competitors. While estimating  $\mathcal{Z}$  for each model, MULTINEST was configured to search the same parameter space as EMCEE.

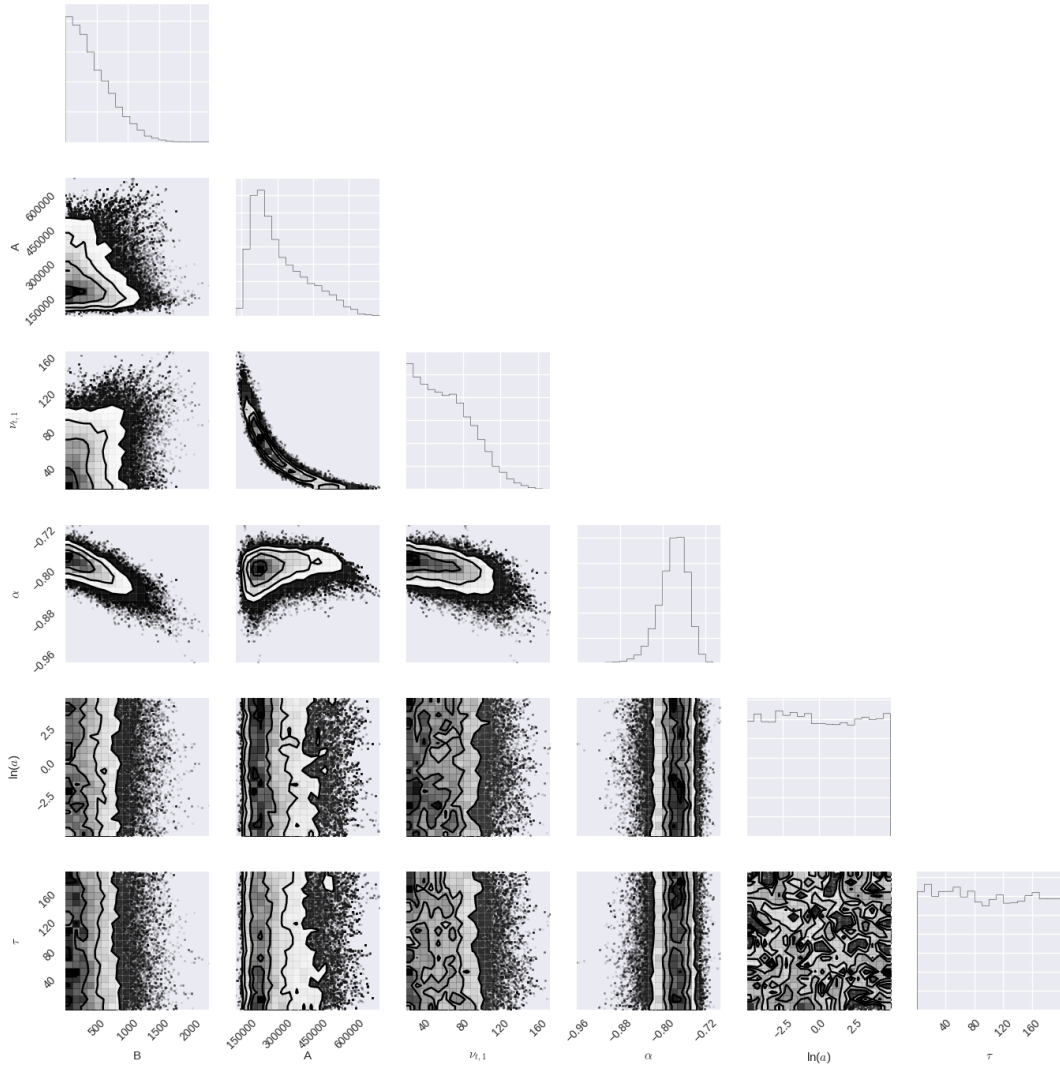


Figure 3.6: Visual depiction of the joint probability of parameters in the sampled model, as sampled by EMCEE.

## 3.6 Results

### 3.6.1 Model Results

Nominal model parameters and their one sigma uncertainties, taken from the posterior distribution constructed by EMCEE, are shown in Table 3.8. Using the sampled posterior distribution, we take the 50<sup>th</sup> percentile as the nominal value, and the 16<sup>th</sup> and 84<sup>th</sup> percentiles represent the one sigma uncertainties. These posterior distributions were also saved and used when estimating derived quantities, including luminosities or thermal fractions, to accurately propagate errors and maintain covariance amongst a given model's fitted parameters.

Figure 3.6 shows an example of the posterior distribution sampled by the EMCEE algorithm displayed as a corner plot (using the python CORNER module described in Foreman-Mackey, 2016). The samples that make up the plot were saved as a PYTHON PICKLE object so that they



could later be loaded when computing model properties and uncertainties.

The final set of SEDs is presented as Figure 3.7. These SEDs include the most preferred model judged strictly by the Bayes evidence values. We include model specific features that were possible additional overlaid components. Highlighted regions of all plotted components represent the one sigma (68%) confidence interval.

Table 3.8: An overview of the most supported models judged strictly by their evidence value and their constrained values. We use the 50<sup>th</sup> percentile of the samples' posterior distribution as the nominal value and use the 16<sup>th</sup> and 84<sup>th</sup> percentiles to provide the  $1\sigma$  uncertainties. Parameters not included in a model are marked by a '-'. We omit parameters constrained that belong to the Matérn covariance function.

Source <i>IRAS</i>	Model	A mJy	B mJy	$\alpha$	$\nu_{t,1}$ GHz	C mJy	D mJy	$\alpha_2$	$\nu_{t,2}$ GHz	I Jy	Temp. K	$\beta$
F00198–7926	C2 1SA	187.9 <sup>+16.7</sup> <sub>-15.2</sub>	0.5 <sup>+0.6</sup> <sub>-0.4</sub>	-1.3 <sup>+0.1</sup> <sub>-0.1</sub>	0.2 <sup>+0.0</sup> <sub>-0.0</sub>	7.6 <sup>+0.8</sup> <sub>-1.0</sub>	0.5 <sup>+0.4</sup> <sub>-0.3</sub>	-	6.2 <sup>+0.7</sup> <sub>-0.6</sub>	0.23 <sup>+0.06</sup> <sub>-0.06</sub>	55.5 <sup>+4.5</sup> <sub>-3.2</sub>	1.3 <sup>+0.3</sup> <sub>-0.2</sub>
F00199–7426	C2 1SAN	6.4 <sup>+2.6</sup> <sub>-3.0</sub>	0.2 <sup>+0.3</sup> <sub>-0.2</sub>	-0.8 <sup>+0.0</sup> <sub>-0.0</sub>	-	46.6 <sup>+21.8</sup> <sub>-13.7</sub>	0.2 <sup>+0.3</sup> <sub>-0.2</sub>	-	0.5 <sup>+0.2</sup> <sub>-0.1</sub>	1.52 <sup>+0.41</sup> <sub>-0.29</sub>	40.1 <sup>+1.8</sup> <sub>-1.9</sub>	1.1 <sup>+0.2</sup> <sub>-0.1</sub>
F01268–5436	SFG NC	0.8 <sup>+0.2</sup> <sub>-0.2</sub>	12.4 <sup>+0.4</sup> <sub>-0.4</sub>	-1.0 <sup>+0.0</sup> <sub>-0.0</sub>	-	-	-	-	-	0.34 <sup>+0.22</sup> <sub>-0.12</sub>	44.7 <sup>+4.6</sup> <sub>-4.4</sub>	1.3 <sup>+0.4</sup> <sub>-0.3</sub>
F01388–4618	C	44.4 <sup>+5.5</sup> <sub>-4.2</sub>	0.2 <sup>+0.2</sup> <sub>-0.1</sub>	-0.7 <sup>+0.0</sup> <sub>-0.0</sub>	0.3 <sup>+0.0</sup> <sub>-0.0</sub>	-	-	-	-	0.59 <sup>+0.25</sup> <sub>-0.19</sub>	45.7 <sup>+3.8</sup> <sub>-3.1</sub>	1.6 <sup>+0.2</sup> <sub>-0.3</sub>
F01419–6826	PL	8.7 <sup>+0.3</sup> <sub>-0.3</sub>	-	-0.7 <sup>+0.0</sup> <sub>-0.0</sub>	-	-	-	-	-	0.82 <sup>+0.37</sup> <sub>-0.32</sub>	41.2 <sup>+3.7</sup> <sub>-2.5</sub>	1.7 <sup>+0.2</sup> <sub>-0.4</sub>
F02364–4751	C	86.5 <sup>+4.7</sup> <sub>-4.6</sub>	0.3 <sup>+0.3</sup> <sub>-0.2</sub>	-0.8 <sup>+0.0</sup> <sub>-0.0</sub>	0.3 <sup>+0.0</sup> <sub>-0.0</sub>	-	-	-	-	1.04 <sup>+0.43</sup> <sub>-0.30</sub>	40.8 <sup>+2.9</sup> <sub>-2.4</sub>	1.3 <sup>+0.3</sup> <sub>-0.2</sub>
F03068–5346	C	147.1 <sup>+205.1</sup> <sub>-19.3</sub>	2.5 <sup>+0.4</sup> <sub>-0.5</sub>	-0.9 <sup>+0.1</sup> <sub>-0.1</sub>	0.1 <sup>+0.0</sup> <sub>-0.1</sub>	-	-	-	-	0.40 <sup>+0.16</sup> <sub>-0.08</sub>	49.7 <sup>+3.0</sup> <sub>-3.4</sub>	1.2 <sup>+0.2</sup> <sub>-0.1</sub>
F03481–4012	PL	15.0 <sup>+0.3</sup> <sub>-0.4</sub>	-	-0.8 <sup>+0.0</sup> <sub>-0.0</sub>	-	-	-	-	-	0.29 <sup>+0.12</sup> <sub>-0.09</sub>	47.3 <sup>+3.8</sup> <sub>-3.0</sub>	1.5 <sup>+0.3</sup> <sub>-0.3</sub>
F04063–3236	C2 1SA	49.4 <sup>+4.4</sup> <sub>-4.0</sub>	0.2 <sup>+0.3</sup> <sub>-0.1</sub>	-1.3 <sup>+0.1</sup> <sub>-0.1</sub>	0.3 <sup>+0.0</sup> <sub>-0.0</sub>	5.2 <sup>+0.4</sup> <sub>-0.4</sub>	0.2 <sup>+0.2</sup> <sub>-0.1</sub>	-	6.5 <sup>+0.6</sup> <sub>-0.7</sub>	0.25 <sup>+0.11</sup> <sub>-0.08</sub>	49.5 <sup>+4.2</sup> <sub>-3.7</sub>	1.3 <sup>+0.3</sup> <sub>-0.2</sub>
F06021–4509	C2	25.8 <sup>+8.9</sup> <sub>-8.8</sub>	0.4 <sup>+0.4</sup> <sub>-0.3</sub>	-1.1 <sup>+0.2</sup> <sub>-0.2</sub>	0.4 <sup>+0.3</sup> <sub>-0.1</sub>	5.0 <sup>+1.2</sup> <sub>-1.0</sub>	0.4 <sup>+0.3</sup> <sub>-0.3</sub>	-1.3 <sup>+0.1</sup> <sub>-0.1</sub>	4.4 <sup>+0.9</sup> <sub>-0.7</sub>	0.09 <sup>+0.01</sup> <sub>-0.01</sub>	59.8 <sup>+1.6</sup> <sub>-1.8</sub>	1.1 <sup>+0.2</sup> <sub>-0.1</sub>
F06035–7102	C2 1SAN	23.2 <sup>+3.6</sup> <sub>-2.7</sub>	0.3 <sup>+0.4</sup> <sub>-0.2</sub>	-1.2 <sup>+0.0</sup> <sub>-0.0</sub>	-	349.8 <sup>+42.2</sup> <sub>-38.6</sub>	0.3 <sup>+0.4</sup> <sub>-0.3</sub>	-	0.4 <sup>+0.0</sup> <sub>-0.0</sub>	0.65 <sup>+0.12</sup> <sub>-0.11</sub>	49.3 <sup>+2.1</sup> <sub>-1.7</sub>	1.1 <sup>+0.1</sup> <sub>-0.0</sub>
F06206–6315	C2 1SA	49.0 <sup>+7.4</sup> <sub>-8.4</sub>	0.6 <sup>+0.6</sup> <sub>-0.4</sub>	-1.3 <sup>+0.2</sup> <sub>-0.1</sub>	0.5 <sup>+0.1</sup> <sub>-0.1</sub>	12.8 <sup>+0.9</sup> <sub>-1.1</sub>	0.5 <sup>+0.4</sup> <sub>-0.4</sub>	-	4.5 <sup>+0.4</sup> <sub>-0.4</sub>	0.67 <sup>+0.13</sup> <sub>-0.10</sub>	45.9 <sup>+1.8</sup> <sub>-1.8</sub>	1.1 <sup>+0.1</sup> <sub>-0.1</sub>
F18582–5558	C2	213.2 <sup>+191.4</sup> <sub>-85.6</sub>	0.3 <sup>+0.4</sup> <sub>-0.2</sub>	-0.9 <sup>+0.1</sup> <sub>-0.1</sub>	0.0 <sup>+0.0</sup> <sub>-0.0</sub>	5.9 <sup>+1.0</sup> <sub>-0.9</sub>	0.1 <sup>+0.1</sup> <sub>-0.1</sub>	-1.3 <sup>+0.2</sup> <sub>-0.1</sub>	5.4 <sup>+0.7</sup> <sub>-0.9</sub>	0.48 <sup>+0.07</sup> <sub>-0.08</sub>	43.4 <sup>+1.5</sup> <sub>-1.4</sub>	1.8 <sup>+0.1</sup> <sub>-0.2</sub>
F20117–3249	C2 1SAN	7.3 <sup>+1.7</sup> <sub>-1.3</sub>	0.6 <sup>+0.6</sup> <sub>-0.4</sub>	-1.1 <sup>+0.1</sup> <sub>-0.1</sub>	-	73.0 <sup>+3.4</sup> <sub>-2.9</sub>	0.5 <sup>+0.6</sup> <sub>-0.4</sub>	-	1.6 <sup>+0.2</sup> <sub>-0.2</sub>	1.14 <sup>+0.57</sup> <sub>-0.38</sub>	37.1 <sup>+2.5</sup> <sub>-2.1</sub>	1.7 <sup>+0.2</sup> <sub>-0.3</sub>
F20445–6218	C	62.0 <sup>+106.3</sup> <sub>-15.7</sub>	0.6 <sup>+0.5</sup> <sub>-0.4</sub>	-0.8 <sup>+0.1</sup> <sub>-0.1</sub>	0.2 <sup>+0.1</sup> <sub>-0.2</sub>	-	-	-	-	0.40 <sup>+0.24</sup> <sub>-0.10</sub>	46.6 <sup>+3.1</sup> <sub>-3.9</sub>	1.3 <sup>+0.3</sup> <sub>-0.2</sub>
F21178–6349	C	28.6 <sup>+9.1</sup> <sub>-7.0</sub>	0.9 <sup>+0.2</sup> <sub>-0.2</sub>	-1.2 <sup>+0.1</sup> <sub>-0.1</sub>	0.4 <sup>+0.1</sup> <sub>-0.1</sub>	-	-	-	-	0.23 <sup>+0.15</sup> <sub>-0.08</sub>	48.2 <sup>+4.6</sup> <sub>-4.4</sub>	1.5 <sup>+0.4</sup> <sub>-0.3</sub>
F21292–4953	PL	21.0 <sup>+0.6</sup> <sub>-0.7</sub>	-	-0.5 <sup>+0.0</sup> <sub>-0.0</sub>	-	-	-	-	-	0.46 <sup>+0.25</sup> <sub>-0.13</sub>	46.7 <sup>+3.5</sup> <sub>-3.6</sub>	1.4 <sup>+0.4</sup> <sub>-0.3</sub>
F21295–4634	C2 1SAN	1.1 <sup>+0.7</sup> <sub>-0.6</sub>	0.3 <sup>+0.2</sup> <sub>-0.2</sub>	-1.0 <sup>+0.1</sup> <sub>-0.1</sub>	-	31.3 <sup>+7.7</sup> <sub>-6.1</sub>	0.3 <sup>+0.3</sup> <sub>-0.2</sub>	-	0.5 <sup>+0.2</sup> <sub>-0.1</sub>	1.27 <sup>+0.54</sup> <sub>-0.44</sub>	39.0 <sup>+2.9</sup> <sub>-2.2</sub>	1.6 <sup>+0.2</sup> <sub>-0.3</sub>
F23389–6139	C2 1SA	421.7 <sup>+14.4</sup> <sub>-14.6</sub>	1.0 <sup>+0.6</sup> <sub>-0.7</sub>	-1.4 <sup>+0.0</sup> <sub>-0.0</sub>	0.4 <sup>+0.0</sup> <sub>-0.0</sub>	91.9 <sup>+6.8</sup> <sub>-6.5</sub>	0.7 <sup>+0.6</sup> <sub>-0.4</sub>	-	3.0 <sup>+0.2</sup> <sub>-0.2</sub>	0.86 <sup>+0.26</sup> <sub>-0.23</sub>	44.7 <sup>+2.7</sup> <sub>-2.3</sub>	1.3 <sup>+0.3</sup> <sub>-0.2</sub>

To examine how our sample resided on the FRC, we compared it to the sample of 1809 objects of Yun et al. (2001). The Yun et al. (2001) sample cross referenced the *IRAS* 2 Jy sample with the NRAO VLA All Sky Survey (NRAO; Condon et al., 1998) to investigate the FRC over many orders of magnitude. To remain consistent with their work, no  $k$ -correction was applied. We see in Fig. 3.8 that our sample is consistent with the trend seen by Yun et al. (2001), where only two of our objects, (IRAS F20117-3249 and IRAS F23389-6139), have a slightly elevated 1.4 GHz luminosity. The  $q$  parameter, which is the logarithmic ratio between the far-infrared flux and 1.4 GHz flux density of an object, is a further useful illustration of the FRC, where  $q$  is defined as

$$q \equiv \log \left( \frac{\text{FIR}}{3.75 \times 10^{12} \text{ W m}^{-2}} \right) - \log \left( \frac{S_{1.4 \text{ GHz}}}{\text{W m}^{-2} \text{ Hz}^{-1}} \right). \quad (3.11)$$

$S_{1.4 \text{ GHz}}$  is in units of  $\text{W m}^{-2} \text{ Hz}^{-1}$ , and FIR is defined as

$$\text{FIR} \equiv 1.26 \times 10^{-14} (2.58 S_{60 \mu\text{m}} + S_{100 \mu\text{m}}) \text{ W m}^{-2} \quad (3.12)$$

where  $S_{60 \mu\text{m}}$  and  $S_{100 \mu\text{m}}$  are the 60 and 100  $\mu\text{m}$  band flux densities from *IRAS* in Jy (Helou et al., 1985). The mean  $q$  value between 60  $\mu\text{m}$  and 1.4 GHz is typically taken as 2.34 for star formation galaxies (Yun et al., 2001). Any deviation from this value can be a critical diagnostic of the physical processes driving some object. IR-excess sources ( $q > 3$ ) may be highly obscured compact starburst galaxies or dust-enshrouded AGN. Radio-excess objects ( $q < 1.6$ ) are caused by excess radio emission originating from an AGN component in the galaxy (Yun et al., 2001). Some of the dispersion may be influenced in part by variation in extinction and dust temperature, as well as varying timescales associated with different SFR indicators.

Our sample objects IRAS F20117–3249 and IRAS F23389–6139 have  $q$  values (1.61 and 1.54, respectively) that are approaching the radio-excess region, indicating the potential presence of AGN activity in the observed 1.4 GHz radio-continuum. There is no classification of IRAS F20117–3249 available in the literature, although it has been designated as a galaxy by Paturel et al. (2003). IRAS F23389-6139, however, has been classified as a starburst based on optical imagery (Duc et al., 1997) and infrared template modelling (Farrah et al., 2003).

### 3.6.2 Thermal Fraction

The thermal fraction of a source is a measure of how much of the observed radio-continuum comprises thermal free-free emission. At increasing frequencies, because of the steep spectral index of non-thermal synchrotron emission, the thermal free-free emission begins to dominate

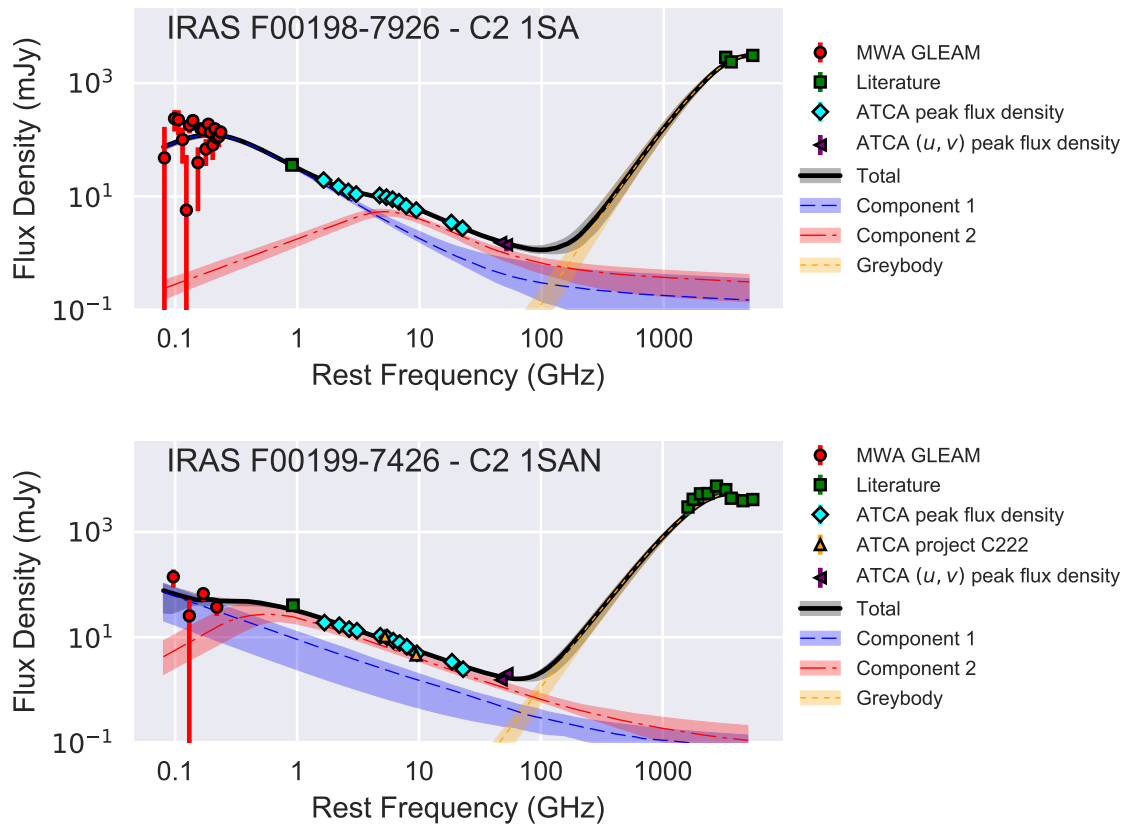


Figure 3.7: The observed data and preferred spectral energy distribution modelling of the SFGs from our sample in RA order. We include any components that make up the most preferred model focusing on the radio continuum. Highlighted regions represent the  $1\sigma$  uncertainty sampled by EMCEE.

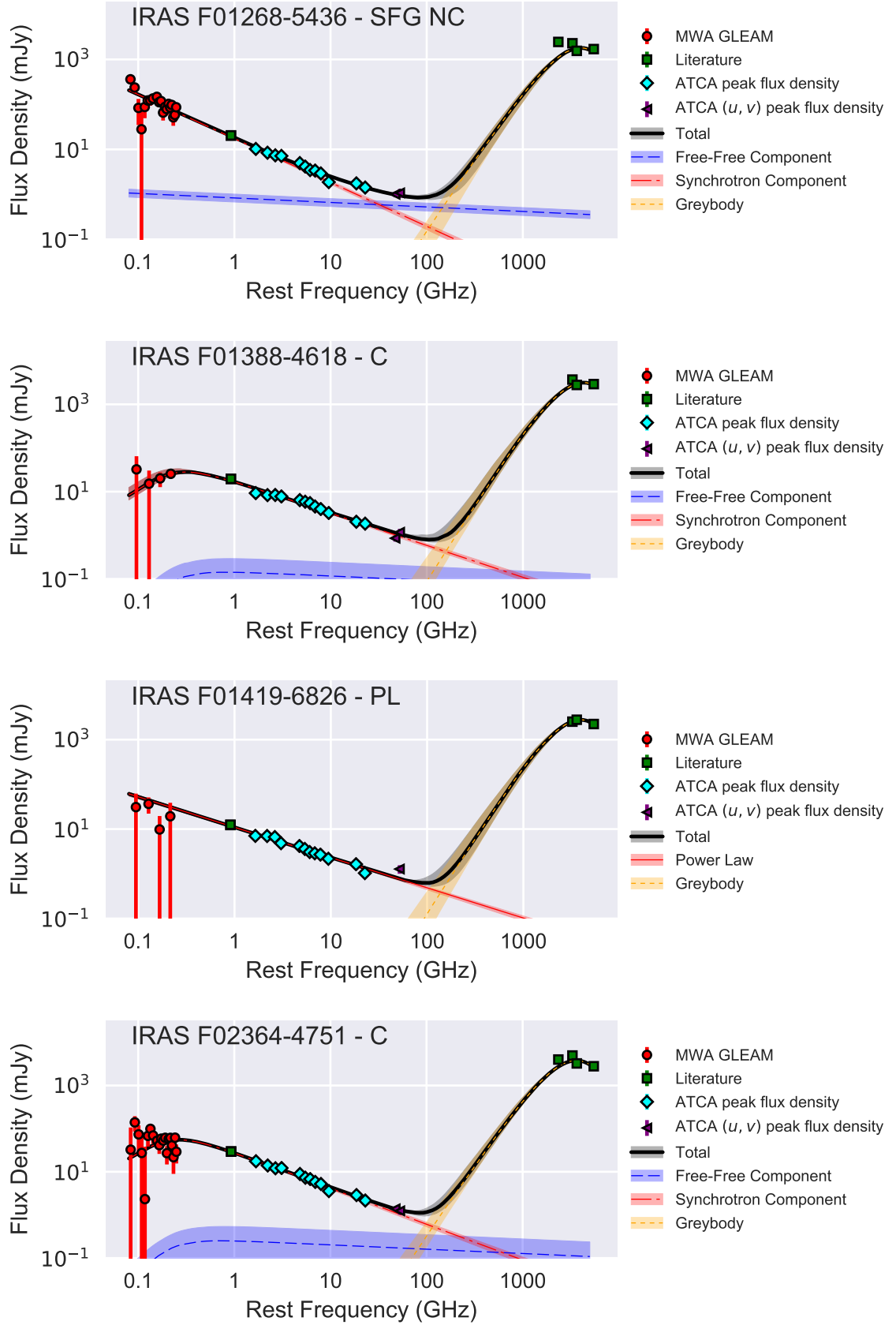


Figure 3.7: (*Continued*) The observed data and preferred SED modelling of the SFGs from our sample in RA order. We include any components that make up the most preferred model focusing on the radio continuum. Highlighted regions represent the  $1\sigma$  uncertainty sampled by EMCEE.

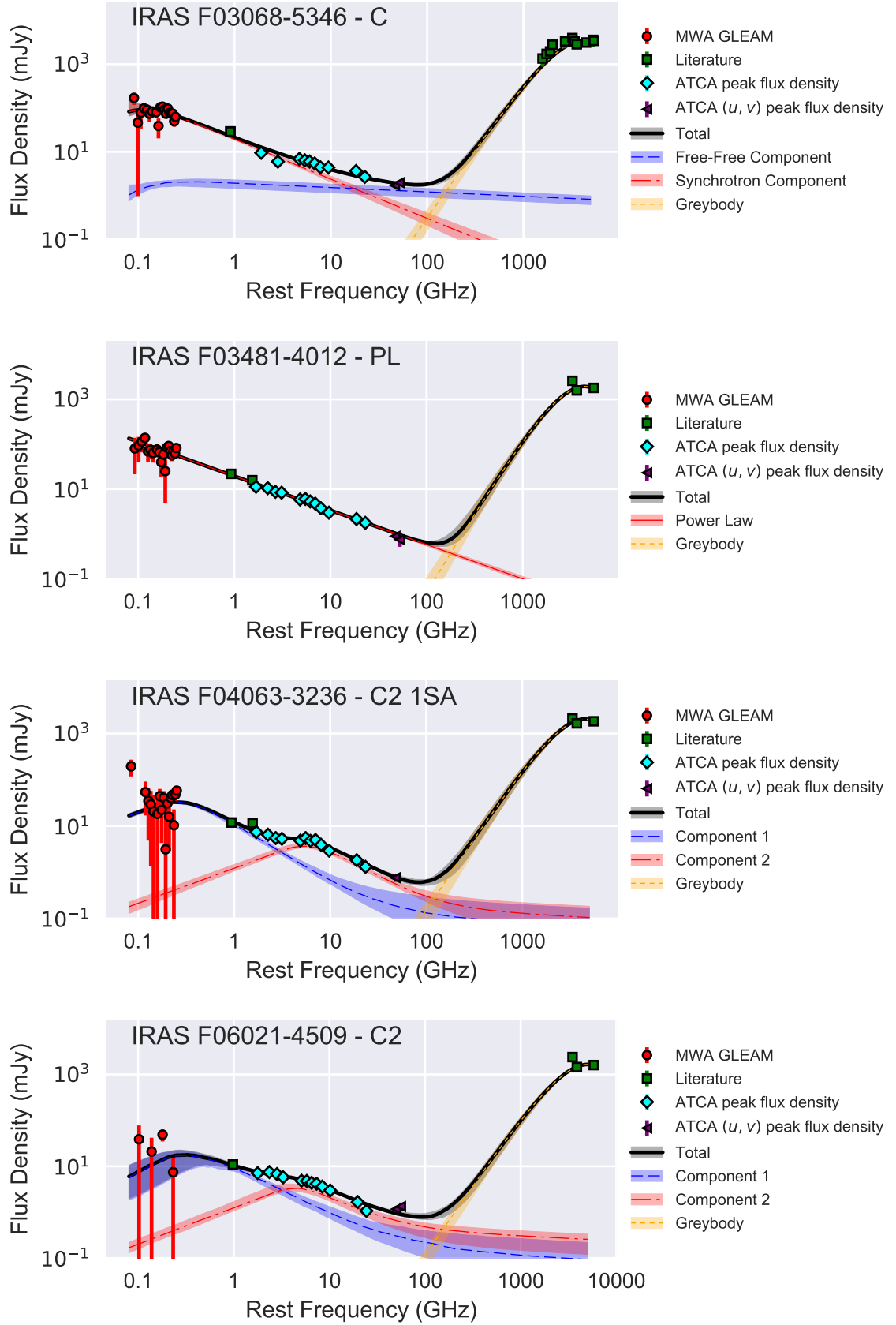


Figure 3.7: (*Continued*) The observed data and preferred SED modelling of the SFGs from our sample in RA order. We include any components that make up the most preferred model focusing on the radio continuum. Highlighted regions represent the  $1\sigma$  uncertainty sampled by EMCEE.

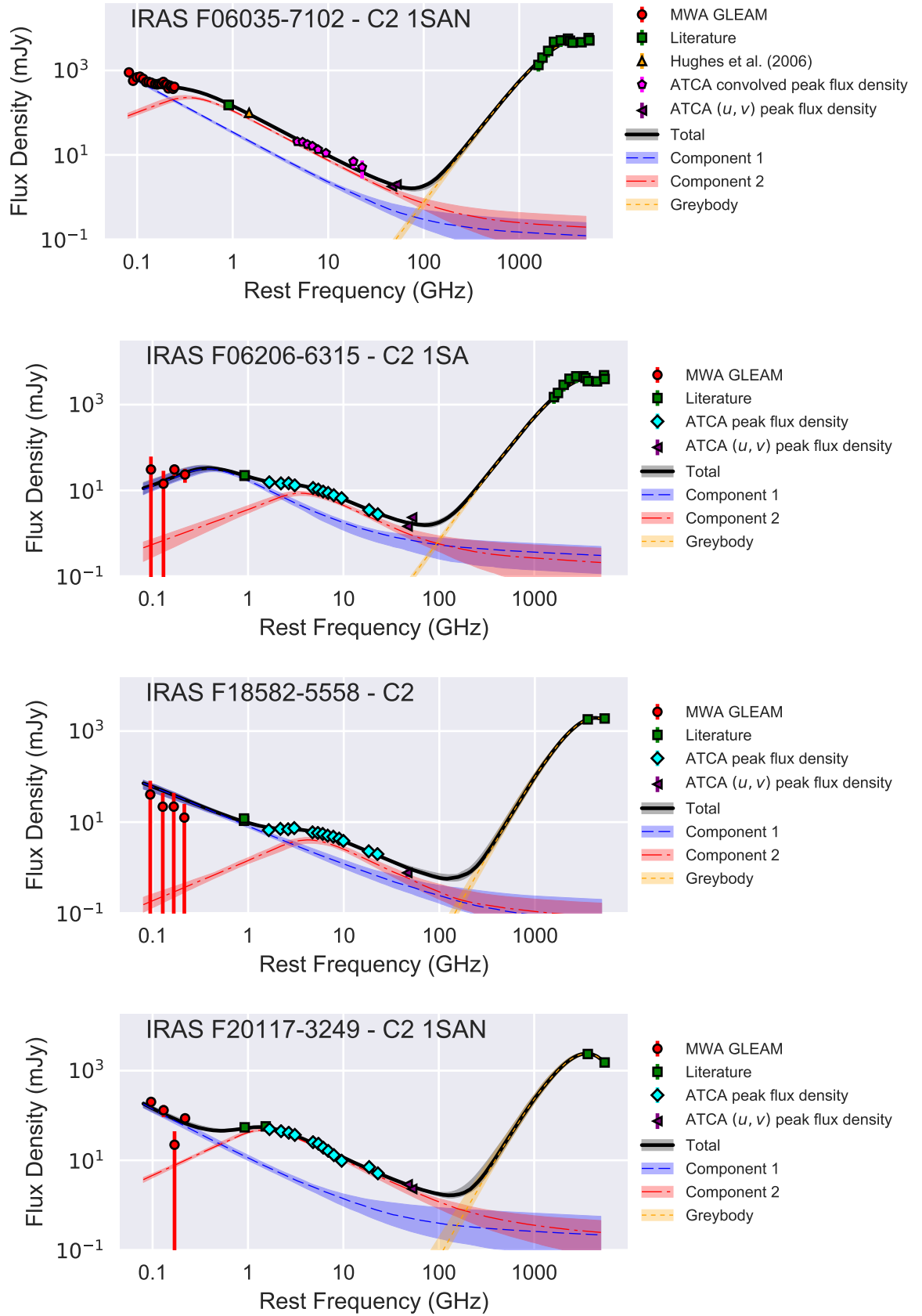


Figure 3.7: (*Continued*) The observed data and preferred SED modelling of the SFGs from our sample in RA order. We include any components that make up the most preferred model focusing on the radio continuum. Highlighted regions represent the  $1\sigma$  uncertainty sampled by EMCEE.

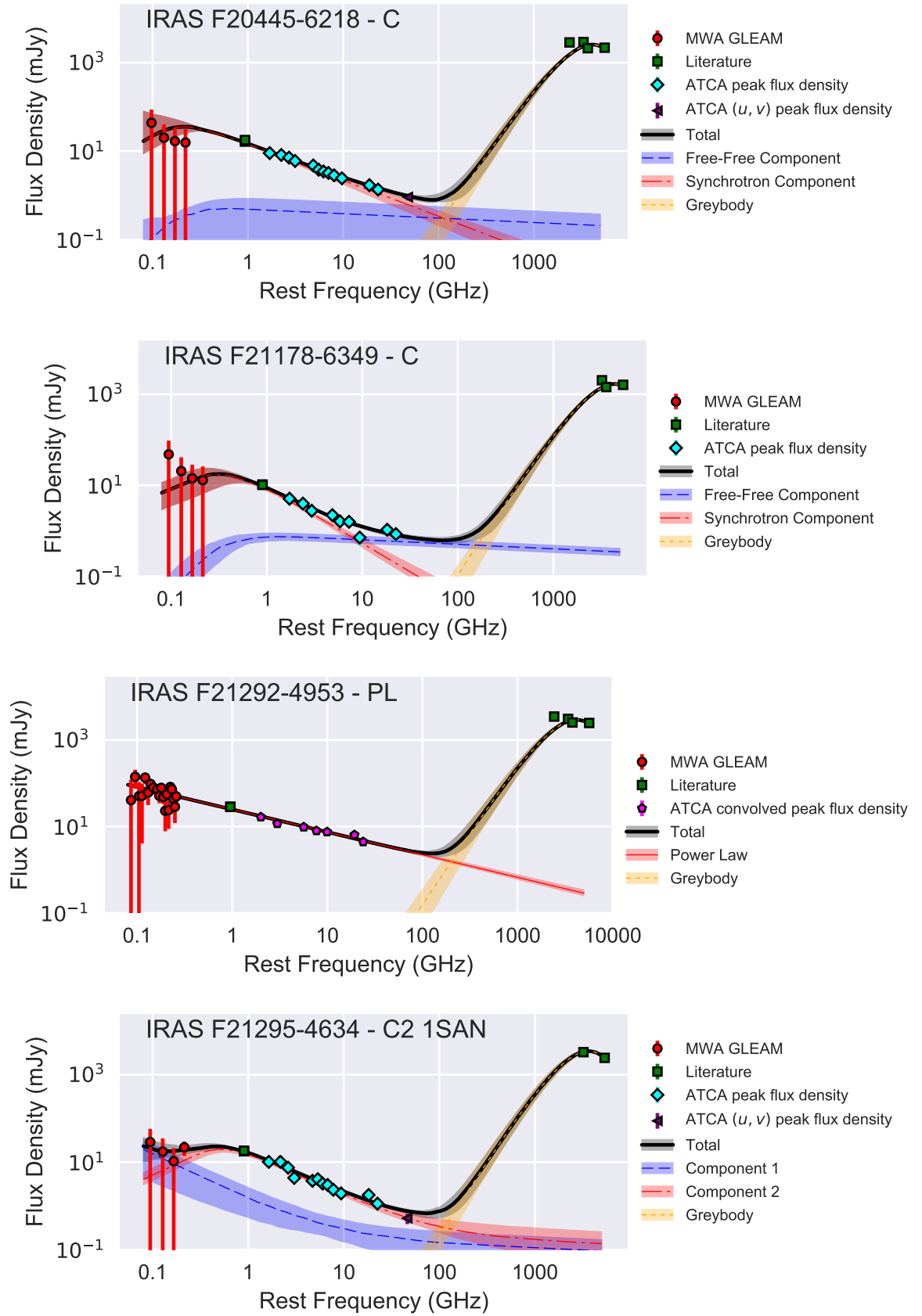


Figure 3.7: (*Continued*) The observed data and preferred SED modelling of the SFGs from our sample in RA order. We include any components that make up the most preferred model focusing on the radio continuum. Highlighted regions represent the 1 $\sigma$  uncertainty sampled by EMCEE.



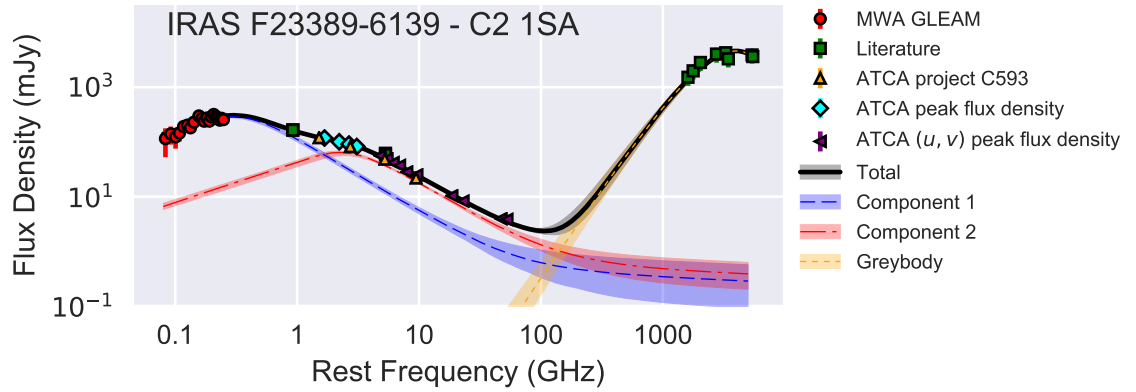


Figure 3.7: (*Continued*) The observed data and preferred SED modelling of the SFGs from our sample in RA order. We include any components that make up the most preferred model focusing on the radio continuum. Highlighted regions represent the  $1\sigma$  uncertainty sampled by EMCEE.

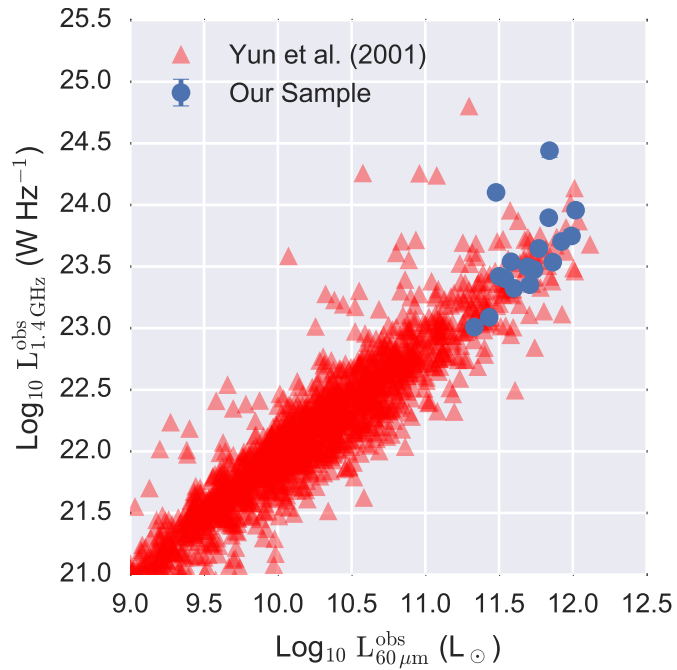


Figure 3.8: A comparison of the  $60\ \mu\text{m}$  and  $1.4\ \text{GHz}$  luminosities of our 19 source sample and Yun et al. (2001). Luminosities have been estimated in the observed frame with no  $k$ -correction applied.

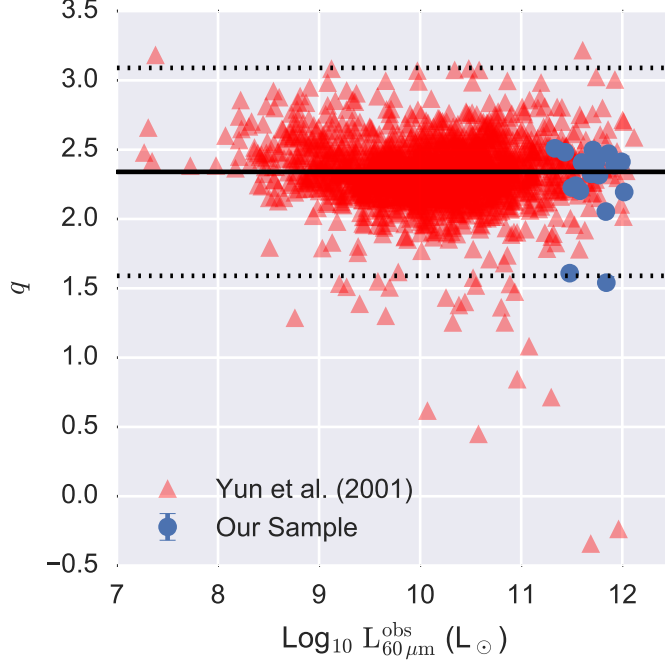


Figure 3.9: The FRC, as parameterised by the  $q$  parameter, of our sample and Yun et al. (2001). The solid horizontal line represents the mean  $q = 2.34$ , as calculated by Yun et al. (2001). The dotted lines represent the radio-excess (*below*) and IR-excess (*above*) objects, defined as three times the SD of  $q$  (SD = 0.25) from the Yun et al. (2001) sample.

the total observed continuum. Ionised H II regions, which thermal free-free emission directly traces, are an excellent probe of current star formation. In the GHz regime, free-free emission represents roughly 5 to 10% of the total radio-continuum (Condon, 1992; Murphy, 2013), and because of its flat spectral index ( $S_\nu \propto \nu^{-0.1}$ ), it is relatively difficult to isolate. The broad coverage of our radio-continuum SEDs however allows us to investigate this property. For each source, using the best fit model, we compute the total amount of thermal emission to derive appropriate nominal thermal fraction values.

We find that at low frequencies, the thermal fraction makes up only a small fraction of the total radio-continuum emission. This is similar to earlier studies (Condon and Yin, 1990; Condon, 1992; Price and Duric, 1992), where at 1.4 GHz, the typical thermal fraction was estimated to be around 10%. In Fig. 3.10a, we show that at 1.4 GHz, the estimated thermal fraction is fairly constant at around 3 to 10%, with the average thermal fraction being 4.6%. This is in line with Murphy (2013), who found in a sample of 31 local starburst galaxies that the thermal fraction at 1.4 GHz is  $\approx 5\%$ . At 40 GHz (Fig. 3.10b), the thermal fraction makes a much larger contribution to the modelled radio-continuum, ranging between 35 to 80% with an average of 47.4%.

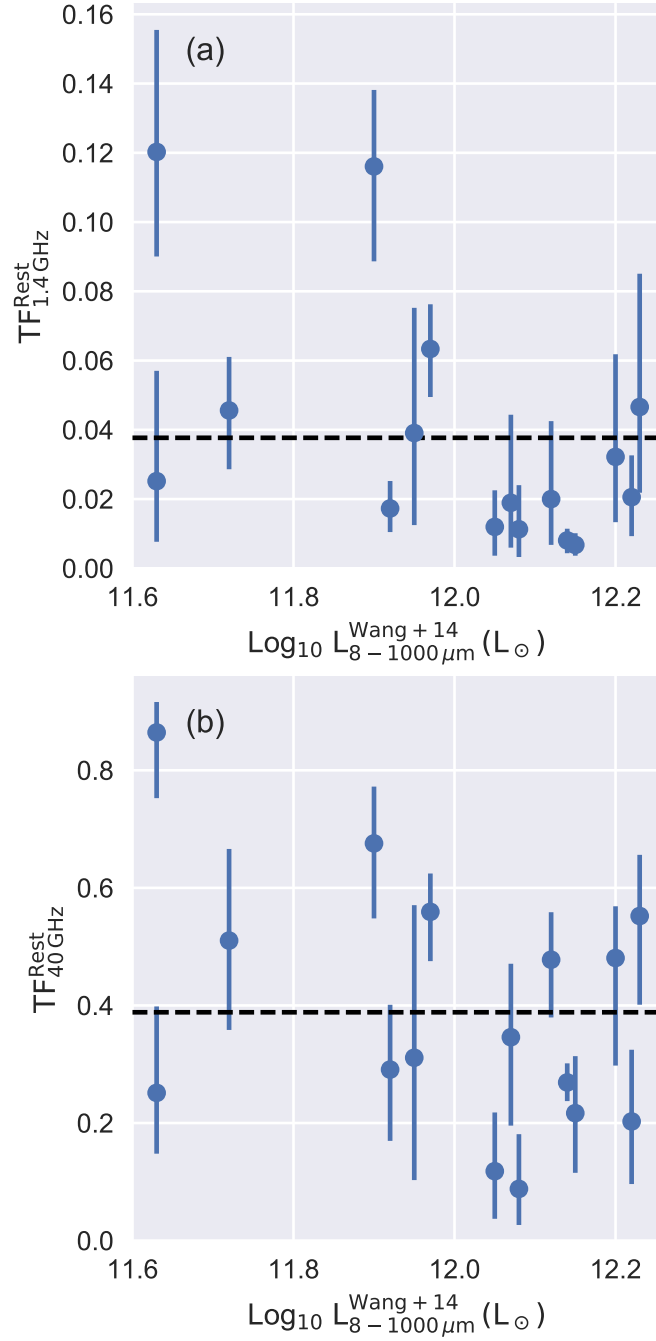


Figure 3.10: A comparison between the total infrared emission and the estimated thermal fraction of the rest frame 1.4 GHz (a) and 40 GHz (b). Dashed horizontal lines represent the average thermal fraction.

### 3.6.3 Spectral curvature and emission measures

Similar to Clemens et al. (2010), the radio-continuum SEDs in our sample of objects are rarely characterised well by a simple power law. The broad frequency range covered by our data shows the presence of multiple bends or turnovers, which we attribute to the effects of FFA. Low frequency data from the MWA GLEAM data show clear cases of low frequency turnovers, as illustrated well by IRAS F01388–4618 and IRAS F23389–6139. At higher frequencies, we see, in a subset of our sources, evidence supporting a ‘kink’ in the radio-continuum spectrum. Similar to the turnover at low frequency, we attribute this to a secondary FFA component with a higher optical depth.

Four objects from our sample had an evidence value that most supported a ‘simple’ model (a power law or the simple normalisation of synchrotron and free-free power law components). Of these four, objects IRAS F01419–6826 had a competing higher-order model. The remaining 15 objects all had higher-order (i.e. turnover due to FFA) models most supported by the evidence, where only source IRAS F03068–5346 had a ‘simple’ competing model.

A common feature seen in our SEDs is the steepening of the radio-continuum spectrum between the 4 to 10 GHz regime. A similar effect was also seen by Clemens et al. (2010). In cases where the MWA GLEAM low frequency measurements indicates a further turnover, this power law is replaced with a higher-order component. This higher-order complexity is supported by both an improved  $\chi^2$  statistic and  $\mathcal{Z}$  value.

The turnover frequency due to FFA is dependent on where the optical depth reaches unity. Generally, it is assumed that the emitting HII regions form a cylinder orientated along the line of sight with constant temperature and density (Condon, 1992). In such scenarios, the free-free opacity is well approximated by

$$\tau_\nu = 3.28 \times 10^{-7} \left( \frac{T_e}{10^4 \text{ K}} \right) \left( \frac{\nu}{\text{GHz}} \right)^{-2.1} \left( \frac{EM}{\text{pc cm}^{-6}} \right), \quad (3.13)$$

where  $T_e$  is the electron temperature of the HII emitting region, typically taken as  $10^4$  K, and EM is the emission measure, defined as

$$\frac{EM}{\text{pc cm}^{-6}} = \int_{\text{los}} \left( \frac{N_e}{\text{cm}^{-3}} \right)^2 d \left( \frac{s}{\text{pc}} \right). \quad (3.14)$$

EM is the integral of the electron density along the line of sight of a HII region of depth  $s$ . Using the above form, for frequencies above the turnover frequency  $\nu_t$ , the free-free spectrum follows a power law of  $\alpha \sim -0.1$ . Once the optical depth reaches unity, the spectrum transitions to the Rayleigh-Jeans law, described well by  $\nu^2$ . Using the turnovers constrained by our modelling, we have estimated the EMs of our sources, outlined in Table 3.9, using Equation 3.14.

Source <i>IRAS</i>	EM <sub>1</sub> 10 <sup>6</sup> cm <sup>-6</sup> pc	EM <sub>2</sub> 10 <sup>6</sup> cm <sup>-6</sup> pc
F00198–7926	0.016	13.851
F00199–7426	–	0.067
F01388–4618	0.021	–
F02364–4751	0.017	–
F03068–5346	0.003	–
F04063–3236	0.029	15.762
F06021–4509	0.038	6.88
F06035–7102	–	0.044
F06206–6315	0.059	7.1
F18582–5558	–	10.599
F20117–3249	–	0.858
F20445–6218	0.01	–
F21178–6349	0.043	–
F21295–4634	–	0.08
F23389–6139	0.044	3.11

Table 3.9: An overview of the emission measures exclusively derived for each source from the model most supported by the evidence. Objects with no low frequency turnover or poorly constrained emission measures are marked by ‘–’.

For systems with multiple intense starburst regions that have been integrated over by a large synthesised radio-telescope beam, their superposition of radio-continuum features will form the observed SED. The orientation of such regions will play a crucial role in the spectral curvature across a broad frequency range. Regions which are small and deep will possess much higher EMs than those which are more widespread and shallow relative to our observing angle. Although the EM is tied to the spatial size of an object, which can vary as a function of frequency with increasing amounts of diffuse synchrotron, we have no evidence to suggest we are resolving our sample, particularly at high frequency where we have obtained critical short spacing data.

### 3.6.4 Far-infrared to radio correlation

The radio-continuum emission is considered an ideal tracer of star formation as it is not affected by dust attenuation. In terms of the local Universe ( $z < 0.2$ ), it is fairly well calibrated by bootstrapping the radio-continuum SFR against the far-infrared SFR via the FRC.

Although understood well in the local Universe, it is unknown whether the FRC will evolve with increasing redshift. As outlined by Murphy (2009), because of the changing composition of the radio-continuum with increasing frequency (which is what would be Doppler shifted to lower frequency) and synchrotron suppression effects that scale with  $(1+z)^4$  caused by inverse-Compton losses, it is thought that the FRC will need to be ‘recalibrated’ to be compatible with the high redshift Universe. Mao et al. (2011) however see no evidence of evolution in the FRC up to  $z \sim 2$  using image stacking techniques, suggesting that the FRC is more physically complex than first thought. As we show in Fig. 3.8, our sample of objects follow the FRC.

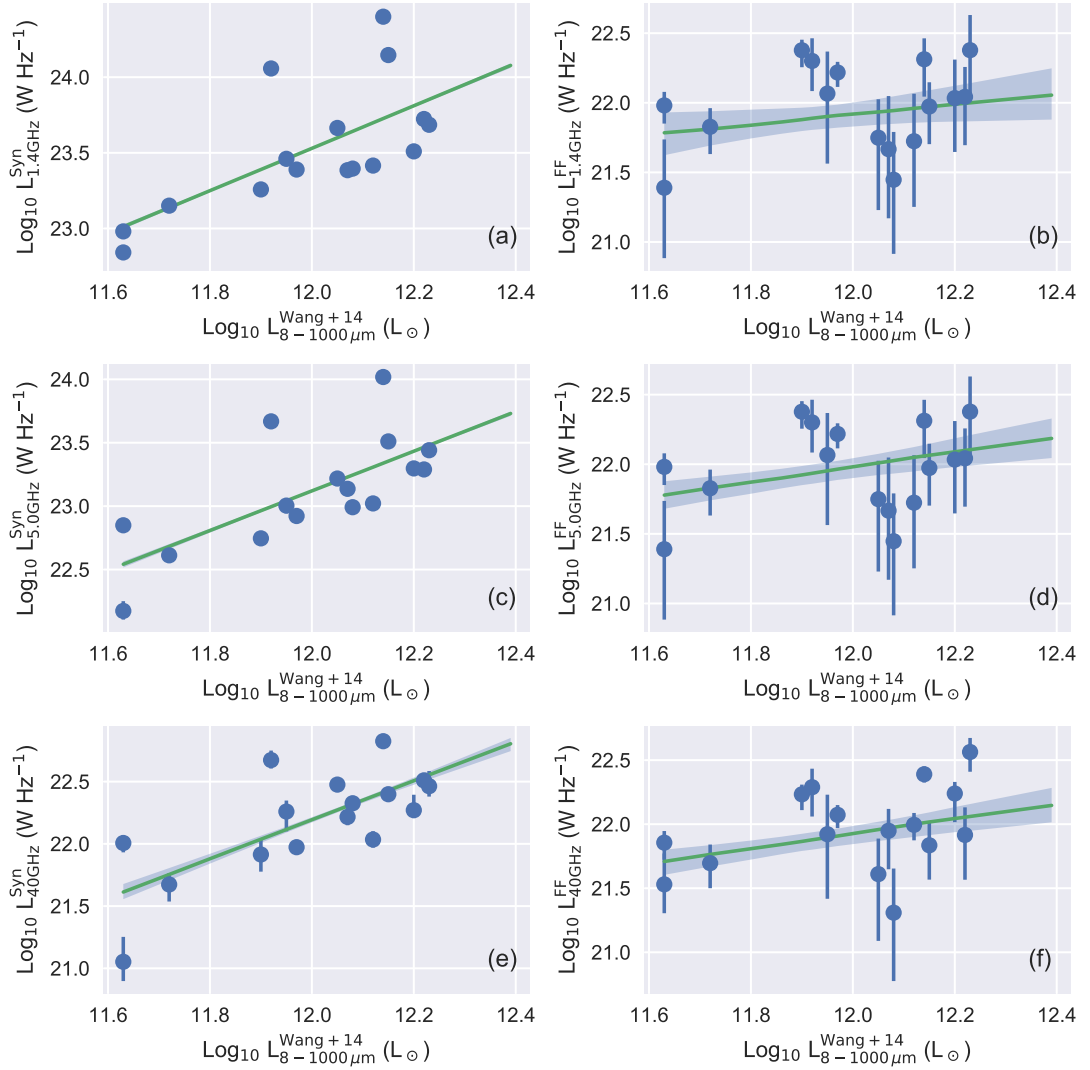


Figure 3.11: A comparison between the total infrared derived SFR, as presented by Wang et al. (2014), and the constrained synchrotron (*a,c,e*) and free-free luminosities (*b, d, f*) at 1.4 GHz, 5.0 GHz, and 40 GHz of sources in our sample. The green line and its highlighted region represent a non-weighted linear regression and the corresponding  $1\sigma$  uncertainty region determined from 1000 realisations.

The synchrotron and free-free emission mechanisms that make up the radio-continuum are both tracers of star formation across different timescales. Given the posterior distribution sampled by EMCEE of the most supported model of each source, we compare in Fig. 3.11 the total far-infrared (taken from Wang et al., 2014) against the decomposed synchrotron and free-free components at 1.4 and 40 GHz. For each comparison, we also include the results of a non-weighted linear fit against multiple realisations (N=1000) of our data, drawn randomly from the posterior distribution. Highlighted regions represent the  $1\sigma$  uncertainty of the best fit parameters of this process.

The total far-infrared correlates well with the modelled synchrotron luminosity for all sources at 1.4 GHz, as demonstrated in Fig. 3.11a. This can simply be attributed to synchrotron emission dominating the radio-continuum at 1.4 GHz (Condon, 1992; Yun et al., 2001; Bell, 2003; Murphy et al., 2006). The two outlying objects, whose synchrotron luminosities are in excess of  $10^{24} \text{ W Hz}^{-1}$  are IRAS F20117–3249 and IRAS F23389–6139.

Free-free emission is a more reliable probe of SFR with these increasing redshifts as it directly traces HII regions ionised by nearby high-mass stars and is unaffected by inverse-Compton losses. Identifying the free-free emission at low frequencies, where it contributes  $\sim 5 - 10\%$  at 1.4 GHz, is difficult and few studies have successfully isolated its signature (Price and Duric, 1992; Clemens et al., 2010; Murphy et al., 2010, 2012; Galvin et al., 2016). This is demonstrated in the top panel of Fig. 3.11b where there is considerable uncertainty associated with the constrained free-free luminosity at 1.4 GHz.

With increasing frequencies, there is a change in the composition of the radio-continuum. Synchrotron emission, due to its steep spectral index, quickly begins to weaken. We show in Fig. 3.11c-e that although there is still a strong correlation between the total infrared and the estimated synchrotron luminosity, it is one with increased uncertainty when compared to the equivalent relation constrained at 1.4 GHz (Fig. 3.11a). The correlation between the total infrared and free-free luminosity at 40 GHz (Fig. 3.11f) is far more constrained than it was at 1.4 and 5.0 GHz (Fig. 3.11b-d).

In Table 3.10, we list the best fit values from a simple linear regression between the total infrared (in units of  $\text{Log}_{10} L_{\odot}$ ) and the decomposed synchrotron and free-free luminosity components at 1.4, 5.0 and 40 GHz (in units of  $\text{Log}_{10} \text{ W Hz}^{-1}$ ). Errors were estimated by drawing 1000 realisations of the luminosities from the posterior distribution sampled by EMCEE. We find these results acceptable given that we have less than one order of magnitude of range in the total infrared luminosities.

Price and Duric (1992) performed a similar analysis for a sample of 31 galaxies. Their study used a single model equivalent to Eq. 3.2 and found that the decomposed synchrotron and

$\nu$ (GHz)	Emission	Gradient	Norm. ( $\text{Log}_{10} \text{ W Hz}^{-1}$ )	$q \pm \sigma_q$
1.4	Syn	$1.40^{+0.03}_{-0.04}$	$6.68^{+0.47}_{-0.41}$	$2.53 \pm 0.38$
5.0	Syn	$1.56^{+0.06}_{-0.05}$	$4.36^{+0.62}_{-0.66}$	$2.94 \pm 0.40$
40.0	Syn	$1.57^{+0.13}_{-0.15}$	$3.39^{+1.77}_{-1.56}$	$3.87 \pm 0.39$
1.4	FF	$0.33^{+0.43}_{-0.33}$	$17.95^{+3.92}_{-5.10}$	$4.09 \pm 0.33$
5.0	FF	$0.53^{+0.27}_{-0.25}$	$15.60^{+2.93}_{-3.27}$	$4.04 \pm 0.34$
40.0	FF	$0.58^{+0.25}_{-0.23}$	$14.97^{+2.74}_{-2.97}$	$4.09 \pm 0.34$

Table 3.10: The fitted gradient and normalisation components of a non-weighted linear fit between the total infrared and decomposed radio-continuum luminosities. Synchrotron and free-free luminosity components are labelled as ‘Syn’ and ‘FF’, respectively. We also provide the mean and SD of the  $q$  parameter, derived using the total infrared luminosity from Wang et al. (2014), for each of the correlations.

free-free components are tightly correlated to the far-infrared across roughly three orders of magnitude. At 5.0 GHz, they estimated the gradient of the synchrotron-FIR and free-free-FIR correlations to be  $1.33 \pm 0.1$  and  $0.93 \pm 0.02$ , respectively. These are comparable to the correlations derived above, particularly the synchrotron-TIR component at  $\nu = 5.0$  GHz. Although we are using the total infrared luminosities, defined as the bolometric luminosity from 8 to  $1000 \mu\text{m}$  derived by Wang et al. (2014) and their IR template fitting routines, the bulk of emission for SFG in this regime is emitted in the FIR (Helou et al., 1988; Condon, 1992). This difference would influence the normalisation component, which is not being compared here.

## 3.7 Discussion

### 3.7.1 Spectral Curvature-Physical Origin?

Fifteen objects in our sample show spectral characteristics that are not consistent with a simple power-law model. Multi-epoch observations and source variability could give a false impression of curvature. For this study, the majority of our data were collected within a two year timespan. MWA GLEAM DR1 conducted its observing campaign between August 2013 to July 2014. Over this timeframe, multiple drift scans were performed across the southern sky before combining all available data into the final image set. Likewise, the majority of our ATCA data were taken between September 2014 and February 2015, with selected frequency bands being observed in compact array configurations up to September 2016. Hence, the bulk of the radio-continuum measurements that make up our sample where curvature has been detected was taken within a three-year timespan. SFGs do not show variability on such timescales at our sensitivities (Mooley et al., 2016).

An inconsistent flux calibration scale may also influence spectral features when comparing



data across a broad frequency range. For ATCA data, PKS 1934–638 is almost exclusively used as a flux calibrator. This gigahertz peaked spectrum source has been well characterised from low to high frequencies and is tied to the spectra of 3C286 and 3C295 which define the Baars et al. (1977) scale (Reynolds, 1994; Partridge et al., 2016). As it was used to provide a flux calibration scale for all ATCA data from 2.1 to 25 GHz for sources in our sample, it is unlikely that high frequency kinks between 4 to 10 GHz are due to a mis-matched flux scale.

At the time of observing the high frequency Q band data, Uranus was the preferred flux calibrating source at ATCA. The flux density accuracy at these Q band frequencies is estimated to be within 10%. An overestimated flux density at these frequencies would increase the amount of free-free emission while model fitting, producing a more pronounced flattening at higher frequencies. Therefore, we have added an additional 10% error in quadrature as a measure to counteract this effect. Low frequency data from SUMSS and MWA GLEAM DR1 both use a large part of the Molonglo reference catalogue (MRC; Large et al., 1981, 1991) to craft a flux calibration scale that is accurate to 2-3% on the Baars et al. (1977) scale. To account for any residual flux calibration mis-match, we injected an additional 5% error in quadrature for all flux density measurements obtained through NED, including measurements from SUMSS or archived ATCA observations (Table 3.4).

Therefore, the curvature features we see in our modelling, we believe are physical in origin. When the derived emission measures (Table 3.9) were compared to similar studies, we found that they are consistent. Clemens et al. (2010) studied a sample of 20 luminous and ULIRGs using data from 244 MHz to frequencies in excess of 23 GHz. Although their SEDs are more sparsely sampled than those in this study, they find evidence that suggests multiple FFA components with varying optical depths. They found emission measures in the range of 0.12 to  $140 \times 10^6 \text{ cm}^{-6} \text{ pc}$ . Similarly, observations using MERLIN of compact sources in M82 at 408 MHz presented by Wills et al. (1997) agree with the emission measures derived from low frequency turnovers for our sample. At higher frequencies, Neff and Ulvestad (2000) also found emission measures in excess of  $10^8 \text{ cm}^{-6} \text{ pc}$  for compact HII regions and supernova remnants observed in the NGC 4038 and NGC 4039 merger system.

Arp 220, the closest ultra-luminous infrared galaxy, has observational evidence of a double starburst nucleus thought to be powered by a recent merger (Smith et al., 1998; Downes and Solomon, 1998; Engel et al., 2011). Using radio recombination lines to constrain turnover features, Anantharamaiah et al. (2000) argued that the radio-continuum SED of Arp 220 is best characterised by three regions of star formation with turnover frequencies of roughly 0.5, 1.4, and 40 GHz. Using their resolved data allowed them to place further constraints on the emitting size and density of the three emission measures, which they modelled as  $1.3 \times 10^5$ ,

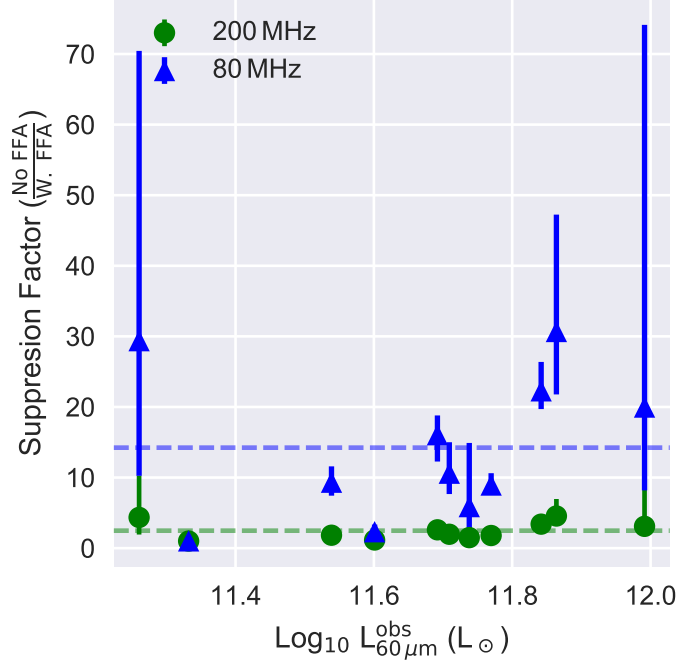


Figure 3.12: A comparison between the observed  $60\ \mu\text{m}$  luminosities and the ratio of the observed radio-continuum with and without the effects of FFA at 80 and 200 MHz. The dashed horizontal lines show the average suppression factor for each group.

$5.0 \times 10^6$ , and  $6.3 \times 10^9\ \text{cm}^{-6}\ \text{pc}$ . Recently, Kapinska et al. (2017) performed radio-continuum modelling of NGC 253 from 70 MHz to 11 GHz. They found that the galaxy was best described as a sum of a discrete central starburst region, modelled as an internally free-free absorbed synchrotron plasma, with an additional synchrotron component that flattens at low frequency.

More broadly, resolved multi-wavelength studies of intense starburst galaxies, in the same class as those in our sample, also show multiple, distinct clumps. Farrah et al. (2001) used the Wide-Field Planetary Camera 2 (WFPC2) on the *Hubble Space Telescope* (*HST*) to study 23 ULIRGs. They found that most observed sources are in some stage of merger with stellar population synthesis modelling, suggesting ages less than several Gyr. Colour maps (based on multiple filters) show a number of distinct ‘knots’ that are clearly distinguished from the surrounding environment which are likely regions of intense starburst activity. Similar *HST* I-band imaging by Borne et al. (2000) also shows that U/LIRGs are often interacting systems in some stage of merger.

### 3.7.2 Effects of FFA on low frequency extrapolations

Euclidean normalised radio source counts of extragalactic objects are a useful cosmological tool (de Zotti et al., 2010). Before low frequency SKA pathfinder projects and all their sky surveys, including MWA and LOFAR, the radio sky at low frequency was extrapolated from slightly higher frequency surveys and assumed power laws. Although useful as an initial estimate,

this approach ignores low frequency turnovers caused by free-free absorption. Understanding the behaviour of starburst galaxies and any deviations from the extrapolated optically thin spectrum will be important for interpreting the well-known uptick in the Euclidean normalised radio source counts (Gruppioni et al., 2003; Seymour et al., 2008).

In our sample, we found that most objects have a well characterised turnover component. In Fig. 3.12, we compare the effects of omitting this feature and the effects that it may have on simple extrapolation. Flux densities without FFA were obtained by removing the frequency-dependent  $\tau$  parameter from the most preferred model. We show an example of this in Fig. 3.13.

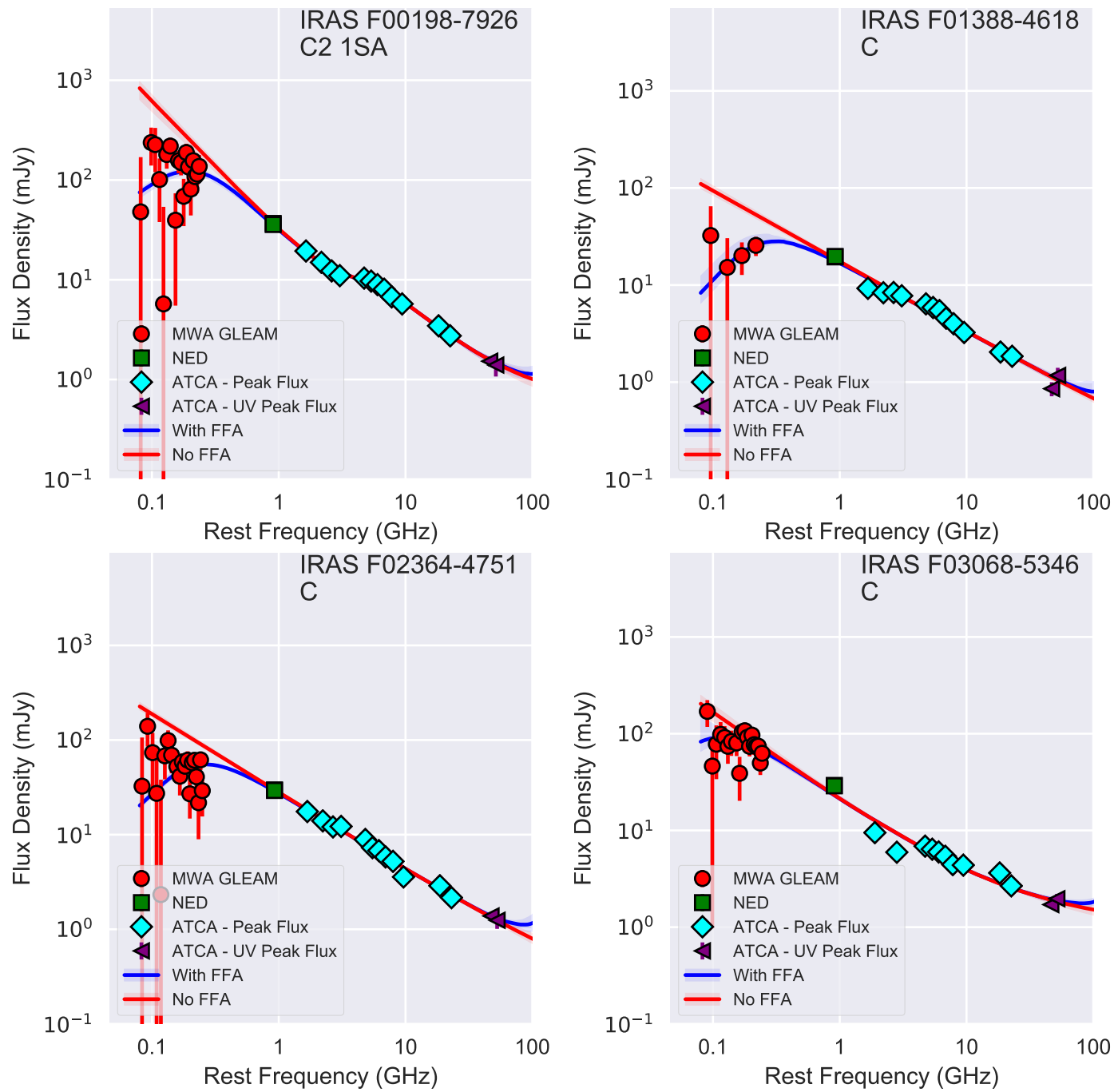


Figure 3.13: The most supported constrained model of objects in this sample showing the effects at low frequencies removed when FFA is removed. All other constrained parameters are unchanged.

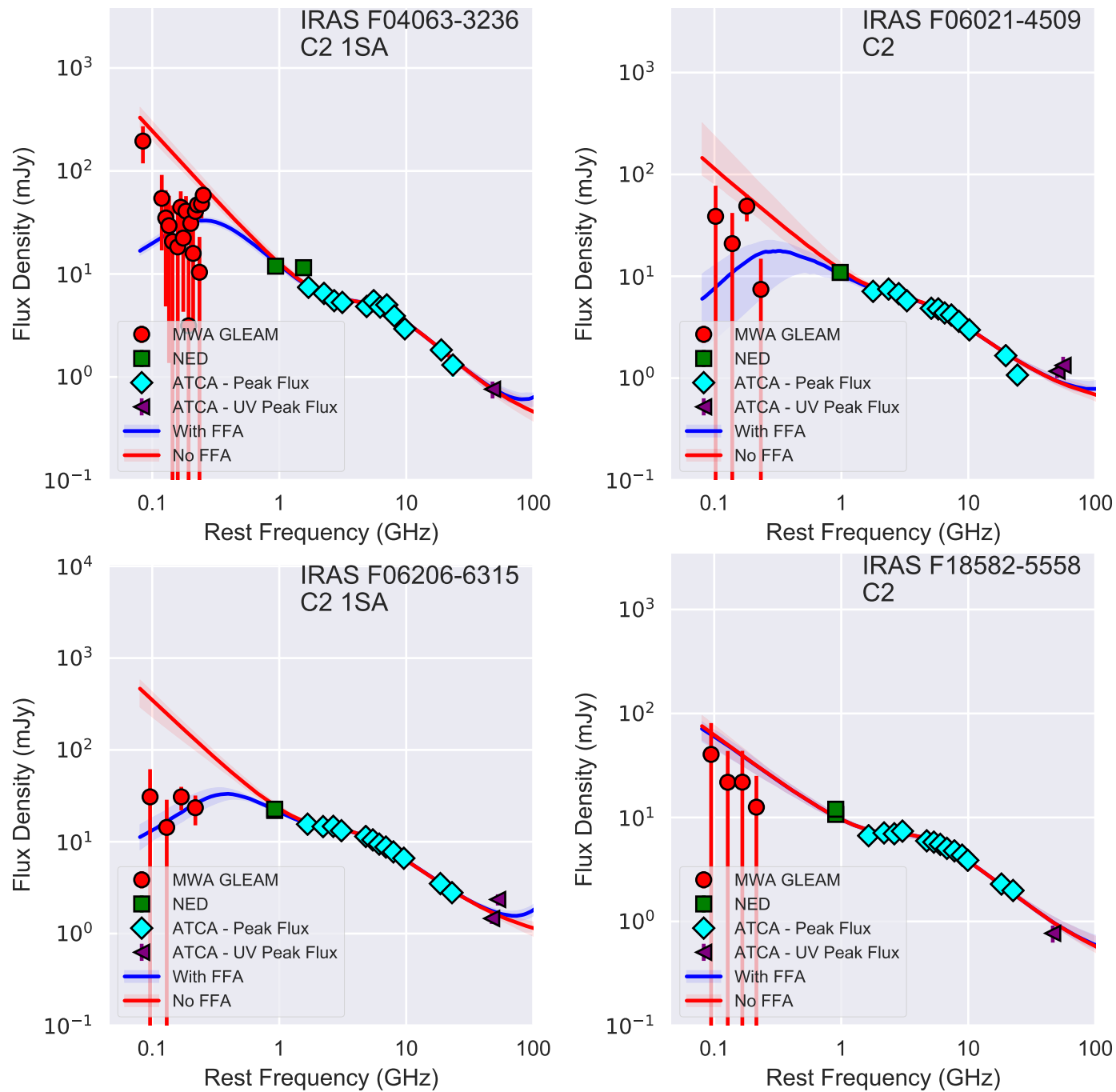


Figure 3.13 (cont.): The most supported constrained model of objects in this sample showing the effects at low frequencies removed when FFA is removed. All other constrained parameters are unchanged.

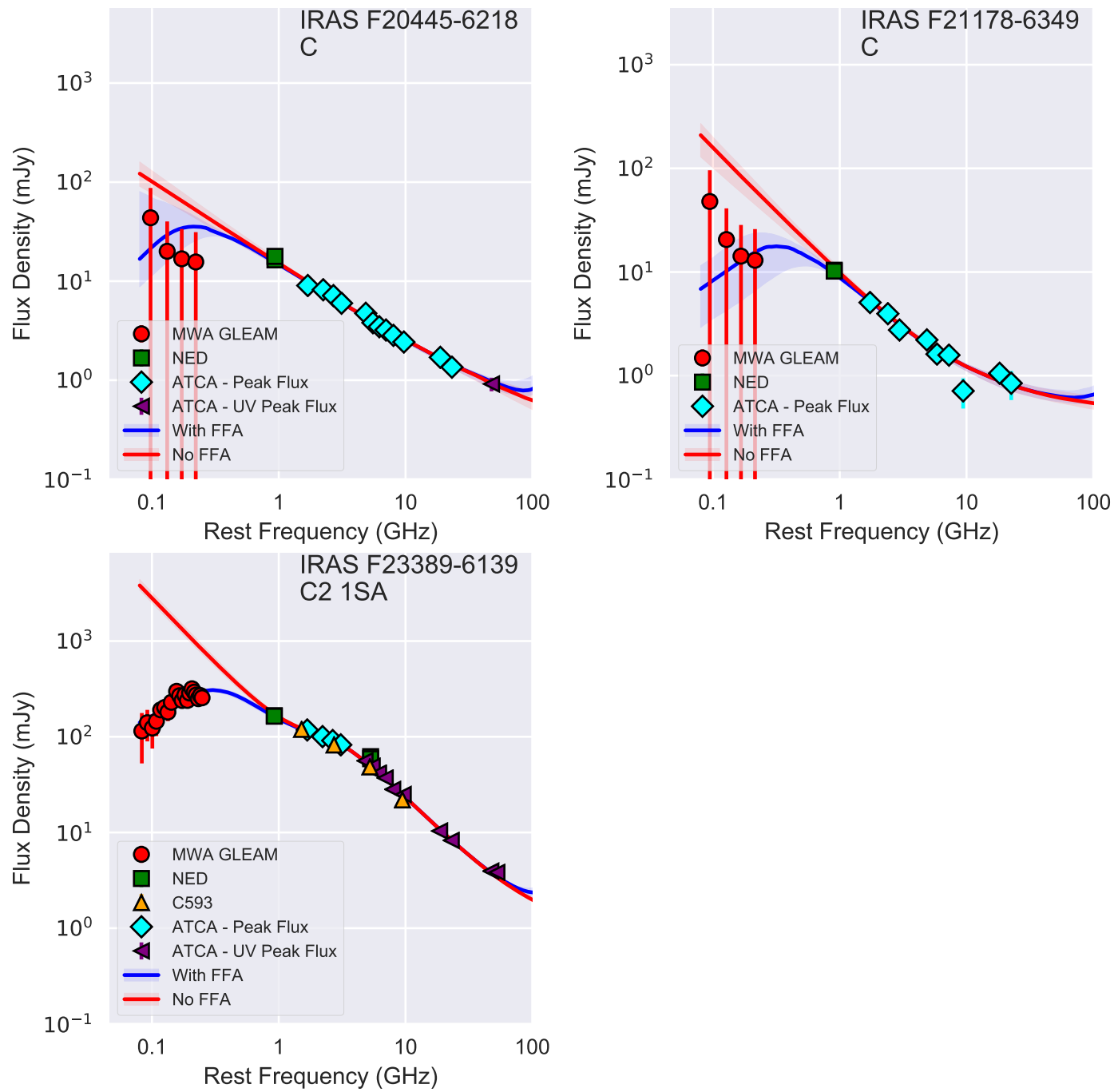


Figure 3.13 (cont.): The most supported constrained model of objects in this sample showing the effects at low frequencies removed when FFA is removed. All other constrained parameters are unchanged.

At the observed 200 MHz (Fig. 3.12), there is only a small difference with the estimated radio-continuum when the effects of FFA are ignored. All but one of our seventeen sources with a low frequency turnover are below a suppression factor of 5, with the average being  $\sim 3.7$  (ie. without FFA, the radio-continuum would be 3.7 times higher than what is observed). At 80 MHz, we find that FFA has a far more significant effect on the observed fluxes. Using the applied modelling, we found that at 80 MHz (Fig. 3.12), the estimated radio-continuum without FFA is, on average,  $\sim 19$  times larger than the observed SED.

Including curvature due to FFA for SFG type sources when estimating low frequency source counts and confusion limits will be important. Earlier studies have typically used simple power-law models with varying spectral indices when extrapolating fluxes between frequencies (Waldrum et al., 2007; Franzen et al., 2016). Similarly, Wilman et al. (2008) performed a semi-empirical simulation of the radio-continuum sky out to  $z = 20$ . In their simulation, a turnover due to FFA was assumed at 1 GHz for all starburst galaxies. Our sample, which is constructed to be representative of high redshift starburst galaxies, has turnovers between 90 to 500 MHz (if they were detected). Incorporating our turnover frequencies into the assumed model of Wilman et al. (2008) will have the effect of *increasing* the modelled flux densities at low frequencies. Galvin et al. (in. prep) is exploring the degree of change and how confusion limits could be affected.

### 3.7.3 Synchrotron Spectral Index

The mean modelled synchrotron spectral index in our sample is  $\alpha = -1.06$ , which is noticeably steeper than the canonical spectral index of  $\alpha \sim -0.8$  often assumed for SFG (Condon, 1992). This is based on the well constrained power-law slope of the distribution of cosmic rays we observe at Earth which directly relates to the synchrotron spectral index. This difference is larger than our modelling uncertainties and seems a real outcome of modelling.

Figure 3.14 shows a comparison between the SFR of my sample against the modelled synchrotron spectral index. I have also included six starburst galaxies from Wang and Fields (2016), who constrained the cosmic ray distribution index using Gamma-ray data from the *Fermi*, High Energy Stereoscopic System (HESS) and Very Energetic Radiation Imaging Telescope Array System (VERITAS) instruments. I have converted these to a spectral index following

$$\alpha = \frac{\gamma - 1}{2}, \quad (3.15)$$

where  $\gamma$  is the cosmic ray power law. This comparison reveals a tentative relationship, where galaxies with a higher SFR have steeper synchrotron spectral indices.

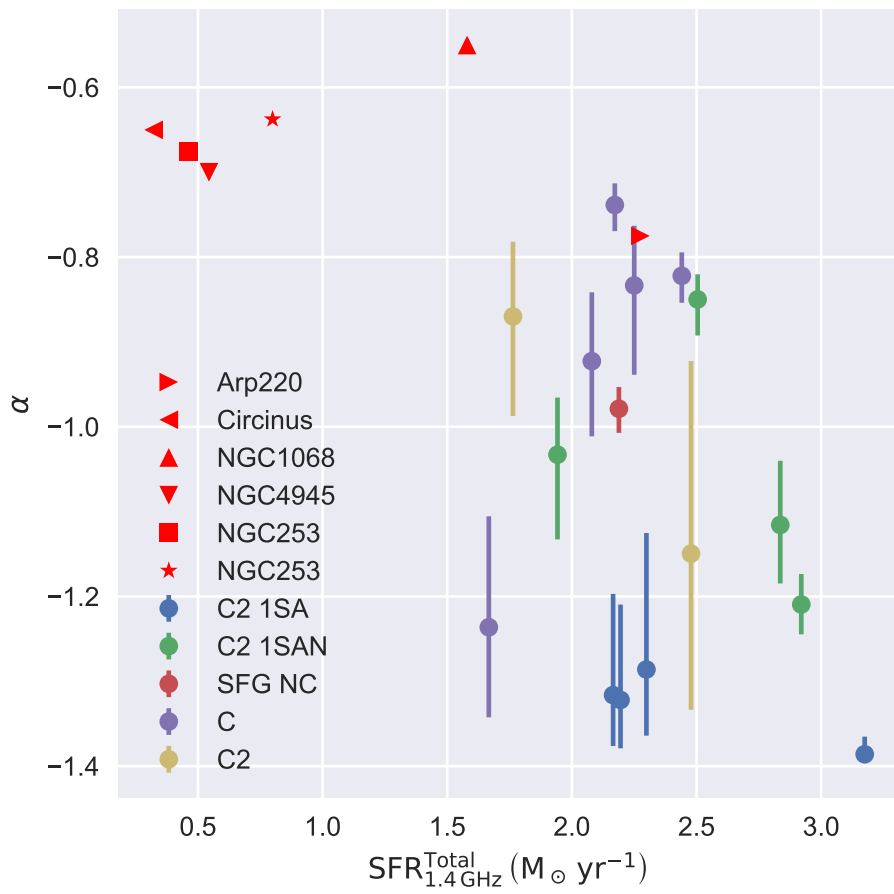


Figure 3.14: Comparison between the SFR and synchrotron spectral index from our modelling and six starburst galaxies from Wang and Fields (2016).



Here, we consider four mechanisms which could explain the spectral index steeper than that of the Milky Way: (i) electron cooling via inverse-Compton losses, (ii) ageing of relativistic electron energy distribution, (iii) a steeper power-law in the relativistic electron energy distribution, or (iv) a different galaxy morphology for extreme starbursts affecting cosmic ray diffusion. We consider (i) to be unlikely as IC losses are weak at low redshifts and when compared with other losses (Lacki and Thompson, 2010). Ageing of the starburst is unlikely as the IR luminosities (which are a more instantaneous tracer of SFR) are still high.

There is some evidence in the literature from GeV and TeV observations of galaxies with higher star formation rate having a steeper cosmic ray power-law index (e.g. Wang and Fields, 2016). This steeper cosmic ray power-law index shows a steeper synchrotron spectrum. Our SFG have even higher SFRs, so they might be expected to have synchrotron spectral indices as steep as we see here. Interestingly, in the case where a single power law is preferred over multiple components with turnovers, the fitted spectral index is lower and closer to the canonical value. One explanation for this and for the lower spectral indices typically seen in deep surveys (Ibar et al., 2009; Huynh et al., 2012), is that simple 2-3 point broadband spectral indices miss the complexity of spectral structure we observe here and ‘average’ over a steeper power law with multiple turnover components.

The final possibility is that powerful starbursts are fundamentally different than lower SFR galaxies previously studied in detail. Lacki and Thompson (2010) describe scenarios where ‘puffy’ starburst galaxies, whose volume density is far less than compact starbursts, can exhibit a steeper cosmic ray distribution index by having a far higher scale height for the cosmic ray distribution. Therefore, we suggest that the steep synchrotron spectral indices modelled in our sample of sources are caused by either a steeper cosmic ray distribution index or a physical difference in the nature of these galaxies compared to nearby lower SFR SFGs.

### 3.8 Conclusion

We have modelled the radio-continuum across a broad frequency range (80 MHz to 45 GHz) for a sample of 19 LIRGS, selected specifically to represent the types of objects to be discovered by SKA and its pathfinder projects at high redshifts. We found that

1. in our sample of 19 objects, the radio continuum of only three (16%) sources were characterised well by a single power-law component over a broad frequency range;
2. Eleven objects show evidence of a low frequency turnover ( $\nu < 800$  MHz), with ten exhibiting features between 400 MHz to 6.5 GHz that are consistent with a higher frequency turnover. Six sources in our sample of 19 show evidence of both a low and mid-to-high

frequency turnover. These could be explained by considering free-free absorption processes acting across multiple regions of star formation, each with different optical depths, that are then integrated over by the large radio synthesised beam;

3. the intrinsic components that make up the radio continuum are correlated with the far-infrared, with the Syn-IR correlations being steeper than the FF-IR trends, similar to the FRC used to calibrate current 1.4 GHz SFR tracers; and
4. without accounting for the effects of FFA, the low frequency radio emission of faint starburst galaxies is susceptible to being overestimated by as much as a factor of 30 when using a simple power-law scaling from a higher frequency, which may influence estimations of low frequency source counts.
5. the mean synchrotron spectral index of our sample is  $\alpha = -1.06$ , which is steeper than the canonical value of  $\alpha = -0.8$ . We suggest that this is associated with a steeper cosmic ray distribution index.

# Chapter 4

## Optical Spectroscopy Data of LIRGS

### 4.1 Motivation

Recombination lines have been extensively used throughout the literature to understand the intrinsic chemical composition of galaxies, their motion, dust composition, and importantly, in the context of this dissertation, their star formation rates.

Once the thermal free-free radio continuum is isolated, it is expected to be a more robust tracer of star formation for the SKA era. To evaluate the effectiveness of the free-free component, we planned to acquire Paschen- $\alpha$  ( $\lambda = 1.875 \mu\text{m}$ , referred to as Pa $\alpha$  hereafter) observations to complement the broadband radio SEDs of my secondary LIRG sample. Pa $\alpha$  is a powerful tracer of star formation that, when compared to other recombination lines, is far more resilient to the effects of dust attenuation (Alonso-Herrero et al., 2006). In the literature, Pa $\alpha$  has been used to calibrate other tracers of star formation and assess their reliability (Calzetti et al., 2005, 2007; Alonso-Herrero et al., 2006; Kennicutt et al., 2007, 2009).

The set of LIRGs described in the previous Chapter was selected to have a redshift in the range of 0.067 to 0.227. This redshift range shifts the Pa $\alpha$  transition to a wavelength not effected by atmospheric opacity, allowing ground-based spectroscopic observations. Although acquiring Integral Field Unit (IFU) Pa $\alpha$  data using the SINFONI instrument on the VLT for these sources has been proposed, they so far are yet to be successful.

An alternative to Pa $\alpha$  as a tracer to star formation is the H $\alpha$  recombination line ( $\lambda = 656.28 \text{ nm}$ ). Although this longer wavelength line is more susceptible to dust extinction effects, it is arguably the most utilised recombination line for tracing star formation. Being in the optical wavelength regime, at low redshifts, this line is observable from ground-based instruments up to

redshifts of  $\sim 0.5$ . As outlined in §1.2.2,  $H\alpha$  is produced by the ionisation of HII regions by the UV emission of nearby HMS. These are the same emitting regions that produce thermal free-free radio emission. The amount of  $H\alpha$  emission is directly proportional to the photoionisation rate and to recent star formation. This makes it an ideal tracer of star formation with time scales that are relatively prompt.

For these reasons, the  $H\alpha$  nebular recombination line is one of the more ideal tracers of star formation to compare against the free-free emission characterised by modelling of the radio-continuum SEDs presented in the previous Chapter.

For calibrating the free-free component of the radio continuum as a tracer to star formation, observations for five nights were allowed on the Australian National University (ANU) 2.3 m WiFeS instrument to acquire spectra between 3000 to 9500 Å. The goal of these data was to characterise the  $H\alpha$  and  $H\beta$  nebular transitions to produce dust corrected star formation rates for the sample of LIRGs studied throughout this project (the sample defined in the previous Chapter). In this Chapter, these data are presented, including an overview of the data reduction process and subsequent processing used to obtain dust corrected  $H\alpha$  luminosities.

## 4.2 Background

Although optical-based measures of star formation are near-instantaneous tracers, their critical flaw is that they are sensitive to the presence of dust. Small grains of dust, whose sizes range from 0.35 nm to approximately  $1\ \mu\text{m}$  (Kennicutt and Evans, 2012), absorb and scatter passing light. In the literature, there is often a distinction made between the terms, extinction, which is the combined absorption and scattering of light, and attenuation, which is the net effect of complex dust geometries on passing light (Calzetti, 2001). Throughout this dissertation, I have used extinction and attenuation interchangeably while, referring to the latter scenario.

Reliable measures of SFR based on optical emission require these effects of dust attenuation to be estimated and corrected for. These measures are increasingly difficult to apply at high redshifts, but in the local Universe, are reasonably accurate and understood (Ly et al., 2012; Domínguez et al., 2013). With only limited or sparse data (which is often the case for high redshift objects), it is difficult to distinguish a dusty starburst object with a high level of extinction from an older, post starburst system (Calzetti, 2001). Breaking this degeneracy requires broadband data with comprehensive stellar reference templates.

Young, high-mass stars ionise the nearby clouds of hydrogen gas with their large amounts of UV emission, exciting their molecular content. This produces both free-free radio-continuum emission and the Balmer series of recombination lines. These lines, the most notable being the

$H\alpha$  and  $H\beta$ , are powerful emission diagnostics. They are observable from ground-based instrumentation, and once a dust extinction correction has been applied, are remarkably accurate tracers of star formation. Acquiring a dust correction is, in of itself, not a straight forward procedure. The amount of extinction depends on the distribution of dust, star formation, and how intermixed the two components are.

To the first order, studies in the literature have found that assuming an order of magnitude of extinction for the  $H\alpha$  line as a ‘rule of the thumb’ to be acceptable. This approach is based on statistical averages of the extinction in nearby local galaxies and as such is meant to be applied to groups of objects in place of individual objects (Kennicutt, 1992). More accurate corrections may be derived using the Balmer decrement method. This approach uses an expected intrinsic ratio between lines in the Balmer series as a way to characterise the unknown degree of dust obscuration (Osterbrock, 1989). The bluer end of a spectrum (where  $H\beta$  resides) is more affected by dust than the redder end (where  $H\alpha$  is); any deviation from the expected  $H\alpha/H\beta$  ratio can be used to estimate a reddening curve (how the dust obscuration changes across wavelength) and consequently recover the intrinsic luminosity of an obscured line (Calzetti et al., 2000).

After correcting for dust obscuration,  $H\alpha$  luminosities have been extensively used in previous studies when assessing consistency among various star formation tracers. Kewley et al. (2002) compared dust corrected  $H\alpha$  luminosities to far-infrared emission and found the two tracers to agree. They also found that the Balmer decrement derived colour excess term,  $E(B - V)$ , correlated well with far-infrared luminosities. Physically, this is explained simply as the dust that produces the far-infrared emission is the same dust that obscures the nebular recombination lines. Hao et al. (2011) also used dust corrected  $H\alpha$  luminosities to calibrate multi-wavelength composite star formation tracers, which incorporate two different emission diagnostics, typically one tracing stellar light directly and another tracing light reprocessed by dust.

Investigating the decomposed free-free radio continuum alongside dust corrected  $H\alpha$  measurements is a more direct comparison that can be made when assessing potential correlation. Both measures are produced by the same nebular emitting matter that has been bombarded by ionising UV radiation from young high-mass stars. For future radio surveys exploring the high redshift Universe, due to inverse-Compton cooling and Doppler shifting effects, the observed radio continuum is going to become increasingly free-free in nature. Understanding how free-free emission itself can be used to calibrate high redshift SFR indicators is critical.

### 4.3 Wide-Field Spectrograph

The Wide-Field Spectrograph (Dopita et al., 2007, 2010) instrument is present on the Mount Stromlo Sliding Springs Observatory 2.3-m telescope managed by the Australian National University. I developed two proposals that were ultimately successful and collectively was awarded competitive nights on the instrument. Data acquired from this instrument is presented in Chapter 4.



Figure 4.1: An image of the ANU 2.3metre telescope that hosts the Wide-Field Spectrograph instrument at the Mount Stromlo Sliding Springs observatory. Image courtesy: [http://rsaa.anu.edu.au/files/styles/acton\\_gallery\\_scale/public/2\\_3m\\_dome\\_telescope\\_daytime.jpg](http://rsaa.anu.edu.au/files/styles/acton_gallery_scale/public/2_3m_dome_telescope_daytime.jpg)

WiFeS is a powerful integral field, image slicing double beam spectrograph. It is made up of 25 individual  $38'' \times 1''$  gratings, thus providing a complete field of view of  $38'' \times 25''$  with  $0.5''$  sampling along each slit. Incoming light is divided into two  $4096 \times 4096$  pixel charge-coupled devices (CCDs), each optimised for their respective blue and red beam. There are five gratings available on WiFeS with different wavelength coverage and resolution, which are outlined in Table 4.1.

	Blue			Red		
	$R = 7000$		$R = 3000$	$R = 7000$		$R = 3000$
Grating	U7000	B7000	B3000	R7000	I7000	R3000
Dichroic	RT480	RT615	RT560	RT480	RT615	RT560
$\lambda_{min}$ (Å)	3290	4180	3200	5290	6830	5300
$\lambda_0$ (Å)	3850	4900	4680	6200	8000	7420
$\lambda_{max}$ (Å)	4380	5580	5900	7060	9120	9800

Table 4.1: The standard WiFeS grating and dichroic sets, their wavelength coverage, and resolution following  $R \sim \lambda/\Delta\lambda$ . This table has been taken from Dopita et al. (2010).

Being a completely robotised instrument, WiFeS is available for remote observations over the internet. All actions required by the observer are performed using the Telescope Automation and Remote Observing System (TAROS) JAVA application. A screen capture of TAROS is

Observation Date	Project ID	Principal Investigator
14-12-2014	4140196	Galvin
15-12-2014	4140196	Galvin
06-10-2015	3150149	Galvin
07-10-2015	3150149	Galvin
08-10-2015	3150149	Galvin

Table 4.2: An overview of the WiFeS observations obtained as a part of this thesis.

shown in Figure 4.2. Through this application, different target sources can be set, positioned in the aperture, and observed. Various observing modes, including classic equal, classic unequal, and nod and shuffle are offered.

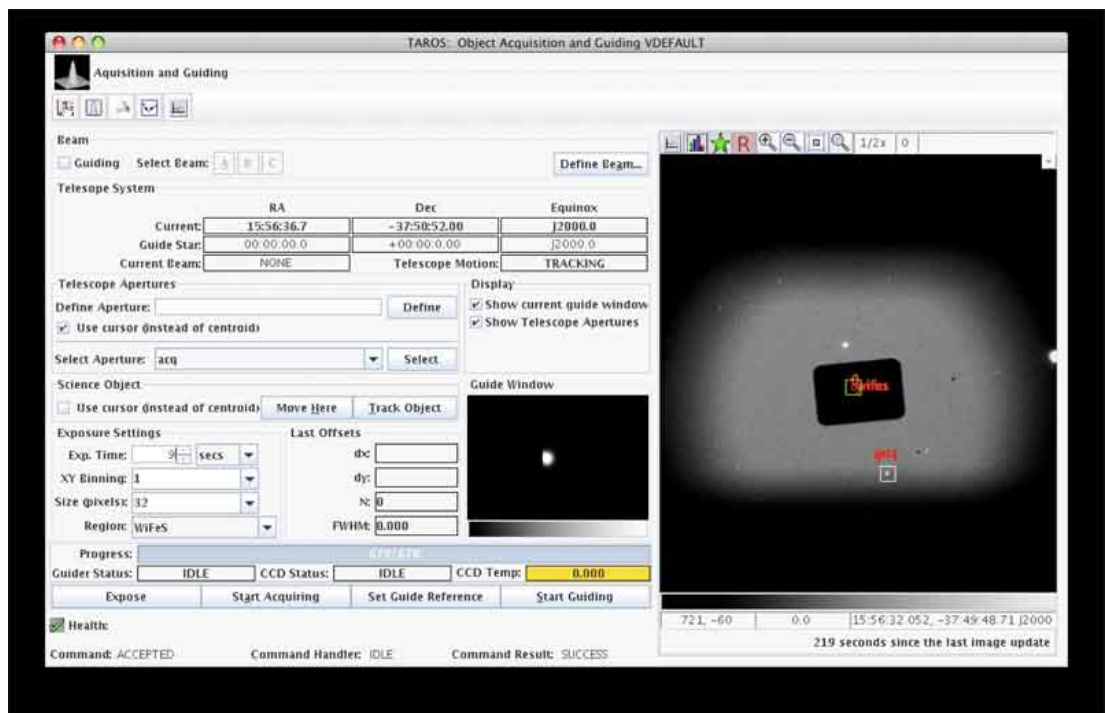


Figure 4.2: A screen capture of the TAROS observing application used by WiFeS. Image taken from Dopita et al. (2010).

Guide stars, which are used to ensure pointing stability, are manually identified and selected by the observer while configuring an exposure. An example of a guide star is shown in the ‘Guide Window’ panel of Figure 4.2.

## 4.4 Optical Spectroscopic Data

Data were collected over five grey nights in December 2014 and October 2015 using the B3000 and R3000 gratings, which provided a spectral resolution of  $R \sim 3000$  ( $R = \lambda/\Delta\lambda$ ). These gratings provide continuous coverage from 3200-9800 Å with a single exposure, and spectral resolutions of  $\sim 0.75$  Å in the blue arm (3200-5900 Å) and  $\sim 1.55$  Å in the red (5300-9800 Å).

At wavelengths larger than 8000 Å the throughput of the R3000 grating slowly diminishes. To remove atmospheric sky lines, I used a nod and shuffle (NAS) exposure strategy to obtain sky frames. NAS will continually switch positions between a target source and the corresponding empty sky position based on user-defined cycles and integration times. The empty sky frames would be used as a model to subtract the corresponding sky lines that are present in the target source exposure. Four of the five nights had excellent seeing conditions with no cloud cover and a typical seeing of 1.5'' throughout the run. The 5<sup>th</sup> night was stormed over, and no usable data could be obtained.

I observed a Copper-Argon (Cu-Ar) arc line lamp multiple times throughout the night to derive a time-dependent wavelength calibration solution. Across each observing night, I used the HD 26169 standard star to derive flux and telluric calibration solutions. Exposures were also taken during the twilight to perform flat-field corrections. Ultimately, depending on various source LST constraints throughout the nights, each source was observed for at least 20 minutes (and an additional 20 minutes on the sky frame), although some sources were observed for upwards of 50 minutes in multiple consecutive exposures that were later co-added during data reduction.

#### 4.4.1 Data Reduction

The optical spectra obtained from the WiFeS instrument were reduced and calibrated using the PYTHON based PYWIFES automated reduction pipeline (Childress et al., 2014). PYWIFES comprises a number of self-contained data analysis and processing modules that operate based on user-defined, metadata structures. It has been specifically developed to reduce data from WiFeS automatically but is aimed at being general enough to be used for any IFU spectroscopic datasets.

##### 4.4.1.1 pywifes operation

I configured the pipeline to perform all data reduction steps, including bias frame subtractions, flat fielding corrections, wavelength calibrations, cosmic ray cleaning, sky frame subtraction, field co-adding, and final flux and telluric calibration. At each stage, the data products were inspected using quality controls built into the individual modules in the pipeline, to ensure an adequate calibration was performed. The final outputs of the PYWIFES pipeline were two separate calibrated red and blue data cubes for each source that contained the flux and variance measures.

The key stages of the PYWIFES pipeline are listed below:

- bias frame subtraction



- flat-field correction
- wavelength calibration
- cosmic ray cleaning
- skyframe subtraction
- co-adding
- flux calibration

PYWIFES operates on a user-defined data structure that encodes raw telescope files that are to be included as part of the data reduction, each file's purpose (e.g. bias frame and sky frame), and any task-specific parameters (e.g. method to isolate lamp lines for use in wavelength calibration and number of processor cores to be used during certain tasks). The default parameters for all tasks included in this data structure were sufficient and did not require manual adjustment.

The final outputs from PYWIFES were a set of FITS files. Encoded in each FITS file were three data cubes, representing the flux calibrated emission per pixel (in units of  $\text{ergs s}^{-1} \text{cm}^{-2} \text{\AA}^{-1}$ ), the corresponding variance per pixel ( $\sigma^2$ ), and flagged pixel masks. For each data cube, the X and Y-axes correspond to RA and DEC sky positions in units of Arcseconds offsets from a reference position, while the Z-axis encodes the observed wavelength in units of Angstrom. A spaxel corresponds to a single pixel, with an X and Y value, that maintains all spectral information along the Z-axis. As WiFeS is a dual-beam spectrograph, each target source had a Flexible Image Transport System (FITS) file for the red and blue arm. Because the pointing model of WiFeS is not absolute, the user manually has to move a target object into the IFU aperture. For absolute positions to be derived, there should be a number of unresolved objects in each field with which other imagery should be compared. This requirement meant that I was unable to obtain the absolute position for these data as I did not have reference sources in the field of view.

While processing data with the PYWIFES pipeline, a bug was discovered by the somewhat unique combination of order science objects that were observed and the NAS strategy used that perturbed the absolute flux calibration applied to the output data products. A thorough overview of the problem is described in Appendix B.5. As part of this work, a patch has been submitted to the developers with an outline to replicate the issue. After the application of this patch, there does not appear to be any other obvious issue related to these data products produced by our adopted observing strategy.

#### 4.4.2 Extracting 1D Spectra

A high signal-to-noise measurement is particularly important when attempting to correct for dust attenuation via the Balmer decrement method to produce accurate SFR measures based on  $H\alpha$  luminosities. For these reasons, I produced a one-dimensional (1D henceforth) spectrum for each source from the potentially resolved WiFeS IFU data cubes.

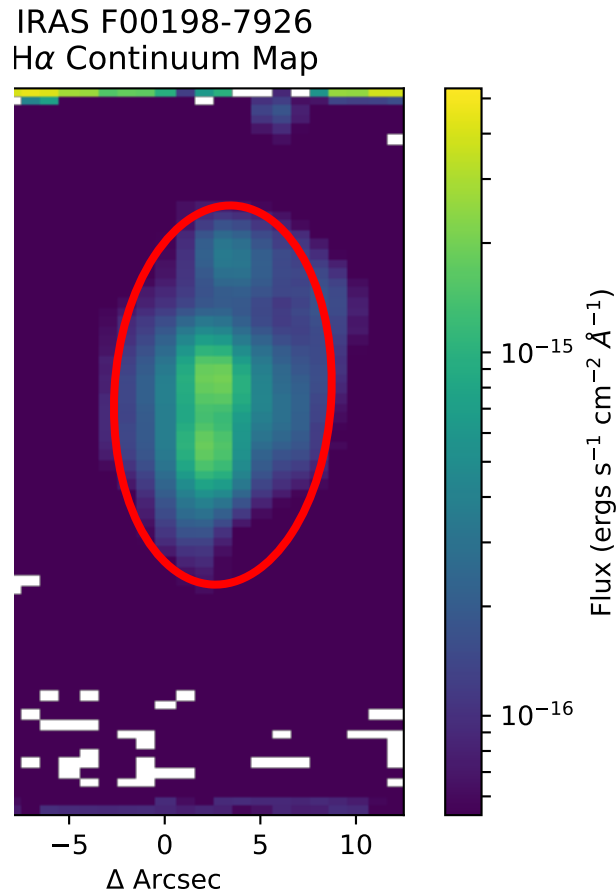


Figure 4.3: The  $H\alpha$  continuum map I produced for IRAS F00198-7926. The overlaid red ellipsis was defined using a multi-Gaussian expansion from codes published by Cappellari (2002).

For each object detected in my sample of WiFeS data, I produced an aperture mask constructed by applying a multi-Gaussian expansion (Cappellari, 2002) on the  $H\alpha$  continuum maps of each source. These continuum maps were created simply by summing all frames along the  $\lambda$ -axis between  $6552.80 \times (1 + z)$  and  $6572.80 \times (1 + z)$  into a single image, where  $z$  is the redshift of a particular object. These ‘continuum maps’ focus on a specific line, in this case  $H\alpha$ , but are wide enough that they may contain stellar continuum emission. An example of one of the  $H\alpha$  continuum maps with an overlaid aperture for IRAS F00198-7926 is shown in Figure 4.3. The overlaid red ellipse is an aperture mask created using a multi-Gaussian expansion implemented using the `FIND_GALAXY` routine from Michele Cappellari’s software page, accessible at

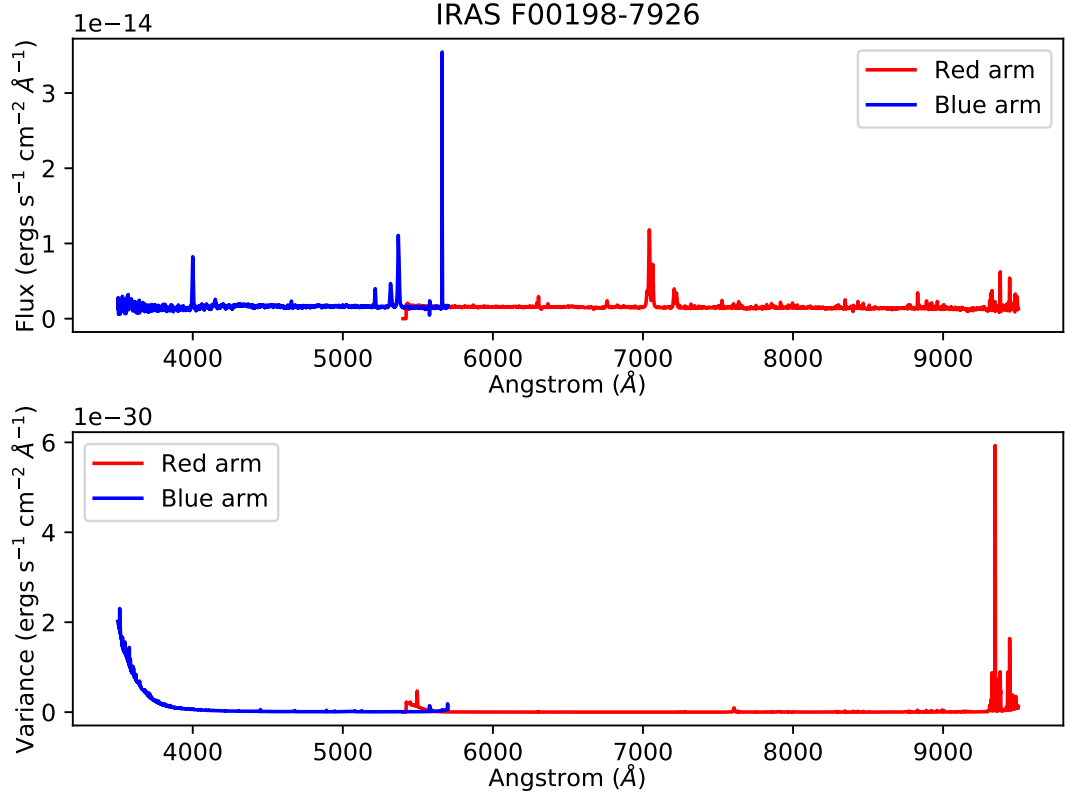


Figure 4.4: The collapsed one-dimensional spectra of IRAS F00198-7926 using an aperture (see Figure 4.3) mask. All spaxels inside this mask were summed together to maximise the SNR of the detected stellar emission lines and stellar continuum. The top panel shows the measured flux, and the bottom panel shows the equivalent variance.

<http://www-astro.physics.ox.ac.uk/~mxc/software/>.

As WiFeS is a dual-beam spectrograph, the single aperture mask created using the  $H\alpha$  continuum map, from the red beam, was also applied to the blue beam data cube. Among my samples, the  $H\alpha$  line was consistently the strongest feature. My initial one-dimensional spectra for each source were produced by summing all spaxels that resided inside the aperture mask (represented as the red ellipse in Figure 4.3) for each frame along the  $\lambda$ -axis of the four data cubes (each FITS file has separate data cubes for flux and variance).

An example of the collapsed one-dimensional spectra of IRAS F00198-7926 is shown in Figure 4.4. Between the blue and red beams of WiFeS, there is complete coverage from 3300 to 9500 Å in the observed frame, with slight overlapping coverage at  $\sim 5500$  Å. Poor sky subtraction at wavelengths above 7000 Å has produced a number of residual artefacts that are in the observed spectrum and are not genuine stellar features. Towards the upper end of the blue beam there remains a residual cosmic ray that was not completely cleaned from the data cubes. Again, this is an erroneous feature that is not real and was subsequently manually removed.

Before modelling the combining of the extracted blue and red spectra into a single dataset, a simple test was performed to ensure that each of the independently calibrated beams shared

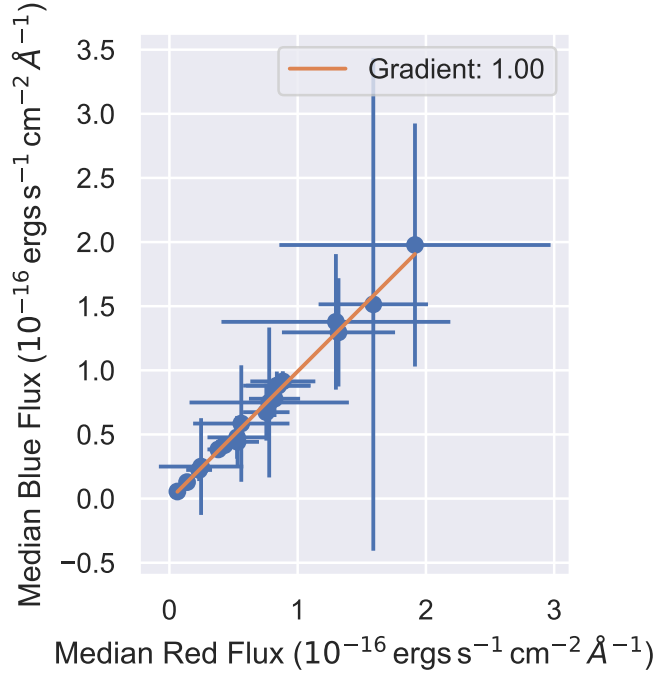


Figure 4.5: A comparison between the median flux measurement of the one-dimensional spectra extracted for each source from their corresponding red and blue data cubes. Overlaid as the orange line is the result of orthogonal distance regression performed against the data.

a consistent flux calibration scale. There is  $600 \text{ \AA}$  of spectral overlap between the upper and lower ends of the R3000 and B3000 gratings, respectively. For each source, the median and SD were measured for the red and blue spectra within this overlapping region. For most sources, this overlapping region contained no emission or absorption features. If data were properly calibrated and shared a consistent absolute flux scale, the stellar continuum should align. By considering the median value, the residual effects of uncleaned cosmic rays and the presence of any emission lines should largely be suppressed, allowing an approximate comparison to be made. The SD was taken as a first order measure of the noise of the continuum.

Results of this test are shown in Figure 4.5. With these 19 measurements, a simple linear model was constrained using orthogonal distance regression to account for errors in both dimensions. This resulted in the following relation:

$$\text{Flux}_{\text{Blue}} = 1.0006 (\pm 0.02) \times \text{Flux}_{\text{Red}} - 0.009 (\pm 0.006), \quad (4.1)$$

where  $\text{Flux}_{\text{Blue}}$  and  $\text{Flux}_{\text{Red}}$  are the median flux values of the blue and red spectra, respectively, between  $5300 \text{ \AA}$  and  $5900 \text{ \AA}$  in units of  $10^{-16} \text{ ergs s}^{-1} \text{ cm}^{-2} \text{ \AA}^{-1}$ . The gradient of this model is indistinguishable from unity, suggesting that the two independently calibrated datasets are on a consistent flux calibration scale with an adequate level of precision.

This agrees with the qualitative assessment made by closely examining a set of spectra where

emission features were present in this overlapping region. Two example spectra of sources IRAS F01268-5436 and IRAS F04063-3236 are shown in Figure 4.6. The redshifts of these sources placed certain spectral emission features in this overlapping region. It is clear that they agree with one another to a high level of precision despite the various edge band effects.

#### 4.4.3 PPXF

After producing integrated 1D-spectra of each source, I proceeded to fit the observed stellar continuum and spectral line features. A naive approach originally adopted was to fit, using least-squares optimisation, a low order polynomial to the stellar continuum and a series of Gaussian-like functions for stellar emission features of the detected transitions. A part of this procedure was the implementation of a rolling box function to calculate a rolling mean and SD, which was used to isolate and fit the continuum. The residuals were then fit with the Gaussian-like shapes, which were configured by hand with initial guesses for the model optimiser for complex or blended features.

For the first order, this method worked well. However, it neglected stellar absorption features and often required multiple Gaussians to model single transitions correctly. The former was particularly troublesome as older stellar populations often produce absorption features in the same  $\lambda$ -region as stellar emission features. The process as a whole was time-consuming because it required some level of manual interaction to create the initial model and corresponding initial parameter guesses for each individual source.

While developing this naive method, I found more sophisticated approaches that can take advantage of the stellar continuum and recover more robust intrinsic galactic properties, including correcting for stellar absorption features. The observed spectra of a galaxy at a certain sky position can be considered as the weighted sum of individual stellar components that have been convolved by a line of sight velocity dispersion (LOSVD) function describing the summed Doppler shifting effects. There exists in the literature stellar template libraries covering a range of stellar parameters, including those that are empirically measured (Valdes et al., 2004; Sánchez-Blázquez et al., 2006) or synthetically derived (Munari et al., 2005; Gustafsson et al., 2008). When combined with optimisation methods, these libraries can be used to constrain intrinsic physical properties of an observed spectrum, including metallicities, stellar ages, and star formation histories.

Figure 4.7 shows an example of a stellar template taken from Sánchez-Blázquez et al. (2006). This example template has a metallicity of  $-1.71$  and is  $\sim 1$  Myr old. I have labelled a number of absorption features from the Balmer series that are present throughout the spectra.

In simple situations, the LOSVD, also referred to as a line profile, is assumed to be Gaussian

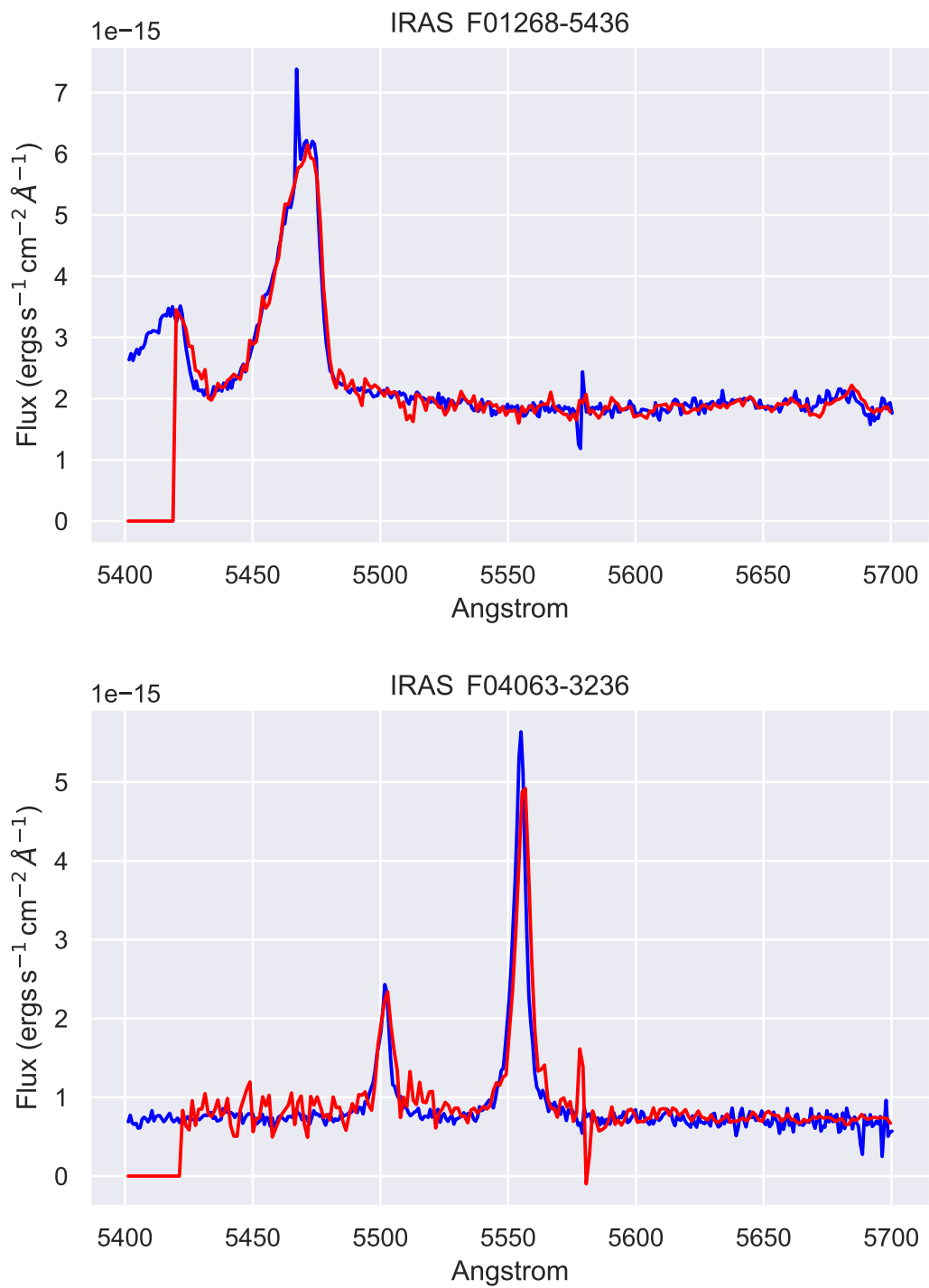


Figure 4.6: The overlapping spectra of two sources which exhibit common spectral features that appear to agree to a high level of precision.

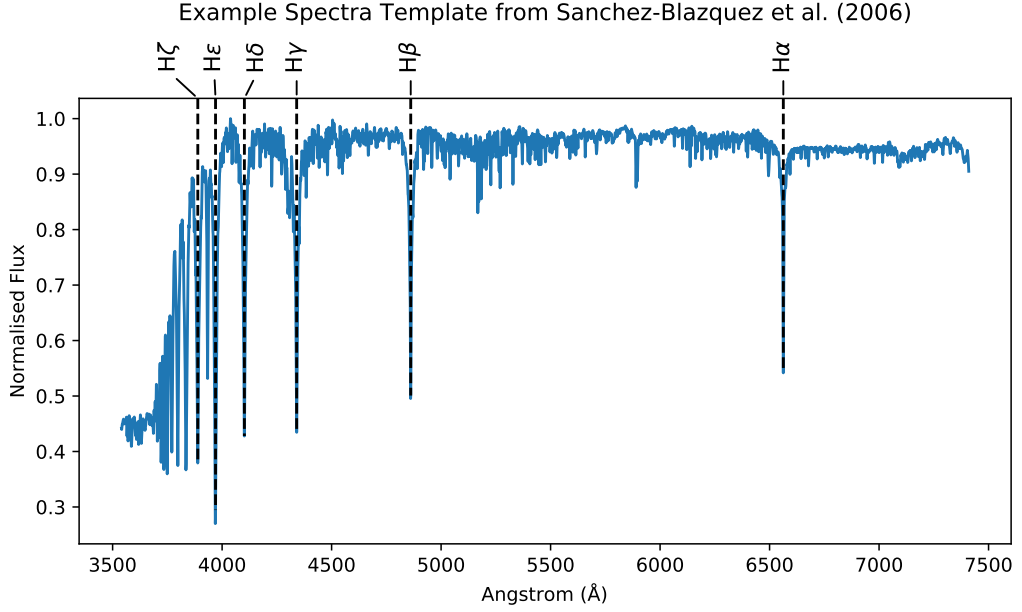


Figure 4.7: An example of a stellar template taken from the MILES template library (Sánchez-Blázquez et al., 2006). Stellar absorption features have been labelled.

in nature. However, there is no guarantee that this holds, especially when working with one-dimensional spectra that cover a summed region in the sky. In such situations, when high order complexity is detected, a number of approaches can be undertaken. The initial thought is to treat these higher-order shapes as the superposition of two individual Gaussian profiles. Although this approach is attractive if there is evidence that suggests the blending of two kinematically distinct stellar populations, it can produce degenerative solutions with highly correlated uncertainties among the six individual parameters.

Alternatively, non-Gaussian line profiles can be parameterised by the Gauss-Hermite series. First described by van der Marel and Franx (1993) and Gerhard (1993), and outlined in § 3.2 of Cappellari (2017), the LOSVD can be written as:

$$\mathcal{L}(y) = \frac{\exp(-y^2/2)}{\sigma\sqrt{2\pi}} \left[ 1 + \sum_{m=3}^M h_m H_m(y) \right], \quad (4.2)$$

$$y = (v - V)/\sigma$$

$v$  is the wavelength vector of a measured spectra,  $V$  is the velocity offset of the convolving Gaussian,  $\sigma$  is the uncertainty vector for the measured spectra, and  $H_m$  is the standardised Hermite polynomial. For stellar kinematic problems, typically only the 3<sup>rd</sup> and 4<sup>th</sup> order Her-

mite polynomials are used, which are described as

$$H_3 = \frac{y(2y^2 - 3)}{\sqrt{3}}, \quad H_4 = \frac{4(y^2 - 3)y^2 + 3}{\sqrt{24}}. \quad (4.3)$$

If some set of observed spectra are considered as nothing more than the weighted sum of stellar templates, it is straightforward to construct a galaxy model that can be used to recover intrinsic components using the stellar continuum. I have adopted this notation from §3.1 of Cappellari (2017), where the galaxy model ( $G_{\text{mod}}$ ) is described as

$$G_{\text{mod}}(x) = \sum_{n=1}^N w_n \left\{ [T_n(x) * \mathcal{L}_n(cx)] \sum_{k=1}^K a_k \mathcal{P}_k(x) \right\} + \sum_{l=0}^L b_l \mathcal{P}_l(x) + \sum_{j=1}^J c_j S_j(x), \quad (4.4)$$

where  $T_n$  are stellar reference templates,  $\mathcal{L}_n$  are the different LOSVDs of each template set,  $c$  is the speed of light,  $\mathcal{P}_k$  and  $\mathcal{P}_l$  are multiplicative and additive polynomials, respectively, to account for low-level discrepancies, and  $S_j$  is the spectrum of the sky (e.g. Weijmans et al., 2008). Alternatively,  $\sum_{k=1}^K a_k \mathcal{P}_k(x)$  can be replaced with some reddening curve that can be used to constrain dust attenuation using the stellar continuum. A common reddening curve,  $k(\lambda)$ , and one that I adopt is that of Calzetti et al. (2000), defined as

$$\begin{aligned} k(\lambda) &= 2.659(-1.857 + 1.040/\lambda) & 0.63 \mu m \leq \lambda \leq 2.20 \mu m \\ &= 2.659(-2.156 + 1.509/\lambda - 0.198/\lambda^2 + 0.011/\lambda^3) \\ & & 0.12 \mu m \leq \lambda < 0.63 \mu m. \end{aligned} \quad (4.5)$$

There have been a number of published codes that aim to solve Equation 4.4. In this thesis, I used the PPXF algorithm, which was first released by Cappellari and Emsellem (2004), later updated by Cappellari (2017), and was obtained from Michele Cappellari's software website at <http://www-astro.physics.ox.ac.uk/~mxc/software/>.

PPXF is particularly powerful because the most recent release can handle stellar emission lines with their own LOSVD that is distinct from the continuum. Alternate public codes, such as GANDALF (Sarzi et al., 2006), often require stellar emission features to be masked out from the stellar continuum and modelled separately.

PPXF solves for the continuum and emission features simultaneously by crafting a set of synthetic templates to represent stellar emission lines. These synthetic templates consist of



	Emission line	Å	Ratio
1	H $\delta$	4101.56	
2	H $\gamma$	4340.47	
3	H $\beta$	4861.33	
4	H $\alpha$	6562.80	
5	[OII]	3726.03	
6	[OII]	3728.82	
7	[SII]	6716.47	
8	[SII]	6730.85	
9	[OIII]	4958.92	0.35 $\times$ [OIII] $\lambda$ 5006.84
10	[OIII]	5006.84	
11	[OI]	6363.67	0.33 $\times$ [OI] $\lambda$ 6300.30
12	[OI]	6300.30	
13	[NII]	6548.03	0.35 $\times$ [NII] $\lambda$ 6583.41
14	[NII]	6583.41	

Table 4.3: The stellar emission lines that I constructed to give to PPXF. For lines that have a known ratio (i.e. a doublet), I have provided the ratio used when constructing its template.

simple Gaussians centred at some transition lab measured wavelengths whose sigma reflects the spectral resolution of the observing instruments. Transitions known to come in pairs (i.e. doublets) with fixed emission ratios were encoded in a single template encoding this known ratio if extinction effects were negligible across their separation. Emission lines used in this manner are described in Table 4.3. The toolkit to craft these templates was included as part of the PPXF software distribution. Ideally, spectra should be modelled in the rest frame. Although the LOSVD measure has a velocity offset component that can account for a redshift, if the degree of Doppler shifting is large, then PPXF will fail to converge to a solution.

I have presented an example of a set of generated templates that were provided to PPXF in Figure 4.8. The code included in the PPXF distribution was modified to encode the instrumental resolution of the WiFeS instrument, which with the B3000 and R3000 gratings follows  $\lambda/\Delta\lambda \sim 3000$ . Although the peaks of each of the synthetic templates may not be consistent, this is accounted for by the weights derived subsequently by PPXF and have no effect on the final modelled spectra or the integrated line fluxes.

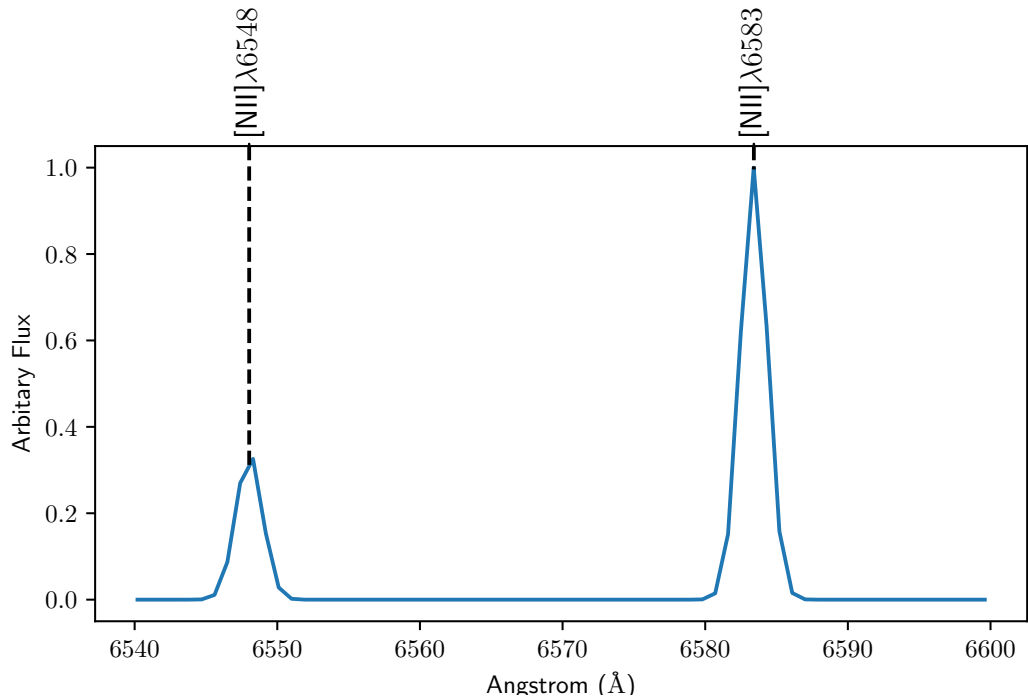
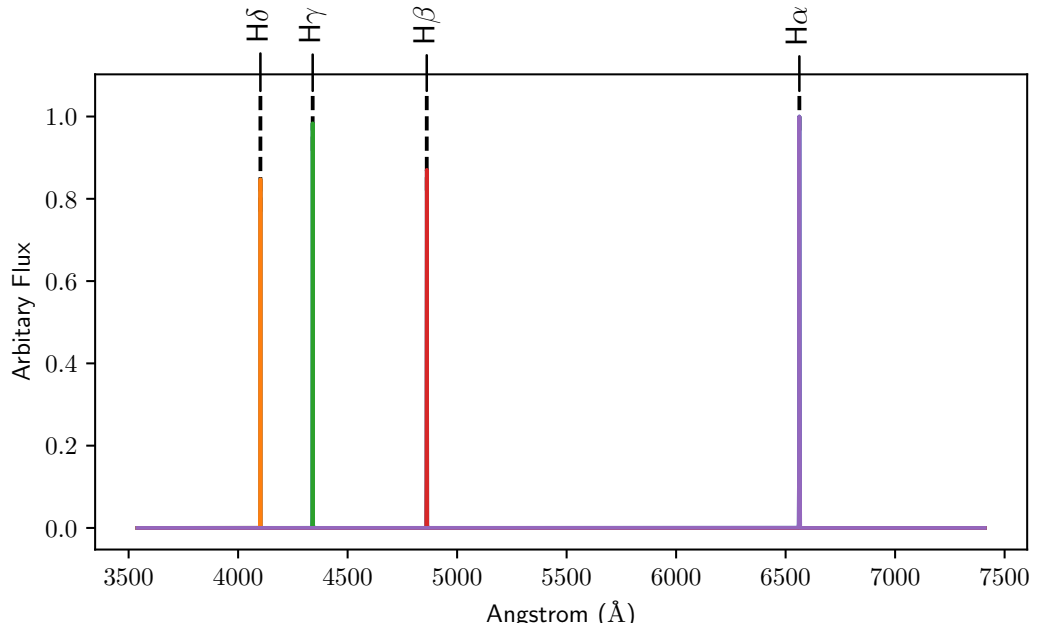


Figure 4.8: Example of the generation of templates, accounting for the WiFeS spectral resolution, to constrain stellar emission lines. Each feature is a Gaussian placed at the known emitted wavelength for each transition. For the case of the [NII] template, the known ratio of the doublet has been encoded into the template. The different colours in the top panel represent distinct templates in the plot, each with their own associate weight to be found by PPXF.

#### 4.4.4 Constraining the stellar continuum and transitions

These collapsed one-dimensional spectra produced for each source, as described in Section 4.4.2, were modelled using version 5.1.15 of PPXF, released on the 22<sup>nd</sup> October 2015.

Following the examples outlined on the PPXF website<sup>1</sup> and included in its distribution, I used 144 template spectra from the MILES stellar template library (Sánchez-Blázquez et al., 2006). These 144 spectra form an intersecting grid of 24 ages and six metallicities and span 3525 to 7500 Å with a spectral resolution of  $R \sim 2000$ . Of the set of reference templates available at the time, I found these to be the most comparable with my own spectra in terms of coverage and spectral resolution. Although my spectra in the WiFeS red arm went upwards of 9000 Å, much of this was contaminated by residual artefacts from an imperfect sky subtraction and contained no emission lines of interest. As the set of MILES stellar reference templates had an upper wavelength limit of 7500 Å, I simply masked out all data above this limit, which included these residual sky lines after shifting my observed spectra to the rest frame.

For most sources, I configured PPXF to solve for two template sets, each with their own distinct LOSVD parameters. The stellar continuum used 144 templates from the MILES library and included the  $H_3$  and  $H_4$  Hermit coefficients when modelling the LOSVD. Stellar emission transitions were modelled using the set of generated templates described in Table 4.3 whose LOSVD was modelled as a pure Gaussian (i.e. a single LOSVD was used for all emission lines). This approach of using a common set of LOSVDs for a set of templates is particularly powerful when attempting to constrain the weak transitions because the properties of the strongest lines often help to reduce, or completely break, degeneracies when trying to identify lines in the low signal-to-noise regime.

Figure 4.9 shows the spectra of IRAS F00198–7926 modelled by PPXF. There are two components that make up this figure. The top panel shows the observed spectra (thin black line) overlaid with the final modelled spectra (thick blue line), the stellar continuum made up of the weighted sum of MILES stellar templates (red line), the generated stellar emission line templates (green lines), and model residuals (lime green scatter around zero). The observed spectra were normalised according to its median value to reduce the numerical precision errors, which led to the ‘Relative Flux’ label. In this case, I do not include a reddening curve (i.e. Equation 4.5) during the modelling of this source.

The bottom panel of Figure 4.9 shows the intersecting grid of 144 MILES stellar templates whose colour represents the corresponding weight constrained by PPXF. These templates have been arranged according to their known ages and metallicities. For IRAS F00198–7926, this template activation map indicates that there are two stellar populations. The strongest being

---

<sup>1</sup><http://www-astro.physics.ox.ac.uk/~mxc/software/>

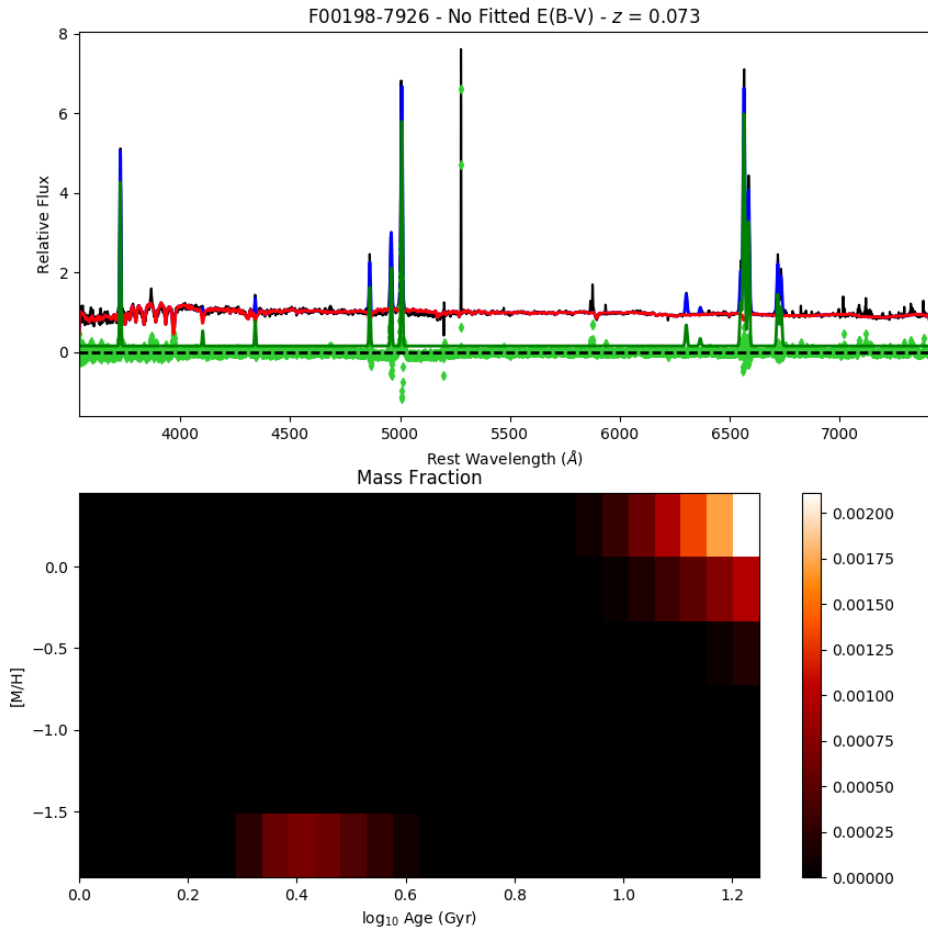


Figure 4.9: An example of the model spectra constrained using the PPXF algorithm. The black line in the top panel is the collapsed one-dimensional spectra obtained from my WiFeS observations. The stellar continuum that has been constrained using the MILES template library is shown in red. Generated templates of the stellar emission lines are shown in green. Residuals of the fit are shown around the dashed line in lime green. The bottom panel shows the multiplicative terms of the MILES templates used that PPXF has constrained, highlighting the activation of a set of distinct old and young stellar reference templates.

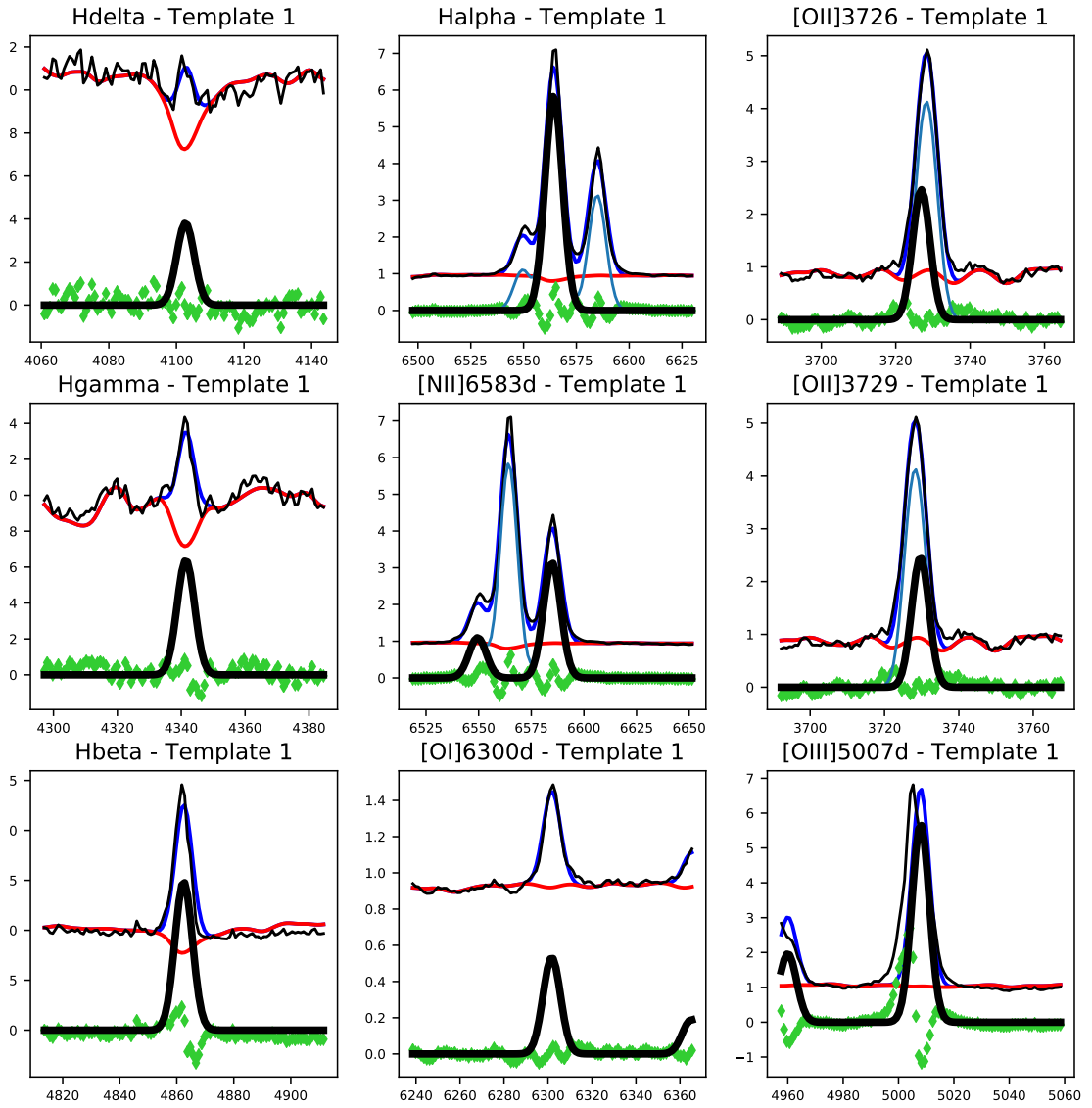


Figure 4.10: I show a zoomed diagnostic plot of each of the lines from the fit shown in Figure 4.9. The thin black line denotes the observed spectra, with the blue line being the modelled spectra. The red line is the stellar continuum described by the MILES stellar templates, with the thick black line being the generated stellar emission line. Where possible, doublets have been encoded in a single template. Some lines rest upon a broad stellar absorption feature, which is described using the MILES templates.

an older population of stellar components with high metallicities ( $\sim \text{Log}_{10} 1.2 \text{ Gyr}$ ,  $[\text{M}/\text{H}] \sim 0.2$ ). There is also a far weaker population of younger stars with ages of  $\sim \text{Log}_{10} 0.4 \text{ Gyr}$ .

To further illustrate the components that PPXF modelled, I present in Figure 4.10 a diagnostic plot showing a zoomed view of a subset of the stellar emission lines of IRAS F00198–7926. The use of stellar reference templates does an excellent job of constraining the stellar continuum on either side of some line. There is also the benefit of accurately being able to estimate the degree of stellar absorption, which can hide a significant fraction of line emission. For instance, lines in the Balmer series, including  $\text{H}\delta$ ,  $\text{H}\gamma$ ,  $\text{H}\beta$ , and  $\text{H}\alpha$ , all have a small absorption component which a simple interpolation from the continuum both sides of the line would have missed (Domínguez et al., 2013). The stellar reference templates, which include these absorption features, require continuum information and the absorptions features at  $\sim 3800 \text{ \AA}$  to reconstruct the likely absorption profile that the  $\text{H}\alpha$  and  $\text{H}\beta$  emission lines reside on. During modelling, this deficit captured by the weighted sum of stellar reference templates is corrected by the weights derived for the synthetic set of templates used to constrain the stellar emission lines.

The remainder of the sample and their PPXF modelled spectra are presented in Appendix B.1 as Figure B.1. For completeness, PPXF modelled each source twice, once where it included the stellar reddening curve as a property to constrain and once without.

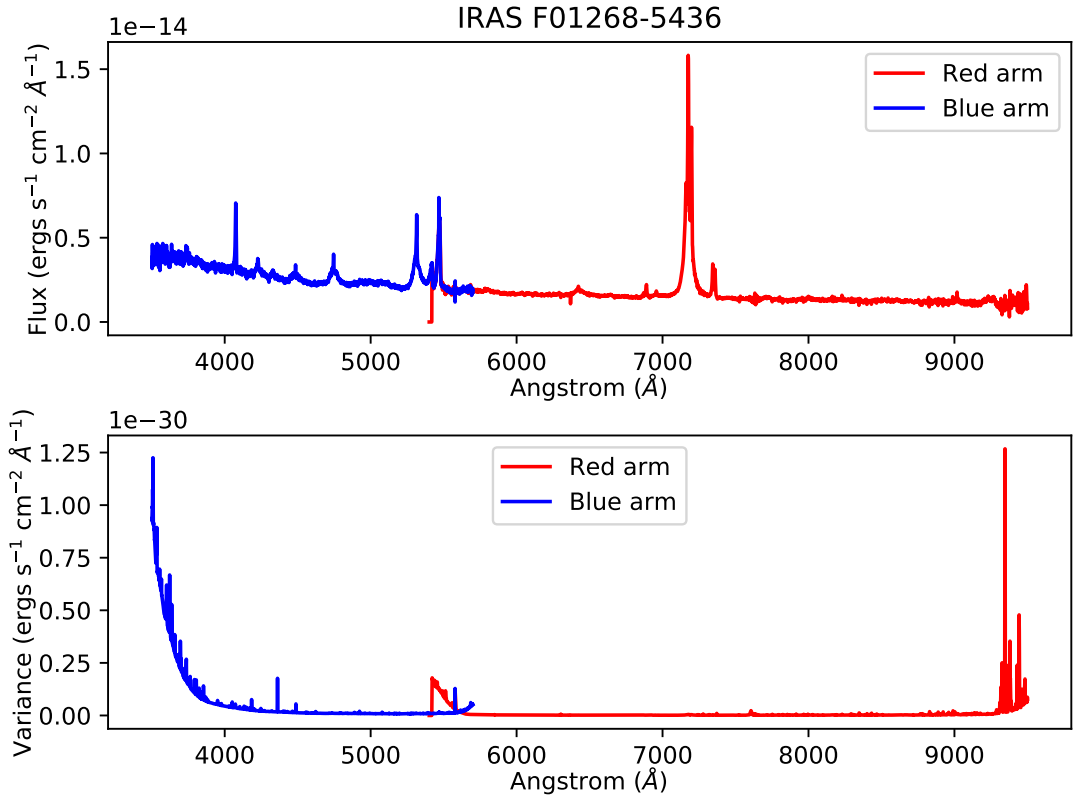


Figure 4.11: The one-dimensional optical spectra of IRAS F01268–5436 exhibiting broadened emission lines and curved stellar continuum after summing spaxels within an aperture mask.

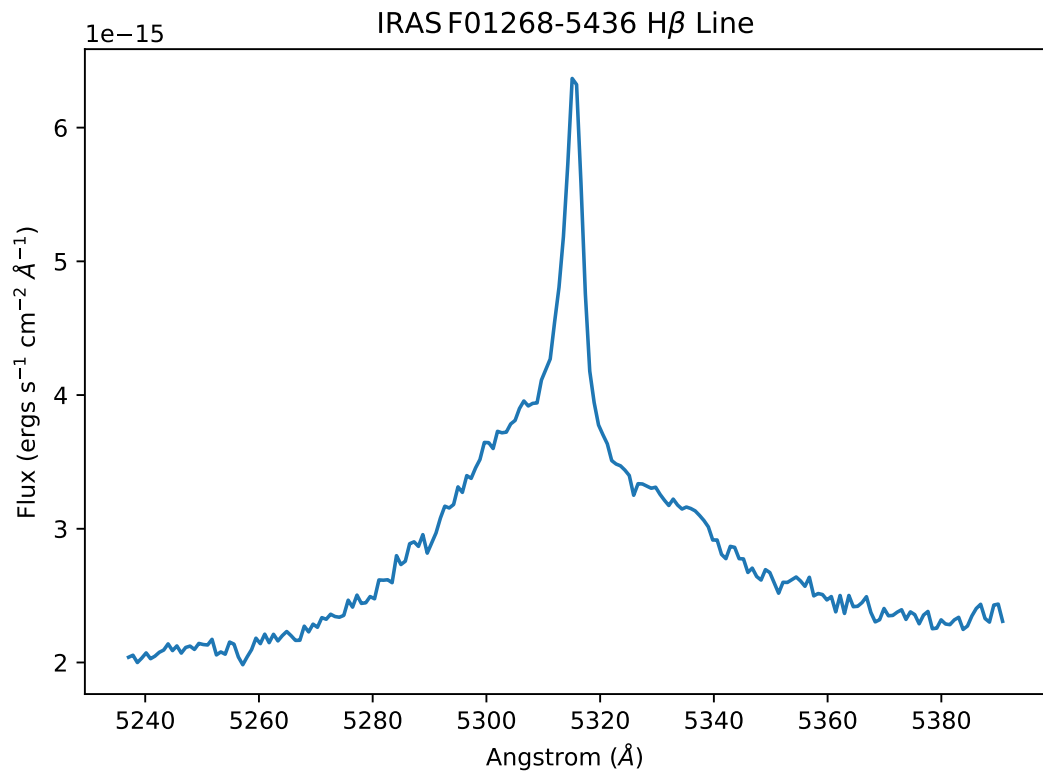


Figure 4.12: The broadened  $H\beta$  emission line of IRAS F01268–5436. There is a low-level broad component sitting on top of a low velocity peak. This broadened feature is modelled with a secondary set of synthetic transition templates with a distinct LOSVD parameter set. I show the  $H\beta$  line and not the  $H\alpha$  line to avoid the nitrogen doublet that slightly obscures the broad component of the  $H\alpha$ .



Figure 4.13: The linear AGN templates generated for IRAS F01268–5436 to help capture the shape at the bluer end of the observed spectrum.

Of our entire sample, a single source exhibited features that indicate the presence of AGN activity. The spectra of IRAS F01268–5436, as presented in Figure 4.11, exhibit broad emission lines and an upward curvature of the stellar continuum. Initial modelling of this source with a single set of synthetic spectral transition templates failed to produce robust fits. Figure 4.12 shows a zoomed-in version of the  $H\beta$  line of this source. There is a low-level broadened component from AGN jet activity, indicating a high level of dispersion, obscuring a secondary narrow  $H\beta$  component more typical of other objects in our sample, and likely associated with star formation. When a single LOSVD parameter set was used to constrain these spectra, PPXF would typically converge on the broadened component in each line and ignore the much narrower feature.

For this single source, I include two synthetic stellar template sets so that PPXF could fit for two distinct LOSVD. For the second set of synthetic stellar templates, I exclude all forbidden transitions, including [OI], [OII], [OIII], [SII], and [NII]. These transitions require low-density environments that are not compatible with the heated, compacted regions surrounding AGN outflows. Differentiating between these two template sets in this manner gave PPXF a strong handle on disentangling the two sets of LOSVD measures and characterising the appropriate template weights for the Balmer series with narrow velocity components.

Another issue I observed when initially fitting the spectra of IRAS F01268–5436 was that the clear slope at the blue end caused a considerable issue with PPXF converging on a robust



solution, particularly when attempting to weigh the set of stellar reference templates optimally. This was particularly evident when attempting to include a reddening curve as a property to constrain, which was unable to capture the upward slope at all. This caused large model residuals for most of the spectra below  $\sim 4000 \text{ \AA}$ . To attempt to capture this shape, I generated a small set of linear templates which I also provided to PPXF. These synthetic templates, shown in Figure 4.13, are used only to help to attempt to capture the shape of the continuum at the blue end and are not particularly physically motivated. For this reason, I configured PPXF to ignore attempting to characterise the LOSVD measure for this template set. Initially, I explored expanding this template set to include power law like shapes below a break frequency and a flat shape above. I found that, ultimately, little difference was made to the residuals of the final model at the cost of increased computation time.

Figure 4.14 shows the result of the PPXF algorithm on the observed optical spectra of IRAS F01268–5436, including a second synthetic set of transitions which excluded the forbidden lines. In this case, there was little information that could be used by PPXF to constrain the age and metallicity of stars that contributed to the stellar continuum. As a result, the algorithm converged on templates that were both young and had small  $[M/H]$  ratios. Such templates have less emission at the bluer end and presumably were activated in an attempt to down-weight the shape of the power-law template included in the fit. I found this to be an acceptable trade-off, as the number one priority was to capture the nebular transitions associated with star formation, which this approach captured adequately.

I also show individual lines modelled by PPXF in Figure 4.15, where I only highlight the templates used to capture the contributions made to the components of the transitions made by regions of low velocity. The addition of a second synthetic set of templates exclusively for the forbidden lines and the linear templates to capture the upward continuum produced adequate fits for individual lines with minimal residuals.

Given the outputs of the PPXF modelling, I was able to calculate robustly constrained integrated line intensities. The integrated area of a one-dimensional Gaussian, or the flux,  $F$ , is

$$F = \sqrt{2\pi} \times A \times \sigma_{total}, \quad (4.6)$$

where  $A$  is the amplitude of a line, given by the maximum value of a template multiplied by the corresponding template weight provided by PPXF, and  $\sigma_{total}$  is the SD of the modelled Gaussian line. When modelling the LOSVD of the stellar emission lines, I limited the modelling

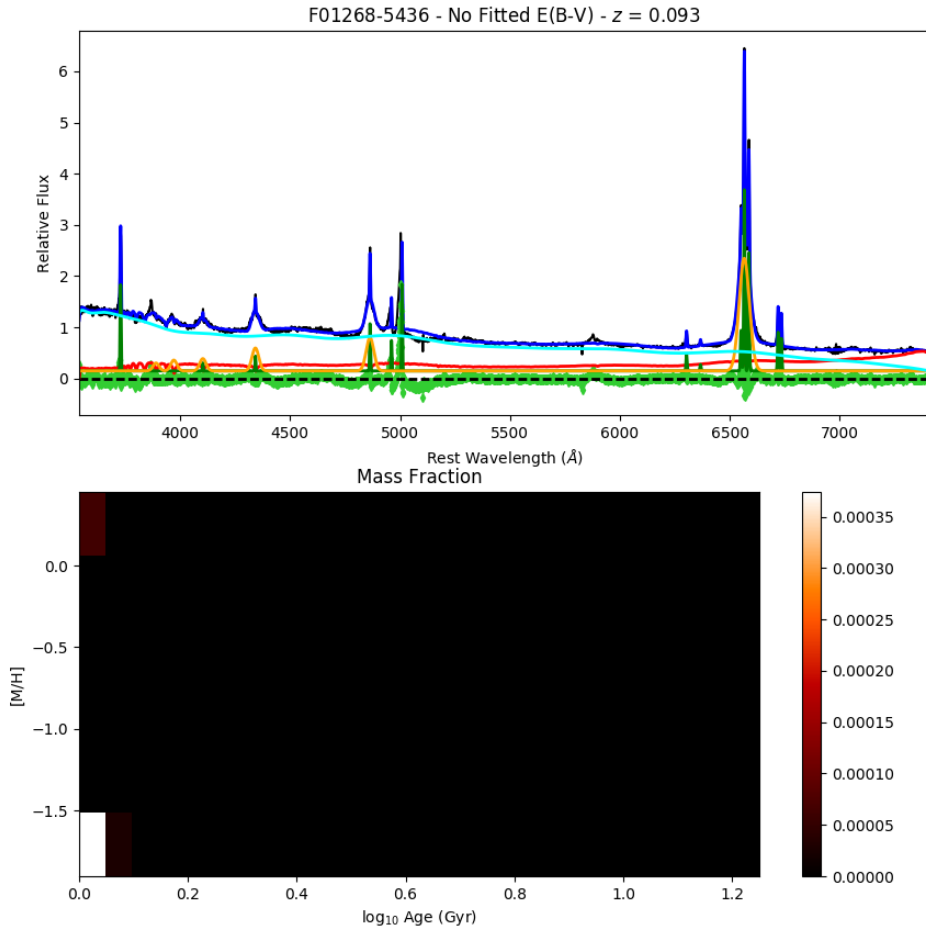


Figure 4.14: The spectra of IRAS F01268–5436 and the model spectra constrained by the PPXF algorithm. The black line in the top panel is the collapsed one-dimensional spectra obtained from my WiFeS observations. The stellar continuum that has been constrained using the MILES template library is shown in red. Generated templates of the stellar emission lines are shown in green. Residuals of the fit are shown around the dashed line in lime green. Two distinct synthetic transition templates have been included, where one excludes forbidden line transitions. The light blue line denotes the power-law template that was included in the fit to capture the slope at the bluer end of the spectra. The bottom panel shows the multiplicative terms of the MILES templates used that PPXF has constrained.

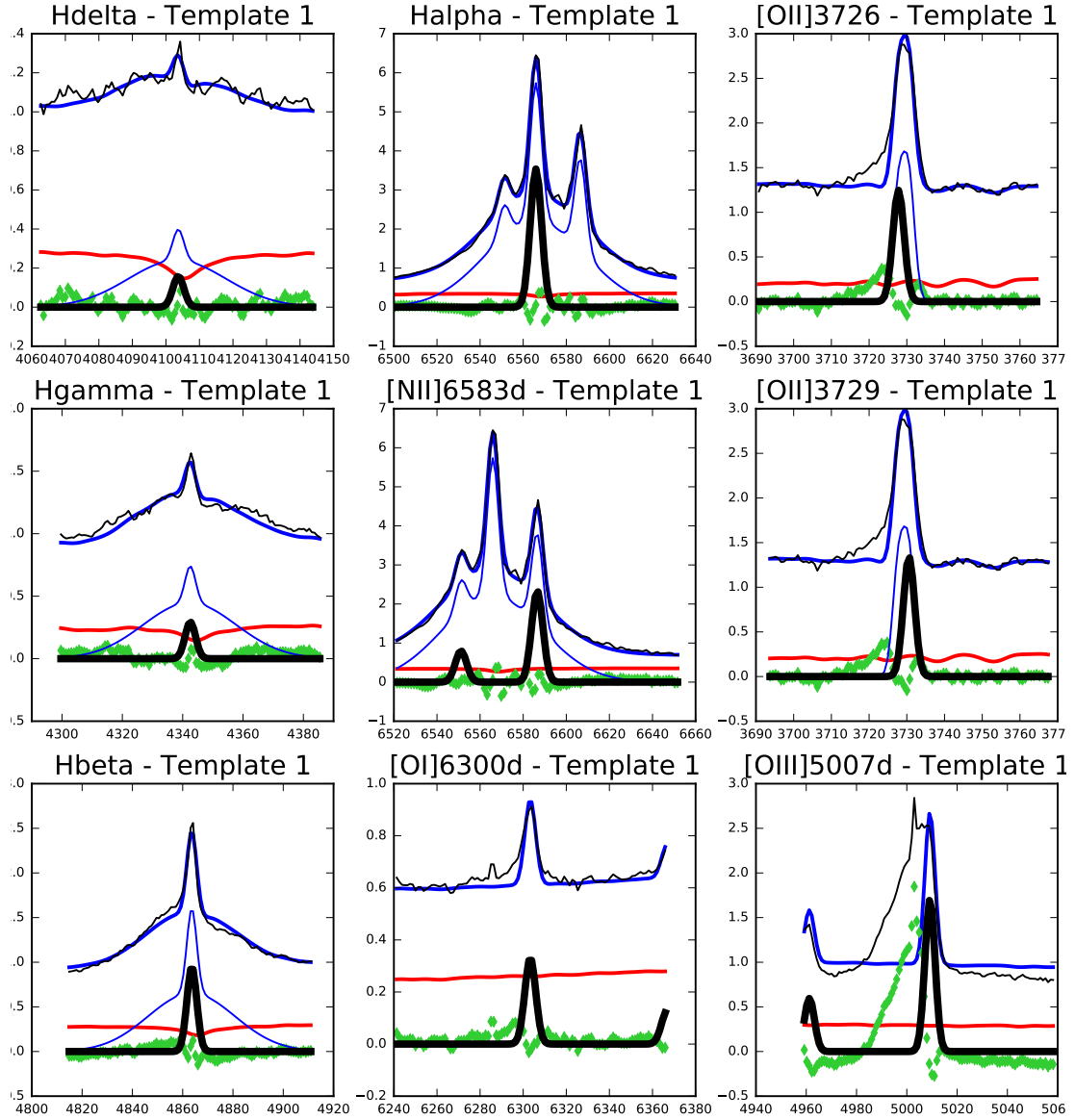


Figure 4.15: A zoomed version of the PPF constrained spectra of IRAS F01268—5436 is shown. The thin black line denotes the observed spectra, with the blue line being the modelled spectra. The red line is the stellar continuum described by the MILES stellar templates, with the thick black line being the generated spectra of each stellar emission line, where possible doublets have been encoded in a single template. Some lines rest upon a broad stellar absorption feature, which is described using the MILES templates. The thin blue line represents the sum total of the thick black line, and a secondary set of synthetic stellar templates included so that PPF could constrain a broadened LOSVD component.

to a simple Gaussian. Hence,  $\sigma_{total}$  is calculated as

$$\sigma_{total} = \sqrt{\sigma_{inst}^2 + \sigma_{kin}^2} \quad (4.7)$$

where  $\sigma_{inst}$  is the instrumental broadening ( $R \sim 3000$ ), and  $\sigma_{kin}$  is the broadening due to LOSVD effects. When modelled with PPXF, this is derived in units of km/s.  $\sigma_{inst}$  is encoded in the stellar line templates as they were generated and can be calculated at any arbitrary wavelength. When calculated in units of  $\text{\AA}$ , the instrumental broadening can be calculated in units of  $\text{\AA}$  following

$$\sigma_{inst} = \frac{\lambda}{2.355 \times 3000}. \quad (4.8)$$

$\sigma_{inst}$  needs to be calculated in units of  $\text{\AA}$  because the spectral pixels and therefore the flux amplitude are in units of  $\text{erg cm}^{-2} \text{s}^{-1} \text{\AA}^{-1}$ . The constant 2.355 is the ratio of Full Width Half Maximum (FWHM) to sigma of a Gaussian distribution, and 3000 is the WiFeS spectral resolution following  $R \sim 3000$ .

The  $\sigma_{kin}$  values outputted by PPXF can be converted from units of km/s to  $\text{\AA}$  as follows:

$$\left( \frac{\sigma_{kin}}{\text{\AA}} \right) = 2.355 \times \left( \frac{\sigma_{kin}}{\text{km/s}} \right) \times \left( \frac{\lambda_{line}}{c} \right), \quad (4.9)$$

where  $\lambda_{line}$  is the wavelength of the line of interest and  $c$  is the speed of light in km/s.

By default, PPXF does not return uncertainties associated with any of its constrained weights or LOSVD parameters. For weak spectra, this is problematic, especially when the Balmer decrement method (see below) is used to estimate and correct for dust attenuation. To characterise how well a parameter is constrained by PPXF, I performed Monte-Carlo simulations to obtain a probability distribution function for each parameter. For each source, I crafted 500 realisations of my data by adding random noise corresponding to the variance vector produced by the PYWIFES pipeline. Similar to the approach outlined in Chapter 3, I performed numerical expressions/evaluations on all realisations of my fitting outputs. Applying steps in this manner allows me to maintain parameter covariances and propagate errors into derived quantities. When quoting values, I supply the 50<sup>th</sup> percentile as the nominal value and take the 16<sup>th</sup> and 84<sup>th</sup> percentiles as the 1- $\sigma$  uncertainties.

#### 4.4.5 Dust attenuation correction

Stellar light can be absorbed or scattered by dust along the line of sight. Depending on the orientation and distribution of such dust, the observed stellar light could only be a fraction of

the actual intrinsic amount emitted by some object. A simple scaling correction factor is not appropriate because there is no guarantee on how dust is arranged. It can be as simple as a single intermediate wall of uniform density or as complex as a mixture of discrete clumps that surround some embedded emitting source.

For the H $\alpha$  line to be used as a *accurate* SFR tracer to calibrate the decomposed radio-continuum components, a dust correction has to be derived and applied to the observed H $\alpha$  integrated line flux. The spectral coverage of the WiFeS instrument allowed me to use the Balmer decrement method, which uses a ‘reference ratio’ to compute the degree of dust attenuation. Dust obscuration varies as a function of wavelength, where, with increasing wavelength, the effect of dust attenuation diminishes.

The Balmer decrement method of estimating dust obscuration exploits this fact. The H $\alpha$  and H $\beta$  stellar transition lines originate from the same emitting matter (i.e. clouds of ionised HII) and are separated by 1,701.47 Å. Using an assumed temperature of  $T = 10^4\text{K}$  and an electron density of  $n_e = 10^2 \text{ cm}^{-3}$  for Case B recombination, which are typical for SFG, the intrinsic theoretical ratio of H $\alpha$ /H $\beta$  is 2.86 (Osterbrock, 1989). Hence, any deviation in the observed ratio of H $\alpha$ /H $\beta$  from the canonical 2.86 value may be attributed to dust obscuration.

Within this framework, the intrinsic flux or luminosity,  $L_{int}$ , of a line can be recovered by following:

$$L_{int}(\lambda) = L_{obs}(\lambda) 10^{0.4A_\lambda} \quad (4.10)$$

$$= L_{obs}(\lambda) 10^{0.4k(\lambda)E(B-V)}, \quad (4.11)$$

where  $L_{int}$  is the total integrated flux or luminosity measurement of some *observed* line,  $k(\lambda)$  is an adopted reddening curve that describes how dust attenuation varies as a function of wavelength, and  $E(B - V)$  is the colour excess, represented as

$$E(B - V) = (B - V)_{obs} - (B - V)_{int} \quad (4.12)$$

and is a measure of the change in  $(B - V)$  because of dust attenuation. Considering H $\alpha$  and H $\beta$  specifically, this  $E(B - V)$  colour excess term can be written as:

$$E(B - V) = \frac{E(\text{H}\alpha - \text{H}\beta)}{k(\lambda_{\text{H}\alpha}) - k(\lambda_{\text{H}\beta})} \quad (4.13)$$

where  $k(\lambda_{\text{H}\alpha})$  and  $k(\lambda_{\text{H}\beta})$  is some adopted reddening curve evaluated at the H $\alpha$  and H $\beta$  wavelengths, respectively. For SFG, the expected ratio of the H $\alpha$  to H $\beta$  emission lines, which is

taken as 2.86, assumes a temperature  $T = 10^4\text{K}$ , and an electron density of  $n_e = 10^2 \text{ cm}^{-3}$  for Case B recombination, typical of SFG (Osterbrock, 1989). With these assumptions Equation 4.13 can be reduced to

$$E(B - V) = 1.97 \log_{10} \left[ \frac{(\text{H}\alpha/\text{H}\beta)_{\text{obs}}}{2.86} \right], \quad (4.14)$$

where  $(\text{H}\alpha/\text{H}\beta)_{\text{obs}}$  is the ratio between the observed  $\text{H}\alpha$  and  $\text{H}\beta$  emission lines. Referring to Equation 4.11, the total extinction,  $A_\lambda$ , in magnitudes at wavelength  $\lambda$  is

$$A_\lambda = k(\lambda) E(B - V), \quad (4.15)$$

and when evaluated at  $\text{H}\alpha$  using the Calzetti et al. (2000) reddening curve, it becomes

$$A_{\text{H}\alpha} = (3.33 \pm 0.80) \times E(B - V). \quad (4.16)$$

Note that this is the colour excess  $E(B - V)$  term and  $A_{\text{H}}$  is *independent* from the reddening curve that PPXF can fit to the stellar continuum. Once Equation 4.16 is derived for some modelled spectra, I use Equation 4.11 to correct the observed  $\text{H}\alpha$  measurement to recover an estimate of the intrinsic  $\text{H}\alpha$  luminosity.

Table 4.4 presents the total integrated  $\text{H}\alpha$  and  $\text{H}\beta$  line fluxes in units of  $\text{ergs/s/cm}^2$  of objects in my sample, the observed  $\text{H}\alpha/\text{H}\beta$  ratio, and the colour correction  $E(B - V)$  term that would then be used to estimate and correct for dust obscuration. This table also includes the intrinsic dust corrected  $\text{H}\alpha$  luminosities estimated using the observed  $\text{H}\alpha/\text{H}\beta$  ratio, and the corresponding SFR of each source. For each quantity, I have provided the  $1\sigma$  range of each quantity after running PPXF on 500 realisations of my spectra. Excluded from these calculations are the systematic uncertainties of the Calzetti et al. (2000) reddening curve, which is taken to be  $\pm 0.8$  in Equation 4.16. When calculating the intrinsic  $\text{H}\alpha$  luminosity, this systematic uncertainty could either decrease or increase the correction by a factor of 2 for each source.

Name <i>IRAS</i>	H $\alpha$ Flux 10 <sup>-14</sup> ergs/s/cm <sup>2</sup>	H $\beta$ Flux 10 <sup>-14</sup> ergs/s/cm <sup>2</sup>	L(H $\alpha_{\text{obs}}$ ) 10 <sup>39</sup> ergs/s	SFR $_{\text{H}\alpha}^{\text{obs}}$ M $_{\odot}$ yr <sup>-1</sup>	H $\alpha$ /H $\beta$	E(B-V)	L(H $\alpha_{\text{ints}}$ ) 10 <sup>39</sup> ergs/s	SFR $_{\text{H}\alpha}^{\text{ints}}$ M $_{\odot}$ yr <sup>-1</sup>
F00198-7926	25.6 <sup>+0.025</sup> <sub>-0.024</sub>	5.0 <sup>+0.031</sup> <sub>-0.032</sub>	330.9 <sup>+0.33</sup> <sub>-0.32</sub>	26.1 <sup>+0.03</sup> <sub>-0.02</sub>	5.1 <sup>+0.0</sup> <sub>-0.0</sub>	0.5 <sup>+0.005</sup> <sub>-0.005</sub>	1521 <sup>+24</sup> <sub>-24</sub>	120 <sup>+2</sup> <sub>-2</sub>
F00199-7426	5.5 <sup>+0.021</sup> <sub>-0.02</sub>	0.6 <sup>+0.023</sup> <sub>-0.019</sub>	127.8 <sup>+0.49</sup> <sub>-0.46</sub>	10.1 <sup>+0.04</sup> <sub>-0.04</sub>	9.2 <sup>+0.3</sup> <sub>-0.3</sub>	1 <sup>+0.03</sup> <sub>-0.03</sub>	2755 <sup>+253</sup> <sub>-247</sub>	218 <sup>+20</sup> <sub>-19</sub>
F01268-5436	19.3 <sup>+0.14</sup> <sub>-0.12</sub>	3.6 <sup>+0.04</sup> <sub>-0.037</sub>	417.1 <sup>+3</sup> <sub>-2.5</sub>	32.9 <sup>+0.2</sup> <sub>-0.2</sub>	5.3 <sup>+0.0</sup> <sub>-0.0</sub>	0.53 <sup>+0.006</sup> <sub>-0.006</sub>	2135 <sup>+50</sup> <sub>-43</sub>	169 <sup>+4</sup> <sub>-3</sub>
F01388-4618	9.6 <sup>+0.03</sup> <sub>-0.029</sub>	1.5 <sup>+0.027</sup> <sub>-0.03</sub>	195.0 <sup>+0.6</sup> <sub>-0.58</sub>	15.4 <sup>+0.05</sup> <sub>-0.05</sub>	6.7 <sup>+0.1</sup> <sub>-0.1</sub>	0.72 <sup>+0.02</sup> <sub>-0.02</sub>	1782 <sup>+103</sup> <sub>-81</sub>	141 <sup>+8</sup> <sub>-6</sub>
F01419-6826	7.2 <sup>+0.032</sup> <sub>-0.032</sub>	1.0 <sup>+0.029</sup> <sub>-0.031</sub>	101.3 <sup>+0.46</sup> <sub>-0.45</sub>	8.0 <sup>+0.04</sup> <sub>-0.04</sub>	6.9 <sup>+0.2</sup> <sub>-0.2</sub>	0.75 <sup>+0.03</sup> <sub>-0.02</sub>	1003 <sup>+83</sup> <sub>-71</sub>	79 <sup>+7</sup> <sub>-6</sub>
F02364-4751	3.1 <sup>+0.035</sup> <sub>-0.034</sub>	0.3 <sup>+0.043</sup> <sub>-0.048</sub>	74.4 <sup>+0.85</sup> <sub>-0.82</sub>	5.9 <sup>+0.07</sup> <sub>-0.06</sub>	10.7 <sup>+2.1</sup> <sub>-1.4</sub>	1.1 <sup>+0.2</sup> <sub>-0.1</sub>	2361 <sup>+1457</sup> <sub>-722</sub>	187 <sup>+115</sup> <sub>-57</sub>
F03068-5346	16.9 <sup>+0.048</sup> <sub>-0.044</sub>	3.9 <sup>+0.04</sup> <sub>-0.039</sub>	229.3 <sup>+0.65</sup> <sub>-0.6</sub>	18.1 <sup>+0.05</sup> <sub>-0.05</sub>	4.4 <sup>+0.0</sup> <sub>-0.0</sub>	0.37 <sup>+0.008</sup> <sub>-0.008</sub>	704 <sup>+19</sup> <sub>-18</sub>	56 <sup>+1</sup> <sub>-1</sub>
F03481-4012	15.5 <sup>+0.032</sup> <sub>-0.032</sub>	3.2 <sup>+0.028</sup> <sub>-0.033</sub>	383.0 <sup>+0.79</sup> <sub>-0.78</sub>	30.3 <sup>+0.06</sup> <sub>-0.06</sub>	4.9 <sup>+0.1</sup> <sub>-0.0</sub>	0.46 <sup>+0.009</sup> <sub>-0.008</sub>	1564 <sup>+43</sup> <sub>-36</sub>	124 <sup>+3</sup> <sub>-3</sub>
F04063-3236	14.1 <sup>+0.056</sup> <sub>-0.18</sub>	3.2 <sup>+0.046</sup> <sub>-0.11</sub>	438.4 <sup>+1.7</sup> <sub>-5.5</sub>	34.6 <sup>+0.1</sup> <sub>-0.4</sub>	4.4 <sup>+0.1</sup> <sub>-0.1</sub>	0.37 <sup>+0.02</sup> <sub>-0.01</sub>	1382 <sup>+67</sup> <sub>-46</sub>	109 <sup>+5</sup> <sub>-4</sub>
F06021-4509	0.9 <sup>+0.02</sup> <sub>-0.019</sub>	0.1 <sup>+0.018</sup> <sub>-0.023</sub>	65.9 <sup>+1.4</sup> <sub>-1.4</sub>	5.2 <sup>+0.1</sup> <sub>-0.1</sub>	12.1 <sup>+5.0</sup> <sub>-2.4</sub>	1.2 <sup>+0.3</sup> <sub>-0.2</sub>	2929 <sup>+4256</sup> <sub>-1299</sub>	231 <sup>+336</sup> <sub>-103</sub>
F06035-7102	21.5 <sup>+0.039</sup> <sub>-0.039</sub>	3.7 <sup>+0.038</sup> <sub>-0.041</sub>	329.6 <sup>+0.6</sup> <sub>-0.59</sub>	26.0 <sup>+0.05</sup> <sub>-0.05</sub>	5.8 <sup>+0.1</sup> <sub>-0.1</sub>	0.6 <sup>+0.01</sup> <sub>-0.009</sub>	2068 <sup>+59</sup> <sub>-56</sub>	163 <sup>+5</sup> <sub>-4</sub>
F06206-6315	4.8 <sup>+0.043</sup> <sub>-0.041</sub>	1.0 <sup>+0.041</sup> <sub>-0.042</sub>	101.8 <sup>+0.92</sup> <sub>-0.87</sub>	8.0 <sup>+0.07</sup> <sub>-0.07</sub>	4.9 <sup>+0.2</sup> <sub>-0.2</sub>	0.46 <sup>+0.04</sup> <sub>-0.03</sub>	424 <sup>+50</sup> <sub>-42</sub>	34 <sup>+4</sup> <sub>-3</sub>
F18582-5558	0.4 <sup>+0.02</sup> <sub>-0.021</sub>	0.0 <sup>+0.011</sup> <sub>-0</sub>	5.1 <sup>+0.27</sup> <sub>-0.28</sub>	0.4 <sup>+0.02</sup> <sub>-0.02</sub>	$\infty$	$\infty$	$\infty$	$\infty$
F20117-3249	7.7 <sup>+0.028</sup> <sub>-0.028</sub>	1.2 <sup>+0.035</sup> <sub>-0.033</sub>	176.6 <sup>+0.65</sup> <sub>-0.64</sub>	13.9 <sup>+0.05</sup> <sub>-0.05</sub>	6.6 <sup>+0.2</sup> <sub>-0.2</sub>	0.72 <sup>+0.02</sup> <sub>-0.02</sub>	1605 <sup>+118</sup> <sub>-120</sub>	127 <sup>+9</sup> <sub>-9</sub>
F20445-6218	3.5 <sup>+0.02</sup> <sub>-0.02</sub>	0.7 <sup>+0.028</sup> <sub>-0.025</sub>	102.2 <sup>+0.57</sup> <sub>-0.58</sub>	8.1 <sup>+0.05</sup> <sub>-0.05</sub>	5.1 <sup>+0.2</sup> <sub>-0.2</sub>	0.49 <sup>+0.03</sup> <sub>-0.03</sub>	457 <sup>+50</sup> <sub>-45</sub>	36 <sup>+4</sup> <sub>-4</sub>
F21178-6349	1.7 <sup>+0.023</sup> <sub>-0.022</sub>	0.1 <sup>+0.028</sup> <sub>-0.02</sub>	22.0 <sup>+0.3</sup> <sub>-0.29</sub>	1.7 <sup>+0.02</sup> <sub>-0.02</sub>	24.4 <sup>+10.5</sup> <sub>-6.9</sub>	1.8 <sup>+0.3</sup> <sub>-0.3</sub>	6077 <sup>+9416</sup> <sub>-3551</sub>	480 <sup>+744</sup> <sub>-281</sub>
F21292-4953	8.1 <sup>+0.024</sup> <sub>-0.53</sub>	1.1 <sup>+0.047</sup> <sub>-0.04</sub>	394.1 <sup>+1.2</sup> <sub>-26</sub>	31.1 <sup>+0.09</sup> <sub>-2</sub>	7.3 <sup>+0.3</sup> <sub>-0.6</sub>	0.8 <sup>+0.03</sup> <sub>-0.07</sub>	4632 <sup>+492</sup> <sub>-1222</sub>	366 <sup>+39</sup> <sub>-97</sub>
F21295-4634	5.9 <sup>+0.05</sup> <sub>-0.054</sub>	1.0 <sup>+0.066</sup> <sub>-0.059</sub>	75.9 <sup>+0.64</sup> <sub>-0.69</sub>	6.0 <sup>+0.05</sup> <sub>-0.05</sub>	5.8 <sup>+0.3</sup> <sub>-0.3</sub>	0.61 <sup>+0.05</sup> <sub>-0.05</sub>	486 <sup>+79</sup> <sub>-68</sub>	38 <sup>+6</sup> <sub>-5</sub>
F23389-6139	2.8 <sup>+0.03</sup> <sub>-0.033</sub>	0.3 <sup>+0.047</sup> <sub>-0.057</sub>	62.2 <sup>+0.67</sup> <sub>-0.74</sub>	4.9 <sup>+0.05</sup> <sub>-0.06</sub>	8.0 <sup>+1.5</sup> <sub>-0.9</sub>	0.88 <sup>+0.1</sup> <sub>-0.1</sub>	942 <sup>+551</sup> <sub>-270</sub>	74 <sup>+44</sup> <sub>-21</sub>

Table 4.4: An overview of the spectral characteristics of objects in my sample. I have included the observed integrated line fluxes of the H $\alpha$  and H $\beta$  emission lines (‘H $\alpha$  flux’ and ‘H $\beta$  flux’ columns, respectively) constrained by PPXF (without including the Calzetti et al. (2000) reddening curve), the observed H $\alpha$  luminosity, L(H $\alpha_{\text{obs}}$ ), the corresponding SFR estimate, SFR $_{\text{H}\alpha}^{\text{obs}}$ , the observed H $\alpha$ /H $\beta$  ratio and derived E(B-V) term, as well as dust corrected H $\alpha$  luminosities, L(H $\alpha_{\text{ints}}$ ), and SFR estimates, SFR $_{\text{H}\alpha}^{\text{ints}}$ . The H $\alpha$ /H $\beta$  are the *observed* ratios before a correction for dust attenuation has been applied. The star formation rates were estimated using Equation 1.6, where SFR (M $_{\odot}$  yr<sup>-1</sup>) = 7.9  $\times$  10<sup>-42</sup>L (H $\alpha$ ). I include the 1 $\sigma$  uncertainties for each item which were obtained after using PPXF on 500 realisations of each spectra.

#### 4.4.6 Reddening curve

Within a typical galaxy, star formation occurs in discrete clumps as opposed to being dispersed and intermixed throughout the entire system and its older stellar populations. Consequently, the degree of dust extinction of the nebular transitions, including the  $H\alpha$  and  $H\beta$  lines, is different from the extinction of the stellar continuum. The relationship between these two different measures is dependent on the possibly complex geometry of the dust and distribution of old and young stars, meaning that a simple numeric derivation is difficult.

Empirically, however, the colour excess term  $E(B - V)$  between these two measures has been observed and constrained. Calzetti (1997, 2013) observed a set of roughly 40 galaxies for which the  $E(B - V)$  term from the Balmer lines and stellar continuum were known and was found to be

$$E(B - V)_{\text{star}} = 0.44 \times E(B - V)_{\text{gas}}. \quad (4.17)$$

Equation 4.17 relates the colour correction  $E(B - V)$  term derived from the  $H\alpha/H\beta$  line ratio,  $E(B - V)_{\text{gas}}$ , to the  $E(B - V)$  term that is constrained using the stellar continuum,  $E(B - V)_{\text{star}}$ , of a galaxy. The  $E(B - V)_{\text{star}}$  term traces dust that is scattered throughout the entire galaxy, whereas  $E(B - V)_{\text{gas}}$  traces dust clumps that are in close proximity with the regions of star formation.

This is an empirically measured relation, and as highlighted by Calzetti et al. (2000), dust geometry in LIRGs could be complex and represent a scenario where it breaks down. Exploring the literature, I found that Babbedge et al. (2005) also suggest that the empirical value of 0.44 of gas to star extinction could be flatter for starburst galaxies. Their work explored whether photometric redshift codes could reliably constrain this quantity, and they found that their  $\chi^2$  minimisation methods preferred gas to star extinction values of  $0.25 \pm 0.2$ .

Objects in my sample are exceptionally powerful in terms of star formation, and because of their presumably complex dust geometry, I elected to constrain my own relation similar to Equation 4.17 with my own data for comparison. For each of the 500 simulated spectra, I performed the same PPXF modelling while using the stellar continuum to constrain the reddening curve shown in Equation 4.5. Figure 4.16 shows the comparison between the  $E(B - V)_{\text{gas}}$  and  $E(B - V)_{\text{star}}$  terms for each source in my sample. Errors represent the  $1\sigma$  interval produced by PPXF modelling of the 500 simulated spectra.

While constraining my own relation, I excluded points where either their  $E(B - V)$  terms were below a  $3\sigma$  significance level. Of the sources whose  $E(B - V)_{\text{star}}$  was constrained to be zero, none had a low significant  $E(B - V)_{\text{gas}}$ . To account for errors in both the dimensions, I drew



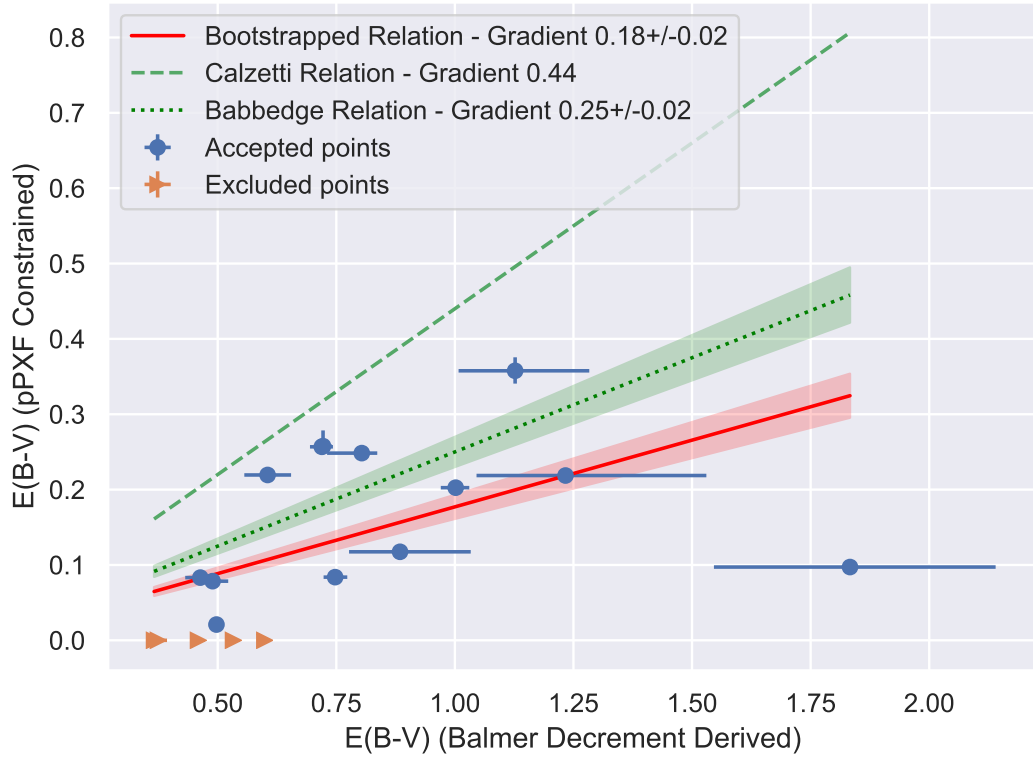


Figure 4.16: A comparison between  $E(B - V)_{\text{gas}}$  and  $E(B - V)_{\text{star}}$  for sources in my sample. I include the empirically measured relationship from Calzetti (1997, 2013), the relation recovered from photometric redshift codes presented by Babbedge et al. (2005), and our own relationship presented in Equation 4.18 constrained using measurements from accepted sources in this sample. The highlighted region represents the uncertainty of Babbedge et al. (2005) and Equation 4.18.

1000 realisations of my data randomly and performed non-weighted least-squares regression to each. I took the mean and SD of these 1000 fits as the best fit value and corresponding uncertainty, respectively. Using the twelve sources passing these criteria, I obtained the following relationship:

$$E(B - V)_{\text{star}} = 0.18 (\pm 0.02) \times E(B - V)_{\text{gas}}. \quad (4.18)$$

The results of this comparison are shown in Figure 4.16, including the sources from this dataset, the Calzetti (1997) and Babbedge et al. (2005) extinction relations, and the extinction relation constrained using the twelve accepted objects which was presented as Equation 4.18.

I found that the gradients between the two models are clearly distinct from one another, even after considering appropriate uncertainties. Of the twelve objects of my sample included as measurements when constraining Equation 4.18, only four appear to be consistent with the Calzetti model shown in Equation 4.17. Rather, the model constrained using my data agrees remarkably well with the relation obtained by Babbedge et al. (2005) and their work with

photometric redshift codes.

This simply implies that the starburst galaxies are remarkably distinct from the normal galaxies we commonly see in the local Universe. Their complex geometries, which often exhibit evidence of merger fuelled star formation, may not be consistent with relations, specially empirically measured ones, that are used for local type objects.

Further investigating this aspect of work would require a larger set of IFU spectroscopic data of galaxies with exceptionally high rates of star formation so as to expand the sample and constrain a more reliable relation. Incorporating an additional set of more typical galaxies will also allow this  $E(B - V)$  comparison to be explored across additional parameter dimensions. Although this would only be empirical, it would allow a more reliable extrapolation and estimation of dust correction methods for low signal-to-noise spectra of high redshift objects.

## 4.5 Three Dimensional Spectra

The IFU on WiFeS provides a field of view of  $38'' \times 25''$ , potentially allowing for the intrinsic structure to be resolved. However, this spatial information was lost when the spectral data cubes were collapsed into a one-dimensional spectrum to maximise the SNR of the stellar emission lines.

To assess if such structures were recoverable in the data cubes, the PPXF method was applied on each spaxel in the entire dataset. With these modelled results, there were 1900 constrained spectra per source, which allowed for the spatial distribution of spectral features to be investigated. The limiting factor in this analysis is the signal to noise of the individual spaxels and the corresponding modelled spectra. Collapsing the data cubes into a one-dimensional spectrum to maximise the SNR was a fundamental component that was incorporated into the time requirements of the WiFeS telescope proposal. Characterising the integrated line flux uncertainties from the constrained PPXF results requires many bootstrapping simulations to be performed. With available computing hardware, this procedure, which has to be carried out on a per spaxel basis, was not possible for this work.

### 4.5.1 IRAS F00198–7926

Obtaining an accurate SFR using the  $H\alpha$  feature first requires the effects of dust extinction to be estimated and corrected. With the spectral coverage of WiFeS, the Balmer decrement was used for this purpose. The success of this approach depends heavily on the SNR of the  $H\alpha$  and  $H\beta$  lines, which are carried through to the colour excess  $E(B-V)$  following Equation 4.14. This method is particularly susceptible to overcorrection of the observed  $H\alpha$  luminosity if the  $H\beta$

line is poorly detected. Examining the set of constrained  $E(B-V)$  measures in Table 4.4 reveals that IRAS F00198–7926 had the most robustly characterised term.

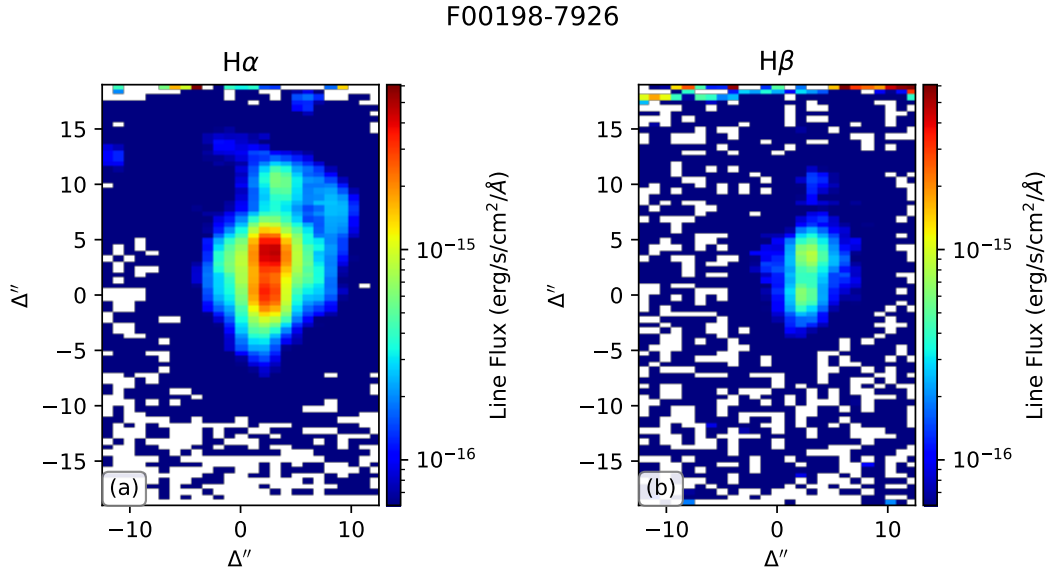


Figure 4.17: The total integrated line fluxes modelled by PPXF of the  $H\alpha$  (left) and  $H\beta$  (right) emission lines in the galaxy IRAS F00198–7923 constrained against each individual spaxel in the data cubes.

Shown in Figure 4.17 are the integrated line intensities of  $H\alpha$  and  $H\beta$  across the observed surface of IRAS F00198–7926. These images were created after running PPXF on each spaxel. In both images, both lines can be clearly detected. The  $H\alpha$  image, in particular, shows two distinct ‘clumps’ of peaking emission. These are also seen in the  $H\beta$  image, although the significance is not the same. Both images also show emission past the main core of the system. The  $H\alpha$  line, in particular, extends far further than the  $H\beta$  line. Without performing simulations to estimate corresponding uncertainties, it is difficult to infer if this is an effect of dust obscuration or simply a weak line that is closer and harder to distinguish from the stellar continuum.

Using the integrated  $H\alpha$  and  $H\beta$  lines fluxes, an estimate of the intrinsic  $H\alpha$  luminosity across the resolved galaxy can be estimated using the Balmer decrement. Shown in Figure 4.18 is the  $H\alpha/H\beta$  ratio across the surface of IRAS F00198–7926, with values clipped between 2.86 and 20. This range was selected in a qualitative manner to attempt to isolate and remove spaxels without real emission and present a more meaningful scale of colour intensity. Pixels comprising noise can produce extreme outliers, making the colour transform meaningless and difficult to interpret. Applying this criterion onto the IRAS F00198–7926  $H\alpha/H\beta$  map masked out 1215 pixels of the available 1900.

A higher  $H\alpha/H\beta$  ratio can be used to infer a larger dust component in that region. At the centre of IRAS F00198–7926, there is a clear dust clump with a mean value of  $\sim 14$ . Extending

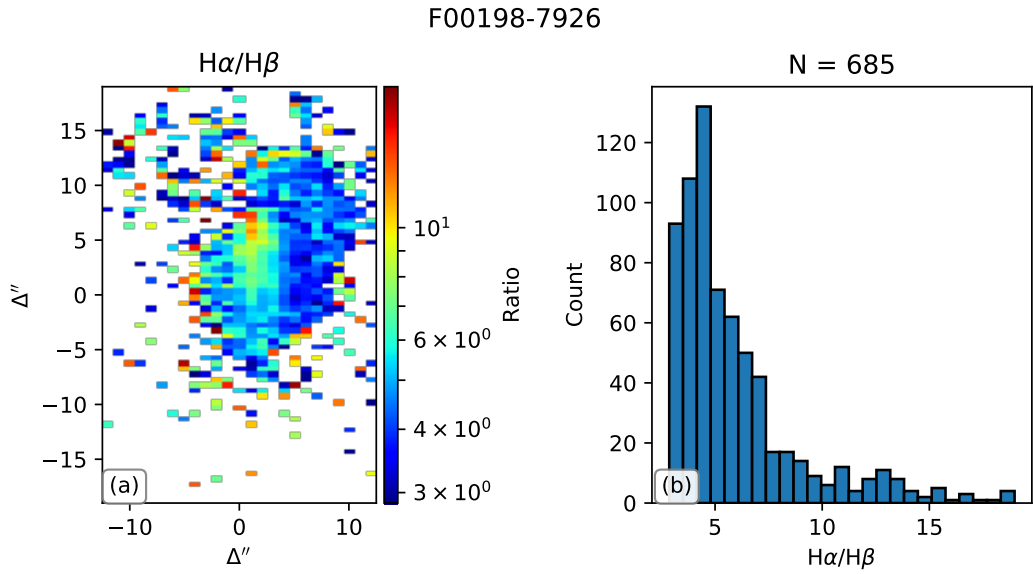


Figure 4.18: (a) The ratio of the integrated fluxes of the  $H\alpha/H\beta$  emission lines, as presented in Figure 4.17, of IRAS F00198–7926 . Pixels with values below 2.86 or above 20.0 are masked out. (b) The distribution of valid pixels in panel (a).

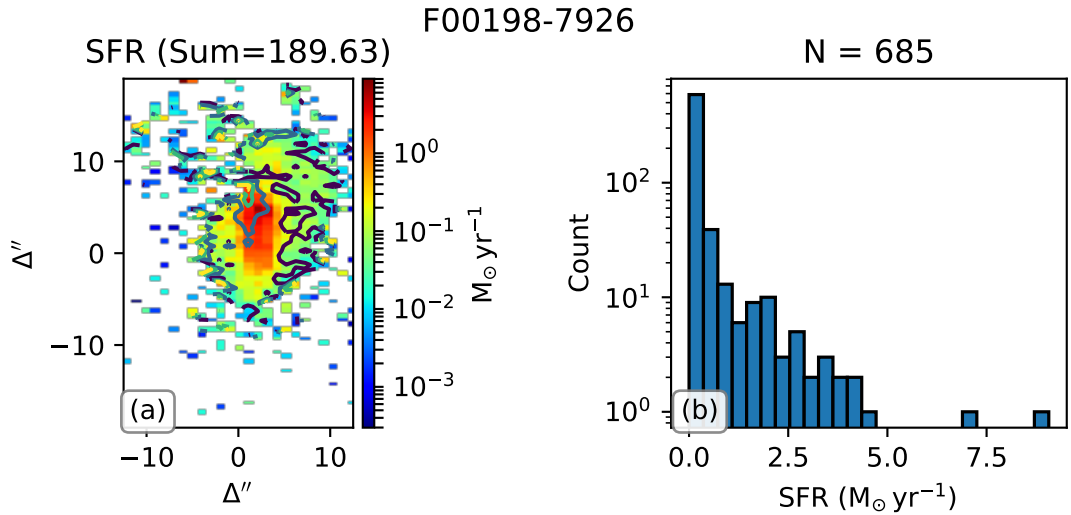


Figure 4.19: (a) A resolved map of IRAS F00198–7926 showing SFR in colour intensity across the galaxy. Pixels whose corresponding  $H\alpha/H\beta$  ratios are outside the range of 2.86 to 20.0 have been masked. Contour overlays show the  $H\alpha/H\beta$  ratio at discrete values of 4, 7, 10, and 13. (b) A distribution of the per pixel SFR value of valid pixels from panel (a).

in a top-down direction from the peak  $H\alpha/H\beta$  pixel is a ‘disc like’ structure. The remainder of the surface of the system shows pixels with values of  $\sim 4$ , indicating only a small amount of dust obscuration. The right panel of Figure 4.18 is a histogram highlighting the distribution of  $H\alpha/H\beta$  ratios in unclipped pixels. This distribution follows a roughly log-normal distribution peaking at  $\sim 4$ .

Using the resolved  $H\alpha/H\beta$  (Figure 4.18a) and integrated  $H\alpha$  line flux (Figure 4.17), the intrinsic  $H\alpha$  luminosity was estimated following Equation 4.11 and its related terms. All pixels were assumed to be at a redshift of 0.0728. From this estimated  $H\alpha$  luminosity, a SFR per pixel was then derived using Equation 5.1. The SFR derived across the surface of IRAS F00198–7923 is shown in Figure 4.19a. Accompanying this map in Figure 4.19b is the distribution of valid SFR pixels.

Located at the centre of IRAS F00198–7926 is a luminous clump with average SFR measures of  $\sim 4 M_{\odot} \text{yr}^{-1}$ . Extending outwards is disc of formation with a much lower SFR measure. Regions with higher SFRs are broadly consistent with regions of higher dust obscuration. The central clump of emitting matter with an  $\text{SFR} > 1 M_{\odot} \text{yr}^{-1}$  does extend beyond the  $H\alpha/H\beta$  contour corresponding to a ratio of 13 by approximately  $4''$ . At a redshift of 0.0728, this corresponds to a physical size of  $\sim 5.4 \text{kpc}$ , assuming the cosmology of Komatsu et al. (2009). The corresponding pixel distribution of SFR shown in Figure 4.19 indicates that there are relatively few pixels whose SFRs are above a rate of  $1 M_{\odot} \text{yr}^{-1}$ .

Much deeper analysis on the significance of these measurements would be dubious without first characterising the parameter uncertainties of PPXF modelling. Attempting to correct for dust obscuration using the Balmer decrement relies critically on the significance of the  $H\beta$  line. An underestimated measurement of the integrated line flux produces an overcorrected  $H\alpha$  luminosity, and subsequently, an overestimated SFR. A potential scenario that cannot be ignored is that the luminous region with an  $\text{SFR} > 1 M_{\odot} \text{yr}^{-1}$  could correspond to a region where the  $H\beta$  is not characterised well and underestimated during modelling. This would produce and overcorrect the  $H\alpha$  luminosity when correcting with the Balmer decrement method. Understanding the uncertainties attached to each spaxel and how they propagate through the PPXF modelling steps is a critical component to interpret the resolved optical spectroscopy correct physically.

This uncertainty analysis is limited by the computational requirements of the bootstrapping procedures that have to be performed with PPXF. As a compromise between preserving spatial information and feasibly running the bootstrapping analysis, spaxels were binned together in a  $4 \times 4$  arrangement, reducing the number of spaxels to model by a factor of 16. A total of 30 realisations of each binned spaxel were modelled with PPXF. Figure 4.20 shows the constrained

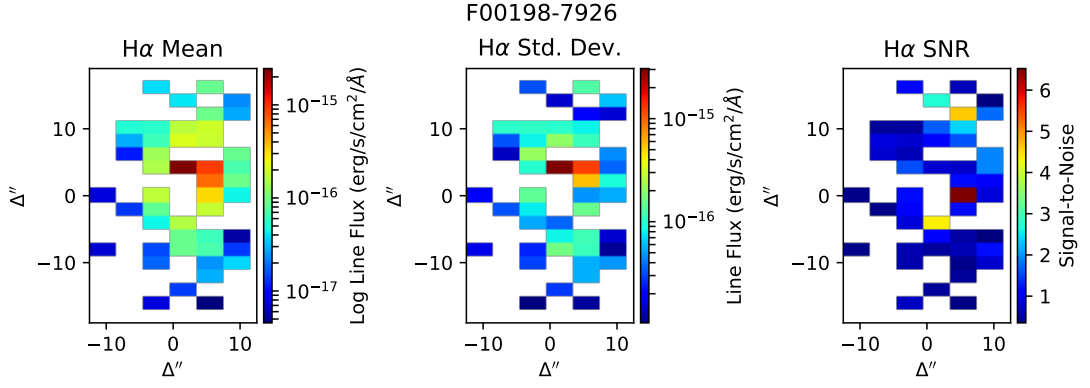


Figure 4.20: The  $H\alpha$  integrated line flux of IRAS F00198–7926 constrained by PPXF after performing 30 bootstrap trials. Pixels that had fewer than 10 successful constrained measurements (e.g. either no line was constrained or their integrated line flux was not a finite number) were masked out in all panels.

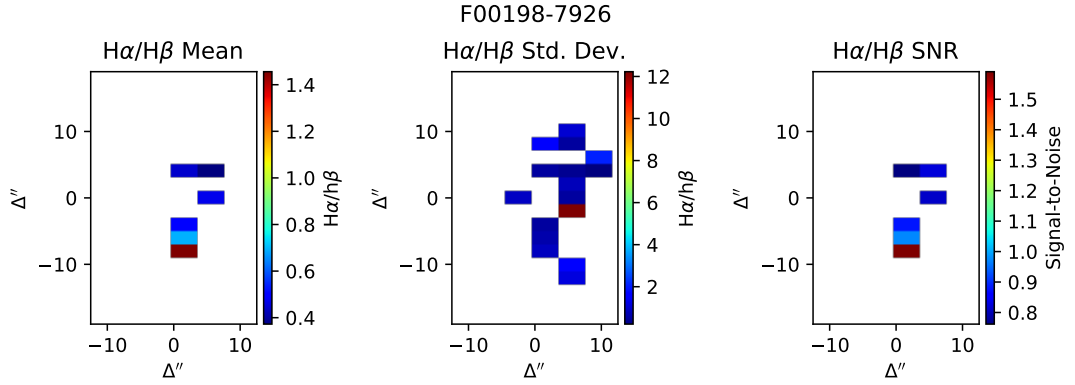


Figure 4.21: The resolved  $H\alpha/H\beta$  ratio across the surface of IRAS F00198–7926 constrained after performing 30 bootstrap trials. Many pixels are masked as there were insufficient statistics from trials with meaningful (i.e. non-zero) results.

$H\alpha$  integrated line flux across the surface of IRAS F00198–7926.

The results shown in Figure 4.20 denote that the  $H\alpha$  line is only marginally detected across the surface of IRAS F00198–7926, with there being relatively few pixels above a SNR of three. Many pixels were excluded for these panels as many of their corresponding generated PPXF trials did not return a meaningfully integrated line flux. There were similar results when inspecting the  $H\beta$  line from this modelling. Because of the very low significance of the modelled lines across the bootstrapped samples, the  $H\alpha/H\beta$  ratio was not reliably constrained, as shown in Figure 4.21. These results were consistent across each of the sources in the sample.

#### 4.5.2 IRAS F02364–4751 - A weak source

To illustrate the importance of characterising the spectral lines correctly when intending to use the Balmer decrement to correct for dust extinction, a similar analysis was performed for IRAS F02364–4751. Its resolved  $H\alpha$  and  $H\beta$  integrated line fluxes are shown in Figure 4.22.

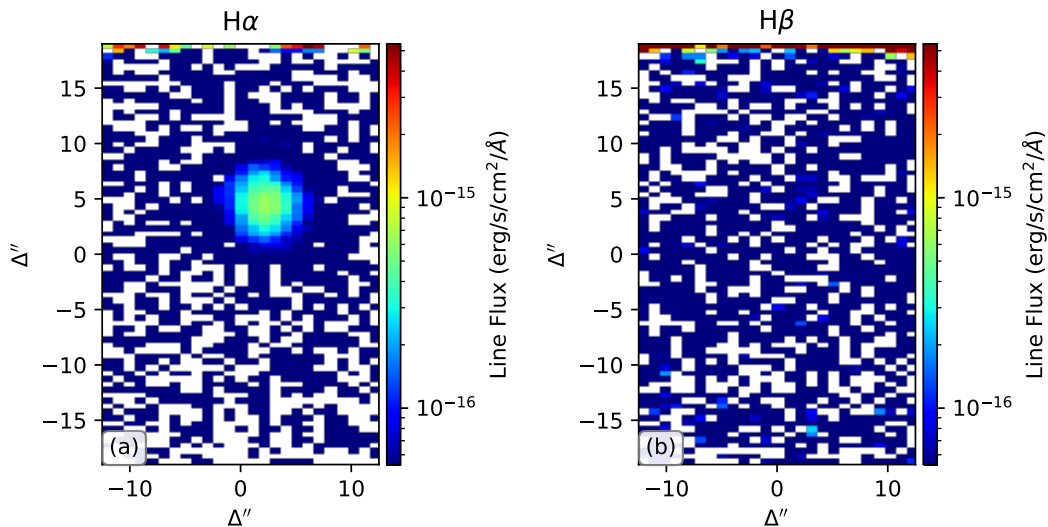


Figure 4.22: The integrated line fluxes of  $H\alpha$  and  $H\beta$  modelled by applying PPXF on individual spaxels of the IRAS F02364–4751 data cubes.

In the  $H\alpha$  panel of Figure 4.22, a strong  $H\alpha$  component, which is upwards of three orders of magnitude brighter than the immediate surrounding area, can be seen. In the corresponding area of the  $H\beta$  map, there is no detectable component.

The difficulty in this scenario is the application of the Balmer decrement to estimate the intrinsic  $H\alpha$  luminosity. Following Equation 4.14, the colour excess term  $E(B-V)$  may be overestimated if the  $H\beta$  line flux is underestimated in the model. Being able to quantify the certainty of the line is critical for managing this effect as spaxels with a poorly detected line can be down-weighted or flagged.

To demonstrate this effect, Figure 4.23a shows the distribution of the  $H\alpha/H\beta$  ratio using the integrated line fluxes taken directly from Figure 4.22. Within the region containing the luminous  $H\alpha$ , now, there are pixels with ratios in excess of 100. Referring to the accompanying histogram (Figure 4.23b), there are a number of extreme outlying pixels, with the highest being  $\sim 920$ . If a clipping range between 2.86 to 20 was applied, in line with Figure 4.18, then there would be 161 pixels remaining.

Using these colour excess measures, the SFR across the surface of IRAS F02364–4751 was estimated. Presented as Figure 4.24a, there is relatively little structure in the resolved SFR map. Note that pixels whose corresponding  $H\alpha/H\beta$  ratios were outside the range of 2.85 to 20 are masked. The majority ( $\sim 90\%$ ) of the un-masked 161 pixels have SFR values much less than one. Integrating this SFR map gives a value of  $127.74 M_{\odot} \text{ yr}^{-1}$ , the bulk of which is contributed by eleven pixels (Figure 4.24b). These pixels also correspond to the most obscured  $H\alpha/H\beta$  ratios that remained after masking.

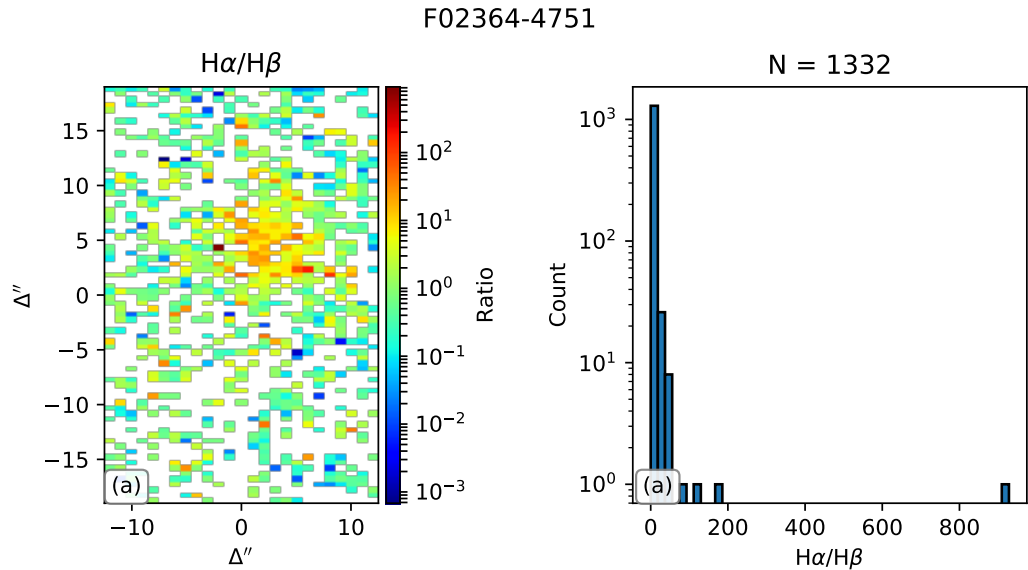


Figure 4.23: The  $H\alpha/H\beta$  ratio across IRAS F02364–4751. Pixels without real values, as is the case when the  $H\beta$  integrated line flux is zero, have been masked. For emphasis, no limiting range has been applied.

Additional figures from the resolved optical spectroscopy for all sources in the LIRGs sample may be found throughout Appendix B.

Whether this is a real, physical effect or an artefact of the modelling is difficult to distinguish. It is certainly possible that this object is heavily embedded in a dusty region, thereby making it appear that no  $H\beta$  emission exists. There may be regions whose optical depth is so high that both the  $H\alpha$  and  $H\beta$  lines are completely obscured, thereby making any attempt to dust correct the observed spectrum incomplete. Inspecting the corresponding uncertainties may be helpful to discern if this was the case or if the poor signal is the main issue. Understanding this behaviour and the spatial distribution of SFR for all LIRGs studied as part of this dissertation would be a critical tool to understand the high order curvature components modelled in their radio continuum. Acquiring IFU data of the near-infrared  $\text{Pa}\alpha$  line, which is less affected by dust obscuration, would be the ideal method to make this determination.

## 4.6 Conclusions

This Chapter describes the optical spectroscopic data obtained on the ANU 2.3 m WiFeS instrument and its data reduction process. The ultimate aim of these data was to acquire strong detections of the Balmer emission lines which can be used to correct for dust obscuration effects and obtain a measure of SFR. As  $H\alpha$  emission is produced by the same ionised clouds of matter as free-free emission, it should be a reliable tool to assess how SFR may manifest in the radio



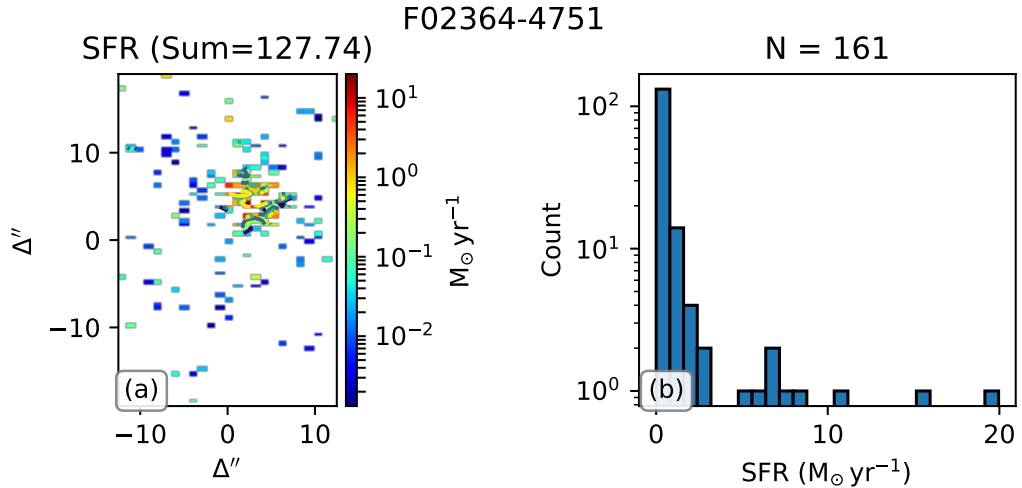


Figure 4.24: The SFR measure across IRAS F02364–475 after estimating and correcting for the effects of dust obscuration.

continuum.

Using the B3000 and R3000 gratings on WiFeS, the optical spectra covering 3000 to 9000 Å of the 19 objects were extracted at a reasonable spectral resolution of  $R \sim 3000$ . This data were reduced using the PYTHON based PYWIFES automated reduction pipeline. Using this pipeline allowed for a comprehensive and repeatable approach to the data reduction process. Issues related to the extraction of the standard star spectrum were identified after initial analysis of the modelled optical spectra and were subsequently corrected with patches to the PYWIFES codebase.

The Balmer decrement method to correct for dust obscuration was applied to recover an estimate of the total intrinsic  $H\alpha$  luminosity. It may still, however, be insufficient for especially obscured regions, where the optical depth ( $\tau_{H\alpha} < 1$ ) may prevent accurate measurement of the total intrinsic  $H\alpha$  luminosity to be recovered.

Colour excess terms derived by PPXF characterising dust extinction effects from local regions to star forming regions and globally across a galaxy were also compared with one another. These two measures are produced by different distributions of dust. Empirically observed relations have been presented in the literature, most notably by Calzetti et al. (2000), who measured the relationship of  $E(B - V)_{\text{stellar}} = 0.44 \times E(B - V)_{\text{gas}}$ . Fitting a similar relationship, a much flatter relation of  $0.18 \pm 0.02$  was constrained. Although the sample size and range of corresponding  $E(B-V)$  measurements are smaller, which increases the difficulty in fitting a reliable and stable relationship, there are arguments in the literature of similar constraints (Babbedge et al., 2005).

An initial investigation of the resolved properties of integrated line intensities,  $H\alpha/H\beta$  ratios,

and SFR was also performed using the individual spaxels within each datacube. The properties of IRAS F00198–7926 suggest that there is a luminous central clump of emission with a higher SFR than the outer, extended region. This interpretation relies critically on the accuracy of the Balmer decrement method to correct for dust obscuration. A similar analysis of IRAS F02364–4751 further highlights the need to properly understand dust obscuration, which relies on the  $H\beta$  emission line for success.

To understand the signal-to-noise profiles of these spatially resolved data, spaxels were binned in a  $4 \times 4$  arrangement. This was a compromise between maintaining spatial information while being able to perform the computationally expensive bootstrapping trials that PPXF requires for error analysis. I found that for many binned spaxels, there was an insufficient signal to reliably constrain a measurable signal of both the  $H\alpha$  and  $H\beta$  lines, thereby making the subsequent dust correction infeasible.

## Chapter 5

# Relating the Radio Continuum to other Star Formation Indicators

### 5.1 Motivation

One of the fundamental goals of the SKA and its pathfinder projects is to characterise the SFH of the Universe. Existing optical tracers of SFR that probe the earliest epochs of the Universe are hampered by an unknown amount of dust obscuration. Radio continuum emission, being impervious to this, is the key to understanding SFR in the distant past at redshifts above two, where optical measures begin to break down. At present, a limitation that we face is the small number of statistics when dealing with radio data in this space and we are unable to constrain the shape of the SFH robustly. Once SKA and its pathfinders begin to produce surveys probing large volumes of the Universe, we will instead face limitations of our understanding of the physics that drive the radio continuum. Knowing how reliable radio-based measures of SFR are will be a critical component of unravelling the SFH of the Universe.

This thesis explores the radio continuum emission of luminous and ultra-luminous infrared galaxies. These objects were specifically targeted because of their exceptionally high SFRs, which are thought to be more similar to the SFR of SFGs at higher redshifts and are expected to represent a large portion of objects to be observed with the next generation of radio surveys. For the 19 LIRGs whose radio continuum were studied in Chapter 3, optical spectroscopic IFU data using the WiFeS telescope have been acquired. These data capture the  $H\alpha$  and  $H\beta$  transitions which trace the same emitting matter that produces the thermal free-free component in the radio continuum. The reduction and modelling of these optical spectroscopic data are described throughout Chapter 4. In this Chapter, I draw conclusions from these modelled components and attempt to identify meaningful SFR indicators.

Being able to compare various indicators of SFR against the decomposed radio components would be an initial step towards understanding and calibrating radio-based SFR tracers compatible with the high redshift Universe. With increasing redshifts, a larger fraction of the observed radio continuum becomes free-free thermal emission not only because of the shifting of the high frequency to longer wavelengths but also because of the suppression of synchrotron emission from inverse-Compton losses. These effects are negligible in the local Universe but are increasingly important to understand at higher redshifts.

Although the atomic physics that drive the manifestations of SFR in the optical spectroscopy are understood well, the presence of dust complicates its use. Before these tracers can be used, the effects of dust obscuration have first to be estimated and accounted for. The Balmer decrement method was used to correct these dust obscuration effects. This approach uses the H $\alpha$  and H $\beta$  spectral features themselves as a way to estimate the obscuring dust.

For reference to the reader, I have outlined the SFR indicators described in Chapter 1 below.

SFRs based on dust corrected H $\alpha$  luminosities were calculated using Equation 2 of Kennicutt (1998), where

$$\text{SFR} (M_{\odot} \text{ yr}^{-1}) = 7.9 \times 10^{-42} L(\text{H}\alpha) (\text{ergs s}^{-1}), \quad (5.1)$$

and is calibrated against a Salpeter (1955) IMF.

For comparison, I have also produced a *composite* SFR measure. A composite SFR is a technique that is new in the literature but appears to be fairly robust. These composite SFRs are based on a simple energy balance model. The purpose of the Balmer decrement correction is to estimate the amount of H $\alpha$  flux that has been absorbed or scattered by dust. This attenuation of starlight is the same process that heats dust to produce infrared emission (Kennicutt et al., 2009). This simple scenario translates to

$$L(\text{H})_{\text{corr}} = L(\text{H}\alpha)_{\text{obs}} + a_{\lambda} L(\text{IR}), \quad (5.2)$$

where  $L(\text{H}\alpha)_{\text{corr}}$  is the intrinsic, unobscured H $\alpha$  luminosity,  $L(\text{H}\alpha)_{\text{obs}}$  is the observed, uncorrected H $\alpha$  luminosity,  $L(\text{IR})$  is some observed bolometric infrared luminosity, and  $a_{\lambda}$  is a scaling factor allowing for the linear combination of the two.

Using the supplied calibrations from Kennicutt et al. (2009), a composite SFR was applied using the following:

$$\text{SFR} (M_{\odot} \text{ yr}^{-1}) = 7.9 \times 10^{-42} [L(\text{H}\alpha)_{\text{obs}} + 0.0024L(\text{TIR})], \quad (5.3)$$

where  $L(\text{TIR})$  is the bolometric luminosity of 8 to 1000  $\mu\text{m}$  derived by Wang et al. (2014)

and the set of best fitting IR templates. Both  $L(\text{H}\alpha)_{\text{obs}}$  and  $L(\text{TIR})$  are in units of  $\text{ergs s}^{-1}$ . Kennicutt et al. (2009) calibrated their composite SFRs against both Salpeter (1955) and Kroupa (2001) IMFs, with Equation 5.3 being calibrated against the former.

I also calculated an SFR based on the total infrared luminosity from Kennicutt (1998) of the form

$$\text{SFR} (\text{M}_{\odot} \text{ yr}^{-1}) = 4.5 \times 10^{-44} L(\text{TIR}) (\text{ergs s}^{-1}), \quad (5.4)$$

which has been calibrated against the Salpeter IMF. The bolometric luminosity  $L(\text{TIR})$  covers 8 to 1000  $\mu\text{m}$ . For the LIRGs sample studied in this thesis, the total infrared luminosity was derived by Wang et al. (2014) and their broadband infrared template fitting codes for each source.

As part of the initial selection criteria for the secondary LIRG sample of objects studied in Chapters 3 and 4, a 1.4 GHz measurement was estimated assuming a M82 radio-continuum spectrum (Condon, 1992) and the SUMSS 843 MHz flux density measurement. As an additional check, this scaled 1.4 GHz luminosity was used to estimate an SFR using the from Yun et al. (2001),

$$\text{SFR} (\text{M}_{\odot} \text{ yr}^{-1}) = 5.9 \times 10^{-22} L_{1.4 \text{ GHz}} (\text{W Hz}^{-1}). \quad (5.5)$$

Yun et al. (2001) bootstrapped the 1.4 GHz SFR against the total infrared SFR from Kennicutt (1998), calibrating it against the Salpeter IMF. The SUMSS measurements were purposely used instead of the 1.4 GHz measurements presented throughout Chapter 3 for two reasons, primarily because they were an additional independent estimate of the SFR. Subsequent to this a more thorough comparison is made between the dust corrected  $\text{H}\alpha$  luminosities and the decomposed radio continuum products in § 5.2.1.

For completeness, I have also considered the SFR calculated by Wang et al. (2014), which is where this sample of sources were selected from. They obtained their SFRs using conversions devised by Rowan-Robinson et al. (1997) and Rowan-Robinson (2001), calibrated against the Salpeter IMF. Wang et al. (2014) calculated SFR following

$$\text{SFR} (\text{M}_{\odot} \text{ yr}^{-1}) = 2.2\epsilon^{-1} 10^{-10} L_{60 \mu\text{m}} (\text{L}_{\odot}) \quad (5.6)$$

where  $\epsilon$  represents the fraction of UV light absorbed by dust, which is taken to be 2/3, and  $L_{60 \mu\text{m}}$  is the 60  $\mu\text{m}$  luminosity taken from their broadband IR fitting.

## 5.2 Initial H $\alpha$ SFR comparisons

The calculated H $\alpha$  luminosities described in the previous Chapter have some degree of uncertainty attached to them. For one, a number of issues were found in the automated PYWIFES pipeline that related to the derivation and application of an absolute flux scale applied to scientific data (Section B.5). By examining the literature, I could locate the H $\alpha$  measurements of IRAS F06035–7102 and IRAS F06206–6315 from Rodríguez-Zaurín et al. (2011) using the Visible Multi-Object Spectrograph (VIMOS) IFU instrument on the Very Large Telescope. Comparing their dust corrected H $\alpha$  fluxes, reported as  $9.98 \times 10^{43}$  erg/s/cm<sup>2</sup> and  $1.06 \times 10^{43}$  erg/s/cm<sup>2</sup> for IRAS F06035–7102 and IRAS F06206–6315, respectively, with those described in Chapter 4 showed that they were consistent within error .

For the remainder of my sample, there were no available measurements that could be used to verify the application of a correct absolute flux scale. As a secondary check, the SFRs of the dust corrected H $\alpha$  luminosities were compared against other multi-wavelength indicators. A consistent result from these comparisons suggests that the WiFeS datacubes and the extracted optical spectrum are calibrated well.

Using each of the SFR measures outlined in Equations 5.1 to 5.6, I examined the amount of correlation among each pair of measures, which is presented as Figure 5.1. To assess the quality of the correlation between each combination, the results of an unweighted linear least-squares fit and sample Pearson correlation coefficient were obtained. This Pearson coefficient test assesses the strength and direction of a linear relation and is calculated as

$$r = \frac{\sum_{i=1}^n (x_i - \bar{x})(y_i - \bar{y})}{\sqrt{\sum_{i=1}^n (x_i - \bar{x})^2} \sqrt{\sum_{i=1}^n (y_i - \bar{y})^2}}, \quad (5.7)$$

where  $x$  and  $y$  are two sets of pairwise samples to be considered,  $n$  is the size of the sets, and  $\bar{x}$  and  $\bar{y}$  are the mean of the sets  $x$  and  $y$ . Evaluating Equation 5.7 returns the sample Pearson correlation coefficient  $r$ , a number between  $-1$  to  $1$  encoding a measure of non-linearity and direction of relationship. A perfectly correlated set of pairwise samples will have a value of one. If they are anti-correlated, the value will be negative. When there is no correlation among the samples, then  $r$  will be zero. Note that  $r$  is not to be confused with the gradient of a linear trend among the sets of  $x$  and  $y$ .

The results of each fit and Pearson correlation coefficients are shown in Table 5.1. Overall, these comparisons show good consistency between the H $\alpha$  and other multi-wavelength SFR tracers that are generally within 0.3 dex of the one to one relation.

Out of the ten individual fits shown in Figure 5.1, only three, (Figures 5.1b, 5.1c, and 5.1i), have a gradient that is consistent with a one to one level. This is mostly because the

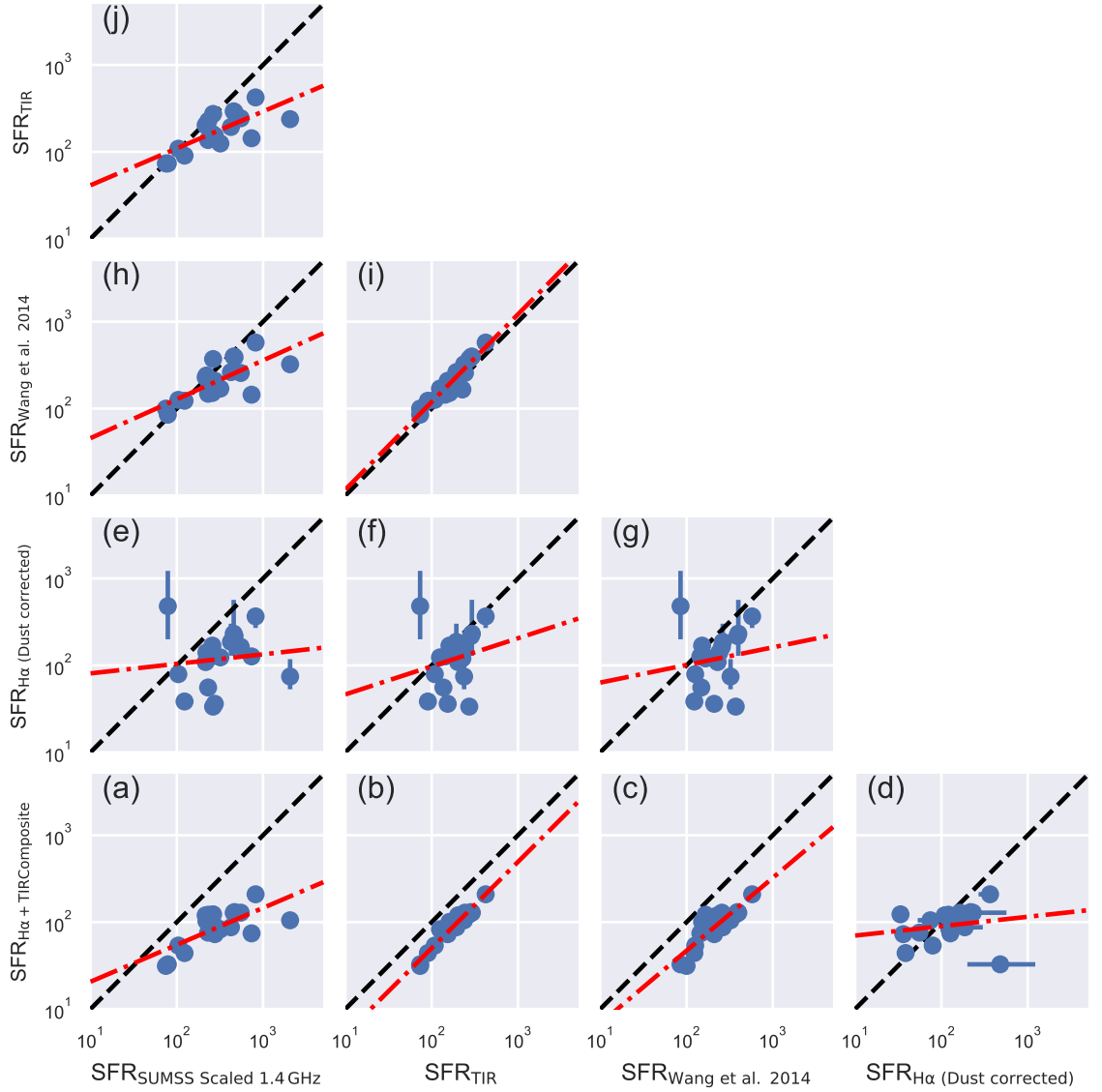


Figure 5.1: A corner plot showing the intersection of various multi-wavelength SFR indicators. Each SFR is in units of  $M_{\odot} \text{ yr}^{-1}$ . Errors on measurements represent the  $1\sigma$  uncertainty as sampled from the posterior distribution from the PPXF simulation fitting. The black dashed line in each plot represents a one to one relation, while the red dash-dot line is the result of a least-squares fit of a straight line in log-log space. The converged parameters and standard errors of each fit are shown in Table 5.1.

Abscissa	Ordinate	Gradient	Normalisation Log $M_{\odot} \text{ yr}^{-1}$	Pearson Coefficient	Figure
SFR <sub>SUMSS Scaled 1.4 GHz</sub>	SFR <sub>H<math>\alpha</math>+TIRComposite</sub>	0.42 $\pm$ 0.10	0.89 $\pm$ 0.25	0.71	5.1a
SFR <sub>TIR</sub>	SFR <sub>H<math>\alpha</math>+TIRComposite</sub>	0.99 $\pm$ 0.06	-0.28 $\pm$ 0.14	0.97	5.1b
SFR <sub>Wang et al. 2014</sub>	SFR <sub>H<math>\alpha</math>+TIRComposite</sub>	0.84 $\pm$ 0.11	-0.00 $\pm$ 0.26	0.87	5.1c
SFR <sub>H<math>\alpha</math> (Dust corrected)</sub>	SFR <sub>H<math>\alpha</math>+TIRComposite</sub>	0.11 $\pm$ 0.14	1.74 $\pm$ 0.30	0.18	5.1d
SFR <sub>SUMSS Scaled 1.4 GHz</sub>	SFR <sub>H<math>\alpha</math> (Dust corrected)</sub>	0.11 $\pm$ 0.24	1.80 $\pm$ 0.61	0.11	5.1e
SFR <sub>TIR</sub>	SFR <sub>H<math>\alpha</math> (Dust corrected)</sub>	0.32 $\pm$ 0.41	1.34 $\pm$ 0.94	0.19	5.1f
SFR <sub>Wang et al. 2014</sub>	SFR <sub>H<math>\alpha</math> (Dust corrected)</sub>	0.20 $\pm$ 0.38	1.60 $\pm$ 0.88	0.13	5.1g
SFR <sub>SUMSS Scaled 1.4 GHz</sub>	SFR <sub>Wang et al. 2014</sub>	0.45 $\pm$ 0.11	1.21 $\pm$ 0.26	0.72	5.1h
SFR <sub>TIR</sub>	SFR <sub>Wang et al. 2014</sub>	1.01 $\pm$ 0.09	0.06 $\pm$ 0.19	0.94	5.1i
SFR <sub>SUMSS Scaled 1.4 GHz</sub>	SFR <sub>TIR</sub>	0.42 $\pm$ 0.10	1.19 $\pm$ 0.24	0.73	5.1j

Table 5.1: An overview of the relations constrained in Figure 5.1. The sample Pearson correlation coefficient of each combination is also included following Equation 5.7.

three unique quantities which make up these two subfigures are based on an aspect of infrared emission. These three sets also have Pearson coefficients approaching one, indicating that there is a meaningful linear trend between the compared quantities.

For the comparisons shown in Figure 5.1a, 5.1h, and 5.1j, the Pearson correlation coefficient suggests that there is a positive linear trend between the modelled quantities. These three comparisons include the SFR based on the scaled SUMSS 1.4 GHz measurement. Given that the 1.4 GHz luminosity of these sources agreed with the sample of Yun et al. (2001) (Figure 3.8), the discrepancy seen here is likely a result of the M82 model used to scale the SUMSS measurement to 1.4 GHz, not accurately reflecting the true spectrum. It appears that the scaled SUMSS measurements overestimate the radio-continuum flux, and consequently, the SFR, when compared with other measures. This agrees with the radio-continuum modelling of these sources, which showed that the synchrotron component was steeper than the typical M82 model of Condon (1992) (Section 3.7.3). The remaining seven fits are poorly constrained with gradients that could be considered to be consistent with zero once accounting for uncertainties in the converged parameters.

Two factors are likely to contribute to the poor fits, the most major being the presence of outliers in the sample. In each comparison, several objects resided a significant distance from the one to one trend, on occasions being upwards of  $\sim 0.5$  dex. Clearly, in the log-log space, this degree of separation has a strong impact on the ability of the fitting methods to converge on a reliable solution. This problem is further aggravated by the range of values in each of the comparisons. With a sample size of only 19, having less than one order of magnitude spread in quantities means that the adopted fitting methods are even more sensitive to the presences of these outliers.

Visually inspecting the presented Figure 5.1 shows that some sources do lie on the one to one relation. This is particularly important for the WiFeS derived SFR measures as it implies



that the flux calibration of the entire sample is accurate to the first order. The large degree of scatter and lack of statistically meaningful correlations, measured by both the linear regression and Pearson coefficient, suggests however, that for individual sources, it may not be accurate.

Assuming the absolute flux calibration of the WiFeS data is accurate, a physical interpretation of the scatter among the dust corrected  $H\alpha$  based SFRs could be related to the optical depth of the  $H\alpha$  recombination line. If the optical depth is greater than one for the  $H\alpha$  line, then the estimated total  $H\alpha$  luminosity obtained through the Balmer decrement will be underestimating the true intrinsic total  $H\alpha$  luminosity. Indeed, it appears that SFR estimates based on the dust corrected  $H\alpha$  luminosity are consistently below the one to one relation for Figures 5.1e-5.1g. The single measurement above the one to one relation for each of these comparisons is IRAS F21178–6349, whose attached uncertainties for modelled spectral components are the largest among this sample (Table 4.4). The application of the Balmer decrement using an ill-constrained  $H\beta$  measurement has likely overestimated the intrinsic  $H\alpha$  luminosity and SFR.

### 5.2.1 Comparing optical features to radio-continuum components

One of the key goals of this dissertation was to investigate the link between the decomposed radio-continuum components and other robust tracers of star formation in preparation for the SKA era of radio-continuum surveys. Understanding the complex nature of the decomposed radio components for intense starburst galaxies will be critical to constrain the SFH in the earliest epochs of the Universe. Using a sample of galaxies which are meant to be representative of the SFRs expected for these objects, I hoped that comparing the decomposed radio-continuum products to other tracers would be able to reveal these intrinsic relationships and assess their reliability. Understanding how these components scale across luminosities and redshifts will be critical to accurately interpret the survey outputs from future radio-continuum surveys.

Of particular interest during this analysis were the spectral emission lines associated with ionised regions of hydrogen. Such regions are excellent tracers of the photoionisation rate of young HMS. Using data obtained from WiFeS, I have attempted to characterise the dust corrected  $H\alpha$  luminosities of all sources in my secondary sample so that I can have another independent, robust measure of SFR to compare the decomposed radio-continuum components against. The free-free continuum component will become especially important to understand higher redshifts. Having an SFR tracer originating from the same emitting matter producing this free-free emission would be a useful tool to understand the limitations of a free-free emission based SFR indicator.

Because these data have uncertainties in both dimensions, traditional non-linear least-

squares methods are not strictly appropriate. I investigated methods which are able to handle this additional constraint, including Orthogonal Diagonal Regression (ODR) (Boggs and Rogers, 1990) and Least Trimmed Squares (LTS) (Simpson, 1997; Rousseeuw and Van Driessen, 2006; Cappellari et al., 2013).

A restriction of both the ODR<sup>1</sup> and LTS<sup>2</sup> codes available was that quantities required symmetric errors in each dimension. The posterior distributions of these data were well sampled for all modelled quantities. For normally distributed data, the 16th and 84th percentiles (which were used as standard errors for reported measurements) were equally spaced around the nominal 50th percentile value, meaning this symmetric error requirement was met. However, using Bayesian fitting for the radio-continuum and optical spectra showed that many of the parameters in the corresponding models had asymmetry around the mean (Figure 3.6).

Initially, I took a conservative approach with these codes and assumed the largest error in both directions. Experimentation found that the LTS codes were more reliable, judged strictly in a ‘by eye’ qualitative sense, but were still susceptible to failing to converge, as shown in Figure 5.2. Forcing symmetric errors in both data dimensions resulted in a poorly constrained fit.

A method similar to the bootstrapping method in Section 5.2 was adopted. Samples were drawn directly from the posterior distributions of each quantity that was being examined. To minimise the effect of outlying sources throughout the bootstrapping analysis, random subsets of sources were chosen following a probability that was in inverse proportion to the variance of their posterior distribution. A larger variance of the posterior distribution relative to others in the sample would result in it being selected fewer times for inclusion in the bootstrapped subsets. If there were errors in both dimensions being considered, then the variance of both sets of posterior distributions were added together in quadrature. This approach allowed for the asymmetric shape of the quantities to be considered while minimising the effects of poorly detected sources and outliers across the small sample size and range.

Shown in Figure 5.3 are a series of comparisons between the dust corrected H $\alpha$  luminosity and the synchrotron, free-free, and total radio-continuum luminosity components at rest frame frequencies of 0.1, 1.4, 5.0 and 40.0 GHz. Overlaid onto each panel is a regression performed using the bootstrapping method outlined above. These data use the H $\alpha$  luminosities, which were corrected for dust obscuration using the Balmer decrement method exclusively. Likewise, the radio-continuum luminosities are computed using the constrained models presented in Chapter 3. If a source does not have a free-free or synchrotron radio component in its most supported

<sup>1</sup>using the implementation within the SCIPY PYTHON package <https://docs.scipy.org/doc/scipy/reference/odr.html>

<sup>2</sup>using the PYTHON implementation by Michele Cappellari <http://www-astro.physics.ox.ac.uk/~mxc/software/#lts>

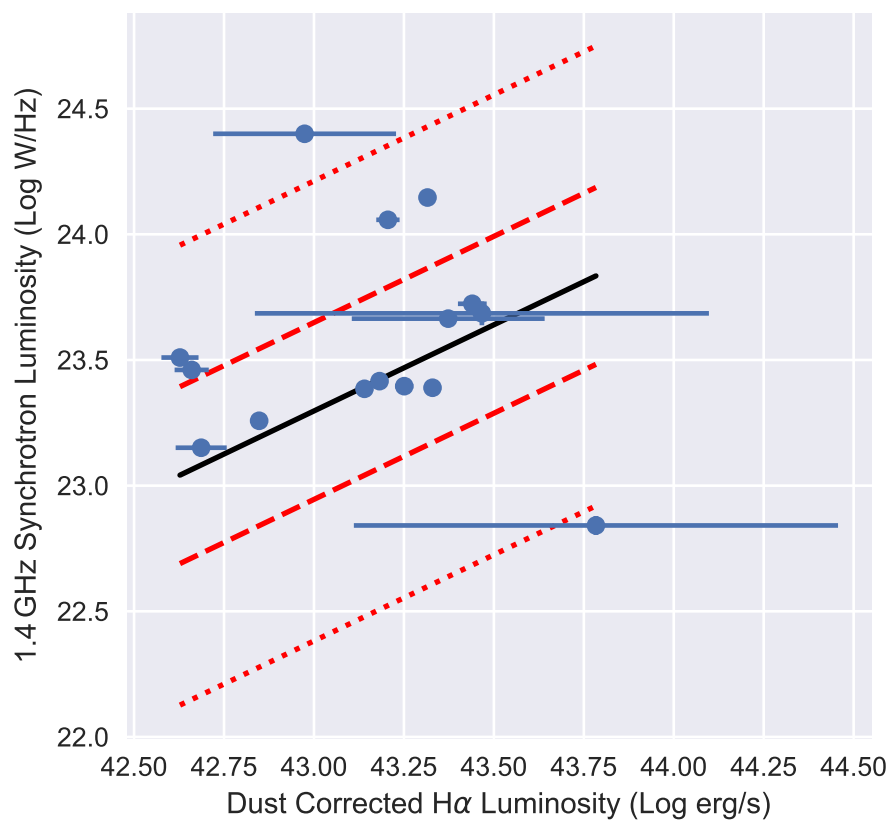


Figure 5.2: An example of the LTS fitting routine applied to data from the modelled quantities obtained from Chapters 3 and 4 from the LIRGs sample. The solid dark lines represent the final solution, whereas the dashed and dotted orange lines represent the 1 and 2.6 sigma confidence interval, as computed directly by the LTS PYTHON package.

model then it is only included when assessing the total radio luminosity at each frequency.

The comparisons made between the  $H\alpha$  and free-free luminosities at each frequency have gradients whose nominal values are each approximately zero with large uncertainties, indicating no trend. The computed Pearson coefficients also have a range of values consistent with zero, suggesting that there are no trends present among the datasets.

Across all frequencies, the comparisons made between the  $H\alpha$  luminosity and the synchrotron and total radio continuum are broadly consistent. Again, in all cases, the one sigma region suggests that a gradient of zero is possible, which suggests no correlation between two quantities. Evaluating the Pearson coefficient implies that some comparisons may have a weak trend. The  $H\alpha$  luminosities against the total radio-continuum luminosity (third column) each have a  $r$  measure of  $\sim 0.4$ , indicating a loose correlation. Although these carry large one sigma uncertainties, in the extreme case for each, the Pearson coefficient remains positive.

There are two potential physical scenarios that may explain the lack of correlation in these modelled quantities.

The first being that the suppression of radio continuum by free-free absorption has masked a significant fraction of the synchrotron and free-free emission. The  $H\alpha$  luminosity, not being affected by this free-free absorption process, will therefore not correlate well in these comparisons. To assess this effect, the same analysis was performed with the exception of ignoring the effects of free-free absorption, if present, in each of the radio-continuum models. Figure 5.4 shows the result of this comparison.

Similar to the comparisons made in Figure 5.3, each panel in Figure 5.4 shows either very weak positive correlations or correlations that are consistent with total independence. Comparisons made between  $H\alpha$  and free-free luminosities show gradients consistent with values of zero. Likewise, the  $H\alpha$  luminosities against both the synchrotron and total radio-continuum luminosities are broadly consistent with one another, but when their uncertainties are considered, these relations are also consistent with noise. The Pearson coefficient also indicates that there is no meaningful trend among all comparisons.

Alternatively, it is possible that these objects are so heavily embedded in dusty regions that the optical depth is sufficiently high to render the Balmer decrement ineffective to recover the intrinsic  $H\alpha$  luminosity. Local (U)LIRGs are known to be especially dusty (Norris, 1985). Performing the Balmer decrement on such objects would lead to a bias of less obscured regions, leading to an underestimated intrinsic  $H\alpha$  luminosity (Kennicutt et al., 2009). Acquiring near infrared spectroscopy IFU data targeting the  $P\alpha$  emission line for this sample would be required to confirm this scenario.

To test this scenario, comparisons similar to those shown in Figures 5.3 and 5.4 using the

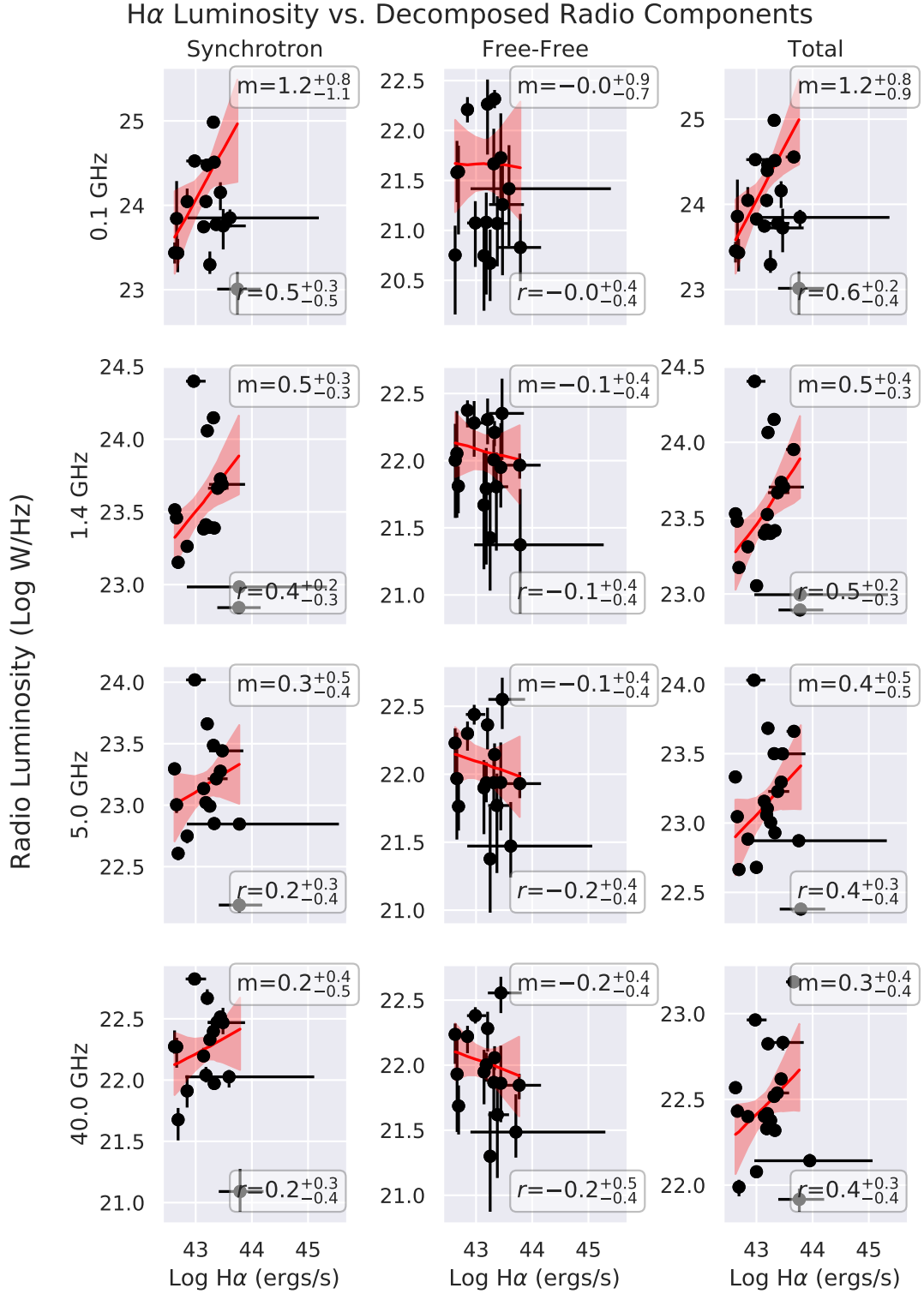


Figure 5.3: A comparison between the dust corrected H $\alpha$  luminosities obtained from the WiFeS dataset and the decomposed radio continuum at multiple frequencies. All radio luminosities are in terms of Log W Hz $^{-1}$  and are in the rest frame. The solid red line and the corresponding highlighted region represent the modelled line of best fit and its one sigma uncertainty. The upper right-hand corner of each panel shows the nominal (i.e. 50<sup>th</sup> percentile) and one sigma uncertainty of the gradient. The Pearson coefficient and its one sigma uncertainties have been calculated and included in the lower right-hand of each panel. Error bars on each measurement represent the one sigma uncertainty from the sampled posterior distribution of each quantity for each source.

## H $\alpha$ Luminosity vs. Decomposed Radio Components Without FFA

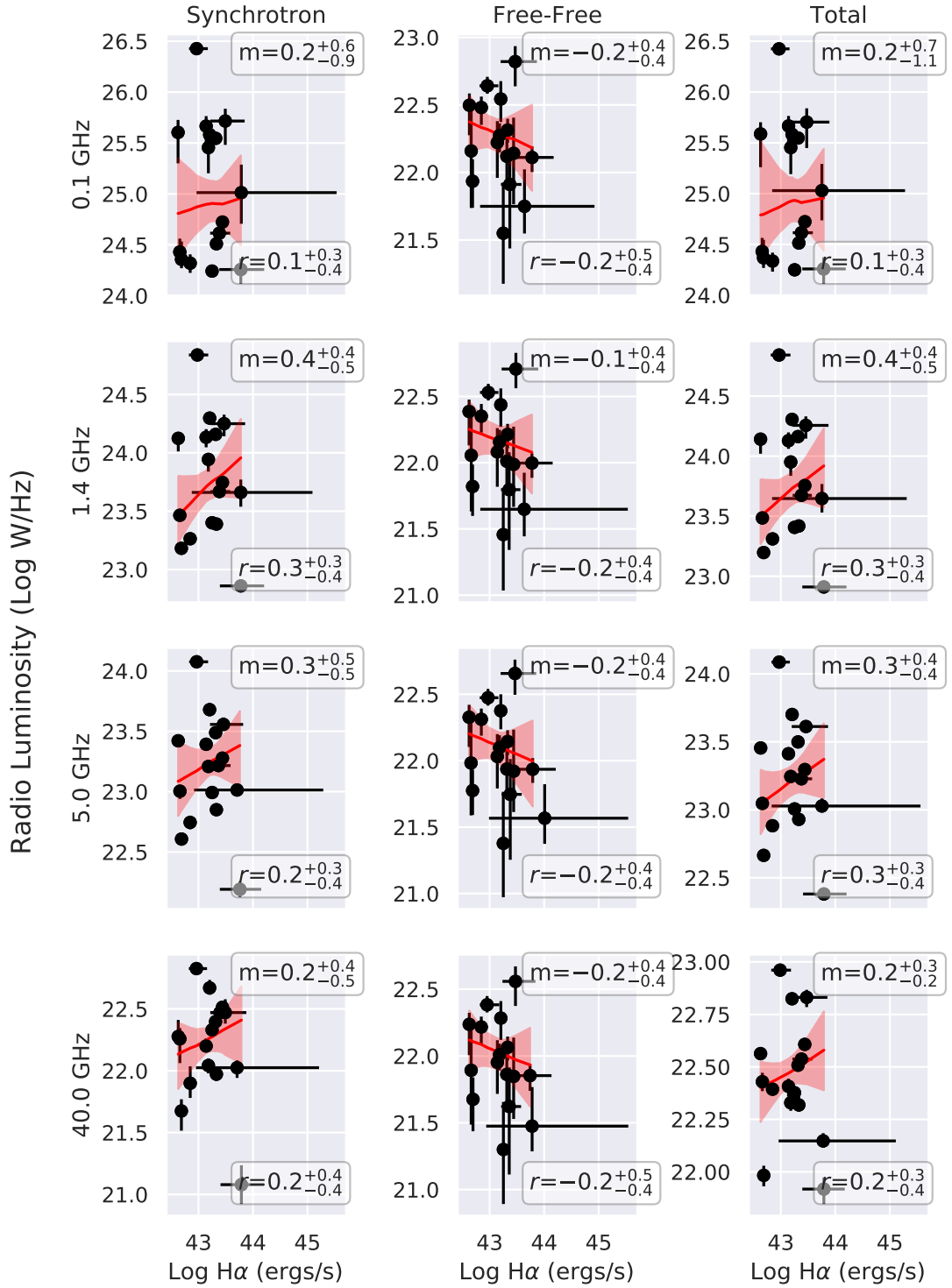


Figure 5.4: A comparison between the dust corrected H $\alpha$  luminosities obtained from the WiFeS dataset and the various radio-continuum components at various frequencies. All radio luminosities are in terms of Log W Hz $^{-1}$ . Each radio-continuum model has been modified to remove the effects of free-free absorption. The solid red line and the corresponding highlighted region represent the modelled line of best fit and its one sigma uncertainty. In the upper right-hand corner of each panel, I denote the nominal (i.e. 50<sup>th</sup> percentile) and one sigma uncertainty of the gradient. The Pearson coefficient and its one sigma uncertainties have been calculated and included in the lower right-hand of each panel. Error bars represent the one sigma uncertainty as indicated by the sampled posterior distribution of each quantity for each source.

composite SFR (Equation 5.3) in place of the  $H\alpha$  luminosity were performed. The basis of this composite tracer is a simple scenario where the energy of optical emission absorbed by dust is reradiated as infrared emission. If extreme dust attenuation is a source of scatter seen in Figures 5.3 and 5.4, using this composite tracer may result in the detection of more meaningful correlations.

These comparisons, presented in Figure 5.5, do indeed appear to have marginally improved trends. This is largely because for these objects, the error introduced by applying the dust correction has been removed. Even so, it is only the comparisons made with the total radio luminosity that is statistically robust and not consistent with noise. Comparing these to the trends made against the total infrared luminosities, presented as Table 3.10, shows that these are not nearly as well constrained. Uncertainties attached to the gradients of all trends in Figure 5.5 are two to three times larger than those in Table 3.10. The difference between units of the total infrared luminosity (Table 3.10) and composite SFRs (Figure 5.5) only affects the normalisation component and would only be a constant offset.

### 5.3 Discussion

Unfortunately, there are no strong correlations among any of the comparisons made between the  $H\alpha$  luminosities and the decomposed radio-continuum components. To assess whether any intrinsic property may have influenced this result, I explored second order features in this space. I show such an example in Figure 5.6, where the thermal fraction evaluated at 1.4 GHz for each object (evaluated from the radio-continuum modelling) is included as the colour of each marker. Investigating other dimensions, including redshift, stellar mass (derived by Wang et al., 2014), the  $q$  parameter, synchrotron spectral index, and turnover frequencies, I was unable to identify any other variable that explains the apparent lack of correlation.

The most likely explanation of this lack of correlation is not physical, rather it is one that is simply related to the detected physical features, their signal to noise and associated modelling uncertainties.

For instance, it is often assumed that the radio-continuum SED of SFG is well characterised by a simple combination of synchrotron and free-free emission. This assumption was built into the time requirements when applying for ATCA time. Finding higher-order features in the SED of these starburst objects was unexpected, and as a consequence, higher-order models with additional parameters had to be used. To detect such features in the radio continuum, if they were present, densely sampled measurements across a broad frequency range are required. This required the ATCA CABB filters to be divided into several sub-bands. Doing so would

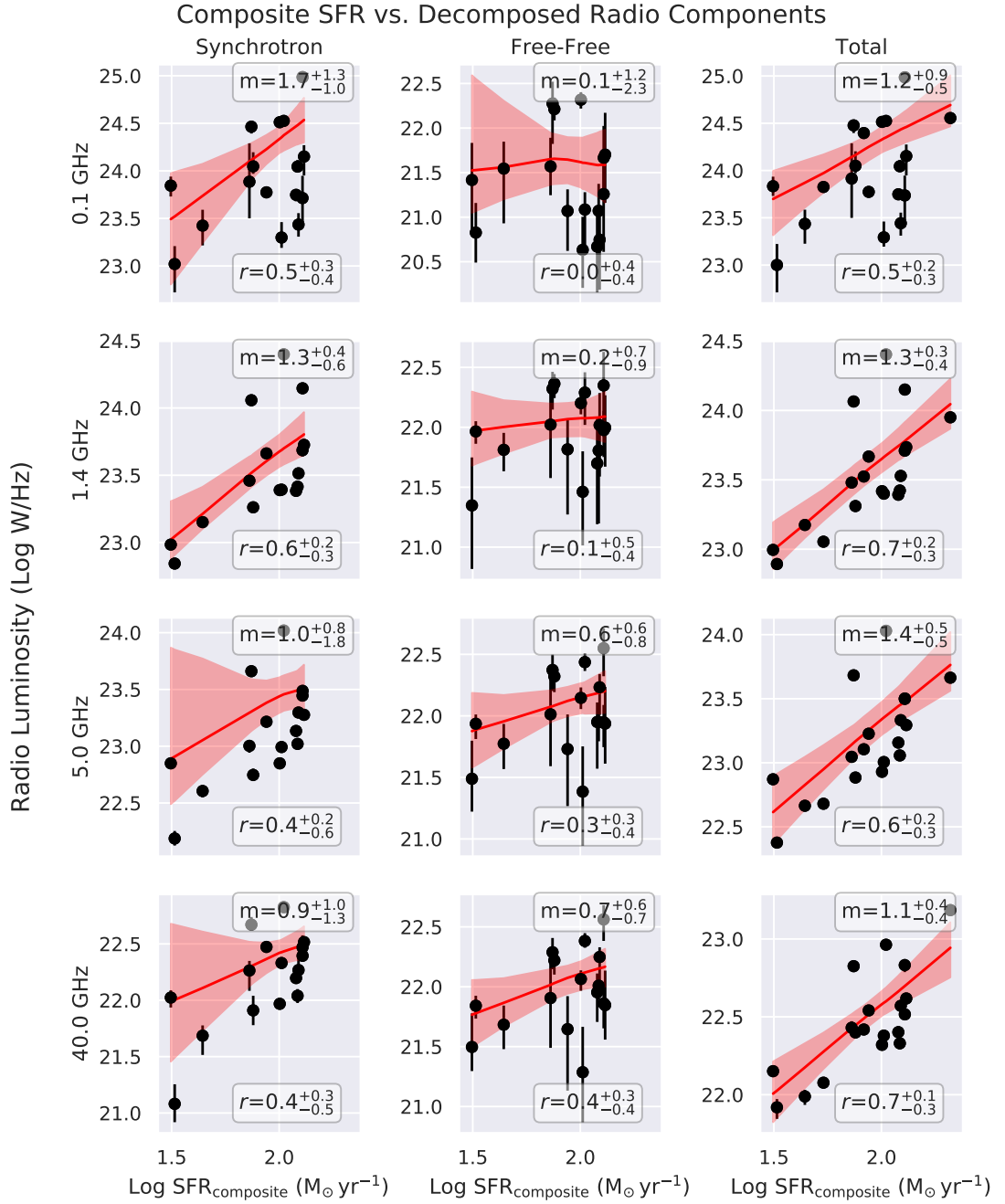


Figure 5.5: A comparison between the composite SFR estimated from Equation 5.3 to the observed  $H\alpha$  measurements obtained using WiFeS and the total infrared luminosity supplied by Wang et al. (2014) compared against the various radio-continuum components at various frequencies. All radio luminosities are in terms of  $\text{Log W Hz}^{-1}$ . The solid red line and the corresponding highlighted region represent the modelled line of best fit and its one sigma uncertainty. In the upper right-hand corner of each panel, the nominal (i.e. 50<sup>th</sup> percentile) and one sigma uncertainty of the gradient are denoted. The Pearson coefficient and its one sigma uncertainties have been calculated and included in the lower right-hand of each panel. Error bars represent the one sigma uncertainty as indicated by the sampled posterior distribution of each quantity for each source.



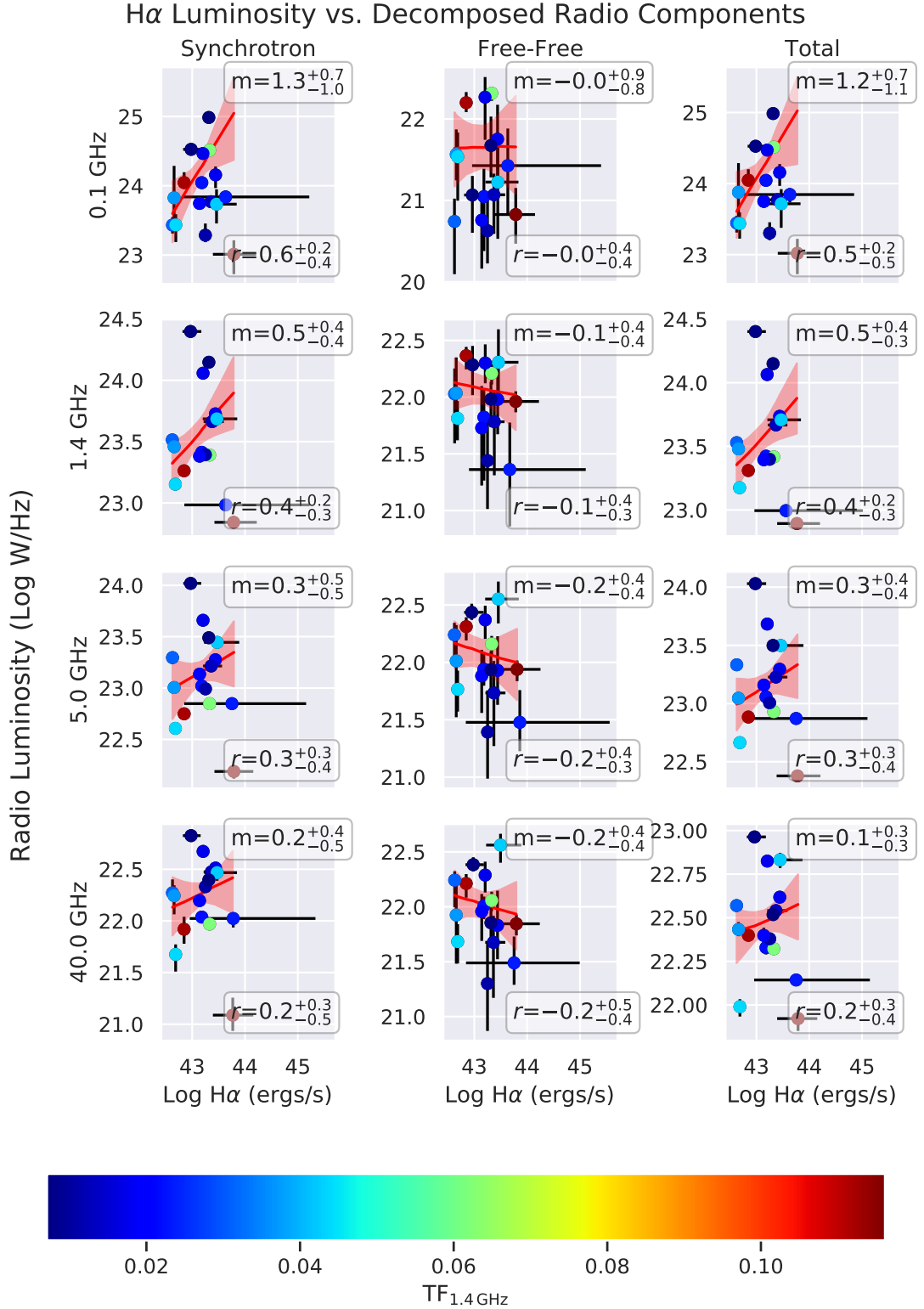


Figure 5.6: A comparison between the dust corrected H $\alpha$  luminosities obtained from the WiFeS dataset and the various radio-continuum components at various frequencies. All radio luminosities are in terms of Log W Hz<sup>-1</sup>. Each radio-continuum model has been modified to remove the effects of free-free absorption, and the colour of each marker represents the nominal thermal fraction at 1.4 GHz constrained by each radio-continuum model. The solid red line and the corresponding highlighted region represent the modelled line of best fit and its one sigma uncertainty. In the upper right-hand corner of each panel, the nominal (i.e. 50<sup>th</sup> percentile) and one sigma uncertainty of the gradient are shown. The Pearson coefficient and its one sigma uncertainties have been calculated and included in the lower right-hand of each panel. Error bars represent the one sigma uncertainty as indicated by the sampled posterior distribution of each quantity for each source.

increase measurement error, and when combined with more complex SED models, would be carried through to constrained quantities.

Further, during this radio-continuum modelling process, the most supported model, as judged strictly by the Bayesian evidence values and the Bayes odds ratio test, may not necessarily be representative of the ‘true’ SED of a source. Rather, it is merely the model that is most supported by the current data. Such discrepancies could influence both the uncertainty and scatter of derived quantities in cases where the model most supported by the data is not necessarily the true underlying behaviour of the source. Such a situation could occur for sources with faint MWA detections (such as those whose fluxes were constrained using the AEGEAN PRIORISED fitting option) or poor high frequency observations, where an incorrect turnover frequency or free-free component could be obtained.

Likewise, when considering the obtained  $H\alpha$  luminosities, several potential issues could contribute to the lack of correlation throughout these comparisons. First, the use of the PYWIFES reduction pipeline introduced a number of flux calibration issues into the final data cubes. I believe I have identified all obvious failure cases relevant to my data that triggered the incorrect calibration scale to be derived and applied. However, I am uncertain whether there exist other fundamental issues with the reduction pipeline and how it was used when operating on my dataset. Tracing these flux calibration issues when initially encountered took a considerable amount of time and effort, especially when considering the size of the codebase and my naive understanding of optical data reduction strategies. It is certainly possible that some scatter in the  $H\alpha$  luminosities of sources in this sample could be the effects of some residual, undiagnosed issue that are not related to flux calibration routines.

More likely though, the obvious source of uncertainty and error in the final  $H\alpha$  luminosities is the method of dust correction used. In this study, I primarily use the Balmer decrement method to characterise and correct for the amount of dust obscuration. Although this method directly traces the dust content in star forming regions (as opposed to the reddening of the stellar continuum which is tracing the attenuation of starlight from an older stellar population), this method is susceptible to the uncertainties associated with  $H\beta$ . For the WiFeS dual-beam spectrograph, the  $H\alpha$  and  $H\beta$  transitions are observed through different beams and filters, each of which has different bandpass responses. Using the  $H\beta$  line in this manner, especially for faint objects, can lead to situations where the correction is overestimated. Poorly constrained  $H\beta$  detections would lead to dust corrected  $H\alpha$  luminosities with larger uncertainties, which would subsequently be carried through to SFR measures.

Finally, when designing the sample selection for objects in this study, I introduced an IR luminosity cut, such that all objects were classified as LIRGs. The premise being after removing

sources with AGN activity, the remainder of these highly luminous objects, which presumably have high luminosities due to high star formation rates, would be representative of objects in the high redshift Universe. A consequence of this selection criteria was that most of the quantities investigated through this project are studied across a relatively small luminosity range. Identifying correlations over a small and incomplete parameter space is difficult and is further complicated when non-negligible outliers exist.

I believe that the lack of detection of meaningful correlations is likely because of a combination of these outlined effects. Comparing the decomposed radio-continuum components across infrared luminosities shows the presences of FRC like relationships, meaning that on some level, the radio-continuum components modelled in Chapter 3 are real. Comparing the H $\alpha$  based SFR measures to other multi-wavelength SFR indicators shows that they are *broadly consistent*, although there is a large scatter and uncertainty attached to them (as illustrated by the poorly constrained correlations shown in Table 5.1). For this reason, I find it likely that the dust corrected H $\alpha$  luminosities are at the centre of the issue. Further investigating this will require revisiting these sources to obtain additional optical spectroscopy observations. Recently, collaborators and I have also submitted a SINFONI VLT proposal to acquire Paschen- $\alpha$  observations of these objects. Paschen- $\alpha$ , being less effected by dust obscuration, could prove to be a more robust tool to compare the decomposed radio-continuum components against.

### 5.3.1 Electron Temperature Variation

When computing the dust correction, I assumed Case B recombination, which in the literature is taken as typical for SFG. In this scenario, the electron temperate,  $T_e$ , is taken to be  $10^4$  K.

As both the thermal free-free radio-continuum and the Balmer series of emission lines trace the same ionised medium, the two quantities can be linked with numerical approximations. Adopting the relation from Condon (1992), the dust corrected H $\beta$  line flux  $F(\text{H}\beta)$  can be related to the thermal free-free component at the radio frequency  $\nu$  at an assumed electron temperature,  $T_e$ , via

$$\left[ \frac{F(\text{H}\beta)}{10^{-12} \text{ erg/s/cm}^2} \right] \sim 0.28 \left( \frac{T_e}{10^4 \text{ K}} \right)^{-0.52} \left( \frac{\nu}{\text{GHz}} \right)^{-0.1} \left( \frac{S_{\text{T}}}{\text{mJy}} \right). \quad (5.8)$$

The radio-continuum SED modelling of 19 LIRGs in Chapter 3 could constrain the thermal free-free component across a broad frequency range. Similarly, an intrinsic H $\beta$  flux for these sources was estimated using the modelled optical spectra as described throughout Chapter 4, with the exception of evaluating the Calzetti et al. (2000) reddening curve in Equation 4.11 at a wavelength of 4861 Å.

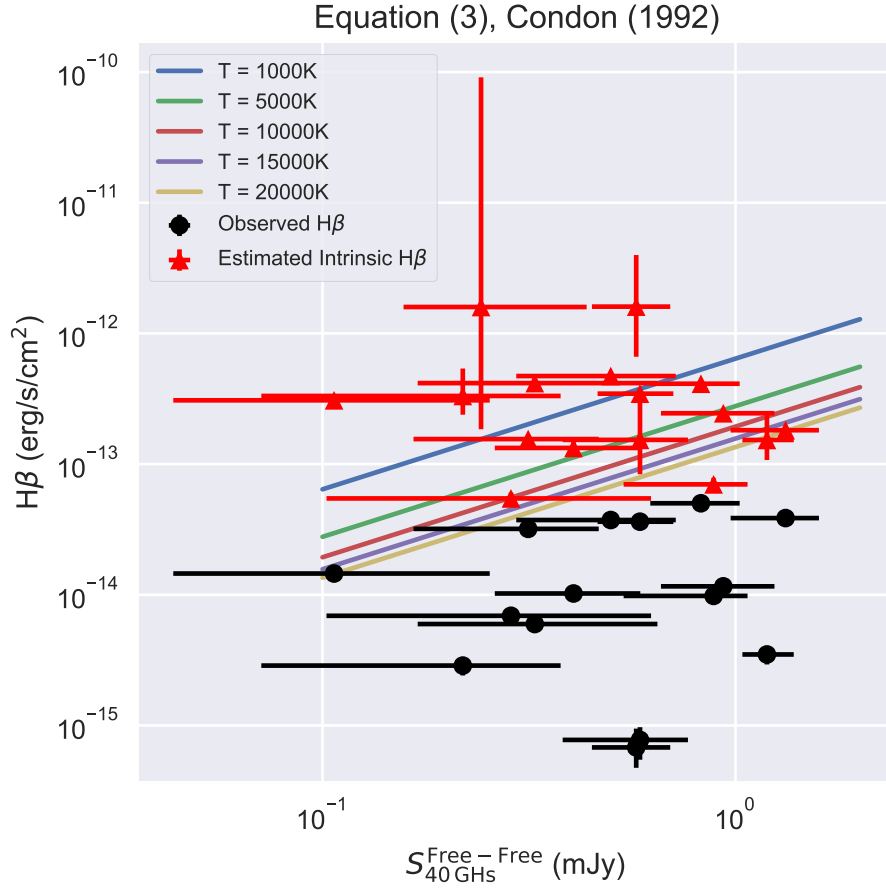


Figure 5.7: A comparison between the free-free radio-continuum flux at 40 GHz and the  $H\beta$  flux from the set of LIRGs studied in this dissertation. Both the observed and intrinsic  $H\beta$  fluxes are included, which have been obtained using the Balmer decrement method. The overlaid colour tracks indicate the effects of varying electron temperatures predicted by Equation 5.8.

Figure 5.7 shows a comparison between the dust corrected  $H\beta$  and thermal free-free radio-continuum fluxes. The colour overlays show tracks of Equation 5.8 evaluated using assumed electron temperatures of 1000, 5000, 10000, and 15000 K. The observed  $H\beta$  fluxes (i.e. modelled intensities without a dust correction being applied) are also included for reference.

As expected, the observed  $H\beta$  fluxes in Figure 5.7 were all below the expected values predicted from Equation 5.8. Clearly, as no dust correction was performed, a sizeable fraction of the intrinsic emission is missing. Once a dust correction was performed, ten objects became consistent with Equation 5.8 evaluated across the range of electron temperatures plotted.

The dust correction applied to these measurements assumes the Case B recombination scenario with  $T_e$  and  $n_e$  set to  $10^4$  K and  $100 \text{ cm}^{-3}$ , respectively. These values are considered to be typical for SFG (Osterbrock, 1989). If the assumed  $H\alpha/H\beta$  ratio of 2.86 used for this sample of objects is accurate, my objects should follow the trend expected following Equation 5.8. Six objects in this sample are far above the expected trend, even when considering uncertainties

and the unusually high electron temperature range overlaid. Three potential scenarios could explain this inconsistency.

The most obvious scenario is that the free-free component constrained using the radio-continuum data underestimates the true amount of free-free emission. Radio-continuum data above 10 GHz are critical to constrain the faint, flat spectrum free-free emission accurately. In this frequency regime, the observed radio-continuum data become sparsely sampled with detections of lower significance. An undetected free-free component may remain that is being missed from these radio data and subsequent modelling. For this scenario to be valid, the radio-continuum data and subsequent modelling would have to be missing upwards of 90% of the actual free-free component. Although possible, this seems to be unlikely, considering the strong correlation observed between the free-free and far-infrared luminosities of these objects.

Alternatively, it is possible that the  $10^4$  K temperature and  $100 \text{ cm}^{-3}$  electron density, which are assumed to be typical for SFG, are not entirely appropriate for these sources. The objects in this LIRG sample were selected to be representative of high redshift objects and their exceptionally high star formation rates, not necessarily the SFGs in the local Universe. Their radio-continuum SEDs, which show higher-order curvature features consistent with multiple regions of free-free absorption, further suggest complex behaviour. The  $\text{H}\alpha/\text{H}\beta$  ratio is largely a function of temperature,  $T$ , following

$$\text{H}\alpha/\text{H}\beta = 2.86 \left( \frac{T}{10^4 \text{ K}} \right)^{-0.07}. \quad (5.9)$$

For this discussion, the effects of a varying electron density can be ignored. Assuming a single electron temperature of  $10^4$  K and electron densities of  $10^2$ ,  $10^4$ , and  $10^6 \text{ cm}^{-3}$ , the corresponding  $\text{H}\alpha/\text{H}\beta$  ratios are 2.86, 2.85, and 2.81, respectively (Groves et al., 2012).

Figure 5.8 shows the effects of adopting a  $\text{H}\alpha/\text{H}\beta$  ratio, the corresponding electron temperatures that would be required, and the resulting dust correction factor applied to estimate the intrinsic line flux or luminosity. A cooler electron temperature or larger  $\text{H}\alpha/\text{H}\beta$  ratio, would reduce the dust correction factor that is applied to the observed flux. An exceptionally large change would have to be applied to bring the six  $\text{H}\beta$  excess sources in Figure 5.7 objects to the expected trend.

Finally, the reddening curve of Calzetti et al. (2000), which was used when dust correcting the optical spectra of these objects, carries a large systematic uncertainty. When evaluated at the wavelength of  $\text{H}\beta$ , the reddening curve  $k(\lambda)$  function is evaluated to be  $4.6 \pm 0.8$ . This large systematic error can easily place these objects onto the expected trend implied by Equation 5.8. Potentially, the Calzetti et al. (2000) reddening curve may not even be appropriate for intense starburst galaxies. Comparing the colour excess  $E(B - V)$  terms derived from the Balmer

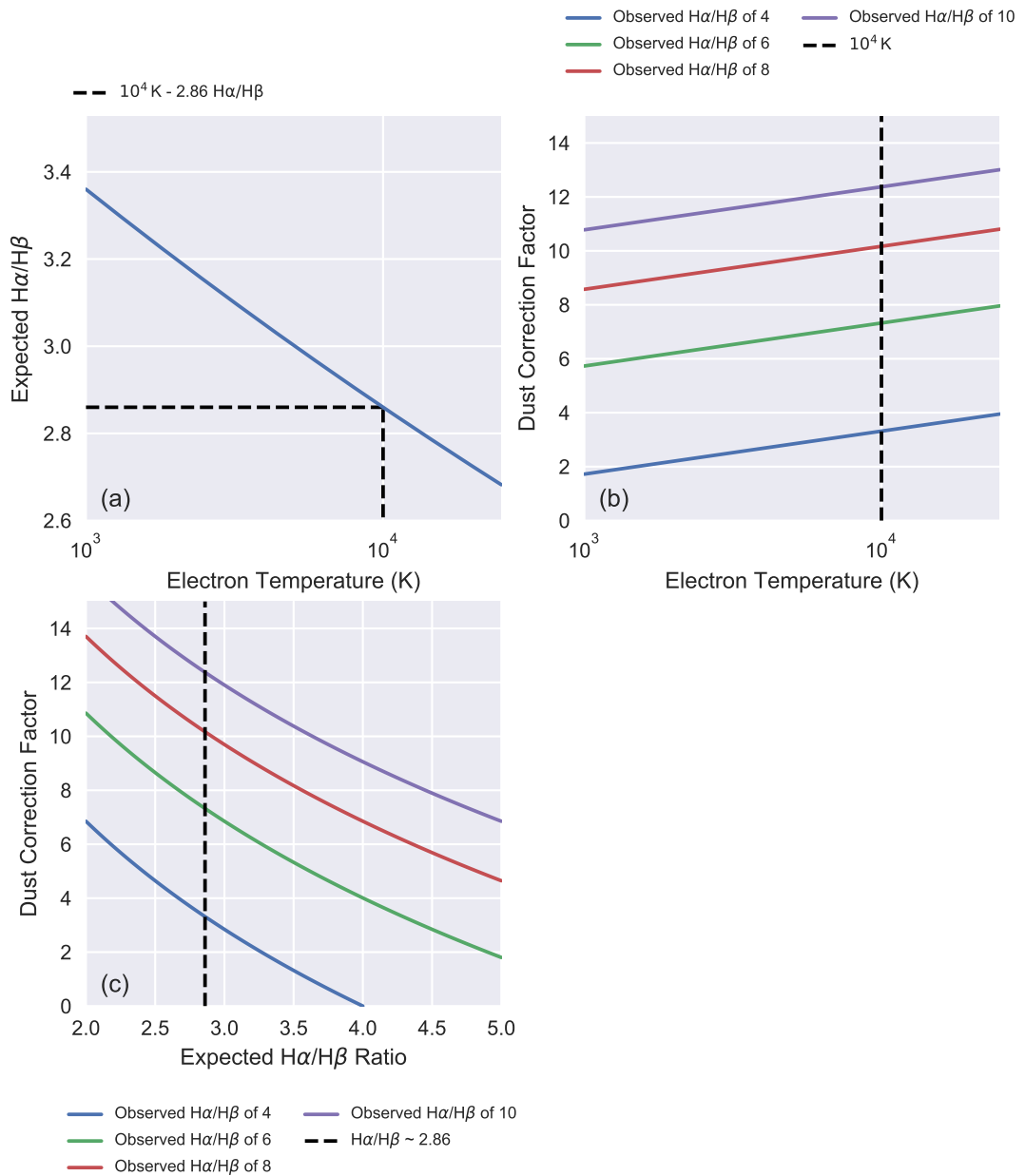


Figure 5.8: Examination of the effects of varying the adopted electron temperature and  $H\alpha/H\beta$  ratio that is used during dust correction using the Balmer decrement method. Panel (a) shows how the  $H\alpha/H\beta$  ratios varies as a function of electron temperature following Equation 5.9. Panel (b) shows how the dust correction factor applied to the observed  $H\beta$  flux changes as a function of electron temperature. Panel (c) shows how the dust correction factor varies across  $H\alpha/H\beta$  ratios. The horizontal and vertical dashed lines in each panel represent the parameters assumed for typical SFG and Case B recombination. Panels (b) and (c) also show how the dust correction factor would vary with different observed  $H\alpha/H\beta$  ratios, where the observed ratio is used to characterise the amount of dust extinction.

decrement and the stellar continuum shows a clear deviation from the empirically measured trend of Calzetti (1997, 2013). The observed trend is much closer to the relation predicted by Babbedge et al. (2005) who used photometric redshift codes to recover colour excess terms for starburst galaxies.

In any case, each scenario would require additional data for further investigation. Obtaining resolved  $\text{Pa}\alpha$  values of these sources would be an initial step.  $\text{Pa}\alpha$  is far less affected by dust attenuation, making measures of SFR more reliable and less susceptible to large errors introduced by the application of an incorrect dust correction term. When combined with the existing WiFeS spectra, the reddening curve can be characterised across a wavelength range spanning three orders of magnitude and may provide insight on how applicable typical reddening curves are for intense starburst objects. Modelling of the WiFeS spectra with PPF seems to suggest that the Calzetti et al. (2000) reddening curve may not be an ideal description of the actual reddening curve (Figure 4.18). Additionally, the resolved IFU data may also indicate discrete regions of intense starburst which may produce the complex features seen in the corresponding radio-continuum SEDs.

Band 3 ALMA data (spanning 84 to 116 GHz) may also be used to investigate the thermal free-free emission of these 19 LIRGs at a frequency regime that is largely devoid of synchrotron emission. With the superb resolution and sensitivity of ALMA, these data would help to separate the synchrotron and free-free emission components better across potentially resolved, discrete regions of star formation. Planned lower frequency bands covering 35 – 50 and 65 – 90 GHz may also be used to construct robust SEDs across a broad frequency range efficiently.

### 5.3.2 Optical and radio-continuum features of IRAS F00198–7926

The radio-continuum SED of IRAS F00198–7926 exhibited evidence of both a low and high frequency turnover due to the effects of Free-Free Absorption (FFA). MULTINEST most preferred the ‘C2 1SA’ model (Equation 3.4), with constrained  $\nu_{t,1}$  and  $\nu_{t,2}$  of  $0.2_{-0.0}^{+0.0}$  GHz and  $6.2_{-0.6}^{+0.7}$  GHz, respectively. An interpretation of this is that there are two distinct regions or populations of star formation with different geometric properties. Equations 3.13 and emission measures showed that the turnover frequency  $\nu_t$  is dependent on the temperature and emission measure (EM) of the emitting medium, where EM is the density of the plasma along the line of sight.

The unresolved radio continuum data cannot relate the discrete turnover components to specific regions of emitting plasma with different EM. However, the resolved WiFeS data cubes may offer the ability to identify these distinct regions.

Figure 5.9 shows the  $\text{H}\alpha$  luminosity of IRAS F00198–8923 after applying a dust correction

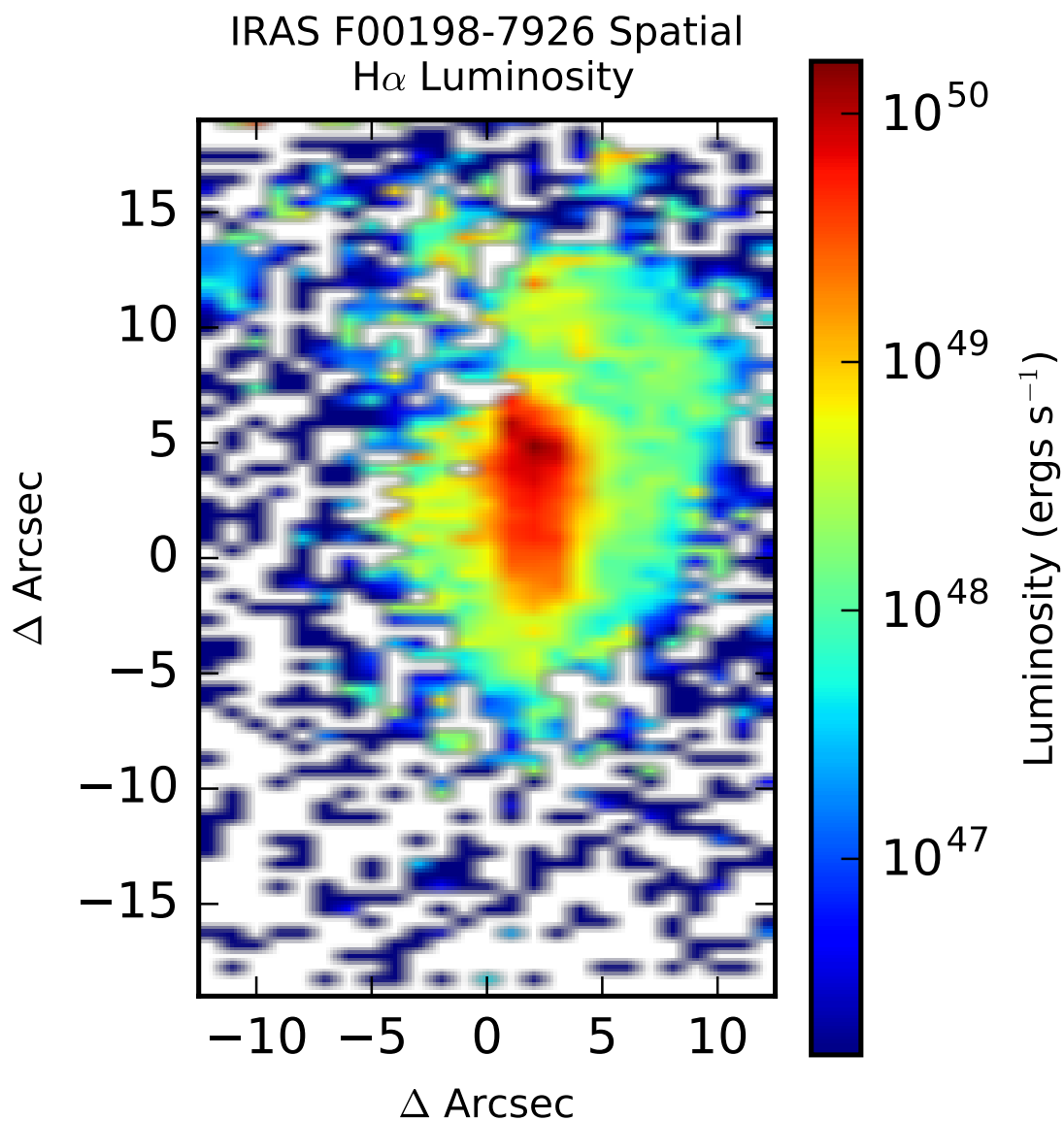


Figure 5.9: The dust corrected  $H\alpha$  luminosity across IRAS F00198-7926 per pixel. A constant redshift of 0.0728 has been assumed.



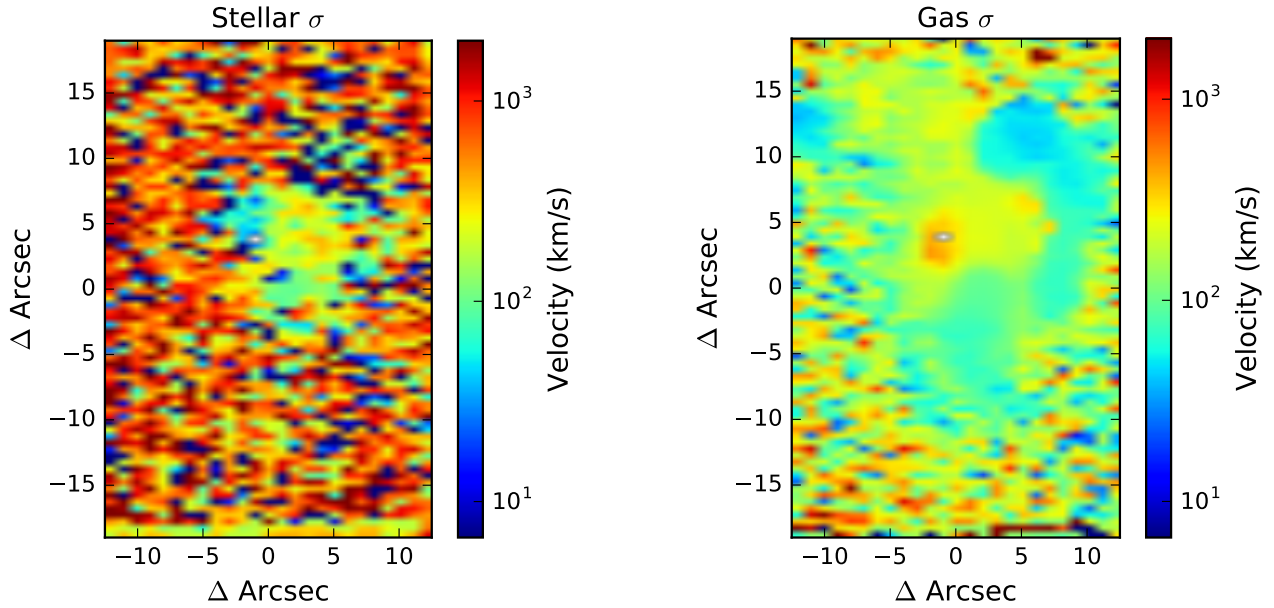


Figure 5.10: The velocity dispersion of IRAS F00198–7926 constrained by PPXF when modelling the LOSVD for the stellar continuum templates of Sánchez-Blázquez et al. (2006) (*left*) and the synthetic templates generated to model the stellar line transitions (*right*). Both show structures at the same approximate location of the luminous clump seen in Figure 5.9.

term. Assuming that the dust attenuation across the object’s surface has been robustly constrained, the dust corrected H $\alpha$  luminosity should be a good proxy for the regions of thermal free-free emission that contributes to the radio-continuum SED.

Within the central field of IRAS F00198–7926 (Figure 5.9) there is a region of approximately 10'' by 5'' that is roughly 1-2 dex more luminous than the surrounding diffuse structure. At a redshift of 0.0728, the physical size corresponds to roughly 15 by 8 kpc. Inspecting the velocity dispersion of the LOSVD parameters (i.e. the  $\sigma$  component) of both the stellar (the template library of Sánchez-Blázquez et al., 2006) and gas (synthetic templates generated to model stellar transitions) templates also shows a fairly clear structure at the same location of this more luminous clump of matter (Figure 5.10).

A potential scenario for IRAS F00198–7923 is that this extra luminous clump, with a higher SFR and a higher density of thermal free-free emission (traced by the dust corrected H $\alpha$  luminosity), produces a higher frequency turnover in the radio continuum. The emission measure (EM) for the higher frequency turnover of IRAS F00198–7926 is estimated to be 13.836 cm $^{-6}$  pc based on a  $\nu_{t,2}$  of 6.2 GHz turnover. Recall that the EM is defined as

$$\frac{EM}{\text{pc cm}^{-6}} = \int_{\text{los}} \left( \frac{N_e}{\text{cm}^{-3}} \right)^2 d \left( \frac{s}{\text{pc}} \right). \quad (5.10)$$

The central clump of H $\alpha$  emitting matter presumably has a higher density because of its

smaller size and more luminous emission, thereby producing the modelled higher turnover frequency in the radio continuum.

This interpretation is speculative without first appropriately characterising uncertainties on a spaxel basis. The initial attempt to bin adjacent spaxels into a more coarse grid suggested that there is an insufficient signal to appropriately perform this type of analysis with the current dataset (Figure 4.21). Because the Balmer decrement method has been used to estimate and correct for dust obscuration, the luminous clump of emitting matter seen in Figure 5.9 could instead be a product of an overcorrected  $H\alpha$  line due to an under constrained  $H\beta$ . Further investigation would have to be carried out along these lines with both a larger sample (in terms of both the optical IFU data as well as the radio-continuum data) and appropriate error characterisation for the resolved  $H\alpha$  and  $H\beta$  components.

Additional consideration would have to be made to attempt to determine whether the  $H\alpha$  line itself has an optical depth above 1, meaning that even an attempt to correct using the Balmer decrement method would be unsuccessful. Such a scenario would require other methods of obtained resolved measures of SFR that trace the ionised regions of matter that produce free-free radio-continuum emission. Ideally, this would be the  $Pa\alpha$  emission line. This scenario has been noted by Norris (1985), where Arp 220 was described as having an optical depth of about 100. Lines observed towards this object are seeing the ratios of emission surrounding the outer part of the galaxy where  $\tau \sim 1$ . It is not unreasonable to expect this to be a problem for the 19 LIRGs studied extensively throughout Chapter 3 and 4, especially considering that the radio continuum for many of these objects contained a secondary turnover at high frequency, suggesting a powerful and dense star forming region in addition to more diffuse and low SFR regions.

Complimenting these data would be resolved radio-continuum images across a broad frequency range. This would allow the turnovers seen in the modelled radio-continuum SEDs of Chapter 3 to be investigated across the surface of each object. Correlating such turnover regions to resolved optical IFUs would offer exciting possibilities to understand the fundamental physical processes that drive SFR and its manifestations.

## 5.4 Conclusions

This Chapter attempts to compare dust corrected  $H\alpha$  luminosities to decomposed radio-continuum components in a set of 19 intense starburst galaxies. Surprisingly, there was no meaningful correlation detected through these comparisons. Incorporating second order physical properties also showed no trends or reasons for this lack of correlation among the datasets.

Considering the fact that FRC like relationships were found in Chapter 3 for the decomposed radio-continuum components and the broad consistency of the  $H\alpha$  SFR based measures with other multi-wavelength indicators, it is likely that the problem is in the optical IFU data. Potentially, there are compounding effects, including weak emission lines with low significance in the modelling, or regions of star formation deeply embedded in dust. In the latter scenario, a Balmer decrement method will be unable to recover an intrinsic  $H\alpha$  luminosity. Given that LIRGs and ULIRGs are known to be especially dusty, this is a likely scenario that needs to be considered.

For a single source in my dataset, I also explored the results of applying PPXF on a per spaxel basis. The source IRAS F00198–7926 was the strongest observed in the sample of 19 LIRGs targeted with WiFeS. Exploring its uncertainties with Monte-Carlo analysis on binned spaxels suggests that there is an insufficient signal to safely interpret the resolved properties constrained by PPXF on a per spaxel basis. That said, inspecting the dust corrected  $H\alpha$  map showed a luminous clump of emitting matter at the central region of the object surrounded by a much weaker, diffuse component. Similar properties were also seen when inspecting the LOSVD characteristics across the object. If such features are genuine and not a symptom of insufficient signals, this suggests a compact region of intense star formation surrounded by diffuse star formation at a much lower rate.

In terms of the radio continuum, IRAS F00198–7926 showed evidence of having two distinct turnovers, which were modelled as being the result of free-free absorption: one at low frequency, constrained by MWA GLEAM data, and the second being at a higher frequency and constrained by ATCA data. Tentatively, it could be argued that the clumpy luminous  $H\alpha$  region, being compact with high thermal activity, could be producing the higher frequency turnover in the radio continuum, with the more diffuse extended region being of lower electron density and producing the low frequency radio continuum turnover. Clarifying whether this is the case will require more data for the remainder of my sample to confirm similar behaviour. It may also be necessary to acquire more radio-continuum data at higher frequencies and extend the sample to characterise the relationship robustly.

## Chapter 6

# Conclusions and Future Work

Much effort has been devoted towards understanding the physical processes that drive star formation and their manifestations across the electromagnetic spectrum. Objects in the local Universe at low redshifts ( $z < 0.2$ ) have allowed a detailed understanding of these signatures to be obtained through densely modelled SEDs. This detailed understanding has allowed accurate measurements of star formation to be obtained with relatively sparse data. Built into these methods are general assumptions that are valid for the greater majority of local objects. The question remains open as to how well these SFR measures scale to the distant, high redshift Universe. Uncertainties arise not only because these assumptions may not necessarily hold but also because this volume of the Universe contains objects that are thought to be fundamentally different from the older galaxies in the local Universe. Understanding these objects and their physical properties requires a deeper knowledge of their structure and processes.

Having an accurate measurement of SFR for objects in the high redshift Universe is critical to constrain the SFH reliably. An understanding of the SFH will allow us to characterise stellar mass growth across cosmic time. Radio-continuum emission has the potential to be the most reliable tracer of star formation for this high redshift Universe.

Optical-based measures require understanding the dust attenuation properties of each galaxy to obtain an intrinsic measure of stellar light. Ignoring the potential for a variety of different reddening curves (an effect that may cause the flatter slope seen in Figure 4.16), the dust correction itself can introduce significant uncertainties, especially for the faint SFGs at high redshifts. Although infrared measurements are mostly optically thin, their usefulness is limited by both source confusion and the inability to be performed on the surface of the Earth because of an opaque atmosphere. This requires space-based observatories, which are expensive and difficult to maintain. Radio emission is not affected by the presence of intervening dust and is easily observable at low lying areas on Earth. The next generation of radio interferometric

telescopes are beginning to become operational, offering orders of magnitude of improvement in terms of sensitivity when compared with conventional instruments. These instruments will be able to reveal a new volume of the Universe in a regime that may offer a superb, unbiased view of the SFH at its earliest epochs.

This dissertation explored the SEDs of samples of LIRGs and ULIRGs across radio, infrared, and optical wavelengths, with an emphasis of understanding the physical processes that make up their radio continuum. These objects, with their exceptionally high SFR, are local objects selected to be representative of the types of SFGs expected to be observed in the high redshift Universe with the SKA and its pathfinder instruments. Although radio-continuum emission is impervious to the effects of dust attenuation, it only offers an indirect method of measuring SFR. At low rest frame frequencies ( $\nu < 2$  GHz), which are the frequencies where most contemporary telescopes operate, the radio continuum is made up of predominately non-thermal synchrotron emission. This type of emission is generated by relativistic electrons accelerating along magnetic field lines. Such electrons can be produced in the shocks of supernova, which gives a mechanism from which the rate of HMS formation can be indirectly measured.

The use of synchrotron emission as a tracer of star formation is complicated because of several factors. Importantly, synchrotron emission is a process that is not exclusive to star formation. AGN are another source of synchrotron emission. If there is a AGN in a galaxy producing synchrotron emission, then the radio continuum cannot be used as an SFR tracer without first characterising the contribution of AGN. Second, SFR tracers at low rest frame radio frequencies have to be calibrated against other SFR tracers. Commonly, this is done using the FRC, which denotes a tight linear relationship spanning many orders of magnitude between radio and infrared luminosities. Although calibrated well in the local Universe (Yun et al., 2001; Bell, 2003), it is unknown how the FRC will evolve with increasing redshifts, with evidence both confirming (Calistro Rivera et al., 2017) and rejecting (Mao et al., 2011) its evolution. Further, it is a non-instantaneous tracer of star formation that may be delayed by upwards of  $10^7$  years Condon (1992), and at higher frequencies, suppression because of inverse-Compton losses can further perturb its typical spectrum.

An alternative to synchrotron emission as a tracer of SFR in the radio continuum is thermal free-free emission. Produced by ionised HII regions, free-free emission is a near-instantaneous measure of SFR. With increasing frequencies, it becomes a larger component of the observed radio continuum. With increasing redshifts, this means that it is becoming a larger component of the observed radio continuum. Inverse-Compton losses should also suppress synchrotron emission in proportion to  $(1+z)^4$ , further highlighting the need to understand the thermal free-free component.

In Chapter 2, I investigate the radio-continuum emission of 12 ULIRGs. Using data from the ATCA from 2.1 to 9.0 GHz and available measurements from the literature, the synchrotron and free-free emission radio-continuum components were modelled and separated using least square optimisation methods. Examining the decomposed components showed that they formed trends similar to the typical FRC. With sufficient data, this suggests that SFR tracers could be calibrated as a function of frequency and redshift. Similar trends were also seen when comparing the observed spectral index of the radio continuum to the modelled thermal fraction of the same sources. Depending on their relative proportions, the steep spectrum synchrotron emission and the flat spectrum free-free emission can have a predictable total spectral index. This comparison also showed that the thermal fraction could be predicted with larger certainty across different assumed synchrotron spectral indices as the total spectral index becomes flatter. A flatter total spectral index indicates a higher thermal fraction.

Exploring various dimensions of the constrained models and their derived properties showed that the thermal fraction of 26 objects appears to have a multi-modal distribution as a function of the  $q$  parameter (Figure 2.14). Exploring the literature, Marvil et al. (2015) equated the two quantities together via calibrated SFRs measures and predicted an increase in the thermal fraction as a function of  $q$ . Marvil et al. (2015) highlighted that this relation source, which would classically be defined as radio excess, could also be interpreted as having a low thermal fraction. Investigating this further, the scatter of the thermal fraction as a function of the  $q$  parameter could be replicated by using an assumed SFH, with an initial burst of star formation with exponential decay and different timescale offsets for each of the emission processes for free-free, synchrotron, and far-infrared emission. Within this framework, it would be possible to estimate the age of a starburst with relatively little information across its SED. Quantifying errors with this approach requires a larger sample of objects with additional methods of estimating the starburst age.

Although the synchrotron and free-free emission components were separated to the first order, associated uncertainties, particularly for free-free emission, were relatively high. To observe the flat spectral shape of free-free emission ( $\alpha = -0.1$ ) requires a broadband and densely sampled SED. Given the  $0.2 < z < 0.5$  range of these objects, a large amount of telescope time would be required to obtain the sensitive radio-continuum observations. It was also noted that the GLEAM survey (Wayth et al., 2015) would not have the sensitivity to detect these objects.

A secondary sample of 20 LIRGs was selected with the long-term aim of characterising their broadband SED from 80 MHz to upwards of  $\sim 90$  GHz. This sample was constructed by initially selecting bright Infrared (IR) objects without signs of AGN activity and enforcing a redshift

range of  $0.067 < z < 0.227$ , which would facilitate ground-based follow up of the Pa $\alpha$  emission line. Competitive time on the ATCA telescope was awarded to cover 2.1 to 90 GHz for these sources. In conjunction with data from the GLEAM catalogue (Hurley-Walker et al., 2017), which has 20 flux density measures covering 72 to 231 MHz, these SEDs values were densely sampled from 80 MHz to 48 GHz (in the observed frame), with near-continuous coverage from 1.1 to 20 GHz. Although high frequency 3 mm data ( $\sim 90$  GHz) were taken, they were ultimately discarded as an adequate calibration solution could not be derived.

These data represent some of the most densely sampled radio continuum of SFGs in the literature. Using sophisticated Bayesian modelling techniques, their SEDs values were fitted with a series of increasingly complex physical models. To prevent overfitting, the Bayes factor was used to infer the model most supported by evidence. Over such a large frequency range, it was found that a simple power-law or two-component synchrotron and free-free model rarely characterised the data well. At low frequencies ( $\nu < 1$  GHz) a turnover caused by FFA was often either constrained or supported by the MWA GLEAM measurements.

Similarly, at higher frequencies, there was often a kink or steepening observed. In such cases, the modelling tended towards a secondary component of FFA with a high EM. Such complexity has been observed in a similar set of LIRGs and ULIRGs by Clemens et al. (2010) and by Anantharamaiah et al. (2000) in their study of the starburst Arp 220.

Physically speaking, these turnovers suggest that there are at least two distinct regions of star formation that the large radio synthesised beam integrates over. The effects of free-free absorption, specifically where optically unity is reached, are directly related to the line-of-sight depth and density of the intermingled volume relativistic and thermal free electrons. The more compact or ‘deep’ the volume, the higher the turnover frequency will become. When unresolved, these features are expressed as flattening, kink like components.

A more complete SED and more sophisticated modelling approach can better characterise and separate the synchrotron and free-free components that make up the radio continuum for these sources when compared to the sample of ULIRGs studied in Chapter 2. Comparing these constrained quantities with total infrared ( $8 - 1000 \mu\text{m}$ ) luminosities from Wang et al. (2014), similar FRC trends were obtained. Given the broadband SEDs, these could also be examined as a function of frequency, where it was shown that at higher frequencies, the FRC like trends against the synchrotron and free-free components steepened with their  $q$  parameters increasing.

Included in these models as a free parameter was the spectral index of synchrotron emission. For some sources, there were two such free parameters, with each being tied to a different emission component. Typically, the spectral index synchrotron emission is taken to be  $-0.8$  (Condon and Yin, 1990; Condon, 1992), yet these indices were found to be steeper, with the

average being  $-1.06$ . This steepening is unlikely to be caused by electron cooling caused by IC losses as all sources are at relatively low redshift ( $z < 0.227$ ) and are competing against other losses (Lacki et al., 2010; Lacki and Thompson, 2010). FIR is a more instantaneous tracer of star formation compared with synchrotron emission; it is not likely that this steepening is caused by spectral ageing. A potential explanation is that the intrinsic cosmic ray power-law index is steeper. Wang and Fields (2016) suggest that this could be the case for starburst objects, a conclusion that is made based on GeV and TeV observation. Lacki et al. (2010) suggest that ‘puffy’ type starbursts, whose volume density is far less than compact starbursts, could also exhibit steeper than expected cosmic ray power laws.

To correctly interpret the radio emission of the types of SFGs expected in the high redshift Universe in the SKA era, it is necessary to understand the complex broadband nature of SFGs. Evidence from this dissertation suggests far more complex behaviour than what is typically exhibited in more local objects with far less star formation. It will be critical to developing newer methods that can fully utilise alternate methods of calibrating and characterising star formation from radio signatures that are separated from the uncertainties of the FRC. The secondary component of this thesis involved exploring how this could be done using optical spectroscopy.

For the sample of LIRGs whose radio-continuum modelling makes up Chapter 3, competitive time was awarded over five nights on the ANU 2.3 m optical telescope WiFeS. This IFU provided a  $36'' \times 25''$  field of view with spectral coverage from 3300 to 9000 Å and a spectral resolution of  $R \sim 3000$ . The goal of these data was to obtain a strong measure of the Balmer series of optical lines, including the  $H\alpha$  and  $H\beta$  transitions which could be used to constrain SFR measurements. To improve the signal of these transitions, an aperture was constructed for each source using multi-Gaussian expansion (Cappellari, 2002) which was used to sum all spaxels, producing one-dimensional spectral.

For these one-dimensional spectra, the PPXF modelling code was used to constrain the stellar continuum and capture the optical emission of absorption profiles. A powerful component of PPXF is its ability to also contain measures of the LOSVD that can affect the continuum and transition features in different ways. Bootstrapping analysis was used to obtain reliable measures of these constrained quantities.

Balmer decrement was used to estimate and correct the effects of dust attenuation. This approach compares the observed  $H\alpha/H\beta$  ratio with an expected one. For SFGs, this expected ratio is 2.86 assuming case B recombination, a temperature of  $T = 10^4$  K, and an electron density of  $n_e = 10^2 \text{ cm}^{-3}$  (Osterbrock, 1989). These ratios are used together to derive a colour excess term,  $E(B - V)$ , which describes the reddening across the spectrum. PPXF can



also constrain a colour excess term by using the stellar continuum of optical spectra. The stellar continuum comprises an older population of stars, whereas the Balmer transition is associated with regions of ionised gas, making these colour excess terms distinct from one another. Depending on the distribution of gas, dust, and star formation, the Balmer transition and stellar continuum can be significantly different from one another and are not easily relatable with numerical approximations.

Calzetti (1997) observed a trend between these two colour excess terms, where  $E(B - V)_{\text{star}} = 0.44 (\pm 0.02) \times E(B - V)_{\text{gas}}$ . By comparing the colour excess terms of the 19 objects in the LIRG sample obtained using the stellar continuum constrained with PPXF and the Balmer decrement method, I observed a much flatter trend of  $E(B - V)_{\text{star}} = 0.18 (\pm 0.02) \times E(B - V)_{\text{gas}}$ . A notable difference between the two samples is that the SFGs that make up the secondary LIRG sample are much more luminous than those from Calzetti (1997). This agrees with the prediction made by Babbedge et al. (2005), who used photometric redshift codes and found that dusty starburst galaxies, like those observed with the WiFeS instrument in this dissertation, have a trend of  $E(B - V)_{\text{star}} = 0.25 (\pm 0.02) \times E(B - V)_{\text{gas}}$ . Potentially, the difference between these colour excess quantities of the LIRG sample are genuine and not an artefact of poorly constrained  $\text{H}\alpha$  and  $\text{H}\beta$  lines. Exploring this further will require additional observations, as even after integrating across an aperture, some sources have weak lines and can produce a highly ill-constrained  $\text{H}\alpha/\text{H}\beta$  ratio whose errors are propagated to the colour excess  $E(B - V)_{\text{gas}}$  term.

Using the obtained  $\text{H}\alpha/\text{H}\beta$  ratios produced with PPXF (along with uncertainties constructed using bootstrapping analysis), a dust corrected  $\text{H}\alpha$  luminosity was estimated for each object. This was performed assuming the Calzetti et al. (2000) reddening curve. Comparing the SFRs derived using the observed and estimated intrinsic  $\text{H}\alpha$  luminosities shows an increase of about an order of magnitude across the sample. Based on the bootstrapping analysis of the PPXF modelled quantities, many of the estimates of the SFR based on the intrinsic  $\text{H}\alpha$  luminosity have a highly asymmetrical distribution, which has likely been introduced by an imbalanced  $\text{H}\alpha/\text{H}\beta$  distribution. These dust corrected SFR measures do not include the systematic uncertainty from Calzetti et al. (2000), which could increase or decrease each SFR by a factor of two. Because of an undetected  $\text{H}\beta$  line, the dust correction for IRASF18582–5558 could not be performed. Otherwise, 12 of the 19 objects had dust corrected SFRs over  $100 M_{\odot} \text{ yr}^{-1}$ .

An aperture for each source was created to improve the SNR of the one-dimensional spectra of each source. In doing so, the structure resolved by WiFeS was lost. To investigate whether the multiple radio-continuum turnover components could be correlated to optically resolved structures (particularly those traced by  $\text{H}\alpha$  emission, which is produced by the same emitting matter as free-free radio emission), the PPXF method was executed against each of the 1,900

spaxels for all sources. Exploring these resolved PPXF parameter maps shows that for many sources, resolved regions seem to appear with more luminous  $H\alpha$  emission. IRAS F00198–7926, one of the brighter objects in the LIRG sample, shows a wide, diffuse region of  $H\alpha$  emission with a dense clump in its centre (Figure 4.19). Care has to be taken when interpreting these as because of computation limitations, bootstrapping analysis cannot be performed on each of the individual 11,900 spaxels. To illustrate the importance of characterising these uncertainties, the resolved  $H\alpha$  and  $H\beta$  integrated fluxes of IRAS F02364–4751 are shown in Figure 4.22. For this source, it appears that there is no discernible  $H\beta$  component. Such situations can cause the  $H\alpha$  luminosity to be overcorrected. Examining the resolved SFR map of this source (Figure 4.24) shows that the bulk of its  $127 M_{\odot} \text{ yr}^{-1}$  is produced by eleven pixels.

As a compromise between retaining spatial information while being able to perform the required bootstrapping analysis to characterise PPXF uncertainties, a  $4 \times 4$  gridding kernel was used to sum adjacent spaxels. This allowed a set of trials to be performed for each summed set of spaxels so that a measure of the reliability of these resolved quantities could be made. The gridded set of spaxels showing the  $H\alpha$  and  $H\alpha/H\beta$  quantities for IRAS F00198–7926 is shown in Figures 4.20 and 4.21. Because of the low signal, no reliable characterisations can be made for the  $H\alpha/H\beta$  ratio across the bootstrapping trials, meaning no dust correction can be made. As IRAS F00198–7926 is one of the brighter objects in the sample, and it is unlikely this type of analysis can be carried out with the current set of WiFeS data. It is hoped that future observations, whether deeper integrations on WiFeS or near-IR observations using the SINFONI instrument on the VLT, will be able to characterise potential dust attenuation better and obtain a more reliable measure of star formation and its spatial distribution.

One of the fundamental goals of this dissertation was to investigate how the decomposed radio-continuum components could be correlated with other measures of star formation independent of the FRC and assess their reliability. Using information from modelling the radio continuum of an initial sample of 12 ULIRGs (Chapter 2), a secondary set of 20 LIRGs was selected (Chapter 3). Using data from the literature and awarded telescope time from ATCA, the radio continuum included dense samples and was modelled with sophisticated Bayesian inference methods to separate synchrotron and free-free radio emission components. Connecting these components to the optical measures of star formation obtained from the optical spectroscopic data collected with WiFeS would provide a measure independent from the FRC capable of assessing and calibrating radio SFR measures for the types of SFGs expected in the high redshift volume of the Universe.

An initial comparison between radio, infrared, and optical SFR measures showed that broadly the radio and infrared tracers agreed reasonably well (Figure 5.1). Any relations that

included an SFR based on a dust corrected  $H\alpha$  luminosity showed no statistically significant trend. This was observed by examining the gradient between the trends and the Pearson coefficient, both of which were consistent with noise with a slight positive gradient (Table 5.1). Trends that included an estimate of SFR using a 1.4 GHz luminosity extrapolated from the 843 MHz SUMSS measurement of each source were positive. Their gradients were each around  $\sim 0.45 \pm 0.1$ , with a Pearson coefficient of  $\sim 0.7$ . The remaining comparisons incorporated some measure of the total infrared luminosity (including the SFR based on the IR and  $H\alpha$  composite tracer). Naturally, these were the strongest trends of the entire set.

Comparing the decomposed radio components across a broad range of frequencies directly with the dust corrected  $H\alpha$  luminosities showed weak, positive trends between the synchrotron and the total radio luminosities (Figure 5.3). These are only tentative as the presence of outliers and a small luminosity range prohibit a meaningful set of trends to be robustly constrained. All comparisons that included the free-free luminosity, although consistent with noise, tended towards an anti-correlation with the dust corrected  $H\alpha$  luminosities judged by both the constrained gradient and range of Pearson coefficients. These should be the strongest trends as the same ionised material produces both the  $H\alpha$  and free-free continuum emission.

Potential second order effects were explored to explain whether there were systematic effects or physical influences causing the scatter. Examining the estimated luminosities without the effects of free-free absorption failed to improve the comparison (Figure 5.4). Similarly, an exhaustive search across additional properties, including the thermal fraction, colour excess terms, free-free absorption produced turnovers, radio spectral indices, and estimated masses (as modelled by Wang et al., 2014), failed to reveal any likely physical basis for the lack of correlation. Exploring these trends as a function of the composite SFR (which is the combination of the uncorrected  $H\alpha$  and total infrared luminosities) instead of the dust corrected luminosity produced similar results.

It was unexpected that no robust trends were present in these comparisons. Determining the exact cause of this discrepancy requires newer datasets. A physical explanation could be that these LIRGs are especially dusty, making the optical depth of  $H\alpha$  larger than one. The Balmer decrement will be unable to correct for the  $H\alpha$  flux so heavily embedded in dust that it is obscured.  $P\alpha\alpha$  would be a better method of obtaining a more reliable measure of SFR for these regions as it is less affected by intervening dust. Although it is possible that the radio luminosities are erroneous, it is unlikely as they form FRC like trends with the total infrared luminosities (Figure 3.8).

Even ignoring the potential of  $H\alpha$  with an unrecoverable optical depth, the dust correction itself carries a large degree of uncertainty. Typical properties assumed for the case of SFGs,

including temperature and electron densities, may not be appropriate for the types of starbursts this LIRG sample represents (Figure 5.8). When coupled with a potentially different reddening curve, as suggested by Figure 4.16, recovering an accurate intrinsic measure of the total  $H\alpha$  luminosity may not be a straight forward task. More broadband SED modelling approaches may be more appropriate. Toolkits similar to MAGPHYS (da Cunha et al., 2008) would be a future piece of work that may be able to constrain internal measures like  $H\alpha$  more accurately.

Alternatively, rather than there being a physical basis, the issue may be with the data obtained by WiFeS and its quality. Checks of the relative scaling between the blue and red arms show they are consistent, and checks comparing constrained lines with measures available in the literature indicate that the absolute flux scale applied was reasonable. There could be faint regions of diffuse star formation that the current data are not sensitive enough to detect. Constructing an aperture over the incomplete surface may lead to a lack of correlation in which case, longer integration times on these sources would be required.

Tentative comparisons were made between the resolved dust corrected  $H\alpha$  luminosity obtained from WiFeS IFU data of IRAS F00198–7926 and its radio continuum. The resolved optical data suggested a luminous clump of emitting matter with a high SFR and a broader diffuse component with a lower SFR (Figure 5.9). Bayesian modelling shows that the radio-continuum spectrum was best described as a combination of two individual FFA components with distinct EMs. This could suggest a scenario where the luminous  $H\alpha$  clump, having a much smaller volume with more intense star formation, could be driving the high EM turnover in the radio-continuum spectrum, with a more diffuse region of star formation contributing to the low frequency turnover. Confirming this scenario would require a more reliable measure of the resolved regions of star formation using either  $H\alpha$  or  $P\alpha\alpha$ , which both trace the same emitting matter as free-free emission.

## 6.1 Future work

Obtaining a robust measure of the SFH of the Universe requires a strong, fundamental understanding of starburst galaxies at high redshifts and how star formation is expressed. My work in this thesis shows that the broadband radio continuum of intense SFGs is not as simple as traditionally thought. Non-thermal synchrotron emission is a volatile emission process that, although has worked reasonably well for the local Universe, makes extrapolating current radio-continuum SFR indicators to the high- $z$  Universe difficult. The uncertainty of how the FRC scales with redshift requires other methods to be considered to evaluate how radio-based SFR measures can be crafted and evaluated.

Maximising the scientific output of the sample of LIRGs studied throughout this thesis requires near-infrared measurements of the Pa $\alpha$  recombination line. Analysis of the optical spectroscopy obtained with the WiFeS instrument suggests that these objects have complex dust distributions which make correcting for its effects difficult. Typical corrections following the Balmer decrement appear to be unable to correctly describe the intrinsic H $\alpha$  luminosity, as assessed by the poor correlation of various SFR measures and comparisons with the decomposed radio-continuum components. Seeking time on a facility with an IFU and resolution to spatially isolate discrete regions of star formation would be ideal. In combination with collaborators, we are seeking time on the SINFONI instrument on the VLT. These data will help understand the physical conditions that may be producing the higher-order spectral features observed in the radio continuum of these objects.

High frequency radio observations above rest frame frequencies of 10 GHz may offer the key to crafting updated, robust SFR tracers compatible with the next generation of radio-continuum surveys. Such data offer a window into the thermal free-free emission that directly traces current SFR. Investigating this type of emission offers several advantages. For objects at higher redshifts, the observed radio continuum is made up of a larger thermal free-free component. The steep spectrum synchrotron quickly becomes a small component of the rest frame radio continuum. Inverse-Compton losses should further suppress the observed synchrotron emission.

Results and lessons learnt from this thesis have helped develop experiments to further understand the high frequency radio continuum of starburst objects. As a principal investigator, I am leading two projects using ATCA that are exploring the high frequency tracers of star formation.

As a direct test of the FRC, a total of 143 hours have been awarded and have been used to observe the radio continuum at 33 and 35 GHz in a sample of 375 objects. At these frequencies, free-free emission contributed upwards of  $\sim 40\%$  of the total radio continuum (Figure 3.10). With a large sample, the FRC can reliably be constrained. If this free-free emission is not affected by IC scattering and is relatively flat, it should be able to be used as a more reliable standard to calibrate radio SFR measures. In conjunction with lower frequency measurements, the remaining synchrotron component is isolated and removed.

The first semesters of observations have been reduced and used to produce an initial FRC at 34 GHz, which is included as Figure 6.1. To the data, a piecewise linear model was fit with the break luminosity being included as a free parameter. There is a strong relation for luminosities above  $L_{60\mu m} > 10^{10} L_{\odot}$  with a well constrained gradient of  $1.3 \pm 0.1$ . At lower luminosities, the correlation is tentative, where the gradient is  $0.8 \pm 0.3$ . This is consistent with the flattening inferred by Bell (2003), where escaping cosmic rays from small galaxies cause the synchrotron

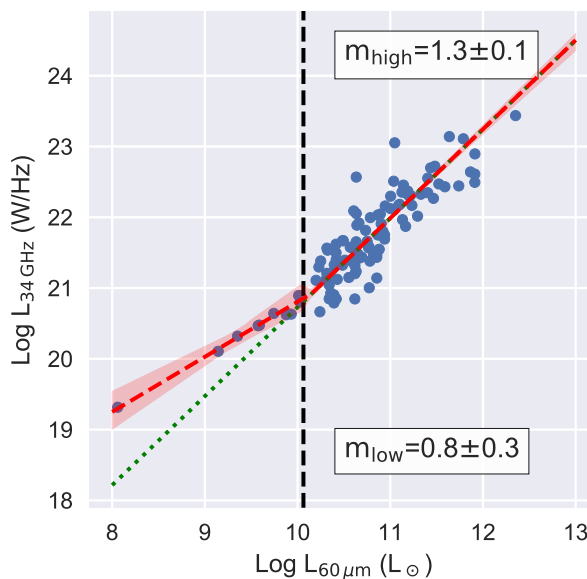


Figure 6.1: The observed far-infrared to radio correlation at 34 GHz. A two-component model has been constrained to the available data.

emission to be under-representative of the true SFR.

Absent from Figure 6.1 are the data taken from a second semester of observations, flux density uncertainties, and upper limits on the non-detections. In conjunction with lower frequency data at 0.83, 1.4, 5.5, and 9.0 GHz of these sources (the majority of which is collected as part of this project or available in the literature), it is planned that the change in observable properties of the FRC could be used to marginalise over average radio SED. The change in normalisation, gradient, and scatter of the FRC across a set of frequencies could be used to attempt to constrain an assumed starburst SED. Incorporating additional dimensions (e.g. redshifts, stellar mass, colour excess terms) may allow for greater understanding of the processes that drive the FRC and where they may break down.

An additional programme using ATCA that I am leading aims to survey the quarter square degree Extended *Chandra* Deep Field South (ECDFS) field at 8.5 GHz down to an RMS of  $2.9 \mu\text{Jy}/\text{beam}$ . Using Square Kilometer Array Design Simulation (SKADS) (Wilman et al., 2008), it is estimated that this programme will detect more than 200 SFGs up to a redshift of three. The ECDFS is a key legacy field that is being targeted by many instruments, including ALMA, the VLT, MeerKAT, and Euclid. One of the goals of this programme is to use the wealth of radio-continuum data to perform broadband SED fitting to isolate the free-free component of a large sample of objects across a meaningful redshift range. These decomposed components will be used as the basis for updated radio SFR measures which can be calibrated against the superb multi-wavelength data of the field.

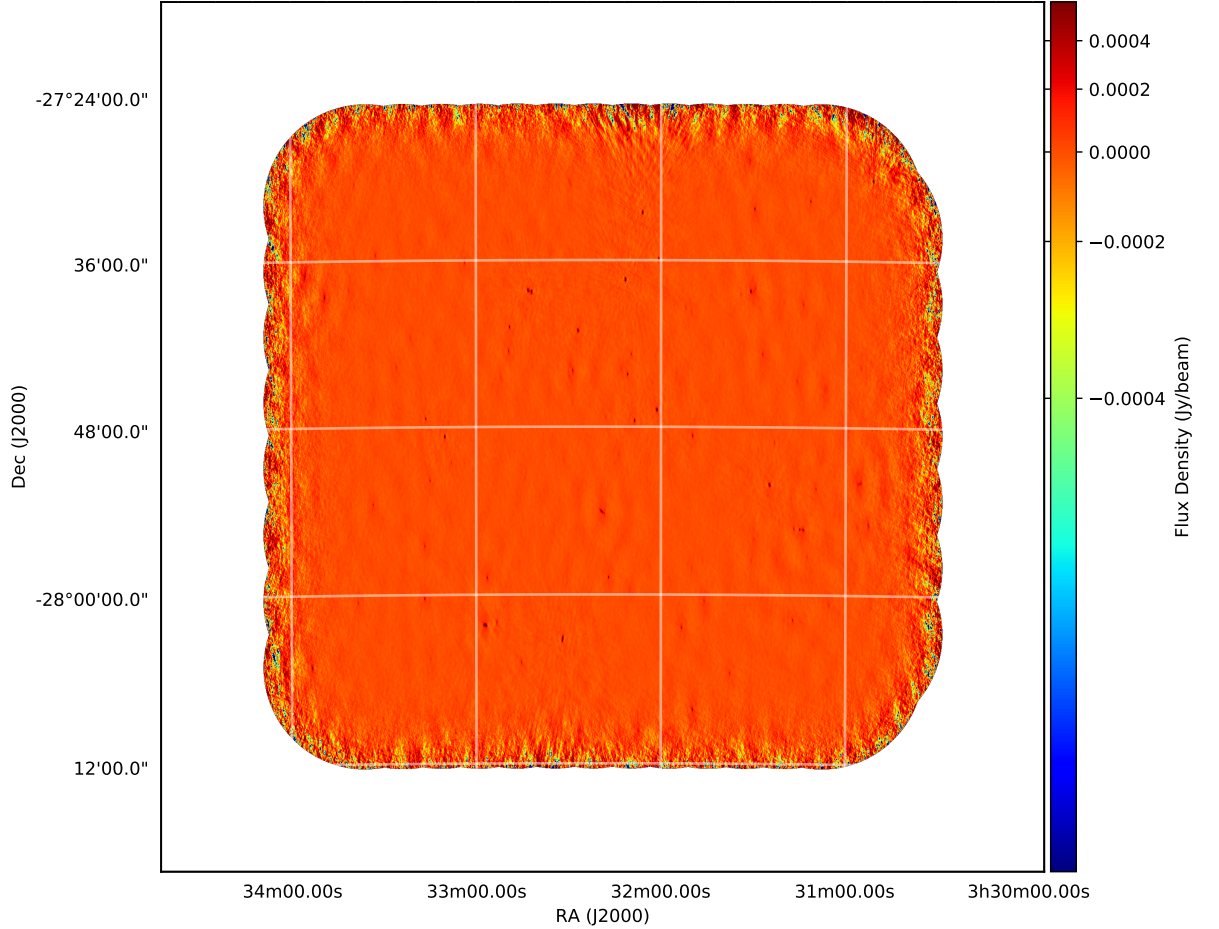


Figure 6.2: An image of the ECDFS at 8.5 GHz. Its RMS varies between 8 to 10  $\mu\text{Jy}/\text{beam}$  across the field.

This is an ongoing project that so far has been awarded 240 hours of competitive time on ATCA. At present, these data have been observed and reduced to create an image whose RMS varies across the field between 8 to 10  $\mu\text{Jy}/\text{beam}$ , from which 83 sources at a  $5\sigma$  level. Source completeness tests have also been performed, and it is estimated that all sources above 150  $\mu\text{Jy}/\text{beam}$  have been detected. By calculating the Euclidean normalised source counts and by comparing with the predictions made by SKADS, the faint SFGs are beginning to be detected (Figure 6.3).

It is hoped that it may be continued as a legacy programme to integrate on the field down to an eventual RMS of 1.1  $\mu\text{Jy}/\text{beam}$ . If successful, this will complement the planned legacy programmes to be performed on MeerKAT that target this field (Jarvis et al., 2016).

During my candidature, the Australia Telescope National Facility (ATNF) called for the community to submit ATCA legacy proposals. These were programmes that required at least 2000 hours of telescope time whose data would create a lasting and meaningful impact on the astronomy community. One of the successful programmes is the GAMA Legacy ATCA Southern

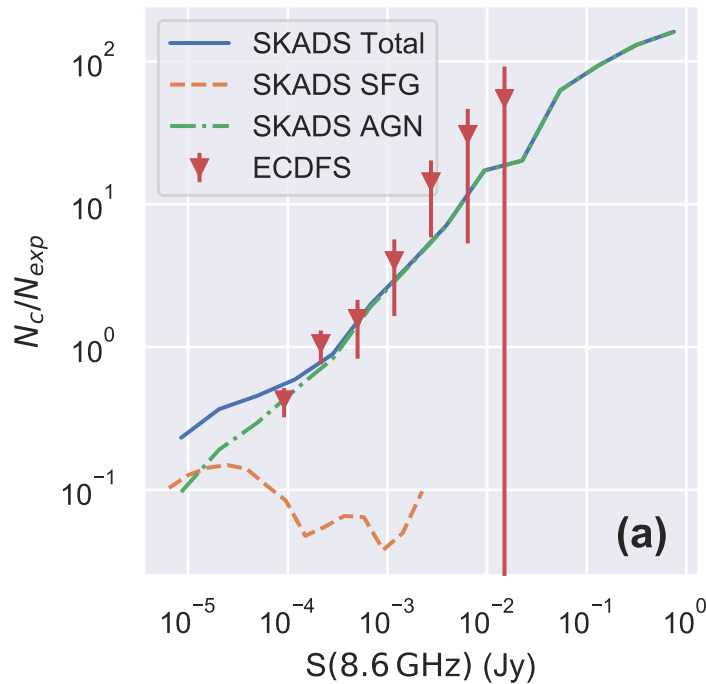


Figure 6.3: The source counts of objects detected in deep 8.5 GHz image of the ECDFS shown as Figure 6.2. Completeness corrections have been applied.

Survey (GLASS). GLASS is observing the 60 degree<sup>2</sup> Galaxy and Mass Assembly (GAMA) G23 field at 5.5 and 9.0 GHz. Across  $\sim 3000$  telescope hours, the survey aims to reach a  $1\sigma$  RMS of  $30 \mu\text{Jy}/\text{beam}$ , enabling for a large population of AGN and SFG sources to be detected.

The G23 field has been extensively studied, not only at radio wavelengths by MWA GLEAM, SUMSS, NVSS, and ASKAP, but also at optical and infrared bands. This allows detailed broadband SED modelling. For instance, Davies et al. (2016) have used the field and its superb data to investigate various SFR tracers, their consistency, and conditions where they may break down. Using the dataset from GLASS, the radio continuum of detected SFGs will be able to be decomposed into the synchrotron and free-free components. These derived properties can then be included in such multi-wavelength analysis.

It is expected that with a  $\sim 30 \mu\text{Jy}/\text{beam}$  RMS, ULIRGs up to a redshift of 0.5 could be detected, and across the entire 60 degrees<sup>2</sup> field, there will be approximately 2500 SFGs. Once this survey is completed, this represents an excellent opportunity to perform broadband radio-continuum decomposition to estimate the synchrotron and free-free components, which can then be examined by other multi-wavelength information.

The SKA era of radio astronomy will be capable of probing the faint SFGs at the earliest epoch of the Universe, a volume that conventional instruments are blind to. Work throughout this dissertation shows that these objects are complex and very different from the typical SFGs



in the local Universe. Scaling existing SFR radio measures will not be a straight forward problem. Crafting more appropriate measures will require a stronger understanding of the free-free emission process that is often overlooked at low frequencies. With a stronger handle on this component, it will be possible to assess how well the FRC behaves at higher redshifts and allow for an independent method of calibrating SFR. It will be interesting to see, once the SKA pathfinders begin operating as designed, how well the local Universe scale is now understood, even if only to a modest redshift.

## Bibliography

- Adelberger, K. L. and Steidel, C. C. (2000). Multiwavelength Observations of Dusty Star Formation at Low and High Redshift. *ApJ*, 544:218–241.
- Allen, D. A., Norris, R. P., Meadows, V. S., and Roche, P. F. (1991a). A large sample of southern IRAS galaxies - Spectral classes and superclustering. *MNRAS*, 248:528–543.
- Allen, D. A., Norris, R. P., Meadows, V. S., and Roche, P. F. (1991b). A large sample of southern IRAS galaxies - Spectral classes and superclustering. *MNRAS*, 248:528–543.
- Alonso-Herrero, A., Rieke, G. H., Rieke, M. J., Colina, L., Pérez-González, P. G., and Ryder, S. D. (2006). Near-Infrared and Star-forming Properties of Local Luminous Infrared Galaxies. *ApJ*, 650:835–849.
- Ambikasaran, S., Foreman-Mackey, D., Greengard, L., Hogg, D. W., and O’Neil, M. (2014). Fast Direct Methods for Gaussian Processes and the Analysis of NASA Kepler Mission Data.
- Anantharamaiah, K. R., Viallefond, F., Mohan, N. R., Goss, W. M., and Zhao, J. H. (2000). Starburst in the Ultraluminous Galaxy Arp 220: Constraints from Observations of Radio Recombination Lines and Continuum. *ApJ*, 537:613–630.
- Andreani, P., Fosbury, R. A. E., van Bemmell, I., and Freudling, W. (2002). Far-infrared/millimetre emission in 3C sources. Dust in radio galaxies and quasars. *A&A*, 381:389–400.
- Baars, J. W. M., Genzel, R., Pauliny-Toth, I. I. K., and Witzel, A. (1977). The absolute spectrum of CAS A - an accurate flux density scale and a set of secondary calibrators. *A&A*, 61:99–106.
- Babbedge, T. S. R., Whitaker, R., and Morris, S. (2005). Can a photometric redshift code reliably determine dust extinction? *MNRAS*, 361:437–450.
- Bell, E. F. (2003). Estimating Star Formation Rates from Infrared and Radio Luminosities: The Origin of the Radio-Infrared Correlation. *ApJ*, 586:794–813.
- Bell, E. F. and Kennicutt, Jr., R. C. (2001). A Comparison of Ultraviolet Imaging Telescope Far-Ultraviolet and H $\alpha$  Star Formation Rates. *ApJ*, 548:681–693.
- Bevington, P. R. (1969). *Data reduction and error analysis for the physical sciences*.
- Blanton, M. R., Bershadsky, M. A., Abolfathi, B., Albareti, F. D., Allende Prieto, C., Almeida, A., Alonso-García, J., Anders, F., Anderson, S. F., Andrews, B., and et al. (2017). Sloan

- Digital Sky Survey IV: Mapping the Milky Way, Nearby Galaxies, and the Distant Universe. *AJ*, 154:28.
- Bock, D. C.-J., Large, M. I., and Sadler, E. M. (1999). SUMSS: A Wide-Field Radio Imaging Survey of the Southern Sky. I. Science Goals, Survey Design, and Instrumentation. *AJ*, 117:1578–1593.
- Boggs, P. T. and Rogers, E. (1990). Orthogonal distance regression. In *Statistical analysis of measurement error models and applications: proceedings of the AMS-IMS-SIAM joint summer research conference*, volume 112, page 186. Contemporary Mathematics.
- Borne, K. D., Bushouse, H., Lucas, R. A., and Colina, L. (2000). Evidence for Multiple Mergers among Ultraluminous Infrared Galaxies: Remnants of Compact Groups? *ApJ*, 529:L77–L80.
- Braun, R., Popping, A., Brooks, K., and Combes, F. (2011). Molecular gas in intermediate-redshift ultraluminous infrared galaxies. *MNRAS*, 416:2600–2606.
- Buat, V. (1992). Global recent star formation in normal galaxies from a multiwavelength study - Comparison with their gas content. *A&A*, 264:444–454.
- Buat, V., Boselli, A., Gavazzi, G., and Bonfanti, C. (2002). Star formation and dust extinction in nearby star-forming and starburst galaxies. *A&A*, 383:801–812.
- Calistro Rivera, G., Williams, W. L., Hardcastle, M. J., Duncan, K., Röttgering, H. J. A., Best, P. N., Brügger, M., Chyży, K. T., Conselice, C. J., de Gasperin, F., Engels, D., Gürkan, G., Intema, H. T., Jarvis, M. J., Mahony, E. K., Miley, G. K., Morabito, L. K., Prandoni, I., Sabater, J., Smith, D. J. B., Tasse, C., van der Werf, P. P., and White, G. J. (2017). The LOFAR window on star-forming galaxies and AGNs - curved radio SEDs and IR-radio correlation at  $0 < z < 2.5$ . *MNRAS*, 469:3468–3488.
- Callingham, J. R., Gaensler, B. M., Ekers, R. D., Tingay, S. J., Wayth, R. B., Morgan, J., Bernardi, G., Bell, M. E., Bhat, R., Bowman, J. D., Briggs, F., Cappallo, R. J., Deshpande, A. A., Ewall-Wice, A., Feng, L., Greenhill, L. J., Hazelton, B. J., Hindson, L., Hurley-Walker, N., Jacobs, D. C., Johnston-Hollitt, M., Kaplan, D. L., Kudrayvtseva, N., Lenc, E., Lonsdale, C. J., McKinley, B., McWhirter, S. R., Mitchell, D. A., Morales, M. F., Morgan, E., Oberoi, D., Offringa, A. R., Ord, S. M., Pindor, B., Prabu, T., Procopio, P., Riding, J., Srivani, K. S., Subrahmanyam, R., Udaya Shankar, N., Webster, R. L., Williams, A., and Williams, C. L. (2015). Broadband Spectral Modeling of the Extreme Gigahertz-peaked Spectrum Radio Source PKS B0008-421. *ApJ*, 809:168.

- Calzetti, D. (1997). UV opacity in nearby galaxies and application to distant galaxies. In Waller, W. H., editor, *American Institute of Physics Conference Series*, volume 408 of *American Institute of Physics Conference Series*, pages 403–412.
- Calzetti, D. (2001). The Dust Opacity of Star-forming Galaxies. *PASP*, 113:1449–1485.
- Calzetti, D. (2013). *Star Formation Rate Indicators*, page 419.
- Calzetti, D., Armus, L., Bohlin, R. C., Kinney, A. L., Koornneef, J., and Storchi-Bergmann, T. (2000). The Dust Content and Opacity of Actively Star-forming Galaxies. *ApJ*, 533:682–695.
- Calzetti, D., Kennicutt, R. C., Engelbracht, C. W., Leitherer, C., Draine, B. T., Kewley, L., Moustakas, J., Sosey, M., Dale, D. A., Gordon, K. D., Helou, G. X., Hollenbach, D. J., Armus, L., Bendo, G., Bot, C., Buckalew, B., Jarrett, T., Li, A., Meyer, M., Murphy, E. J., Prescott, M., Regan, M. W., Rieke, G. H., Roussel, H., Sheth, K., Smith, J. D. T., Thornley, M. D., and Walter, F. (2007). The Calibration of Mid-Infrared Star Formation Rate Indicators. *ApJ*, 666:870–895.
- Calzetti, D., Kennicutt, Jr., R. C., Bianchi, L., Thilker, D. A., Dale, D. A., Engelbracht, C. W., Leitherer, C., Meyer, M. J., Sosey, M. L., Mutchler, M., Regan, M. W., Thornley, M. D., Armus, L., Bendo, G. J., Boissier, S., Boselli, A., Draine, B. T., Gordon, K. D., Helou, G., Hollenbach, D. J., Kewley, L., Madore, B. F., Martin, D. C., Murphy, E. J., Rieke, G. H., Rieke, M. J., Roussel, H., Sheth, K., Smith, J. D., Walter, F., White, B. A., Yi, S., Scoville, N. Z., Polletta, M., and Lindler, D. (2005). Star Formation in NGC 5194 (M51a): The Panchromatic View from GALEX to Spitzer. *ApJ*, 633:871–893.
- Calzetti, D., Kinney, A. L., and Storchi-Bergmann, T. (1994). Dust extinction of the stellar continua in starburst galaxies: The ultraviolet and optical extinction law. *ApJ*, 429:582–601.
- Calzetti, D., Wu, S.-Y., Hong, S., Kennicutt, R. C., Lee, J. C., Dale, D. A., Engelbracht, C. W., van Zee, L., Draine, B. T., Hao, C.-N., Gordon, K. D., Moustakas, J., Murphy, E. J., Regan, M., Begum, A., Block, M., Dalcanton, J., Funes, J., Gil de Paz, A., Johnson, B., Sakai, S., Skillman, E., Walter, F., Weisz, D., Williams, B., and Wu, Y. (2010). The Calibration of Monochromatic Far-Infrared Star Formation Rate Indicators. *ApJ*, 714:1256–1279.
- Cappellari, M. (2002). Efficient multi-Gaussian expansion of galaxies. *MNRAS*, 333:400–410.
- Cappellari, M. (2017). Improving the full spectrum fitting method: accurate convolution with Gauss-Hermite functions. *MNRAS*, 466:798–811.

- Cappellari, M. and Emsellem, E. (2004). Parametric Recovery of Line-of-Sight Velocity Distributions from Absorption-Line Spectra of Galaxies via Penalized Likelihood. *PASP*, 116:138–147.
- Cappellari, M., Scott, N., Alatalo, K., Blitz, L., Bois, M., Bournaud, F., Bureau, M., Crocker, A. F., Davies, R. L., Davis, T. A., de Zeeuw, P. T., Duc, P.-A., Emsellem, E., Khochfar, S., Krajnović, D., Kuntschner, H., McDermid, R. M., Morganti, R., Naab, T., Oosterloo, T., Sarzi, M., Serra, P., Weijmans, A.-M., and Young, L. M. (2013). The ATLAS<sup>3D</sup> project - XV. Benchmark for early-type galaxies scaling relations from 260 dynamical models: mass-to-light ratio, dark matter, Fundamental Plane and Mass Plane. *MNRAS*, 432:1709–1741.
- Chabrier, G. (2003). Galactic Stellar and Substellar Initial Mass Function. *PASP*, 115:763–795.
- Chabrier, G. (2005). The Initial Mass Function: From Salpeter 1955 to 2005. In Corbelli, E., Palla, F., and Zinnecker, H., editors, *The Initial Mass Function 50 Years Later*, volume 327 of *Astrophysics and Space Science Library*, page 41.
- Childress, M. J., Vogt, F. P. A., Nielsen, J., and Sharp, R. G. (2014). PyWiFeS: a rapid data reduction pipeline for the Wide Field Spectrograph (WiFeS). *Ap&SS*, 349:617–636.
- Clemens, M. S., Scaife, A., Vega, O., and Bressan, A. (2010). Starburst evolution: free-free absorption in the radio spectra of luminous IRAS galaxies. *MNRAS*, 405:887–897.
- Condon, J. J. (1992). Radio emission from normal galaxies. *ARA&A*, 30:575–611.
- Condon, J. J., Cotton, W. D., Greisen, E. W., Yin, Q. F., Perley, R. A., Taylor, G. B., and Broderick, J. J. (1998). The NRAO VLA Sky Survey. *AJ*, 115:1693–1716.
- Condon, J. J. and Yin, Q. F. (1990). A new starburst model applied to the clumpy irregular galaxy Markarian 325. *ApJ*, 357:97–104.
- Cortese, L., Boselli, A., Franzetti, P., Decarli, R., Gavazzi, G., Boissier, S., and Buat, V. (2008). Ultraviolet dust attenuation in star-forming galaxies - II. Calibrating the A(UV) versus  $L_{TIR}/L_{UV}$  relation. *MNRAS*, 386:1157–1168.
- Crocker, A. F., Calzetti, D., Thilker, D. A., Aniano, G., Draine, B. T., Hunt, L. K., Kennicutt, R. C., Sandstrom, K., and Smith, J. D. T. (2013). Quantifying Non-star-formation-associated 8  $\mu$ m Dust Emission in NGC 628. *ApJ*, 762:79.
- da Cunha, E., Charlot, S., and Elbaz, D. (2008). A simple model to interpret the ultraviolet, optical and infrared emission from galaxies. *MNRAS*, 388:1595–1617.

- da Cunha, E., Walter, F., Smail, I. R., Swinbank, A. M., Simpson, J. M., Decarli, R., Hodge, J. A., Weiss, A., van der Werf, P. P., Bertoldi, F., Chapman, S. C., Cox, P., Danielson, A. L. R., Dannerbauer, H., Greve, T. R., Ivison, R. J., Karim, A., and Thomson, A. (2015). An ALMA Survey of Sub-millimeter Galaxies in the Extended Chandra Deep Field South: Physical Properties Derived from Ultraviolet-to-radio Modeling. *ApJ*, 806:110.
- Davies, L. J. M., Driver, S. P., Robotham, A. S. G., Grootes, M. W., Popescu, C. C., Tuffs, R. J., Hopkins, A., Alpaslan, M., Andrews, S. K., Bland-Hawthorn, J., Bremer, M. N., Brough, S., Brown, M. J. I., Cluver, M. E., Croom, S., da Cunha, E., Dunne, L., Lara-López, M. A., Liske, J., Loveday, J., Moffett, A. J., Owers, M., Phillipps, S., Sansom, A. E., Taylor, E. N., Michalowski, M. J., Ibar, E., Smith, M., and Bourne, N. (2016). GAMA/H-ATLAS: a meta-analysis of SFR indicators - comprehensive measures of the SFR- $M_*$  relation and cosmic star formation history at  $z < 0.4$ . *MNRAS*, 461:458–485.
- de Jong, T., Klein, U., Wielebinski, R., and Wunderlich, E. (1985). Radio continuum and far-infrared emission from spiral galaxies - A close correlation. *A&A*, 147:L6–L9.
- de Zotti, G., Massardi, M., Negrello, M., and Wall, J. (2010). Radio and millimeter continuum surveys and their astrophysical implications. *A&A Rev.*, 18:1–65.
- DeBoer, D. R., Gough, R. G., Bunton, J. D., Cornwell, T. J., Beresford, R. J., Johnston, S., Feain, I. J., Schinckel, A. E., Jackson, C. A., Kesteven, M. J., Chippendale, A., Hampson, G. A., O’Sullivan, J. D., Hay, S. G., Jacka, C. E., Sweetnam, T. W., Storey, M. C., Ball, L., and Boyle, B. J. (2009). Australian SKA Pathfinder: A High-Dynamic Range Wide-Field of View Survey Telescope. *IEEE Proceedings*, 97:1507–1521.
- Dole, H., Lagache, G., Puget, J.-L., Caputi, K. I., Fernández-Conde, N., Le Floc’h, E., Papovich, C., Pérez-González, P. G., Rieke, G. H., and Blaylock, M. (2006). The cosmic infrared background resolved by Spitzer. Contributions of mid-infrared galaxies to the far-infrared background. *A&A*, 451:417–429.
- Domínguez, A., Siana, B., Henry, A. L., Scarlata, C., Bedregal, A. G., Malkan, M., Atek, H., Ross, N. R., Colbert, J. W., Teplitz, H. I., Rafelski, M., McCarthy, P., Bunker, A., Hathi, N. P., Dressler, A., Martin, C. L., and Masters, D. (2013). Dust Extinction from Balmer Decrements of Star-forming Galaxies at  $0.75 \leq z \leq 1.5$  with Hubble Space Telescope/Wide-Field-Camera 3 Spectroscopy from the WFC3 Infrared Spectroscopic Parallel Survey. *ApJ*, 763:145.
- Dopita, M., Hart, J., McGregor, P., Oates, P., Bloxham, G., and Jones, D. (2007). The Wide Field Spectrograph (WiFeS). *Ap&SS*, 310:255–268.

- Dopita, M., Rhee, J., Farage, C., McGregor, P., Bloxham, G., Green, A., Roberts, B., Neilson, J., Wilson, G., Young, P., Firth, P., Busarello, G., and Merluzzi, P. (2010). The Wide Field Spectrograph (WiFeS): performance and data reduction. *Ap&SS*, 327:245–257.
- Downes, D. and Solomon, P. M. (1998). Rotating Nuclear Rings and Extreme Starbursts in Ultraluminous Galaxies. *ApJ*, 507:615–654.
- Dressel, L. L. and Condon, J. J. (1978). The Arecibo 2380 MHz survey of bright galaxies. *ApJS*, 36:53–75.
- Duc, P.-A., Mirabel, I. F., and Maza, J. (1997). Southern ultraluminous infrared galaxies: an optical and infrared database. *A&AS*, 124.
- Eddington, A. S. (1927). The conditions of emission of forbidden lines. *MNRAS*, 88:134–138.
- Einstein, A. (1905). Über einen die Erzeugung und Verwandlung des Lichtes betreffenden heuristischen Gesichtspunkt. *Annalen der Physik*, 322:132–148.
- Engel, H., Davies, R. I., Genzel, R., Tacconi, L. J., Sturm, E., and Downes, D. (2011). Arp 220: Extinction and Merger-induced Star Formation. *ApJ*, 729:58.
- Farrah, D., Afonso, J., Efstathiou, A., Rowan-Robinson, M., Fox, M., and Clements, D. (2003). Starburst and AGN activity in ultraluminous infrared galaxies. *MNRAS*, 343:585–607.
- Farrah, D., Rowan-Robinson, M., Oliver, S., Serjeant, S., Borne, K., Lawrence, A., Lucas, R. A., Bushouse, H., and Colina, L. (2001). HST/WFPC2 imaging of the QDOT ultraluminous infrared galaxy sample. *MNRAS*, 326:1333–1352.
- Feroz, F., Hobson, M. P., and Bridges, M. (2009). MULTINEST: an efficient and robust Bayesian inference tool for cosmology and particle physics. *MNRAS*, 398:1601–1614.
- Fisher, K. B., Huchra, J. P., Strauss, M. A., Davis, M., Yahil, A., and Schlegel, D. (1995). The IRAS 1.2 Jy Survey: Redshift Data. *ApJS*, 100:69.
- Foreman-Mackey, D. (2016). corner.py: Scatterplot matrices in python. *The Journal of Open Source Software*, 24.
- Foreman-Mackey, D., Hogg, D. W., Lang, D., and Goodman, J. (2013). emcee: The MCMC Hammer. *PASP*, 125:306–312.
- Franzen, T. M. O., Jackson, C. A., Offringa, A. R., Ekers, R. D., Wayth, R. B., Bernardi, G., Bowman, J. D., Briggs, F., Cappallo, R. J., Deshpande, A. A., Gaensler, B. M., Greenhill, L. J., Hazelton, B. J., Johnston-Hollitt, M., Kaplan, D. L., Lonsdale, C. J., McWhirter, S. R.,

- Mitchell, D. A., Morales, M. F., Morgan, E., Morgan, J., Oberoi, D., Ord, S. M., Prabu, T., Seymour, N., Shankar, N. U., Srivani, K. S., Subrahmanyam, R., Tingay, S. J., Trott, C. M., Webster, R. L., Williams, A., and Williams, C. L. (2016). The 154 MHz radio sky observed by the Murchison Widefield Array: noise, confusion, and first source count analyses. *MNRAS*, 459:3314–3325.
- Galvin, T. J., Seymour, N., Filipović, M. D., Tothill, N. F. H., Marvil, J., Drouart, G., Symeonidis, M., and Huynh, M. T. (2016). Characterizing the radio continuum emission from intense starburst galaxies. *MNRAS*, 461:825–838.
- Gerhard, O. E. (1993). Line-of-sight velocity profiles in spherical galaxies: breaking the degeneracy between anisotropy and mass. *MNRAS*, 265:213.
- Gooch, R. (2011). Karma: Visualisation Test-Bed Toolkit. Astrophysics Source Code Library.
- Goodman, J. and Weare, J. (2010). Ensemble samplers with affine invariance. *Commun. Appl. Math. Comput. Sci.*, 5(1):65.
- Gregory, P. C., Scott, W. K., Douglas, K., and Condon, J. J. (1996). The GB6 Catalog of Radio Sources. *ApJS*, 103:427.
- Gregory, P. C., Vavasour, J. D., Scott, W. K., and Condon, J. J. (1994). The Parkes-MIT-NRAO (PMN) map catalog of radio sources covering  $-88$  deg less than  $\delta$  less than  $-37$  deg at 4.85GHz. *ApJS*, 90:173–177.
- Groves, B., Brinchmann, J., and Walcher, C. J. (2012). The Balmer decrement of Sloan Digital Sky Survey galaxies. *MNRAS*, 419:1402–1412.
- Gruppioni, C., Pozzi, F., Zamorani, G., Ciliegi, P., Lari, C., Calabrese, E., La Franca, F., and Matute, I. (2003). The radio-mid-infrared correlation and the contribution of 15- $\mu$ m galaxies to the 1.4-GHz source counts. *MNRAS*, 341:L1–L6.
- Gustafsson, B., Edvardsson, B., Eriksson, K., Jørgensen, U. G., Nordlund, Å., and Plez, B. (2008). A grid of MARCS model atmospheres for late-type stars. I. Methods and general properties. *A&A*, 486:951–970.
- Hambly, N. C., MacGillivray, H. T., Read, M. A., Tritton, S. B., Thomson, E. B., Kelly, B. D., Morgan, D. H., Smith, R. E., Driver, S. P., Williamson, J., Parker, Q. A., Hawkins, M. R. S., Williams, P. M., and Lawrence, A. (2001). The SuperCOSMOS Sky Survey - I. Introduction and description. *MNRAS*, 326:1279–1294.
- Han, Y. and Han, Z. (2012). Decoding Spectral Energy Distributions of Dust-obscured Starburst-Active Galactic Nucleus. *ApJ*, 749:123.



- Hancock, P. J., Murphy, T., Gaensler, B. M., Hopkins, A., and Curran, J. R. (2012). Compact continuum source finding for next generation radio surveys. *MNRAS*, 422:1812–1824.
- Hao, C.-N., Kennicutt, R. C., Johnson, B. D., Calzetti, D., Dale, D. A., and Moustakas, J. (2011). Dust-corrected Star Formation Rates of Galaxies. II. Combinations of Ultraviolet and Infrared Tracers. *ApJ*, 741:124.
- Helou, G. (1986). The IRAS colors of normal galaxies. *ApJ*, 311:L33–L36.
- Helou, G., Khan, I. R., Malek, L., and Boehmer, L. (1988). IRAS observations of galaxies in the Virgo cluster area. *ApJS*, 68:151–172.
- Helou, G., Soifer, B. T., and Rowan-Robinson, M. (1985). Thermal infrared and nonthermal radio - Remarkable correlation in disks of galaxies. *ApJ*, 298:L7–L11.
- Helou, G. and Walker, D. W., editors (1988). *Infrared astronomical satellite (IRAS) catalogs and atlases. Volume 7: The small scale structure catalog*, volume 7.
- Hildebrand, R. H. (1983). The Determination of Cloud Masses and Dust Characteristics from Submillimetre Thermal Emission. *QJRAS*, 24:267.
- Hopkins, A. M. (2004). On the Evolution of Star-forming Galaxies. *ApJ*, 615:209–221.
- Hopkins, A. M., Connolly, A. J., Haarsma, D. B., and Cram, L. E. (2001). Toward a Resolution of the Discrepancy between Different Estimators of Star Formation Rate. *AJ*, 122:288–296.
- Hughes, A., Staveley-Smith, L., Kim, S., Wolleben, M., and Filipović, M. (2007). An Australia Telescope Compact Array 20-cm radio continuum study of the Large Magellanic Cloud. *MNRAS*, 382:543–552.
- Hughes, A., Wong, T., and et al. (2006). A multiresolution analysis of the radio-FIR correlation in the Large Magellanic Cloud. *MNRAS*, 370:363–379.
- Hurley-Walker, N., Callingham, J. R., Hancock, P. J., Franzen, T. M. O., Hindson, L., Kapińska, A. D., Morgan, J., Offringa, A. R., Wayth, R. B., Wu, C., Zheng, Q., Murphy, T., Bell, M. E., Dwarakanath, K. S., For, B., Gaensler, B. M., Johnston-Hollitt, M., Lenc, E., Procopio, P., Staveley-Smith, L., Ekers, R., Bowman, J. D., Briggs, F., Cappallo, R. J., Deshpande, A. A., Greenhill, L., Hazelton, B. J., Kaplan, D. L., Lonsdale, C. J., McWhirter, S. R., Mitchell, D. A., Morales, M. F., Morgan, E., Oberoi, D., Ord, S. M., Prabu, T., Shankar, N. U., Srivani, K. S., Subrahmanyam, R., Tingay, S. J., Webster, R. L., Williams, A., and Williams, C. L. (2017). GaLactic and Extragalactic All-sky Murchison Widefield Array (GLEAM) survey - I. A low-frequency extragalactic catalogue. *MNRAS*, 464:1146–1167.

- Huynh, M. T., Hopkins, A. M., Lenc, E., Mao, M. Y., and et. al. (2012). The ATLAS 5.5 GHz survey of the extended Chandra Deep Field South: catalogue, source counts and spectral indices. *MNRAS*, 426:2342–2358.
- Ibar, E., Ivison, R. J., Biggs, A. D., Lal, D. V., Best, P. N., and Green, D. A. (2009). Deep multi-frequency radio imaging in the Lockman Hole using the GMRT and VLA - I. The nature of the sub-mJy radio population. *MNRAS*, 397:281–298.
- Ivison, R. J., Magnelli, B., Ibar, E., Andreani, P., Elbaz, D., Altieri, B., Amblard, A., Arumugam, V., Auld, R., Aussel, H., Babbedge, T., Berta, S., Blain, A., Bock, J., Bongiovanni, A., Boselli, A., Buat, V., Burgarella, D., Castro-Rodríguez, N., Cava, A., Cepa, J., Chagnial, P., Cimatti, A., Cirasuolo, M., Clements, D. L., Conley, A., Conversi, L., Cooray, A., Daddi, E., Dominguez, H., Dowell, C. D., Dwek, E., Eales, S., Farrah, D., Förster Schreiber, N., Fox, M., Franceschini, A., Gear, W., Genzel, R., Glenn, J., Griffin, M., Gruppioni, C., Halpern, M., Hatziminaoglou, E., Isaak, K., Lagache, G., Levenson, L., Lu, N., Lutz, D., Madden, S., Maffei, B., Magdis, G., Mainetti, G., Maiolino, R., Marchetti, L., Morrison, G. E., Mortier, A. M. J., Nguyen, H. T., Nordon, R., O’Halloran, B., Oliver, S. J., Omont, A., Owen, F. N., Page, M. J., Panuzzo, P., Papageorgiou, A., Pearson, C. P., Pérez-Fournon, I., Pérez García, A. M., Poglitsch, A., Pohlen, M., Popesso, P., Pozzi, F., Rawlings, J. I., Raymond, G., Rigopoulou, D., Riguccini, L., Rizzo, D., Rodighiero, G., Roseboom, I. G., Rowan-Robinson, M., Saintonge, A., Sanchez Portal, M., Santini, P., Schulz, B., Scott, D., Seymour, N., Shao, L., Shupe, D. L., Smith, A. J., Stevens, J. A., Sturm, E., Symeonidis, M., Tacconi, L., Trichas, M., Tugwell, K. E., Vaccari, M., Valtchanov, I., Vieira, J., Vigroux, L., Wang, L., Ward, R., Wright, G., Xu, C. K., and Zemcov, M. (2010). The far-infrared/radio correlation as probed by Herschel. *A&A*, 518:L31.
- Jarvis, M., Seymour, N., Afonso, J., Best, P., Beswick, R., Heywood, I., Huynh, M., Murphy, E., Prandoni, I., Schinnerer, E., Simpson, C., Vaccari, M., and White, S. (2015). The star-formation history of the Universe with the SKA. *Advancing Astrophysics with the Square Kilometre Array (AASKA14)*, page 68.
- Jarvis, M., Taylor, R., Agudo, I., Allison, J. R., Deane, R. P., Frank, B., Gupta, N., Heywood, I., Maddox, N., McAlpine, K., Santos, M., Scaife, A. M. M., Vaccari, M., Zwart, J. T. L., Adams, E., Bacon, D. J., Baker, A. J., Bassett, B. A., Best, P. N., Beswick, R., Blyth, S., Brown, M. L., Bruggen, M., Cluver, M., Colafrancesco, S., Cotter, G., Cress, C., Davé, R., Ferrari, C., Hardcastle, M. J., Hale, C. L., Harrison, I., Hatfield, P. W., Klockner, H. R., Kolwa, S., Malefahlo, E., Marubini, T., Mauch, T., Moodley, K., Morganti, R., Norris, R. P., Peters, J. A., Prandoni, I., Prescott, M., Oliver, S., Oozeer, N., Rottgering, H. J. A., Seymour,

- N., Simpson, C., Smirnov, O., and Smith, D. J. B. (2016). The MeerKAT International GHz Tiered Extragalactic Exploration (MIGHTEE) Survey. In *Proceedings of MeerKAT Science: On the Pathway to the SKA. 25-27 May*, page 6.
- Jeffs, B. D., Warnick, K. F., Landon, J., Waldron, J., Jones, D., Fisher, J. R., and Norrod, R. D. (2008). Signal Processing for Phased Array Feeds in Radio Astronomical Telescopes. *IEEE Journal of Selected Topics in Signal Processing*, 2:635–646.
- Jonas, J. L. (2009). MeerKAT - The South African Array With Composite Dishes and Wide-Band Single Pixel Feeds. *IEEE Proceedings*, 97:1522–1530.
- Kapinska, A. D., Staveley-Smith, L., Crocker, R., Meurer, G. R., Bhandari, S., Hurley-Walker, N., Offringa, A. R., Hanish, D. J., Seymour, N., Ekers, R. D., Bell, M. E., Callingham, J. R., Dwarakanath, K. S., For, B.-Q., Gaensler, B. M., Hancock, P. J., Hindson, L., Johnston-Hollitt, M., Lenc, E., McKinley, B., Morgan, J., Procopio, P., Wayth, R. B., Wu, C., Zheng, Q., Barry, N., Beardsley, A. P., Bowman, J. D., Briggs, F., Carroll, P., Dillon, J. S., Ewall-Wice, A., Feng, L., Greenhill, L. J., Hazelton, B. J., Hewitt, J. N., Jacobs, D. J., Kim, H.-S., Kittiwisit, P., Line, J., Loeb, A., Mitchell, D. A., Morales, M. F., Neben, A. R., Paul, S., Pindor, B., Pober, J. C., Riding, J., Sethi, S. K., Udaya Shankar, N., Subrahmanyan, R., Sullivan, I. S., Tegmark, M., Thyagarajan, N., Tingay, S. J., Trott, C. M., Webster, R. L., Wyithe, S. B., Cappallo, R. J., Deshpande, A. A., Kaplan, D. L., Lonsdale, C. J., McWhirter, S. R., Morgan, E., Oberoi, D., Ord, S. M., Prabu, T., Srivani, K. S., Williams, A., and Williams, C. L. (2017). Spectral energy distribution and radio halo of NGC 253 at low radio frequencies. *ArXiv e-prints*.
- Kass, R. E. and Raftery, A. E. (1995). Bayes factors. *Journal of the american statistical association*, 90(430):773–795.
- Kennicutt, R. C. and Evans, N. J. (2012). Star Formation in the Milky Way and Nearby Galaxies. *ARA&A*, 50:531–608.
- Kennicutt, Jr., R. C. (1983). The rate of star formation in normal disk galaxies. *ApJ*, 272:54–67.
- Kennicutt, Jr., R. C. (1992). The integrated spectra of nearby galaxies - General properties and emission-line spectra. *ApJ*, 388:310–327.
- Kennicutt, Jr., R. C. (1998). Star Formation in Galaxies Along the Hubble Sequence. *ARA&A*, 36:189–232.
- Kennicutt, Jr., R. C., Armus, L., Bendo, G., Calzetti, D., Dale, D. A., Draine, B. T., Engelbracht, C. W., Gordon, K. D., Grauer, A. D., Helou, G., Hollenbach, D. J., Jarrett, T. H.,

- Kewley, L. J., Leitherer, C., Li, A., Malhotra, S., Regan, M. W., Rieke, G. H., Rieke, M. J., Roussel, H., Smith, J.-D. T., Thornley, M. D., and Walter, F. (2003). SINGS: The SIRTf Nearby Galaxies Survey. *PASP*, 115:928–952.
- Kennicutt, Jr., R. C., Calzetti, D., Walter, F., Helou, G., Hollenbach, D. J., Armus, L., Bendo, G., Dale, D. A., Draine, B. T., Engelbracht, C. W., Gordon, K. D., Prescott, M. K. M., Regan, M. W., Thornley, M. D., Bot, C., Brinks, E., de Blok, E., de Mello, D., Meyer, M., Moustakas, J., Murphy, E. J., Sheth, K., and Smith, J. D. T. (2007). Star Formation in NGC 5194 (M51a). II. The Spatially Resolved Star Formation Law. *ApJ*, 671:333–348.
- Kennicutt, Jr., R. C., Hao, C.-N., Calzetti, D., Moustakas, J., Dale, D. A., Bendo, G., Engelbracht, C. W., Johnson, B. D., and Lee, J. C. (2009). Dust-corrected Star Formation Rates of Galaxies. I. Combinations of H $\alpha$  and Infrared Tracers. *ApJ*, 703:1672–1695.
- Kennicutt, Jr., R. C., Tamblyn, P., and Congdon, C. E. (1994). Past and future star formation in disk galaxies. *ApJ*, 435:22–36.
- Kewley, L. J., Geller, M. J., and Jansen, R. A. (2004). [O II] as a Star Formation Rate Indicator. *AJ*, 127:2002–2030.
- Kewley, L. J., Geller, M. J., Jansen, R. A., and Dopita, M. A. (2002). The H $\alpha$  and Infrared Star Formation Rates for the Nearby Field Galaxy Survey. *AJ*, 124:3135–3143.
- Kirkpatrick, A., Pope, A., Alexander, D. M., Charmandaris, V., Daddi, E., Dickinson, M., Elbaz, D., Gabor, J., Hwang, H. S., Ivison, R., Mullaney, J., Pannella, M., Scott, D., Altieri, B., Aussel, H., Bournaud, F., Buat, V., Coia, D., Dannerbauer, H., Dasyra, K., Kartaltepe, J., Leiton, R., Lin, L., Magdis, G., Magnelli, B., Morrison, G., Popesso, P., and Valtchanov, I. (2012). GOODS-Herschel: Impact of Active Galactic Nuclei and Star Formation Activity on Infrared Spectral Energy Distributions at High Redshift. *ApJ*, 759(2):139.
- Klaas, U., Haas, M., and et al. (2001a). Infrared to millimetre photometry of ultra-luminous IR galaxies: New evidence favouring a 3-stage dust model. *A&A*, 379:823–844.
- Klaas, U., Haas, M., and et al. (2001b). Infrared to millimetre photometry of ultra-luminous IR galaxies: New evidence favouring a 3-stage dust model. *A&A*, 379:823–844.
- Komatsu, E., Dunkley, J., Nolte, M. R., Bennett, C. L., Gold, B., Hinshaw, G., Jarosik, N., Larson, D., Limon, M., Page, L., Spergel, D. N., Halpern, M., Hill, R. S., Kogut, A., Meyer, S. S., Tucker, G. S., Weiland, J. L., Wollack, E., and Wright, E. L. (2009). Five-Year Wilkinson Microwave Anisotropy Probe Observations: Cosmological Interpretation. *ApJS*, 180:330–376.

- Kroupa, P. (2001). On the variation of the initial mass function. *MNRAS*, 322:231–246.
- Kroupa, P. and Weidner, C. (2003). Galactic-Field Initial Mass Functions of Massive Stars. *ApJ*, 598:1076–1078.
- Lacki, B. C. and Thompson, T. A. (2010). The Physics of the Far-infrared-Radio Correlation. II. Synchrotron Emission as a Star Formation Tracer in High-redshift Galaxies. *ApJ*, 717:196–208.
- Lacki, B. C., Thompson, T. A., and Quataert, E. (2010). The Physics of the Far-infrared-Radio Correlation. I. Calorimetry, Conspiracy, and Implications. *ApJ*, 717:1–28.
- Large, M. I., Cram, L. E., and Burgess, A. M. (1991). A machine-readable release of the Molonglo Reference Catalogue of Radio Sources. *The Observatory*, 111:72–75.
- Large, M. I., Mills, B. Y., Little, A. G., Crawford, D. F., and Sutton, J. M. (1981). The Molonglo Reference Catalogue of Radio Sources. *MNRAS*, 194:693.
- Leitherer, C. and Heckman, T. M. (1995). Synthetic properties of starburst galaxies. *ApJS*, 96:9–38.
- Li, Y., Calzetti, D., Kennicutt, R. C., Hong, S., Engelbracht, C. W., Dale, D. A., and Moustakas, J. (2010). Spitzer 70  $\mu\text{m}$  Emission as a Star Formation Rate Indicator for Sub-galactic Regions. *ApJ*, 725:677–691.
- Lilley, A. E. and Palmer, P. (1968). Tables of Radio-Frequency Recombination Lines. *ApJS*, 16:143.
- Lonsdale, C. J., Cappallo, R. J., Morales, M. F., Briggs, F. H., and et al. (2009). The Murchison Widefield Array: Design Overview. *IEEE Proceedings*, 97:1497–1506.
- Ly, C., Malkan, M. A., Kashikawa, N., Ota, K., Shimasaku, K., Iye, M., and Currie, T. (2012). Dust Attenuation and  $\text{H}\alpha$  Star Formation Rates of  $z \sim 0.5$  Galaxies. *ApJ*, 747:L16.
- Lynds, R. (1971). The Absorption-Line Spectrum of 4c 05.34. *ApJ*, 164:L73.
- Madau, P. and Dickinson, M. (2014). Cosmic Star-Formation History. *ARA&A*, 52:415–486.
- Madau, P., Pozzetti, L., and Dickinson, M. (1998). The Star Formation History of Field Galaxies. *ApJ*, 498:106–116.
- Mao, M. Y., Huynh, M. T., Norris, R. P., Dickinson, M., Frayer, D., Helou, G., and Monkiewicz, J. A. (2011). No Evidence for Evolution in the Far-infrared-Radio Correlation out to  $z \sim 2$  in the Extended Chandra Deep Field South. *ApJ*, 731:79.

- Mao, M. Y., Norris, R. P., Emonts, B., Sharp, R., Feain, I., Chow, K., Lenc, E., and Stevens, J. (2014). Star formation in the ultraluminous infrared galaxy F00183-7111. *MNRAS*, 440:L31–L35.
- Mao, Y.-W., Kennicutt, Jr., R. C., Hao, C.-N., Kong, X., and Zhou, X. (2012). Characterizing Ultraviolet and Infrared Observational Properties for Galaxies. I. Influences of Dust Attenuation and Stellar Population Age. *ApJ*, 757:52.
- Markwardt, C. B. (2009). Non-linear Least-squares Fitting in IDL with MPFIT. In Bohlender, D. A., Durand, D., and Dowler, P., editors, *Astronomical Data Analysis Software and Systems XVIII*, volume 411 of *Astronomical Society of the Pacific Conference Series*, page 251.
- Marvil, J., Owen, F., and Eilek, J. (2015). Integrated Radio Continuum Spectra of Galaxies. *AJ*, 149:32.
- Mauch, T., Murphy, T., Buttery, H. J., Curran, J., Hunstead, R. W., Piestrzynski, B., Robertson, J. G., and Sadler, E. M. (2003). SUMSS: a wide-field radio imaging survey of the southern sky - II. The source catalogue. *MNRAS*, 342:1117–1130.
- Mauch, T., Murphy, T., and et al. (2013). Sydney University Molonglo Sky Survey (SUMSS V2.1) (Mauch+ 2008). *VizieR Online Data Catalog*, 8081:0.
- Miller, G. E. and Scalo, J. M. (1978). On the birthplaces of stars. *PASP*, 90:506–513.
- Mooley, K. P., Hallinan, G., Bourke, S., Horesh, A., Myers, S. T., Frail, D. A., Kulkarni, S. R., Levitan, D. B., Kasliwal, M. M., Cenko, S. B., Cao, Y., Bellm, E., and Laher, R. R. (2016). The Caltech-NRAO Stripe 82 Survey (CNSS). I. The Pilot Radio Transient Survey In 50 deg<sup>2</sup>. *ApJ*, 818:105.
- Moré, J. J. (1978). *The Levenberg-Marquardt algorithm: Implementation and theory*, pages 105–116. Springer Berlin Heidelberg, Berlin, Heidelberg.
- Moshir, M. (1990). IRAS Faint Source Catalogue, version 2.0. In *IRAS Faint Source Catalogue, version 2.0 (1990)*, page 0.
- Moshir, M., Kopman, G., and Conrow, T. A. O. (1992). *IRAS Faint Source Survey, Explanatory supplement version 2*.
- Moustakas, J. and Kennicutt, Jr., R. C. (2006). An Integrated Spectrophotometric Survey of Nearby Star-forming Galaxies. *ApJS*, 164:81–98.
- Munari, U., Sordo, R., Castelli, F., and Zwitter, T. (2005). An extensive library of 2500 10 500 Å synthetic spectra. *A&A*, 442:1127–1134.

- Murakami, H., Baba, H., Barthel, P., Clements, D. L., and et al. (2007). The Infrared Astronomical Mission AKARI. *PASJ*, 59:S369.
- Murphy, E., Sargent, M., Beswick, R., Dickinson, C., Heywood, I., Hunt, L., Huynh, M., Jarvis, M., Karim, A., Krause, M., Prandoni, I., Seymour, N., Schinnerer, E., Tabatabaei, F., and Wagg, J. (2015). The Astrophysics of Star Formation Across Cosmic Time at  $>10$  GHz with the Square Kilometre Array. *Advancing Astrophysics with the Square Kilometre Array (AASKA14)*, page 85.
- Murphy, E. J. (2009). The Far-Infrared-Radio Correlation at High Redshifts: Physical Considerations and Prospects for the Square Kilometer Array. *ApJ*, 706:482–496.
- Murphy, E. J. (2013). The Role of Merger Stage on Galaxy Radio Spectra in Local Infrared-bright Starburst Galaxies. *ApJ*, 777:58.
- Murphy, E. J., Bremseth, J., Mason, B. S., Condon, J. J., Schinnerer, E., Aniano, G., Armus, L., Helou, G., Turner, J. L., and Jarrett, T. H. (2012). The Star Formation in Radio Survey: GBT 33 GHz Observations of Nearby Galaxy Nuclei and Extranuclear Star-forming Regions. *ApJ*, 761:97.
- Murphy, E. J., Condon, J. J., Schinnerer, E., Kennicutt, R. C., Calzetti, D., Armus, L., Helou, G., Turner, J. L., Aniano, G., Beirão, P., Bolatto, A. D., Brandl, B. R., Croxall, K. V., Dale, D. A., Donovan Meyer, J. L., Draine, B. T., Engelbracht, C., Hunt, L. K., Hao, C.-N., Koda, J., Roussel, H., Skibba, R., and Smith, J.-D. T. (2011). Calibrating Extinction-free Star Formation Rate Diagnostics with 33 GHz Free-free Emission in NGC 6946. *ApJ*, 737:67.
- Murphy, E. J., Helou, G., Braun, R., Kenney, J. D. P., Armus, L., Calzetti, D., Draine, B. T., Kennicutt, Jr., R. C., Roussel, H., Walter, F., Bendo, G. J., Buckalew, B., Dale, D. A., Engelbracht, C. W., Smith, J. D. T., and Thornley, M. D. (2006). The Effect of Star Formation on the Far-Infrared-Radio Correlation within Galaxies. *ApJ*, 651:L111–L115.
- Murphy, E. J., Helou, G., Condon, J. J., Schinnerer, E., Turner, J. L., Beck, R., Mason, B. S., Chary, R.-R., and Armus, L. (2010). The Detection of Anomalous Dust Emission in the Nearby Galaxy NGC 6946. *ApJ*, 709:L108–L113.
- Murphy, E. J., Stierwalt, S., Armus, L., Condon, J. J., and Evans, A. S. (2013). Radio and Mid-infrared Properties of Compact Starbursts: Distancing Themselves from the Main Sequence. *ApJ*, 768:2.
- Nardini, E., Risaliti, G., Watabe, Y., Salvati, M., and Sani, E. (2010). The role of nuclear activity as the power source of ultraluminous infrared galaxies. *MNRAS*, 405:2505–2520.

- Neff, S. G. and Ulvestad, J. S. (2000). VLA Observations of the Nearby Merger NGC 4038/4039: H II Regions and Supernova Remnants in the “Antennae”. *AJ*, 120:670–696.
- Netzer, H. (1990). AGN emission lines. In Blandford, R. D., Netzer, H., Woltjer, L., Courvoisier, T. J.-L., and Mayor, M., editors, *Active Galactic Nuclei*, pages 57–160.
- Niklas, S., Klein, U., and Wielebinski, R. (1997). A radio continuum survey of Shapley-Ames galaxies at  $\lambda$  2.8cm. II. Separation of thermal and non-thermal radio emission. *A&A*, 322:19–28.
- Norris, R. P. (1985). The nature of the megamaser galaxy IC 4553 (Arp 220). *MNRAS*, 216:701–711.
- Norris, R. P., Afonso, J., Bacon, D., Beck, R., Bell, M., Beswick, R. J., Best, P., Bhatnagar, S., Bonafede, A., Brunetti, G., Budavári, T., Cassano, R., Condon, J. J., Cress, C., Dabbech, A., Feain, I., Fender, R., Ferrari, C., Gaensler, B. M., Giovannini, G., Haverkorn, M., Heald, G., Van der Heyden, K., Hopkins, A. M., Jarvis, M., Johnston-Hollitt, M., Kothes, R., Van Langevelde, H., Lazio, J., Mao, M. Y., Martínez-Sansigre, A., Mary, D., Mcalpine, K., Middelberg, E., Murphy, E., Padovani, P., Paragi, Z., Prandoni, I., Raccanelli, A., Rigby, E., Roseboom, I. G., Röttgering, H., Sabater, J., Salvato, M., Scaife, A. M. M., Schilizzi, R., Seymour, N., Smith, D. J. B., Umana, G., Zhao, G.-B., and Zinn, P.-C. (2013). Radio Continuum Surveys with Square Kilometre Array Pathfinders. *PASA*, 30:e020.
- Norris, R. P., Hopkins, A. M., Afonso, J., Brown, S., Condon, J. J., Dunne, L., Feain, I., Hollow, R., Jarvis, M., Johnston-Hollitt, M., Lenc, E., Middelberg, E., Padovani, P., Prandoni, I., Rudnick, L., Seymour, N., Umana, G., Andernach, H., Alexander, D. M., Appleton, P. N., Bacon, D., Banfield, J., Becker, W., Brown, M. J. I., Ciliegi, P., Jackson, C., Eales, S., Edge, A. C., Gaensler, B. M., Giovannini, G., Hales, C. A., Hancock, P., Huynh, M. T., Ibar, E., Ivison, R. J., Kennicutt, R., Kimball, A. E., Koekemoer, A. M., Koribalski, B. S., López-Sánchez, Á. R., Mao, M. Y., Murphy, T., Messias, H., Pimblet, K. A., Raccanelli, A., Randall, K. E., Reiprich, T. H., Roseboom, I. G., Röttgering, H., Saikia, D. J., Sharp, R. G., Slee, O. B., Smail, I., Thompson, M. A., Urquhart, J. S., Wall, J. V., and Zhao, G.-B. (2011). EMU: Evolutionary Map of the Universe. *PASA*, 28:215–248.
- Norris, R. P., Lenc, E., Roy, A. L., and Spoon, H. (2012). The radio core of the ultraluminous infrared galaxy F00183-7111: watching the birth of a quasar. *MNRAS*, 422:1453–1459.
- Osterbrock, D. E. (1989). *Astrophysics of gaseous nebulae and active galactic nuclei*.
- Partridge, B., López-Cañiego, M., Perley, R. A., Stevens, J., Butler, B. J., Rocha, G., Walter,



- B., and Zacchei, A. (2016). Absolute calibration of the radio astronomy flux density scale at 22 to 43 ghz using planck. *The Astrophysical Journal*, 821(1):61.
- Paturel, G., Petit, C., Prugniel, P., Theureau, G., Rousseau, J., Brouty, M., Dubois, P., and Cambrésy, L. (2003). HYPERLEDA. I. Identification and designation of galaxies. *A&A*, 412:45–55.
- Perley, R., Napier, P., Jackson, J., Butler, B., Carlson, B., Fort, D., Dewdney, P., Clark, B., Hayward, R., Durand, S., Revnell, M., and McKinnon, M. (2009). The Expanded Very Large Array. *IEEE Proceedings*, 97:1448–1462.
- Perley, R. A., Chandler, C. J., Butler, B. J., and Wrobel, J. M. (2011). The Expanded Very Large Array: A New Telescope for New Science. *ApJ*, 739:L1.
- Prandoni, I. and Seymour, N. (2015). Revealing the Physics and Evolution of Galaxies and Galaxy Clusters with SKA Continuum Surveys. *Advancing Astrophysics with the Square Kilometre Array (AASKA14)*, page 67.
- Price, R. and Duric, N. (1992). New results on the radio-far-infrared relation for galaxies. *ApJ*, 401:81–86.
- Reynolds, J. (1994). A revised flux scale for the AT compact array. Technical report, ATNF Memo.
- Rodríguez-Zaurín, J., Arribas, S., Monreal-Ibero, A., Colina, L., Alonso-Herrero, A., and Alfonso-Garzón, J. (2011). VLT-VIMOS integral field spectroscopy of luminous and ultraluminous infrared galaxies. III. The atlas of the stellar and ionized gas distribution. *A&A*, 527:A60.
- Rouan, D. (2011). Grey body. In Gargaud, M., Amils, R., Quintanilla, J., Cleaves, Henderson-James (Jim), I., Irvine, W., Pinti, D., and Viso, M., editors, *Encyclopedia of Astrobiology*, pages 695–695. Springer Berlin Heidelberg.
- Rousseeuw, P. J. and Van Driessen, K. (2006). Computing lts regression for large data sets. *Data Mining and Knowledge Discovery*, 12(1):29–45.
- Rowan-Robinson, M. (2000). Hyperluminous infrared galaxies. *MNRAS*, 316:885–900.
- Rowan-Robinson, M. (2001). The Star Formation History of the Universe: An Infrared Perspective. *ApJ*, 549:745–758.
- Rowan-Robinson, M., Mann, R. G., Oliver, S. J., Efstathiou, A., Eaton, N., Goldschmidt, P., Mobasher, B., Serjeant, S. B. G., Sumner, T. J., Danese, L., Elbaz, D., Franceschini,

- A., Egami, E., Kontizas, M., Lawrence, A., McMahon, R., Norgaard-Nielsen, H. U., Perez-Fournon, I., and Gonzalez-Serrano, J. I. (1997). Observations of the Hubble Deep Field with the Infrared Space Observatory - V. Spectral energy distributions, starburst models and star formation history. *MNRAS*, 289:490–496.
- Roy, A. L., Norris, R. P., Kesteven, M. J., Troup, E. R., and Reynolds, J. E. (1998). Seyfert galaxies and the radio-far-infrared correlation. *MNRAS*, 301:1019–1030.
- Salpeter, E. E. (1955). The Luminosity Function and Stellar Evolution. *ApJ*, 121:161.
- Sánchez-Blázquez, P., Peletier, R. F., Jiménez-Vicente, J., Cardiel, N., Cenarro, A. J., Falcón-Barroso, J., Gorgas, J., Selam, S., and Vazdekis, A. (2006). Medium-resolution Isaac Newton Telescope library of empirical spectra. *MNRAS*, 371:703–718.
- Sarzi, M., Falcón-Barroso, J., Davies, R. L., Bacon, R., Bureau, M., Cappellari, M., de Zeeuw, P. T., Emsellem, E., Fathi, K., Krajnović, D., Kuntschner, H., McDermid, R. M., and Peletier, R. F. (2006). The SAURON project - V. Integral-field emission-line kinematics of 48 elliptical and lenticular galaxies. *MNRAS*, 366:1151–1200.
- Sault, R. J., Teuben, P. J., and Wright, M. C. H. (2011). MIRIAD: Multi-channel Image Reconstruction, Image Analysis, and Display. Astrophysics Source Code Library.
- Sault, R. J. and Wieringa, M. H. (1994). Multi-frequency synthesis techniques in radio interferometric imaging. *A&AS*, 108:585–594.
- Schinckel, A. E. T. and Bock, D. C.-J. (2016). The Australian SKA Pathfinder: project update and initial operations. In *Ground-based and Airborne Telescopes VI*, volume 9906 of *Proc. SPIE*, page 99062A.
- Seymour, N., Dwelly, T., Moss, D., McHardy, I., Zoghbi, A., Rieke, G., Page, M., Hopkins, A., and Loaring, N. (2008). The star formation history of the Universe as revealed by deep radio observations. *MNRAS*, 386:1695–1708.
- Seymour, N., Huynh, M., Dwelly, T., Symeonidis, M., Hopkins, A., McHardy, I. M., Page, M. J., and Rieke, G. (2009). Investigating the far-IR/radio correlation of star-forming Galaxies to  $z = 3$ . *MNRAS*, 398:1573–1581.
- Seymour, N., McHardy, I. M., and Gunn, K. F. (2004). Radio observations of the 13<sup>h</sup> XMM-Newton/ROSAT Deep X-ray Survey Area. *MNRAS*, 352:131–141.
- Simpson, D. G. (1997). *Introduction to Rousseeuw (1984) Least Median of Squares Regression*, pages 433–461. Springer New York, New York, NY.

- Smith, D. J. B., Hardcastle, M. J., Jarvis, M. J., Maddox, S. J., and et al. (2013). Isothermal dust models of Herschel-ATLAS galaxies. *MNRAS*, 436:2435–2453.
- Smith, H. E., Lonsdale, C. J., Lonsdale, C. J., and Diamond, P. J. (1998). A Starburst Revealed—Luminous Radio Supernovae in the Nuclei of ARP 220. *ApJ*, 493:L17–L21.
- Spoon, H. W. W., Armus, L., Marshall, J. A., Bernard-Salas, J., Farrah, D., Charmandaris, V., and Kent, B. R. (2009). High-Velocity Neon Line Emission From the ULIRG IRAS F00183-7111: Revealing the Optically Obscured Base of a Nuclear Outflow. *ApJ*, 693:1223–1235.
- Steidel, C. C., Giavalisco, M., Pettini, M., Dickinson, M., and Adelberger, K. L. (1996). Spectroscopic Confirmation of a Population of Normal Star-forming Galaxies at Redshifts  $Z > 3$ . *ApJ*, 462:L17.
- Strauss, M. A., Davis, M., Yahil, A., and Huchra, J. P. (1990). A redshift survey of IRAS galaxies. I - Sample selection. *ApJ*, 361:49–62.
- Strauss, M. A., Huchra, J. P., Davis, M., Yahil, A., Fisher, K. B., and Tonry, J. (1992). A redshift survey of IRAS galaxies. VII - The infrared and redshift data for the 1.936 Jansky sample. *ApJS*, 83:29–63.
- Sullivan, M., Mobasher, B., Chan, B., Cram, L., Ellis, R., Treyer, M., and Hopkins, A. (2001). A Comparison of Independent Star Formation Diagnostics for an Ultraviolet-selected Sample of Nearby Galaxies. *ApJ*, 558:72–80.
- Symeonidis, M., Vaccari, M., Berta, S., Page, M. J., Lutz, D., Arumugam, V., Aussel, H., Bock, J., Boselli, A., Buat, V., Capak, P. L., Clements, D. L., Conley, A., Conversi, L., Cooray, A., Dowell, C. D., Farrah, D., Franceschini, A., Giovannoli, E., Glenn, J., Griffin, M., Hatziminaoglou, E., Hwang, H.-S., Ibar, E., Ilbert, O., Ivison, R. J., Floc’h, E. L., Lilly, S., Kartaltepe, J. S., Magnelli, B., Magdis, G., Marchetti, L., Nguyen, H. T., Nordon, R., O’Halloran, B., Oliver, S. J., Omont, A., Papageorgiou, A., Patel, H., Pearson, C. P., Pérez-Fournon, I., Pohlen, M., Popesso, P., Pozzi, F., Rigopoulou, D., Riguccini, L., Rosario, D., Roseboom, I. G., Rowan-Robinson, M., Salvato, M., Schulz, B., Scott, D., Seymour, N., Shupe, D. L., Smith, A. J., Valtchanov, I., Wang, L., Xu, C. K., Zemcov, M., and Wuyts, S. (2013). The Herschel census of infrared SEDs through cosmic time. *MNRAS*, 431:2317–2340.
- Takeuchi, T. T., Buat, V., and Burgarella, D. (2005). The evolution of the ultraviolet and infrared luminosity densities in the universe at  $0 < z < 1$ . *A&A*, 440:L17–L20.
- Terlouw, J. P. and Vogelaar, M. G. R. (2015). *Kapteyn Package, version 2.3*. Kapteyn

Astronomical Institute, Groningen. Available from <http://www.astro.rug.nl/software/kapteyn/>.

Tingay, S. J., Goeke, R., Bowman, J. D., Emrich, D., and et al. (2013). The Murchison Widefield Array: The Square Kilometre Array Precursor at Low Radio Frequencies. *PASA*, 30:e007.

Valdes, F., Gupta, R., Rose, J. A., Singh, H. P., and Bell, D. J. (2004). The Indo-US Library of Coudé Feed Stellar Spectra. *ApJS*, 152:251–259.

van der Kruit, P. C. (1971). Observations of core sources in Seyfert and normal galaxies with the Westerbork synthesis radio telescope at 1415 MHz. *A&A*, 15:110–122.

van der Kruit, P. C. (1973). High-resolution Radio Continuum Observations of Bright Spiral Galaxies at 1415 MHz: A General Discussion. *A&A*, 29:263.

van der Marel, R. P. and Franx, M. (1993). A new method for the identification of non-Gaussian line profiles in elliptical galaxies. *ApJ*, 407:525–539.

van Haarlem, M. P., Wise, M. W., Gunst, A. W., Heald, G., McKean, J. P., Hessels, J. W. T., de Bruyn, A. G., Nijboer, R., Swinbank, J., Fallows, R., Brentjens, M., Nelles, A., Beck, R., Falcke, H., Fender, R., Hörandel, J., Koopmans, L. V. E., Mann, G., Miley, G., Röttgering, H., Stappers, B. W., Wijers, R. A. M. J., Zaroubi, S., van den Akker, M., Alexov, A., Anderson, J., Anderson, K., van Ardenne, A., Arts, M., Asgekar, A., Avruch, I. M., Batejat, F., Bähren, L., Bell, M. E., Bell, M. R., van Bemmell, I., Bennema, P., Bentum, M. J., Bernardi, G., Best, P., Birzan, L., Bonafede, A., Boonstra, A.-J., Braun, R., Bregman, J., Breitling, F., van de Brink, R. H., Broderick, J., Broekema, P. C., Brouw, W. N., Brüggem, M., Butcher, H. R., van Cappellen, W., Ciardi, B., Coenen, T., Conway, J., Coolen, A., Corstanje, A., Damstra, S., Davies, O., Deller, A. T., Dettmar, R.-J., van Diepen, G., Dijkstra, K., Donker, P., Doorduyn, A., Dromer, J., Drost, M., van Duin, A., Eislöffel, J., van Enst, J., Ferrari, C., Frieswijk, W., Gankema, H., Garrett, M. A., de Gasperin, F., Gerbers, M., de Geus, E., Griebmeier, J.-M., Grit, T., Gruppen, P., Hamaker, J. P., Hassall, T., Hoeft, M., Holties, H. A., Horneffer, A., van der Horst, A., van Houwelingen, A., Huijgen, A., Iacobelli, M., Intema, H., Jackson, N., Jelic, V., de Jong, A., Juette, E., Kant, D., Karastergiou, A., Koers, A., Kollen, H., Kondratiev, V. I., Kooistra, E., Koopman, Y., Koster, A., Kuniyoshi, M., Kramer, M., Kuper, G., Lambropoulos, P., Law, C., van Leeuwen, J., Lemaitre, J., Loose, M., Maat, P., Macario, G., Markoff, S., Masters, J., McFadden, R. A., McKay-Bukowski, D., Meijering, H., Meulman, H., Mevius, M., Middelberg, E., Millenaar, R., Miller-Jones, J. C. A., Mohan, R. N., Mol, J. D., Morawietz, J., Morganti, R., Mulcahy, D. D., Mulder,

- E., Munk, H., Nieuwenhuis, L., van Nieuwpoort, R., Noordam, J. E., Norden, M., Noutsos, A., Offringa, A. R., Olofsson, H., Omar, A., Orrú, E., Overeem, R., Paas, H., Pandey-Pommier, M., Pandey, V. N., Pizzo, R., Polatidis, A., Rafferty, D., Rawlings, S., Reich, W., de Reijer, J.-P., Reitsma, J., Renting, G. A., Riemers, P., Rol, E., Romein, J. W., Roosjen, J., Ruiter, M., Scaife, A., van der Schaaf, K., Scheers, B., Schellart, P., Schoenmakers, A., Schoonderbeek, G., Serylak, M., Shulevski, A., Sluman, J., Smirnov, O., Sobey, C., Spreeuw, H., Steinmetz, M., Sterks, C. G. M., Stiepel, H.-J., Stuurwold, K., Tagger, M., Tang, Y., Tasse, C., Thomas, I., Thoudam, S., Toribio, M. C., van der Tol, B., Usov, O., van Veelen, M., van der Veen, A.-J., ter Veen, S., Verbiest, J. P. W., Vermeulen, R., Vermaas, N., Vocks, C., Vogt, C., de Vos, M., van der Wal, E., van Weeren, R., Weggemans, H., Weltevrede, P., White, S., Wijnholds, S. J., Wilhelmsson, T., Wucknitz, O., Yatawatta, S., Zarka, P., Zensus, A., and van Zwieten, J. (2013). LOFAR: The LOw-Frequency ARray. *A&A*, 556:A2.
- Véron-Cetty, M.-P. and Véron, P. (2006). A catalogue of quasars and active nuclei: 12th edition. *A&A*, 455:773–777.
- Voelk, H. J. (1989). The correlation between radio and far-infrared emission for disk galaxies - A calorimeter theory. *A&A*, 218:67–70.
- Waldram, E. M., Bolton, R. C., Pooley, G. G., and Riley, J. M. (2007). Some estimates of the source counts at Planck Surveyor frequencies, using the 9C survey at 15 GHz. *MNRAS*, 379:1442–1452.
- Wang, B. and Heckman, T. M. (1996). Internal Absorption and the Luminosity of Disk Galaxies. *ApJ*, 457:645.
- Wang, L., Rowan-Robinson, M., Norberg, P., Heinis, S., and Han, J. (2014). The Revised IRAS-FSC Redshift Catalogue (RIFSCz). *MNRAS*, 442:2739–2750.
- Wang, X. and Fields, B. D. (2016). Are Starburst Galaxies Proton Calorimeters? *ArXiv e-prints*.
- Wayth, R. B., Lenc, E., Bell, M. E., and et, a. (2015). GLEAM: The GaLactic and Extragalactic All-Sky MWA Survey. *PASA*, 32:e025.
- Weijmans, A.-M., Krajnović, D., van de Ven, G., Oosterloo, T. A., Morganti, R., and de Zeeuw, P. T. (2008). The shape of the dark matter halo in the early-type galaxy NGC 2974. *MNRAS*, 383:1343–1358.
- Wills, K. A., Pedlar, A., Muxlow, T. W. B., and Wilkinson, P. N. (1997). Low-frequency observations of supernova remnants in M82. *MNRAS*, 291:517.

- Wilman, R. J., Miller, L., Jarvis, M. J., Mauch, T., Levrier, F., Abdalla, F. B., Rawlings, S., Klöckner, H.-R., Obreschkow, D., Olteanu, D., and Young, S. (2008). A semi-empirical simulation of the extragalactic radio continuum sky for next generation radio telescopes. *MNRAS*, 388:1335–1348.
- Wilson, W. E., Ferris, R. H., Axtens, P., Brown, A., Davis, E., Hampson, G., Leach, M., Roberts, P., Saunders, S., Koribalski, B. S., Caswell, J. L., Lenc, E., Stevens, J., Voronkov, M. A., Wieringa, M. H., Brooks, K., Edwards, P. G., Ekers, R. D., Emonts, B., Hindson, L., Johnston, S., Maddison, S. T., Mahony, E. K., Malu, S. S., Massardi, M., Mao, M. Y., McConnell, D., Norris, R. P., Schnitzeler, D., Subrahmanyan, R., Urquhart, J. S., Thompson, M. A., and Wark, R. M. (2011). The Australia Telescope Compact Array Broad-band Backend: description and first results. *MNRAS*, 416:832–856.
- Wu, H., Cao, C., Hao, C.-N., Liu, F.-S., Wang, J.-L., Xia, X.-Y., Deng, Z.-G., and Young, C. K.-S. (2005). PAH and Mid-Infrared Luminosities as Measures of Star Formation Rate in Spitzer First Look Survey Galaxies. *ApJ*, 632:L79–L82.
- Yamamura, I., Makiuti, S., Ikeda, N., Fukuda, Y., and et al. (2010). VizieR Online Data Catalog: AKARI/FIS All-Sky Survey Point Source Catalogues (ISAS/JAXA, 2010). *VizieR Online Data Catalog*, 2298.
- Yun, M. S. and Carilli, C. L. (2002). Radio-to-Far-Infrared Spectral Energy Distribution and Photometric Redshifts for Dusty Starburst Galaxies. *ApJ*, 568:88–98.
- Yun, M. S., Reddy, N. A., and Condon, J. J. (2001). Radio Properties of Infrared-selected Galaxies in the IRAS 2 Jy Sample. *ApJ*, 554:803–822.
- Zhu, Y.-N., Wu, H., Cao, C., and Li, H.-N. (2008). Correlations between Mid-Infrared, Far-Infrared,  $H\alpha$ , and FUV Luminosities for Spitzer SWIRE Field Galaxies. *ApJ*, 686:155–171.

# Appendix A

## Submitted Papers

This appendix chapter contains two additions: papers written and submitted during my candidature. Both papers were completed during my PhD candidature and are original work.

### A.1 NGC 7793

I have attached a paper that I wrote as the first author investigating NGC 7793. This work involved imaging archived ATCA data to produce a series of sensitive radio continuum images. These were then used to identify discrete sources and estimate spectral indices. Although not a key component of my PhD project, the work this paper is based on, including data reduction and analysis, was performed during my candidature. I claim complete ownership of this work as first author.

This paper was submitted to and accepted by the ‘Astrophysics and Space Science’ Journal in 2014 and has since been cited three times.

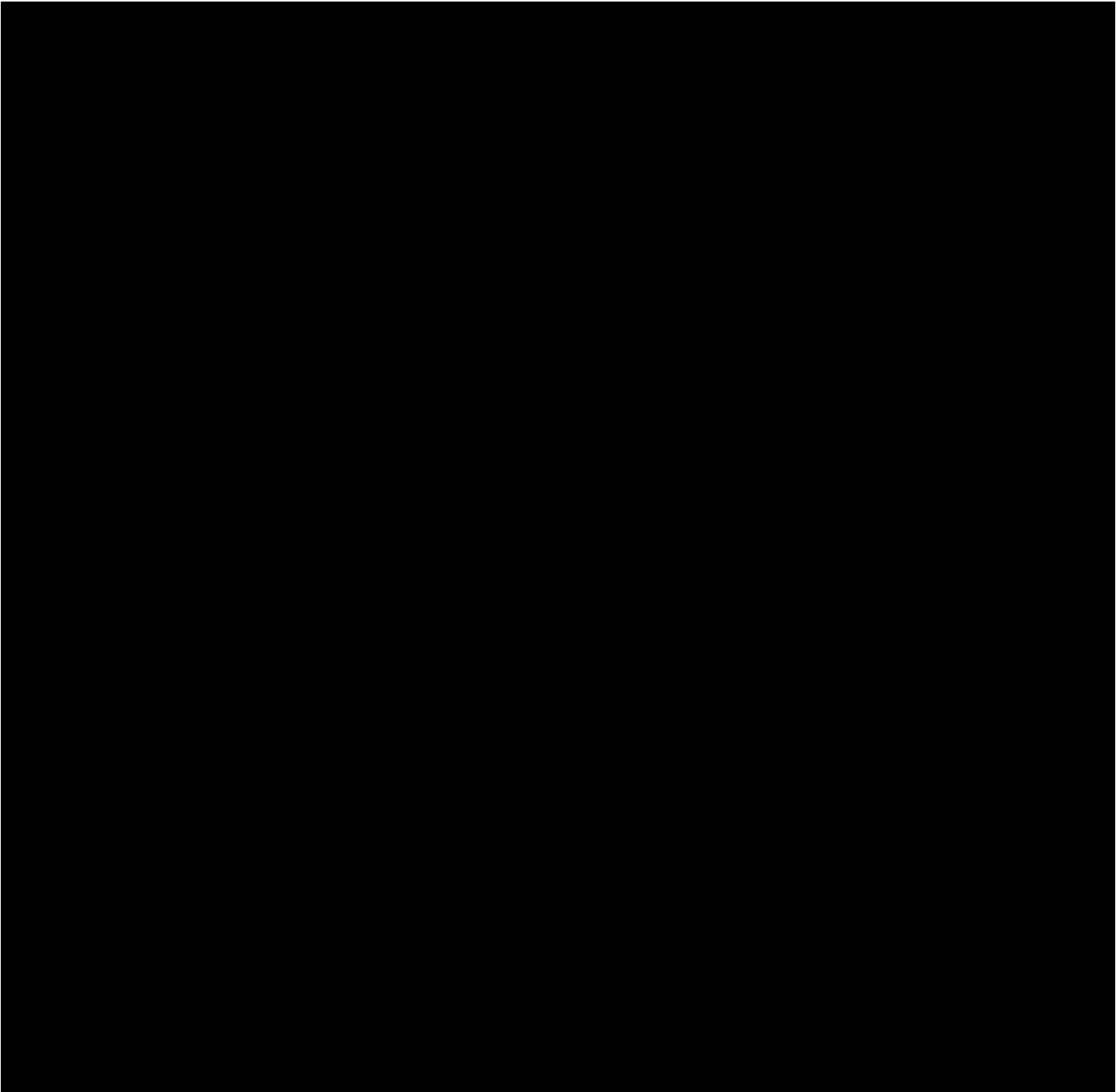
#### A.1.1 NGC 7793 Paper

---

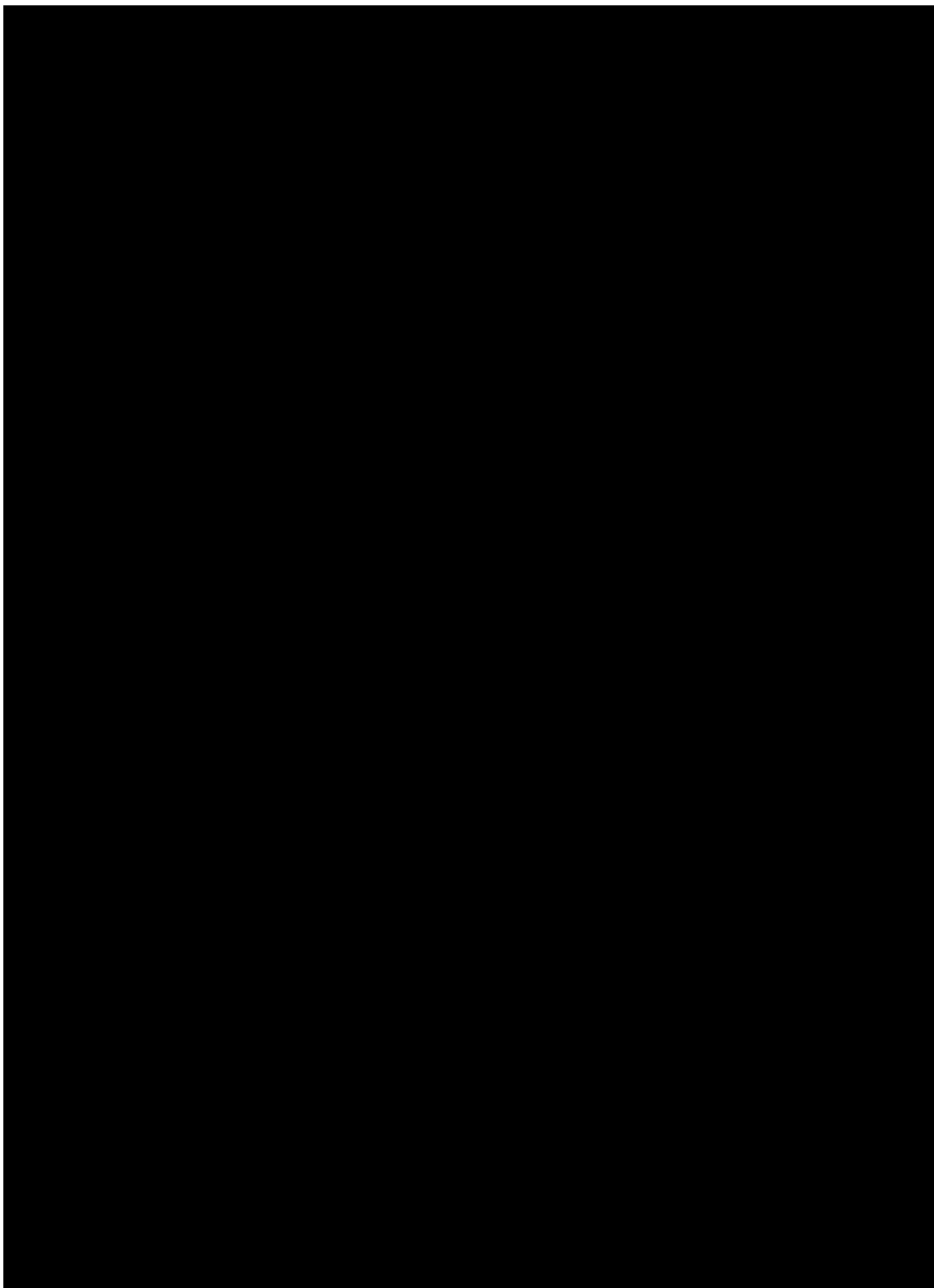
# Radio-Continuum Study of the Nearby Sculptor Group Galaxies. Part 3: NGC 7793 at $\lambda=12.2, 6$ and $3$ cm

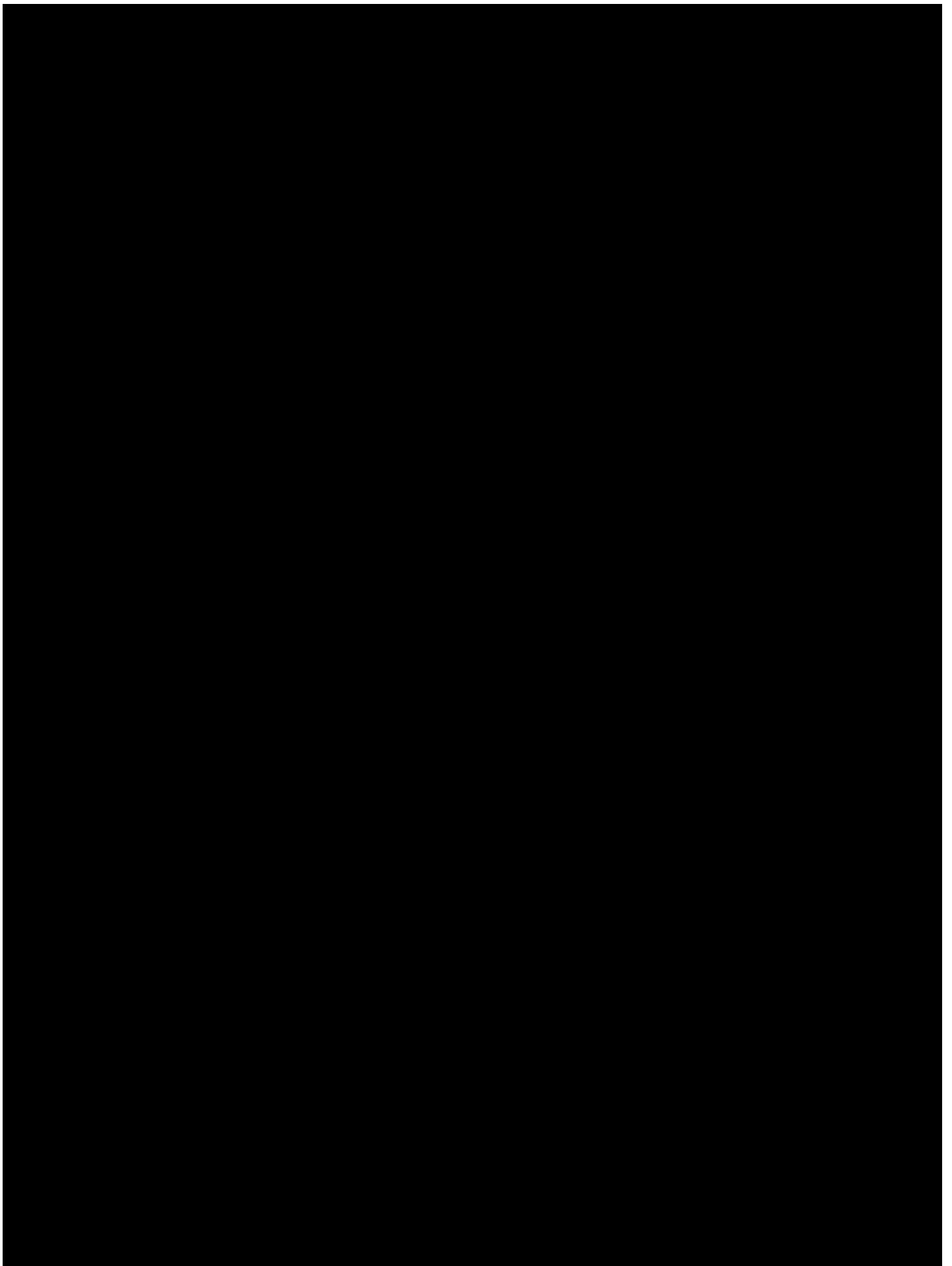
Timothy J. Galvin, Miroslav D. Filipović, Nicholas  
F. H. Tothill, Evan J. Crawford, Andrew N.  
O'Brien • Nicholas Seymour •  
Thomas G. Pannuti, Alekzander R. Kosakowski, Biswas Sharma

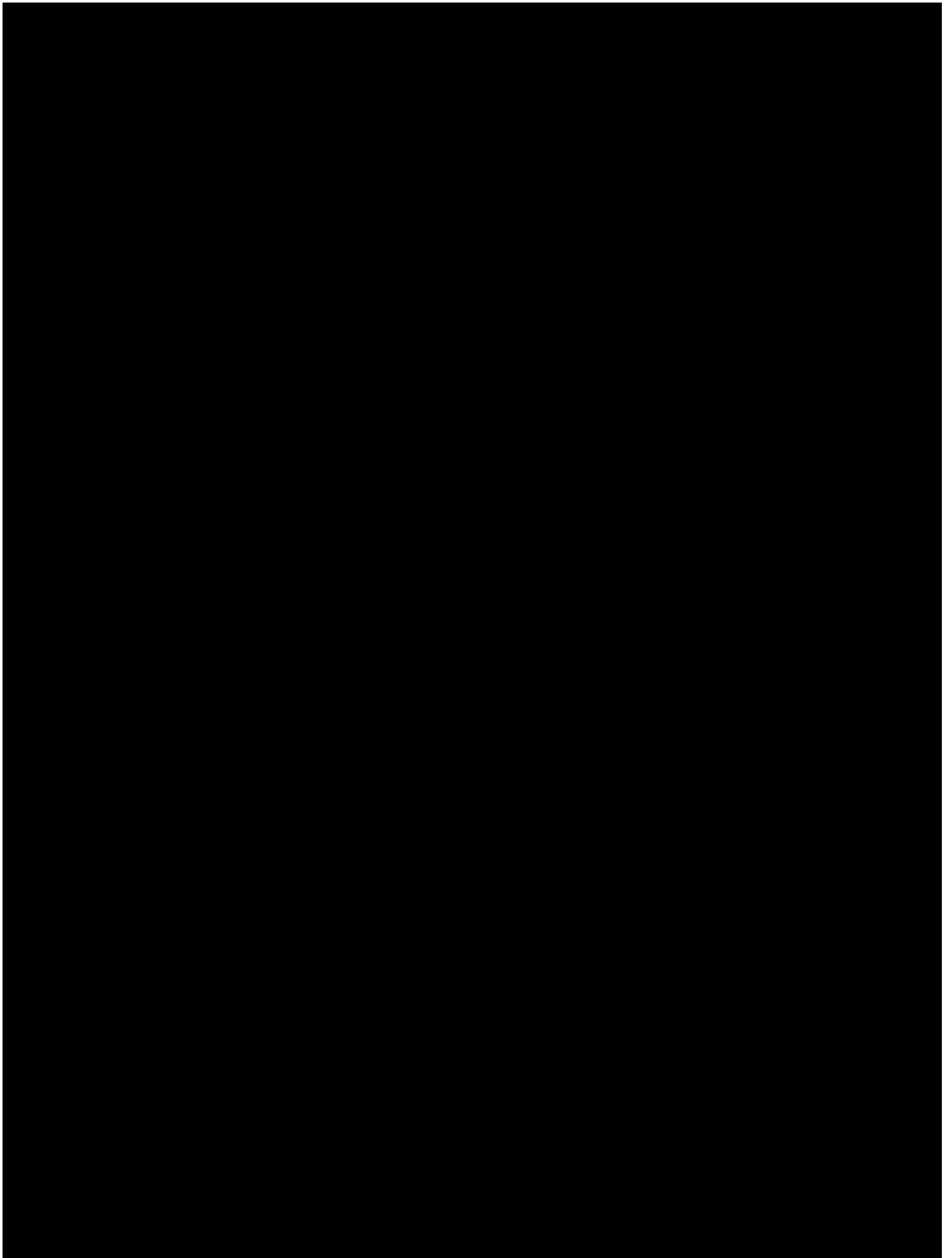
<https://rdcu.be/b4ZM8>

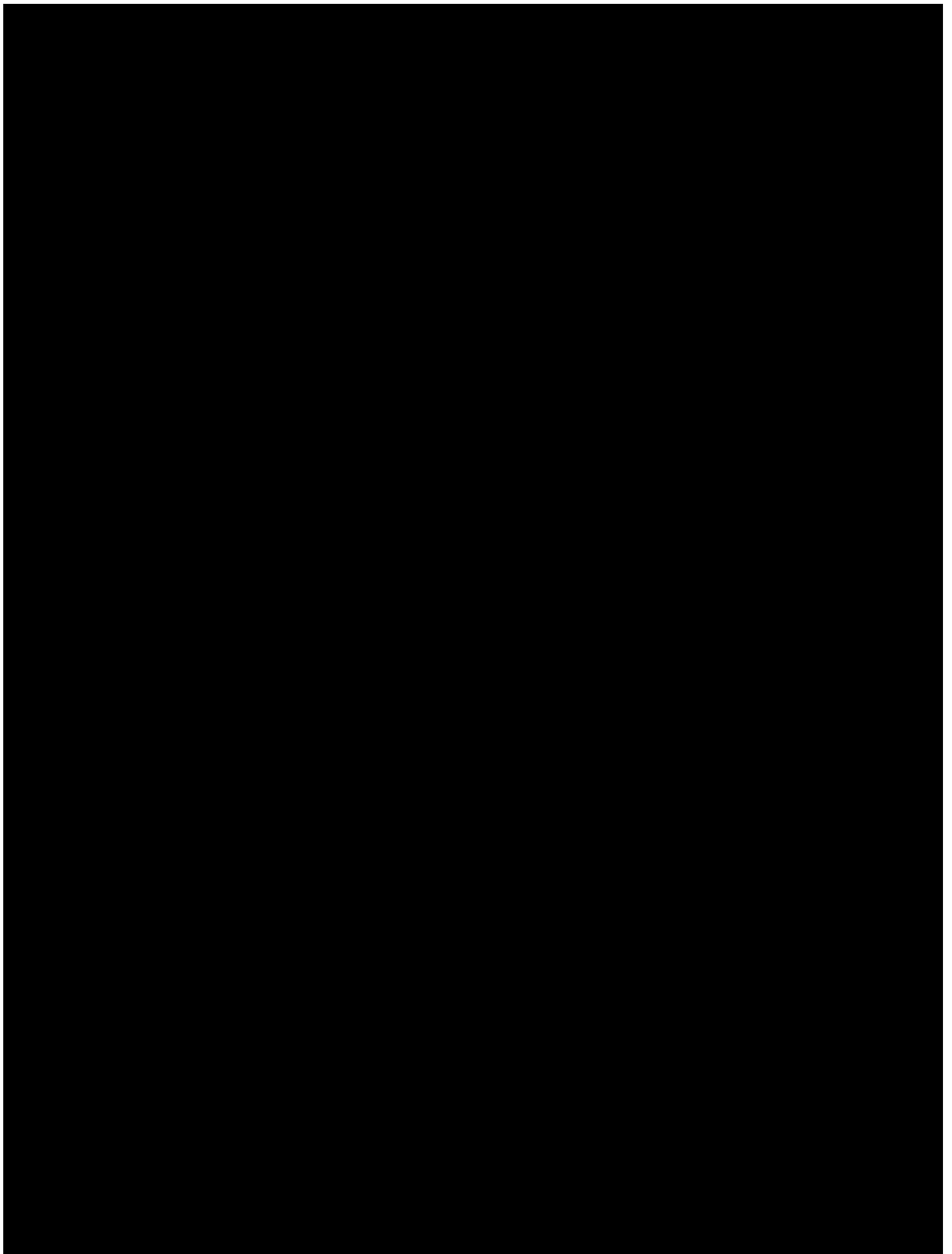


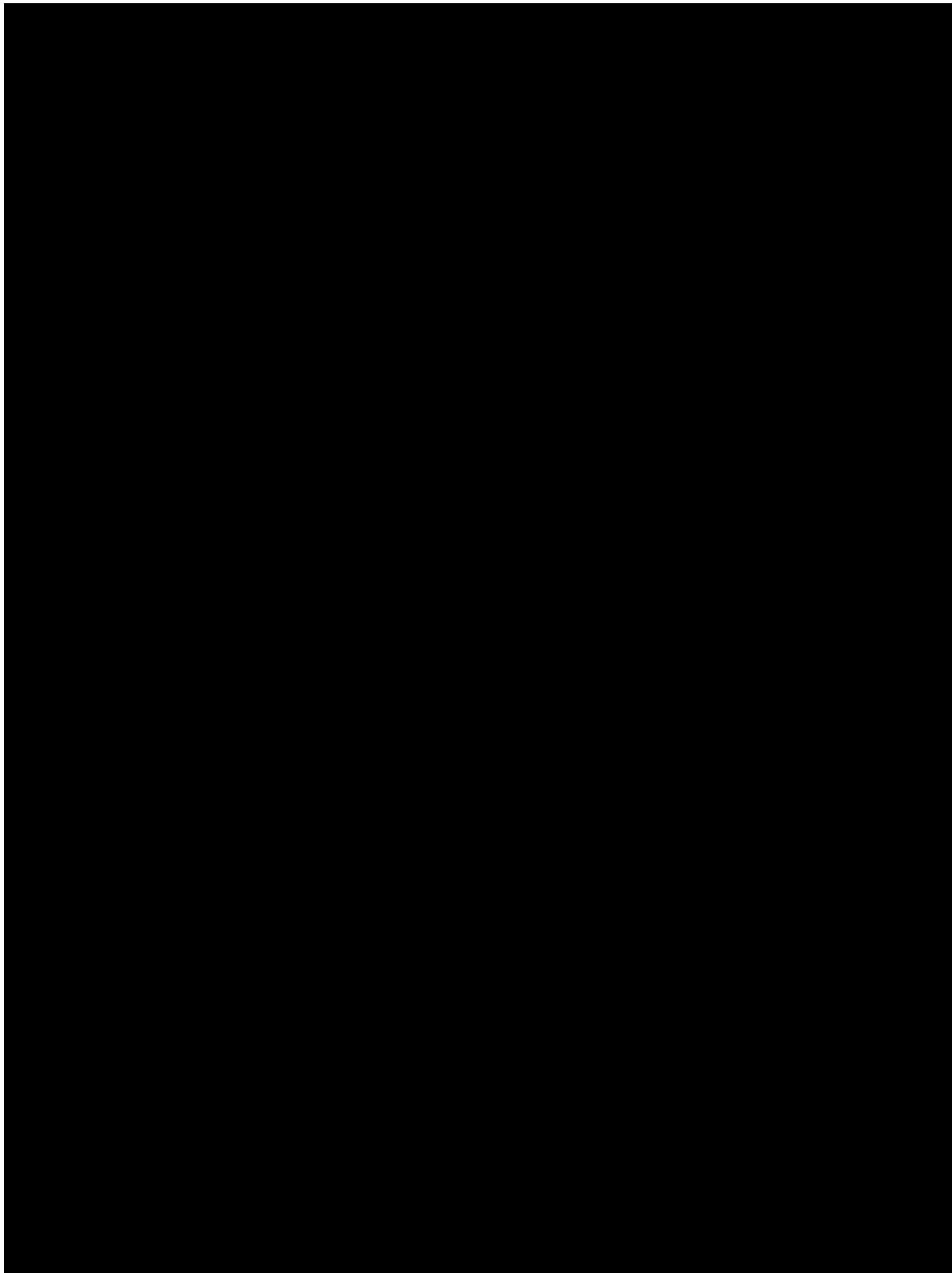


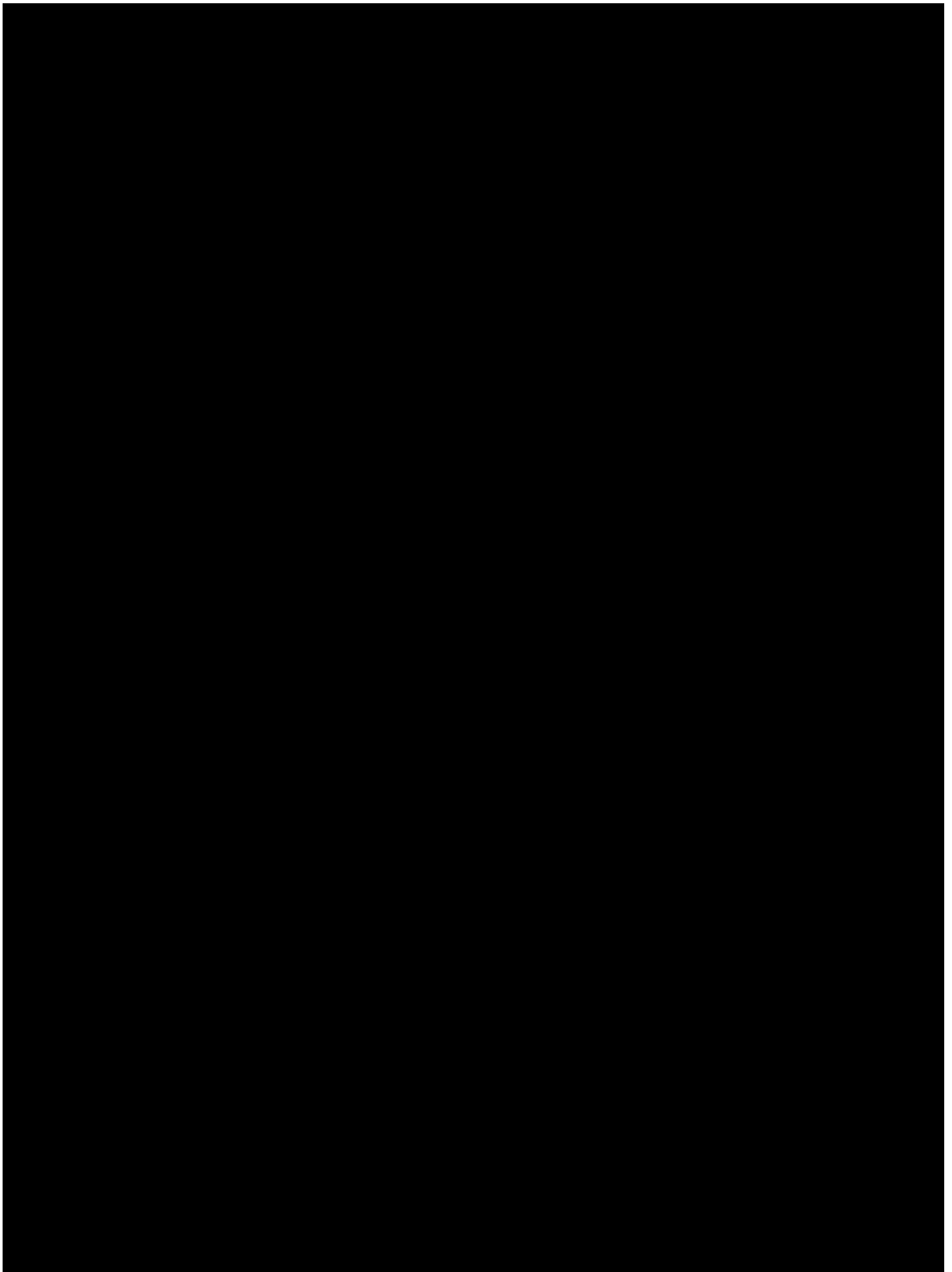


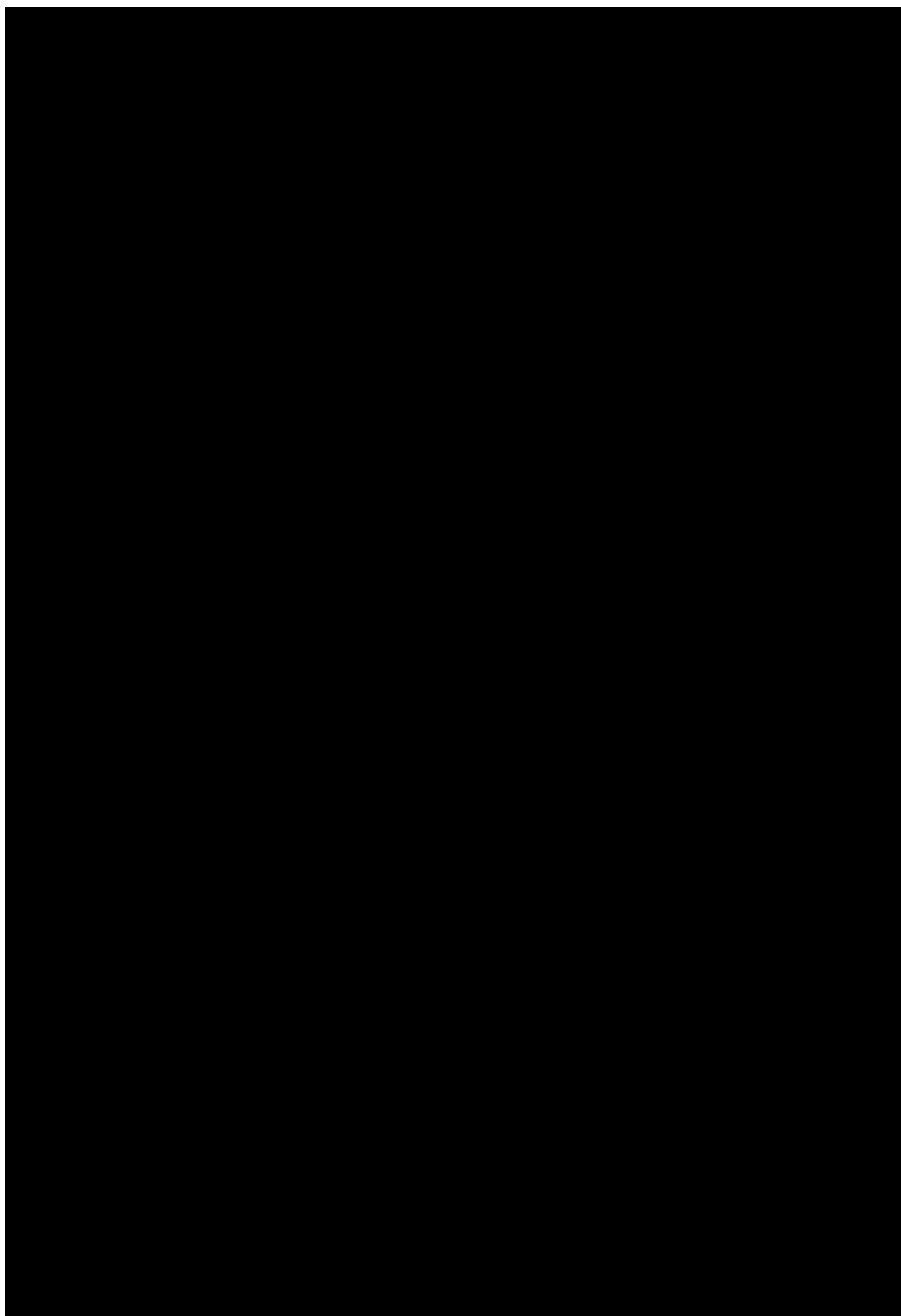


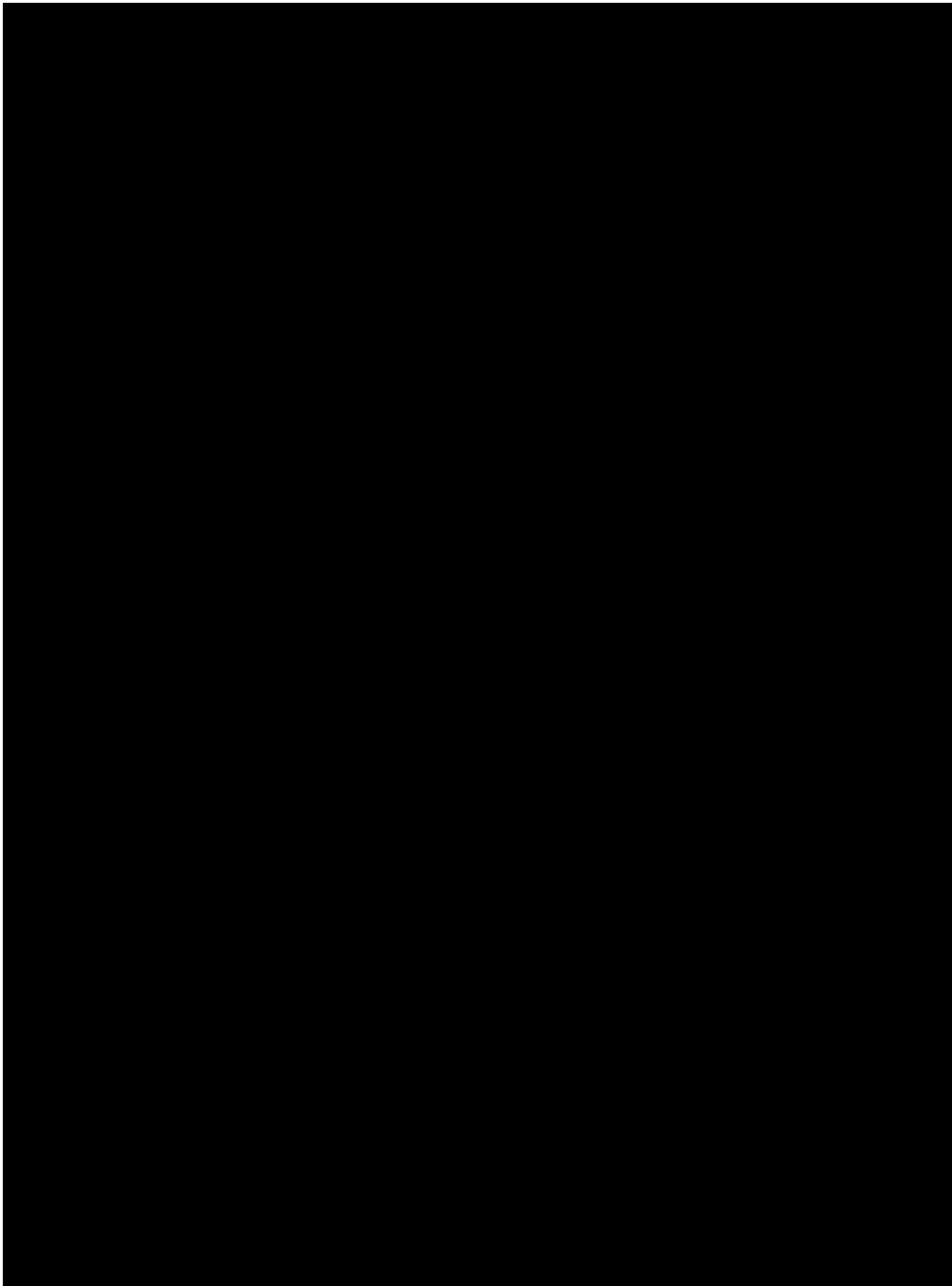














## **A.2 M31**

I have attached a paper that I wrote as first author that published a table of discrete sources detected in M31 using archival VLA data which were imaged while I was an Honours student. Using multi-wavelength data available in the literature, I extracted a population of supernova remnants and supernova remnant candidates. Although this paper does not form a major component of my PhD project, I analysed the existing images I created during my candidature.

This paper was submitted to and accepted by the ‘Serbian Astronomical Journal’ in 2014 and has been cited once.

### **A.2.1 M31 Paper**

<http://saj.matf.bg.ac.rs/index.php?id=189>

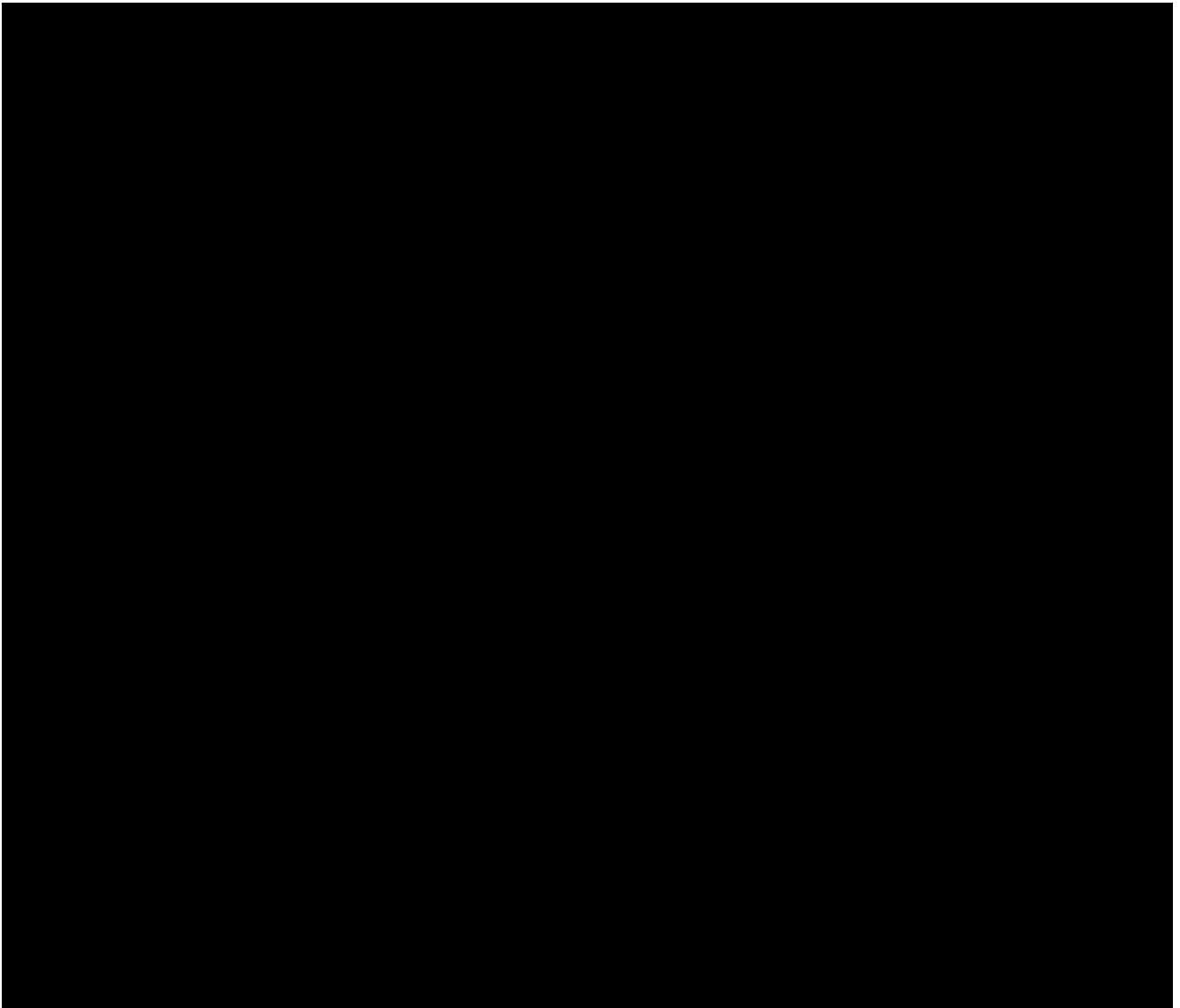
Serb. Astron. J. № 189 (2014), 1 - 5

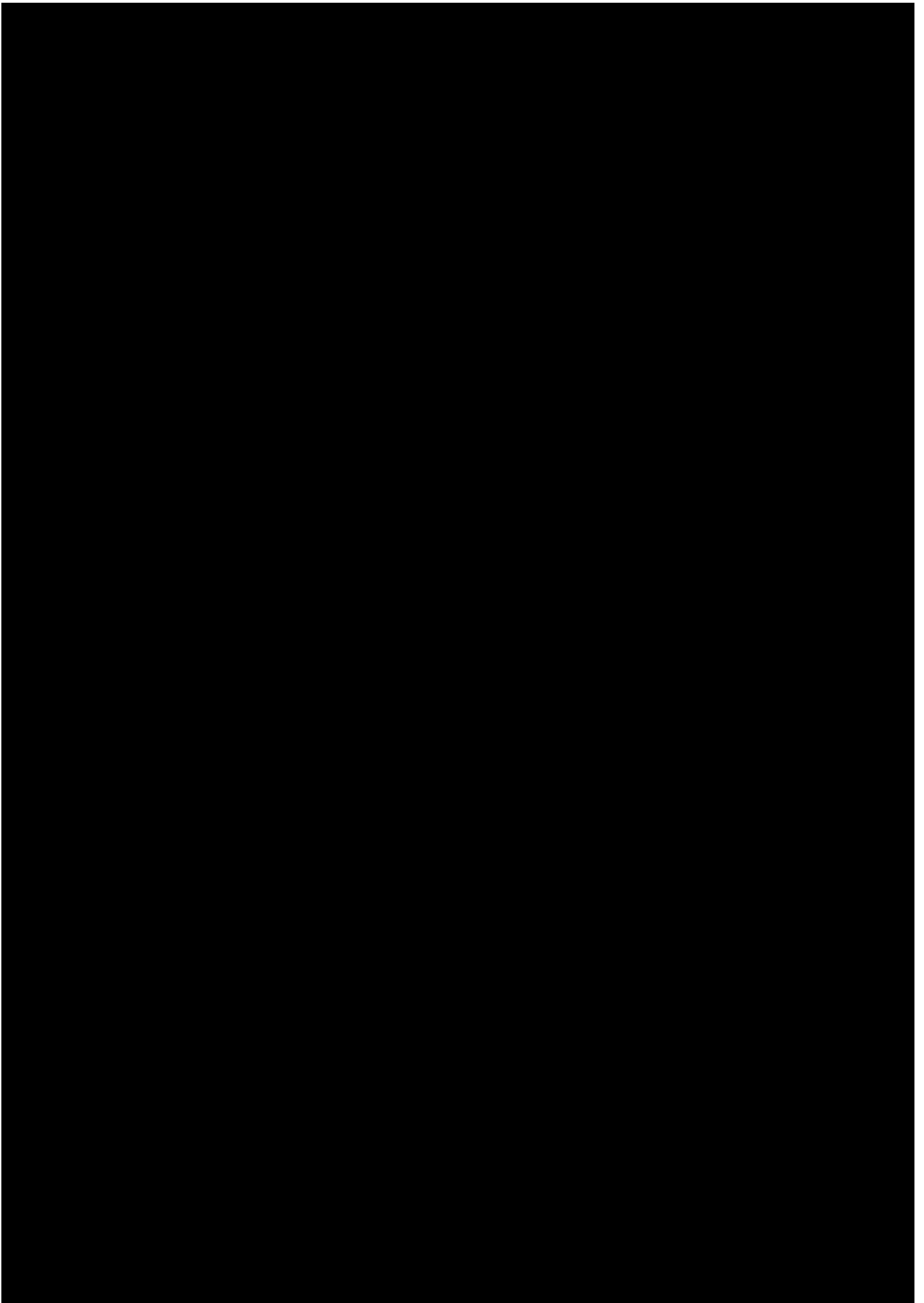
Editorial

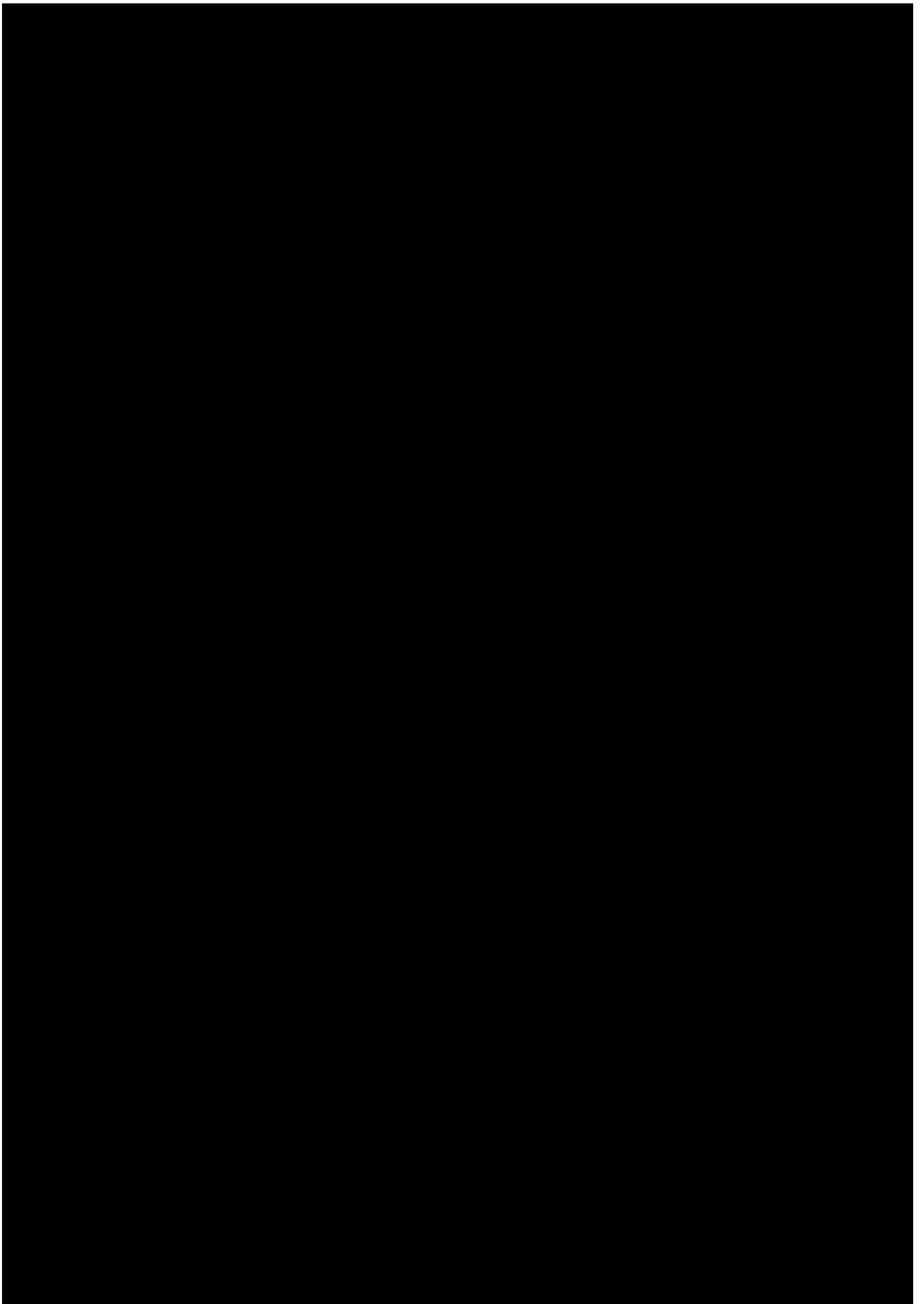
**20 CM VLA RADIO-CONTINUUM STUDY OF M 31 –  
IMAGES AND POINT SOURCE CATALOGUES DR2:  
EXTRACTION OF A SUPERNOVA REMNANT SAMPLE**

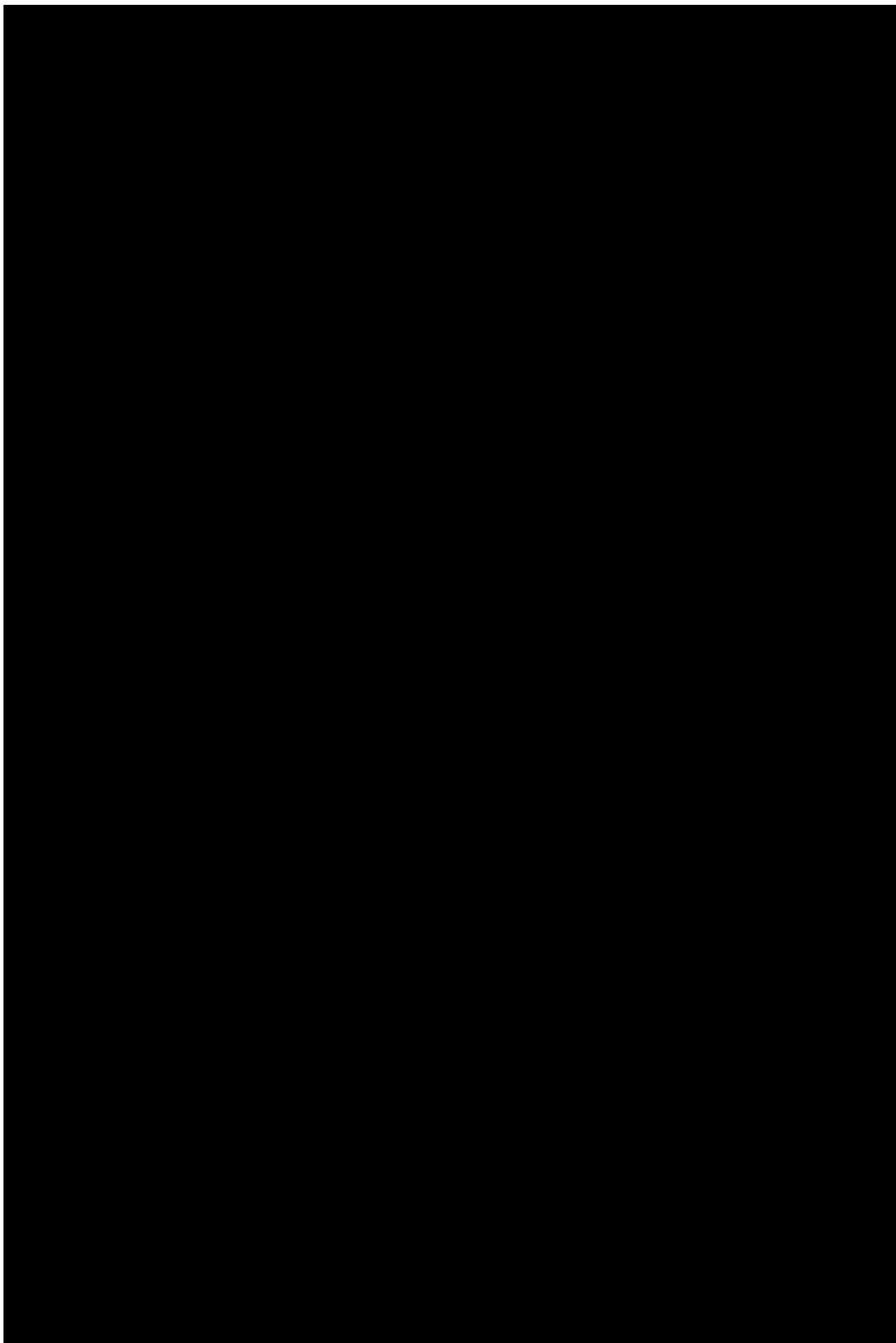
**T. J. Galvin, M. D. Filipović**

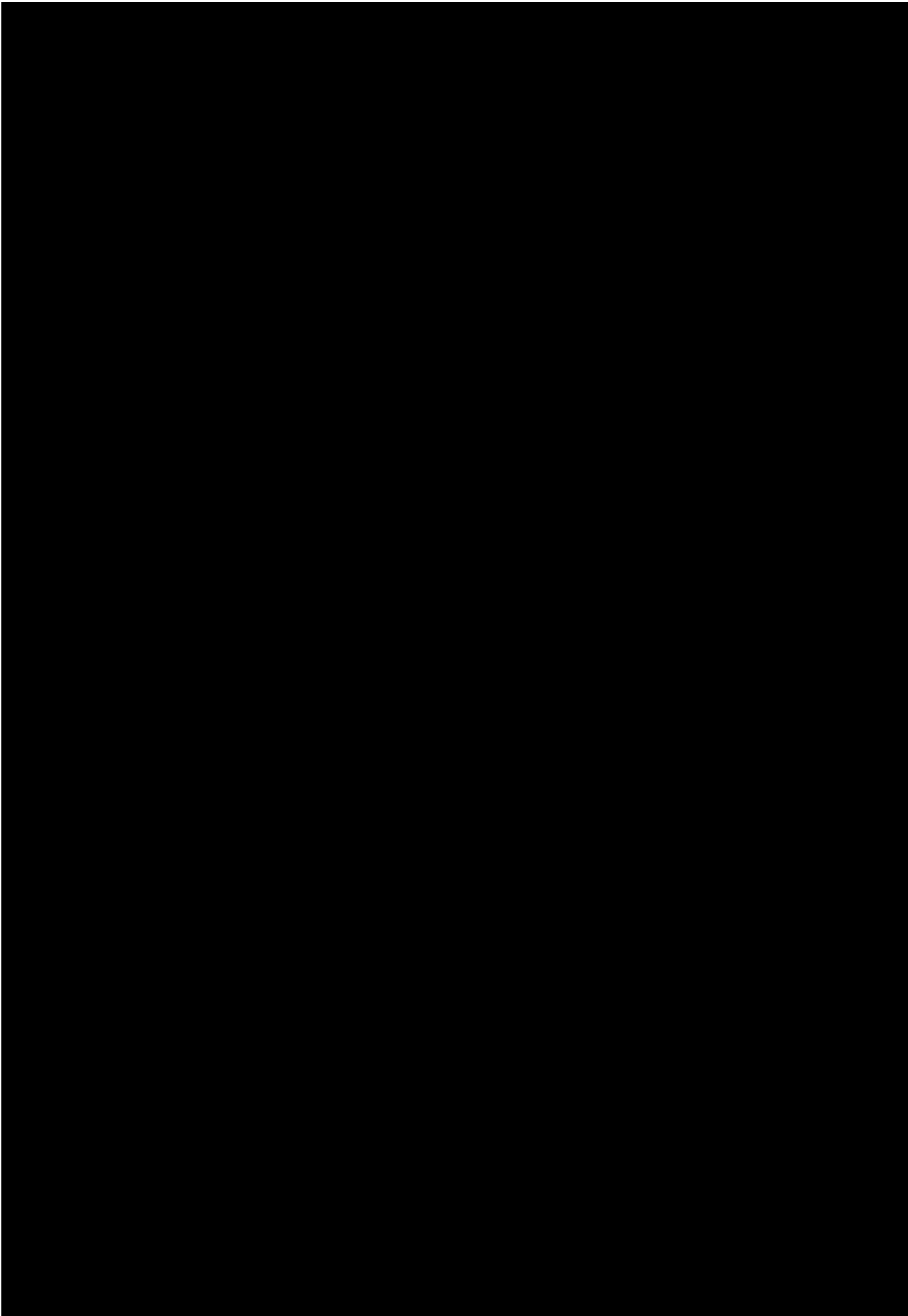
<sup>1</sup>*University of Western Sydney, Locked Bag 1797, Penrith South DC, NSW 2751, Australia  
E-mail: 136525304@student.uws.edu.au, m.filipovic@uws.edu.au*

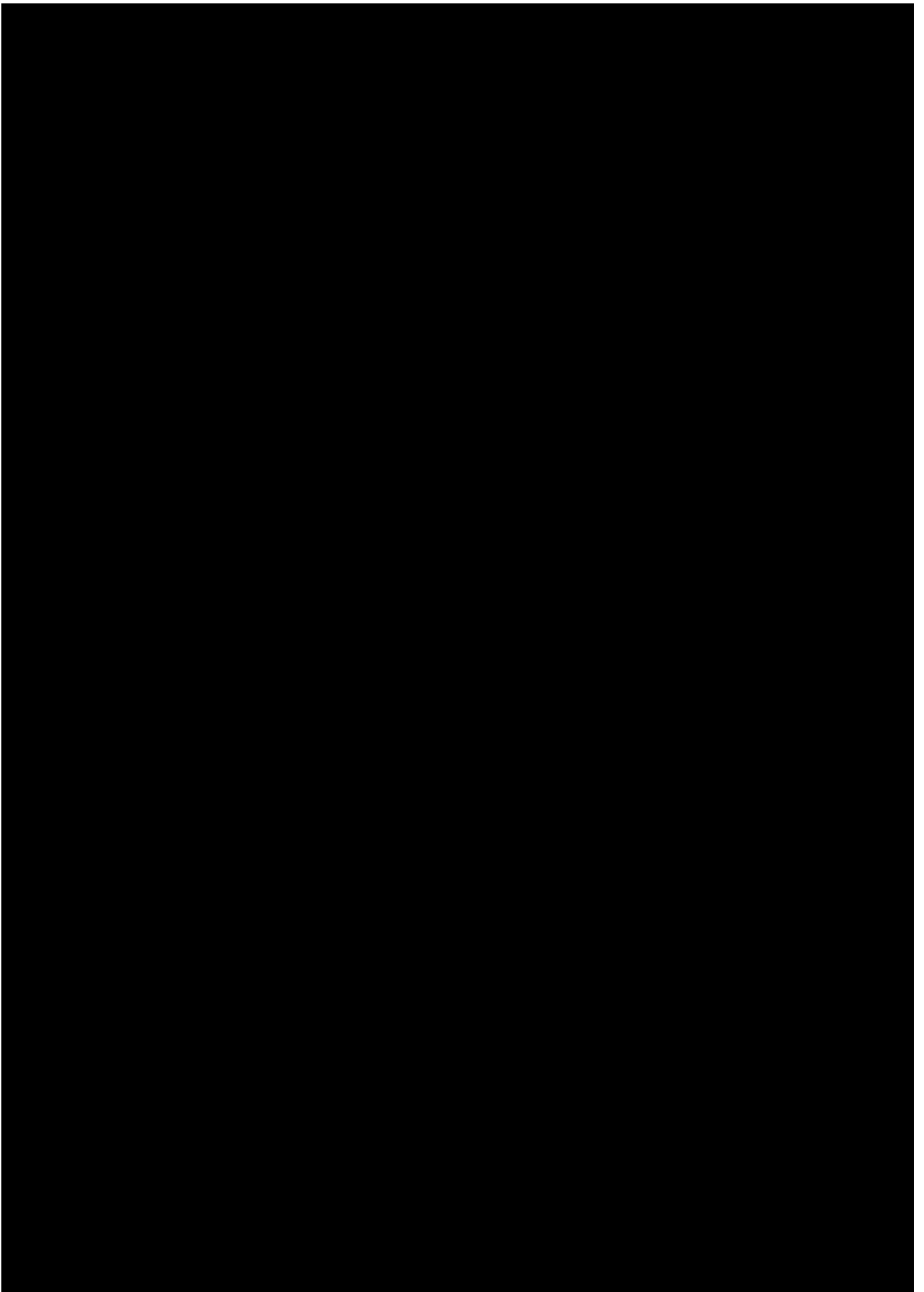


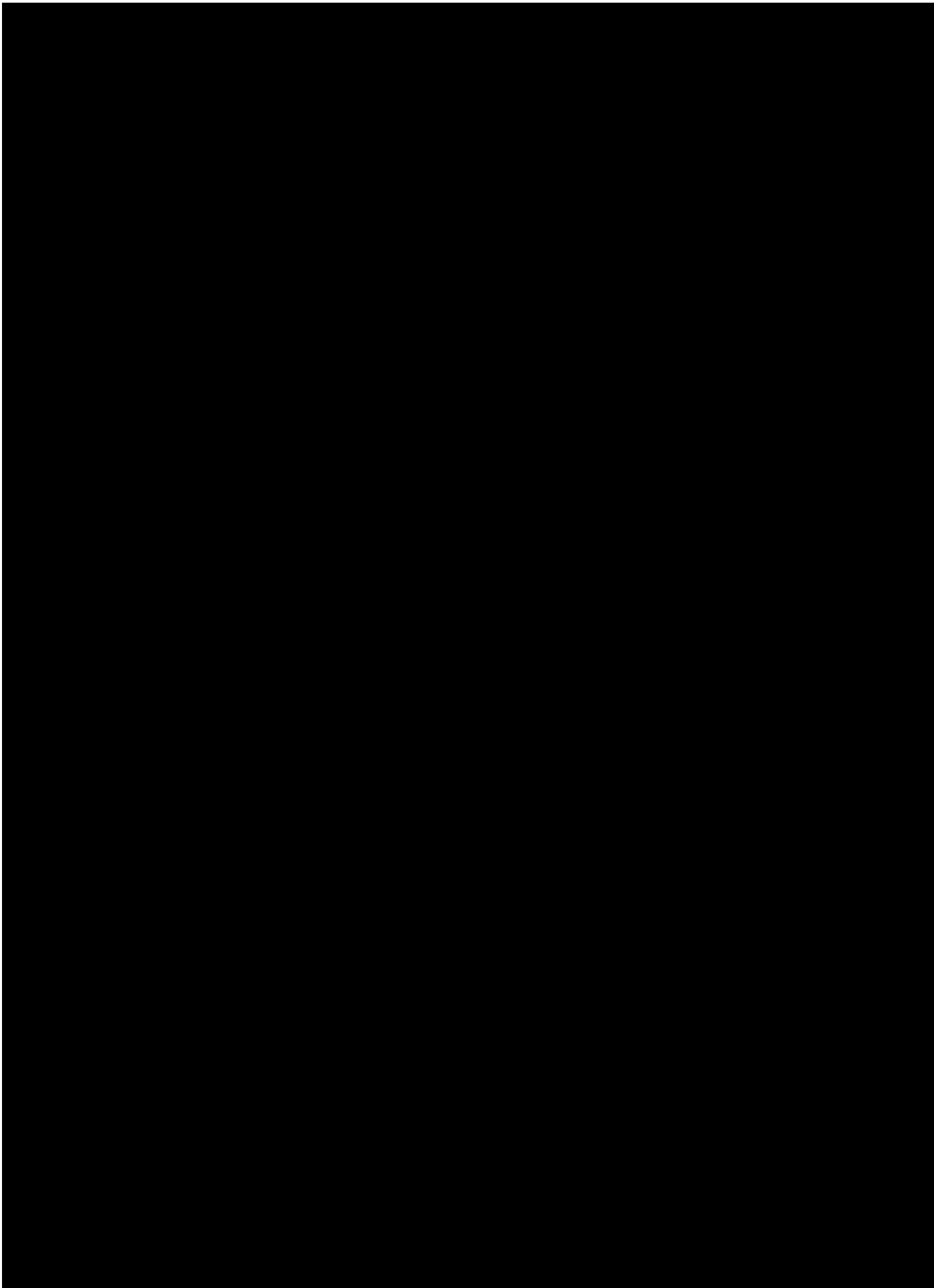




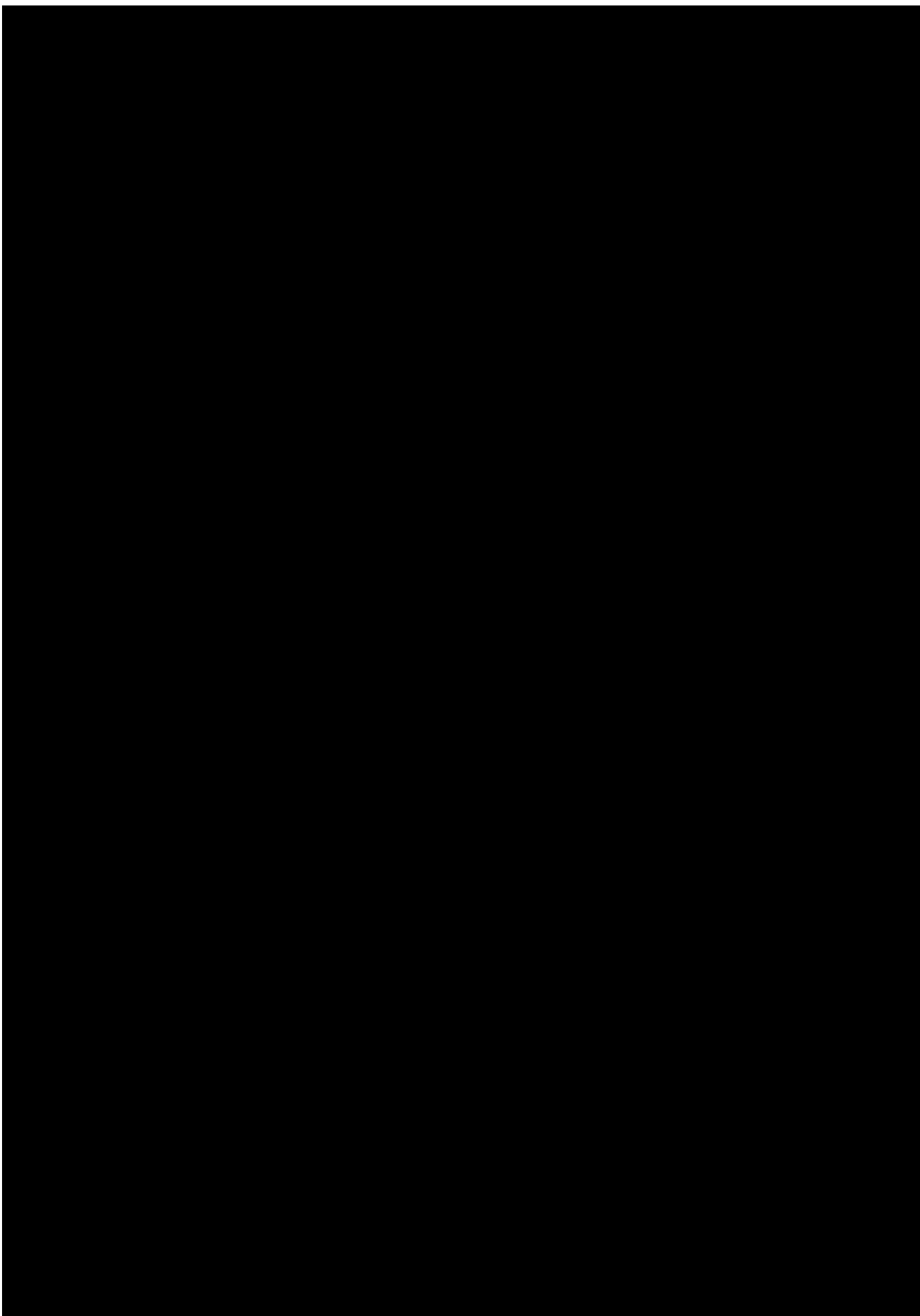


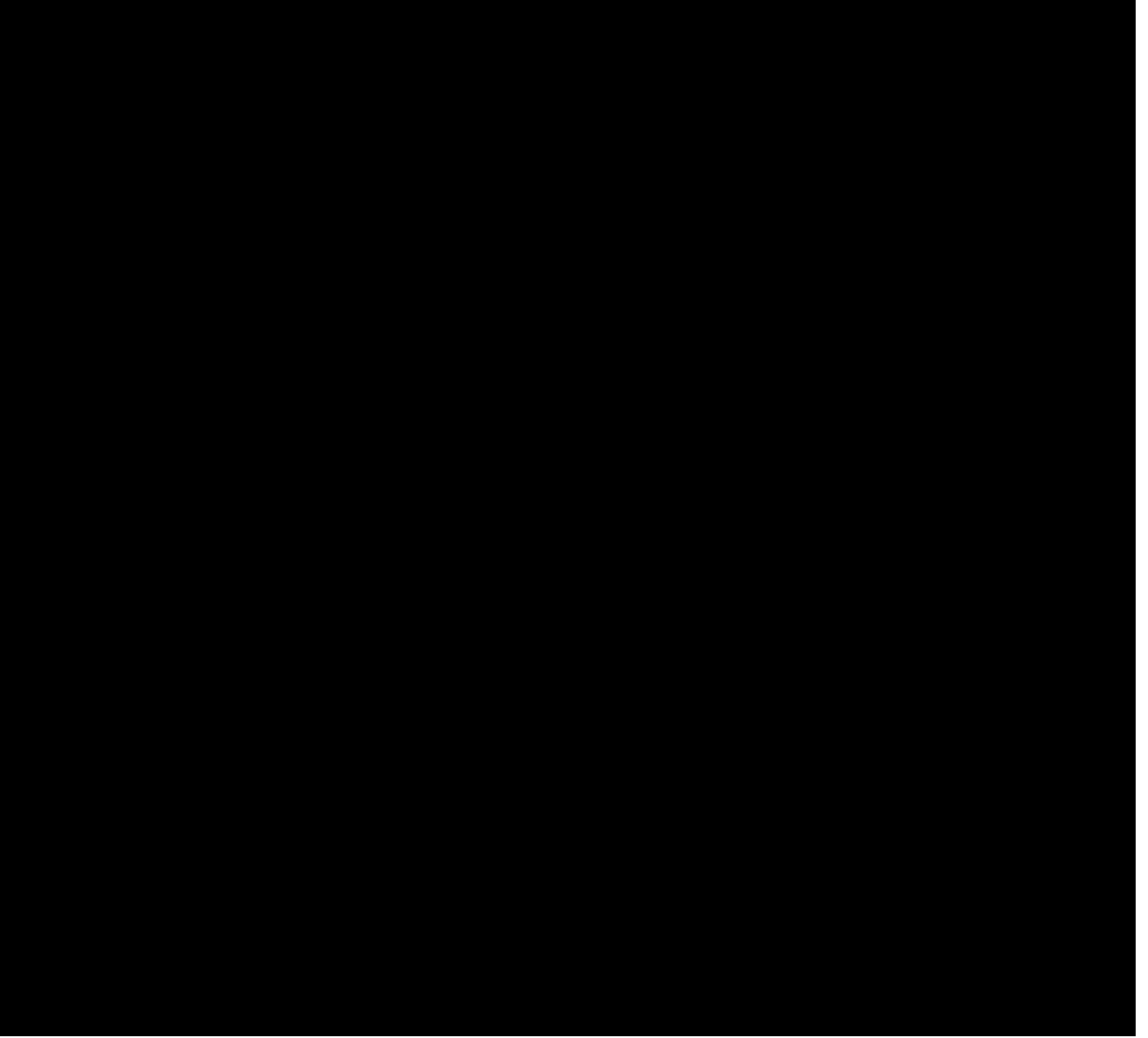


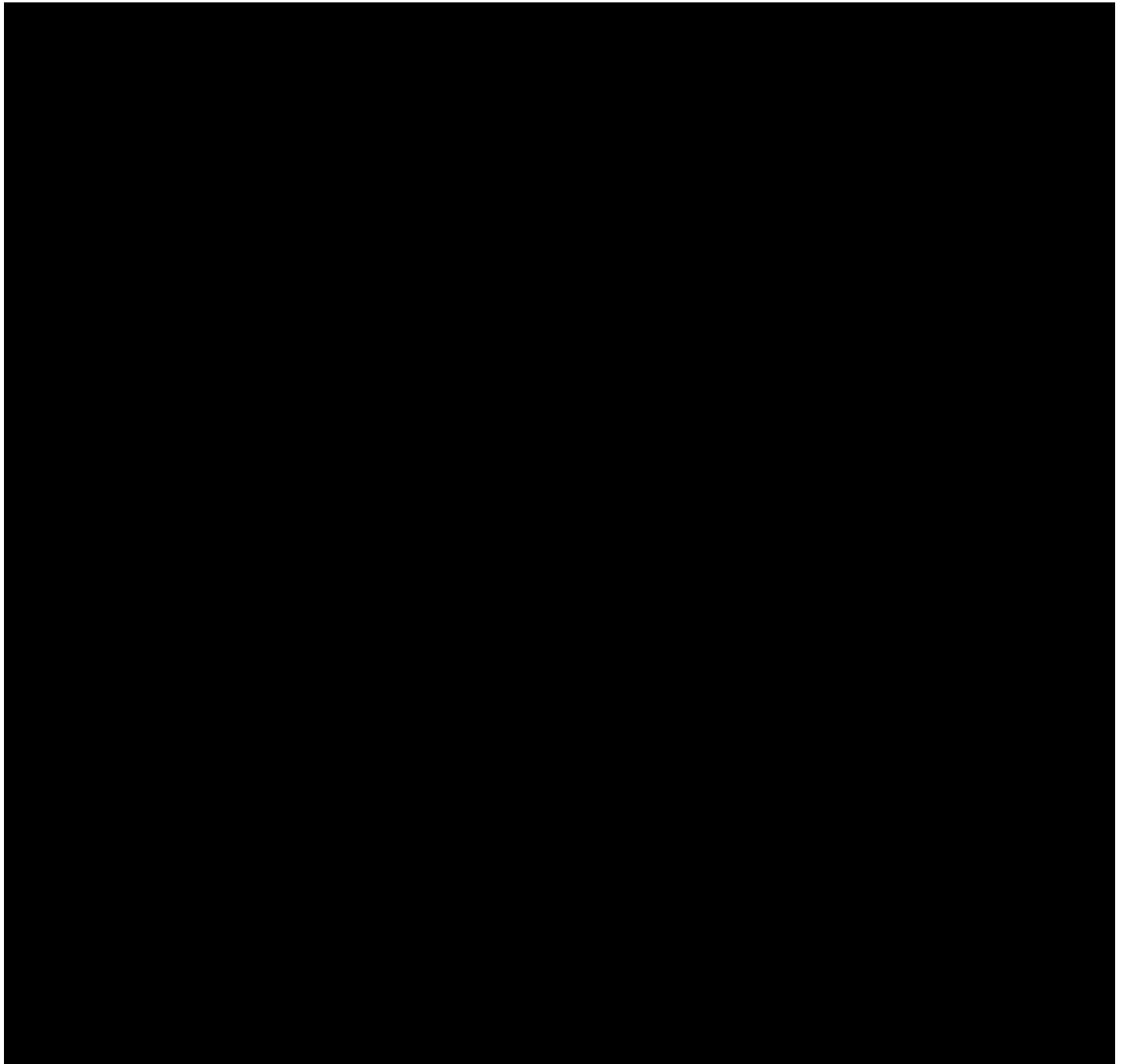




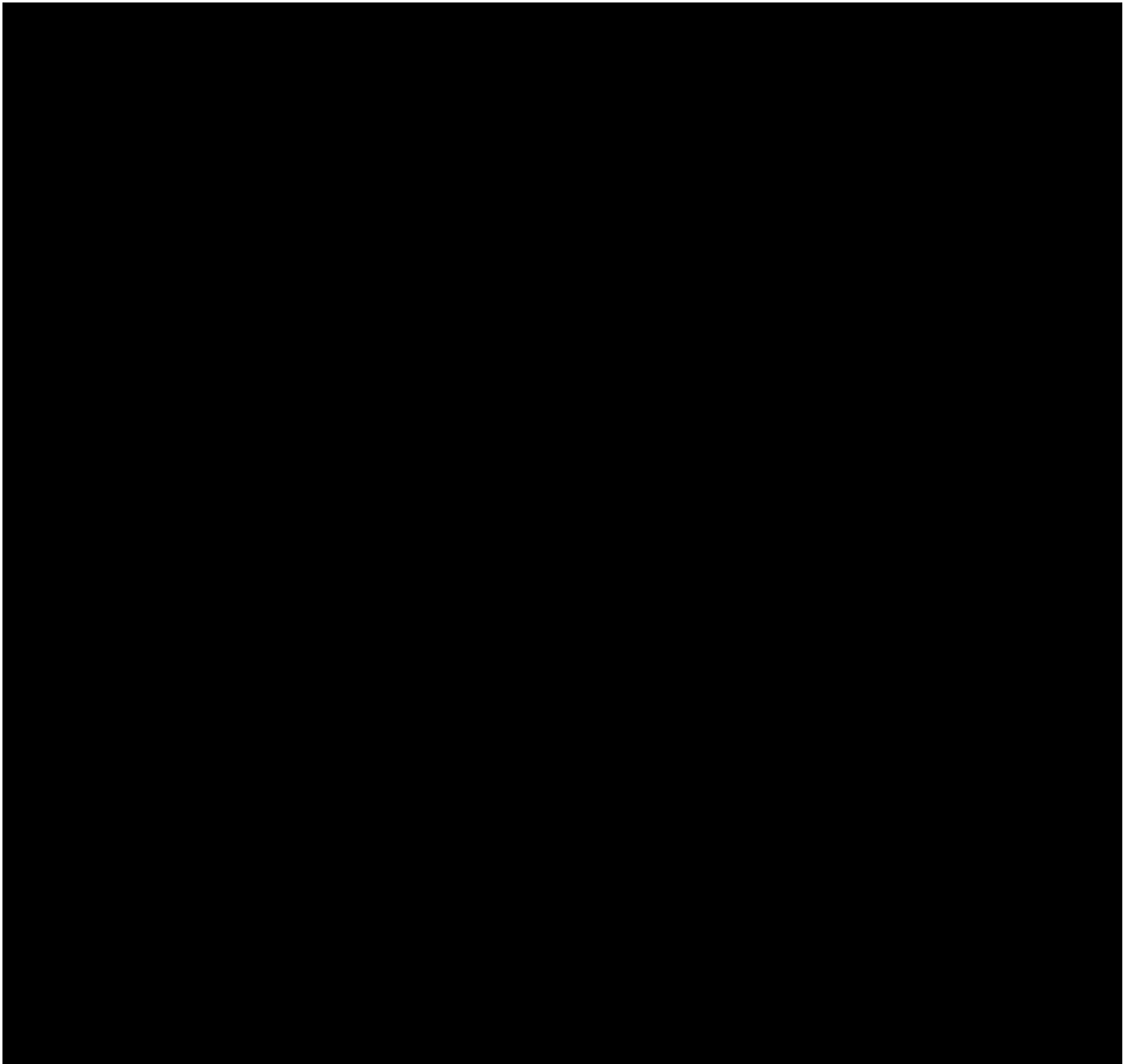




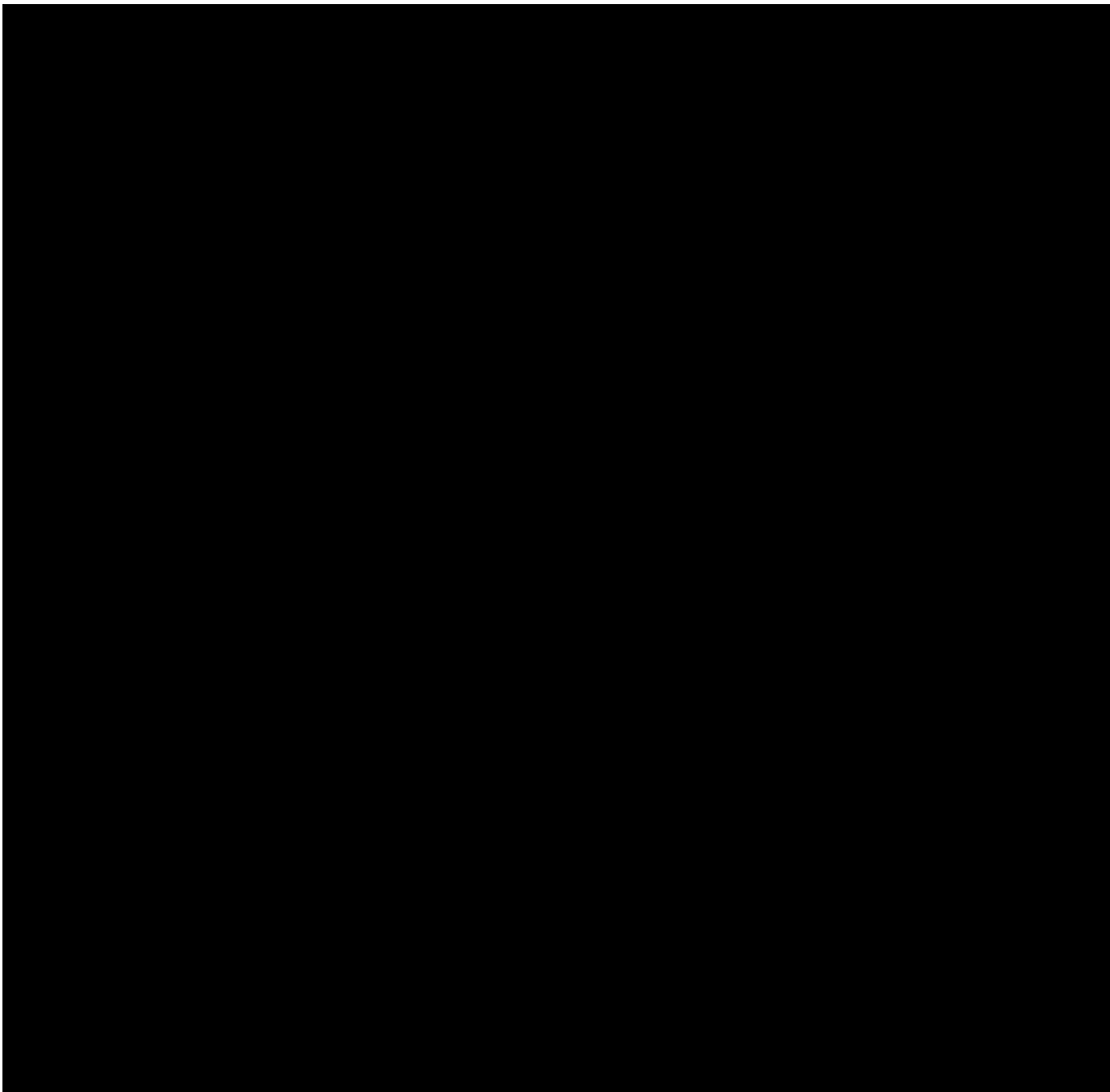


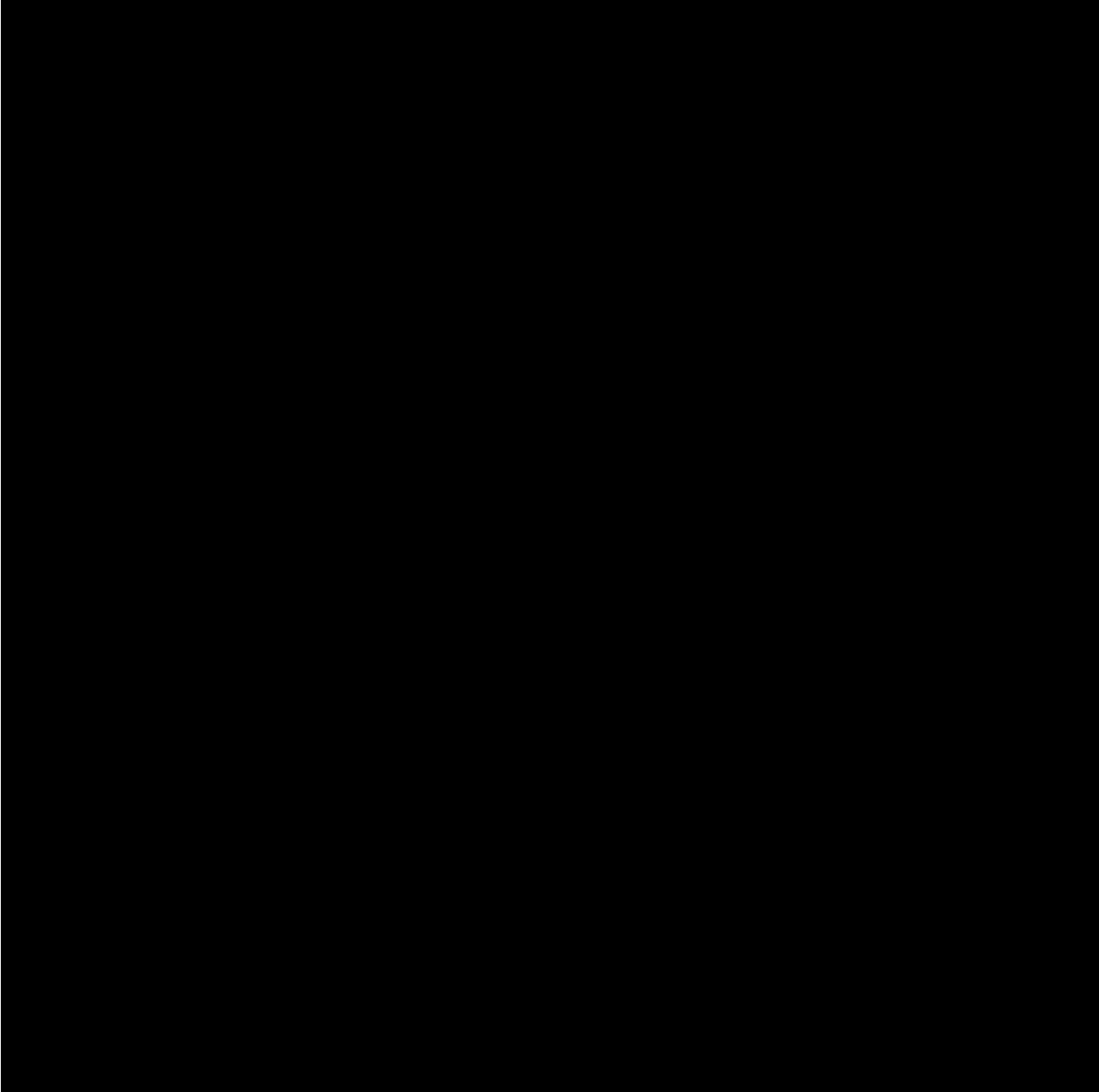








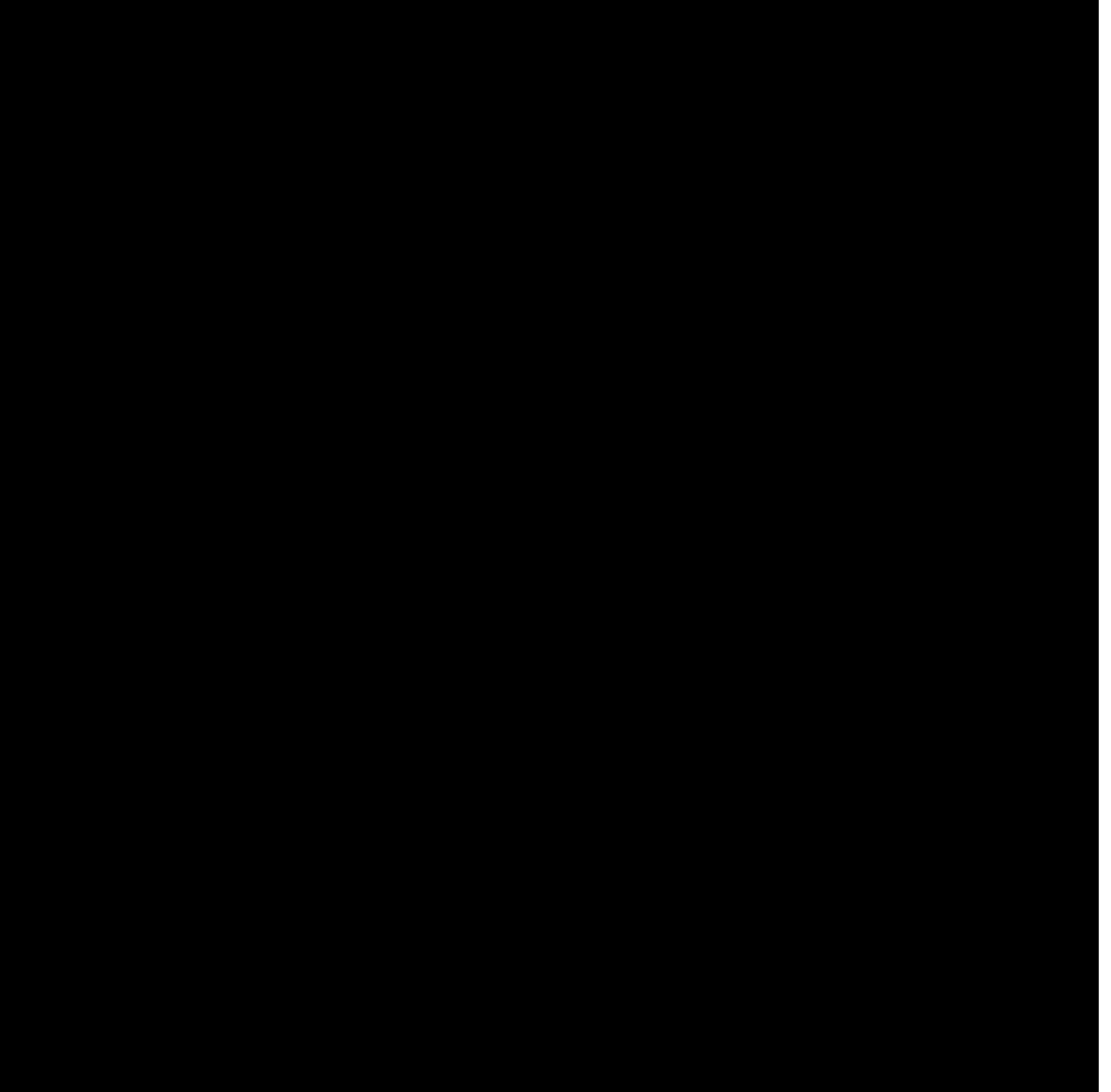




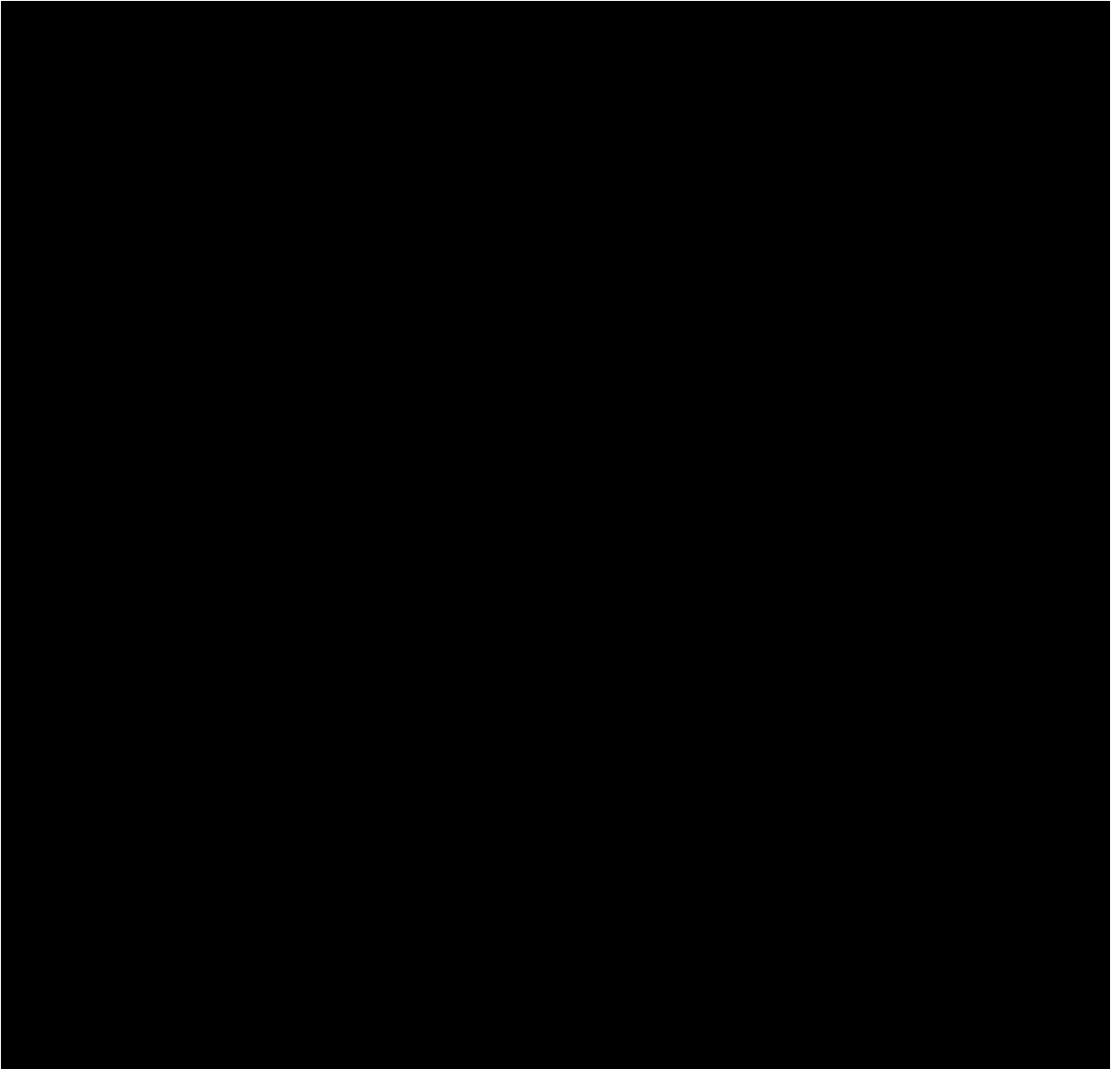


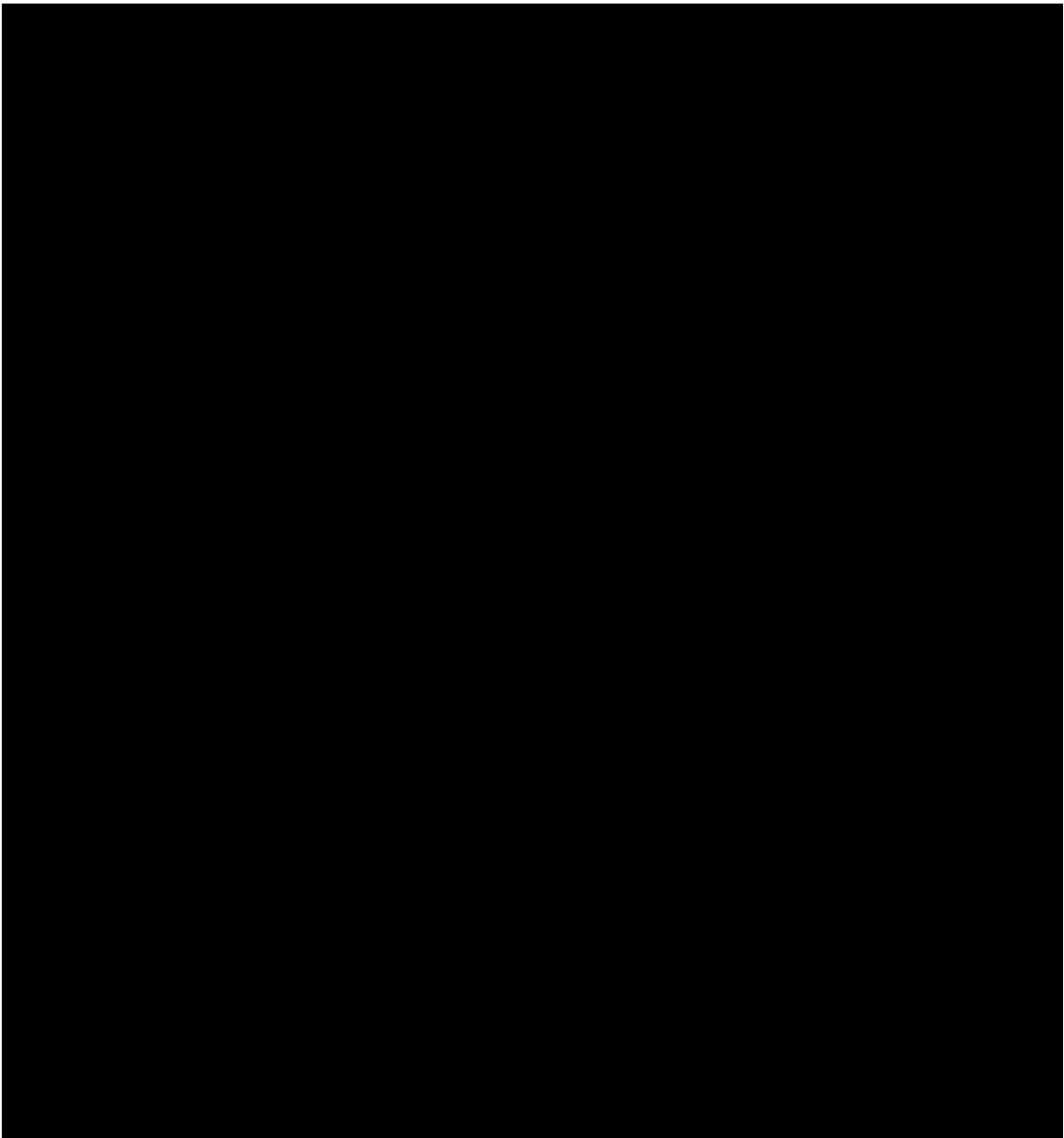


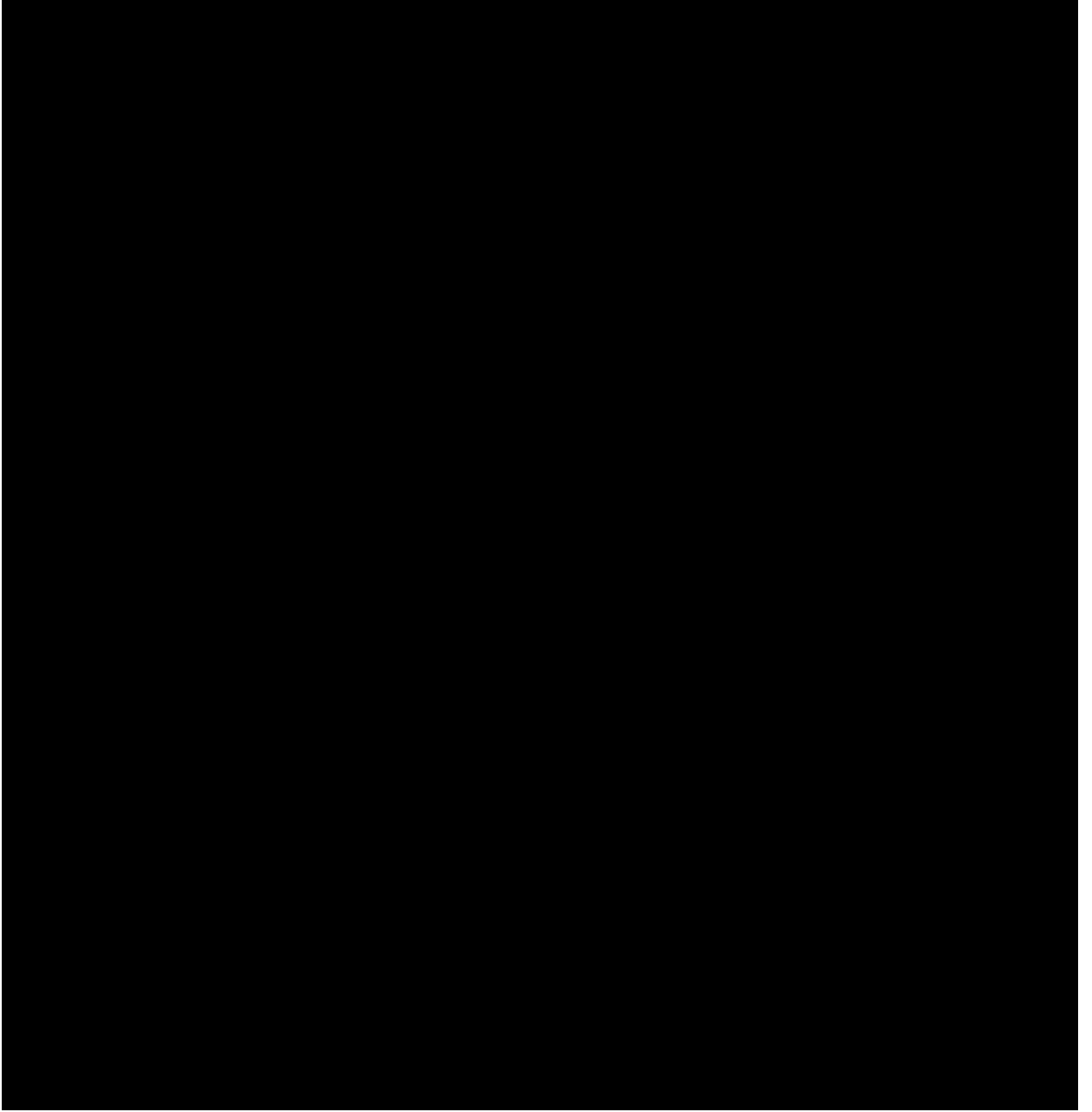


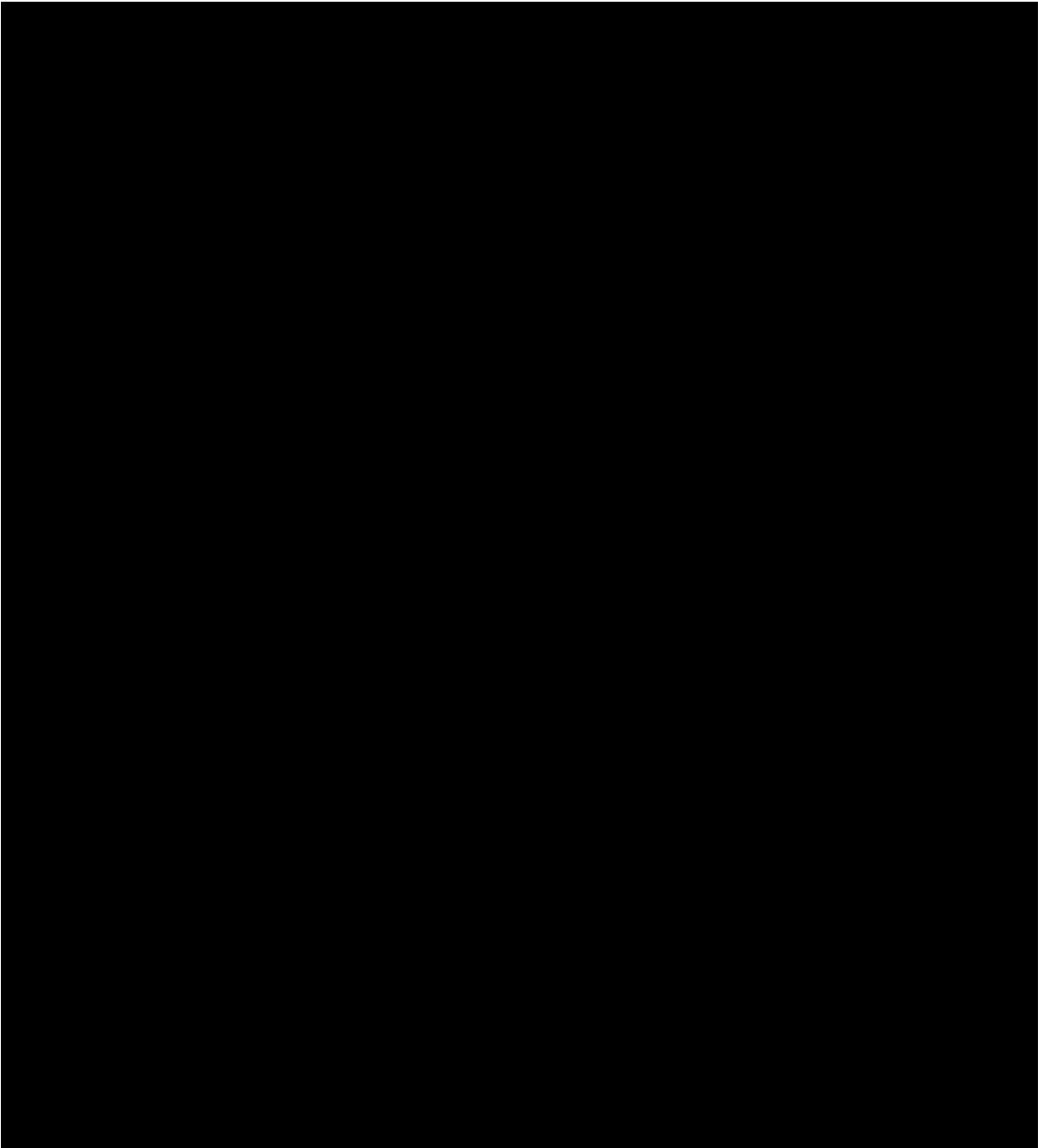




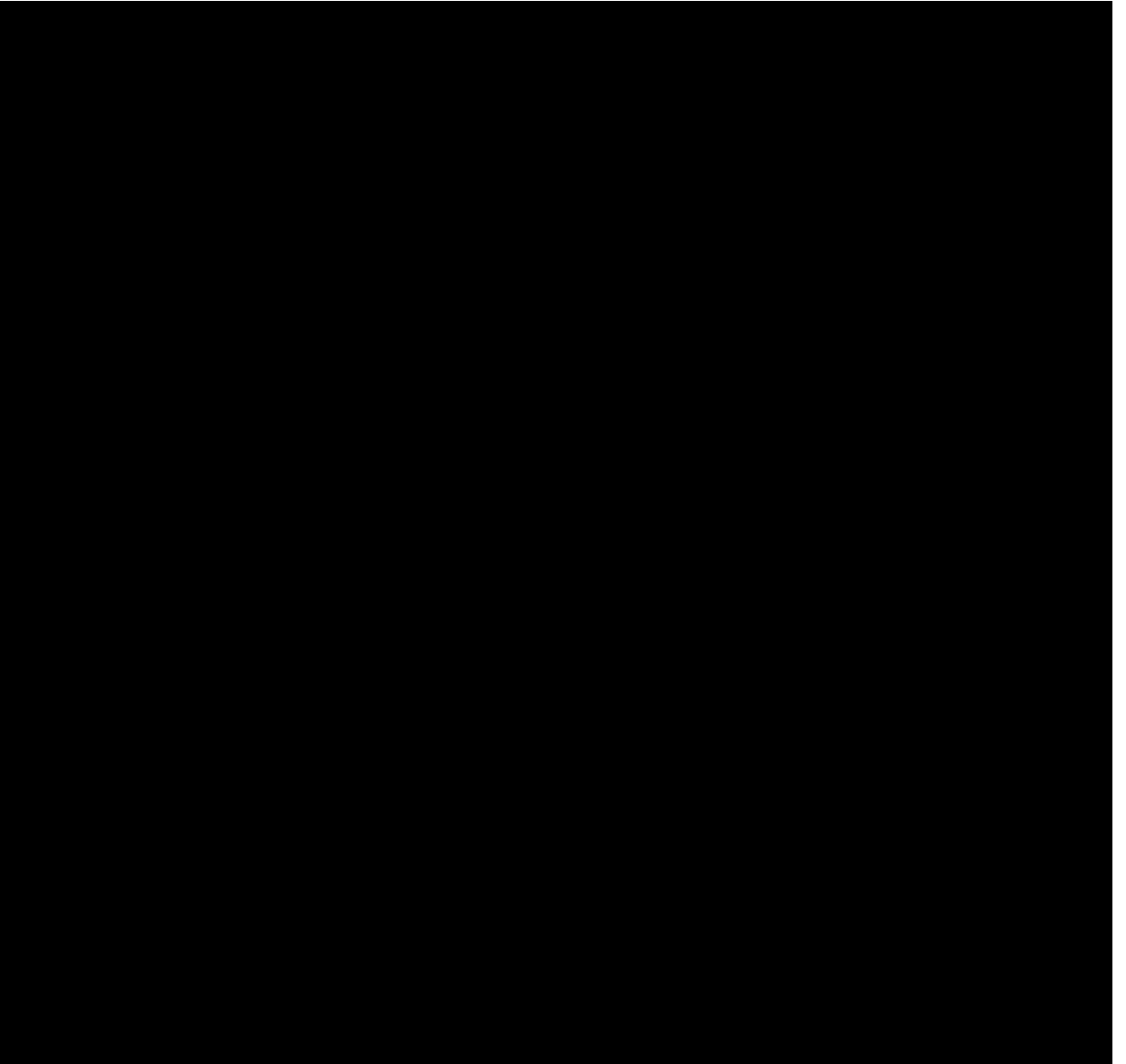


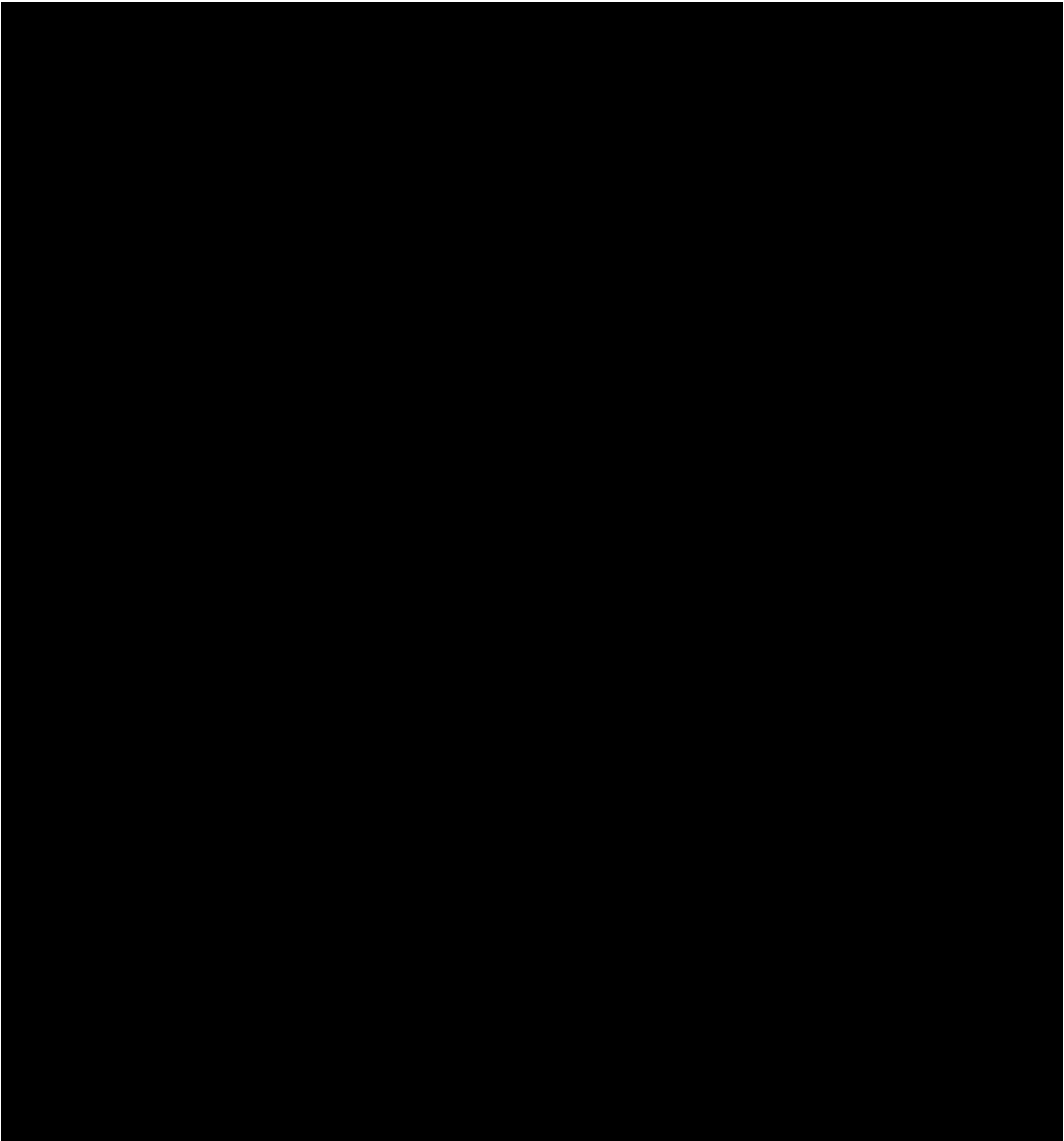












## Appendix B

# WIFES Supplementary Data and Figures

This section of the Appendices includes Figures related to the processing of the WiFeS dataset, including the modelled one-dimensional spectra of each source, resolved modelling of the  $H\alpha$  and  $H\beta$  recombination lines, resolved dust obscuration measures, and resolved star formation rates.

### B.1 PPXF modelled galaxy spectra

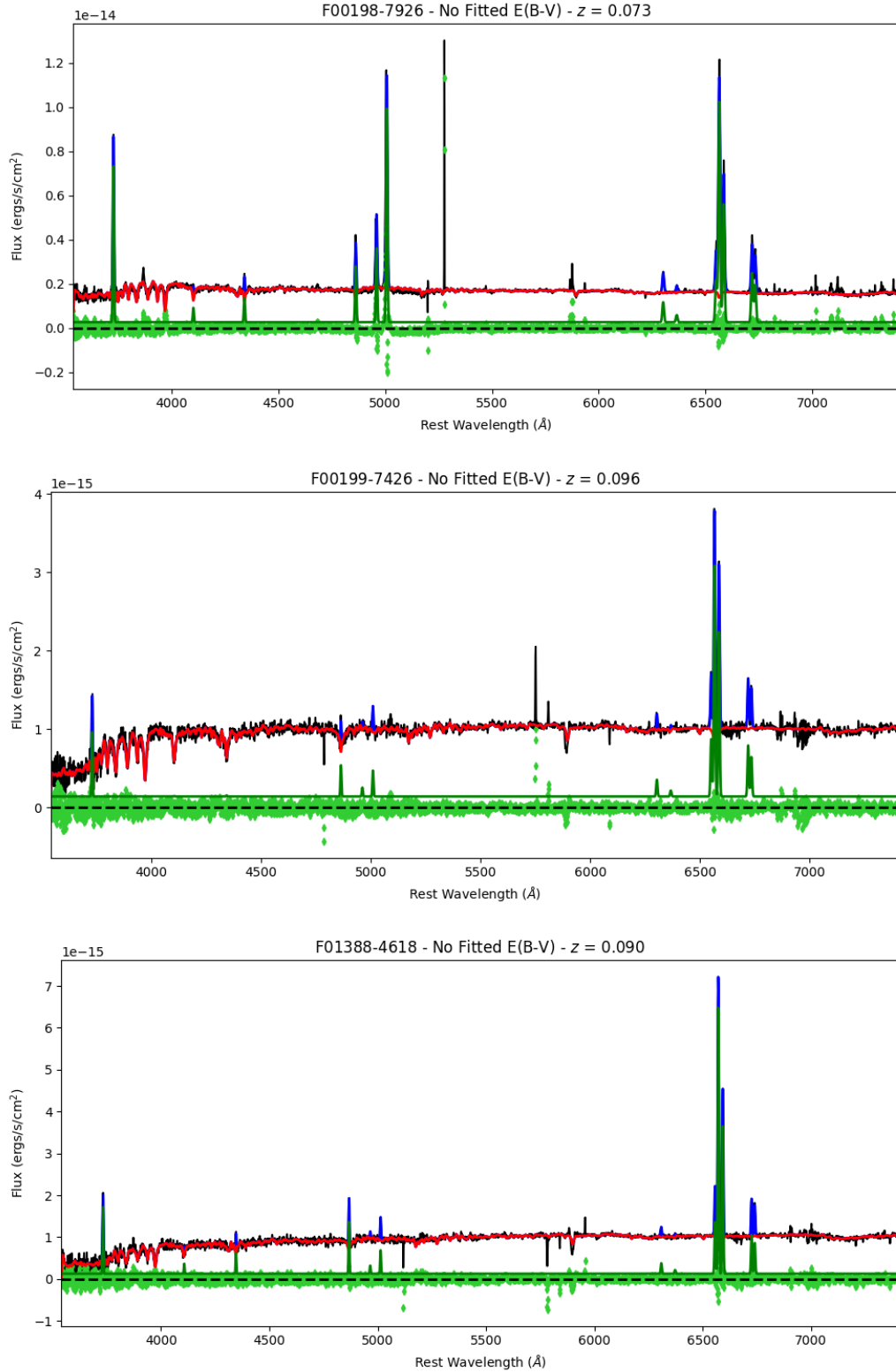


Figure B.1: An example of the model spectra constrained using the PPXF algorithm. The black line is the collapsed one-dimensional spectra obtained from my WiFeS observations. The stellar continuum that has been constrained using the MILES template library is shown in red. Generated templates of the stellar emission lines are shown in green. Residuals of the fit are shown around the dash line in lime green.

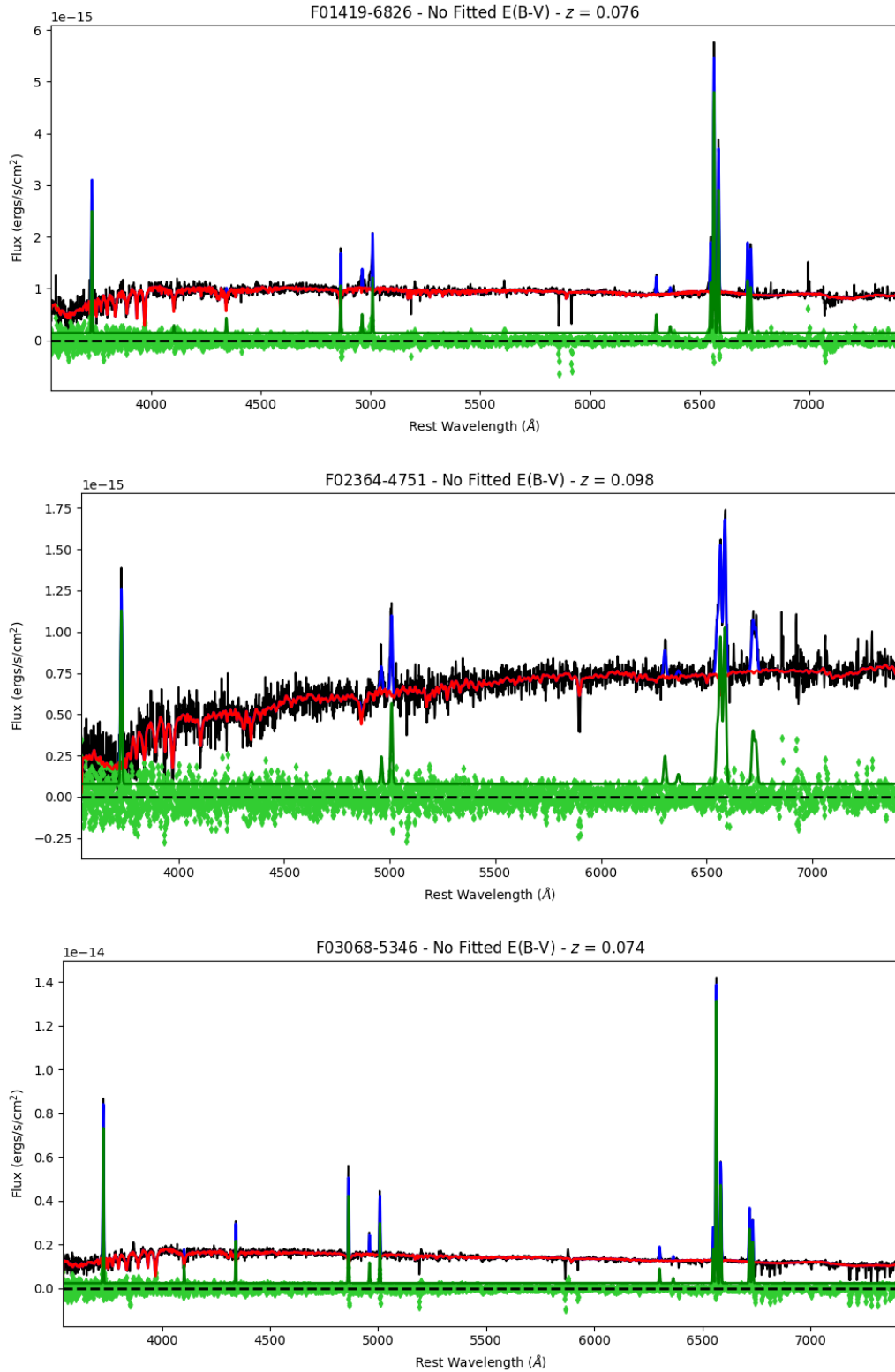


Figure B.1 (cont.): An example of the model spectra constrained using the PPF algorithm. The black line is the collapsed one-dimensional spectra obtained from my WiFeS observations. The stellar continuum that has been constrained using the MILES template library is shown in red. Generated templates of the stellar emission lines are shown in green. Residuals of the fit are shown around the dash line in lime green.

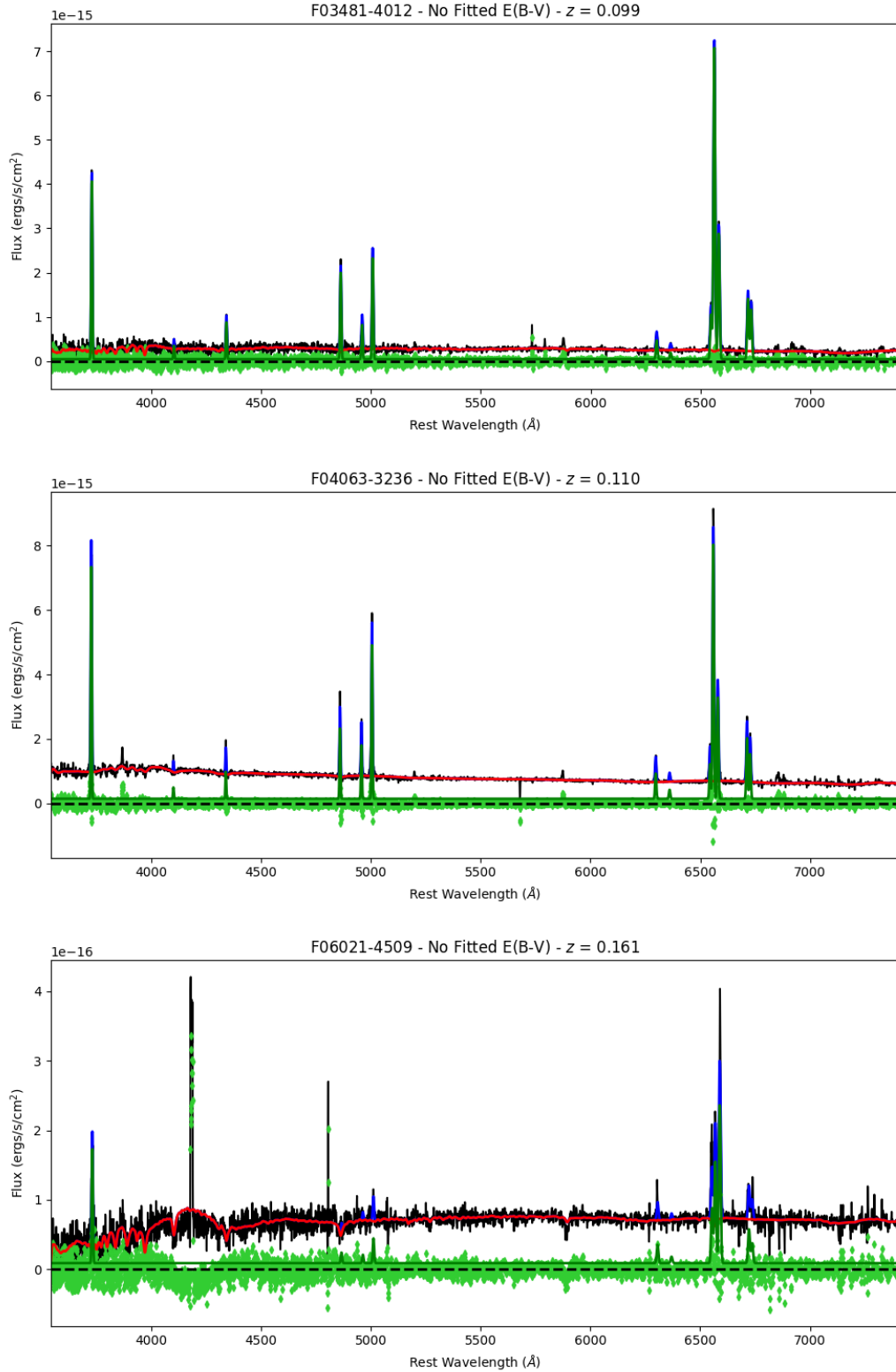


Figure B.1 (cont.): An example of the model spectra constrained using the PPXF algorithm. The black line is the collapsed one-dimensional spectra obtained from my WiFeS observations. The stellar continuum that has been constrained using the MILES template library is shown in red. Generated templates of the stellar emission lines are shown in green. Residuals of the fit are shown around the dash line in lime green.

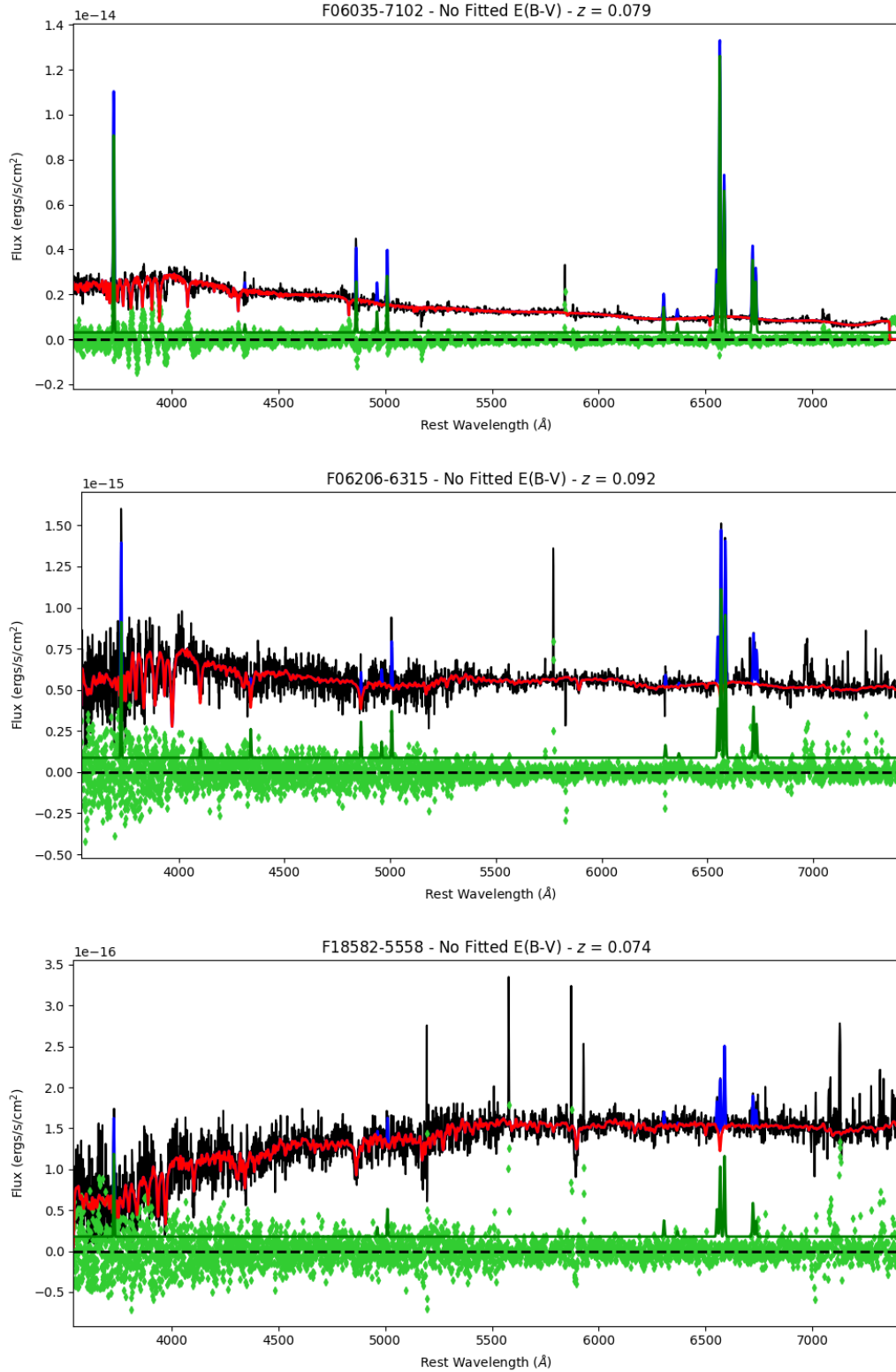


Figure B.1 (cont.): An example of the model spectra constrained using the PPXF algorithm. The black line is the collapsed one-dimensional spectra obtained from my WiFeS observations. The stellar continuum that has been constrained using the MILES template library is shown in red. Generated templates of the stellar emission lines are shown in green. Residuals of the fit are shown around the dash line in lime green.

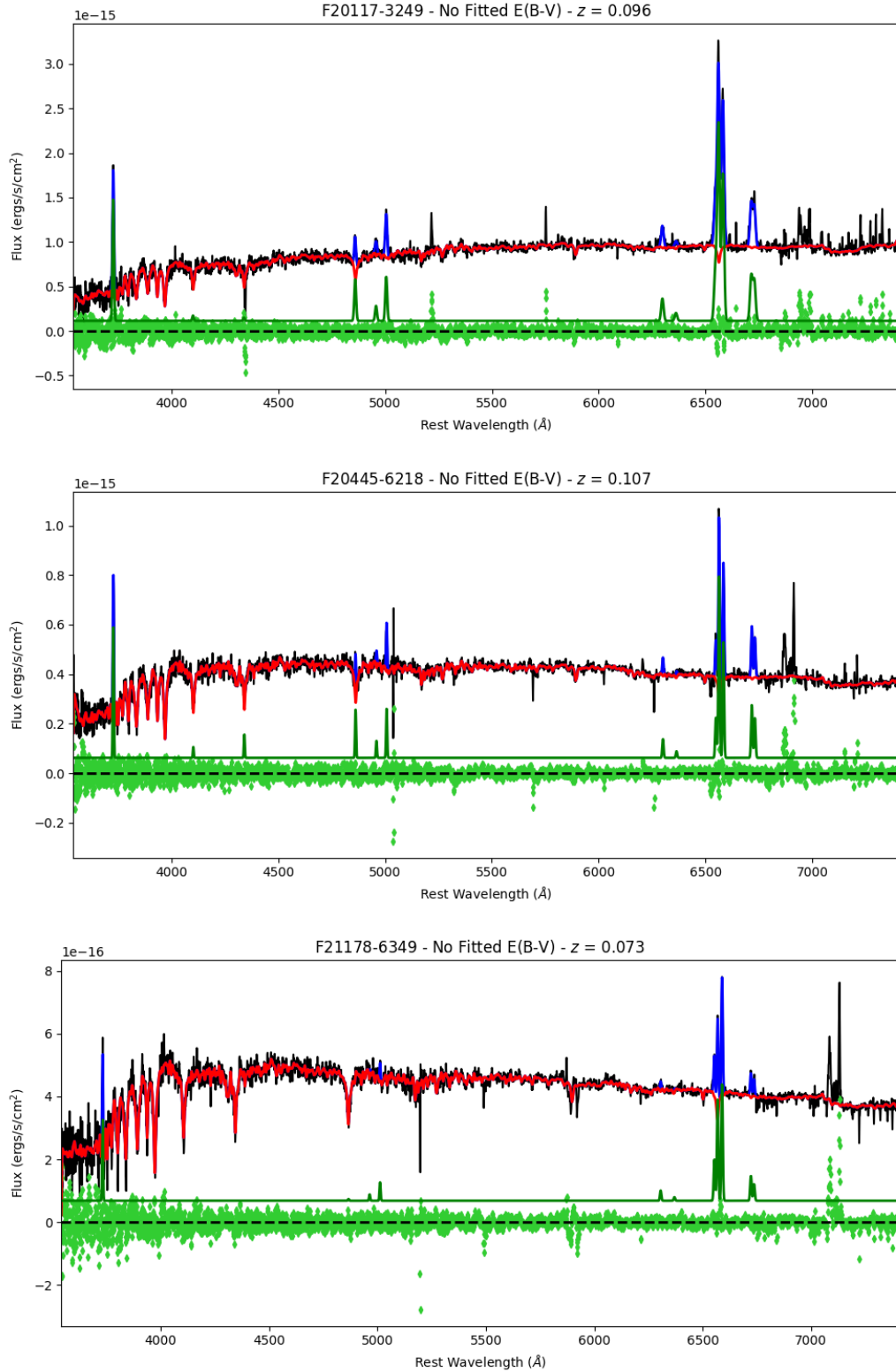


Figure B.1 (cont.): An example of the model spectra constrained using the PPXF algorithm. The black line is the collapsed one-dimensional spectra obtained from my WiFeS observations. The stellar continuum that has been constrained using the MILES template library is shown in red. Generated templates of the stellar emission lines are shown in green. Residuals of the fit are shown around the dash line in lime green.



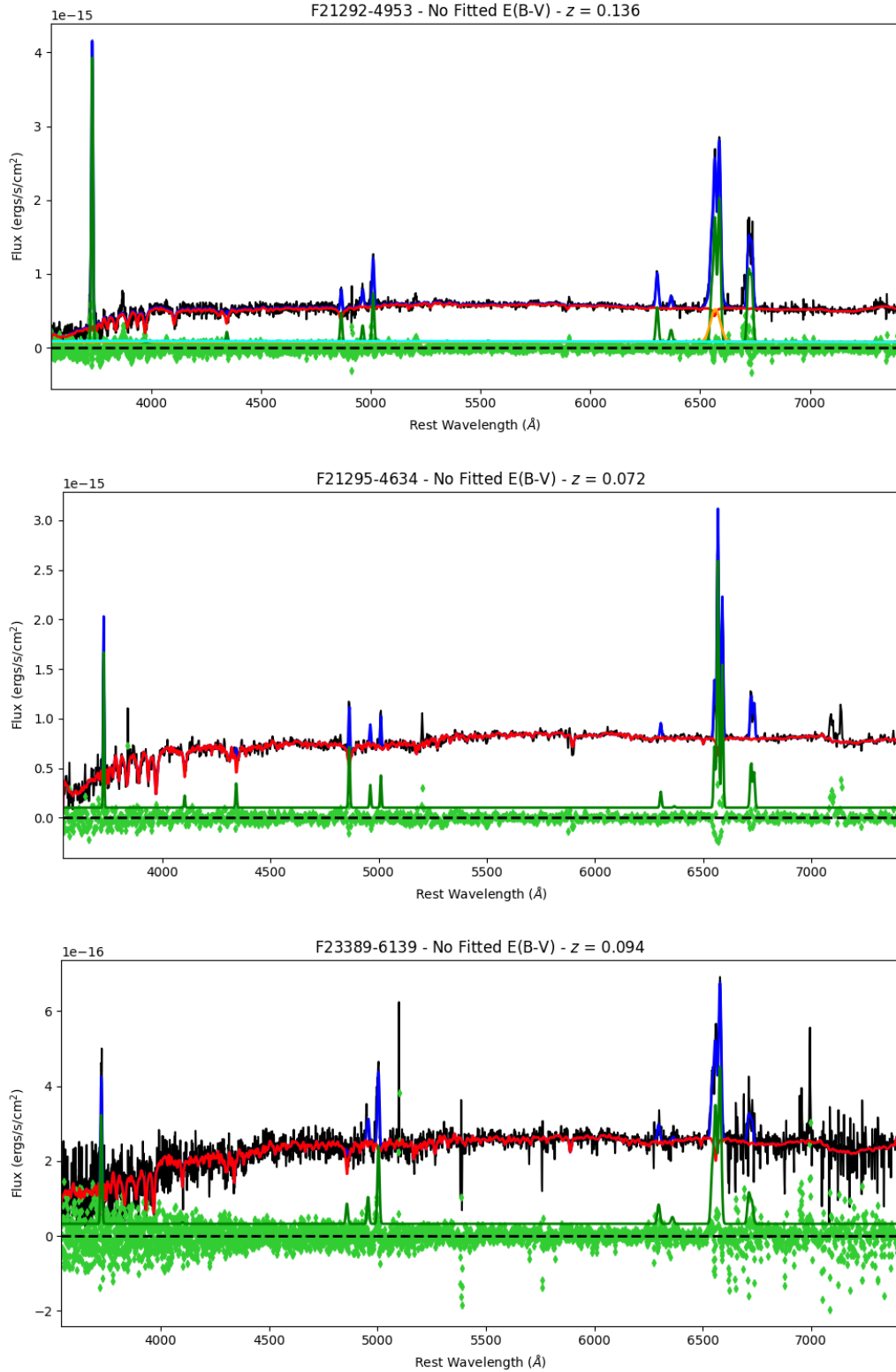
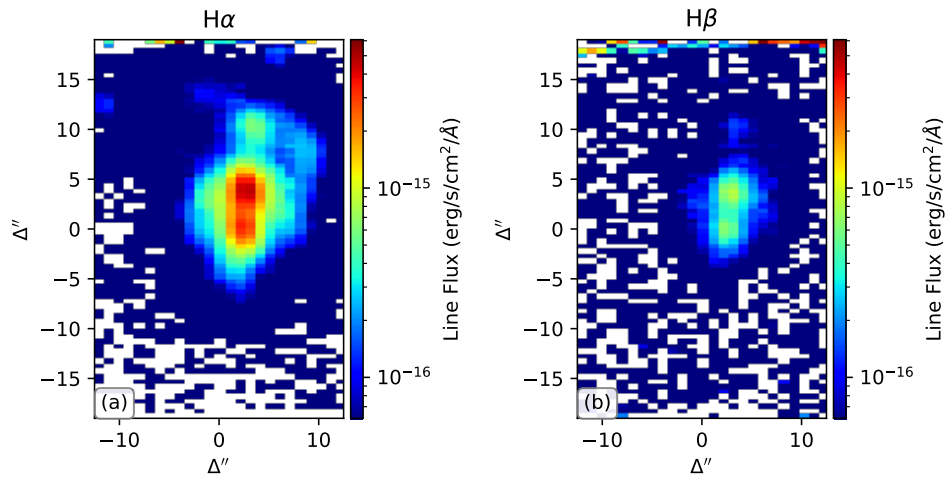


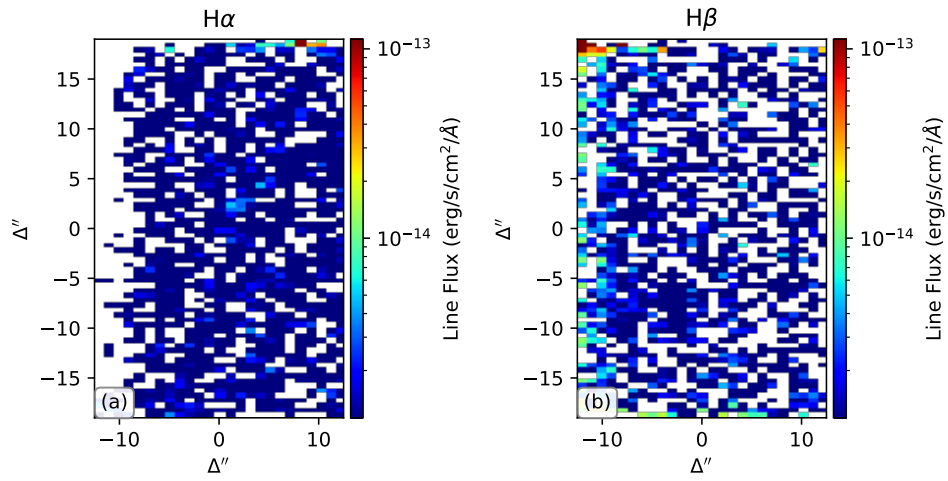
Figure B.1 (cont.): An example of the model spectra constrained using the PPXF algorithm. The black line is the collapsed one-dimensional spectra obtained from my WiFeS observations. The stellar continuum that has been constrained using the MILES template library is shown in red. Generated templates of the stellar emission lines are shown in green. Residuals of the fit are shown around the dash line in lime green.

## B.2 Resolved Optical Modelling

F00198-7926



F00199-7426



F01388-4618

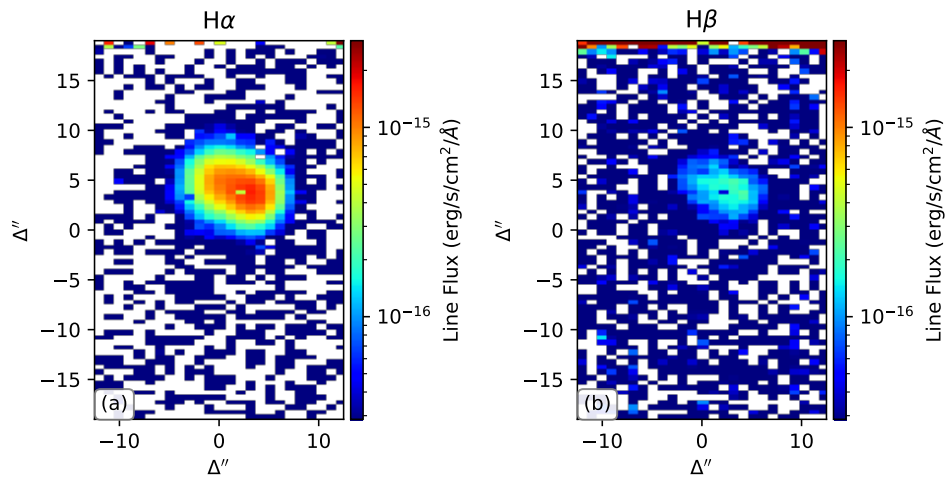
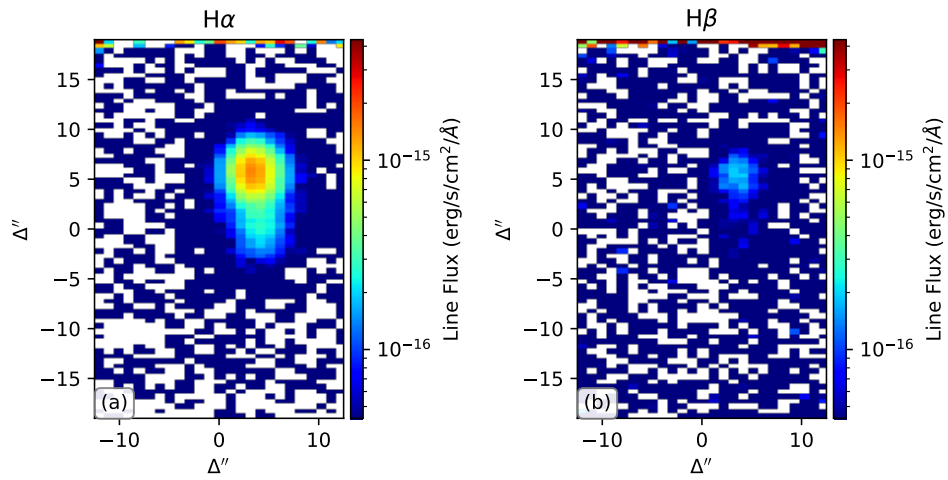
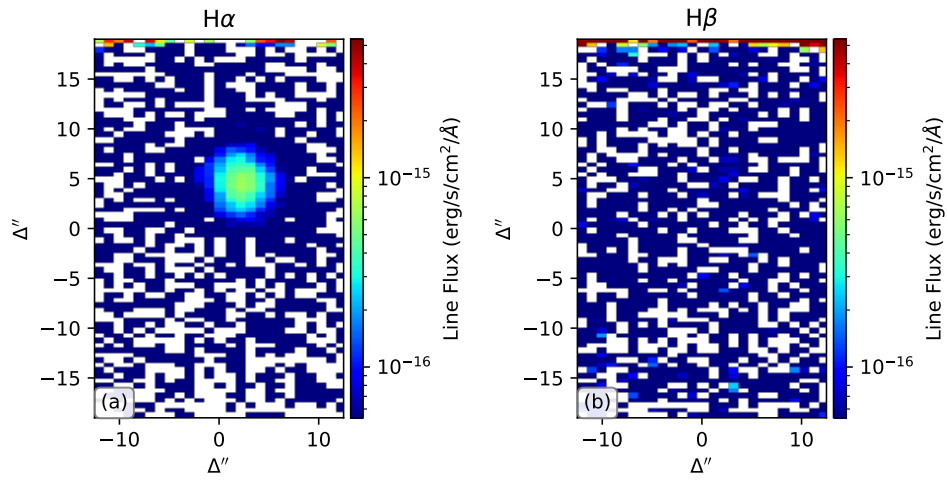


Figure B.2: The integrated fluxes of the H $\alpha$  and H $\beta$  lines constrained by applying PPXF to each of the 1,900 individual spaxels.

F01419-6826



F02364-4751



F03068-5346

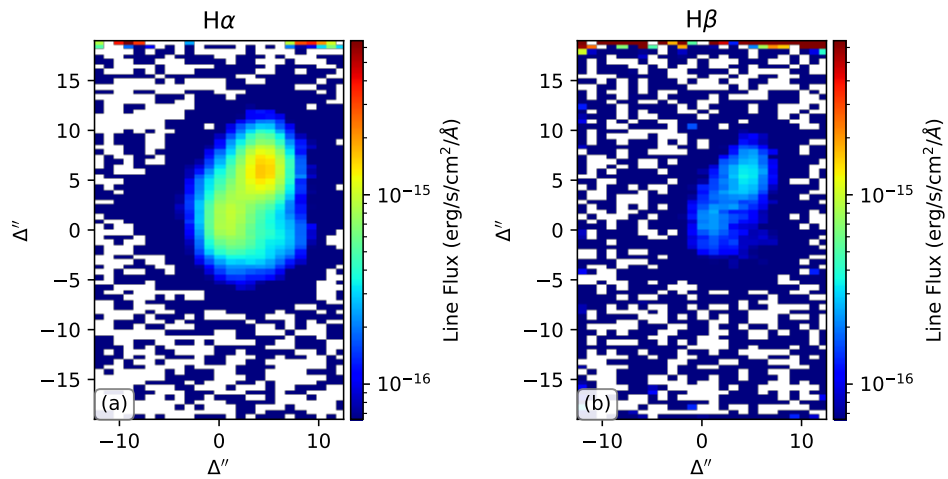
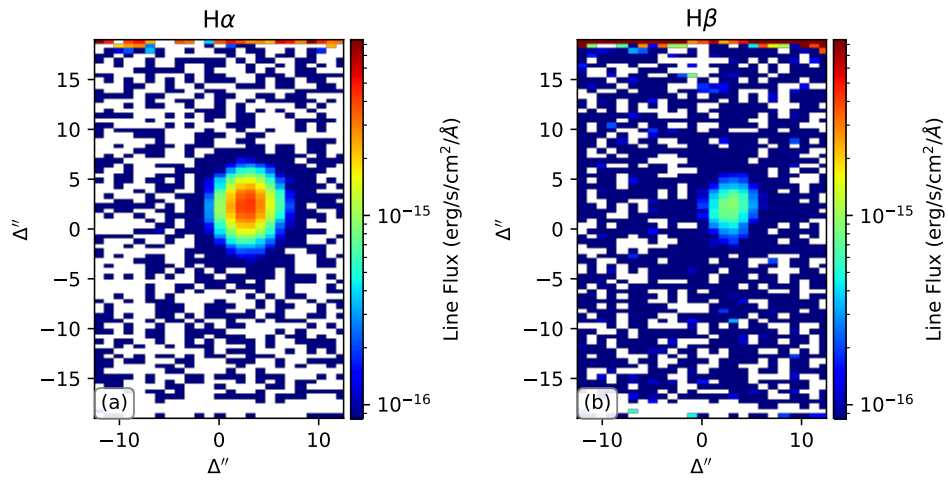
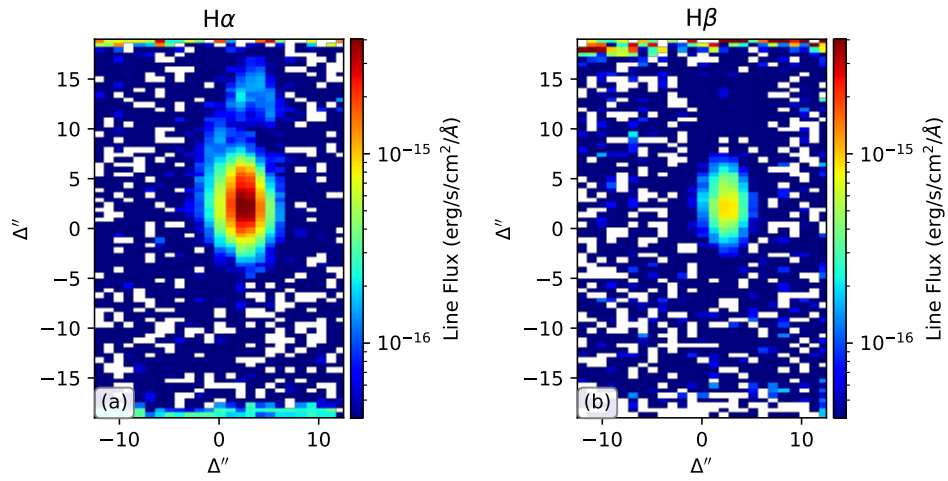


Figure B.2 (cont.): The integrated fluxes of the H $\alpha$  and H $\beta$  lines constrained by applying PPXF to each of the 1,900 individual spaxels.

F03481-4012



F04063-3236



F06021-4509

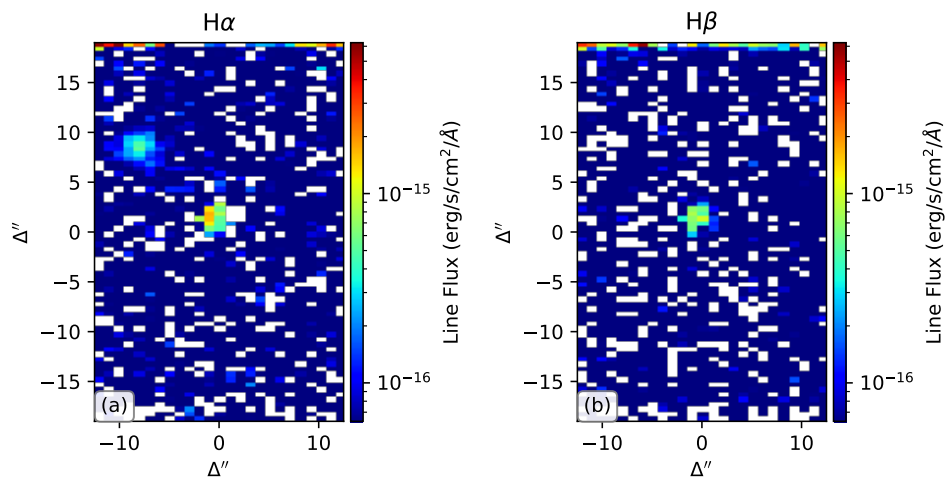
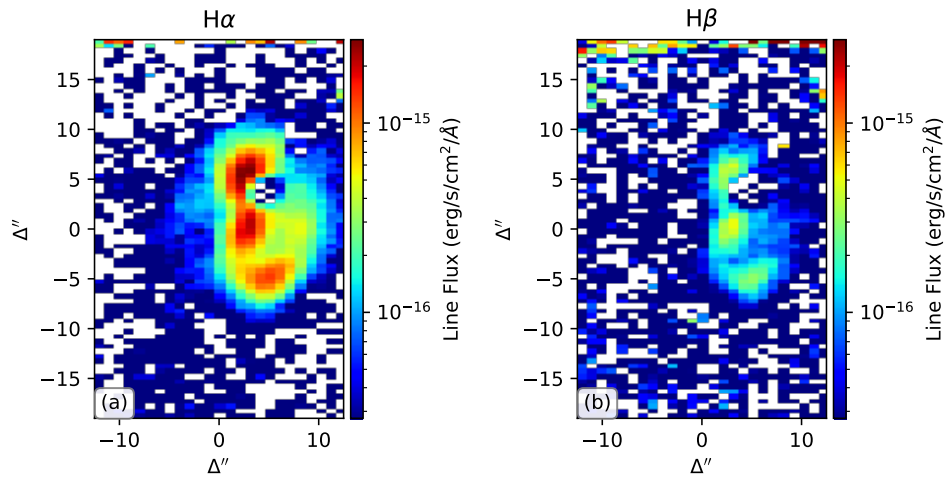
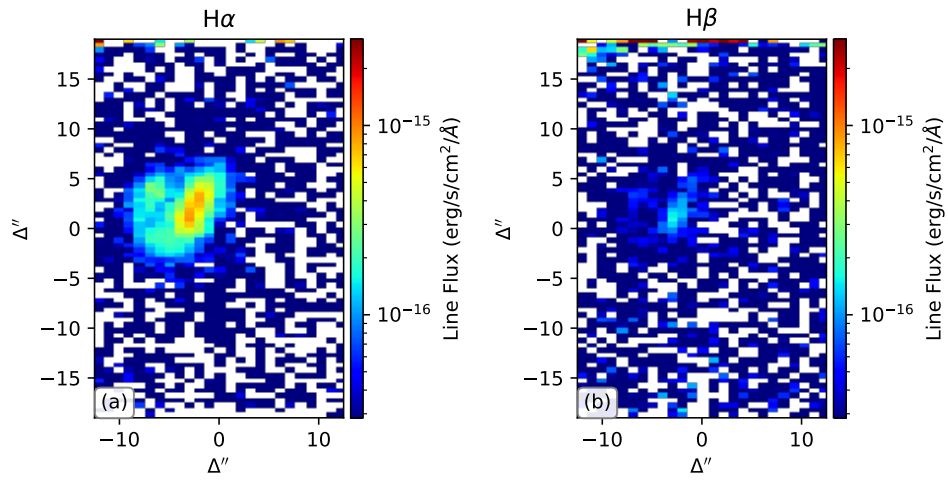


Figure B.2 (cont.): The integrated fluxes of the H $\alpha$  and H $\beta$  lines constrained by applying PPXF to each of the 1,900 individual spaxels.

F06035-7102



F06206-6315



F18582-5558

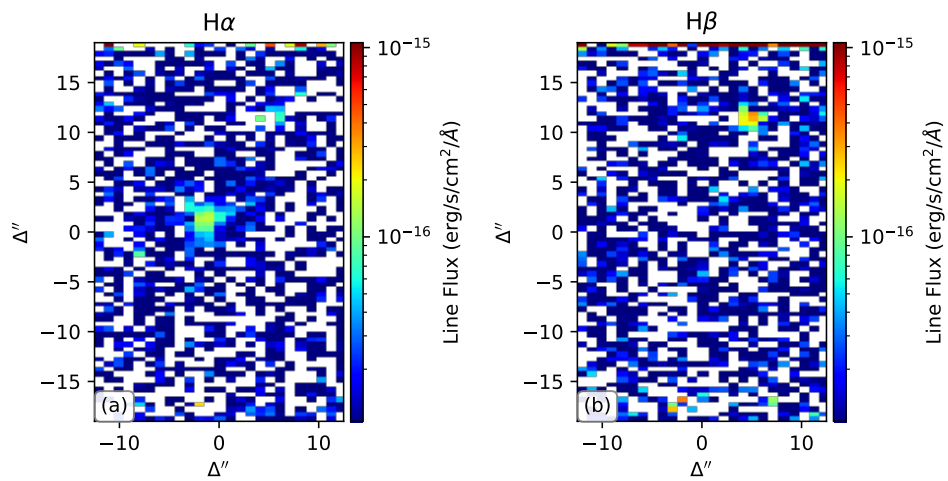


Figure B.2 (cont.): The integrated fluxes of the H $\alpha$  and H $\beta$  lines constrained by applying PPXF to each of the 1,900 individual spaxels.

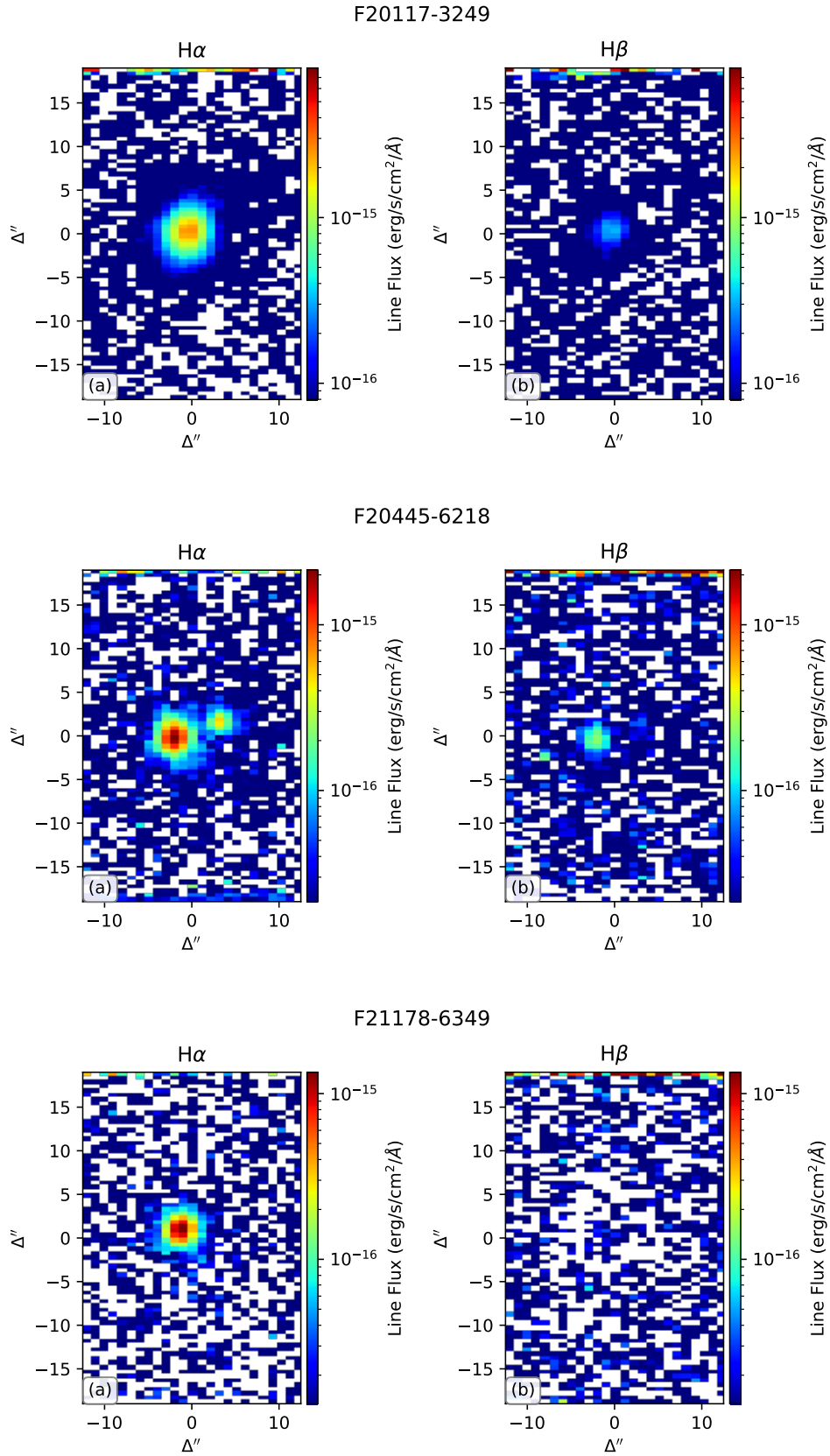
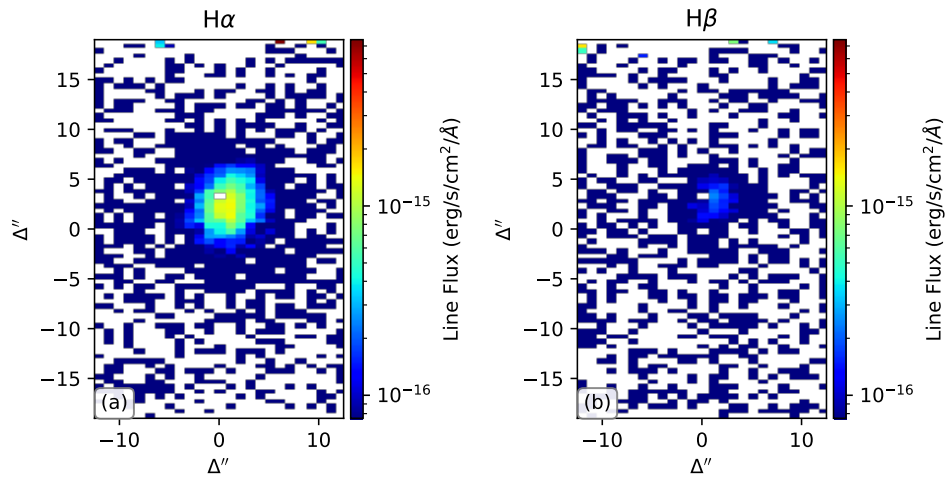
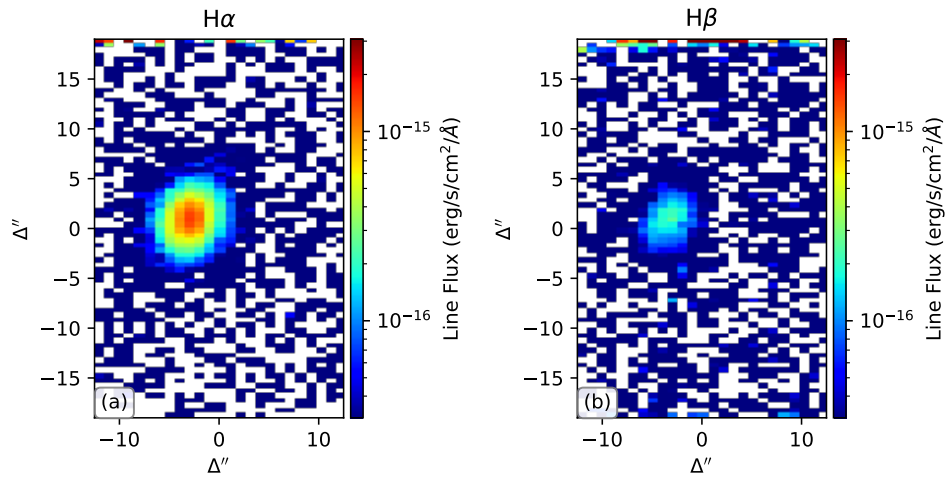


Figure B.2 (cont.): The integrated fluxes of the H $\alpha$  and H $\beta$  lines constrained by applying PPXF to each of the 1,900 individual spaxels.

F21292-4953



F21295-4634



F23389-6139

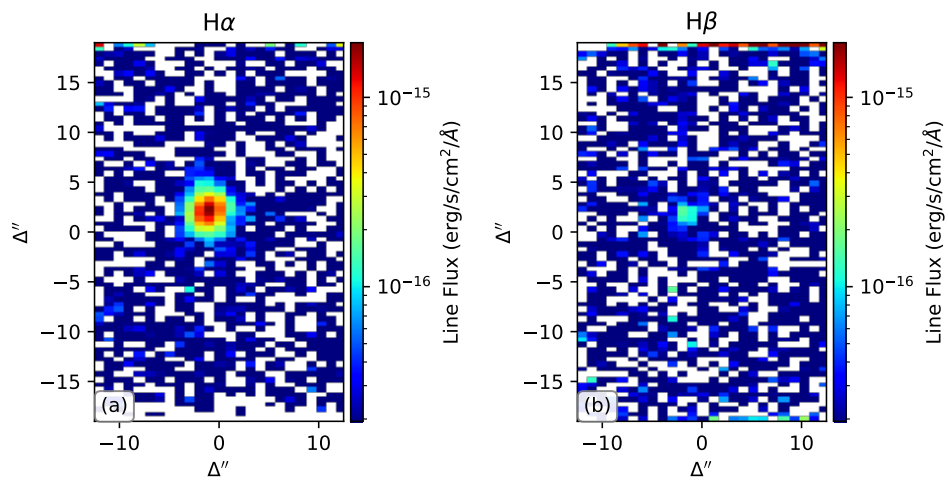


Figure B.2 (cont.): The integrated fluxes of the H $\alpha$  and H $\beta$  lines constrained by applying PPXF to each of the 1,900 individual spaxels.



### B.3 Resolved Dust Obscuration

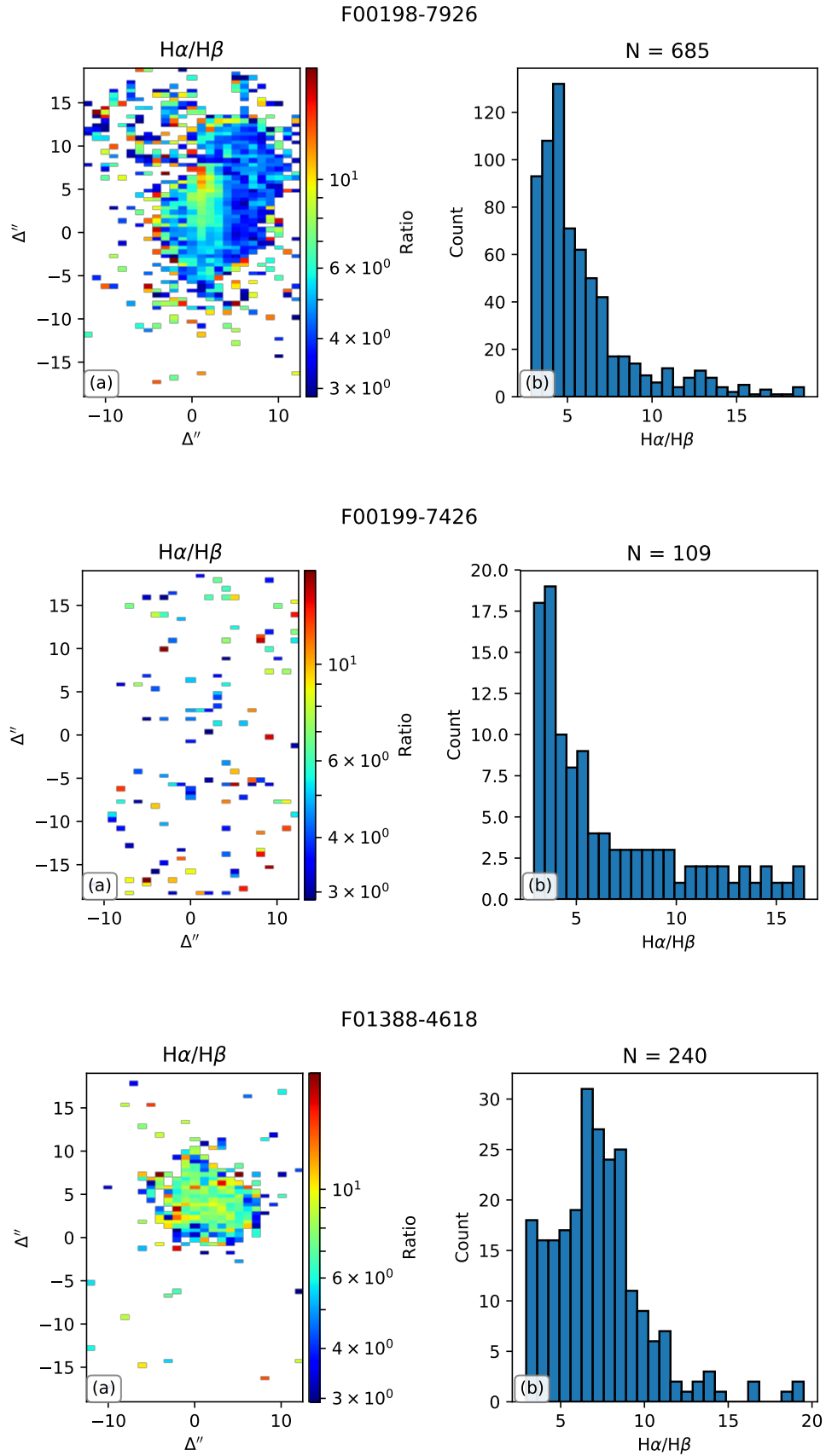


Figure B.3: (a) The  $H\alpha/H\beta$  ratios obtained by applying PPXF across each of the 1,900 individual spaxels. Pixels outside the range of 2.86 to 20 were masked out. (b) The corresponding distribution of  $H\alpha/H\beta$  ratios of valid pixels. The total number of valid pixels is included in the figure title.

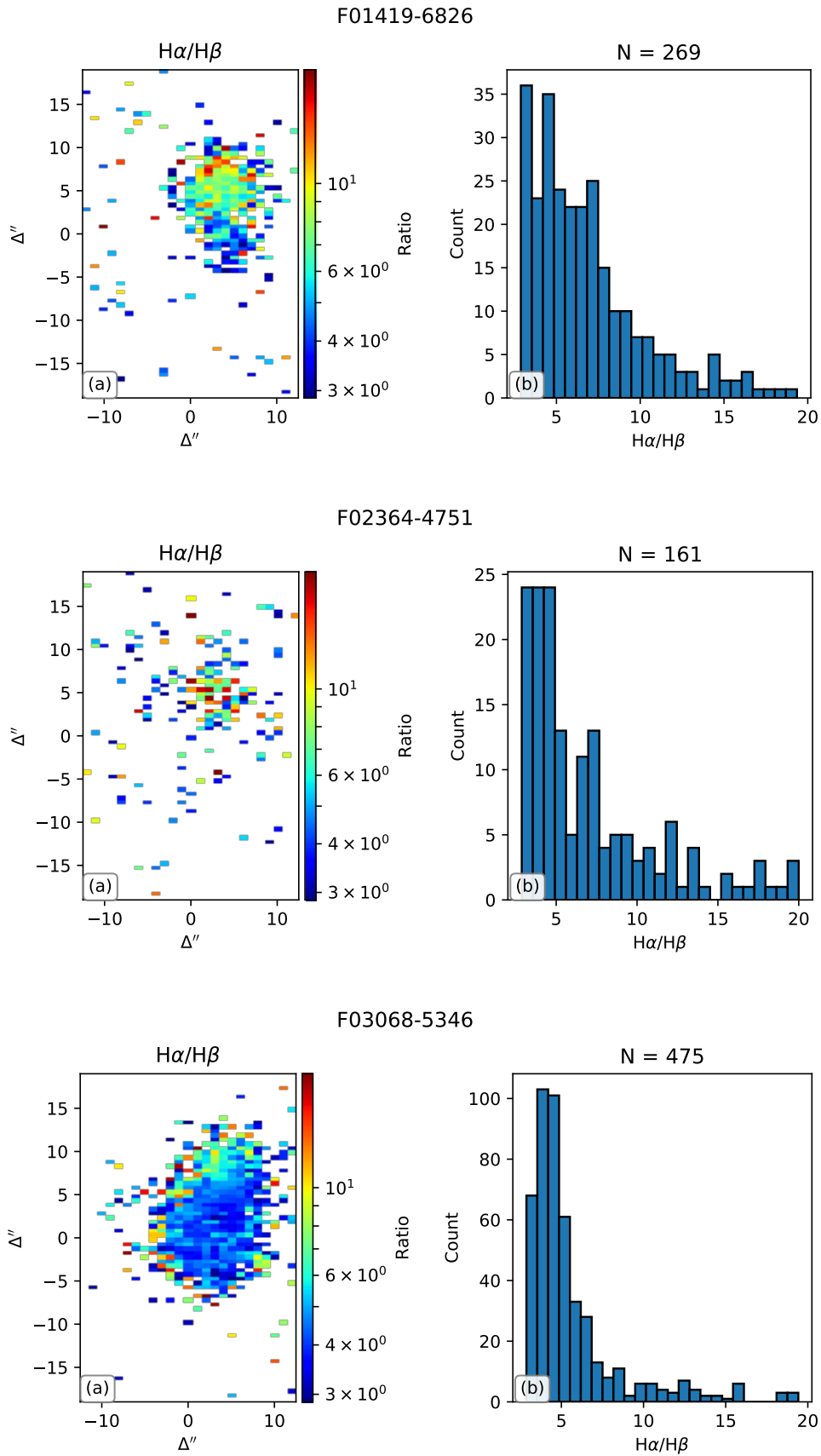


Figure B.3 (cont.): (a) The H $\alpha$ /H $\beta$  ratios obtained by applying PPXF across each of the 1,900 individual spaxels. Pixels outside the range of 2.86 to 20 were masked out. (b) The corresponding distribution of H $\alpha$ /H $\beta$  ratios of valid pixels. The total number of valid pixels is included in the figure title.

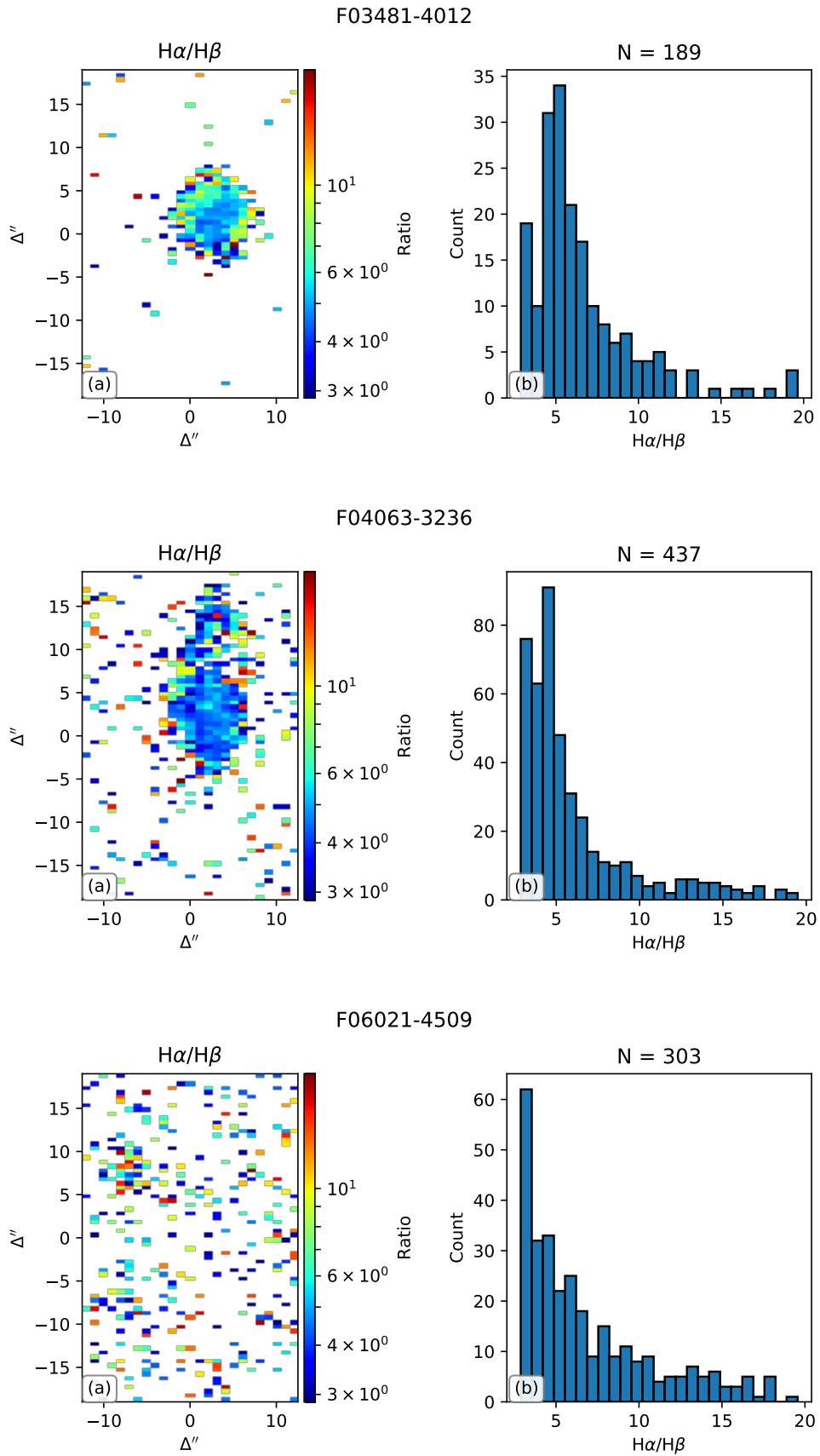


Figure B.3 (cont.): (a) The  $H\alpha/H\beta$  ratios obtained by applying PPXF across each of the 1,900 individual spaxels. Pixels outside the range of 2.86 to 20 were masked out. (b) The corresponding distribution of  $H\alpha/H\beta$  ratios of valid pixels. The total number of valid pixels is included in the figure title.

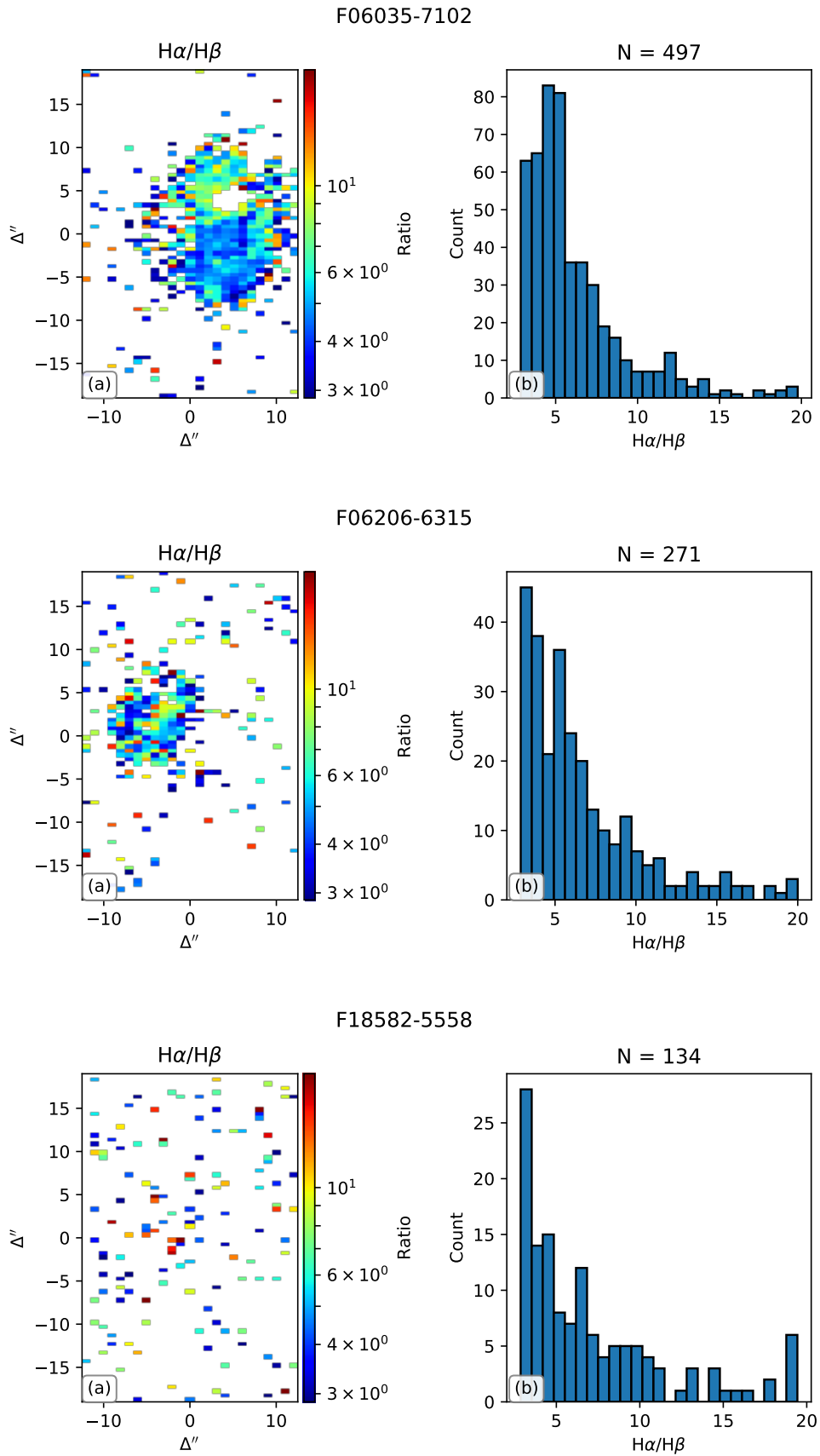


Figure B.3 (cont.): (a) The  $H\alpha/H\beta$  ratios obtained by applying PPXF across each of the 1,900 individual spaxels. Pixels outside the range of 2.86 to 20 were masked out. (b) The corresponding distribution of  $H\alpha/H\beta$  ratios of valid pixels. The total number of valid pixels is included in the figure title.

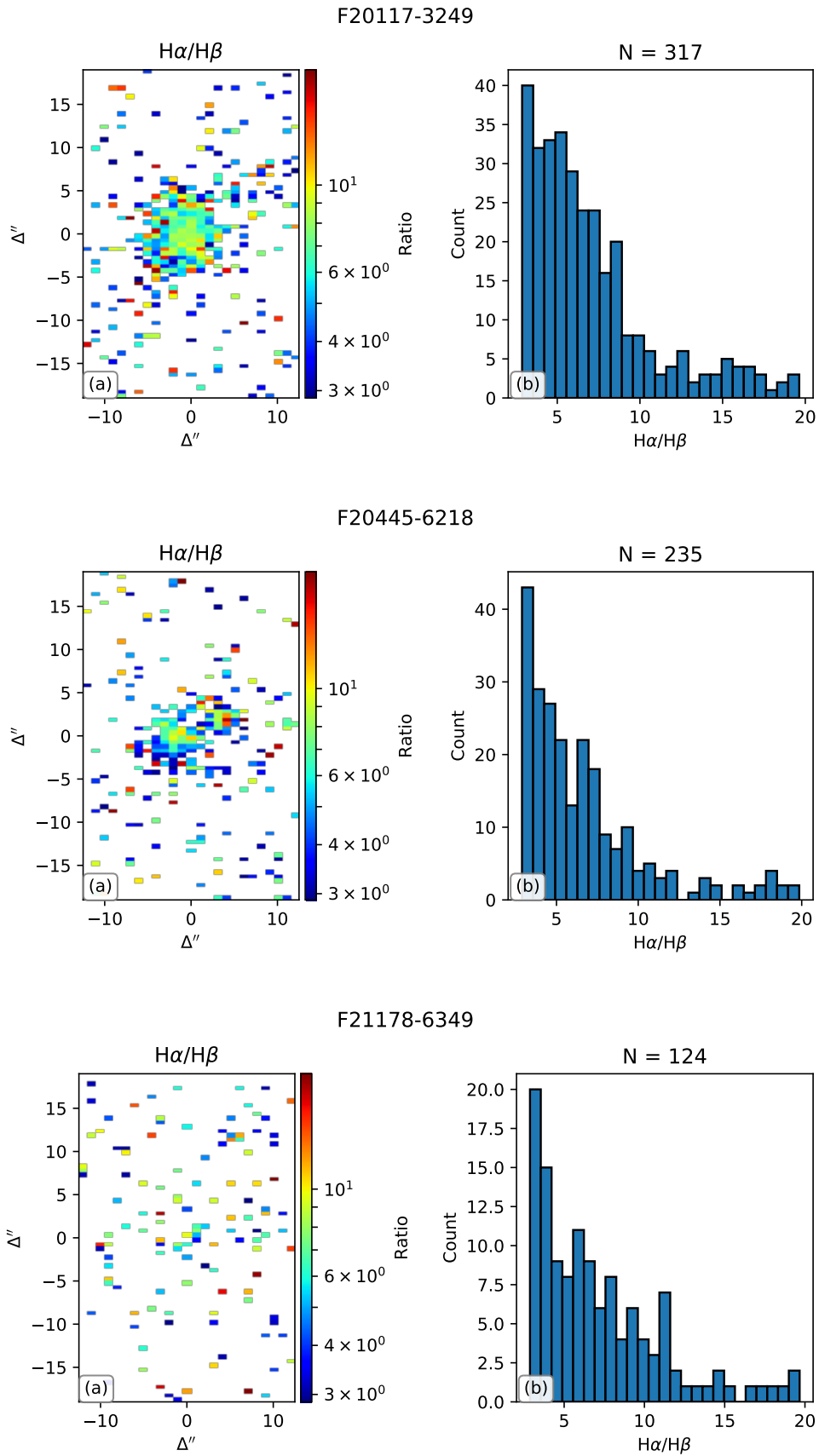


Figure B.3 (cont.): (a) The H $\alpha$ /H $\beta$  ratios obtained by applying PPXF across each of the 1,900 individual spaxels. Pixels outside the range of 2.86 to 20 were masked out. (b) The corresponding distribution of H $\alpha$ /H $\beta$  ratios of valid pixels. The total number of valid pixels is included in the figure title.

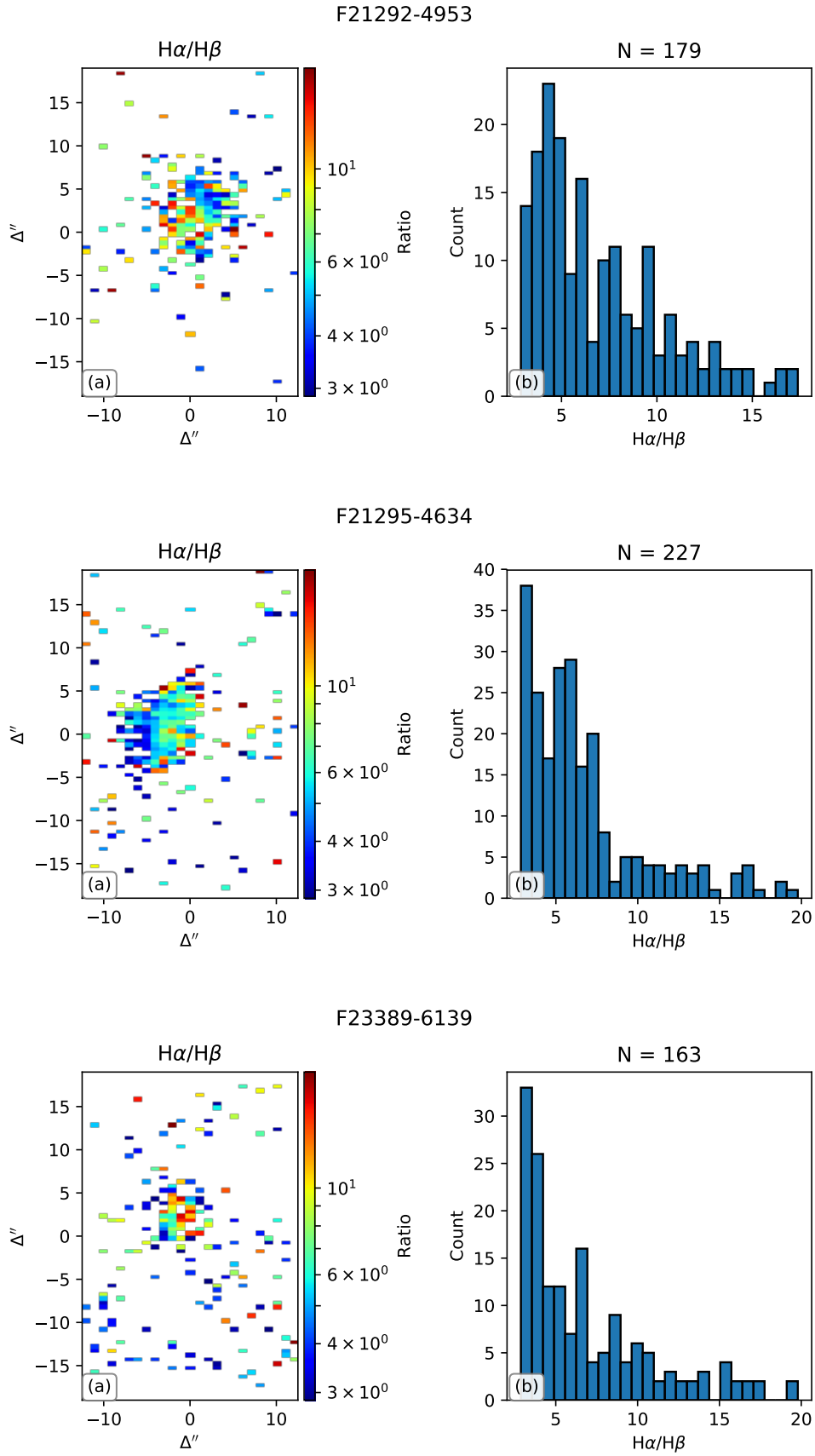


Figure B.3 (cont.): (a) The H $\alpha$ /H $\beta$  ratios obtained by applying PPXF across each of the 1,900 individual spaxels. Pixels outside the range of 2.86 to 20 were masked out. (b) The corresponding distribution of H $\alpha$ /H $\beta$  ratios of valid pixels. The total number of valid pixels is included in the figure title.

## B.4 Resolved Star Formation Rate

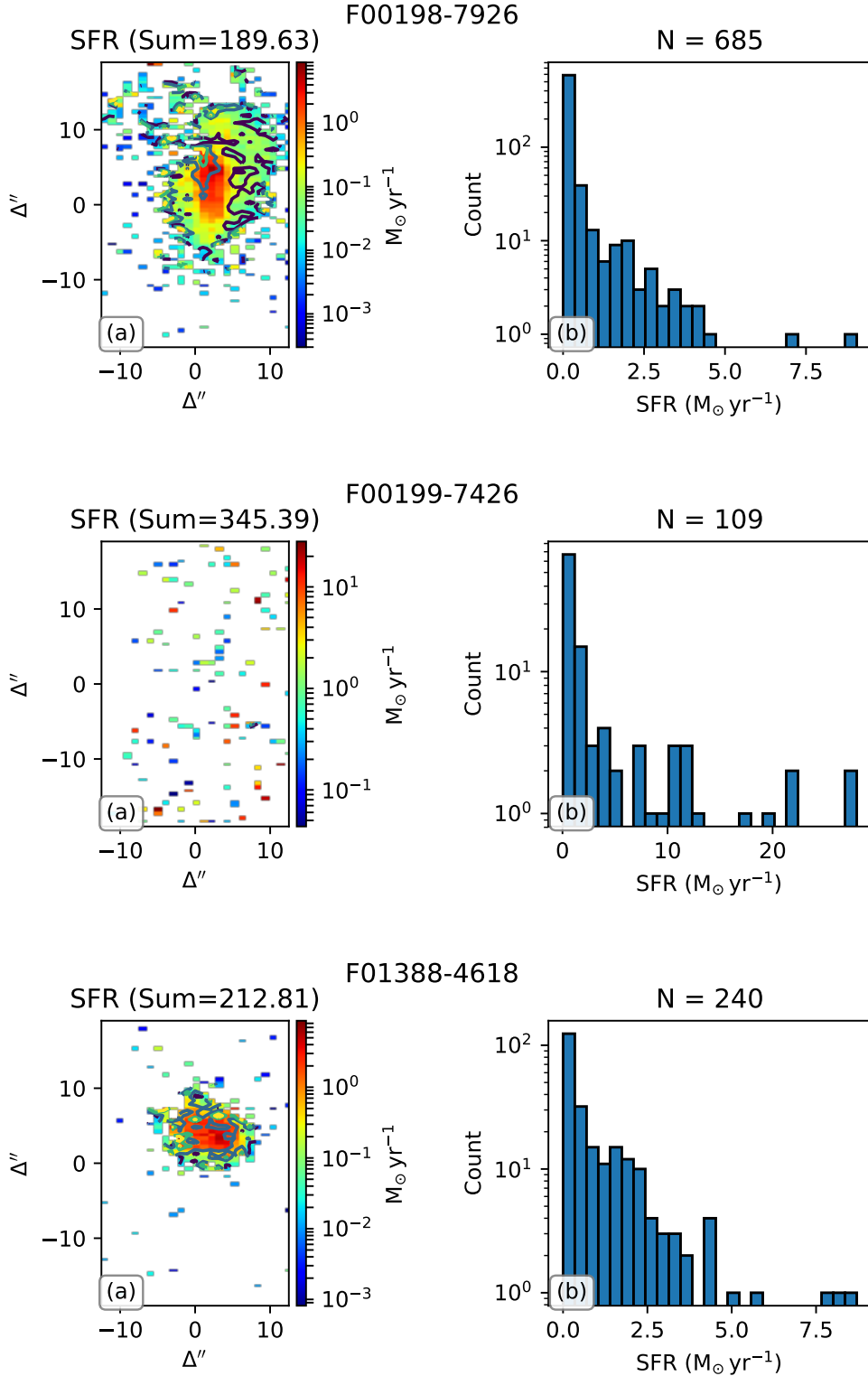


Figure B.4: (a) The SFR rate obtained using Equation 5.1 after applying a dust obscuration correction using the Balmer decrement method. Pixels whose corresponding  $H\alpha/H\beta$  ratios were outside the range of 2.86 to 20 were masked out. The total SFR of all pixels summed is included in the figure title. (b) The corresponding distribution of SFR of valid pixels. The total number of valid pixels is included in the figure title.



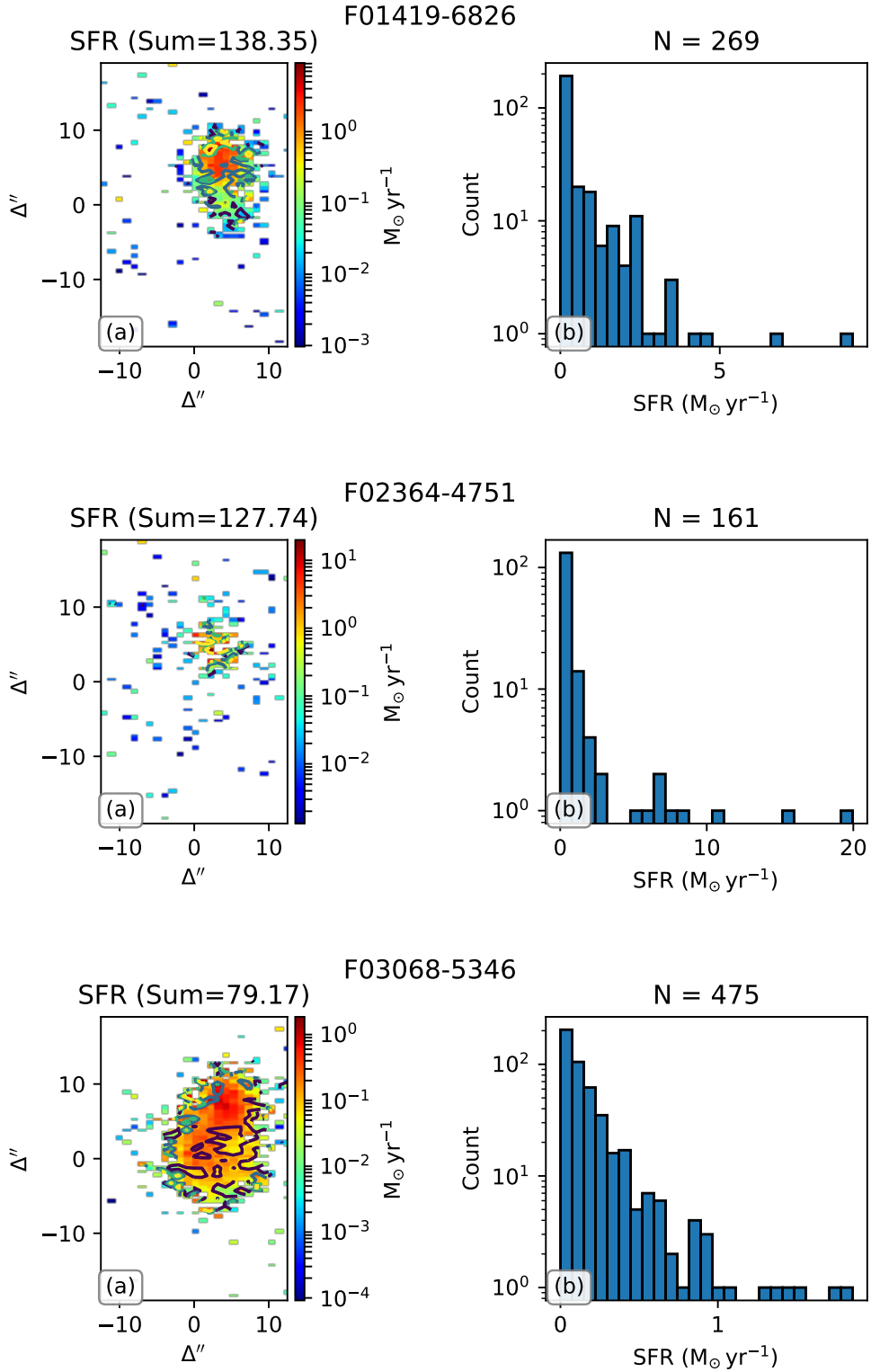


Figure B.4 (cont.): (a) The SFR rate obtained using Equation 5.1 after applying a dust obscuration correction using the Balmer decrement method. Pixels whose corresponding  $H\alpha/H\beta$  ratios were outside the range of 2.86 to 20 were masked out. The total SFR of all pixels summed is included in the figure title. (b) The corresponding distribution of SFR of valid pixels. The total number of valid pixels is included in the figure title.

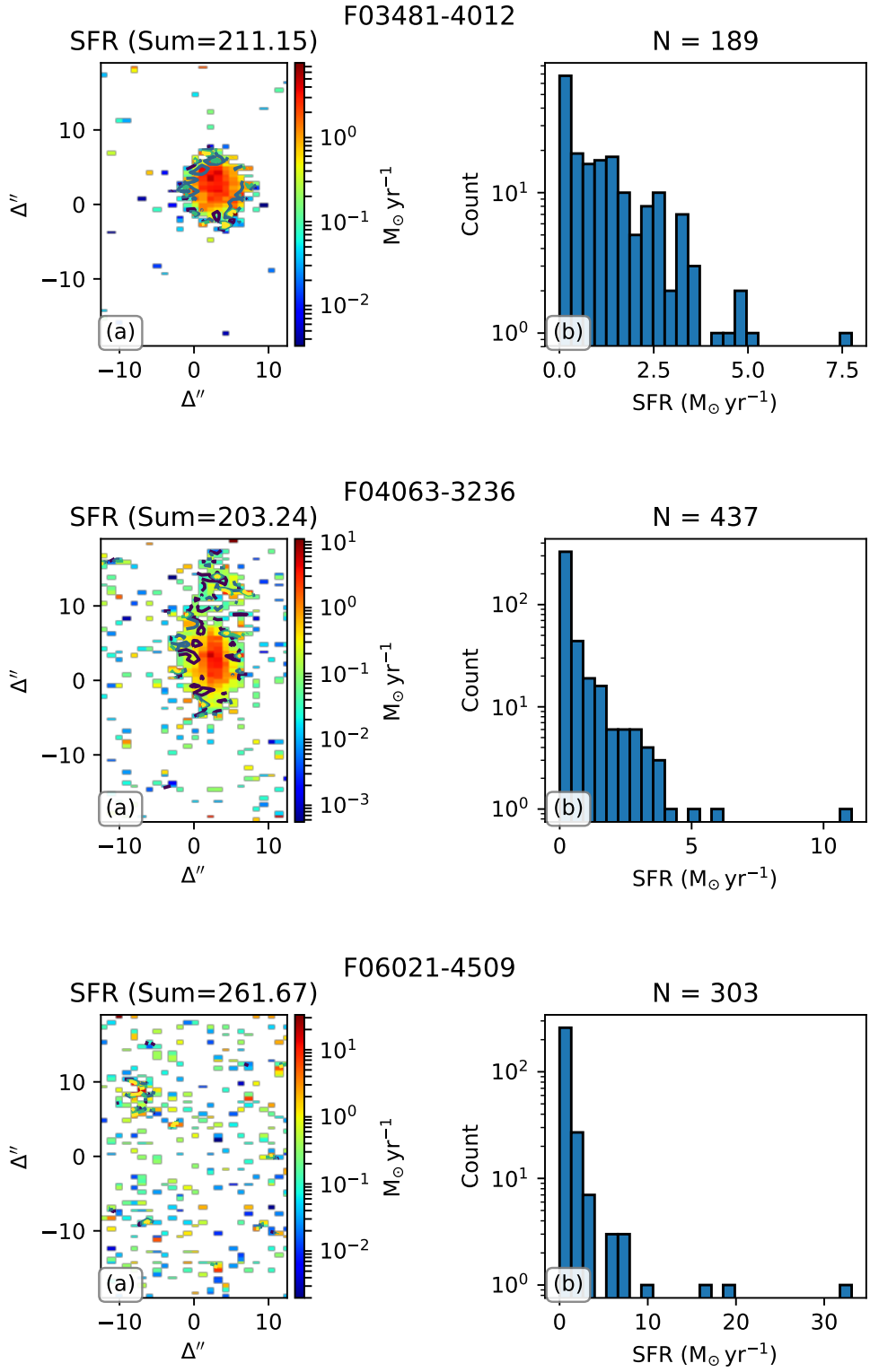


Figure B.4 (cont.): (a) The SFR rate obtained using Equation 5.1 after applying a dust obscuration correction using the Balmer decrement method. Pixels whose corresponding  $H\alpha/H\beta$  ratios were outside the range of 2.86 to 20 were masked out. The total SFR of all pixels summed is included in the figure title. (b) The corresponding distribution of SFR of valid pixels. The total number of valid pixels is included in the figure title.

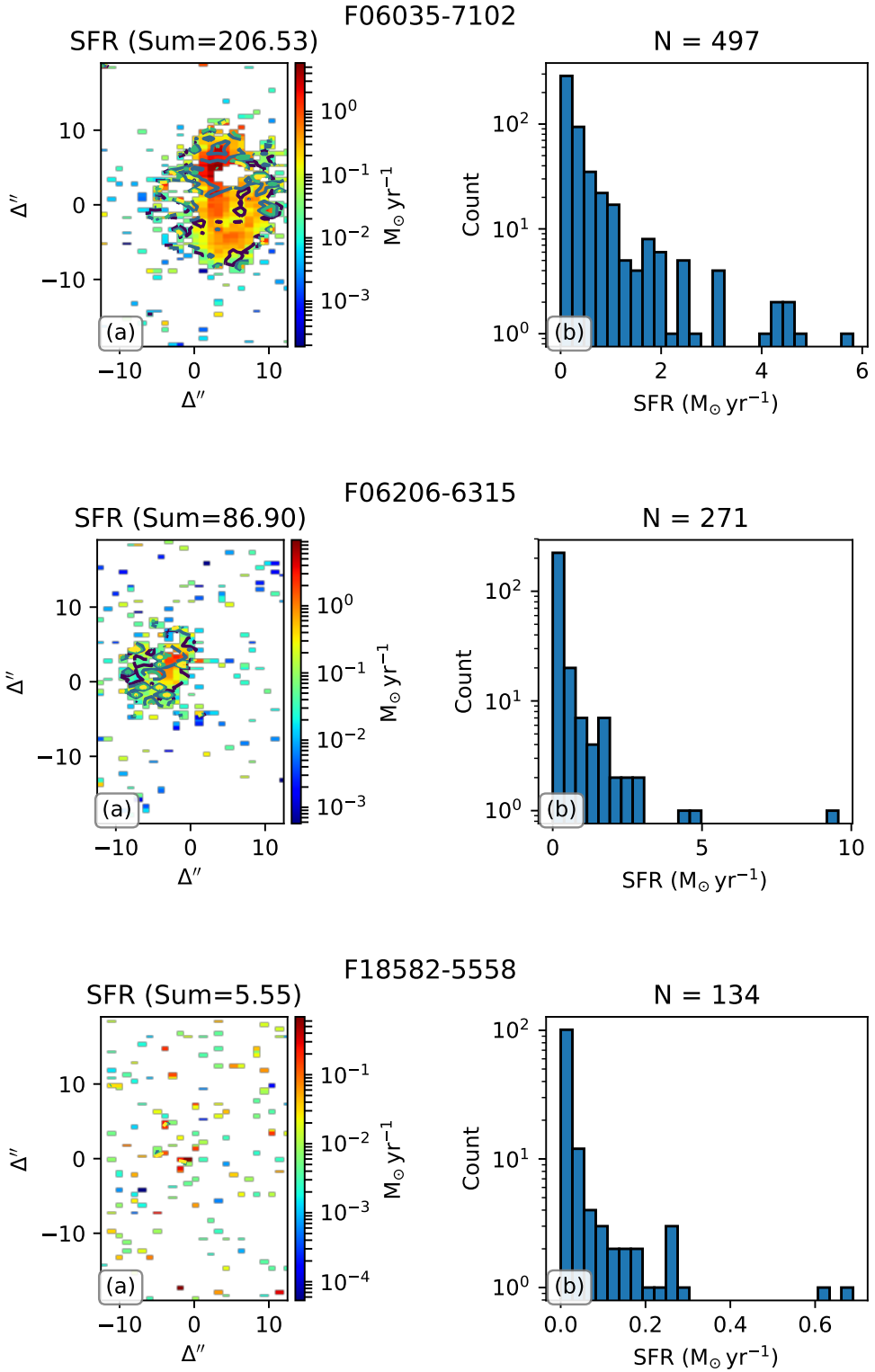


Figure B.4 (cont.): (a) The SFR rate obtained using Equation 5.1 after applying a dust obscuration correction using the Balmer decrement method. Pixels whose corresponding  $H\alpha/H\beta$  ratios were outside the range of 2.86 to 20 were masked out. The total SFR of all pixels summed is included in the figure title. (b) The corresponding distribution of SFR of valid pixels. The total number of valid pixels is included in the figure title.

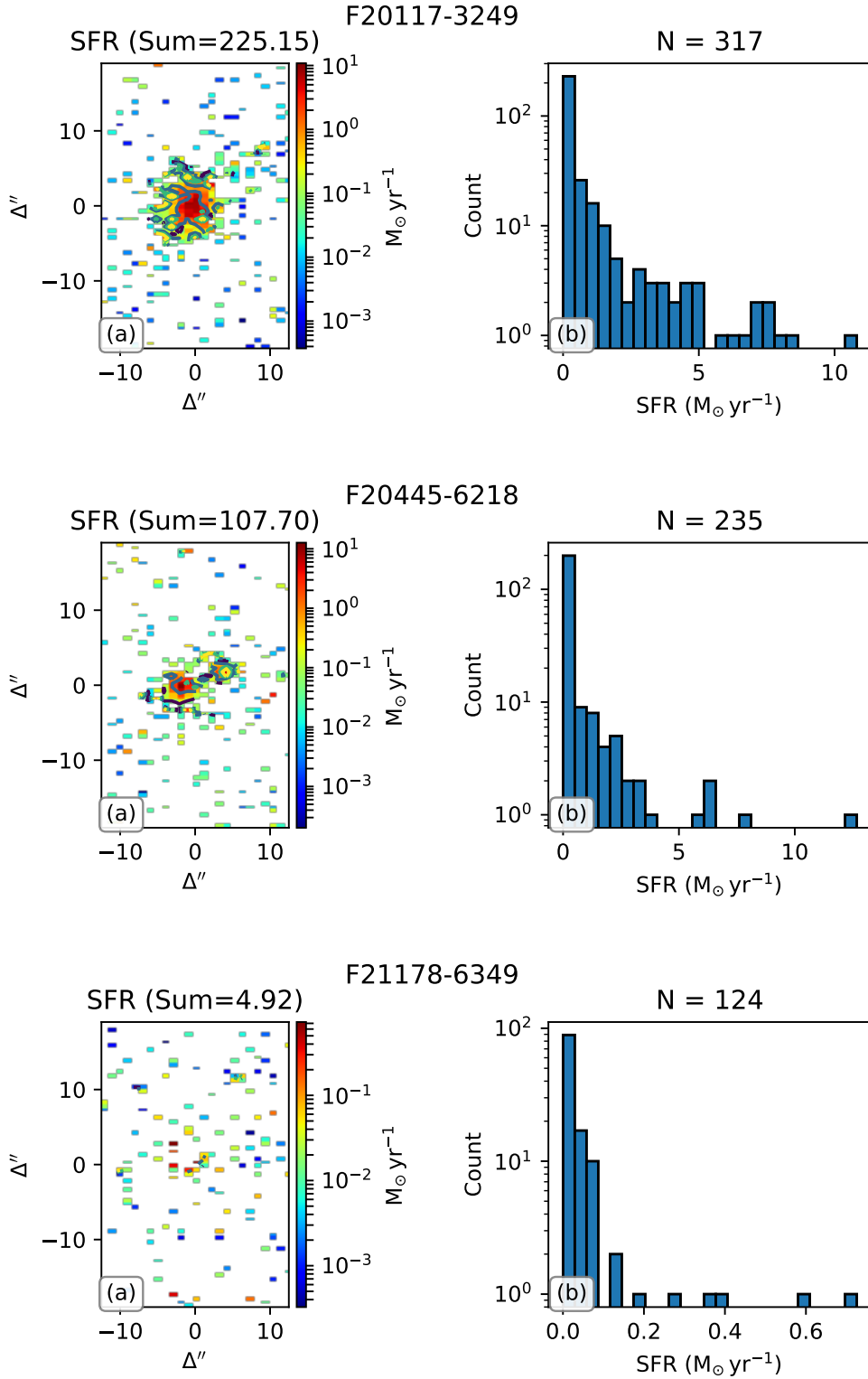


Figure B.4 (cont.): (a) The SFR rate obtained using Equation 5.1 after applying a dust obscuration correction using the Balmer decrement method. Pixels whose corresponding  $H\alpha/H\beta$  ratios were outside the range of 2.86 to 20 were masked out. The total SFR of all pixels summed is included in the figure title. (b) The corresponding distribution of SFR of valid pixels. The total number of valid pixels is included in the figure title.

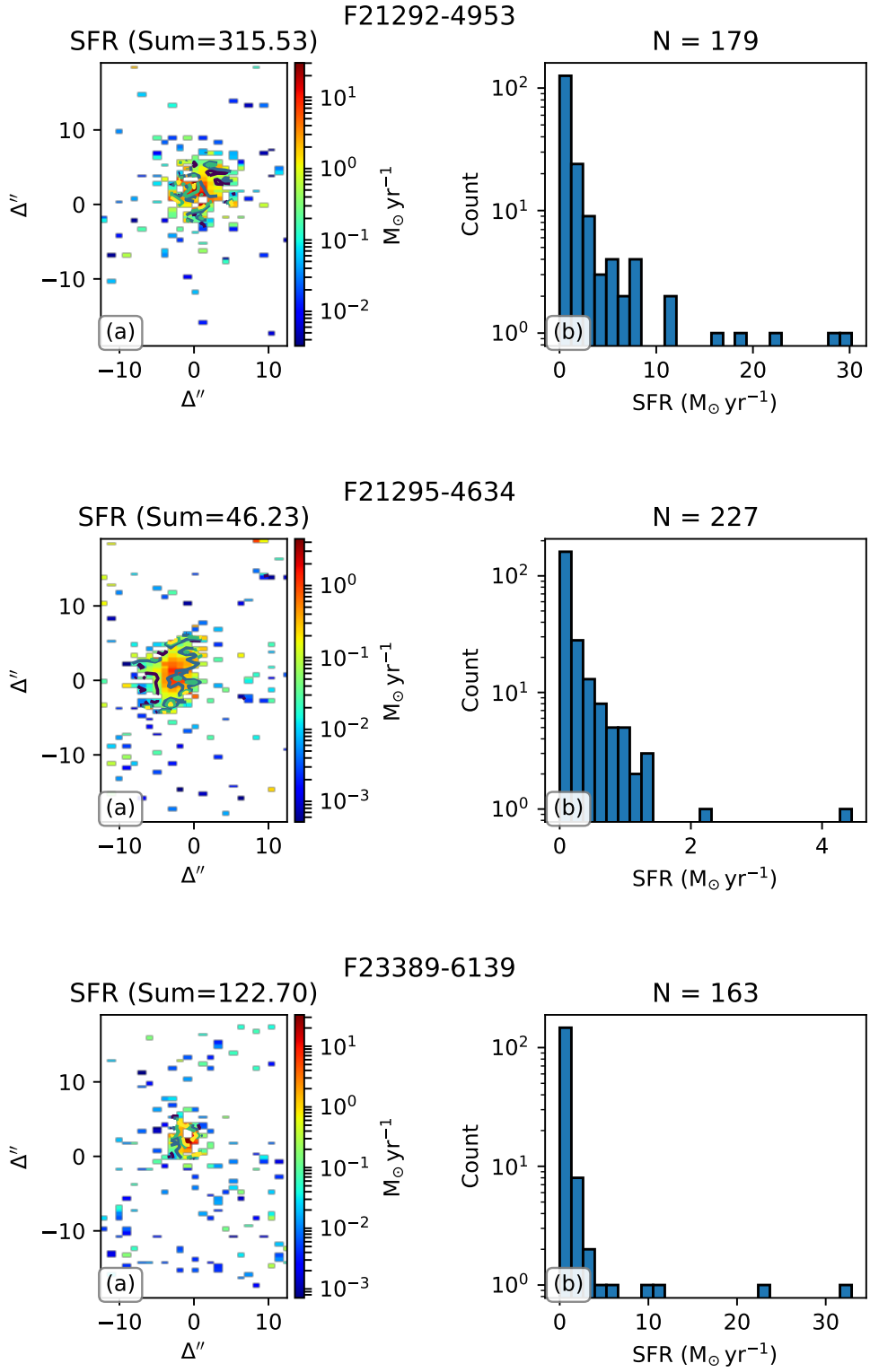


Figure B.4 (cont.): (a) The SFR rate obtained using Equation 5.1 after applying a dust obscuration correction using the Balmer decrement method. Pixels whose corresponding  $H\alpha/H\beta$  ratios were outside the range of 2.86 to 20 were masked out. The total SFR of all pixels summed is included in the figure title. (b) The corresponding distribution of SFR of valid pixels. The total number of valid pixels is included in the figure title.

## B.5 pywifes Flux Calibration Issue

After initially examining the outputs of PYWIFES and modelling the one-dimensional spectra (see subsequent sections for a description of the procedures used), I found considerable discrepancies between the  $H\alpha$  and other multi-wavelength based star formation rate indicators. Figure B.5 shows an early plot to examine the inconsistent dust corrected  $H\alpha$  star formation tracers against other multi-wavelength indicators. In this Figure, there does appear to be some degree of correlation among the top two panels; however, SFRs derived using the dust corrected  $H\alpha$  luminosities are too high by a factor of  $\sim 10$ .

For some time, the working assumption was that the adopted dust correction process itself was incorrect and that there was a type of unit or normalisation error present in the PYTHON code. This was based on the correlation shown in Figure B.5, which is based on measurements *after* the dust correction was performed.

After eliminating the dust correction itself as the root of the discrepancy, a thorough examination of the PYWIFES source code was performed. Individual tasks of the pipeline were executed directly while stepping through the codebase with numerous breakpoints and custom logging messages. This analysis revealed that the problem was caused by the extraction of the standard star spectrum with an incorrect exposure time included under the ‘EXPTIME’ FITS header field.

PYWIFES incorrectly assumed that based on the presence of a user specified flag, all exposures were performed using a NAS strategy and failed to confirm this using the metadata preserved in the FITS header of each image file. This affected where the pipeline would recalculate the ‘EXPTIME’ field based on information available from the science sources. When the spectrum of the standard star is compared with its reference spectrum, it is down-weighted by the incorrect exposure duration placed in ‘EXPTIME’ attribute.

To help other users of the PYWIFES software, an issue has been submitted onto its GITHUB project page with an initial fix. A problem summary and basic code fix may be found at <https://github.com/PyWiFeS/pipeline/pull/12>. Strictly, this submitted code segment does not fix the root cause of the problem. The correct approach for eliminating the issue would require a consistent check of the exposure type in each FITS file to determine the correct code path to adopt while processing.

A secondary issue associated with the flux calibration module of the PYWIFES pipeline was also uncovered by this dataset during processing in a scenario not included in the previous code patch. When co-adding multiple exposure of a single standard star together, the ‘EXPTIME’ field is not correctly recomputed when NAS information is also present. The simple solution in this case was to rerun the reduction pipeline while ensuring that only a single standard star

## Balmer Decrement - Integrated Flux Density

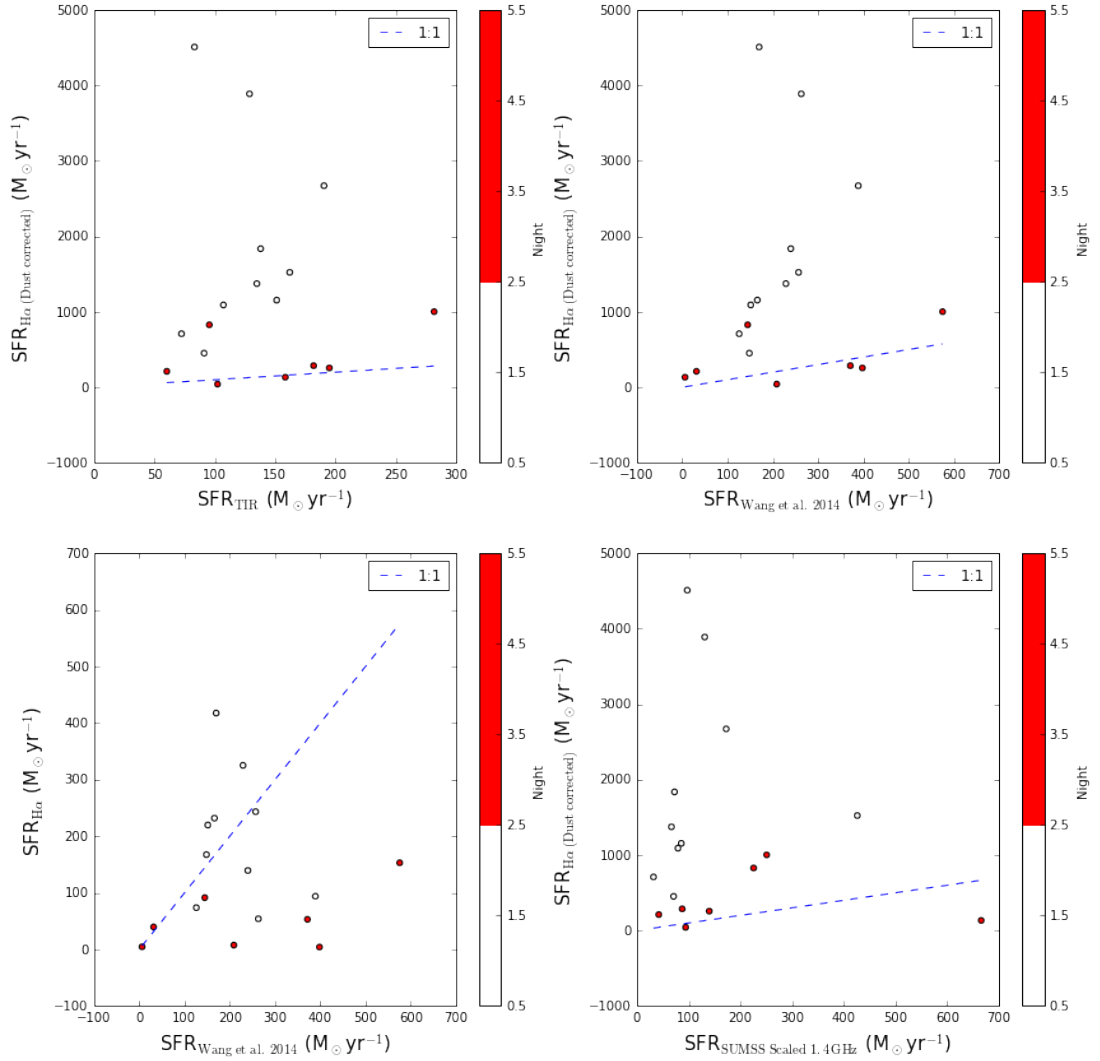


Figure B.5: An early diagnostic plot made to investigate the discrepancy between dust corrected  $H\alpha$  and other multi-wavelength star formation tracers. Subplots with the y-axis label  $SFR_{H\alpha(\text{DustCorrected})}$  show the comparisons made with the dust corrected  $H\alpha$  luminosities, corrected exclusively via the Balmer decrement method. The y-axis label  $SFR_{H\alpha}$  used the observed  $H\alpha$  uncorrected for dust attenuation. As a marker colour, I include the observing semester that data were acquired in, where nights 1 and 2 were obtained in semester one and are represented as open face circles, and nights 3, 4, and 5 were obtained in semester two and are represented as red face circles. This is a historical Figure that cannot be reproduced because I have since corrected the dataset, so I present it as is. At this point, no attempt was yet made to characterise and propagate spectra uncertainties, although a clear systematic offset can clearly be seen.

exposure was used when extracting the standard star spectrum.